Small Specimen Test Techniques Applied to

Nuclear Reactor Vessel Thermal Annealing and Plant Life Extension

Corwin/Haggag/Server, editors

STP 1204

STP 1204

Small Specimen Test Techniques Applied to Nuclear Reactor Vessel Thermal Annealing and Plant Life Extension

William R. Corwin, Fahmy M. Haggag, and William L. Server, editors

ASTM Publication Code Number (PCN)
04-012040-35

ASTM
1916 Race Street
Philadelphia, PA 19103

Library of Congress Cataloging in Publication Data

Small specimen test techniques applied to nuclear reactor vessel thermal annealing and plant life extension/William R. Corwin, Fahmy M. Haggag, and William L. Server, editors.
p. cm. — (STP ; 1204)
"Contains papers presented at the symposium of the same name held in New Orleans, Louisiana, on 29–31 Jan. 1992 . . . sponsored by ASTM Committee E-10 on Nuclear Technology and Applications"—Foreword.
"ASTM publication code number (PCN) 04-01204-35."
Includes bibliographical references and indexes.
ISBN 0-8031-1869-4
1. Nuclear pressure vessels—Testing—Congresses. 2. Annealing of metals—Congresses. 3. Nuclear power plants—Maintainability—Congresses. I. Corwin, W. R. II. Haggag, Fahmy M. III. Server, W. L. IV. ASTM Committee E-10 on Nuclear Technology and Applications. V. Series: ASTM special technical publication; 1204.
TK9211.5.S57 1993
621.48'3—dc20 93-20768
CIP

Photocopy Rights

Peer Review Policy

Each paper published in this volume was evaluated by three peer reviewers. The authors addressed all of the reviewers' comments to the satisfaction of both the technical editor(s) and the ASTM Committee on Publications.

The quality of the papers in this publication reflects not only the obvious efforts of the authors and the technical editor(s), but also the work of these peer reviewers. The ASTM Committee on Publications acknowledges with appreciation their dedication and contribution to time and effort on behalf of ASTM.

Printed in Ann Arbor, MI
October 1993

Foreword

This publication, *Small Specimen Test Techniques Applied to Nuclear Reactor Vessel Thermal Annealing and Plant Life Extension*, contains papers presented at the symposium of the same name held in New Orleans, Louisiana, on 29–31 Jan. 1992. The symposium was sponsored by ASTM Committee E-10 on Nuclear Technology and Applications. Cochairmen were William R. Corwin, Oak Ridge National Laboratory, Fahmy M. Haggag, Oak Ridge National Laboratory, and William L. Server, ATI Incorporated.

Contents

NOVEL BEND AND PUNCH TESTING TECHNIQUES

Overview

The Symposium on Small Specimen Test Techniques and Their Application to Nuclear Reactor Vessel Thermal Annealing and Plant Life Extension may have marked a turning point in expanding the overall interest in ASTM Subcommittee E10.02 activities in radiation embrittlement for commercial power reactors. The symposium, which was held in New Orleans, Louisiana, on 29–31 Jan. 1992, was organized to bring together, in a single meeting, both the diverse interests and capabilities of the scientific testing community and the needs of the commercial light-water-cooled power-reactor industry. Participants came from all over the world with speakers from twelve countries presenting 40 papers covering three wide-ranging topics: (1) unique small and miniature specimens, as well as nondestructive, nonintrusive, and in-situ test techniques for measuring mechanical and fracture properties; (2) application of those techniques to assess irradiation-induced embrittlement; (3) actual examples of the use of these techniques to verify results of thermal annealing of vessels and to evaluate potential reactor-vessel life extension. The strong interest in the topics addressed at the symposium was apparently fueled by the maturing of miniature specimen testing technology and the simultaneous recognition of the very real need for continued and extended-life operation of installed nuclear reactor capacity, which amounts to many billions of dollars.

This symposium was the third in a related series of meetings on small specimen testing technology organized by ASTM Subcommittee E10.02 on Behavior and Use of Nuclear Structural Materials. The first was the Symposium on the Use of Small-Scale Specimens for Testing Irradiated Materials, which was held in Albuquerque, New Mexico in September 1983 and resulted in the publication of *The Use of Small-Scale Specimens for Testing Irradiated Materials, ASTM STP 888*. The primary driving force behind that symposium was the need of the fusion reactor materials research community to assess effects of the very high levels of irradiation expected in the first wall of a fusion reactor. The severely limited volume of materials which can be irradiated in test reactors to high levels of embrittlement results in the need for small specimen technology. The second meeting was a Workshop on Subsize Specimen Technology, held in New Orleans, Louisiana in January 1986 and sponsored jointly by ASTM Committees E10 on Nuclear Technology and Applications, E24 on Fracture Testing, and E28 on Mechanical Testing. The thrust of the workshop was to examine the needs for testing the relatively small sizes of material available to the irradiation effects research community and to compare those needs with the size requirements stipulated by existing testing standards. In contrast with the two earlier meetings, which focused exclusively on testing techniques, the recent symposium explicitly included the needs of and applications to commercial nuclear power reactors. In addition, the program of the recent symposium was strongly augmented by presentations of the continued development of testing technology within the fusion reactor research community. The final program of the symposium benefited significantly from the incorporation of numerous presentations from the International Energy Agency's planned workshop on small specimen test techniques, following an agreement to merge their workshop with the already-planned ASTM symposium. It is expected that the collection of the papers within this resulting special technical publication, which documents the recent symposium, will provide a resource for both researchers and end users in this field.

In the area of applications, a combination of Russian and Finnish authors provided an understanding of the usefulness of small specimen test techniques for commercial-nuclear-power plant-life extension. Their work described the application of small-specimen testing and sampling techniques to evaluate the potential for continued operation of various former eastern block pressurized-water-reactor pressure vessels.

In the sessions on nondestructive and nonintrusive testing techniques, novel approaches were described for obtaining materials information on thermal aging and embrittlement by electromagnetic and electrochemical techniques with little or no damage to the piece of material being sampled. A novel automated ball indentation technique was successfully applied to measure yield strength and flow properties in a range of metallic materials including welds and heat-affected zones and was further applied to nondestructively examine a structural component in situ (a circumferential weld in a stainless steel pipe). Application of these types of techniques will be very valuable in determining the degree of recovery following thermal annealing of nuclear pressure vessels.

Numerous novel and improved methods for obtaining and applying data from small specimens was described in the various sessions on testing techniques. Improvements in both correlation methods with standard-size specimens and test techniques were described by the authors of papers dealing with impact testing of subsize Charpy V-notch type specimens. The portion of the symposium related to fracture toughness provided new insight into both the limitations and possible ways to correct and utilize measurements made using very small fracture toughness specimens. Innovative experimental approaches to obtaining fracture toughness data with small amounts of test material included techniques for using very small-sized compact tension specimens as well as those describing radically new specimen designs. Improvements and innovations in some of the punch and disk testing, which had been described at the previous symposium on small-scale specimen testing in Albuquerque, were reported. New approaches for automating the remote testing and evaluating the preparation of irradiated tension specimens were described as well as new means of obtaining their required elongation information by techniques as sophisticated as laser interferometry.

As a result of the keen interest in and obvious applications for the small-specimen, nondestructive, nonintrusive, and in-situ testing techniques described at the meeting, it was agreed to initiate a follow-on activity with the explicit purpose of evaluating the type of materials property data generated by these various methods. ASTM Subcommittee E10.02 plans to coordinate such activities, which will include the distribution of one or more common sets of material for examination by interested parties. The eventual goal is to compare results from numerous nonstandard techniques with results from standardized tests and with each other. While this activity might eventually involve comparisons of material before and after irradiation, it is anticipated that the variations in materials properties, such as would result from irradiation-induced embrittlement, would initially be simulated (possibly by thermal treatments or cold work) to minimize handling of activated materials and to facilitate a much wider degree of participation in comparison testing.

Once the level of overall accuracy and the degree of reproducibility of data generated by the techniques described in this volume can be more fully evaluated among themselves and against other standardized tests, it will be possible to better ascertain and potentially improve the confidence of application of that data for integrity evaluations of reactor pressure vessels or any other structures. In the meantime, these testing techniques continue to provide a means of obtaining materials property information for situations where extraction of samples from vessels of other structural components is not desirable or possible and when the amount of available material is too limited to utilize conventional, standardized techniques.

William R. Corwin
Oak Ridge National Laboratory, Oak Ridge, TN; symposium co-chairman and editor

Fahmy M. Haggag
Oak Ridge National Laboratory, Oak Ridge, TN; symposium co-chairman and editor

William L. Server
ATI Incorporated, San Ramos, CA; symposium co-chairman and editor

Nondestructive and Nonintrusive Testing Techniques

James F. Stubbins,[1] *Wei-Ja Shong,*[1] *Michael Giacobbe,*[1]
Abderrafi M. Ougouag,[1] *and John G. Williams*[2]

Pressure Vessel Steel Embrittlement Monitoring by Magnetic Properties Measurements

REFERENCE: Stubbins, J. F., Shong, W.-J., Giacobbe, M., Ougouag, A. M., and Williams, J. G., **"Pressure Vessel Steel Embrittlement Monitoring by Magnetic Properties Measurements,"** *Small Specimen Test Techniques Applied to Nuclear Reactor Vessel Thermal Annealing and Plant Life Extension, ASTM STP 1204,* W. R. Corwin, F. M. Haggag, and W. L. Server, Eds., American Society for Testing and Materials, Philadelphia, 1993, pp. 5–15.

ABSTRACT: The magnetic properties of specimens of one heat of A533B nuclear pressure vessel grade steel have been examined in the as-received condition and after neutron irradiation to various fluence levels up to 4×10^{18} cm^{-2} ($E > 0.1$ MeV) in the University of Illinois advanced TRIGA reactor core at two temperatures, approximately 120 and 260°C. The effect of certain heat treatments was also investigated. The magnetic properties were measured by an automated hysteresis curve-tracing method using a miniature transformer which incorporated the specimens in its core. Changes in magnetic hysteresis energy loss were correlated with neutron fluence in the case of certain irradiated specimens and with microhardness measurements in the case of heat-treated specimens. At the higher irradiation temperatures, no significant changes in either the magnetic hysteresis properties or the microhardness were noted for the present fluences. The relationship between the observed magnetic properties response and irradiation-induced embrittlement is discussed.

KEYWORDS: magnetic properties, hysteresis loss, coercivity, remanence, radiation effects, nuclear pressure vessel steels

The potential for the use of magnetic properties as an indication of the degree of accumulated radiation-induced damage in ferromagnetic materials is virtually unexplored. While past irradiation damage studies [*1,2*] have established that some features of the magnetic hysteresis response of ferromagnetic materials are effected by irradiation, they did not attempt to correlate the observed magnetic properties changes with other materials mechanical properties changes. The understanding of irradiation-induced properties changes has progressed markedly since those studies, and a much better understanding of the microstructural response of materials to irradiation now exists. Furthermore, the earlier magnetic properties work centered on a few select materials, none of which are directly relevant to structural applications. In the present work, nuclear pressure vessel steels are studied to determine the effects of irradiation on both mechanical and magnetic properties. Radiation-induced magnetic properties changes in this class of materials have received scant attention [*3–5*], though there is potential for the use of magnetic properties as an indication of bulk properties changes which would also influence mechanical performance.

[1] Department of Nuclear Engineering, University of Illinois, 103 S. Goodwin Ave., Urbana, IL 61801.
[2] Department of Nuclear Engineering, University of Arizona, Tuscon, AZ 85721.

Steels, including those grades employed for nuclear pressure vessels and support systems, are ferromagnetic. In fact, this ferromagnetism extends to temperature well in excess of those where they are employed for nuclear applications; the Curie temperature of Fe is 770°C. This may provide a means for recording and analyzing materials properties changes over a range of temperatures of interest to operating nuclear reactors. Furthermore, magnetic properties measurement techniques are relatively simple and amenable to automation, even in adverse environments; thus real-time monitoring may be possible.

The aim of the present work was to correlate changes in magnetic properties of nuclear pressure vessel steels with the onset and evolution of irradiation-induced embrittlement of those materials. As far as the authors are aware, there is no precedent for the application of magnetic properties such as remanence, coercivity, saturation magnetization, or hysteresis loss for the monitoring of damage dosimetry and pressure vessel embrittlement. The basis for a correlation between magnetic and mechanical properties stems from the fact that the principal feature controlling magnetic hysteresis response is the pinning of magnetic domain walls. The microstructural features capable of pinning these walls are the same as those which influence the flow of dislocations. Thus, the level of materials hardening should correlate directly with the energy to move magnetic domain walls and align magnetic domains.

While scant theory exists regarding the precise effects of fine microstructural features on magnetic hysteresis response, a few recent studies on hard magnetic materials show that magnetic remanence, at least, was dramatically affected by very low doses of neutrons. Cost and Brown [*6–8*] found that Fe-Nd-B and Co-Sm permanent magnets lost their field strength when subjected to (epithermal) neutron irradiation. The changes were very sensitive to dose, so sensitive that large changes in magnetic remanence were found after only 10^{15} or 10^{16} n/cm^2 ($E > 0.1$ MeV). No similar data are available for the response of magnetic properties of low alloy steels to irradiation.

Experimental

Definitions

The magnetic hysteresis is a familiar property of ferromagnetic materials. Several features of the hysteresis response are a possible means of judging the degree of domain wall pinning and the level of domain alignment under an applied magnetic field. In particular, the magnetic remanence, coercivity, saturation magnetization, and the hysteresis loss are readily quantifiable with standard magnetic properties measurement techniques. These are defined as follows (see Fig. 1). Saturation magnetization, M_s, is the upper limit to the magnetization of the material that can be achieved by an externally applied field, H. The magnetic remanence, B_r, is the level of magnetism remaining in the specimen after the applied field, H, is removed, that is, set to zero. The coercivity, H_c, is the further field which must be applied to remove the magnetic remanence, that is, set back to zero. The hysteresis loss is the area of the hysteresis curve. It should be noted that it is often difficult to reach full magnetic saturation; values of B are found to increase with the increase of H even after the tips of the hysteresis loop are closed [*9*]. In the present work, only small changes in the hysteresis response were found by increasing the applied field beyond the point where the hysteresis loop closes at the tips even though the value of B continued to rise with H. Alternate definitions of effective or technical magnetic saturation have been proposed based on the width of the loop at $B = 0$, that is, the coercivity [*10*] or by an extrapolation of the closed part of the loop back to the $H = 0$ axis [*9*].

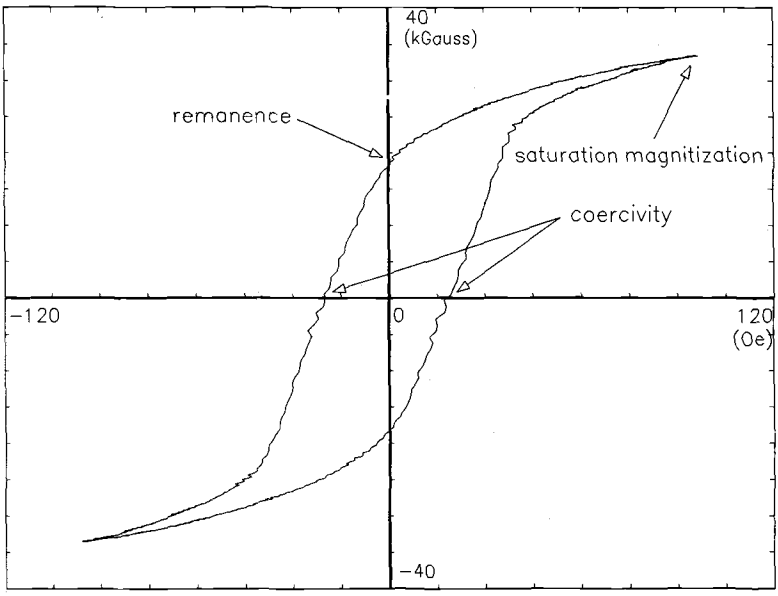

FIG. 1—*Typical hysteresis loop of A533B pressure vessel steel. The positions of the remanence, coercivity, and effective magnetic saturation are indicated. The hysteresis loss is the area of the curve.*

Magnetic Properties Measurement Technique

A major point in the development of present measurement techniques is that magnetic properties are bulk properties and are amenable to measurement in very small volumes of materials. In fact, the development of eddy currents during such measurement can be a major disadvantage to the use of large sample volumes. Small specimen sizes have additional advantages in that only small volumes of material are activated during irradiation and that self-shielding effects are minimized during irradiation. Low specimen activity allows magnetic property measurements to be performed after only short "cooling" periods, and also aids other handling processes.

While several specimen configurations are possible, the present technique employed specimens in the shape of cylindrical pins with a diameter of 1.51 mm and a length of 12.8 mm. The specimen and yoke configuration for measurements is depicted in Fig. 2, where the

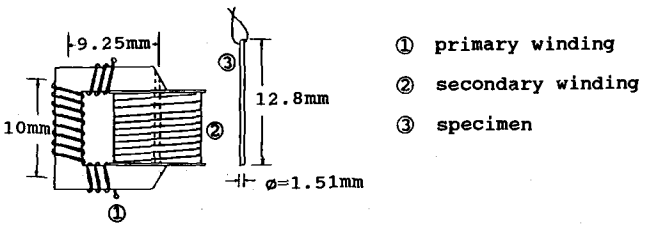

FIG. 2—*Magnetic properties measurement specimen, yoke, and sensing reel arrangement. For magnetic properties measurement, the specimen is inserted into the yoke/reel apparatus on the right-hand side.*

primary windings on the yoke and the secondary winding coil for properties measurement are also shown. The primary windings around the yoke, 40 turns, were to sustain the heavy current necessary to generate strong magnetic flux. The secondary loop coil, a plastic reel with 800 turns of fine copper wire, was designed to induce a large, more accurately measurable voltage from its interaction with the magnetic field generated in the specimen. Specimens were inserted through the yoke and reel arrangement for measurements. This specimen and yoke arrangement was linked between a primary driver circuit where the magnetic field was applied to the yoke and a secondary monitoring circuit where the hysteresis response of the specimen was measured.

The circuit for magnetic properties measurement is depicted in Fig. 3. The primary side current was provided by a programmable power supply operated in a current control mode. The current source amplified a 60-Hz sinusoidal input signal from a signal generator. The maximum current intensity was set sufficiently high to extend the hysteresis loop beyond

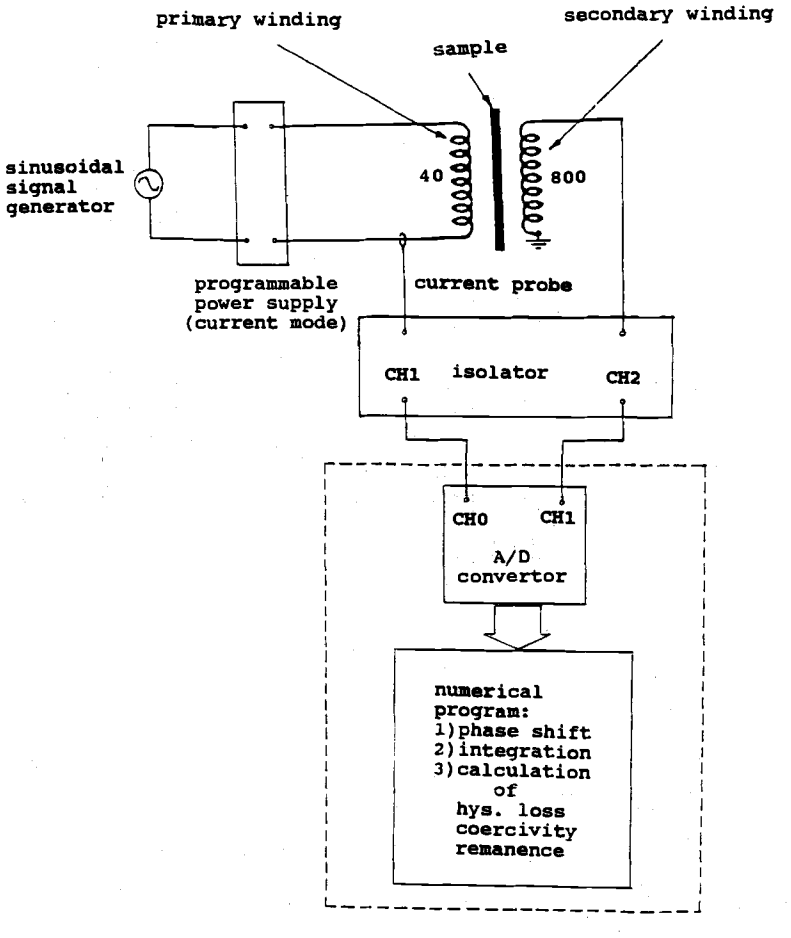

FIG. 3—*The primary circuit and the secondary or integrating circuit for making magnetic property measurements.*

the point of closure at the tips. It was found that, while true magnetic saturation was not reached, the values of magnetic properties of interest were influenced to only a minor extent by increasing the applied field toward full saturation once the loop closes. The maximum and minimum values of the H field which meet the above criterion were then used for all subsequent measurements. The primary current was monitored using a current probe which was not directly connected to the circuit. This avoided any direct heating effect which might induce inaccuracy in measuring under high current conditions. The signal sensed by the current probe was out of phase with the primary current; however, the phase shift was constant and was adjusted numerically in the data acquisition and processing stage.

During measurement, it was necessary to apply the high current intensity for only a few seconds to allow the diagnosis of required signals on both primary and secondary sides of the circuit. Prior to and following measurement, the current source was disconnected to decrease potential heating of the yoke and specimen. Further cooling was applied by a cooling fan directed across the yoke-specimen assembly. Measurements of the operating temperature of the yoke reveal that heating was minimal; temperature rises of 2 to 3°C above ambient were typical.

The secondary circuit is a simple system which monitors the potential (voltage) across the pick-up coil windings. The variation in voltage is a direct measure of the magnetic response of the specimen. The integration of the current produced in the pin, a necessary step for the determination of the hysteresis response, was performed by the data acquisition and analysis system. Repeated tests on a standard specimen showed acceptable standard deviations of all measured parameters and established the reliability and applicability of this numerical integration method. Variations in measurements were less than 2.5% in all cases.

In a previous description of magnetic properties monitoring techniques [5], a secondary integration circuit was employed to monitor magnetic hysteresis response. This circuit was found to have the useful feature that the hysteresis response could be monitored directly from the charging and discharging of the capacitor in the circuit. However, the components, principally the capacitor, on the secondary side were found to provide possible inaccuracies in the desired measurements. While the results were amenable to correction, a simpler means of avoiding such difficulties was available, that is, the elimination of the secondary side circuit. The change to measure only the voltage variation across the specimen coil also eliminated any possibility of mutual inductance in the secondary circuit, which could also have complicated the measurements.

Material and Irradiation

Specimens for magnetic properties measurements were cut from a plate of A533B nuclear pressure vessel steel. The composition of the plate and its heat treatment history are given in Table 1. These steel specimens were fabricated in the shape of cylindrical pins with

TABLE 1—*Chemical composition (wt. %) of A533B Cl. I plate.*[a]

C	Mn	P	S	Si	Mo	Ni	Cu	Cr
0.19	1.32	0.013	0.013	0.22	0.54	<0.05	0.12	<0.05

[a] Plate donated by Combustion Engineering; the plate had received a post-weld heat treatment cycle to simulate typical nuclear pressure vessel fabrication practices.

diameter 1.51 mm and length 12.8 mm and blocks with dimensions of 2 by 2 by 6 mm. The cylindrical specimens were designed to be inserted in the slot of a miniature yoke, Fig. 2, to take magnetic properties determinations, while blocks were used to measure the microhardness of the material.

Specimen were irradiated for varying numbers of cycles at full power (1.5 MW) in the University of Illinois advanced TRIGA reactor. Irradiation periods were typically 8 h, and several irradiation periods were required to reach the desired fluences. The maximum total accumulated fluence was 4×10^{18} n/cm^2 ($E > 0.1$ MeV). Prior to irradiation, samples were vacuum encapsulated. Samples were placed both in the central core region and in a cadmium-lined location at the periphery of the core to obtain two flux and fluence levels. Nickel wires were employed to determine neutron fluences.

Besides the dose rate difference, the irradiation temperature was higher in the core central position than in the peripheral position. Thermal paint was applied to separate block specimens to estimate the irradiation temperature. From color changes of the paint, the temperature at the central core location was determined to fall between 250 and 280°C. Temperature in the core peripheral region was approximately 120°C.

In addition to the irradiations, specimens were heat treated either to intentionally alter the steel microstructure or to establish whether the thermal cycles associated with the irradiations at 250 to 280°C had any influence on the materials hardness or magnetic properties in the absence of radiation. The former heat treatments were described previously [5] and are listed as HT1 through HT4 in Table 2. The latter heat treatments were carried out on six batches of specimens, aged at 260°C for a number of 8-h aging cycles. Magnetic parameters and hardness values were determined following each of the cycles. The specimen with the most cycles at 260°C is listed as HT5 in Table 2. A complete listing of the irradiation and heat treatment parameters are provided in Table 2.

Results and Discussion

Results of the magnetic properties measurements are shown in Fig. 4 for two pins irradiated in the core peripheral region to doses of 5.22×10^{17} and 6.34×10^{17} n/cm^2 ($E > 0.1$ MeV) where the irradiation temperature was on the order of 120°C. A loop from the as-received condition is also shown for comparison. The loops showed a notable increase in the effective magnetic saturation point; however, similar values for the remanence, B_r (value of B at $H = 0$), and the coercivity, H_c (value of H at $B = 0$), were nearly identical within experimental error. The hysteresis losses, noted in Table 2, increased with the dose for the irradiated specimens.

For specimens irradiated at higher temperatures, smaller changes in magnetic response following irradiation were observed. Figure 5 shows the hysteresis loops for two of ten specimens irradiated to doses up to 4×10^{18} n/cm^2 ($E > 0.1$ MeV). Both specimens again exhibited higher saturation magnetization than the as-received pin, though in these cases the differences were very small. Similar values of coercivities and remanences were found again regardless of specimen exposure. Furthermore, while the two irradiated conditions were very different neutron doses, the hysteresis loops nearly overlapped, suggesting that effects other than radiation damage had influenced magnetic properties. This is consistent with no notable changes in hardness measured at those conditions.

To separate temperature and irradiation effects, specimens were heated and cooled to simulate the thermal cycles which the pins irradiated at 260°C experienced. The results of two specimens from the set which received the heat treatments only are depicted in Fig. 6. The changes in the hysteresis response due to heat treatment are similar to those found

TABLE 2—*Properties of irradiated and heat treated A533B steel specimens.**

Condition	Fluence (10E18 n/cm²)	Hysteresis Loss, 10E6 erg/cm³			Coercivity, Oe			Remanence, kG			DPH†
		Pre	Post	Ratio	Pre	Post	Ratio	Pre	Post	Ratio	
Control		1.81	1.81	1.00	17.47	17.47	1.00	17.35	17.35	1.00	291
Irradiation Temperature, 260°C											
	0.65	1.70	1.80	1.06	16.51	17.46	1.06	16.56	17.24	1.07	...
	0.65	1.79	1.83	1.02	17.22	17.95	1.04	17.74	17.40	0.98	...
	1.32	1.82	1.82	1.00	17.73	17.42	0.98	17.80	17.40	0.98	334
	1.32	1.64	1.70	1.03	16.49	17.32	1.05	16.69	16.94	1.01	341
	2.28	1.72	1.88	1.09	16.12	17.54	1.09	15.93	17.47	1.10	328
	2.28	1.80	1.82	1.01	17.17	18.01	1.05	18.10	17.62	0.97	319
	2.98	1.82	1.83	1.01	17.56	17.63	1.00	18.24	17.56	0.96	258
	2.98	1.62	1.68	1.03	16.57	16.96	1.02	16.54	16.96	1.02	276
	3.64	1.84	1.82	0.99	17.55	17.76	1.01	18.39	17.59	0.96	291
	3.64	1.83	1.82	0.99	17.74	17.27	0.97	18.27	17.38	0.95	291
Irradiation Temperature, 120°C											
	0.52	...	1.86	...	...	17.03	...	...	17.42	...	...
	0.63	...	1.93	...	...	17.15	...	...	17.53	...	...
Heat Treatments											
HT1	...	...	1.70	...	...	17.22	...	...	14.76	...	85
HT2	...	...	1.70	...	...	17.15	...	...	17.27	...	81
HT3	...	...	1.74	...	...	16.92	...	...	16.26	...	83
HT4	...	1.79	1.81	1.01	17.56	17.90	1.02	17.33	17.50	1.01	271
HT5	...	1.83	1.81	0.99	17.65	17.05	0.97	17.44	17.32	0.99	234

* To avoid oxidation or loss of carbon, each specimen was vacuum encapsulated for heat treatment.
† Measured with a 100 gm load.
HT1: 910°C for 30 min, furnace cool.
HT2: 900°C for 20 min, furnace cool to 800°C, air cool.
HT3: 900°C for 20 min, furnace cool to 800°C, air cool, 700°C for 48 h, air cool.
HT4: 260°C for 8 h, air cool.
HT5: 260°C for 43 h (8 + 8 + 3 + 8 + 8 + 8), air cooled between each interval.

during irradiation at 260°C and were small in all cases. This was again consistent with the small observed changes in specimen hardness in those cases.

Other heat treatments were carried out to alter the as-received materials microstructure; the heat treatment conditions are noted in Table 2 [*5*]. These heat treatments resulted in substantial softening of the material. The hysteresis responses of these specimens are shown in Fig. 7. Observable changes were shown in most of the standard magnetic properties.

A comparison of the hysteresis curves from unirradiated, irradiated, and thermally treated specimens in Figs. 4 to 7 shows that the effective magnetic saturation rises with irradiation exposure and may be affected by heat treatment. Even at low neutron dose differences, deviations in the values are apparent in the figures. These changes are best reflected in the hysteresis loss, which correlates with increases in the effective magnetic saturation.

Values for the hysteresis losses are given in Table 1. The changes with dose fluctuate for the irradiations at higher temperature, but rise consistently for the two points available at 120°C. (The value for the control is a useful baseline for the 120°C irradiations.) These trends, however, need to be tracked to higher doses in all cases to determine the full influence of irradiation on magnetic properties changes. The doses reported here are still low in terms of irradiation-induced mechanical properties changes.

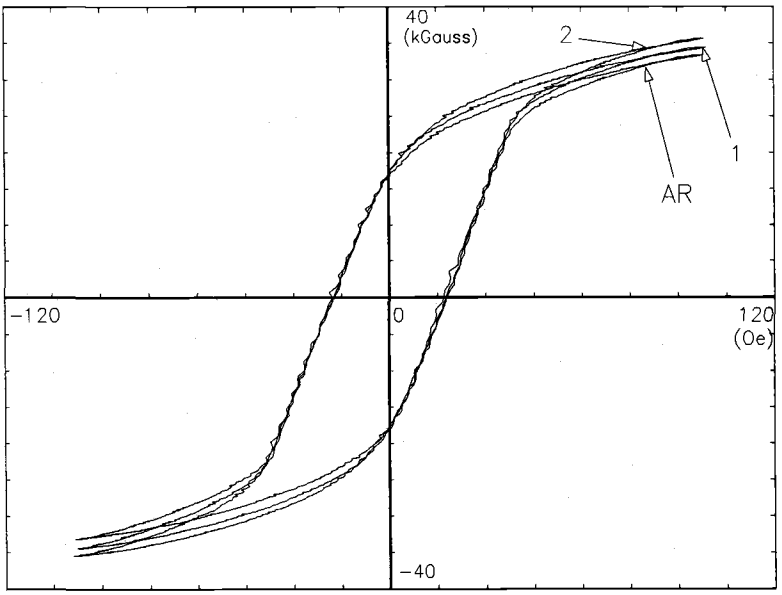

FIG. 4—*The hysteresis loops for specimens irradiated at approximately 120°C: AR = as received (unirradiated) condition; 1: 5.22 × 10¹⁷ n/cm² (E > 0.1 MeV) and 2: 6.34 × 10¹⁷ n/cm² (E > 0.1 MeV).*

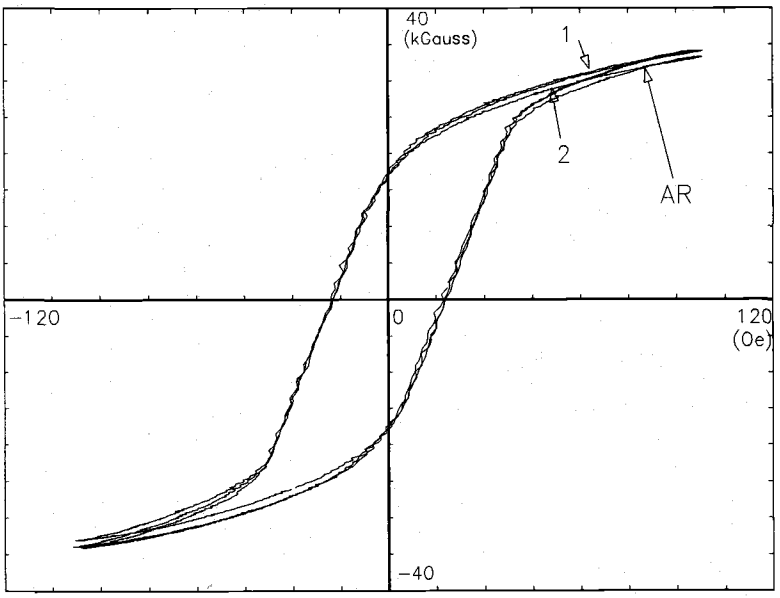

FIG. 5—*The hysteresis loops for specimens irradiated at approximately 260°C: AR = as received (unirradiated) condition; 1: 6.5 × 10¹⁷ n/cm² (E > 0.1 MeV) and 2: 2.28 × 10¹⁸ n/cm² (E > 0.1 MeV).*

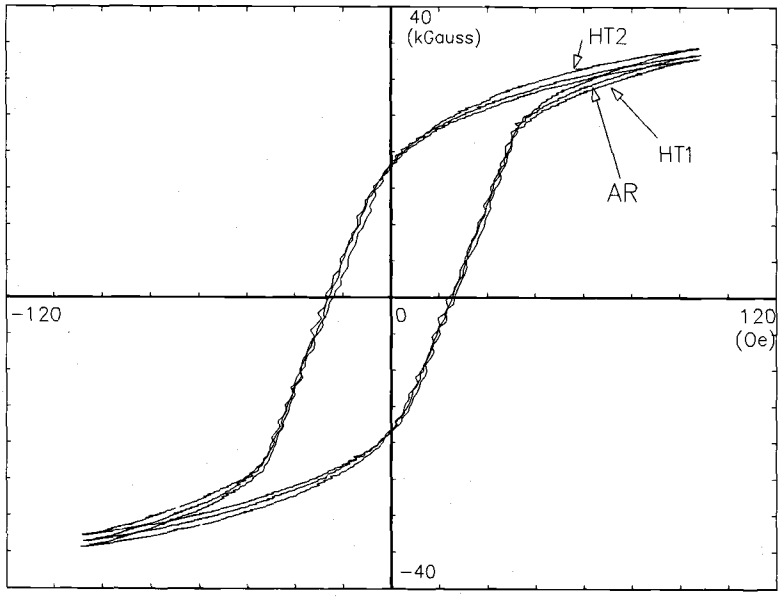

FIG. 6—*The hysteresis loops for specimens heat-treated with thermal cycles to simulate the reactor exposures at 260°C; AR = as received; HT1: 260°C for 8 h and HT2: cycled to 260°C for 8 h twice, for 3 h once, then for 8 h three times. These thermal cycles were the same the specimens (1 and 2) received during their irradiation cycles (see Fig. 5 for comparable irradiation results).*

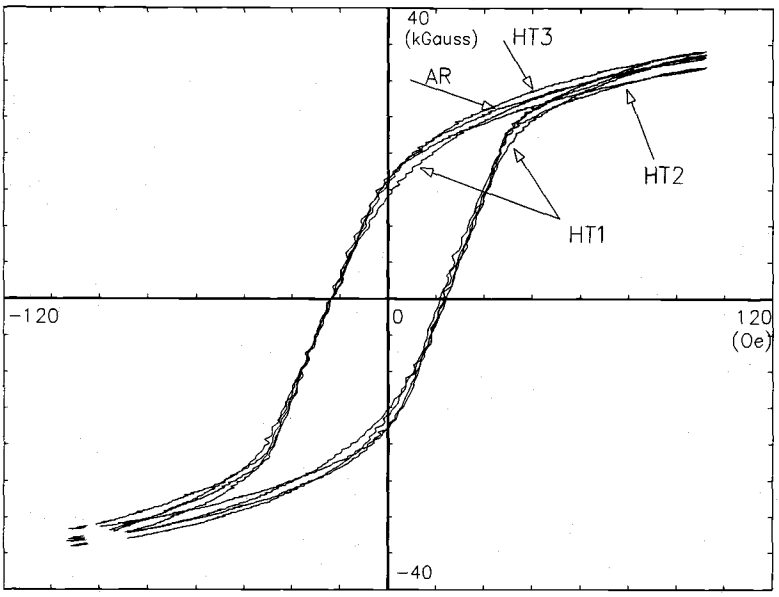

FIG. 7—*The hysteresis loops for specimens heat treated to various annealing conditions: AR = as received, 1: 910°C for 30 min, furnace cool; 2: 900°C for 20 min, furnace cool to 800°C, air cool; and 3: 900°C for 20 min, furnace cool to 800°C, air cool, 700°C for 48 h, air cool.*

The magnetic properties of the A533B pressure vessel steel examined here were found fairly radiation resistant at the higher irradiation temperature and more sensitive to irradiation at the lower temperature. Earlier work by Gordon and Sery [*1*] show small irradiation-induced effects in high purity Fe. However, the lack of pronounced changes in the higher irradiation temperature tests here may be more directly associated with the low fluences. The lower temperature irradiations show a greater degree of sensitivity which is consistent with observed temperature dependencies of post-irradiation mechanical properties changes. Further work is underway to clarify the temperature and dose effects.

Conclusions

A nondestructive method for monitoring irradiation-induced changes in magnetic properties of nuclear pressure vessel steels was described, and typical measurements on small specimens were carried out. The technique involves the examination of very small volumes of material, but measures bulk properties. It was shown to be sensitive to magnetic properties changes following irradiation to less than 1×10^{18} n/cm^2 ($E > 0.1$ MeV) at approximately 120°C. To date, irradiations to higher doses at approximately 260°C have not produced changes in either microhardness or magnetic properties. Changes in both microhardness and magnetic properties were found after certain thermal aging studies. In all cases where changes were seen, increases in the hysteresis loss correlated with increased microhardness. In cases where no irradiation-induced magnetic properties changes were found, the microhardness was also found not to change.

Acknowledgments

This work was supported by the U.S. Department of Energy under contract number DE-FG07-90ER13030.

References

[*1*] Gordon, D. I. and Sery, R. S., "Irradiation of Iron and 7-59 Mo Permalloy with 2 MeV Electrons," *Journal of Applied Physics,* Vol. 35, No. 3, 1964, pp. 879–880.

[*2*] Chen, C. W., *Magnetism and Metallurgy of Soft Magnetic Materials,* Vol. XV in *Selected Topics in Solid State Physics,* North Holland Publishing Co., Amsterdam, 1977, Chapter 7, Part 1.

[*3*] El-Kalla, E. H., Rahman, F. A., and Maaty, A. A., "The Effect of Neutron Irradiation on the Magnetic Properties of Low Carbon Steels," *International Journal of Radiation Applications and Instrumentation, Part A: Applied Radiation and Isotopes,* Vol. 40, No. 2, 1989, pp. 159–162.

[*4*] Kwon, O.-Y., Ono, K., Lucas, G. E., and Oddette, G. R., "Detection of Irradiation Effects on Reactor Pressure Vessel Steels by Magneto-Acoustic Emission," *Proceedings*, Ninth International Conference on NDE in the Nuclear Industry, Tokyo, Japan 24–28 April 1988, American Society for Metals, Metals Park, OH.

[*5*] Stubbins, J. F., Williams, J. G., Ougouag, A. M., Patel, J. U., and Shong, W.-J., "Measurement of Irradiation Damage in Nuclear Pressure Vessel Steels by Magnetic Properties Changes," *Proceedings,* Fifth International Symposium on Environmental Degradation of Materials in Nuclear Power Systems—Water Reactors, E. P. Simonen, Ed., American Nuclear Society, Monterey, CA, 1992, pp. 719–724.

[*6*] Cost, J. R., Brown, R. D., Giorgi, A. L., and Stanley, J. T., "Radiation Effects in Rare-Earth Permanent Magnets," *IEEE Transactions on Magnetics,* Vol. 24, 1988, pp. 2016–2019.

[*7*] Brown, R. D. and Cost, J. R., "Radiation-Induced Changes in Magnetic Properties of Fe-Nd-B Permanent Magnets," *IEEE Transactions on Magnetics,* Vol. 25, 1989, pp. 3117–3120.

[*8*] Cost, J. R. and Brown, R. D., "Sm-Co Permanent Magnets: Effects of Fast Neutron Irradiation," *Metallurgical Transactions A,* Vol. 21A, 1990, pp. 1817–1821.

[*9*] Takahashi, M. in *Physics and Engineering Applications of Magnetism,* Y. Ishikawa and N. Miura, Eds., Springer-Verlag, Berlin, 1991, Vol. 92, p. 164.

[*10*] Jiles, D., *Introduction to Magnetism and Magnetic Materials,*, Chapman and Hall, London, 1991.

DISCUSSION

R. Odette[1] (*written discussion*)—(1) Does saturation mean fully saturated in your experiments? (2) Are there concerns that the multiple cycles influence the fine scale microstructure induced by irradiation?

J. F. Stubbins et al. (*authors' closure*)—(1) The specimens are loaded to effective saturation, the point past where the tips of the hysteresis loop close. Full saturation may not be reached to very high applied field strengths, but is not necessary for the determination of the hysteresis loss, the remanence, or the coercivity. (2) We have no evidence that the fine scale microstructure is influenced by the application of induced magnetic fields. It is likely that the fine structure is stable with respect to the applied fields. In the present case, we see no change in the hysteresis response in measured properties from the first to the last cycle which would indicate that the microstructure has been effected.

W. R. Corwin[2] (*written discussion*)—(1) Is there any value in changing the experimental parameters of the magnetic measurement (e.g., frequency or amplitude of driving function) to enhance measured differences? (2) If adequate magnetic changes occur to correlate with embrittlement, would it be possible to also measure them using a flat probe for in-situ RPV measurements?

J. F. Stubbins et al. (*authors' closure*)—(1) We have not found that changes in frequency, over a limited range of frequencies, make a difference in the results. The driver current amplitude is set so that the effective saturation magnetization is exceeded. If lower amplitudes were used, full effective saturation would not be achieved and the results would vary with amplitude. However, for amplitudes above the effective saturation level, little, if any, changes are found as a function of amplitude. (2) In situ measurements may be possible, but would probably be difficult. For instance, the materials properties would vary as a function of distance through the wall thickness of a typical pressure vessel due to differences in exposure fluences and temperatures during operation. Thus, the technique would have to differentiate between properties responses at various vessel wall depths.

[1] University of California, Santa Barbara, Department of Chemical and Nuclear Engineering, Santa Barbara, CA 93106.
[2] ORNL, Oak Ridge National Laboratory, Oak Ridge, TN.

Yutaka Nishiyama,[1] *Kiyoshi Fukaya,*[1] *Masahide Suzuki,*[1] *Motokuni Eto,*[1] *and Tetsuo Shoji*[2]

Electrochemical Evaluation of Thermal Aging Embrittlement of 2¼Cr-1Mo Steel for a Nuclear Pressure Vessel

REFERENCE: Nishiyama, Y., Fukaya, K., Suzuki, M., Eto, M., and Shoji, T., **"Electrochemical Evaluation of Thermal Aging Embrittlement of 2¼Cr-1Mo Steel for a Nuclear Pressure Vessel,"** *Small Specimen Test Techniques Applied to Nuclear Reactor Vessel Thermal Annealing and Plant Life Extension, ASTM STP 1204,* W. R. Corwin, F. M. Haggag, and W. L. Server, Eds., American Society for Testing and Materials, Philadelphia, 1993, pp. 16–26.

ABSTRACT: A nondestructive test technique using an electrochemical method was investigated for evaluating thermal aging embrittlement of 2¼Cr-1Mo steel for a nuclear pressure vessel. Agings were conducted at temperatures ranging from 400 to 500°C for up to 50 000 h. In the anodic polarization curve measured in calcium nitrate solution, a secondary peak, which is higher for embrittled materials than for the deembrittled ones, was observed in the passive potential region. Changes in the secondary peak can be correlated with the degree of the embrittlement evaluated by the shift in Charpy ductile-to-brittle transition temperature (ΔDBTT).

KEYWORDS: 2¼Cr-1Mo steel, electrochemical technique, nondestructive examination, thermal aging embrittlement, impact toughness, phosphorus segregation, intergranular attack

A normalized and tempered (NT) 2¼Cr-1Mo steel has been selected as the pressure vessel material of the first high-temperature, gas-cooled reactor (HTTR) in Japan. The pressure vessel will be subjected to a temperature of about 400°C during normal operation. It is well known that low-alloy ferritic steels suffer toughness degradation mainly due to intergranular segregation of impurity atoms when they are subjected to temperatures between 375 to 500°C. On irradiation embrittlement of this material, the results of neutron irradiation experiments conducted around 400°C to a neutron fluence of 1×10^{22} n/m^2 ($E > 1$MeV), which is equivalent to the total fluence of the pressure vessel exposed during the service life, showed that NT 2¼Cr-1Mo steels did not exhibit significant radiation embrittlement [*1–3*]. Hence, the evaluation of aging embrittlement in terms of the shifts in Charpy ductile-to-brittle transition temperature (ΔDBTT) in service is the main concern for the estimation of remaining life of the HTTR pressure vessel.

In the surveillance program of a reactor pressure vessel (RPV), it is desirable to monitor the material degradation directly from the RPV in a nondestructive way. Spatial limitations in the reactor core and the expense of a large number of irradiated specimens would be alleviated if nondestructive test techniques are found to be reliable. Recent studies have demonstrated that the electrochemical technique provides a wide range of applicability to

[1] Japan Atomic Energy Research Institute, Tokai-mura, Ibaraki-ken, 319-11, Japan.
[2] Research Institute for Fracture Technology, Tohoku University, Aramaki, Sendai, 980, Japan.

the nondestructive detection of several kinds of aging damages in high-temperature component materials [*4,5*]. The technique makes use of the preferential dissolution of specific microstructures due to the presence of carbides and segregated impurity atoms, which often cause toughness degradation. The present study was conducted to develop the electrochemical technique for the nondestructive evaluation of aging embrittlement of 2¼Cr-1Mo steel. Anodic polarization curves in calcium nitrate solution were measured on aged 2¼Cr-1Mo steels to establish the correlation between the electrochemical parameter and the degree of embrittlement. The dependence of aging temperature on the correlation is also discussed.

Experimental Procedure

Material used in the present study was a NT 2¼Cr-1Mo steel plate of 160-mm thickness designated as A387 Gr.22 Cl.2 in accordance with the ASTM Specification for Pressure Vessel Plates, Alloy Steels, Chromium-Molybdenum (ASTM A 387/A 387M). Table 1 shows the chemical composition at the quarter thickness position and at heat-treatment conditions. The microstructure of this steel consists mainly of bainite with a small amount of proeutectoid ferrite.

Isothermal agings in air were conducted at temperatures ranging from 400 to 500°C for up to 50 000 h. The blocks for the thermal aging experiment were cut from the quarter thickness position of the original plate and had the dimensions of 230 by 60 by 20 mm^3. After these aging treatments, Charpy V-notch impact specimens (CVN) of 10 by 10 by 55 mm^3 with a 45°, 2-mm-deep notch were machined from the blocks.

Coupons with dimensions of 10 by 10 by 5 mm^3 for anodic polarization tests were cut from the undamaged edge portion of CVN bars fractured in the lower shelf region, as illustrated in Fig. 1. An installed copper wire was soldered to one end of the coupon, which was mounted in epoxy resin. After mechanically polishing the surface to a 1-μm diamond finish, the coupon was cleaned with acetone. The edge of the coupon was coated with electrically insulated lacquer to prevent crevice corrosion. The schematic diagram of the anodic polarization test apparatus is shown in Fig. 2. A solution of 55% $Ca(NO_3)_2$ deaerated by bubbling nitrogen gas at 30°C was used. Anodic polarization curves (potential-current density curves) were determined in a three-electrode corrosion cell with a platinum (Pt) and saturated calomel electrode (SCE) as counter and reference electrodes, respectively. The potential of the specimen was measured with respect to SCE (mV versus SCE). The potential of the specimen was scanned from an open circuit potential to transpassive potential at a rate of 0.5 mV/s.

Results and Discussion

Effect of Thermal Aging on Charpy Impact Properties

Shifts in the 68 J (50 ft · lbf) Charpy ductile-to-brittle transition temperature (ΔvTr_{50}) as a function of aging time are shown in Fig. 3. Initial embrittlement was most rapid at 500°C,

TABLE 1—*Test material (chemical composition weight percent and heat treatment conditions[a]).*

	Chemical Composition, wt%										
Position	C	Si	Mn	P	Ni	Cr	S	Cu	Mo	As	Sn
¼ t	0.15	0.05	0.55	0.008	0.11	2.33	0.01	0.07	0.90	0.006	0.008

[a] Heat treatment: 900/930°C—6.5 h, water cooled; 670/690°C—7 h, air cooled; and PWHT, 680/710°C—20 h.

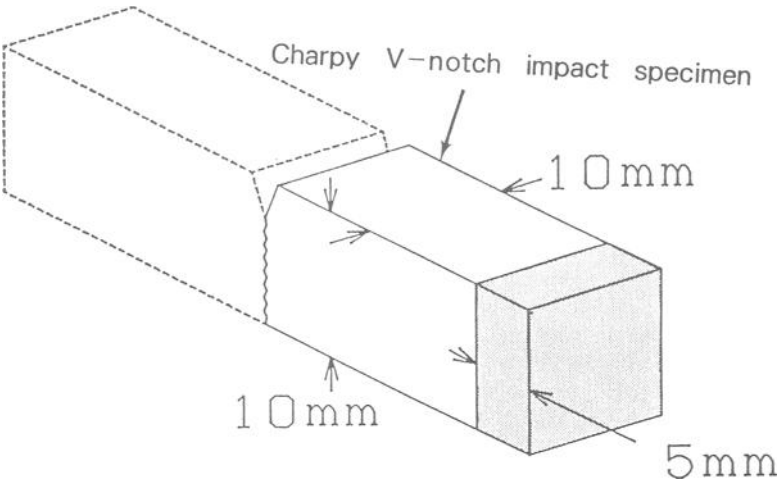

FIG. 1—*Shape and dimension of the coupon cut from the undamaged portion of a broken Charpy V-notch impact bar for the anodic polarization test.*

whereas for long aging time the lower temperature aging caused more severe embrittlement. The most severe embrittlement seems to be at 400°C. This temperature dependence of embrittlement can be interpreted as one of the characteristics of reversible temper embrittlement caused by impurity segregation to prior austenite grain boundaries [*6*]. Figure 4 shows the fracture surfaces of CVN specimens tested in the lower shelf region for as-received and embrittled (450°C × 10 000 h aged) materials. The aging altered the fracture appearance from the entirely transgranular to mixed transgranular plus intergranular fracture. Auger

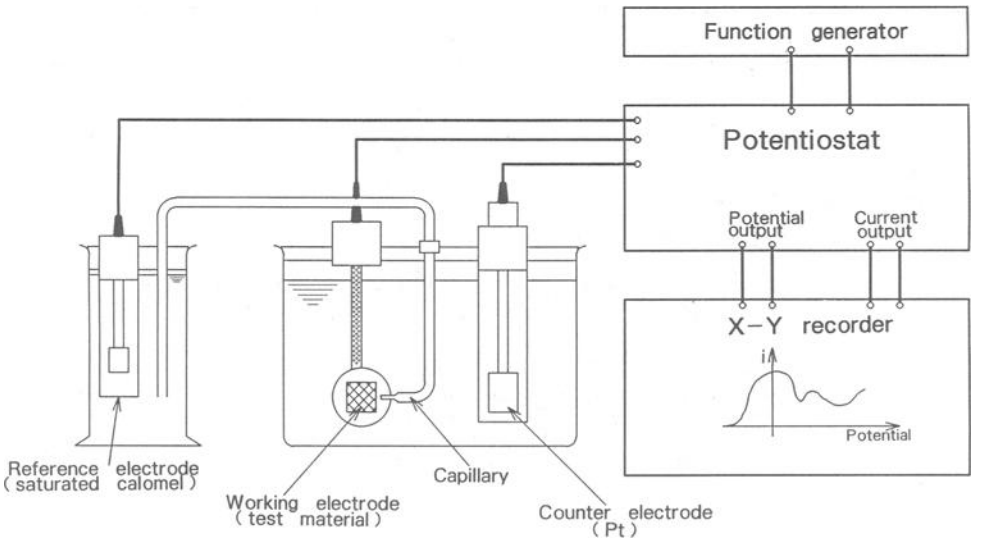

FIG. 2—*Schematic diagram of the electrochemical polarization test apparatus.*

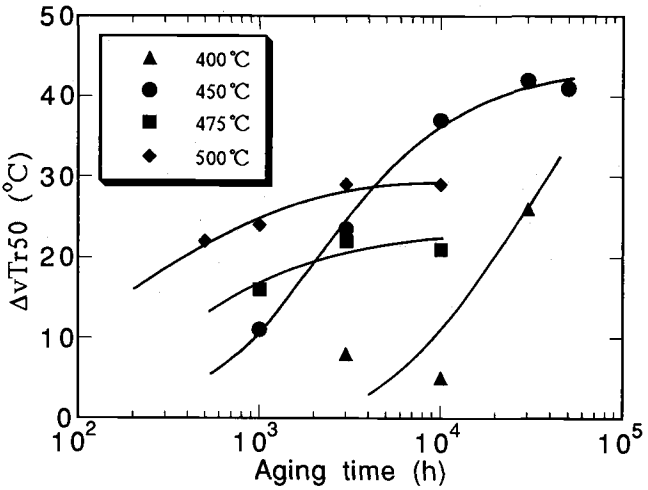

FIG. 3—*Shifts in the 68 J (50 ft-lbf) Charpy ductile-to-brittle transition temperature* (ΔvTr_{50}) *as a function of aging.*

electron spectroscopy (AES) analysis revealed that phosphorus segregates on intergranular facets. Thus, we conclude that the aging embrittlement of this steel is caused mainly by phosphorus segregation to prior austenite grain boundaries.

Anodic Polarization Curves

As stated previously, electrochemical techniques for evaluating material degradation are based on the preferential dissolution due to the presence of precipitates or impurity atoms, which often cause embrittlement. It is well known that grain boundaries with segregated phosphorus are selectively dissolved in picric acid solution. Hence, chemical etching and electrochemical polarization methods on the basis of this phenomenon have been proposed to evaluate the degree of embrittlement [*5*]. However, the sensitivity of these methods was insufficient for the precise and quantitative evaluation of embrittlement. Recently, for 1Cr-0.5MoV steel aged at 400°C for up to 6000 h, Watanabe and Shoji [*4*] have shown that the change in the anodic polarization curve measured in hot calcium nitrate solution was correlated with the shift of the Charpy fracture appearance transition temperature (ΔFATT). This method was found to be more sensitive for evaluating phosphorus-induced embrittlement than the picric acid method.

Figure 5 shows typical anodic polarization curves for as-received and 450°C × 10 000 h aged materials. After passing through the primary peak, both materials began to passivate around 0 mV. There was no significant change in curves between as-received and aged materials up to this potential. Subsequently, a secondary peak, which is higher for aged materials than for as-received ones, was observed around 140 mV in the passive potential region. To clarify this increase in the secondary peak, potentiostatic etching at 140 mV for 20 min following the anodic polarization up to this potential was performed for as-received, 450°C × 3000 h, and 450°C × 10 000 h aged materials. Scanning electron microscopy (SEM) photographs of these specimen surfaces shown in Fig. 6 reveal that the preferential dissolution at grain boundaries becomes clearer with increased aging time. In addition, as shown in Fig. 6*d*, an initiation of intergranular penetration in the cross section was observed for

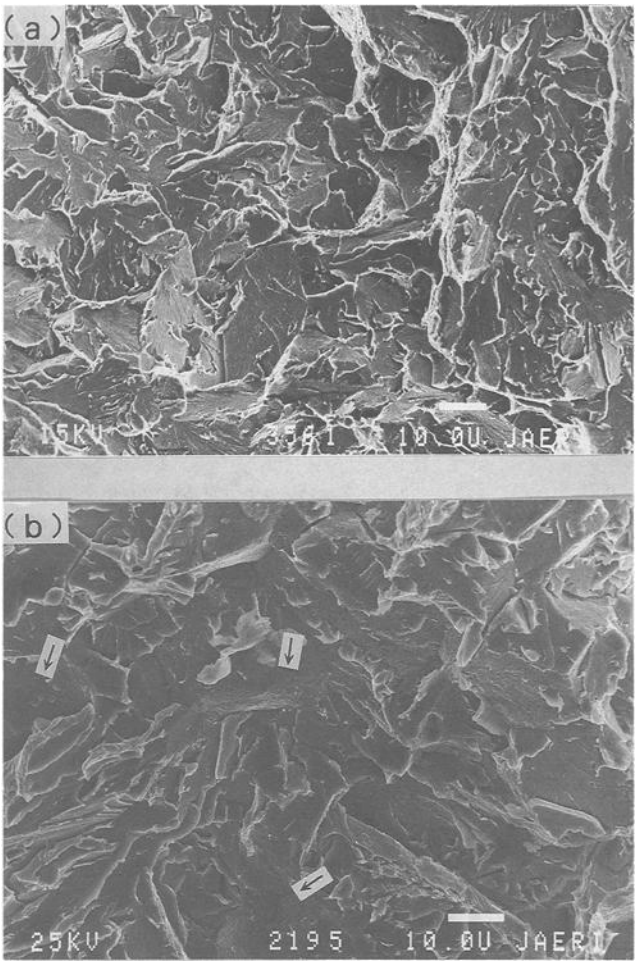

FIG. 4—*Scanning electron micrographs of fracture surfaces in Charpy specimens;* (a) *as-received and* (b) *thermally aged (450°C × 10 000 h), both tested in the lower shelf region. Arrows indicate intergranular facets.*

450°C × 10 000 h aged material. It was confirmed that this intergranular dissolution did not occur up to 0 mV in low-alloy ferritic steels [*4*]. Therefore, it is concluded that the increase in the secondary peak around 140 mV corresponds to the intergranular corrosion.

Secondary Peak in the Passive Potential Region

It has been suggested that the intergranular corrosion of iron alloys in hot calcium nitrate solution is associated with segregated phosphorus atoms that prevent the formation of a passive layer [*7,8*]. It has been also suggested that carbon (primarily as carbide) at grain boundaries is related to intergranular corrosion [*7*]. Since 2¼Cr-1Mo steel contains many

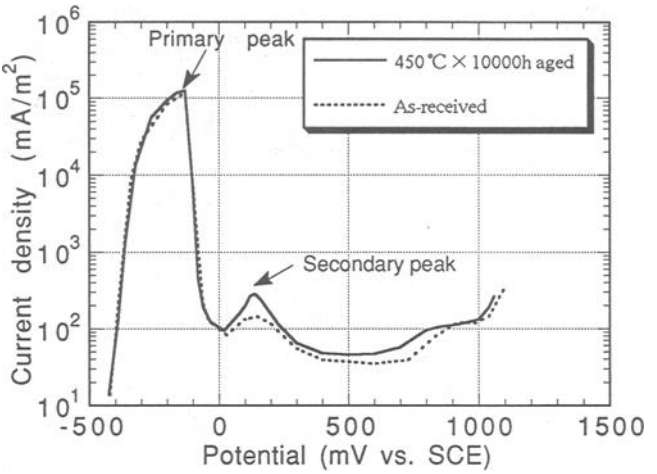

FIG. 5—*Anodic polarization curves for as-received and 450°C × 10 000 h aged materials in 55% $Ca(NO_3)_2$ solution at 30°C.*

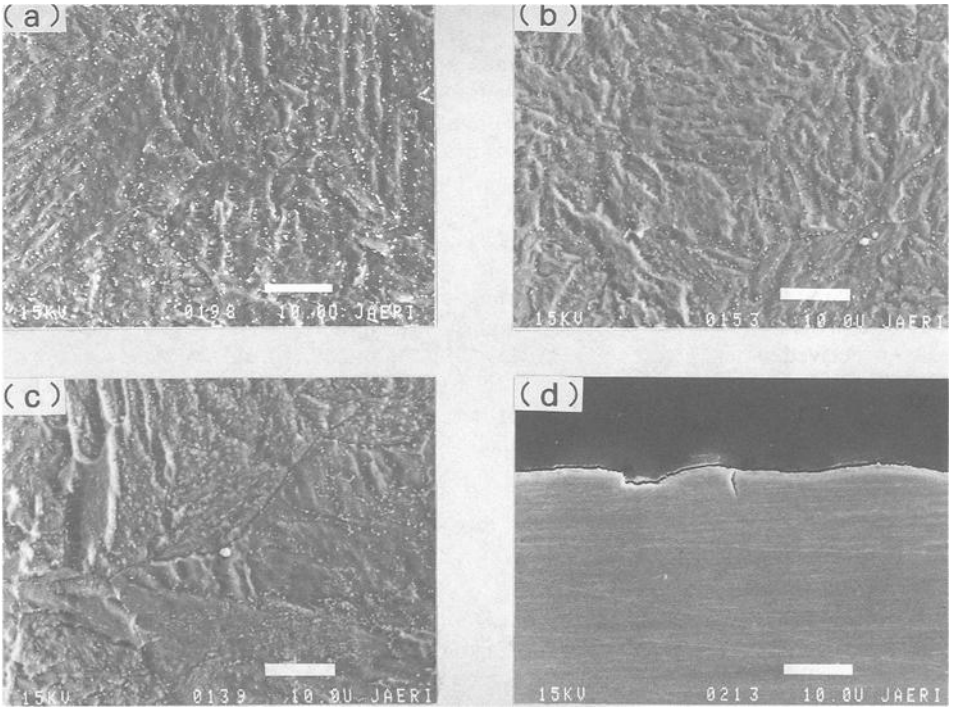

FIG. 6—*Scanning electron micrographs of specimen surfaces potentiostatically etched at 140 mV for 20 min:* (a) *as-received;* (b) *450°C × 3000 h aged;* (c) *450°C × 10 000 h aged; and* (d) *intergranular attack in a cross section of 450°C × 10 000 h aged material.*

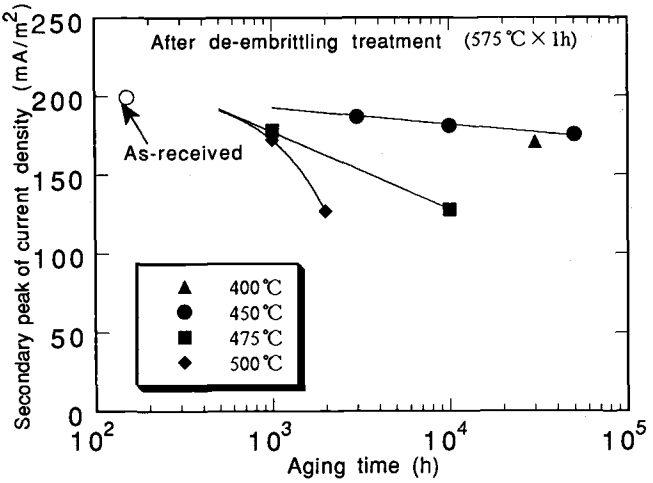

FIG. 7—*Secondary peak of the current density of thermally aged materials after deembrittling treatment (575°C × 1 h) as a function of aging time.*

types of carbides which have formed during tempering treatments, the carbide evolution during the aging may also affect the intensity of the secondary peak.

Figure 7 shows the secondary peak of the current density of aged materials after deembrittling treatment as a function of aging time. Since this deembrittling treatment of 575°C for 1 h lowered the Charpy ductile-to-brittle transition temperature to the initial level [*3*], the decrease in the secondary peak observed on materials aged above 475°C may correspond to carbide evolution. Materials aged below 450°C exhibited no significant decrease in the secondary peak. This indicates that the aging below 450°C would cause no carbide evolution. Cheruvu [*9*] showed that carbides originally formed in the tempering treatment are stable in low-alloy ferritic steels exposed to long-term service below 450°C. Figure 8 shows the transmission electron micrographs of carbon extraction replicas and the typical energy-dispersive X-ray (EDX) spectrum of the carbide observed at grain boundaries. The relative peak ratios in the EDX spectra indicated that most of the carbides present at grain boundaries of the as-received material were those of M_7C_3 [*10*]. On the other hand, carbides which had globular morphology were found in 500°C × 2000 h aged material. These carbides were identified as the M_2C type from the EDX spectra [*10*]. No precipitates of the M_6C type of carbides were detected. Thus we consider that M_2C carbides or changes of grain boundary chemistry accompanied by this precipitation impeded the intergranular corrosion, resulting in the decrease in the secondary peak.

As expected from the above results, changes in the secondary peak before and after the deembrittling treatment (designated as "ΔI_p") represent the degree of phosphorus segregation regardless of carbide evolution. ΔI_p values are plotted as a function of aging time in Fig. 9. For aging above 475°C, there was no significant increase in ΔI_p. ΔI_p for the materials aged below 450°C increased with increased aging. In particular, ΔI_p as the cause of aging at 400°C sharply increased after the longest incubation period. This dependence of ΔI_p on aging time and temperature seems analogous to that of ΔDBTT shown in Fig. 4. Thus, ΔI_p is expected to be a representative parameter for evaluating the degree of embrittlement.

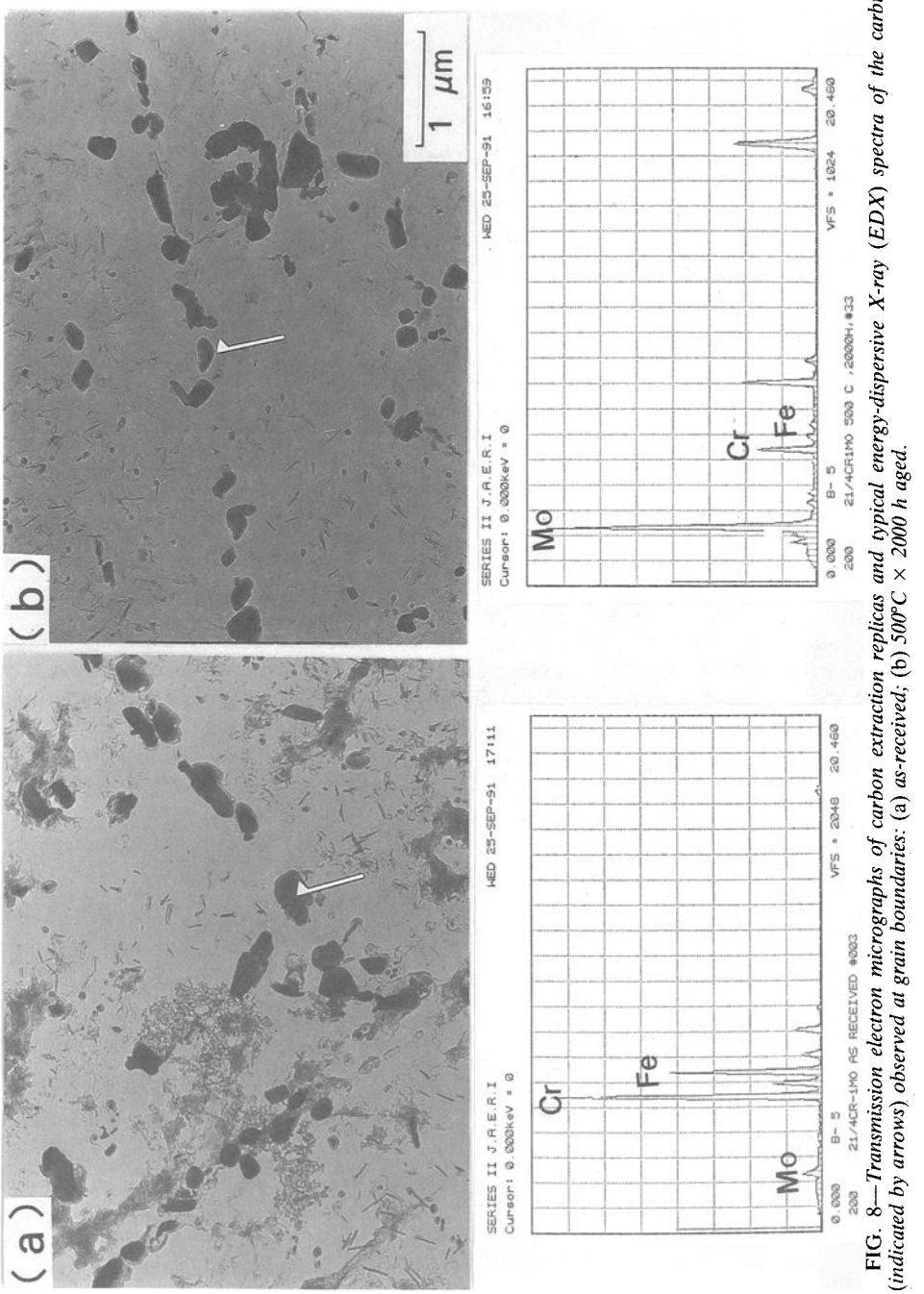

FIG. 8—*Transmission electron micrographs of carbon extraction replicas and typical energy-dispersive X-ray (EDX) spectra of the carbides (indicated by arrows) observed at grain boundaries:* (a) *as-received;* (b) *500°C × 2000 h aged.*

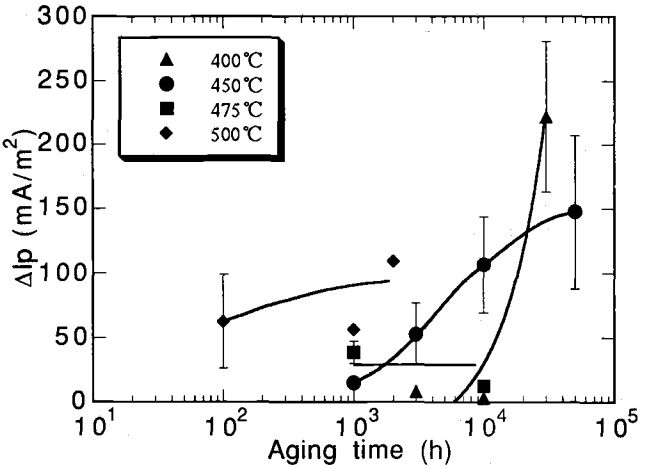

FIG. 9—*Change of the peak current density before and after the deembrittling treatment* (ΔI_p) *as a function of aging.*

Quantitative Evaluation of Thermal Aging Embrittlement

Figure 10 shows the correlation between ΔI_p and ΔvTr_{50} for the materials aged at 400 and 450°C. ΔI_p has a good correlation with the degree of embrittlement, although it depends on the aging time. Thus, it is suggested that the electrochemical technique, i.e., measuring the anodic polarization curve, has the potential to be applied as a nondestructive monitor of the embrittlement. It is noted that the aging at 400°C exhibits the larger increase in ΔI_p than that at 450°C when the comparison is made for a given ΔvTr_{50}. Figure 11 shows the size distribution of the intergranular attack in the cross section for 400°C × 30 000 h and 450°C × 10 000 h aged materials potentiostatically etched at 140 mV. It is clear that aging at 400°C for 30 000 h caused the more intergranular attacks and the longer depth, while

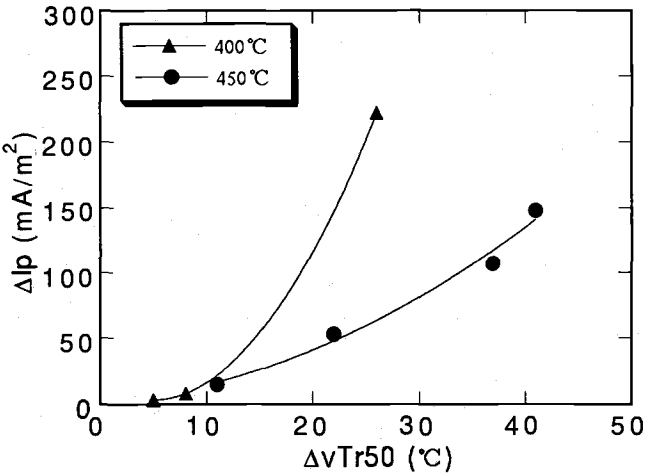

FIG. 10—*Correlation between* ΔI_p *and* ΔvTr_{50} *for 400 and 450°C aged materials.*

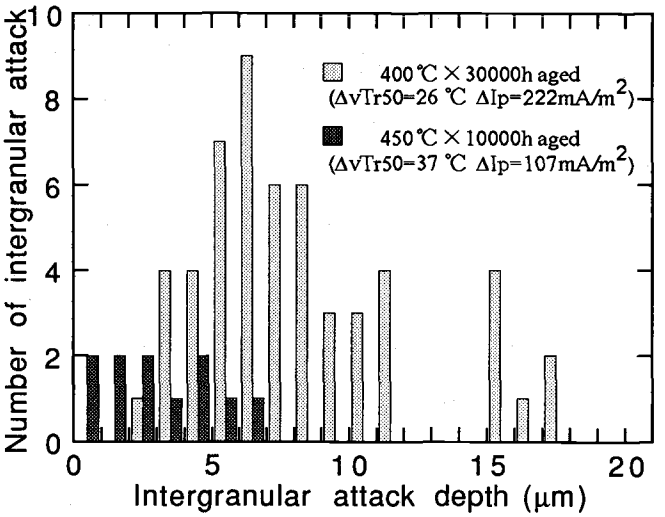

FIG. 11—*Size distribution of the intergranular attack in the cross section for 400°C × 30 000 h and 450°C × 10 000 h aged materials after potentiostatic etching at 140 mV.*

showing less ΔvTr_{50} than that at 450°C for 10 000 h. Since the service temperature of the HTTR pressure vessel will be around 400°C, the degree of embrittlement in service can be evaluated more sensitively by the ΔI_p measurement in Fig. 10.

Küpper et al. [*11*] have studied the intergranular corrosion of Fe-P alloys with 0.003 to 2.5 wt% P in a 55% $Ca(NO_3)_2$ solution at 60°C. The equilibrium for phosphorus segregation to grain boundaries was established by annealing at temperatures between 400 and 800°C, and the curent-time curves at a constant potential in the passive potential region were measured for these materials with varying phosphorus concentration. Their results showed that the alloy with a high concentration of phosphorus exhibited a short incubation period for the onset of intergranular corrosion. From these results, it is assumed that ΔI_p is significantly affected by phosphorus concentration at grain boundaries. Since the potential of samples was scanned in the present experiment, those grain boundaries with higher concentration of phosphorus would be more critical for the increase in the secondary peak. From the thermodynamics of segregation [*12*], the equilibrium concentration of phosphorus at 400°C would be higher than that at 450°C. Consistent with this fact, the most severe embrittlement will be achieved at 400°C after long-term aging, as shown in Fig. 3. We believe that a high concentration of phosphorus in the scatter of concentration from one grain boundary to others builds up even before the equilibrium is attained at 400°C, although a statistical analysis of phosphorus concentration on intergranular facets was not done in this study. Consequently, this high concentration of phosphorus is believed to be related to the larger increase in the secondary peak for a given ΔvTr_{50}.

Summary and Conclusions

A nondestructive test technique based on the measurement of electrochemical properties has been described for the evaluation of the degree of embrittlement of 2¼Cr-1Mo steel for a nuclear pressure vessel. Thermal aging at temperatures from 400 to 500°C for up to 50 000 h caused phosphorus segregation to grain boundaries, resulting in ΔDBTT. In the

anodic polarization curve in a 55% $Ca(NO_3)_2$ solution at 30°C, embrittled materials exhibited the higher secondary peak of the current density, which may be attributed to the intergranular corrosion around 140 mV in the passive potential region. This phenomenon corresponds to the presence of intergranular segregation of phosphorus, which prevents the formation of a passive layer. However, at higher aging temperatures, it was found that the precipitation of Mo_2C-type carbide decreased the secondary peak.

The degree of embrittlement in terms of ΔDBTT was correlated with the change of secondary peaks for the aged and deembrittled materials (ΔI_p). This result indicates that the aging embrittlement can be evaluated nondestructively by the anodic polarization measurement. However, ΔDBTT predicted by a given ΔI_p decreases with increasing aging temperature. This discrepancy was inferred in terms of the high concentration of phosphorus, which builds up before the higher equilibrium concentration is attained at lower temperature aging, and in the scatter of concentration from one grain boundary to others.

Acknowledgment

We wish to acknowledge Dr. Yutaka Watanabe of Tohoku University for his valuable discussions.

References

[1] Suzuki, M., Fukaya, K., Kodaira, T., and Oku, T., "Effect of Microstructure and Thermal Aging on Neutron Irradiation Embrittlement of 2¼Cr-1Mo Steel for a Nuclear Pressure Vessel," *Influence of Radiation Material Properties, ASTM STP 956,* F. A. Garner, C. H. Henager, and N. Igata, Eds., American Society for Testing and Materials, Philadelphia, 1987, pp. 98–110.

[2] Suzuki, M., Fukaya, K., Kodaira, T., and Oku, T., "Temper and Neutron Irradiation Embrittlement in 2¼Cr-1Mo Steels for Pressure Vessels of High-Temperature Gas-Cooled Reactor," *Nuclear Technology,* Vol. 66, September 1984, pp. 619–629.

[3] Oku, T., Kodaira, K., Fukaya, K., Suzuki, M., Tanaka, Y., Iwadate, T., Suzuki, K., and Sato, I., "Study on 2¼Cr-1Mo Steel for High Temperature Gas-Cooled Reactor Material Characterization of Forged Low Si 2¼Cr-1Mo Steel," *Nuclear Engineering and Design,* Vol. 119, 1990, pp. 177–186.

[4] Watanabe, Y. and Shoji, T., "The Evaluation of In-Service Materials Degradation of Low-Alloy Steels by Electrochemical Method," *Metallurgical Transactions A,* Vol. 22A, September 1991, pp. 2091–2097.

[5] Shoji, T. and Takahashi, H., "Nondestructive Evaluation of Materials Degradation during Service Operation by Means of Electrochemical Method," *Life Extension and Assessment of Fossil Power Plants, EPRI CS5208,* R. B. Dooley and R. Viswanathan, Eds., Electric Power Research Institute, Palo Alto, CA, 1987, pp. 745–759.

[6] Gould, G. C., "Temper Embrittlement in High Purity 3.5Ni, 1.75Cr, 0.20C Steel," *Temper Embrittlement in Steel, ASTM STP 407,* American Society for Testing and Materials, Philadelphia, 1968, pp. 90–105.

[7] Tauber, G. and Grabke, H. J., "Electrochemical and Auger-Spectroscopic Studies on the Intergranular Corrosion of Iron in Nitrate Solutions," *Corrosion Science,* Vol. 19, 1979, pp. 793–798.

[8] Jones, R. H., Arey, B. W., Bear, D. R., and Friesel, M. A., "Grain-Boundary Chemistry and Intergranular Stress Corrosion of Iron Alloys in Calcium Nitrate," *Corrosion,* June, 1989, pp. 494–502.

[9] Cheruvu, N. S., "Degradation of Mechanical Properties of Cr-Mo-V and 2.25Cr-1Mo Steel Components After Long-Term Service at Elevated Temperature," *Metallurgical Transactions A,* Vol. 20A, January 1989, pp. 87–97.

[10] Titchmarsh, J. M., "The Identification of Second-Phase Particles in Steels Using an Analytical Transmission Electron Microscope," UKAEA Report AERE-R9661, AEA Technology, Harwell Laboratory, Oxon, UK, December 1979.

[11] Kupper, J., Erhart, H., and Grambke, H., "Intergranular Corrosion of Iron-Phosphorus Alloys in Nitrate Solutions," *Corrosion Science,* Vol. 21, No. 3, 1981, pp. 227–238.

[12] McLean, D., *Grain Boundaries in Metals,* Oxford University Press, London, UK, 1957.

Fahmy M. Haggag[1]

In-Situ Measurements of Mechanical Properties Using Novel Automated Ball Indentation System

REFERENCE: Haggag, F. M., **"In-Situ Measurements of Mechanical Properties Using Novel Automated Ball Indentation System,"** *Small Specimen Test Techniques Applied to Nuclear Reactor Vessel Thermal Annealing and Plant Life Extension, ASTM STP 1204,* W. R. Corwin, F. M. Haggag, and W. L. Server, Eds., American Society for Testing and Materials, Philadelphia, 1993, pp. 27–44.

ABSTRACT: Determination of the integrity of any metallic structure is required either to ensure that failure will not occur during the service life of the components (particularly following any weld repair) or to evaluate the lifetime extension of the structure. A portable/in-situ stress-strain microprobe system was developed to evaluate nondestructively in situ the integrity of metallic components [including base metal, welds, and heat-affected zones (HAZs)]. The microprobe system utilizes an innovative automated ball indentation (ABI) technique to determine several key mechanical properties (yield strength, true-stress/true-plastic-strain curve, strain-hardening exponent, Lüders strain, elastic modulus, and an estimate of the local fracture toughness). This paper presents ABI test results from several metallic samples. The microprobe system was used successfully to nondestructively test in-situ a circumferentially welded Type 347 stainless steel pipe. Four V-blocks were used to mount the testing head of the microprobe system, allowing a 360° inspection of property gradients in the weld and its HAZ.

KEYWORDS: in-situ testing, structural integrity, automated ball indentation, spherical indenter, cyclic loading, partial unloading, field apparatus, microprobe, welds, heat-affected zone, yield strength, flow properties, pipes, nuclear pressure vessel steels, nondestructive testing

The ABI test is based on strain-controlled multiple indentations (at the same penetration location) of a polished surface by a spherical indenter (0.25 to 1.57-mm diameter). The microprobe system and test methods [*1*] are based on well demonstrated and accepted physical and mathematical relationships which govern metal behavior under multiaxial indentation loading. A summary of the ABI test technique is presented here, and more details are given elsewhere [*1–14*]. The microprobe system currently utilizes an electromechanically driven indenter, high-resolution penetration transducer and load cell, a personal computer (PC), a 16-bit data acquisition/control unit, and copyrighted ABI software. Automation of the test, where a 486 PC and a test controller were used in innovative ways to control the test (including a real-time graphic and digital display of load-depth test data) as well as to analyze test data (including tabulated summary and macro-generated plots), make it simple, rapid (less than 10 min for a complete ABI test), accurate, economical, and highly reproducible. Results of ABI tests (at several strain rates) on various base metals, welds, and HAZs at different metallurgical conditions are presented and discussed in this paper. Ex-

[1] Advanced Technology Corporation, 115 Clemson Drive, Oak Ridge, TN 37830-7665.

FIG. 1—*The portable/in-situ stress-strain microprobe system configured for laboratory bench-top testing (the testing head has a specimen support platen).*

cellent agreement was obtained between ABI-derived data and those from conventional ASTM methods. All ABI tests were performed using a commercially available portable/in-situ stress-strain microprobe system,[2] the mechanics of which are described elsewhere [*1*].

A bench-top configuration of the microprobe (Figs. 1 and 2) was used to test laboratory base metal and weld specimens (Figs. 2 and 3) and resistance spot welds and their HAZs in 1020 carbon steel and 2219 aluminum sheets. A Charpy V-notch (CVN) block is shown underneath the ball indenter in Fig. 2. Gradients in the yield strength and flow properties and correlations to the material microstructure in the weld and HAZ areas are discussed in Ref 7. A 347 stainless steel (SS) flat specimen was also tested and the ABI results compared

[2] Portable/In-Situ Stress-Strain Microprobe System, Model PortaFlow-P1, U.S. Patent No. 4,852,397, Advanced Technology Corporation, 115 Clemson Drive, Oak Ridge, TN 37830-7665.

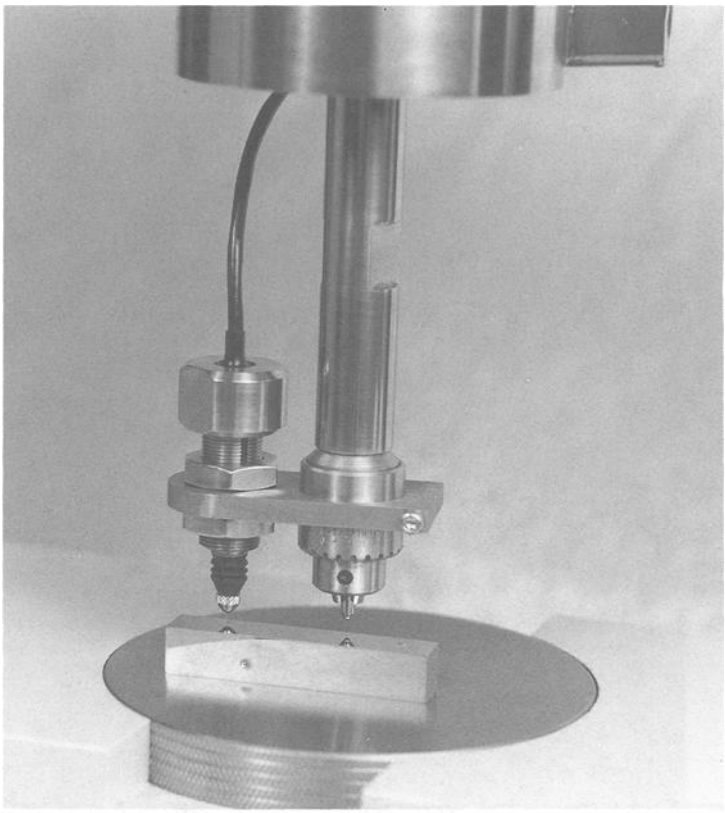

FIG. 2—*Details of the ball indenter and the LVDT of the microprobe system (a Charpy V-notch block is shown underneath the indenter).*

to its material certification. The in-situ configuration (Fig. 4) was used successfully to test a 114-mm outer diameter 347 SS pipe containing a circumferential weld (308 SS).

Portable/In-Situ Stress-Strain Microprobe System and ABI Testing

Figures 1 and 4 show the different components of the microprobe system used in this work. These include: (1) a compact testing head (Fig. 1 is the bench-top configuration with a support platen for laboratory specimen testing, while Fig. 4 shows the in-situ configuration where the testing head is mounted on a stainless steel pipe), (2) a small electronics cabinet which contains the data acquisition/control unit, other boards for signal conditioning and control, and the driver of the electric servo motor, and (3) a portable 486 personal computer. Other testing head mounts such as magnetic holders (either permanent or electric) can be used when appropriate.

The ABI test is based on multiple indentation cycles (at the same penetration location) on a polished metallic surface by a spherical indenter. Each cycle consists of indentation, unload, and reload sequences. Values of indentation penetration speed (strain rate), data acquisition rate, indentation target delta displacement (penetration depth for each cycle), unload target delta load, indentation maximum (final) load, and indentation maximum (final)

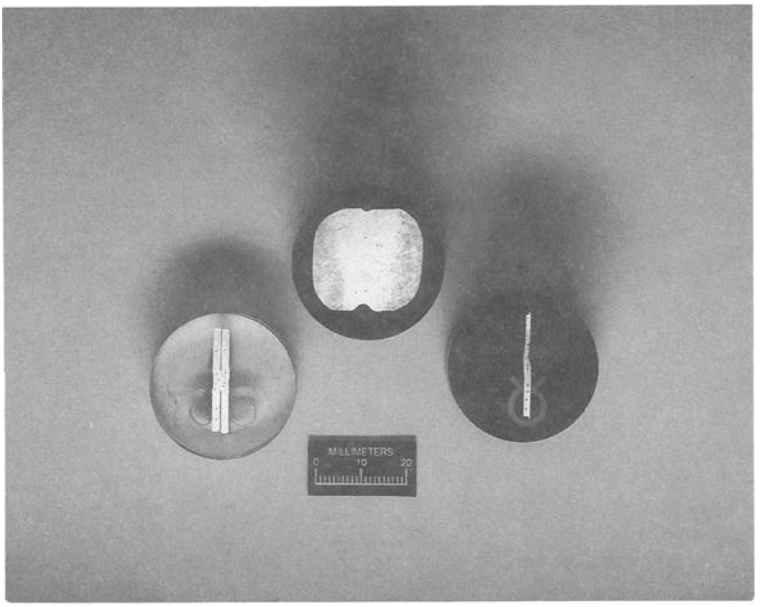

FIG. 3—*Example of weld samples used in laboratory automated ball indentation (ABI) tests.*

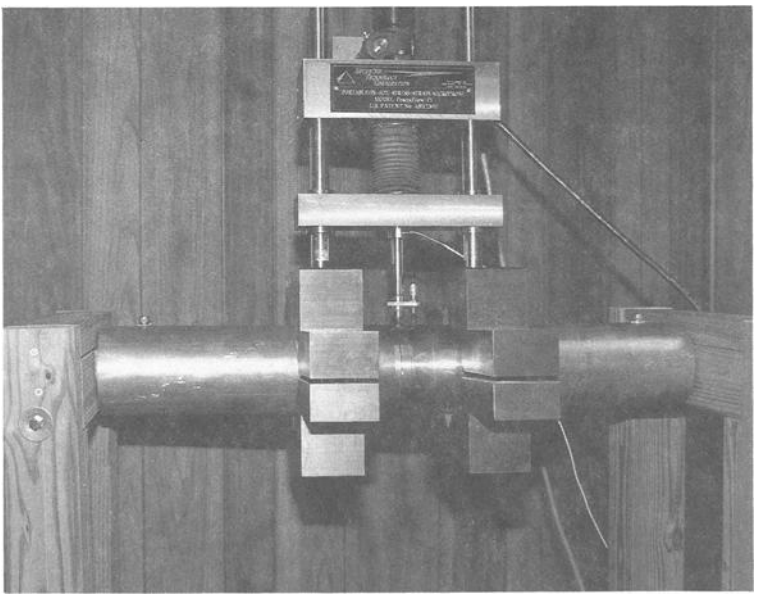

FIG. 4—*The testing head of the microprobe system is mounted on a circumferentially welded 347 SS pipe (114 mm diameter) using four 90° V-blocks.*

displacement (penetration depth) are input before the test starts. The computer program checks all test values against limits to detect operator error. Once the test is started, operation is automatic until either maximum load or maximum displacement is reached, but the operator can abort the test at any time if system malfunction is detected. Current test values for indentation load and depth are displayed digitally on the computer monitor in engineering units as well as in real-time graphics (penetration depth as X-axis versus indentation load as Y-axis) so the operator can monitor the test progress. The ABI test data are saved in memory during the test and then stored on the computer hard disc following test completion and full material sample unloading. The applied loads and associated displacements (depth of penetration of the indenter into the specimen) are measured using a load cell and a spring-loaded linear variable differential transducer (LVDT). The test setup of the current work used tungsten carbide ball indenters varying in size from 0.25 to 1.57-mm diameter. Appropriate capacity load cells were used for the selected indenter size. Details of the ball indenter and the LVDT are shown in Fig. 2. The load-displacement data from each unloading sequence are fitted with a first degree polynomial and the fit extrapolated to obtain the displacement corresponding to zero load. These displacements and the maximum cycle load and displacement values from each indentation sequence are used to determine the yield strength, produce the ABI-derived true-stress/true-plastic-strain curve, and to estimate fracture toughness. The ABI analyses are based primarily on elasticity and plasticity theories and some empirical correlations as described in Refs *1* through *14*. The primary equations used in these analyses are given in the next section.

ABI Data Analysis

The main problem in determining yield strength from ball indentation tests is due to the inhomogeneous or Lüders strain behavior. In a uniaxial tension test the Lüders strain is the inhomogeneous plateau (horizontal portion) of the stress-strain curve where it is confined mostly to a defined volume of the specimen gage section. Hence, the inhomogeneous (Lüders) and homogeneous (work hardening) behaviors in a tension test are well defined and separated from each other. In contrast, in an ABI test the material has less constraint at the surface around the indentation. With increasing indentation loads, an increasing volume of material is forced to flow under multiaxial compression caused by the indenter, and more material pileup and Lüders strain occur around the indentation. Thus, in an ABI test both inhomogeneous and homogeneous material behavior occur simultaneously during the entire test. Consequently, an accurate determination of yield strength should be based on the entire load-displacement curve of the ABI test as explained later. It should be emphasized here that, e.g., for an ABI test consisting of eight cycles, there will be eight yielding processes of new material each time the indenter has penetrated deeper into the test material, as well as eight processes of work hardening of both old and new material. Hence, the yield strength analysis in ABI testing should account for this simultaneous occurrence of yielding and strain hardening of test material under ABI multiaxial compression. Schematics of the ABI load-displacement plot and the profile of indentation (exaggerated to show material pileup) are shown in Figs. 5 and 6, respectively. The ABI load-displacement curve will not exhibit any Lüders plateau (e.g., as the case in uniaxial tensile tests of carbon steel materials).

Flow Properties

The homogeneous plastic flow portion of the true-stress (σ_t)/true-plastic-strain (ϵ_p) curve can be represented by the familiar power law equation

$$\sigma_t = K \epsilon_p^n \tag{1}$$

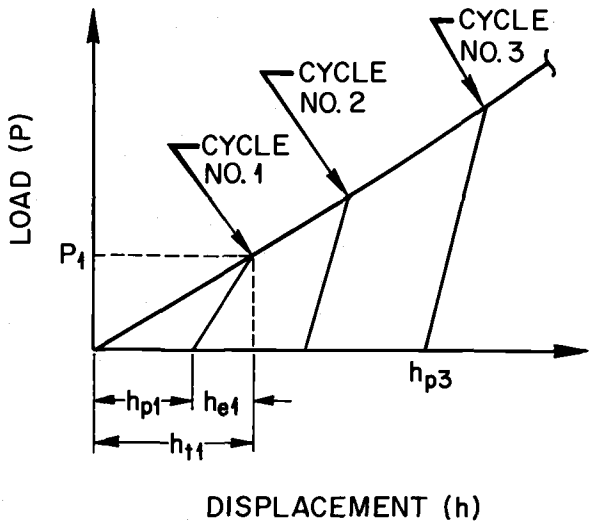

FIG. 5—*Schematic representation of the relationship between indentation load and penetration depth of the ball indenter as observed by increased cyclic loading. Elastic unloading slopes are not parallel because of increased spherical deformation volume as the load is increased.*

where

n = strain-hardening exponent, and
K = strength coefficient.

It should be noted that this representation is not a necessary requirement for determining the indentation-derived σ_t-ϵ_p data as will be shown later (Eqs 2 and 3), but it can be used to determine the strain-hardening exponent over the ϵ_p range of interest. Furthermore, a single power curve may not fit the entire σ_t-ϵ_p curve as noted in ASTM Test Method for Tensile Strain-Hardening Exponent (n-Values) of Metallic Sheet Materials (E 646-78).

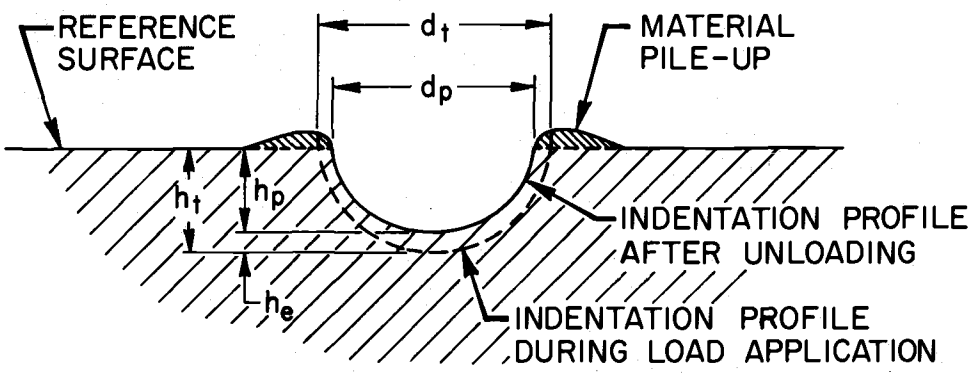

FIG. 6—*Illustration of ball indentation geometries before and after load application (the material pileup is exaggerated).*

The computer program is used to solve the following equations and to thereby determine the flow curve from the ABI data.

$$\epsilon_p = 0.2\, d_p/D \tag{2}$$

$$\sigma_t = 4P/\pi d_p^2 \delta \tag{3}$$

where

$$d_p = \{0.5\, CD\, [h_p^2 + (d_p/2)^2]/[h_p^2 + (d_p/2)^2 - h_p D]\}^{1/3} \tag{4}$$

$$C = 5.47P(1/E_1 + 1/E_2) \tag{5}$$

$$\delta = \begin{cases} 1.12 & \phi \leq 1 \\ 1.12 + \tau \ln\phi & 1 < \phi \leq 27 \\ \delta_{max} & \phi > 27 \end{cases} \tag{6}$$

$$\phi = \epsilon_p E_2/0.43\sigma_t \tag{7}$$

$$\delta_{max} = 2.87\alpha_m \tag{8}$$

$$\tau = (\delta_{max} - 1.12)/\ln(27) \tag{9}$$

In the above equations, σ_t is the true stress, ϵ_p is the true-plastic-strain, d_p is the plastic indentation diameter, D is the diameter of the ball indenter, P is the applied indentation load, h_p is the plastic indentation depth, E_1 is the elastic modulus of the indenter, E_2 is the elastic modulus of the test material, δ is a parameter whose value depends on the stage of development of the plastic zone beneath the indenter, α_m is a parameter proportional to the strain rate sensitivity of the test material or specimen (e.g., for low strain-rate-sensitive materials $\alpha_m = 1.0$), and "ln" is the natural logarithm.

It can be seen that d_p appears on both sides of Eq 4; the computer program solves this equation by iteration. Equations 3, 6, and 7 also have to be solved by iteration, since σ_t depends on δ, which depends on ϕ, which depends on σ_t. The computer program is used also to fit the ABI-derived σ_t-ϵ_p data (calculated using Eqs 2 and 3) by linear regression analysis to the relationship of Eq 1 and to determine the strain-hardening exponent (n) and the strength coefficient (K). The previous equations provide means for predicting the homogeneous portion of the stress/strain curve from indentation data.

Yield Strength

For each ABI loading cycle, the total penetration depth (h_t) is measured while the load is being applied, then converted to a total indentation diameter (d_t) using the following equation

$$d_t = 2(h_t D - h_t^2)^{0.5} \tag{10}$$

Data points from all loading cycles up to $d_t/D = 1.0$ are fit by linear regression analysis to the following relationship

$$P/d_t^2 = A(d_t/D)^{m-2} \tag{11}$$

where P is the applied indentation load, m is Meyer's coefficient, and A is a test material (or specimen) parameter obtained from the regression analysis of test data of d_i/D versus P/d_i^2. The test material parameter (A) is then used to calculate the yield strength (σ_y) of the material using the following equation

$$\sigma_y = B_m A \tag{12}$$

where B_m is a material-type constant (e.g., a single value of $B_m = 0.2285$ (Ref *2*) is applicable to all carbon steels whether cold rolled, hot rolled, or irradiated). The value of B_m for each class or type of material is determined from regression analysis of various tensile yield-strength values (measured from specimens with different heat treatments and flow properties and machined from different orientations) and their corresponding "A" values as measured from entire ABI curves (up to $d_i/D = 1.0$). In Eq 12 above, the units of A and σ_y should be the same. The ABI approach to determine yield strength eliminates the need to measure material pileup except for residual stress evaluation and thereby significantly reduces testing time and thus cost. A major reason for the success of the above ABI procedure for determining yield strength from ABI measurements is that the yield strength, strength coefficient, Lüders strain (ϵ_L), and strain hardening exponent are governed by the following relationship [*8*]

$$\ln (K/\sigma_y) = \epsilon_L - n \cdot \ln \epsilon_L \tag{13}$$

Previous work by Au et al. [*10*] on ferritic steel was not successful in determining the yield strength of ferritic steels from instrumented ball indentation. In that work, backward extrapolation of their true-stress/true-plastic-strain curve could result in underestimating the yield strength by as much as 70% or more. The current ABI procedure for calculating the yield strength is applicable to all metallic materials whether they exhibit Lüders strain or not. However, the value of B_m will be different for each class of materials (e.g., 0.191 for SS) and should be determined experimentally. Furthermore, empirical Eq 12 might be written in the following generic form

$$\sigma_y = b_m + B_m A \tag{14}$$

where b_m is a class-of-material yield-strength offset-constant. The values of b_m and B_m can be determined from the linear regression analysis of plotting σ_y values from tensile tests versus "A" values obtained from ABI tests on the same materials.

Results and Discussion

The bench-top configuration of the stress-strain microprobe was used to test laboratory specimens of A533, A537, and A508 nuclear pressure vessel steels obtained from the Electric Power Research Institute (EPRI). The ABI-measured yield strength and strain-hardening exponent were in very good agreement with those from tension test results (Ref *15*) as shown in Table 1. It should be noticed that, in Ref *15*, tension test results were reported from one specimen only for each material. If more tension specimens were tested (e.g., duplicates in each of the three orientations), a statistical comparison between average ABI and average tension test results could have been made. The ABI-measured strain-hardening exponent was compared to the tensile true uniform elongation since for materials exhibiting a power-law flow curve, it can be mathematically proven that the two values should be equal (see Appendix). Several resistance spot welds made from 1020 carbon steel and 2219 alu-

TABLE 1—*Comparison of ABI and uniaxial test results on four heats of nuclear pressure vessel steels.*

Heat No. and Specimen No.	ABI-True Stress/ True-Plastic Strain Equation	ABI-Yield Strength, MPa	Uniaxial Tensile (Ref *15*)	
			Yield, MPa	Uniform Elongation, %
1b K	σ_t(MPa) = 1006 $\epsilon_p^{0.138}$	428		
EEB-T22	σ_t(MPa) = 972 $\epsilon_p^{0.135}$	426	445	13.9
SA 533-B	σ_t(MPa) = 999 $\epsilon_p^{0.139}$	424		
1b L	σ_t(MPa) = 1060 $\epsilon_p^{0.137}$	451		
EFB-T33	σ_t(MPa) = 1045 $\epsilon_p^{0.140}$	435	453	12.1
SA 533-B	σ_t(MPa) = 1069 $\epsilon_p^{0.139}$	450		
5b A	σ_t(MPa) = 912 $\epsilon_p^{0.143}$	373		
GCB-T69	σ_t(MPa) = 854 $\epsilon_p^{0.141}$	359	355	18.9
SA 508 Cl 1	σ_t(MPa) = 829 $\epsilon_p^{0.135}$	362		
	σ_t(MPa) = 849 $\epsilon_p^{0.139}$	369		
7b A	σ_t(MPa) = 989 $\epsilon_p^{0.138}$	424		
GBB-T54	σ_t(MPa) = 960 $\epsilon_p^{0.131}$	435	386	13.6
SA 537 Cl 2	σ_t(MPa) = 902 $\epsilon_p^{0.126}$	436		

minum sheets were also tested successfully (weld nugget, HAZ, and base metal) at various strain rates. The ABI results and the microstructural evaluation are given in detail in Ref 7. An example of the true-stress/true-plastic-strain curves of these spot welds is shown in Fig. 7. This figure shows that the microprobe system is capable of determining the gradients of yield strength and flow properties in very small areas. Such a capability is essential in determining the structural integrity of spot welds and in improving the welding procedures. Figure 7 shows that the weld nugget and HAZ stress-strain curves are higher than the base metal for the 1020 carbon steel (weld over-matching), while the weld nugget and HAZ stress-strain curves were lower than the aluminum base metal (weld under-matching).

In-Situ ABI Testing of Structural Components

A flat 347 stainless steel (SS) specimen obtained from an aerospace alloy (Heat No. F846) was tested prior to testing the 347 SS pipe to establish a comparison between ABI and tension test results. The ABI-measured (from one seven-cycle test) yield strength of 315.8 MPa was in good agreement with the tensile yield strength of 317.2 MPa (indicated on this material's test report). A total of five ABI tests were then performed on the 114 mm outer diameter 347 SS pipe (5 mm thick) containing a circumferential weld (308 SS). The testing head of the portable/in-situ stress-strain microprobe system was clamped on the pipe using four 90° V-blocks as shown in Fig. 4. This mounting method allowed the head to be rotated 360° and clamped rigidly for ABI testing at any location of the weld, HAZ, or the base metal. A value of B_m = 0.191 (Ref *2*) was used for all ABI tests on stainless steel samples and pipe materials.

The engineering ultimate strength (UTS) can be calculated from the ABI test results as follows

$$\text{UTS} = K \cdot (n/e)^n \tag{15}$$

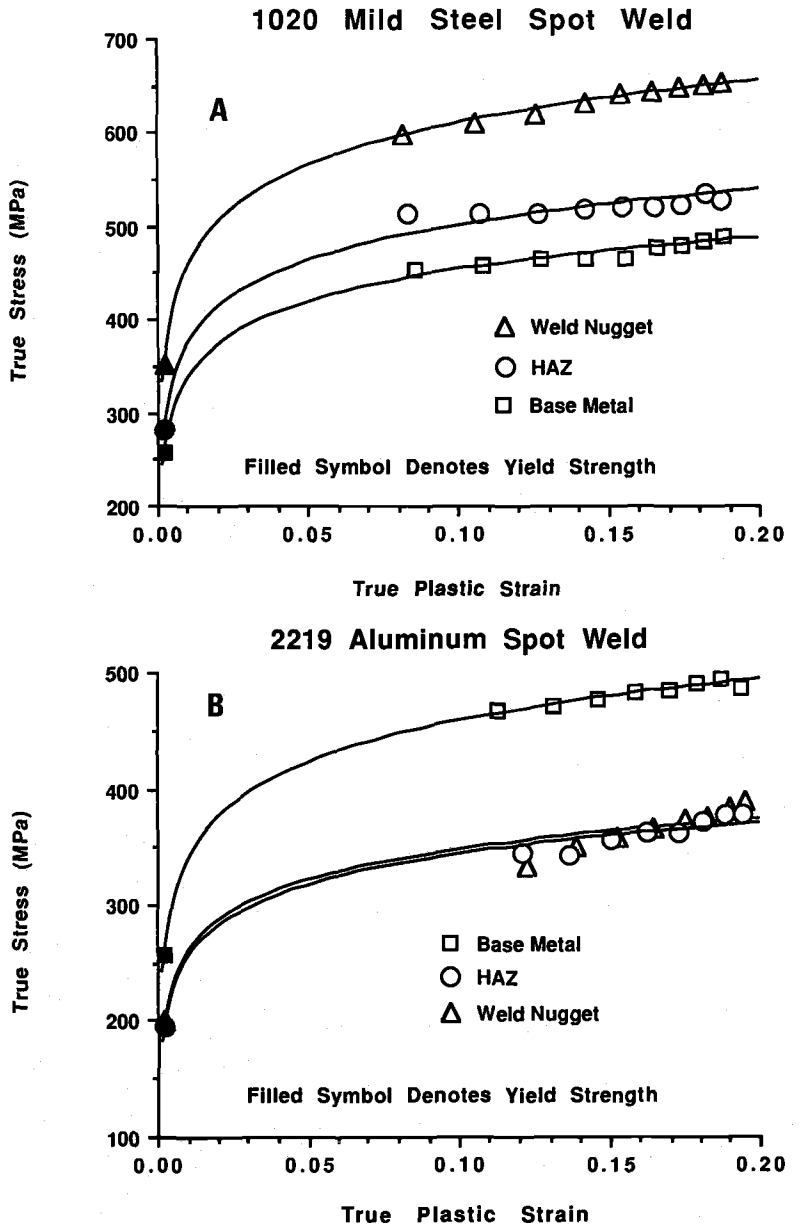

FIG. 7—*Example of ABI test results on spot welds:* (a) *1020 steel and* (b) *2219 aluminum.*

The Brinell hardness number (HB) can also be determined from the ABI test using the maximum indentation load (P_{max} in kg) and the final impression diameter (d_f in mm) and the indenter diameter (D in mm) using the following equation (from ASTM Test Method for Brinell Hardness of Metallic Materials, ASTM E 10-84)

$$HB = 2P_{max}/[\pi D(D - (D^2 - d_f^2)^{0.5})] \tag{16}$$

An example of the in-situ ABI test results from the welded 347 SS pipe is shown in Fig. 8, and the results are summarized in Table 2.

The above ABI test results show that the flow properties measured by the microprobe at three circumferential weld areas are in good agreement with each other and are consistently slightly lower than those at the base metal and the HAZ test locations. The above in-situ tests also successfully demonstrate the potential applicability of the microprobe system to nondestructively test welded pipes and pressure vessels in the petroleum, fossil and nuclear power plants, etc.

Fracture Toughness

A simple technique is described [*2,4*] for estimating the fracture toughness by coupling the ABI-derived flow properties with a modified but empirically calibrated critical fracture strain model. This technique is currently limited to ductile fracture applications.

The critical fracture strain model for ductile fracture prediction can be expressed in the form [*16,17*]

$$K_{JIc} = \text{constant } (\epsilon_f^* \cdot l_0^* \cdot E \cdot \sigma_y)^{0.5} \tag{17}$$

where K_{JIc} is the initiation fracture toughness calculated from J_{Ic}, ϵ_f^* is the critical fracture strain, l_0^* is the characteristic distance ahead of the crack tip over which the strain must exceed ϵ_f^*, E is the elastic modulus, and σ_y is the yield strength. The modification [*18*] of this model involved: (1) the use of measured uniform strain from tension tests or the strain-hardening exponent from ABI tests instead of the critical fracture strain value required in the original model, and (2) the assumption of an empirically calibrated value for the characteristic distance, l_0^*, for each class of material. The ABI test technique used in this work provides an alternative method to determine the yield strength, σ_y, and the strain-hardening exponent, n, (for most metals exhibiting a power law behavior one can mathematically prove that the strain-hardening exponent, n, is equal to the uniform ductility, ϵ_u) in a nondestructive manner, which will be more favorable over tension testing for field applications and when limited materials are available.

The determination of the critical fracture strain, ϵ_f^*, requires testing of several circumferentially notched round tension specimens, each having a different value of its notch root radius. Since this approach is costly, values of the critical fracture strain, ϵ_f^*, were not determined for the materials used in this work and "n" values were used instead.

The modified critical strain model can now be written as

$$K_{JIc} = \text{constant } (n \cdot l_0^* \cdot E \cdot \sigma_y)^{0.5} \tag{18}$$

The characteristic distance, l_0^*, for ductile fracture is usually a multiple of the interparticle spacing and should be regarded as essentially an empirically obtained quantity. Although this dimension is presumably of relevance to the microstructural aspects of fracture initiation, it is plausibly related to the yield strength, strain-hardening exponent (a measure of work hardening), and the strength coefficient of the test material. However, more research is needed to better quantify and define this dimension in order to be able to use this method of estimating fracture toughness for applications where this characteristic distance is expected to change (e.g., due to radiation embrittlement).

Since the critical fracture strain, ϵ_f^*, values were not determined experimentally, strain-hardening values were used in the calculations [*2,4*]. Although such a substitution has no theoretical basis, it was considered reasonable since the critical fracture strain is often

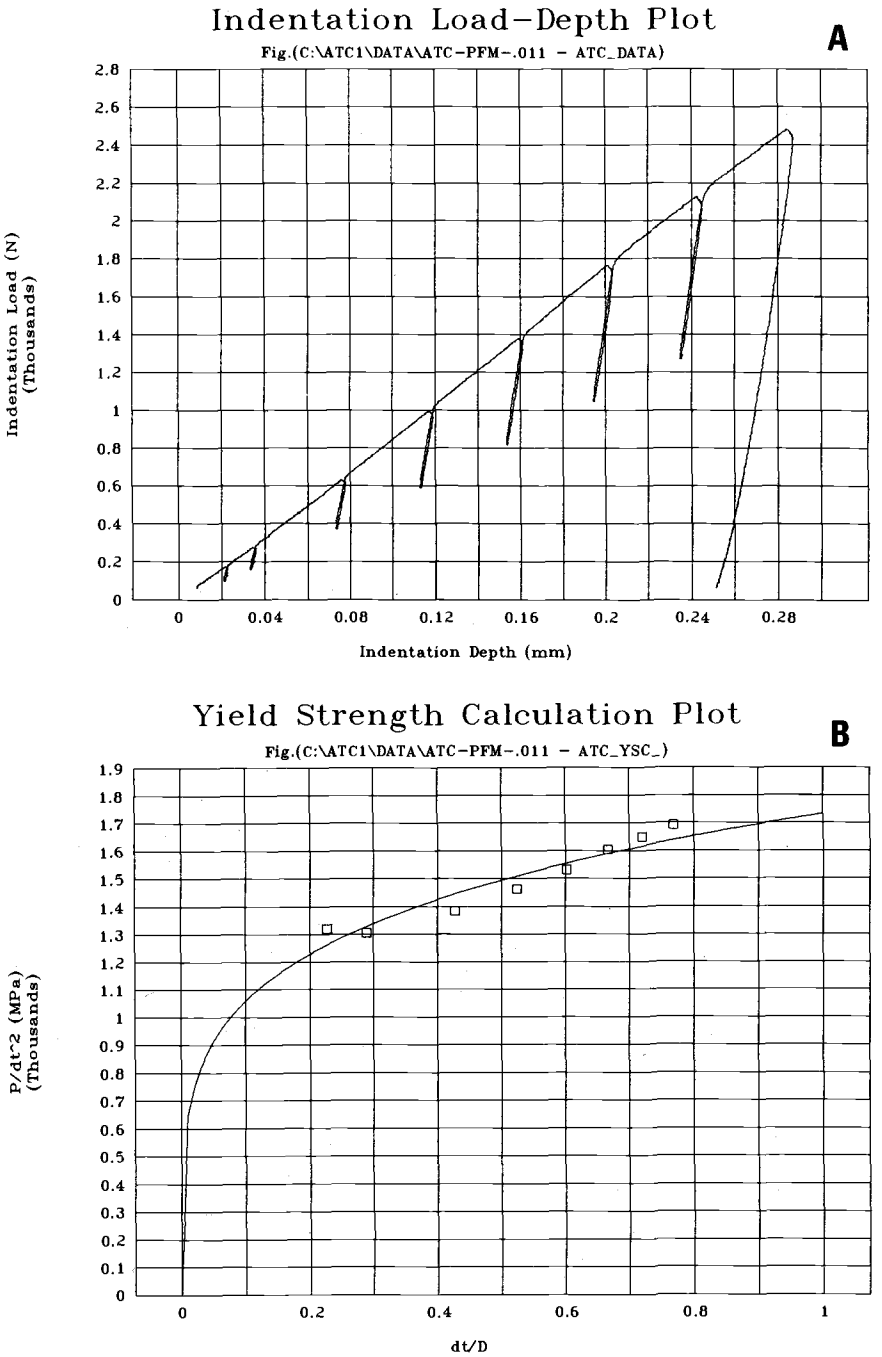

FIG. 8—*In-situ ABI test results of the HAZ in welded 347 stainless steel pipe using a 1.57-mm-diameter tungsten carbide ball indenter:* (a) *indentation load-depth plot,* (b) *yield strength calculation plot,* (c) *true-stress/true-plastic-strain data and curve fitting,* (d) *log true-stress/log true-plastic-strain* (*slope is equal to strain-hardening exponent,* n).

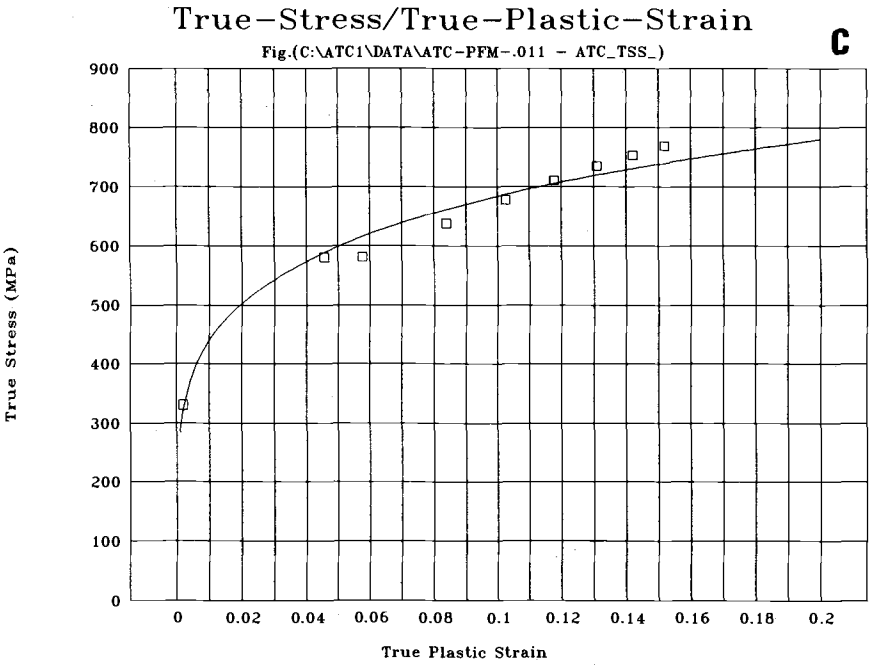

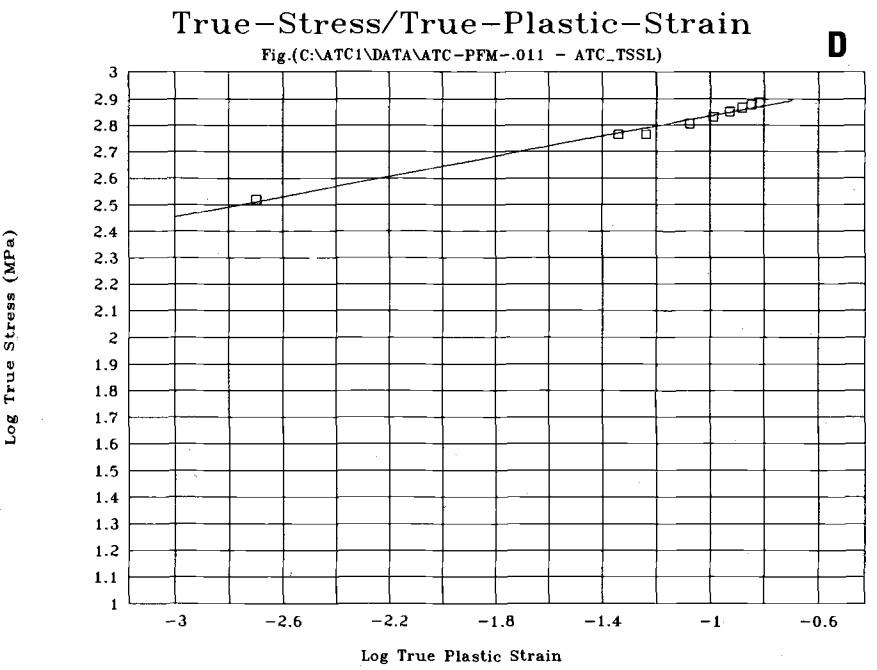

FIG. 8—*Continued.*

TABLE 2—*Summary of in-situ ABI test results from welded 347 SS pipe.*

Test Area	ABI-True Stress/ True-Plastic Strain Equation	ABI-Yield Strength, MPa	Ultimate Strength, MPa	Brinell Hardness
Weld Metal (308 SS)				
Test No. 1	$\sigma_t(\text{MPa}) = 990\ \epsilon_p^{0.198}$	283	589	169
Test No. 2	$\sigma_t(\text{MPa}) = 920\ \epsilon_p^{0.190}$	283	555	164
Test No. 3	$\sigma_t(\text{MPa}) = 971\ \epsilon_p^{0.190}$	300	586	172
HAZ				
Test No. 4	$\sigma_t(\text{MPa}) = 1060\ \epsilon_p^{0.191}$	331	638	186
Base Metal (347 SS)				
Test No. 5	$\sigma_t(\text{MPa}) = 1097\ \epsilon_p^{0.197}$	325	654	188

proportional to the uniform strain for a smooth tensile specimen [*19*]. The proportionality constant would thus be included in the constant coefficient of Eq 18. The value of 3.00 for this constant is good for steels whether in the irradiated [*18*] or deformed [*20*] condition; however, this value might be different for other classes of materials such as titanium or aluminum alloys, and further research is needed to determine the appropriate value of this constant via empirical calibration.

For estimating fracture toughness in certain applications, ABI testing can augment or replace tension testing because it is simple, fast, nondestructive, and can be performed in-situ, using the field microprobe apparatus, to evaluate deformed components and aged and embrittled structural components (provided that characteristic distance values are available from open literature). Furthermore, the ABI technique uses a very small volume of test material. Hence, it could prove valuable in new alloy development and when limited amounts of material are available. Other applications might include weld characterization and qualification, testing of near-net-shape manufactured components, and residual life assessment.

A new empirical model, used successfully in this work for estimating the fracture toughness in A508 Class 4 forging, is described by the following equation

$$K_{\text{JIc}} = \text{constant}\ (K \cdot d \cdot n \cdot \sigma_y)^{0.5} \tag{19}$$

where d is the grain size of the test material, K is the strength proportionality constant, n is the strain-hardening exponent, and σ_y is the yield strength. The remaining parameter needs to be estimated and verified by correlations with more extensive database. This model eliminates the need for the characteristic distance and uses three parameters measured from ABI tests (namely, σ_y, K, and n). Furthermore, the grain size could be determined, nondestructively, in the field for structural components using portable metallography equipment. However, more fracture toughness and ABI measurements are needed to quantify the applicability of this model to many heats of materials.

A total of twelve ABI tests were conducted on a 12-mm-thick slice of A508 Class 4 forging obtained from Westinghouse Plant Apparatus Division, Pa. The fracture toughness of this material measured from 25.4-mm-thick specimen tested at room temperature (Specimen I.D.: BW281, composition F, 2004) was 204 MPa$\sqrt{\text{m}}$. Using the results from the twelve ABI tests and the model of Eq 18 and using an assumed characteristic distance (l_0^*) of 350 μm (0.01378 in.)—as reported earlier for A533 Grade B Class 1 steel by Ritchie et al. [*17*]—the average estimated fracture toughness was 207 MPa$\sqrt{\text{m}}$ with a standard deviation of 4 MPa$\sqrt{\text{m}}$.

Another twelve ABI tests were conducted on the side surfaces far from the fracture planes of four 25.4-mm-thick compact specimens (1TCS) of the same A508 Class 4 forging material used above. These specimens were tested previously according to ASTM Test Method for J_{Ic}, A Measure of Fracture Toughness (E 813-89), and their fracture toughness values for Specimens 1 through 4 were 292, 249, 196, and 180 MPa$\sqrt{m}$, respectively. The results are summarized in Table 3, where a value of 350 μm was assumed for the characteristic distance for the model of Eq 18. For estimating fracture toughness from ABI test results using the model of Eq 19, the constant was taken as 97 and measured grain size values of 50, 41, 52, and 39 μm were used for Specimens 1 through 4, respectively. Table 3 shows a fair agreement between 13 each ABI-estimated fracture toughness values using the models of Eqs 18 and 19 and those measured from four J_{Ic} tests. These results also demonstrate the need for further development of the proposed models.

In summary, the results of the ABI tests on several metallic samples and structural components (including welds and HAZs) are reproducible and show excellent agreement with the results from standard tension tests. Furthermore, automation of the ball indentation test makes it accurate, simple, strain rate controlled, fast (less than 10 min per test), and economical (cheaper than a destructive tension test, particularly for irradiated materials) for both field and laboratory applications. It should be emphasized here that results from ABI tests conducted under multiaxial compression loading may not correlate with results from uniaxial tension tests conducted on materials that exhibit different behavior under tensile or compression loading, such as those fabricated from powder compacts. Some fracture toughness values estimated from ABI data are in good agreement with those measured using the unloading compliance technique. For others, better correlations need to be

TABLE 3—*Comparison of estimated (using ABI data) and measured fracture toughness values for A508 class 4 forging tested at room temperature.*

Specimen/ ABI Test No.	ABI Yield Strength, MPa	ABI Flow Properties Equation, MPa	ABI Estimated Fracture Toughness, MPa$\sqrt{m}$		Measured Fracture Toughness, MPa$\sqrt{m}$ (From J_{Ic})
			Eq 18	Eq 19	
Specimen No. 1					
Test No. 13	560	$\sigma_t = 1275\ \epsilon_p^{0.134}$	220	212	
Test No. 14	547	$\sigma_t = 1276\ \epsilon_p^{0.138}$	221	213	292
Test No. 19	538	$\sigma_t = 1330\ \epsilon_p^{0.141}$	221	218	
Specimen No. 2					
Test No. 22	578	$\sigma_t = 1319\ \epsilon_p^{0.134}$	225	199	
Test No. 23	565	$\sigma_t = 1371\ \epsilon_p^{0.140}$	227	204	249
Test No. 21	555	$\sigma_t = 1330\ \epsilon_p^{0.135}$	220	196	
Specimen No. 3					
Test No. 27	561	$\sigma_t = 1350\ \epsilon_p^{0.140}$	226	227	
Test No. 28	567	$\sigma_t = 1421\ \epsilon_p^{0.143}$	229	237	196
Test No. 25	576	$\sigma_t = 1198\ \epsilon_p^{0.122}$	214	203	
Test No. 24	585	$\sigma_t = 1182\ \epsilon_p^{0.124}$	217	204	
Specimen No. 4					
Test No. 16	566	$\sigma_t = 1175\ \epsilon_p^{0.124}$	214	174	
Test No. 29	574	$\sigma_t = 1248\ \epsilon_p^{0.127}$	217	182	180

developed and verified. A larger database is needed to quantify the accuracy of estimated fracture toughness values. Furthermore, the microprobe capabilities for nondestructive in-situ testing of structural components (base metal, weld, HAZ) have been demonstrated. Such capabilities will be very useful in testing nuclear pressure vessels during their design service life and before and after their thermal annealing. Moreover, the use of the microprobe for in-situ testing could eliminate both cutting of boat samples from nuclear pressure vessel and machining of irradiated specimens. For nuclear pressure vessels with a thin layer of inside stainless steel cladding, local areas (approximately 3 mm in diameter) of the cladding can be ABI tested and then removed (drilled) such that the thick ferritic steel material underneath can be ABI tested successfully.

Conclusions

1. The ABI technique was very successful in accurately determining the yield strength and measuring the flow properties of welds in several metallic materials (e.g., A533-B-1, A508, A537, 1020, 347 SS, 308 SS, and 2219 aluminum).
2. The gradients in mechanical properties of weld metals and their HAZs were successfully determined from ABI tests conducted on both laboratory specimens as well as on structural components (114 mm outer diameter 347 stainless steel pipe containing a circumferential weld).
3. The ABI results from tests conducted on curved structures were in excellent agreement with those from tests conducted on similar flat specimens.
4. In-situ (field) ABI tests on pipes were proven to be *nondestructive,* accurate, reproducible, and fast (less than 10 min per test). Hence, the microprobe system could be used for life-time extension evaluation of nuclear power plant components (e.g., pressure vessels and their supports). One prime example could be to determine the degree of ductility recovery of aged nuclear pressure vessels following their thermal annealing.
5. Preliminary results of fracture toughness estimation methods from ABI measurements show varying degrees of agreement with conventional data and should be investigated further.

APPENDIX

Relationship between True Uniform Elongation and Strain-Hardening Exponent

The homogeneous plastic flow portion of the true-stress (σ_t)/true-plastic-strain (ϵ_p) curve can be represented by the familiar power law equation

$$\sigma_t = K \epsilon_p^n \tag{A1}$$

where

n = strain-hardening exponent
K = strength coefficient

Load = P
Cross-sectional area of tensile specimen = A
Instantaneous specimen gage length = l
Volume of specimen gage section = V

$$P = \sigma_t A \tag{2}$$

$$dP = \sigma_t dA + A\, d\sigma_t \tag{3}$$

Since necking occurs at maximum load, $dP = 0$

$$d\sigma_t/\sigma_t = -dA/A \tag{4}$$

From constancy of volume ($V = Al$), $dV = A\,dl + l\,dA = 0$

$$-dA/A = dl/l \tag{5}$$

Since $dl/l \equiv d\epsilon_p$ (6)
Combining Eqs 4, 5, and 6

$$\sigma_t = d\sigma_t/d\epsilon_p \tag{7}$$

From Eqs 1 and 7

$$K\,\epsilon_p^n = K\,n\,\epsilon_p^{n-1} \tag{8}$$

At necking, the true-plastic strain (ϵ_p) equals the true uniform elongation (ϵ_u).
Therefore from Eq 8

$$n = \epsilon_u \tag{9}$$

Hence, the true uniform elongation is numerically equal to the strain-hardening exponent.

References

[1] Haggag, F. M., "Field Indentation Microprobe for Structural Integrity Evaluation," U.S. Patent No. 4,852,397, 1 Aug. 1989.

[2] Haggag, F. M., Nanstad, R. K., Hutton, J. T., Thomas, D. L., and Swain, R. L., "Use of Automated Ball Indentation Testing to Measure Flow Properties and Estimate Fracture Toughness in Metallic Materials," *Applications of Automation Technology to Fatigue and Fracture Testing, ASTM STP 1092*, A. A. Braun, N. E. Ashbaugh, and F. M. Smith, Eds., American Society for Testing and Materials, Philadelphia, 1990, pp. 188–208.

[3] Haggag, F. M., Nanstad, R. K., and Braski, D. N., "Structural Integrity Evaluation Based on an Innovative Field Indentation Microprobe," *Innovative Approaches to Irradiation Damage and Failure Analysis*, D. L. Marriott, T. R. Mager, and W. H. Bamford, Eds., PVP Vol. 170, American Society of Mechanical Engineers, New York, 1989, pp. 101–107.

[4] Haggag, F. M. and Nanstad, R. K., "Estimating Fracture Toughness Using Tension or Ball Indentation Tests and a Modified Critical Strain Model," *Innovative Approaches to Irradiation Damage and Failure Analysis*, D. L. Marriott, T. R. Mager, and W. H. Bamford, Eds., PVP Vol. 170, American Society of Mechanical Engineers, New York, 1989, pp. 41–46.

[5] Haggag, F. M., Wong, H., Alexander, D. J., and Nanstad, R. K., "The Use of Field Indentation Microprobe in Measuring Mechanical Properties of Welds," *Recent Trends in Welding Science and Technology, TWR'89*, Proceedings of the 2nd International Conference on Trends in Welding Research, Gatlinburg, TN, 14–18 May, 1989, 1990, pp. 843–849.

[6] Haggag, F. M., "Application of Flow Properties Microprobe to Evaluate Gradients in Weldment Properties," *International Trends in Welding Sciences and Technology*, S. A. David and J. M. Vitek, Eds., ASM, Metals Park, OH, 1993, pp. 629–635.

[7] Haggag, F. M. and Bell, G. E. C., "Measurement of Yield Strength and Flow Properties in Spot Welds and Their HAZs at Various Strain Rates," *International Trends in Welding Science and Technology*, S. A. David and J. M. Vitek, Eds., ASM, Metals Park, OH, 1993, pp. 637–642.

[8] Haggag, F. M., "The Role of Lüders Strain in Predicting Flow Properties in Steels from an Instrumented Hardness Test," M.S. thesis, Department of Chemical and Nuclear Engineering, University of California, Santa Barbara, CA, 1980.

[9] Haggag, F. M. and Lucas, G. E., "Determination of Lüders Strains and Flow Properties in Steels from Hardness/Microhardness Tests," *Metallurgical Transactions A*, Vol. 14A, 1983, pp. 1607–1613.

[10] Au, P., Lucas, G. E., Sheckherd, J. W., and Odette, G. R., "Flow Property Measurements from Instrumented Hardness Tests," *Non-destructive Evaluation in the Nuclear Industry,* American Society for Metals, Metals Park, OH, 1980, pp. 597–610.

[12] Tabor, D., *The Hardness of Metals,* Clarendon Press, Oxford, 1951.

[13] Francis, H. A., "Phenomenological Analysis of Plastic Spherical Indentations," *Transactions of the ASME,* July 1976, pp. 272–281.

[14] George, R. A., Dinda, S., and Kasper, A. S., "Estimating Yield Strength from Hardness Data," *Metal Progress,* May 1976, pp. 30–35.

[15] Server, W. L. and Oldfield, W., "Nuclear Pressure Vessel Steel Data Base," EPRI Report NP-933, Electric Power Research Institute, Palo Alto, CA, 1978.

[16] Pandey, R. K., and Banerjee, S., "Strain Induced Fracture in Low Strength Steels," *Engineering Fracture Mechanics,* Vol. 10, 1978, pp. 817–829.

[17] Ritchie, R. O., Server, W. L., and Waullaert, R. A., "Critical Fracture Stress and Fracture Strain Models for Prediction of Lower and Upper Shelf Toughness in Nuclear Pressure Vessel Steels," *Metallurgical Transactions A,* Vol. 10A, 1979, pp. 1557–1570.

[18] Haggag, F. M., Reuter, W. G., and Server, W. L., "Recovery of Fracture Toughness of Irradiated Type 347 Stainless Steel Due to Thermal Stress Relief: Metallographic and Fractographic Studies," *Proceedings of the 2nd International Symposium on Environmental Degradation of Materials in Nuclear Power Systems-Water Reactors,* Monterey, CA, 9–12 Sept. 1985, pp. 509–514.

[19] Pavinich, W. A., "The Effect of Neutron Fluence and Temperature on the Fracture Toughness and Tensile Properties for a Linde 80 Submerged Arc Weld," *Proceedings of the 2nd International Symposium on Environmental Degradation of Materials in Nuclear Power Systems-Water Reactors,* Monterey, California, 9–12 Sept. 1985, pp. 485–495.

[20] Haggag, F. M., Server, W. L., Lucas, G. E., Odette, G. R., and Sheckherd, J. W., "The Use of Miniaturized Tests to Predict Flow Properties and Estimate Fracture Toughness in Deformed Steel Plates," *Journal of Testing and Evaluation,* JTEVA, Vol. 1, No. 1, January 1990, pp. 62–69.

Charpy Impact Testing

Arvind S. Kumar,[1] *Brian S. Louden,*[1] *Frank A. Garner,*[2] *and Margaret L. Hamilton*[2]

Recent Improvements in Size Effects Correlations for DBTT and Upper Shelf Energy of Ferritic Steels

REFERENCE: Kumar, A. S., Louden, B. S., Garner, F. A., and Hamilton, M. L., **"Recent Improvements in Size Effects Correlations for DBTT and Upper Shelf Energy of Ferritic Steels,"** *Small Specimen Test Techniques Applied to Nuclear Reactor Vessel Thermal Annealing and Plant Life Extension, ASTM STP 1204,* W. R. Corwin, F. M. Haggag, and W. L. Server, Eds., American Society for Testing and Materials, Philadelphia, 1993, pp. 47–61.

ABSTRACT: Currently available correlations for the effects of specimen size on the upper shelf energy (USE) were developed for relatively ductile steels and do not serve as well when the steels become embrittled. Size effects correlations were developed recently for the impact properties of less ductile HT9 to be applied to other initially more ductile steels as they lose their ductility during irradiation. These new correlations successfully predict the ductile brittle transition temperature (DBTT) and USE of full-size Charpy specimens based on subsize specimen data. The new DBTT and the USE correlations were tested against published experimental data on other ferritic steels and shown to perform successfully at lower USE, particularly when both notched and precracked specimens as well as notched-only specimens were employed.

KEYWORDS: upper shelf energy, ductile brittle transition temperature, normalization, correlation, HT9 size effect, precrack, embrittlement

Neutron-induced embrittlement of ferritic steels is of great importance for pressure vessels of existing fission reactors and for structural applications in breeder reactors and future fusion reactors. The development of a comprehensive database on embrittlement, however, requires large irradiation volumes at uniform temperatures and neutron fluxes. The current irradiation facilities are extremely limited in irradiation space. In addition, there is invariably only a limited amount of archival material available for irradiation.

It generally requires approximately ten full-size Charpy specimens to obtain the ductile brittle transition temperature (DBTT) and the upper shelf energy (USE) of steels. Acquiring data at several neutron fluences, compositions, and temperatures for a comprehensive database, therefore, is not possible in a reasonable period of time. Therefore, it is necessary to rely on subsize specimens for determining the impact properties of irradiated materials. The volume occupied by one full-size specimen is equivalent to eighteen third-size specimens, almost sufficient to provide two impact energy versus temperature curves.

For fusion and breeder reactor applications, both the temperatures and displacement levels required are larger than those of fission reactor pressure vessel steels. The use of high flux facilities, such as the High Flux Isotope Reactor (HFIR) and the Fast Flux Test Facility

[1] Chairman and professor of nuclear engineering, and graduate student, respectively, University of Missouri, Rolla, MO 65401.

[2] Staff scientist and senior scientist, respectively, Pacific Northwest Laboratory, Richland, WA 99352.

(FFTF), is associated with other experimental difficulties. HFIR is a highly thermalized reactor with a large gamma heating rate (20 to 50 W/g). This can cause large temperature differences across full-size (1 by 1 by 5.5 cm) Charpy impact specimens, leading to difficulties in maintaining a uniform specimen temperature. Fast reactor facilities, such as the FFTF, do not suffer as much from the large gamma heating problem, since the gamma heating rate is lower (4 to 5 W/g). However, the minimum irradiation temperature for FFTF is 360°C, above the values relevant for current fission reactor surveillance work and for some fusion reactor applications.

Another option is to irradiate specimens in relatively low-power (1 to 10 MW) research reactors and to develop size effects correlations that are valid for all similar steels at comparable service temperatures and levels of embrittlement.

The subsize Charpy specimens used in this study and others [*1–9*] are considerably smaller than the full-size specimens. Decreasing the specimen dimensions lowers both the USE and the DBTT. Furthermore, the reduced dimensions of subsize specimens lead toward a plane stress condition, in contrast to the approximately plane strain conditions operating in full-size specimens. A plane strain condition promotes brittle failure, whereas plane stress promotes ductile failure, thereby reducing the apparent DBTT. In addition, the reduced fracture volume of subsize specimens reduces their USE. The reductions in USE and DBTT due to reduced specimen dimensions require that methodologies be developed for predicting USE and DBTT of full-size specimens from subsize specimen data since it is the properties of full-size impact specimens that are used in structural design. A number of attempts have been made in the past to develop the required methodologies, including the development of correlation factors that can be used to normalize USE and DBTT. The normalized values are equal to the ratios of the measured values and the respective normalization factors and are intended to be invariant with specimen size.

Prior efforts to correlate subsize and full-size USE involved the use of mainly ductile materials (USE $>$ 200 J) in the unirradiated state [*3–10*]. A normalization factor equal to the fracture volume below the notch root has worked well to normalize the USE of these materials. The fracture volume was taken as Bb^2 in the studies of Lucas et al. [*5,6*] and as $(Bb)^{3/2}$ in the studies of Corwin et al. [*3,4*], where B is the specimen width and b is the ligament size. Neither of these normalization factors was successful in correlating subsize and full-size specimen data for ferritic materials HT9 and A533B when they were tested [*10,11*] in a relatively brittle condition (USE $\sim$ 100 J).

In an earlier stage of the current study, a normalization factor was developed for correlating the USE of full-size and subsize specimens of brittle materials [*10*]. The normalization factor worked well for HT9 in the T-L orientation, having a full-size USE of 129 J. The normalization factor also worked well for other materials in a relatively brittle state (USE $\sim$ 100 J), such as the 9Cr-1Mo-V-Nb in the quenched T-L and L-T conditions [*4*] and 12Cr-1Mo-V-W steel in the L-T orientation [*3*] used by other investigators. It has been found that the same normalization factor also works well for A533B pressure vessel steel [*12*] in a brittle state (USE $\sim$ 60 J). The success of this correlation relies on the fact that all of the specimen dimensions and the stress concentration factor at the notch root are important in the fracture of brittle materials, and these are all taken into account in the correlation.

However, none of the correlations developed so far work well for both ductile and brittle materials. Figure 1 shows how the earlier correlations of Corwin et al. [*3,4*] and the current authors [*10*] compare. Proximity of the normalized USE of full-size (marked 1), half-size (marked 2), and third-size (marked 3) specimens shows a good correlation. Note that Corwin's model works better at high USE and our earlier model worked better at low USE. Such a situation exists when a normally ductile steel, such as a reactor pressure vessel, embrittles significantly under neutron irradiation.

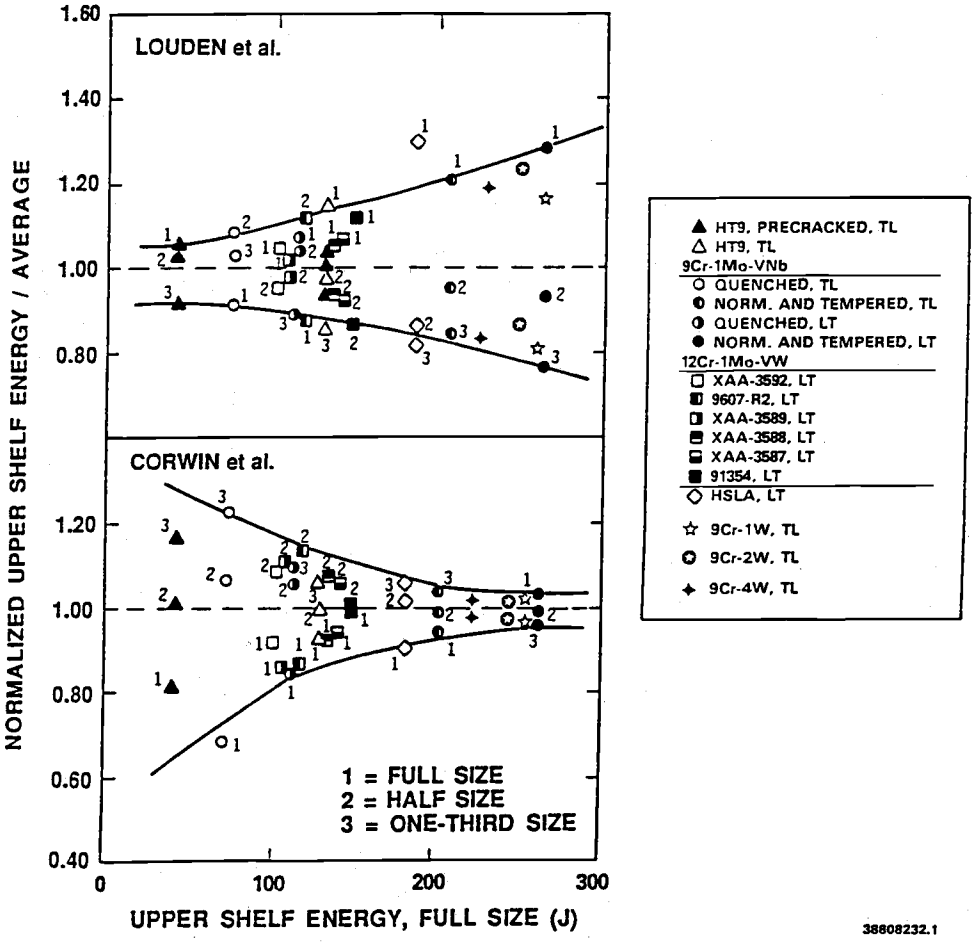

FIG. 1—*Comparison of normalized USEs of various materials. The numbers 1, 2, and 3 refer to full-, half-, and third-size specimens. All specimens are notched-only except those labeled precracked. TL means that the specimen axis is perpendicular to the rolling direction. LT means that the axis of the specimen is parallel to the rolling direction. The specimen geometries are shown in Fig. 2:* (a) *normalization of Louden et al.* [10]; (b) *normalization of Corwin et al.* [3,4].

A normalization factor was developed in this study to correlate the USE of full-size and subsize specimens without regard to the ductile or brittle nature of the material. This approach is based on the partitioning of the USE into two contributions, that is, that required for crack initiation and that for crack propagation. To accomplish this partition, both precracked and notched-only specimens were used. Whereas the USE of notched-only specimens is the sum of both crack initiation and propagation energies, the USE of precracked specimens reflects only crack propagation. The difference in USE values for the two types of specimens is thus a good estimate of the crack initiation energy. The utility of this partition will be expanded on in later sections of the paper.

In addition to the correlation for USE, a correlation methodology is also presented to predict the shift in DBTT for full-size specimens based on subsize data. No other correlations in the published literature have been successful.

Experimental Procedure

Dimensions for both full-size and subsize specimens are given in Fig. 2. The full-size specimen dimensions are in accordance with ASTM Methods for Notched Bar Impact Testing of Metallic Materials (E 23–92). While there are no standards available for subsize specimens, the dimensions used in this study for half- and third-size specimens are similar to those used in other investigations [*1–8*]. Note that the half-size and third-size specimens have the same length in order to allow sufficient span for the striker to pass through the specimen placement apparatus.

All specimens used in this study were machined from HT9 plate material of heat 9607R2, which was manufactured by Electralloy Corporation for the U.S. DOE fusion materials program. The chemical composition and tensile properties of this heat are given elsewhere [*13*]. A series of heat treatments was performed on the plate stock to produce a tempered martensitic structure with a hardness of 255 DPH and a prior austenite grain size of ASTM 5 to 6. All specimens were taken from the base material in the transverse (T-L) orientation, in which the long axis of the specimen lies perpendicular to the rolling direction and the direction of elongation of the grains is the same as the direction in which the crack propagates. Specimens in this orientation will have the least resistance to fracture and will therefore provide a minimum estimate of fracture energy.

Adjustable anvils and interchangeable crossheads made possible the testing of different size specimens on the same instrumented drop tower. Data from each test were recorded on a digital oscilloscope and transferred to a desktop computer for storage and analysis.

Calibration of the instrumented hammer was performed by adjusting the load signal gain so that the maximum load obtained during dynamic testing was the same as the maximum

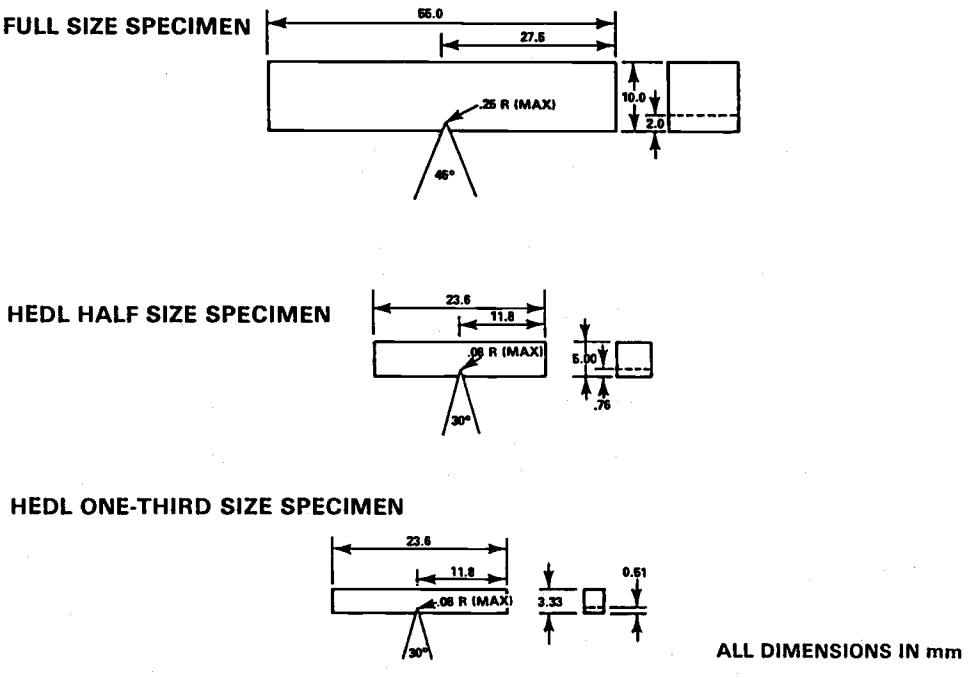

FIG. 2—*Dimensions of full-size and subsize Charpy specimens.*

load determined during the slow bend testing of a strain-rate insensitive alloy (6061 aluminum in the T51 heat-treatment) [*1*]. In addition, a static calibration of the load cell was performed to ensure that its response was linear over the desired range.

The impact velocity of the crosshead was calibrated by attaching a 1-cm-long flag to the crosshead positioned so that the flag passed an infrared sensor just prior to impact, causing a change in voltage during interruption by the flag. The duration of this change was measured and the velocity was calculated as the average of at least ten calibration runs.

Temperature control for full-size specimens was accomplished in a conditioning chamber where high temperatures were attained with a heated stream of air and low temperatures were reached by using cold nitrogen gas. Temperature control was achieved by adjusting the rate of gas flow into the conditioning chamber. Each specimen was kept at the test temperature for 5 to 10 min prior to testing to ensure temperature stabilization to within 2°C. Temperature control for the subsize specimens used the same sources of heated or cooled gas as the full-size specimens, but because the conditioning chamber was designed specifically for full-size specimens, the miniature specimens were manually placed and aligned in the testing position and the gas was directed across the specimen surface. A thermocouple spot-welded across from the notch (opposite the surface being impacted) was used to monitor the temperature for each test. The uncertainties in temperature were measured to be very small (<5°C) as documented by Hu and Gelles [*1*].

Specimen placement for full-size specimens was achieved by air-driven pistons that moved the specimen from its initial position into and out of the conditioning chamber and finally into the testing position using a rotary positioning arm. ASTM E 23-92 provides for a maximum 5-s delay between obtaining the desired temperature and impacting the specimen. For full-size specimens, the elapsed time between the exit of the sample from the conditioning chamber and the impact was approximately 0.2 s. For subsize specimens, no specimen transfer was involved.

Results and Discussion

The results of the impact testing on HT9 in the T-L orientation are shown in Fig. 3 and Tables 1 and 2. The methodologies of correlating the DBTT and USE of full-size and subsize data are presented below. The DBTT is defined as the temperature at which the impact energy is equal to half of the sum of USE and lower shelf energy. Since the lower shelf energy is very small in comparison to USE, DBTT is determined at half of USE in those cases in which lower shelf energy data are not available.

DBTT Correlation

The DBTT shift due to irradiation-induced embrittlement in some ways is similar to the shift induced by precracking the Charpy specimens since the precracking increases the DBTT in a manner similar to irradiation. The DBTT shifts due to precracking are larger for subsize specimens than for full-size specimens. The smaller the size, the larger the shift in DBTT. Figure 3 shows the fracture energy of full-, half-, and third-size specimens as a function of the test temperature. Both notched-only and precracked specimen test results are presented.

The assumptions underlying the DBTT correlation are as follows. It is assumed that the fracture is controlled by the maximum elastic tensile stress, σ', ahead of the crack tip. The maximum tensile stress can be raised to the critical stress for crack propagation, σ_f^*, by the strain hardening in the plastically deformed zone at the crack tip. When the stress at the crack tip reaches the critical value, σ_f^*, also called the fracture stress, the crack propagates.

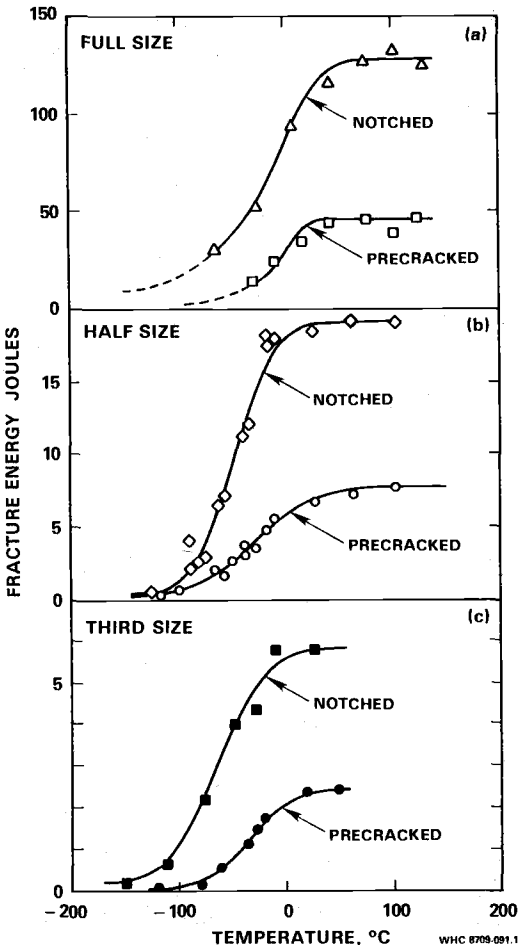

FIG. 3—*Dependence of fracture energy on temperature for both notched, precracked, and notched-only specimens:* (a) *full-size;* (b) *half-size;* (c) *third size.*

It has been shown by Lucas et al. [5] that this fracture stress is a material property and is independent of specimen size.

It is proposed that a normalized value of DBTT can be defined as the ratio of the measured value of DBTT and σ'. Furthermore, it is hypothesized that σ' controls the fracture process. Therefore, σ' is assumed to be the same for notched and precracked specimens.

TABLE 1—*HT-9 Charpy data—DBTT* [10].

Specimen Size	DBTT, K		ΔDBTT,[a] K
	Notched-only	Precracked	
Full size	259	266	7
Half size	226	246	20
Third size	209	239	30

[a] ΔDBTT = precracked DBTT − notched DBTT.

TABLE 2—*HT-9 Charpy data—USE* [10].

Specimen Size	USE, J		Ratio[a]
	Notched-only	Precracked	
Full size	129	44	2.9
Half size	19	8	2.4
Third size	6	2	3

[a] Ratio = notched USE/precracked USE.

In order to calculate σ' we must know the specimen dimensions, the stress concentration factor, K_t, at the notch root, and P_m, the maximum load developed in the Charpy impact test. σ' is given by

$$\sigma' = (K_t)(3P_mL)/(2Bb^2) \tag{1}$$

where B is the specimen width and b is the ligament size. The value of P_m was not investigated in this study. In addition, the value of P_m was not available from other published studies. An alternative approach was used to calculate it based on the fracture stress, σ_f^*, data of Lucas et al. [5]. In another paper, Lucas et al. [6] showed that the fracture stress is related to P_m by the equation

$$\sigma_f^* = 6.52P_m/Bb$$

which leads to tl ɜ equation

$$P_m = \sigma_f^* Bb/6.52 \tag{2}$$

Equation 1 then reduces to

$$\sigma' = 0.23K_tL\sigma_f^*/b \tag{3}$$

The stress concentration factor, K_t, is given by the following equation [14]

$$K_t = \frac{2(b/R + 1) - f(b/R + 1)^{1/2}}{4(b/R + 1)/g - 3f}$$

$$f = \frac{2(b/R + 1)(b/R)^{1/2}}{(b/R + 1)\arctan (b/R)^{1/2} + (b/R)^{1/2}}$$

$$g = \frac{4(b/R)^{3/2}}{3[(b/R)^{1/2} + (b/R - 1)\arctan (b/R)^{1/2}]}$$

where R is the radius of the notch root, and b is defined above. The calculated values of K_t are 4.8, 7.6, and 6.3 for full-, half-, and third-size specimens, respectively. Note that K_t for the third-size specimen is smaller than that for the half-size specimen.

Figure 4 shows the normalized DBTT of the full-size specimens plotted against the normalized DBTT of the subsize specimens. The data of Lucas et al. [6] for three steel compositions are shown in addition to the notched-only and precracked specimen data for HT9

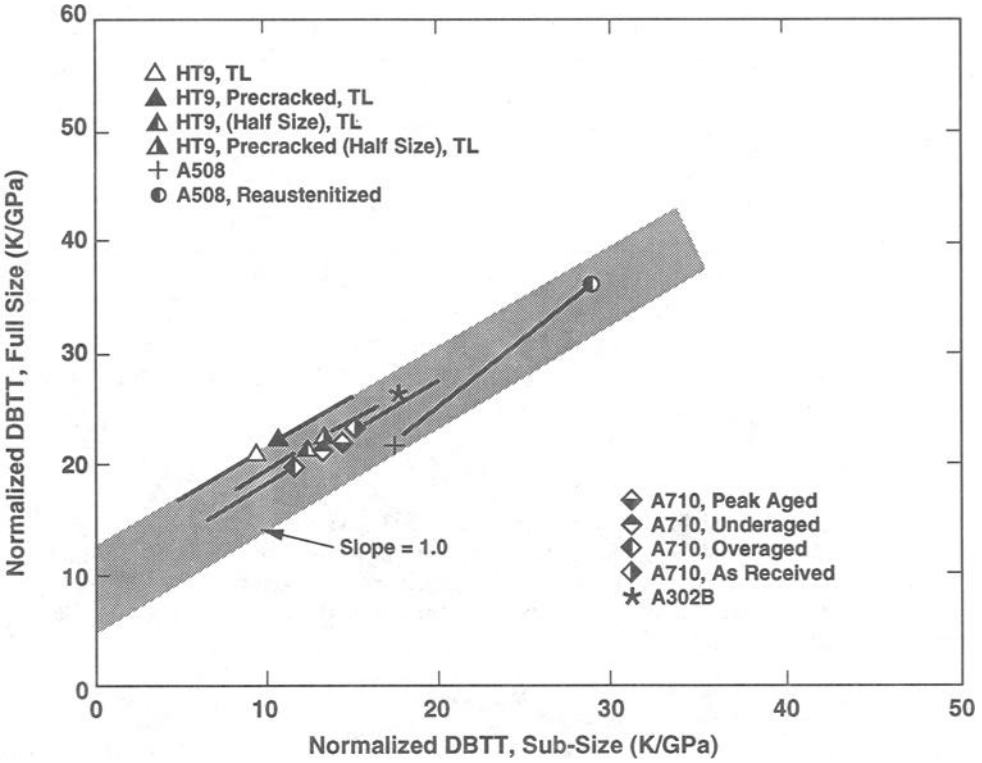

FIG. 4—*Comparison of normalized DBTT for various materials. All subsize specimen data points correspond to third-size specimens except those marked half size. The dimensions for HT9 are given in Fig. 1; the third-size specimens of all of the other materials used by Lucas et al. were 3.3 by 3.3 by 18.3 mm with a 0.67-mm-deep notch and a root radius of 0.076 mm. Note that for specimen groups of one size and one material, the data points can be connected with a line of slope near unity.*

used in this study. The DBTT data for HT9 are presented in Table 1. The data of Lucas et al. were only available for full- and third-size specimens.

The topmost line joins data points marked (△) and (▲) where △ represents notched third-size specimens and ▲ represents the precracked third-size specimens of HT9. The line has a slope of approximately unity. Similarly, the notched and precracked half-size data of HT9 are joined by a line of slope ~1.

The data of Lucas et al. [*6*] on A710, in four different thermally aged conditions, are also connected by a line of slope unity. In addition, the data on the A508 in the two conditions also lie on a line with a slope approximately equal to unity.

The above-mentioned variation of the normalized values of DBTT ($DBTT_n$) with precracking or thermal aging leads to the conclusion that

$$(DBTT_n)_{\text{full size}} = (DBTT_n)_{\text{subsize}} + \text{constant} \tag{4}$$

Alexander and Klueh [*15*] reached a similar conclusion with one exception. In their case the DBTT was not normalized. The constant in Eq 4 is dependent on both specimen size and material. For a given material and specimen size, however, the constant is independent of the alloy pretreatment condition (thermomechanical treatment). In this context, the embrittlement introduced by precracking represents another alloy condition. Therefore, the

shifts in $DBTT_n$ due to thermal treatment or precracking are equal for full-size and subsize specimens

$$\Delta(DBTT_n)_{\text{full size}} = \Delta(DBTT_n)_{\text{subsize}} \tag{5}$$

Because the embrittlement introduced by precracking can be considered a simulation of the embrittlement introduced by a thermomechanical treatment or by irradiation, the shift in $DBTT_n$ due to neutron irradiation will probably be the same for full-size and subsize specimens. Tests are in progress to confirm this proposal [*12*].

Hu and Gelles [*1*] irradiated precracked half-size specimens of HT9 base metal to 3×10^{22} n/cm^2 ($E > 0.1$ MeV) or ~15 dpa in EBR-II at temperatures ranging from 390 to 450°C. The results are shown in Fig. 5. The choice of precracked specimens in these experiments was based on the observations that the precracked data had less scatter than the notched data had in tests of the unirradiated material. The shift in DBTT, ΔDBTT, was 124°C for irradiation at 390°C, but with increasing irradiation temperature, the ΔDBTT decreased. Based on the ΔDBTT correlation methodology described above, the predicted ΔDBTT for precracked full-size specimens at 390°C and 3×10^{22} n/cm^2 would be ~83°C since the ratio of ΔDBTT and σ' must be the same for full-size and half-size specimens. The values of σ' for full-size and half-size HT9 specimens are 13.25 and 20.31 GPa, respectively, as calculated by Eq 4.

USE Correlation

For correlating the upper shelf energy (USE) of full-size and subsize specimens, testing of both notched and precracked specimens is required. The difference (ΔUSE) between the USE of notched and precracked specimens provides an estimate of the energy expended in plastic deformation and strain hardening to raise the maximum normal stress below the notch root to the fracture level. ΔUSE is thus an estimate of the crack initiation energy and should scale with the fracture volume equal to Bb^2, where B is the specimen width and b is the ligament size. The USE of Charpy specimens can thus be written as the sum of two terms as follows

$$\text{USE} = \Delta\text{USE} + \text{USE}_p \tag{6}$$

where ΔUSE is the crack initiation energy and USE_p is the crack propagation energy. USE_p is equal to the upper shelf energy of precracked specimens. The crack initiation energy can be written from the above equation as the difference between the upper shelf energy of notched-only and precracked specimens and is given by

$$\Delta\text{USE} = \text{USE} - \text{USE}_p \tag{7}$$

A normalized value of ΔUSE (ΔUSE_n) is defined as the ratio of the measured ΔUSE and the fracture volume. It is proposed that ΔUSE_n be equal for full-size and subsize specimens.

$$(\Delta\text{USE/Fracture volume})_{\text{full size}} = (\Delta\text{USE/Fracture volume})_{\text{subsize}} \tag{8}$$

The measured values of USE and ΔUSE_n are presented in Table 3 for the HT9 specimens used in this study. The last column in the table is the ratio of the ΔUSE_n and the average of the ΔUSE_n values of full-, half-, and third-size specimens. The normalized values are within ±7% of the average value, showing an excellent correlation.

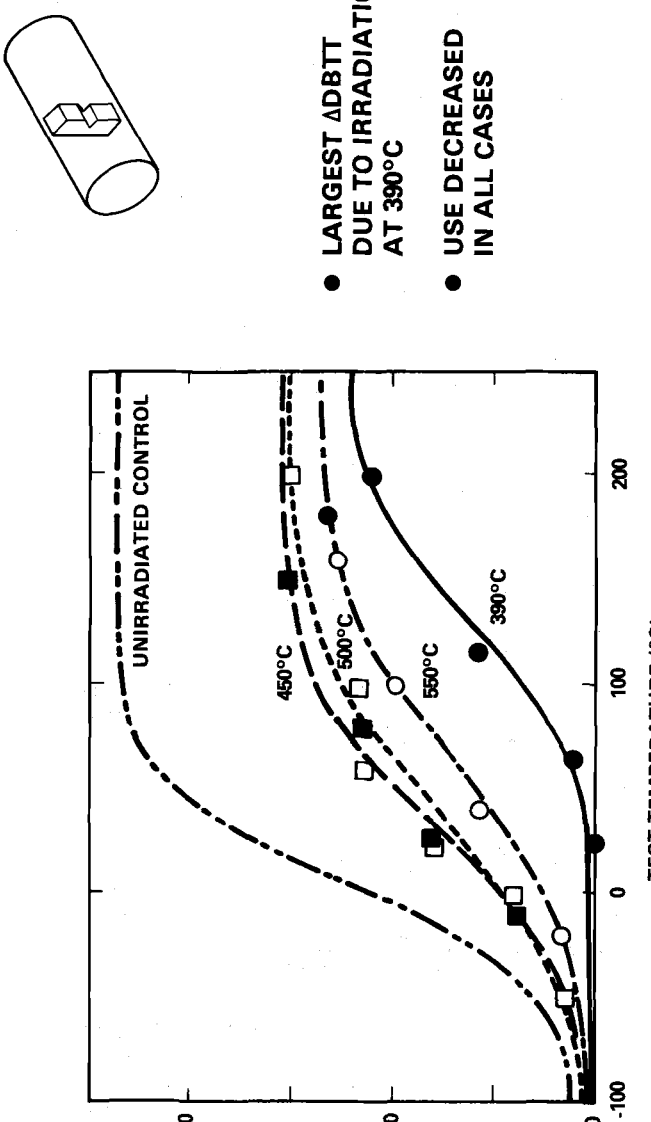

FIG. 5—*Results of Charpy impact tests of half-size specimens of HT9 irradiated to 3 × 10^{22} n/cm² (E > 0.1 MeV) or ~15 dpa in EBR-II at temperatures ranging from 390 to 450°C showing normalized fracture energy as a function of test temperature. The normalized energy is equal to the measured value divided by the product of the ligament size and the width.*

TABLE 3—*HT-9 Charpy—USE* [11].

Specimen Size	Notched-only, J	Precracked, J	ΔUSE Fracture Volume, J/cm³	ΔUSE_n,[a] Average[b]
Full size	129	44	133	1.01
Half size	19.1	8.0	123	0.93
Third size	5.9	2.3	140	1.06

[a] ΔUSE_n = ΔUSE/fracture volume.
[b] Average of ΔUSE_n of full-, half-, and third-size specimens.

A similar agreement between ΔUSE_n of full-size and subsize specimens of A533B pressure vessel steel was observed in the work of Rosinski et al. [*12*]. The normalized values were within ±8% of the average values of ΔUSE_n, showing once again an excellent correlation.

Having determined ΔUSE_n of full-size specimens from subsize data, one must determine USE_p in order to predict USE of full-size specimens. It is shown in Table 2 that the ratio of USE and USE_p is invariant with specimen size. Therefore

$$(USE/USE_p)_{\text{full size}} = (USE/USE_p)_{\text{subsize}} \tag{9}$$

Equations 7 through 9 are three equations in three unknowns, USE, ΔUSE, and USE_p, for full-size specimens. The corresponding values for subsize specimens are to be determined by experimental measurements. USE of full-size specimens can thus be determined by testing subsize specimens and using Eqs 7 through 9.

Alexander and Klueh [*15*] have also analyzed the effects of specimen size on the USE of a number of steels. The data were obtained from the work of Corwin and Houghland [*4*], Abe et al. [*9*], Lucas et al. [*6*], Alexander and Klueh [*15*], Klueh et al. [*16–19*], and Corwin et al. [*3*]. The analysis of Alexander and Klueh [*15*] involves normalization of USE values by the fracture volume equal to $(Bb)^{3/2}$. The normalization works well for steels having USE > 150 J.

However, when we examine their normalized data for those steels that have low values of USE, the normalized values of full-, half-, and third-size specimens are substantially different. In addition, Alexander and Klueh [*15*] did not include two steel conditions from the work of Corwin and Houghland [*4*]. These were 9Cr-1Mo-V-Nb steels in the quenched T-L and L-T orientations. The USE for these steels was quoted to be 111 and 72 J, respectively. Table 4 compiles the USE for five steels with low USE selected from the tables of Alexander and Klueh [*15*]. It also includes the 9Cr-1Mo-V-Nb steels in the quenched T-L and L-T orientations from Corwin and Houghland [*4*]. The full-size USE of these steels ranges from 64 to 115 J. When these values are normalized by the fracture volume, the largest difference between the full-size and subsize normalized values is 76%. This occurs when the full-size USE is 72 J for the Alloy 30176, as shown in the last column of Table 4.

The variation of the normalized USE values of subsize specimens with those of the full-size specimens in the work of Alexander and Klueh [*15*] is presented in Figs. 6 and 7. It is to be emphasized that USE values in the figures are normalized and not the actual values. Proximity of the data points to the diagonals in the figures represents a perfect correlation. It is important to note that all of the data points lie considerably above the diagonal, i.e., the subsize specimens exhibit a substantially higher ductility than the full-size specimens. It is evident that the volume normalization used by Alexander and Klueh [*15*], Corwin et al. [*3*], and Corwin and Houghland [*4*] is not adequate for normalizing the USE values of low-ductility steels.

TABLE 4—*Steels with low USE compiled from tables in Refs* 4 *and* 15.

Alloy	Nominal Composition	Specimen Size	Upper Shelf Energy, J	Normalized USE, J/cm³
3589	12Cr-1Mo-V-W-2Ni	Full	106	148
3589	12Cr-1Mo-V-W-2Ni	Half	17.8	182
3592	12Cr-1Mo-V-W-2Ni[a]	Full	101	141
3592	12Cr-1Mo-V-W-2Ni[a]	Half	16.5	169
9607-R2	12Cr-1Mo-V-W	Full	115	161
9607-R2	12Cr-1Mo-V-W	Half	20.8	213
9607-R2	12Cr-1Mo-V-W	Third	5.9	206
A302B	1.5Mn-0.2C	Full	64	89
A302B	1.5Mn-0.2C	Third	3.8	131
A508B[b]	0.6Mn-0.6Ni-0.6Mo-0.2C	Full	74	103
A508B[b]	0.6Mn-0.6Ni-0.6Mo-0.2C	Third	4.1	143
30176	9Cr-1Mo-V-Nb[c]	Full	111	153
30176	9Cr-1Mo-V-Nb[c]	Half	18.9	194
30176	9Cr-1Mo-V-Nb[c]	Third	5.7	199
30176	9Cr-1Mo-V-Nb[d]	Full	72.0	100
30176	9Cr-1Mo-V-Nb[d]	Half	15.3	156
30176	9Cr-1Mo-V-Nb[d]	Third	5.1	176

[a] Adjusted.
[b] Reaustenitized.
[c] Quenched, L-T.
[d] Quenched, T-L.

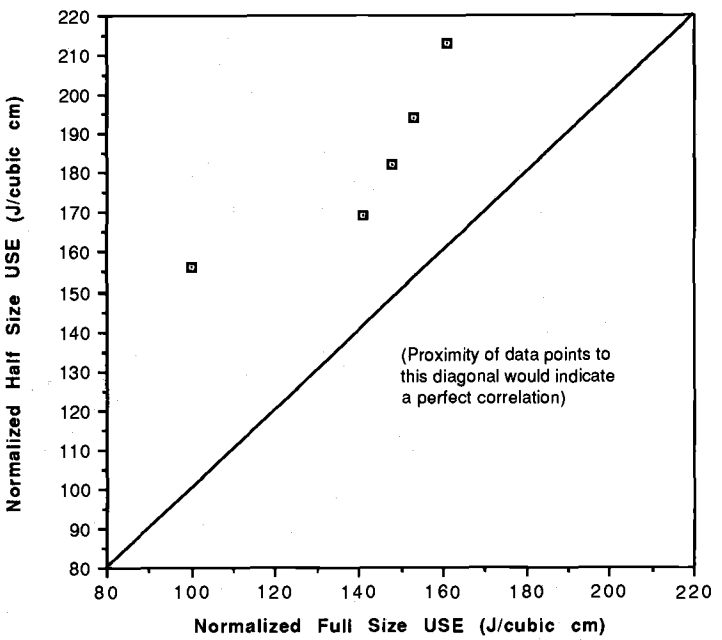

FIG. 6—*Normalized USE of half-size specimens as a function of normalized USE of full-size specimens from Corwin and Houghland* [4] *and Alexander and Klueh* [15].

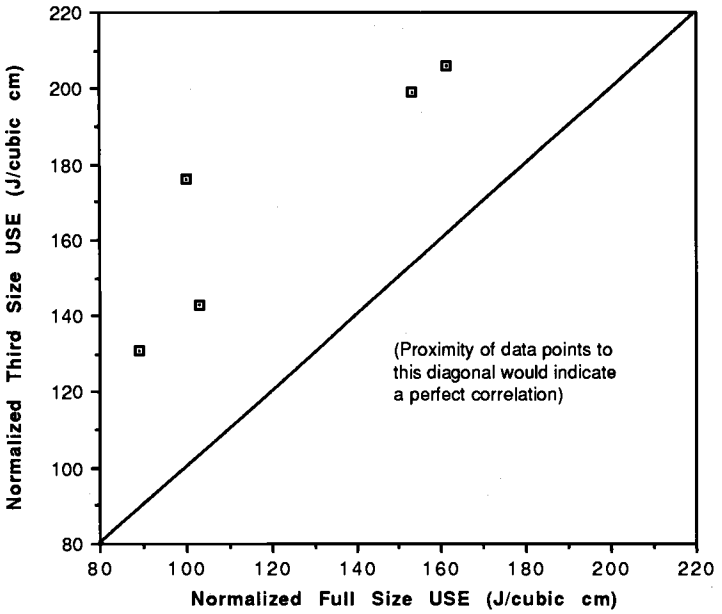

FIG. 7—*Normalized USE of third-size specimens as a function of normalized USE of full-size specimens from Corwin and Houghland* [4] *and Alexander and Klueh* [15].

Conclusion

Volume normalization of USE works well for correlating the USE of full-size and subsize specimens of only high-ductility materials (USE > 150 J). The technique proposed in this paper is expected to be applicable to materials over a wider range of USE values (200 J > USE > 50 J).

This technique uses the difference, ΔUSE, between the USE for notched-only and precracked specimens (USE_p) and correlates it with fracture volume. A normalized value of ΔUSE (ΔUSE_n) is defined as the ratio of the measured ΔUSE and the fracture volume. ΔUSE_n is invariant with specimen size.

$$(\Delta USE/\text{Fracture volume})_{\text{full size}} = (\Delta USE/\text{Fracture volume})_{\text{subsize}}$$

where

$$\Delta USE = USE - USE_p$$

Furthermore, it is shown experimentally that,

$$(USE/USE_p)_{\text{full size}} = (USE/USE_p)_{\text{subsize}}$$

The above equations with the unknowns, USE and USE_p, can be solved to obtain USE for full-size specimens if USE and USE_p for subsize specimens are known from experimental measurements.

In addition, the normalized DBTT shifts due to thermomechanical treatments were found to be independent of specimen size. Normalized DBTT is the ratio of the measured value of DBTT and σ', the maximum elastic tensile stress ahead of the crack tip. If σ' for subsize specimens is known from experimental data, then σ' for full-size specimens can be calculated from Eq 3. The shift in DBTT due to environmental exposure or thermomechanical treatments for full-size specimens can be determined using the following equation if the experimental value of the shift in DBTT for subsize specimens is known.

$$\Delta(\mathrm{DBTT}/\sigma')_{\text{full size}} = \Delta(\mathrm{DBTT}/\sigma')_{\text{subsize}}$$

References

[1] Hu, W. L. and Gelles, D. S., in *Proceedings,* Conference on Ferritic Alloys for Use in Nuclear Energy Technologies, Snowbird, UT, June 1983, p. 631.

[2] Powell, R. W., Johnson, G. D., Hamilton, M. L., and Garner, F. A., in *Proceedings,* ANS International Conference on Reliable Fuels for Liquid Metal Reactors, Tucson, AZ, September 1986, pp. 4–17.

[3] Corwin, W. R., Klueh, R. L., and Vitek, J. M., *Journal of Nuclear Materials,* Vols. 122–123, 1984, p. 343.

[4] Corwin, W. R. and Houghland, A. M., in *The Use of Small-Scale Specimens for Testing Irradiated Material, ASTM STP 888,* W. R. Corwin and G. E. Lucas, Eds., American Society for Testing and Materials, Philadelphia, 1986, p. 325.

[5] Lucas, G. E., Odette, G. R., Sheckherd, J. W., McConnell, P., and Perrin, J., in *The Use of Small-Scale Specimens for Testing Irradiated Material, ASTM STP 888,* W. R. Corwin and G. E. Lucas, Eds., American Society for Testing and Materials, Philadelphia, 1986, p. 305.

[6] Lucas, G. E., Odette, G. R., Sheckherd, J. W., and Krishnadev, M. R., *Fusion Technology,* Vol. 10, 1986, p. 728.

[7] McConnell, P., Sheckerd, J. W., Perrin, J. S., and Wullaert, R. A., *The Use of Small-Scale Specimens for Testing Irradiated Material, ASTM STP 888,* W. R. Corwin and G. E. Lucas, Eds., American Society for Testing and Materials, Philadelphia, 1986, p. 353.

[8] Ferguson, B. L., *Proceedings,* American Institute of Mining, Metallurgical, and Petroleum Engineers, (AIME) Annual Meeting on "What Does the Charpy Test Really Tell Us?," Denver, CO, A. R. Rosenfield et al., Eds., February 1978, American Society for Metals, Metals Park, OH, pp. 90–107.

[9] Abe, F., Noda, T., Araki, H., Okada, M., Narai, M., and Kayano, H., *Journal of Nuclear Materials,* Vol. 150, 1987, pp. 292–301.

[10] Louden, B. S., Kumar, A. S., Garner, F. A., Hamilton, M. L., and Hu, W. L., *Journal of Nuclear Materials,* Vols. 155 to 157, 1988, pp. 662–667.

[11] Kumar, A. S., Garner, F. A., and Hamilton, M. L., in *Effects of Radiation on Materials: 14th International Symposium (Volume II), ASTM STP 1046,* N. H. Packan, R. E. Stoller, and A. S. Kumar, Eds., American Society for Testing and Materials, Philadelphia, 1990, pp. 487–495.

[12] Rosinski, S. T., Kumar, A. S., Cannon, N. S., and Hamilton, M. L., "Application of Subsize Specimens in Nuclear Plant Life Extension," this publication, pp. 405–416.

[13] Lechtenberg, T. A., ADIP Semiannual Progress Report, DOE/ER-0045/8, March 1983, p. 363.

[14] Neuber, H., *Theory of Notch Stresses,* 2nd ed., Springer Publishers, Berlin, 1958, p. 71.

[15] Alexander, D. J. and Klueh, R. L., "Specimen Size Effects in Charpy Impact Testing," *Charpy Impact Test: Factors and Variables, ASTM STP 1072,* J. M. Holt, Ed., American Society for Testing and Materials, Philadelphia, 1990.

[16] Klueh, R. L., Vitek, J. M., and Grossbeck, M. L., *Journal of Nuclear Materials,* Vol. 103–104, 1981, pp. 887–892.

[17] Klueh, R. L., Vitek, J. M., and Grossbeck, M. L., in *Effects of Radiation on Materials: Eleventh Conference, ASTM STP 782,* H. R. Brager and J. S. Perrin, Eds., American Society for Testing and Materials, Philadelphia, 1982, pp. 648–664.

[18] Klueh, R. L., *Metallurgical Transactions A,* Vol. 20A, 1989, pp. 463–470.

[19] Klueh, R. L. and Corwin, W. R., *Journal of Materials Engineering,* Vol. 11, 1989, pp. 169–175.

DISCUSSION

D. J. Alexander[1] (*written discussion*)—Your transition temperature, T_0, is defined at the midpoint of the hyperbolic tangent function, that is, midway between the upper and lower shelves. The example you showed for full-, half-, and third-size specimens indicates a lower shelf of about 30 J for full-size specimens. This seems very high. If additional specimens had been tested at lower temperatures, I am sure the lower shelf would be reduced. This will shift T_0 for full-size specimens to lower temperatures and increase the shift in transition temperature due to precracking for full-size specimens. Please comment on the effects of this change.

A. S. Kumar et al. (*authors' closure*)—Thank you for your comment. We have recalculated the transition temperatures, assuming that the lower shelf is close to zero. The effect of this assumption leads to a shift in the transition temperature of 7 K due to precracking. This value is slightly larger than the value calculated earlier, but is still within the uncertainties of any Charpy data.

A. Kohyama[2] (*written discussion*)—Do you have data indicating some effect of the precracking condition? In other words, how do you optimize the precracking condition to obtain a sufficiently sharp crack with a negligibly small determination zone? How much concern do you have about this variable after neutron irradiation?

A. S. Kumar et al. (*authors' closure*)—The precracking conditions employed in this study were in accordance with ASTM Test Method for Plane-Strain Fracture Toughness of Metallic Materials (E 399), and are described for this study in great detail in Ref *1*. We have confidence in these procedures, which were originally developed by the U.S. breeder reactor program. We have no data from our studies in EBR-II [*2*] that indicate any problem after neutron irradiation.

[*1*] "Alloy Development for Irradiation Performance Quarterly Progress Report for Period Ending June 30, 1980," compiled and edited by B. G. Ashdown, Oak Ridge National Laboratory, DOE/ER-0045/3, U.S. Department of Energy.

[*2*] Hu, W. L. and Gelles, D. S., in *Proceedings*, Conference on Ferritic Alloys for Use in Nuclear Energy Technologies, Snowbird, UT, June 1983, published by the American Institute of Mining, Metallurgical, and Petroleum Engineers, Warrendale, PA, 1984, p. 631.

[1] Oak Ridge National Laboratory, PO Box 2008, Oak Ridge, TN 37831-6151.
[2] University of Tokyo, Hongo, Bunkyo-ku, Tokyo 113, Japan.

Michael P. Manahan Sr.,[1] *James Williams,*[2] *and Richard P. Martukanitz*[3]

Laser Weld Reconstitution of Conventional Charpy and Miniaturized Notch Test (MNT) Specimens

REFERENCE: Manahan, M. P., Williams, J., and Martukanitz, R. P., **"Laser Weld Reconstitution of Conventional Charpy and Miniaturized Notch Test (MNT) Specimens,"** *Small Specimen Test Techniques Applied to Nuclear Reactor Vessel Thermal Annealing and Plant Life Extension, ASTM STP 1204,* W. R. Corwin, F. M. Haggag, and W. L. Server, Eds., American Society for Testing and Materials, Philadelphia, 1993, pp. 62–76.

ABSTRACT: As nuclear power plants approach end-of-license (EOL) and consideration is given to license renewal, there is an ever increasing need to expand the amount of data obtainable from the original surveillance specimens. A laser welding technique to reconstitute broken Charpy specimens is being developed to produce both conventional and miniaturized Charpy specimens. This paper reports on early laser welding development efforts and summarizes previous proof-of-principle experiments on a 1/16 scale miniaturized Charpy test. In order to benchmark the laser welding procedure, the laser-reconstituted specimen data have been compared with the original specimen data. In addition, the microstructure after welding has been examined to ensure that the material in the vicinity of the notch is essentially unchanged after the welding process. Data which characterize the thermal transient during welding are obtained by attaching thermocouples to the specimens. Other important considerations include perturbation of the stress field near the notch, dynamic stress waves, and contact of the weld region with the tup.

Precise control of welding parameters has been demonstrated, heat-affected zones as small as 0.25 mm can be achieved, and sufficient penetration depth can be obtained to enable welding thick sections (1T or greater) to yield conventional Charpy specimens or fracture toughness specimens and thin sections (~5 mm) to yield Miniaturized Notch test (MNT)[4] specimens.

KEYWORDS: Miniaturized Notch Test, Charpy test, laser weld, reconstitution

Miniaturized specimen technology (MST) permits the characterization of mechanical behavior while using a minimum volume of material. Hence, it has many applications, such as nuclear pressure vessel surveillance, failure analysis, and post-irradiation testing. It can also be used to characterize the mechanical behavior of in-service structures and components in cases where small pieces of material can be safely cut out. This paper focuses on the use

[1] President, MPM Research & Consulting, 915 Pike Street, Lemont, PA 16851; adjunct professor of Nuclear Engineering, The Pennsylvania State University, 231 Sackett Building, University Park, PA 16802.

[2] Master's degree candidate, Nuclear Engineering Department, The Pennsylvania State University, 231 Sackett Building, University Park, PA 16802.

[3] Research assistant, Applied Research Laboratory, The Pennsylvania State University, State College, PA 16804.

[4] The processes described are explained in part in U.S. Patent No. 4,567,774, dated 4 Feb. 1986. A patent application on further improvements of the methodology is pending.

of innovative test techniques and the application of laser welding to obtain dynamic Charpy data from very small samples of material.

Reference *1* reported the first successful Charpy specimen miniaturization at a 1/16 size scale (as compared to conventional Charpy specimens). Since this specimen was designed close to the continuum limit of the material, further miniaturization in the cross-sectional dimensions is not possible. However, it may be possible to decrease the length requirement provided a suitable welding procedure can be perfected. To this end, several candidate welding technologies have been investigated and the laser welding process has been pursued. The laser welding approach also has the advantage of easy adaptation to larger cross sections for welding J_{IC} specimens. An example application is welding 1T J_{IC} specimen blanks used in surveillance capsule reinsertion programs [*2*]. This paper presents the results of a laser weld benchmark study using conventional Charpy specimens and summarizes the Miniaturized Notch Test (MNT). Based on the data reported herein, it is feasible to apply laser welding to fabricate MNT specimens using very small volumes of irradiated material.

Laser Weld Reconstitution

Although laser welding was chosen as the preferred method for reconstitution of radioactive materials, several other candidate methods were investigated. The welding approaches considered include: laser welding, electron beam welding, flash welding, arc stud welding, and friction welding. Since reconstitution is geared towards high-activity, hot-cell applications, an important requirement for the welding process is that it should be amenable to remote handling. Another key concern is the amount of material disturbed during the welding process. Two important parameters are the heat-affected zone (HAZ) and the net disturbed material (NDM). We have defined the NDM as the maximum distance (measured normal to the fracture surface) over which metallurgical transformation and/or microstructural changes have occurred. This distance is larger than the HAZ since most welding processes do not produce a planar HAZ which is parallel to the fracture plane. For laser welding, narrow HAZs can be obtained by optimization of three key weld process parameters: laser power, beam velocity, and focal length.

Laser Weld Penetration and HAZ

For the reconstitution of conventional Charpy V-notch specimens, it is desirable to have a single pass weld depth of at least one half of the Charpy thickness (5 mm). This minimum depth enables welding using a two-pass approach. Since the material ablation profile is parabolic, it is possible to adjust the welding parameters to achieve an essentially planar weld parallel to the fracture surface by using a two-pass procedure. In addition, it is best to use run-on and run-off tabs to avoid material distortion as the laser exits the material. The desired 5-mm depth was successfully achieved using a 3.0 kW CO_2 continuous wave laser at a power of 2700 W and speeds of 1.27 and 1.54 cm/s, respectively.

The peak temperature during welding was measured experimentally by attaching thermocouples to the specimen. A computer-controlled data acquisition system was used to collect data at small time intervals during welding to determine the peak of the thermal transient. For nuclear pressure vessel applications, the critical temperature of the fracture process region is taken to be 288°C to ensure that the radiation damage has not been affected. However, future work should focus on determining the maximum temperature allowable for short duration temperature pulses. Based on these measurements, we have concluded that a region extending 4 mm on either side of the weld plane contains material which is

above reactor operating temperature for a short time during laser welding. Therefore, a 10-mm insert was chosen as the smallest insert for laser welding research on conventional Charpy specimens.

Plastic Zone Size Considerations

Other researchers have experimented with inserts as small as 10 mm using arc stud welding and had only limited success [*3,4*]. The poor results obtained using a 10-mm insert may be due to metallurgical changes, plastic zone interference, and/or contact of the tup with the hard HAZ region. At the present time, there are not sufficient data available to come to a definitive conclusion. The concern is that in minimizing the insert size, the weld planes, along with their HAZs, will perturb the plastic zone and influence the local stress field. The Belgians [*4*] have reported a truncation of the plastic zone for the arc stud welding approach when using a 10-mm insert.

The plastic zone normal to the crack plane (PZN) was calculated for test temperatures ranging through the transition region to the upper shelf. These results are summarized in Table 1 for the A302B steel. Based on these PZN data, it was estimated that plastic zone and HAZ interaction will not occur for a 20-mm insert until a 130°C (266°F) test temperature has been reached. For the unirradiated modified A302B material used in the current study, we concluded that inserts larger than about 15 mm would be needed to test on the upper shelf.

The PZN data were compared with earlier arc stud weld data. Battelle Laboratories conducted a study for EPRI on reconstituted Charpy specimens for insert sizes of 22.5 and 10 mm [*3*]. SCK-CEN of Belgium conducted a reconstitution study on A533B HSST 03 steel with 10-mm inserts [*4*]. Both studies used unirradiated A533B steel for Charpy reconstitution, and limited irradiated data were generated in the Battelle work. Overall, application of the PZN criterion for defining the minimum insert size is consistent with the literature data.

At the present time, it is not possible to draw firm conclusions concerning the importance plastic zone and HAZ interaction effects. The preliminary analysis reported here seems to suggest that when the PZN distance is approximately equal to the distance from the crack

TABLE 1—*Change in the plastic zone normal to the crack plane (PZN) as a function of temperature, strain rate, and irradiation for A533 Type B steel with an NDT = −17.8°C (°F).*

	Plastic Zone Normal to Crack Plane (PZN)[a]			
Temperature °C (°F)	Unirradiated Static,[b] PZN, mm (in.)	Irradiated Static, PZN, mm (in.)	Unirradiated Dynamic,[c] PZN_D, mm (in.)	Irradiated Dynamic, PZN_D, mm (in.)
−73.3 (−100)	0.913 (0.0360)	0.574 (0.0226)	0.374 (0.015)	0.229 (0.009)
−45.6 (−50)	1.24 (0.0489)	0.657 (0.0259)	0.510 (0.020)	0.269 (0.0106)
−17.8 (0)	2.27 (0.0894)	0.752 (0.0296)	0.806 (0.032)	0.325 (0.0128)
10 (50)	6.52 (0.257)	0.973 (0.0383)	1.56 (0.062)	0.425 (0.0167)
37.8 (100)	29.34 (1.15)	1.65 (0.0649)	3.95 (0.156)	0.637 (0.0251)
65.6 (150)	34.91 (1.37)	4.32 (0.170)	12.41 (0.489)	1.18 (0.0463)
93.3 (200)	35.96 (1.42)	17.98 (0.708)	28.33 (1.11)	2.79 (0.109)
121.1 (250)	36.95 (1.45)	28.28 (1.11)	29.23 (1.15)	8.34 (0.328)
148.9 (300)	37.88 (1.49)	29.02 (1.14)	30.07 (1.18)	22.9 (0.901)

[a] $PZN = \left(\frac{K}{\sigma_{eff}}\right)^2 \left(\frac{1}{2\pi}\right) \cos^2\left(\frac{\theta}{2}\right) \left[1 + 3\sin^2\left(\frac{\theta}{2}\right)\right] \sin(\theta)$; where: $\theta = 70.83$ for PZN = PZN (max).

[b] Static strain rate = 1×10^{-2}/s; dynamic strain rate = 3×10^{2}/s.

[c] Fluence = 3.2×10^{18} n/cm^2.

plane to the HAZ, energy loss may occur. However, other phenomena such as stress wave reflection during dynamic impact, residual stresses, and the interaction of the relatively hard HAZ with the tup must be carefully assessed in the future.

Comparison of Laser Weld and Conventional Charpy Data

Figure 1 shows the comparison of the laser weld reconstituted data with the conventional specimen data. The laser weld specimens were prepared from the broken halves of the conventional specimens. As shown in Fig. 1, the laser weld specimens prepared using 14 and 20-mm inserts compare well with the conventional specimen data. However, the laser weld specimens prepared using 10-mm inserts yield Charpy energy data below the conventional specimen level above the mid-transition temperature region. Future work should be focused on validating the use of 10-mm inserts for characterization of the 41 J transition temperature.

Miniaturized Notch Test (MNT)

Progress on the development of the MNT has been reported in References *1*, *5*, *6*. This section briefly reviews the key findings related to the MNT. It is anticipated that laser weld reconstitution technology will evolve and eventually be used to reconstitute miniature specimens.

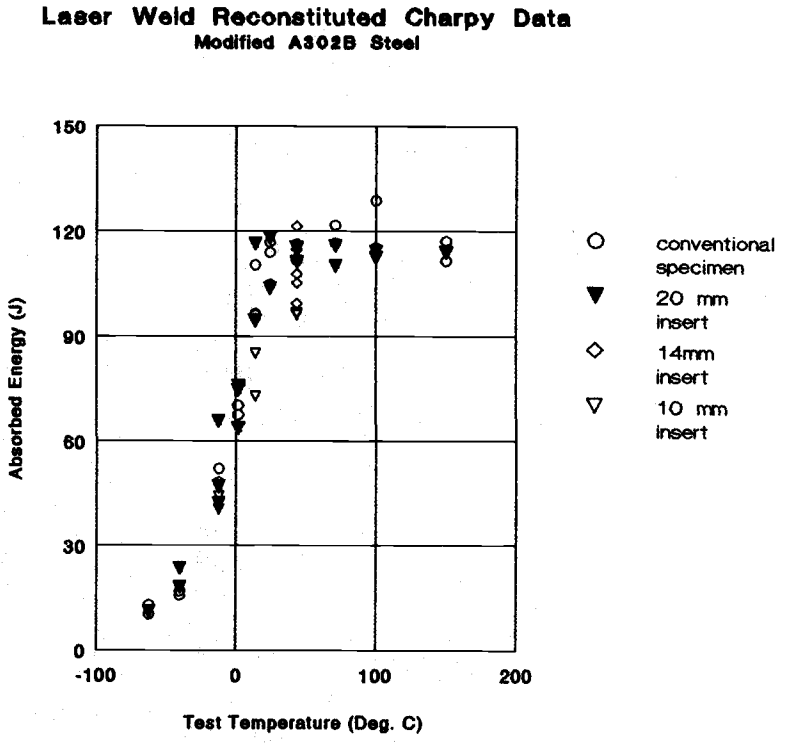

FIG. 1—*Comparison of laser weld data with conventional Charpy specimen data.*

In order to achieve successful test results at the 1/16 size scale, two key developments were necessary: (1) modify the stress field in the vicinity of the crack plane; and (2) develop an energy-based parameter and index that can be related back to the standard specimen test (energy and the 41 J index). An important limitation in miniaturizing any specimen is the extent of the material's microstructural inhomogeneities. The usual guideline dictates that the specimen be at least five to ten times as large as the characteristic heterogeneity dimension. Material for this work was taken from a special heat of ASTM A508 steel provided by Oak Ridge National Laboratory (ORNL) for crack arrest research as part of the Heavy Section Steel Technology (HSST) Program. Conventional mechanical property and microstructural data are available for three different heat treatments, designated 6, 5A, and 6R, in order of increasing toughness and increasing tempering temperature. Microscopy analysis indicated carbon segregates in slender bands about 0.25 mm wide. As a result of these findings, the minimum specimen dimension should be in the range of 3 to 5 mm. For a tension specimen, this minimum size limits the diameter or thickness, and, for a fracture behavior specimen, this minimum limits the dimensions of the crack plane.

Stress Field Modification

Early MNT tests demonstrated that 1/16 size scale miniature Charpy specimens, when tested in the transition region or upper shelf, yield data which cannot be properly analyzed nor related to conventional Charpy data. Figure 2 illustrates the severe nonplanar fracture surface which results. Therefore, to overcome this difficulty, the stress field in the vicinity of the crack plane must be modified. Stress field modification to achieve plane-strain conditions is discussed in Ref *7* in these proceedings. In the case of the MNT, achieving plane strain is neither necessary nor desirable. The fundamental objective is to modify the stress field so that flat fracture is obtained. In the current research, this is accomplished by side grooving the MNT specimen and locating the root of the side-groove notch such that the tensile fields at the root of the notch overlap and produce through thickness tensile stress. MNT specimens which have been stress field modified are shown in Fig. 2. Thus, the experimental hurdle of achieving flat fracture in MNT specimens designed at the continuum limit has been overcome.

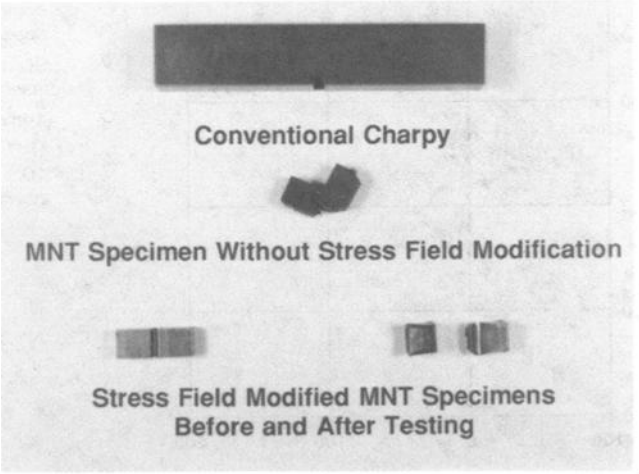

FIG. 2—*Photograph of MNT specimens tested at the same temperature showing the effects of stress field modification.*

MNT Energy-Based Parameter

Several ductile-brittle transition temperature (DBTT) criteria are used in different industries. Since nuclear pressure vessel surveillance is the application of current interest, the 41-J (30 ft-lb) energy absorption level was used as a reference. For the three heat treatments, the Charpy DBTTs are as follows: heat treatment 6, 40°C; heat treatment 5A, −7°C; and heat treatment 6R, −29°C. The key element of data interpretation is to be able to find a physically based parameter and an appropriate index that relate the miniature and conventional specimens. In this context, the term "parameter" means the range variable (e.g., energy, fracture appearance, lateral expansion) and the term "index" means the transition temperature indicator (41-J, 0.89-mm lateral expansion).

The criterion by which the parameters and indices were judged is that the fracture mode in the miniature specimen must be the same as that in the conventional specimen for a given parameter and index level. As shown in Table 2 for the material tested, the MNT specimen exhibits 70% shear at the 41-J index level compared to the conventional CVN specimen, which exhibits only 4% shear. Therefore, the absorbed energy alone is not considered to be a valid parameter for DBTT characterization with MNT specimens for the A508 steel.

It is well established [*8*] that the total energy absorbed in fracturing a Charpy specimen can be further partitioned into pre- and post-maximum load energies. The pre-maximum load energy can be partitioned into elastic stored energy, crack formation energy, and plastic deformation energy. The miniature specimen differs from the conventional one in size and in geometry. Since the miniature specimen has a different span-to-width ratio, different anvil and punch geometry, and has side grooves, the crack initiation energy and its ratio to total energy is different in the two specimen types and, therefore, is not a useful parameter.

The post-maximum load energy (PME) can be partitioned into elastic stored energy, plastic deformation energy, and stable crack propagation energy. The elastic stored energy is available to drive the cleavage fracture for tests conducted in the transition region. The remaining PME is associated with the plastic deformation work and work that goes into propagating a stable crack. Therefore, the PME would be less sensitive to differences in specimen geometry and correlates well with fracture appearance (i.e., percent shear). In the present study, it has been assumed in the analysis that the onset of the maximum load corresponds to crack initiation. While this assumption is reasonable for some materials and test temperatures, it was not actually measured in the test program. In future studies, this question should be resolved by using the electric potential method during testing.

By partitioning the total energy into pre- and post-maximum load energies and plotting these data against test temperature, it can be shown that the pre-maximum load energy does not show a conspicuous transition in fracture behavior. As stated earlier, pre-maximum load energy is associated with elastic stored energy, crack initiation, and plastic deformation near the notch. On the other hand, the PME exhibits a distinct transition because this parameter

TABLE 2—*Percent shear fracture appearance for MNT and conventional Charpy specimens for two indices.*

	Percent Shear Fracture Area at 512 kJ/m^2	Percent Shear Fracture Area at 41 J
Standard specimens[a]	~4	~4
Miniature specimens[a]	~1	>70

[a] All three materials.

is directly associated with the fracture process. Figures 3 and 4 illustrate this behavior for the Heat Treatment 6 material. The other two materials, 5A and 6R, exhibit the same behavior.

Crack initiation was defined as the complete formation of a full-width crack across the length of the notch. If crack initiation, as defined here, is complete when maximum load is reached, the PME should correlate with percent shear for various specimen sizes and shapes regardless of material. Assuming this to be the case, it was thus considered theoretically sound to use PME as a parameter for ductile fracture transition characterization. Differences in specimen size result in the absolute values of PME being different among specimen types. However, the relative proportion of the energy that goes into crack propagation and plastic deformation should correlate with fracture appearance for specimens of different sizes and

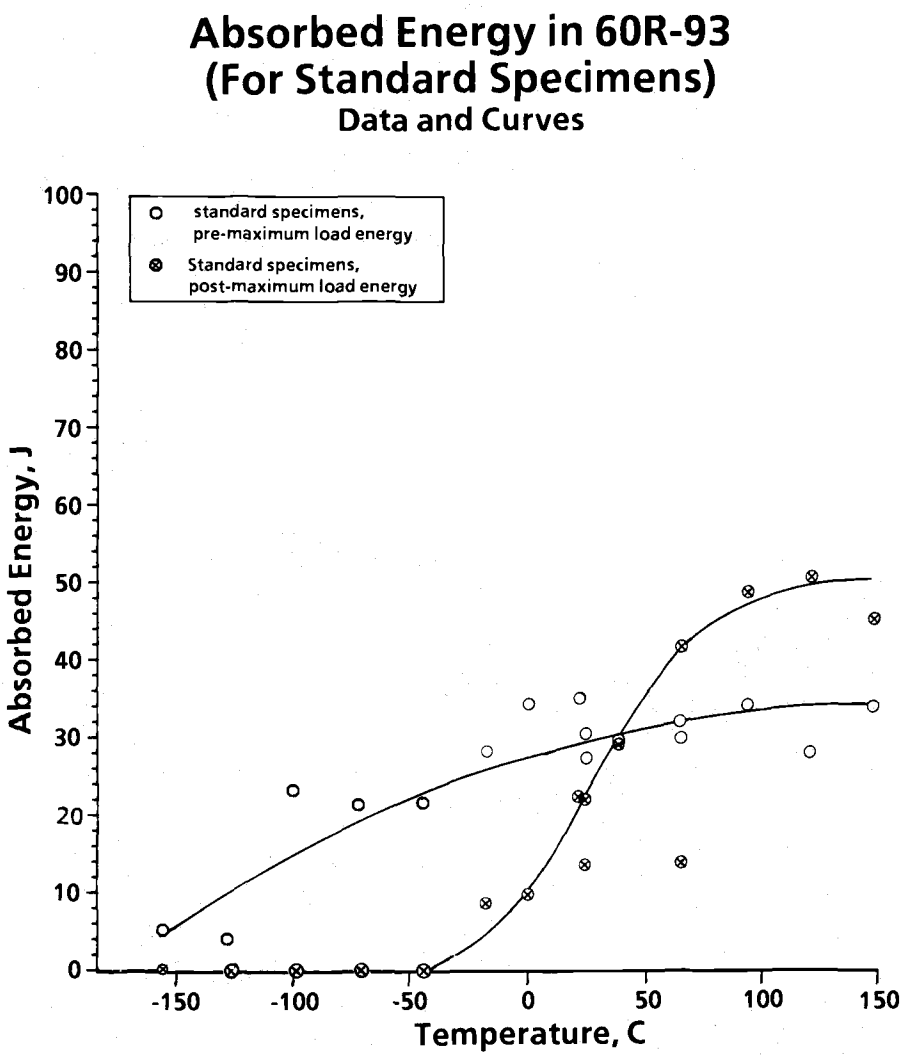

FIG. 3—*Pre- and post-maximum load energies compared (standard specimens, Heat Treatment 6).*

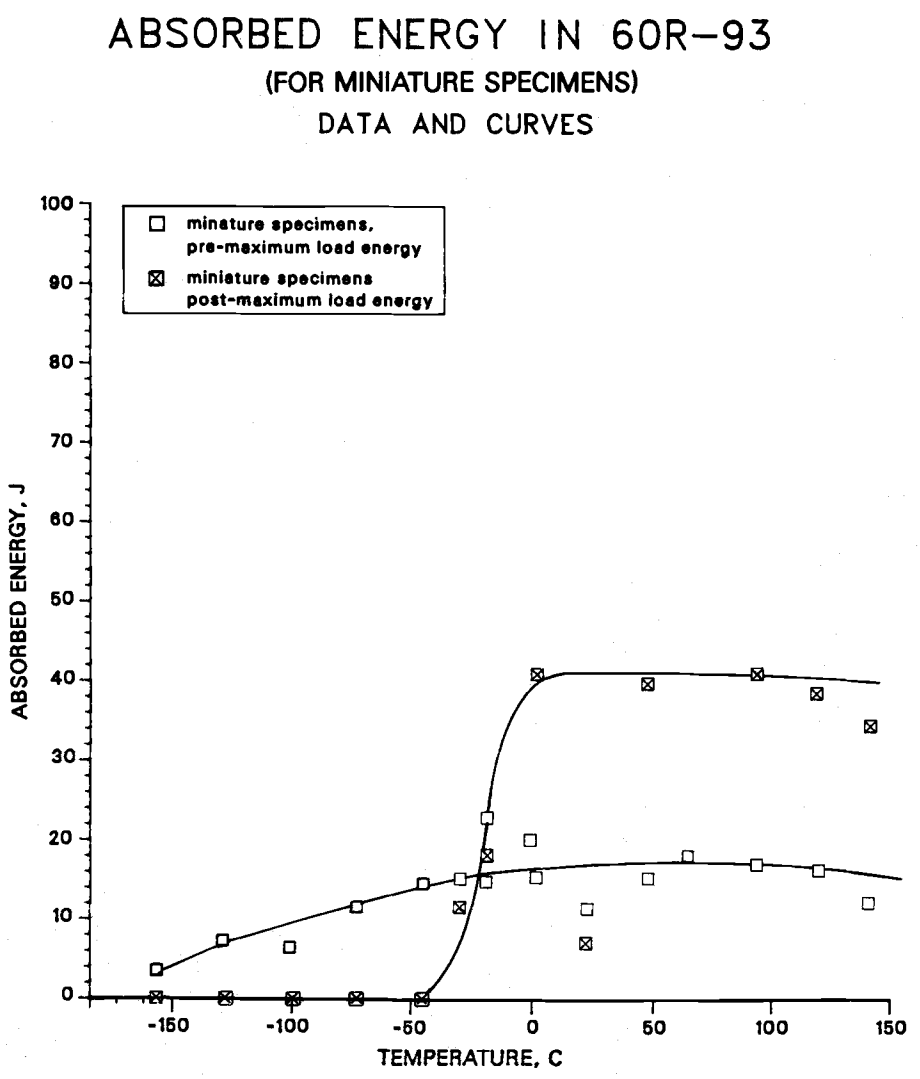

FIG. 4—*Pre- and post-maximum load energies compared (miniature specimens, Heat Treatment 6).*

shapes. Therefore, the absolute values of PME can be converted to percentages by dividing by the total energy (excluding shear lip formation energy). As stated previously, the total energy used in the calculations is defined as the sum of the absorbed energy up to the onset of cleavage. Therefore, any energy absorbed in the formation of shear lips was not included. A MCFRAC [9] plot of percent shear fracture appearance versus percent PME is given in Fig. 5. This figure shows that the data for all three materials in both specimen geometries fit the same curve. A correlation of this kind now allows the use of two criteria, one based on energy and the other on fracture appearance. It is recognized that this correlation is most likely base alloy dependent.

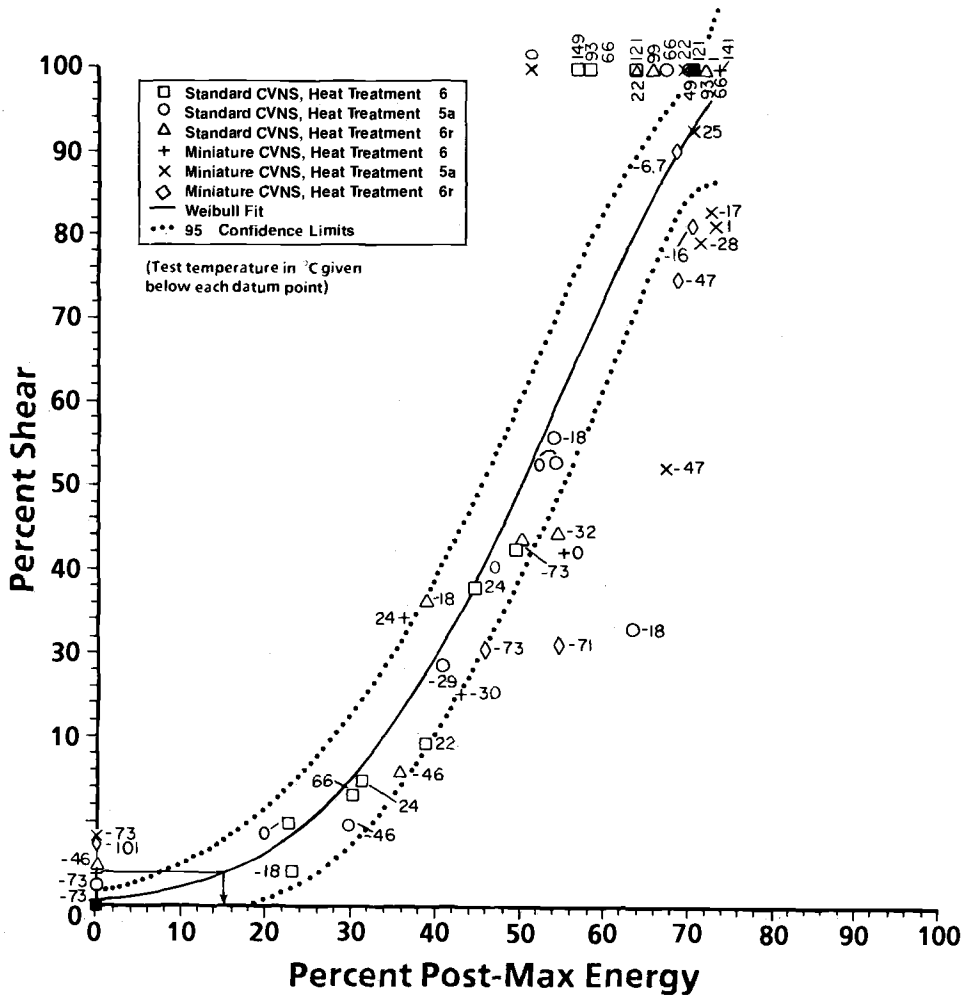

FIG. 5—*Percent PME as a fracture transition criterion (both specimen sizes).*

MNT Indices

As discussed in Ref *1*, either percent shear or present PME can be used as valid MNT parameters. Since the regulations within the nuclear industry are based on the 41 J index with absorbed energy as the parameter, the percent PME is preferable since it can be related directly to the conventional specimen absorbed energy and does not require tedious fracture surface analysis. Figure 5 provides the correlation for obtaining these indices for both specimen dimensions. This technique can be used to relate any specimen geometries that yield notched specimen fracture transition data. In particular, a Charpy energy level of 41 J corresponds to ~4% shear fracture appearance. Referring to Fig. 5, this level of shear corresponds to ~15% PME. Thus, when fracture appearance is used as the MNT parameter, the corresponding index is 4% shear. When percent PME is chosen as the MNT parameter, a value of 15% PME is used as the index. Therefore, when the PME parameter is plotted

against test temperature (Figs. 6–8), transition temperatures for each material may be obtained at the 15% PME level. Table 3 summarizes these transition temperatures.

On comparing these transition temperatures with the standard dynamic CVN transition temperatures, correction factors due to rate effect and size effect are obtained. This is illustrated schematically in Fig. 9. The average shift due to rate effect for the conventional CVN is 45.3°C [*10*]. This shift was determined by averaging the static to dynamic shift at the 41-J level for the three materials using conventional Charpy specimens. As discussed earlier, this is in reasonable agreement with the correlation presented in Ref *11*.

Table 4 presents the shifts due to rate and size effect. These data can be used to relate the MNT data with conventional, dynamic Charpy data for the ASTM A508 steel. The

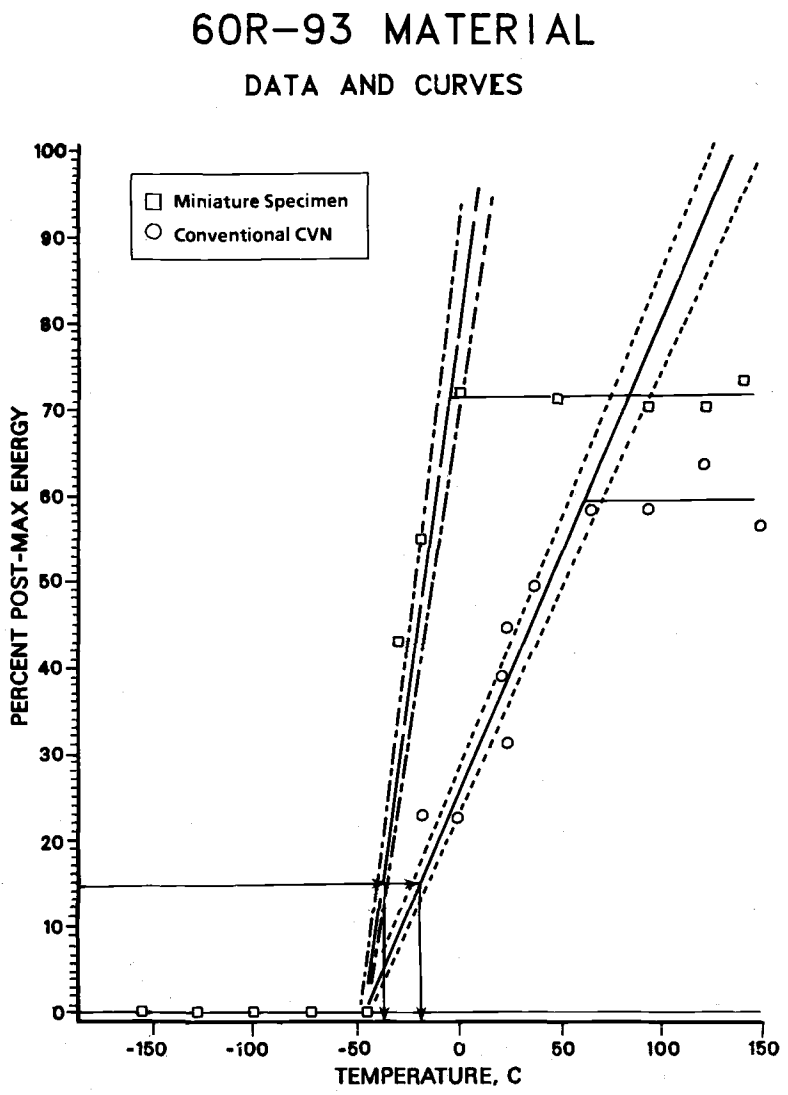

FIG. 6—*Transition temperature from 15% PME index (heat treatment 60R-93 material, both specimen sizes).*

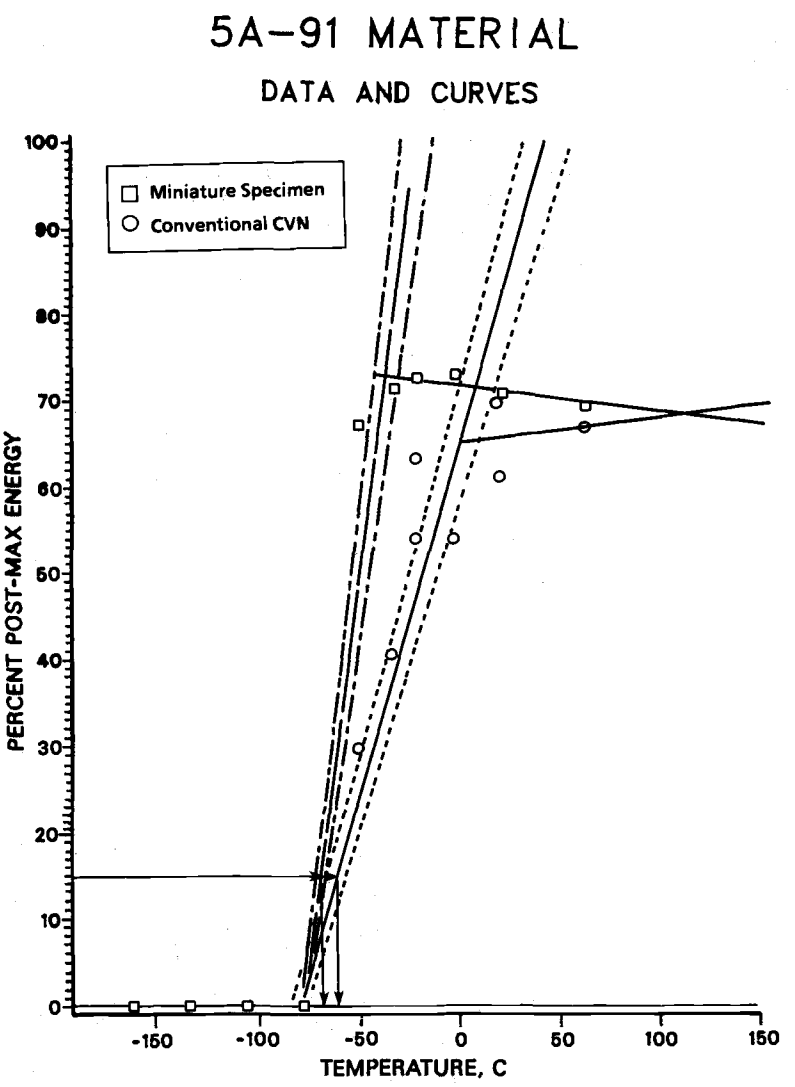

FIG. 7—*Transition temperature from 15% PME index (heat treatment 5A-91 material, both specimen sizes).*

dynamic 41-J transition temperature is obtained by adding the rate effect shift (44.1°C) and the size effect shift (21.3°C) to yield a 41-J dynamic conventional Charpy transition temperature. This is the approach that would be used in cases where the MNT is used to test irradiated pressure vessel steels and there is no archival material available for testing.

In cases where unirradiated archival material is available, it is possible to machine unirradiated and irradiated MNT specimens and measure the shift directly. The strategy would be to first develop the unirradiated MNT data, test the surveillance capsule Charpy specimens, machine the irradiated MNT specimens from the broken Charpy specimens, and test and/or reinsert the MNT specimens back into the reactor to generate plant life extension data.

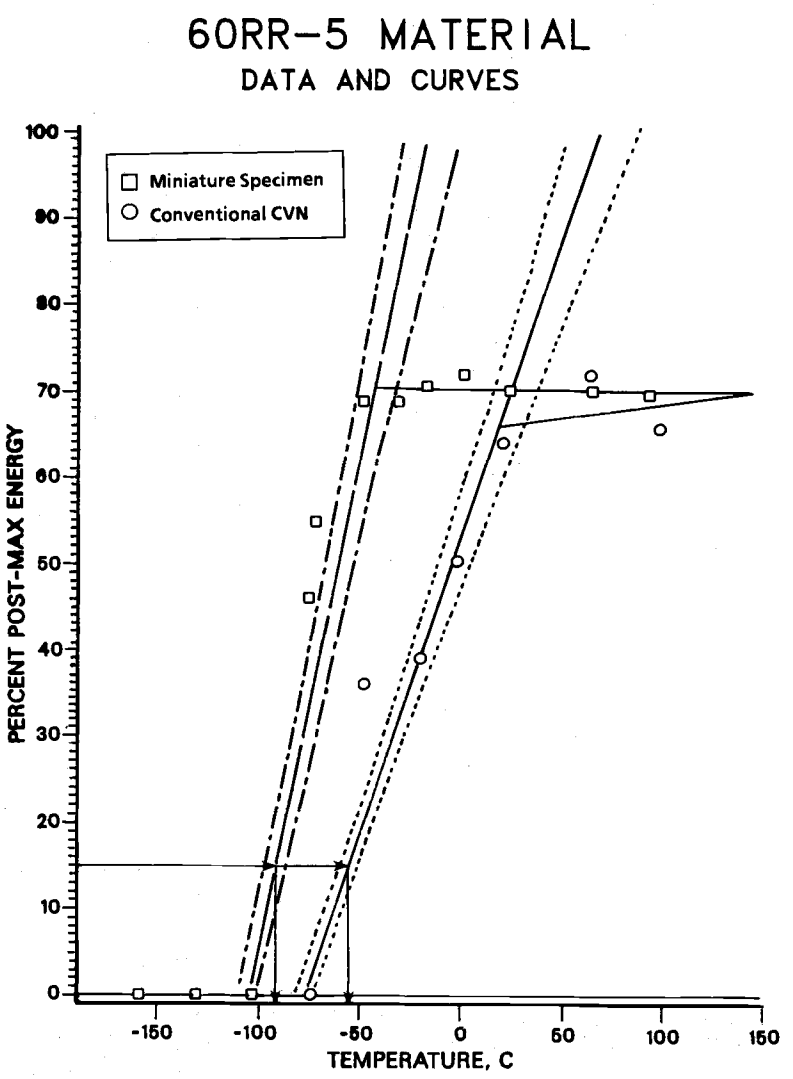

FIG. 8—*Transition temperature from 15% PME index (heat treatment 60RR-5 material, both specimen sizes).*

TABLE 3—*Standard CVN and MNT slow-bend transition temperatures.*

	Heat Treatment					
	6		5A		6R	
Indices	Standard CVN, °C (°F)	MNT, °C (°F)	Standard CVN, °C (°F)	MNT, °C (°F)	Standard CVN, °C (°F)	MNT, °C (°F)
15% PME	−18 (0)	−37 (−35)	−57 (−70)	−65 (−85)	−54 (−65)	−90 (−130)

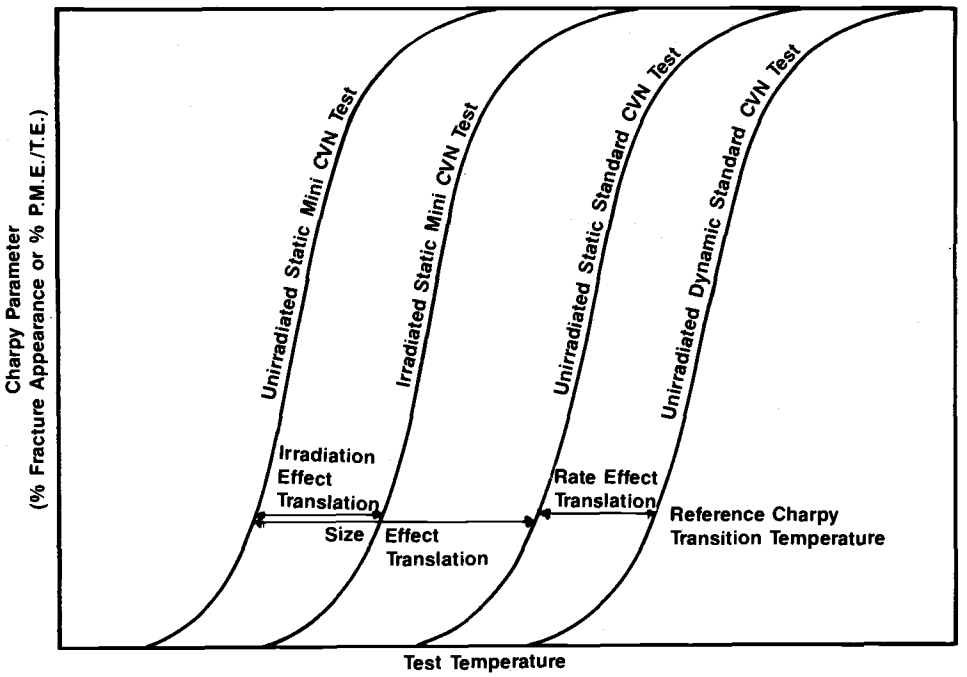

FIG. 9—*Relationship between reference Charpy transition temperature and irradiated miniature Charpy slow-bend transition temperature.*

Summary and Conclusions

Study of alternative weld technologies revealed that laser welding is readily adaptable for hot cell applications. Preliminary work has demonstrated that the required penetration depth can be realized and the control parameters adjusted to yield fairly flat weld planes parallel to the fracture surface. Comparison of laser-welded specimen data with that of conventional specimens showed excellent agreement. Continued successful development will enable reconstitution of 1/16 size scale MNT specimens as well as thicker section J_{IC} bend specimens. The miniaturized specimen design required only 6% of the volume of a standard Charpy specimen. These specimens have proven satisfactory for measuring transition temperature shifts due to heat treatment of a reactor-grade pressure vessel steel. Fracture appearance has been demonstrated to be a useful miniature specimen parameter. For applications in the nuclear industry, conventional dynamic ASTM A508 steel Charpy specimens exhibit ~4% shear at the 41-J energy level. Therefore, the appropriate index for miniature specimens is 4% shear for this material.

A new parameter, percent normalized PME, has been benchmarked for an ASTM A508 steel. This parameter is easier to use than fracture appearance since the data analysis can be easily automated. Like fracture appearance, percent normalized PME can be used to relate miniature specimen data with conventional dynamic, ASTM Test Methods for Notched Bar Impact Testing of Metallic Materials (E 23) specimen data. For the ASTM A508 material investigation, the result is a 41-J DBTT with accuracy equal to that obtained using conventional ASTM test practices. The data obtained thus far are sparse at the 15% normalized PME level. Future studies should provide data at the 15% normalized PME level to more accurately assess the uncertainty of the method.

TABLE 4—*Shifts due to rate and size effects.*

Heat Treatment	Standard Specimen Impact Transition Temperature, °C	Standard Specimen Slow-Bend Transition Temperature, °C	MNT Specimen Slow-Bend Transition Temperature, °C	(Rate Effect) Standard Specimen Impact to Slow-Bend Shift, °C	(Size Effect) Standard Slow-Bend to MNT Slow-Bend Shift, °C
	41 J	15% Normalized PME Index			
6	40	−18	−37	58	19
5A	−7	−57	−65	50	8
6R	−29	−54	−90	25	36

References

[1] Manahan, M. P. and Charles, C., "A Generalized Methodology for Obtaining Quantitative Charpy Data From Test Specimens of Nonstandard Dimensions," *Nuclear Technology*, Vol. 90, May 1990.
[2] Manahan, M. P., "Oyster Creek Pressure Vessel Re-Insertion Capsule Design," MPM Research & Consulting, final report to General Electric Nuclear, 25 Sept. 1990.
[3] Perrin, J., Wullaert, R., McConnell, P., Server, W., and Fromm, E., "Reconstituted Charpy Impact Specimens," EPRI, Battelle Columbus Laboratories, 2nd Fracture Control Corporation, Research Project 2055-3, NP-2759, December 1982.
[4] Fabry, A., Puzzolante, J. L., VonWalle, E., Vandermeulen, W., Vandevelde, J., and Von Ransbeeck, T., "Changing the Notch Orientation of Charpy V Specimens by Stud Welding of Broken Remnants," SCK-CEN, Belgium.
[5] Manahan, M. P., "Determination of Fracture Behavior of Ferritic Steels Using Miniaturized Specimens," *Journal of Nuclear Materials*, 1989, pp. 321–330.
[6] Manahan, M. P., "Determination of Charpy Transition Temperature of Ferritic Steels Using Miniaturized Specimens," *Journal of Materials Science*, 1990, pp. 3429–3438.
[7] Manahan, M. P., "Miniaturized Fracture Toughness Testing During the Plant Life Extension Period," invited paper presented at the American Society for Testing and Materials Second International Conference on Subsize Specimens, January 1992.
[8] Hertzberg, R. W., *Deformation and Fracture Mechanics of Engineering Materials*, 3rd ed., Wiley, New York, 1989.
[9] Manahan, M. P., "*S*tatistical *A*nalysis *M*ethodology for *M*echanics of *Frac*ture, SAM McFRAC: Users Manual," code package based on the Werbull statistic for Charpy and fracture toughness data analyses, 1989.
[10] Manahan, M. P., Rosenfield, A. R., and Vanecho, J. A., "Final report on Miniaturized Fracture Mechanics Feasibility Study to Corporate Technical Development," Battelle Columbus Laboratories, Columbus, OH, 1985.
[11] Rolfe, S. T. and Barsom, J. M., *Fracture and Fatigue Control in Structure*, Prentice-Hall, Englewood Cliffs, NJ, 1977.

Kenichi Hamada,[1] *Shinji Sato,*[1] *and Akira Kohyama*[1]

Fracture Toughness Evaluation of Neutron-Irradiated Composites by a Miniaturized Charpy Test

REFERENCE: Hamada, K., Sato, S., and Kohyama, A., **"Fracture Toughness Evaluation of Neutron-Irradiated Composites by a Miniaturized Charpy Test,"** *Small Specimen Test Techniques Applied to Nuclear Reactor Vessel Thermal Annealing and Plant Life Extension, ASTM STP 1204,* W. R. Corwin, F. M. Haggag, and W. L. Server, Eds., American Society for Testing and Materials, Philadelphia, 1993, pp. 77–89.

ABSTRACT: The impact properties of advanced metal matrix composites (MMCs) such as unidirectionally reinforced silicon carbide (SiC)/aluminum (Al) and C/Al have been investigated based on recent improvements in their mechanical properties. This paper details the effects of test temperature and neutron irradiation on the fracture toughness of these MMCs. The materials used were sheets of PCS-SiC/Al and PAN-C/Al. Miniaturized Charpy V-notched specimens were tested in an instrumented Charpy impact tester. Neutron irradiation was performed in the Japanese Materials Testing Reactor (JMTR), a light water reactor (LWR) at Oarai. The fracture energy increased with increasing test temperature and with neutron irradiation. SiC/Al was rather more insensitive to neutron fluence than C/Al, which was related to the difference in interfacial structure between the two systems.

KEYWORDS: metal matrix composites, aluminum matrix, silicon carbide fiber, carbon fiber, Charpy impact test, fracture toughness, strength properties, miniaturized specimens, miniaturized testing

Metal matrix composites (MMCs) with aluminum (Al) alloy matrices are known to be superior in strength-to-weight ratio, in stiffness-to-weight ratio, and in resistance to a variety of environments. They are, therefore, being considered as future aeronautic and space materials. In addition, aluminum matrix composites are also considered potential materials for nuclear applications because of their good mechanical properties at elevated temperatures and low radio activation characteristics [*1,2*]. Aluminum matrix composite wires, reinforced with either silicon carbide (SiC) fiber or carbon (C) fiber, have been developed as advanced structural materials for operation in such severe environments. Tensile strength as high as 1.7 and 1.5 GPa have been observed at room temperature and at 723 K, respectively [*3*]. Sheet-forming processes have been successfully developed and have been applied to produce composite plates, the largest of which is 2 by 200 by 1000 mm. The plates were produced from composite wires by a hot rolling [*4*] method and by a hot pressing [*5*] method with a degradation in strength of less than 10 and 5%, respectively, from the original wire strength. A number of studies have been performed on the fracture toughness of high-performance composites [*6*]. It is important to understand the effects of neutron irradiation for potential nuclear applications, but data other than that of the authors have not yet been published [*7*].

[1] Department of Materials Science, The University of Tokyo, Hongo, Bunkyo-ku, Tokyo 113, Japan.

Attempts to utilize small specimens for mechanical testing have had a long history [*8*] with recent emphasis on radiation studies, where the major motivation to reduce specimen size derives from the limited availability of irradiation space, the high cost of irradiation, and the need to miniaturize the radiation dose to personnel involved in post-irradiation tests. Miniaturized mechanical tests on thin plates of aluminum matrix composites are also used to evaluate the mechanical properties of full-size structural components in aerospace applications.

The objectives of this study are first to establish an impact test technique using small specimens as a valid testing method for evaluating the fracture toughness of high-performance composites and second to investigate the effects of test temperature and neutron irradiation on the fracture toughness of aluminum matrix composites.

Experimental

The materials used were sheets made from wire preforms of MMCs with pure aluminum matrices, as summarized in Table 1. Reinforcement was in the form of the multi-filament continuous fibers referred to as Nicalon and Torayca, which are a polycarbosilane (PCS) type of SiC fiber and a polyacrylonitril (PAN) type of C fiber, respectively. The composite wires were made using a liquid metal infiltration method from the test plants of Nippon Carbon (for SiC/Al) and Toray (for C/Al) [*9*]. The sheet materials of the MMCs were made from the composite wires by a hot rolling method [*4*] for SiC/Al and a hot pressing method [*5*] for SiC/Al. The maximum temperatures in both processes were 770 K for the hot rolling process and 803 K for the hot pressing process. The sheet insert method was used in the hot pressing process, where foils of the aluminum alloy A2017 were inserted among the layers of aligned composite wires and then the stack of the sandwiches was encapsulated in an evacuated metal container [*5*].

Mechanical properties were measured using an instrumented Charpy tester recently developed for testing miniaturized specimens [*10*]. The machine was a hydraulic drop tower, and the capacity of the load washer was 600 kg. The maximum loads encountered were about 25 kg. The miniaturized Charpy V-notched (CVN) specimens, with dimensions of 2 by 2 by 20 mm, were cut out from the sheet materials and were tested at temperatures ranging from 150 to 530 K. The geometries of the specimen and the test stage and the tap cross-section for the miniaturized Charpy test are shown in Fig. 1.

Neutron irradiation was performed in the Japan Materials Testing Reactor (JMTR) at Oarai establishment, JAERI under the following irradiation conditions: neutron flux ($E >$ 0.1 MeV)—4.2×10^{17} n/m^2 s; irradiation temperature—438 ± 15 K; irradiation time—533 equivalent full power hour; and total neutron fluence—8.0×10^{23} n/m^2. Post-irradiation examinations such as Charpy tests and SEM observations were carried out at the Oarai Branch of the Institute for Materials Research, Tohoku University.

TABLE 1—*Materials used.*

Material	Reinforcement (fiber diameter)	Matrix	Forming Method	Fiber Volume Fraction, %
SiC/Al C/Al	PCS-SiC (ϕ = 12 μm)	A1050	Hot roll	40
	M40J (ϕ = 5 μm)	A1080	Hot press (A2017 Sheet Insert)	45

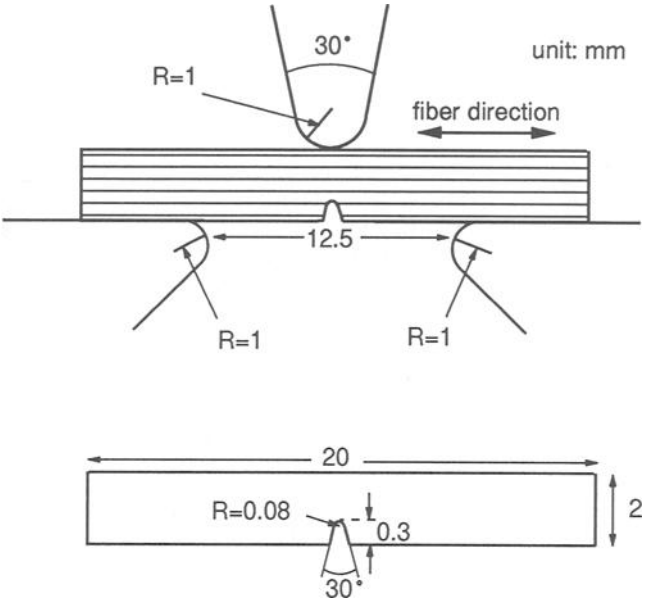

FIG. 1—*Miniaturized specimen and test component.*

Results and Discussion

A typical load-displacement curve for the instrumented Charpy test is shown in Fig. 2. A gradual transition in the deformation process from elastic to plastic was not evident in the figure, and the sharp transition from increasing to decreasing loads observed at the maximum load suggests catastrophic crack initiation and propagation immediately after micro-yielding. The jagged appearance of the load-displacement curve during the fracture process seems to correspond to crack arrest followed by instantaneous crack initiation at interfaces or in the vicinity of interfaces. The absorbed energy, E, is divided into two parts, $E1$ and $E2$, at the point of load maximum as shown in the figure. The former should correspond to the elastic stored energy up to the initiation point of catastrophic cracks, while the latter should correspond to the absorbed energy during crack propagation to failure. Dynamic flexural strength, σ_f, was calculated in the following discussion as

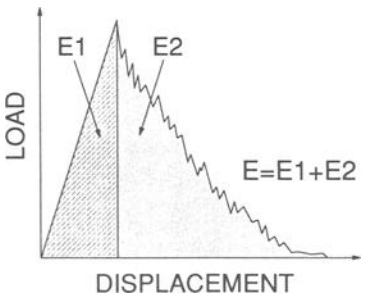

FIG. 2—*Typical load-displacement curve from an instrumented Charpy test.*

where P is the maximum load, L is the flexural span, x is the specimen width, and y is the specimen thickness at the bottom of the notch.

SiC/Al

The absorbed energies, E, $E1$, and $E2$, are shown in Fig. 3. Although the number of specimens tested was quite limited and the intrinsic nature of data scattering made it difficult to draw trend lines, trend zones of test temperature dependence were indicated. They have a tendency to increase gradually with increasing test temperature over the temperature range tested, both before and after neutron irradiation. For unirradiated specimens, the total absorbed energy, E, was approximately 1.3 times larger at 530 K than at 150 K. The limited neutron irradiation data indicate a fair amount of improvement in fracture toughness at the higher temperatures. The majority of this improvement is attributed to an increase in $E2$ without significant changes in $E1$. The slight increase in $E1$ with test temperature in unirradiated specimens is due to the increase in the displacement to the point of load maximum because of the temperature-dependent softening of the matrix. The corresponding temperature dependence of flexural strength is shown in Fig. 4. The $E1$ values and the flexural

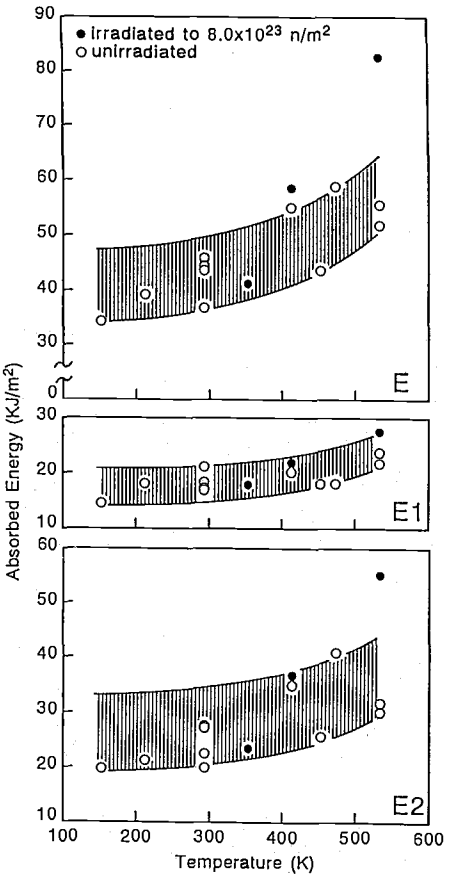

FIG. 3—*Test temperature dependence of absorbed energies* E, E*1 and* E*2 for PCS-SiC/A1050.*

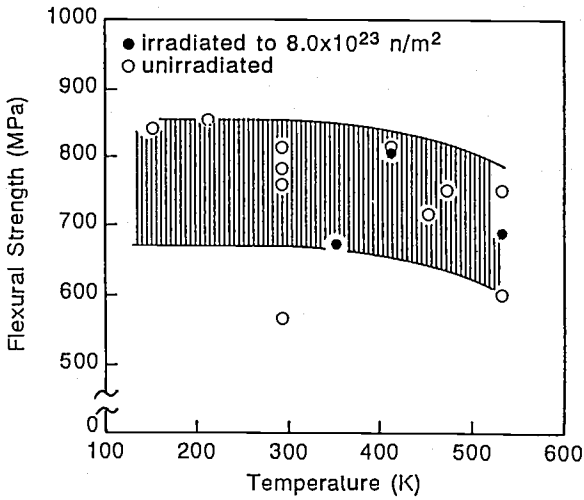

FIG. 4—*Test temperature dependence of flexural strength in PCS-SiC/A1050.*

strength for irradiated specimens are within the trend zones indicated in the figures, which suggests the weak irradiation effects on these properties. The tension test results on the same materials [*11*] showing the slight irradiation strengthening of fibers and the flexural test results showing no detectable irradiation strengthening may indicate irradiation-induced softening of the matrix. Although the temperature dependence of the flexural strength looks larger than that of $E1$, this difference is reasonable since the $E1$ value is proportional to the product of the maximum load and the displacement at the point of load maximum, and while the displacement increases with the temperature-dependent softening of the matrix, the decrease of the maximum load with increasing temperature is less significant.

For SiC/Al, a characteristic fracture behavior has been confirmed by "in situ" observation under a scanning electron microscope [*12*] and is briefly reviewed as follows.

The process of macroscopic failure: the main crack from the bottom of the saw notch propagated forward by linkage of the deformed regions near the main crack tip with that at the fracture surface of the fiber that was fractured prior to the matrix failure. Failure of fibers along the pass of the main crack was not introduced directly by the main crack propagation, and any evidence of crack bridging during the process was hardly seen.

As the strain at failure of the fiber was smaller than that of the matrix, fibers were fractured prior to matrix failure and even prior to plastic deformation of the matrix, in general. Fiber failure should introduce an increase in matrix stress due to the failure of responsible fiber to sustain a major part of the local stress. Together with the stress concentration at the fiber failure location, the formation of a large deformation zone was predicted and proved. As the size of these regions strongly affects the maximum distance between the main crack and a neighboring deformed region, larger deformed regions resulted in larger distance of linkage. As the $E2$ value strongly depends on crack propagation distance, the size change of the deformation regions has a great influence on the change of $E2$. In general, the larger strength difference between fibers and matrix produces the larger deformation regions. Thus, the temperature dependence of the $E2$ values for the unirradiated specimens was correlated with that of the size of the deformation regions, which was caused by the temperature-dependent softening of the matrix and the temperature-insensitive strength of the fibers. In the same way, the largest $E2$ value observed in the irradiated specimen at 530 K could be

interpreted by the largest strength difference caused mainly by strengthening of the fibers [*11*].

Figure 5 shows the fracture characteristics seen in the CVN specimens tested. At 530 K, however, the uneven and granular surface became more significant and the distances of crack linkage became greater than those at the lower temperature. This result is consistent with the explanation of the process mentioned above. The significant lateral expansion observed in the irradiated specimen tested at 530 K also supports the explanation because larger deformed regions of matrix were correlated with the large total deformation of the matrix near the fracture surface. Another important feature of the fracture surface is the lack of fiber pullouts both with and without neutron irradiation. This is due to the strong interfacial strength and sound interfacial microstructure, as reported in Ref *3*.

These results suggest that there is no degradation in fracture toughness during irradiation at about 440 K up to 1×10^{24} n/m^2, but Ref *11* suggests that there is a risk of degradation at higher neutron fluences due to the fluence dependence of fiber strength. On the other hand, at about 723 K, the interfacial reaction induced by irradiation [*3*] may cause a degradation in fracture toughness. At intermediate temperatures, the successful application of these materials is likely. The results from recent three point bend tests on an irradiated

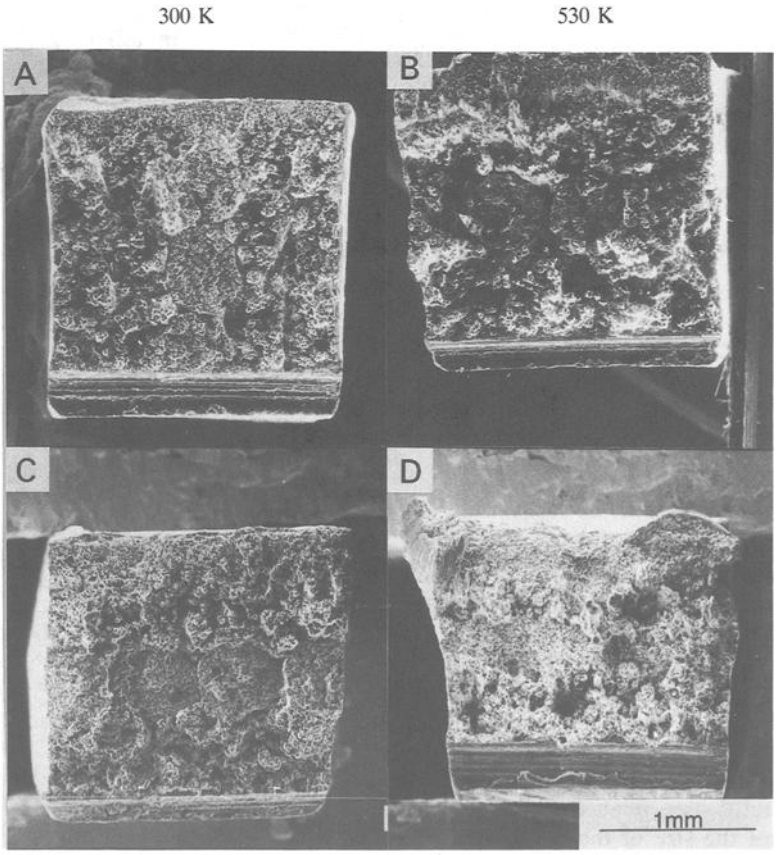

FIG. 5—*Fracture surfaces of PCS-SiC/A1050 after Charpy testing at 300 and 530 K:* (A, B) *unirradiated;* (C, D) *irradiated to 8.0* $\times$ *10^{23} n/m^2 at 438* $\pm$ *15 K in JMTR.*

specimen from the Fast Flux Test Facility at 645 K [*13*] suggest that the strength will be maintained to fluences as high as 3.5×10^{26} n/m^2.

C/Al

Figures 6 and 7 detail the results of tests on C/Al specimens. The figures are analogous to Figs. 3 and 4 for SiC/Al. The absorbed energies increased gradually with increasing test temperature above 450 K both with and without neutron irradiation. For unirradiated specimens, the total absorbed energy, E, was approximately 1.3 times larger at 530 K than at 150 K. Although the limited amount of data on irradiated specimens limit the insights that can be made with respect to neutron irradiation effects, there was some indication that fracture toughness improved with irradiation, independent of test temperature. The majority of this improvement is attributed to an increase in $E2$, while $E1$ did not change. The $E2$ values obtained for the unirradiated specimens were consistent with the softening of the matrix at higher temperatures. Figure 8 illustrates the characteristics of the fracture surfaces seen in the CVN specimens tested. At 300 and 530 K, uneven and granular surfaces were observed for specimens both with and without irradiation, while lateral expansion was not observed in either condition. There is no clear evidence as to the reason for the increase in

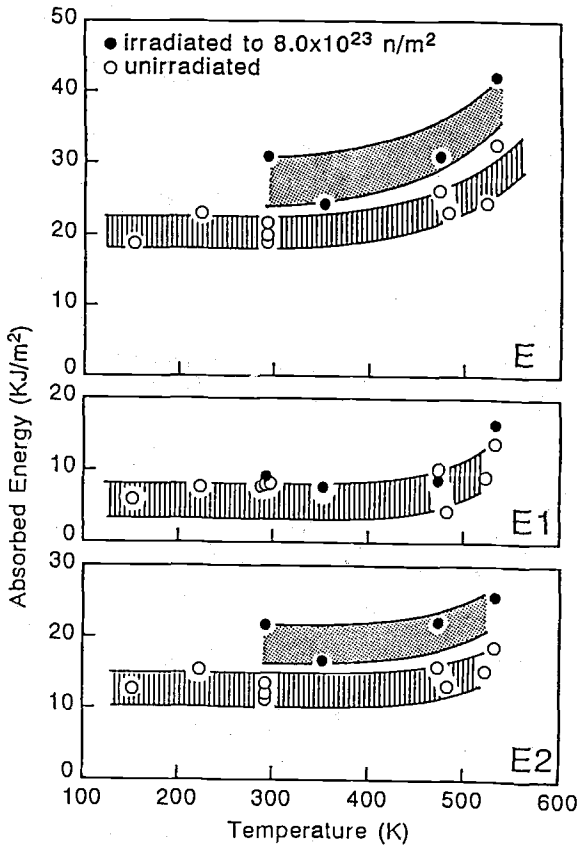

FIG. 6—*Test temperature dependence of absorbed energies* E, E*1, and* E*2 for M40J/A1080.*

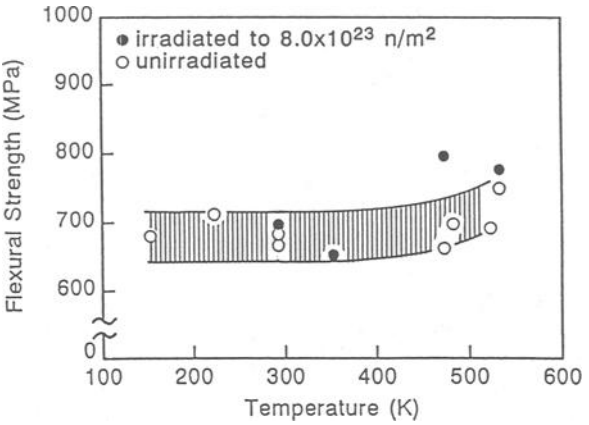

FIG. 7—*Test temperature dependence of flexural strength in M40J/A1080.*

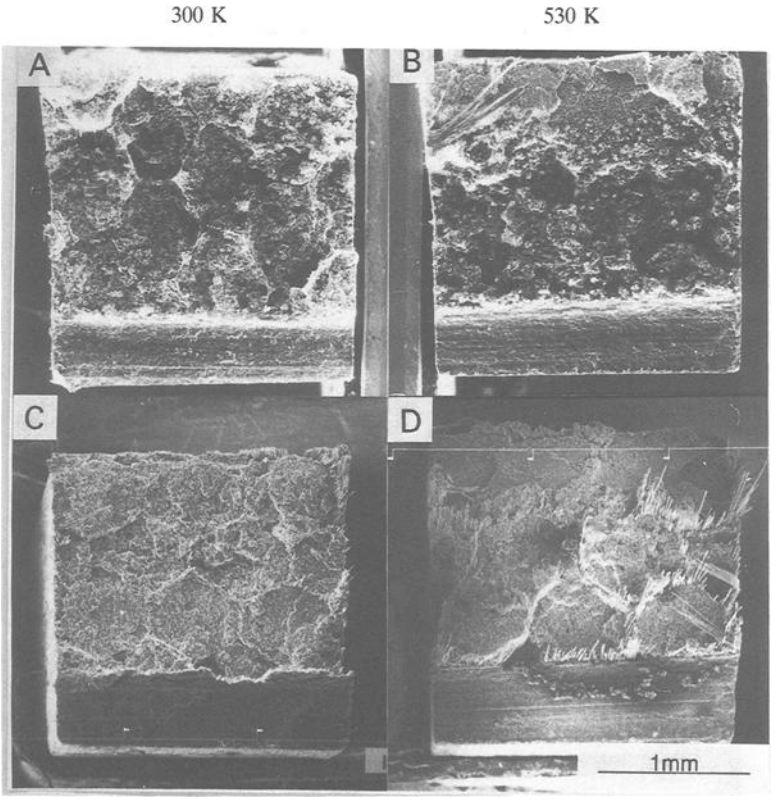

FIG. 8—*Fracture surfaces of M40J/A1080 after Charpy testing at 300 and 530 K:* (A, B) *unirradiated;* (C, D) *irradiated to 8.0 × 10^{23} n/m² at 438 ± 15 K in JMTR.*

$E2$ with irradiation, but the change in the number and length of fiber pullouts on the fracture surface and the flatness of the matrix surface suggest a change in the interfacial strength that could be related to the fracture toughness changes. The weaker interfacial strength of M40J/A1080 than SiC/Al induced debonding of the interface near the fiber fractures that occurred prior to propagation of the main crack, and the long debonded interface promoted flat crack propagation [*12*]. For the irradiated specimens, the improvement in interfacial strength implied by the reduction in the number of fiber pullouts was responsible for the increase of $E2$ independent of test temperature. The short debonding interface results in an increased distance between the main crack and the prior area of deformation, and the longer crack propagation distance causes an increase in $E2$. The increase in flexural strength at higher temperatures is related to a reduction of the high residual thermal stress at the interface that arises from the negative coefficient of linear expansion of the fiber. It is known that the tensile strength of M40J/A1080 composite wires improved from 1.2 to 1.6 GPa after heat treatment at 543 K for 1 h [*14*], and it would appear that the radiation-induced improvement in $E2$ can be attributed to this type of reduction of the high residual thermal stress at the interface. Another important feature of the fracture surface is the long fiber pullouts that appear after neutron irradiation, as shown in Fig. 9. These are most likely due to the weaker interfacial strength at the area near the inserted sheet, A2017. But this happened in the most optimized materials presently available, and the improvement of the interfacial strength near the inserted sheets was known to degrade the strength of the composites [*5*]. Neutron irradiation and the thermal history during the irradiation were believed to induce degradation of the interfacial strength. The origin of this degradation is not clarified yet, but the radiation and/or thermally induced diffusion of some detrimental elements from the A2017 sheet inserts or from their surfaces might be a possibility.

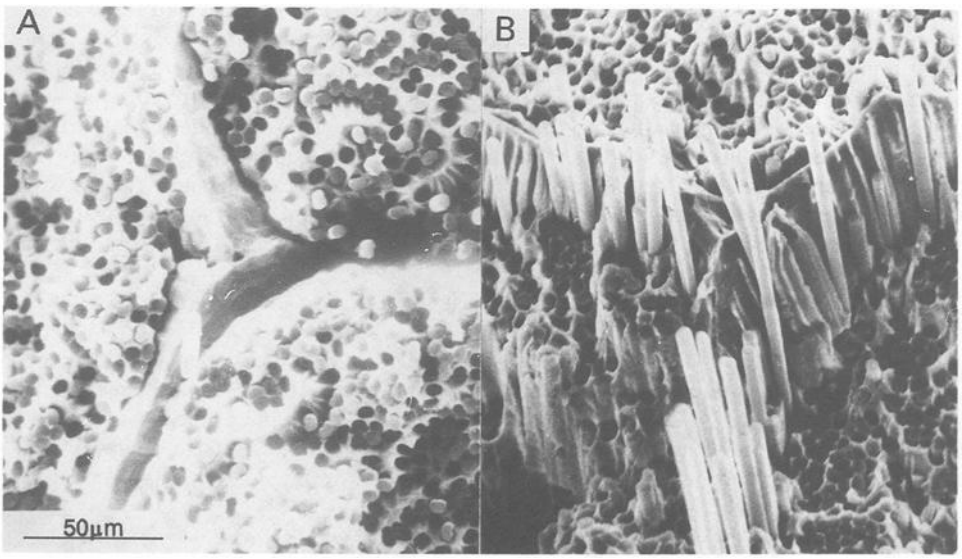

FIG. 9—*Fracture surface of M40J/A1080 showing the bonded structure of the wire preforms:* (A) *unirradiated, tested at 300 K;* (B) *irradiated to 8.0* $\times$ 10^{23} *n/m² at 438* $\pm$ *15 K in JMTR (tested at 530 K).*

Future Application

Dynamic Fracture Toughness

Instrumented impact testing methods were investigated for evaluating the dynamic stress intensity factor at rupture initiation, K_{IC} [*15*]. The K_{IC} values for some ceramic matrix composites are reported for composite materials in Ref *16,* where instrumented Charpy impact testing was applied. In this work, the same testing method was selected and ASTM Test Method for Plane Strain Fracture Toughness of Metallic Materials (E 399) was applied to evaluate K_{IC}. In this study, the depth of saw notch was accounted as the precrack length defined in E 399. This treatment was based on the fact that mostly the fibers at the bottom of the notch were cracked in the process of saw cutting and on the assumption that the cracks at the bottom of the saw notch are sharp enough to be treated as the precrack. The maximum load was treated as the load at the rupture because the lack of plastic deformation and the sharp load drop at the point of load maximum showed that the specimens were under plane strain conditions and that the point of load maximum was the point of catastrophic crack initiation. Thus, K_{IC} is defined as

$$K_{IC} = (PL/x^{3/2}y) \times f(t)$$

where P, L, x, and y are as defined as above, $t = a/x$, a = crack length, and $f(t) = 3t^{1/2}[1.99 - t(1 - t)(2.15 - 3.93t + 2.7t^2)]/[2(1 + 2t)(1 - t)^{3/2}]$.

Figure 10 shows the temperature dependence of K_{IC} for SiC/Al and C/Al. The dependence is similar to that of the flexural strength, reflecting that the maximum load was the sole variable in the data set of K_{IC} in the figure. Yet, the values at room temperature for unirradiated specimens seem quite reasonable compared with values from ceramic matrix composites [*15*], and this may rationalize the assumption to treat the notch depth as the precrack length. Although the trend zones in Fig. 10 are drawn based on the trend seen in the maximum load, the K_{IC} values look nearly temperature independent and show no detectable effect of neutron irradiation. The possible slight temperature dependence at the higher temperature region, shown as trend zones, may correspond to the softening of the matrix and/or changes in interfactial properties at the higher temperature region, but there is no clear evidence for their effect on the K_{IC} of these composites. Despite the importance and strong need for this type of data, the authors have not seen any explanation for the temperature and irradiation dependence of K_{IC} for metal matrix composites. Future work will involve testing precracked specimens and in-situ observations of crack propagation to arrive at clearer insights.

Size Effects and Normalization

It is well known that Charpy impact data on metals exhibit a dependence on specimen size. The major motivation for specimen size considerations are to reduce specimen size for neutron irradiation and to evaluate thin plates with a variety of plate thickness. Previous investigations of stainless steels have provided methods to compensate size effects by normalizing the absorbed energy [*17,18*]. After trials, the following equation was selected

$$\text{normalized } E = E/(Bb)^{3/2}$$

where E is the absorbed energy, B is the specimen width, and b is the ligament size. Figure 11 shows the dependence of absorbed energy on specimen size together with the normalized values. The absorbed energies for the SiC/Al composite show a similar dependence on

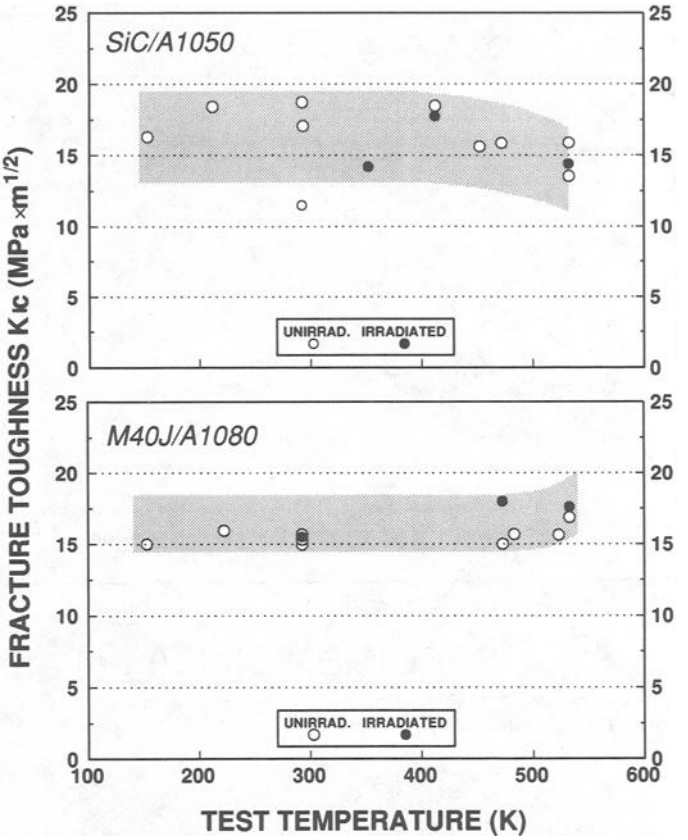

FIG. 10—*Test temperature dependence of* K_{IC} *for PCS-SiC/A1050 and M40J/A1080.*

specimen size as those for ferritic steels. Furthermore, after the normalization, the two sets of data for steels and composites indicate the independency on specimen size. Thus, these sets of data indicate that it is appropriate to apply this equation to metal matrix composites. But the data are still too limited to be conclusive. An ongoing study that includes neutron-irradiated specimens will hopefully provide affirmative data.

Conclusions

The fracture toughness of high-performance composites was investigated using an instrumented Charpy impact tester for miniaturized specimens. This method has proved successful in research on the effects of test temperature and neutron irradiation on the fracture toughness of such materials.

Advanced aluminum matrix composites exhibited an increase in fracture toughness with neutron irradiation in a fission reactor, JMTR. The improvement was attributed primarily to an increase in $E2$, the energy absorbed after the maximum load, usually taken to be the energy of crack propagation. For SiC/Al, the increase in $E2$ with temperature was interpreted to be due to an enhancement of the difference in strength between the matrix and the fiber. This phenomenon was more pronounced after neutron irradiation. $E2$ increased

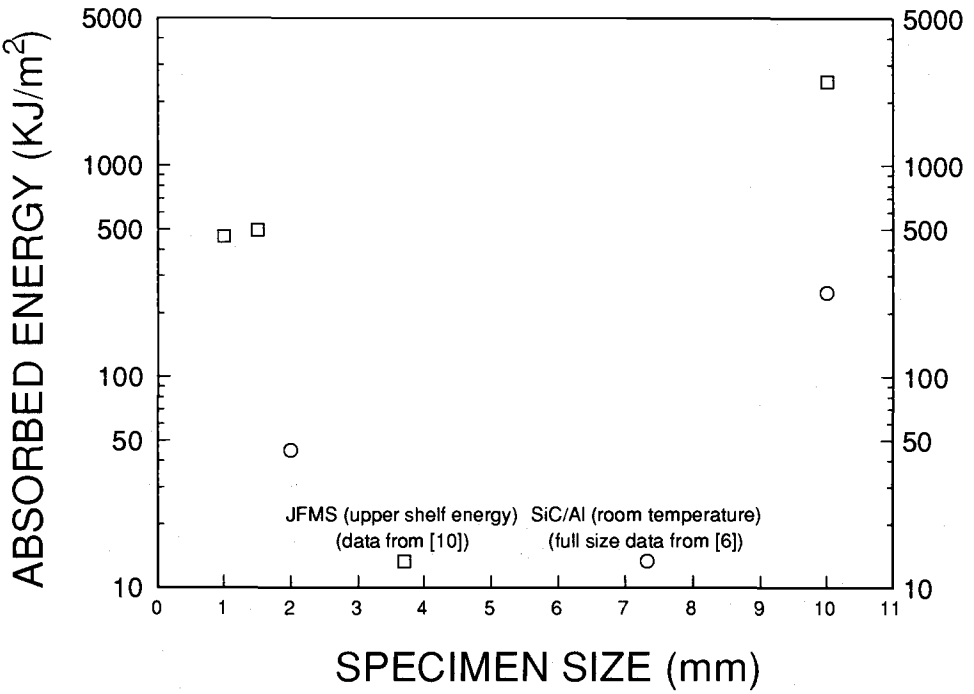

FIG. 11—*Specimen size effects for the total absorbed energy and the normalized energy of stainless steels* [10,16] *and SiC/Al* [6, *this study*].

with neutron irradiation for C/Al, primarily due to the radiation-induced modification of the C/Al interface, where the interfacial strength was weaker before irradiation than after.

Acknowledgments

The authors wish to express their sincere appreciation to Mr. M. Narui and Professor H. Kayano of the Oarai Branch of the Institute for Materials Research, Tohoku University, for their fruitful discussions and encouragement in this work.

References

[1] Hopkins, G. R. and Chin, J., *Journal of Nuclear Materials*, Vols. 141–143, 1986, pp. 148–151.
[2] Kohyama, A., Tezuka, H., Igata, N., Imai, Y., Teranishi, H., and Ishikawa, T., *Journal of Nuclear Materials*, Vols. 141–143, 1986, pp. 96–101.
[3] Kohyama, A., Tezuka, H., Kondo, M., and Sato, S., in "Evolution of Advanced Materials," AIM and ASM–Europe, American Society for Metals, Metals Park, OH, 1989, pp. 405–410.
[4] Sakakibara, T., in *Proceedings*, 6th Symposium on R & D of Composite Materials for Future Industries, Japanese Industrial Technology Association, Tokyo, 1989, pp. 395–403.
[5] Fujiwara, C., in *Proceedings*, 6th Symposium on R & D of Composite Materials for the Future Industries, Japanese Industrial Technology Association, Tokyo, 1989, pp. 385–394.
[6] Imai, Y., Tanaka, Y., Ichikawa, H., Kagawa, Y., and Kishi, T., *Journal of the Japan Society for Composite Materials*, Vol. 16, 1990, pp. 36–39.
[7] Kohyama, A., Tezuka, H., and Saito, S., *Proceedings*, 2nd International Conference on Composite Interfaces, Elsevier, New York, 1988, pp. 125–139.

[8] *The Use of Small-Scale Specimens for Testing Irradiation Materials,* W. R. Corwin and G. E. Lucas, Eds., ASTM STP 888, 1986.
[9] Kohyama, A., in *Proceedings,* 7th Symposium on R & D of Composite Materials for the Future Industries, 1989, pp. 257–272.
[10] Kayano, H., Kurishita, H., Kimura, A., Narui, M., Yamazaki, M., and Suzuki, Y., *Journal of Nuclear Materials,* Vols. 179–181, 1991, pp. 425–428.
[11] Kohyama, A., Sato, S., and Hamada, K., *Effects of Radiation on Materials,* 15th International Symposium, Effects of Radiation on Materials, *ASTM STP 1125,* 1992, pp. 785–796.
[12] Kohyama, A., Niwa, N., and Sato, S., *Key Engineering Materials,* Vols. 79–80, Trans Tech Publications, Aedermannsdorf, Switzerland, pp. 279–294.
[13] Kohyama, A., Sato, S., and Hamada, K., Collected Abstracts of the 109th Annual Meeting of the Japan Institute of Metals, October 1991, Hiroshima, 1991, pp. 198.
[14] Tezuka, H., Doctoral Thesis, Department of Materials Science, The University of Tokyo, 1990.
[15] Server, W. L., *Journal of Testing and Evaluation,* Vol. 6, 1978, pp. 29–34.
[16] Macke, T., Quenisset, J. M. Neuilly, D., Rocher, J. P., and Naslain, R., *Composites Science and Technology,* Vol. 37, Elsevier Science Publishers Ltd., England, 1990, pp. 267–278.
[17] Abe, F., Noda, T., Arai, H., Narui, M., and Kayano, H., *Journal of Nuclear Materials,* Vol. 150, 1987, pp. 292–301.
[18] Corwin, W. R. and Hougland, A. M., in *The Use of Small-Scale Specimens for Testing Irradiated Materials, ASTM STP 888,* W. R. Corwin and G. E. Lucas, Eds., 1986, pp. 325–338.

Fracture Toughness Testing

Ted L. Anderson[1] *and Robert H. Dodds, Jr.*[2]

Simple Constraint Corrections for Subsize Fracture Toughness Specimens

REFERENCE: Anderson, T. L. and Dodds, R. H., Jr., **"Simple Constraint Corrections for Subsize Fracture Toughness Specimens,"** *Small Specimen Test Techniques Applied to Nuclear Reactor Vessel Thermal Annealing and Plant Life Extension, ASTM STP 1204*, W. R. Corwin, F. M. Haggag, and W. L. Server, Eds., American Society for Testing and Materials, Philadelphia, 1993, pp. 93–105.

ABSTRACT: Loss of constraint triaxiality with plastic deformation severely limits the applicability of small specimens to fracture toughness measurement in the ductile-brittle transition region. In earlier work, the authors developed a framework for correcting cleavage fracture toughness data for constraint loss. The present article presents a simple constraint correction equation that increases the measuring capacity of fracture toughness specimens, that is, it is now possible to measure higher *valid* toughness values with small specimens than was previously possible. At present, the constraint correction can be applied only to the low-to-mid transition region, but ongoing work is aimed at extending the approach to the upper transition region, where cleavage is preceded by stable tearing. Current work is also addressing three-dimensional effects.

KEYWORDS: fracture toughness, cleavage, constraint, size effects, *J* integral

Fracture toughness tests on small specimens are common in the nuclear power industry, where limited material is available from surveillance capsules. The relevance of these data to large structures is unclear, however, since fracture toughness can be size dependent. Small fracture toughness specimens often experience a loss in crack tip triaxiality, which typically results in an apparent elevation of material toughness.

Most of the existing ASTM standards for fracture toughness include size requirements which are designed to ensure that measured values are not influenced by constraint loss. For example, the standard for K_{IC} testing, the ASTM Test Method for Plane-Strain Fracture Toughness of Metallic Materials (E 399–83), specifies the following minimum specimen dimensions for valid results

$$B,\ a \geq 2.5 \left(\frac{K_{IC}}{\sigma_{YS}}\right)^2 \tag{1a}$$

$$0.45 \leq a/W \leq 0.55 \tag{1b}$$

where B is specimen thickness, a is crack length, W is specimen width, and σ_{YS} is the yield strength. For all practical purposes, the above size requirements preclude the use of small specimens for K_{IC} measurements on ferritic steels. Consider, for example, a steel with K_{IC} = 100 MPa$\sqrt{m}$ and σ_{YS} = 400 MPa, where the assumed K_{IC} value corresponds to the

[1] Department of Mechanical Engineering, Texas A&M University, College Station, TX 77843.
[2] Department of Civil Engineering, University of Illinois, Urbana, IL.

lower transition region of a typical pressure vessel steel. For this material, the specimen thickness and crack length must be at least 156 mm (6.1 in.) for a valid test. The size requirements would be even more prohibitive in the upper transition region and the upper shelf.

Standard tests based on the J integral have considerably more lenient size requirements. The current ASTM Test Method for J_{IC}, A Measure of Fracture Toughness (E 813-87) includes the following requirements on specimen dimensions

$$B, b \geq \frac{25J_{IC}}{\sigma_Y} \tag{2}$$

where b ($= W - a$) is the uncracked ligament length and σ_Y is the flow stress, defined as the average of yield and tensile strength. One reason for the relaxed size requirements is that the J integral takes account of nonlinear material behavior, while the K_{IC} methodology is based on a linear elastic material assumption. Another important factor is the fracture mechanism. The J_{IC} test, as defined in ASTM E 813–87, quantifies the resistance to initiation of stable crack growth in metals. This ductile crack growth mechanism is predominantly strain controlled and is relatively insensitive to stress triaxiality at the crack tip. Stress-controlled fracture mechanisms such as cleavage, however, are very sensitive to in-crack tip constraint. Consequently, the authors [*1*,*2*] have proposed the following size limits for critical J values measured at the onset of cleavage

$$B, b \geq \frac{200J_c}{\sigma_Y} \tag{3}$$

Equation 3 is eight times more restrictive than Eq 2, but is typically five to ten times more lenient than Eq 1. This size requirement has been incorporated into several draft standards, including an update of ASTM E 813.

Upper shelf toughness measurements with subsize specimens are usually feasible because Eq 2 does not place significant restrictions on specimen dimensions in most cases. However, it is more difficult to obtain valid measurements of cleavage fracture toughness in the transition region because the size requirements are more stringent.

The recommended size limits in Eq 3 are based on a micromechanics model combined with elastic-plastic finite element analysis and experimental validation [*1–4*]. This recent work not only provides the basis for setting size limits for data that are not affected by constraint loss, but also includes a framework for *correcting* the data when the size limits are not met. Consequently, it is possible to infer useful information from subsize specimen data that ordinarily would be considered invalid. This article describes the basis of this methodology, provides simple equations to correct fracture toughness data for constraint loss, and outlines limitations of the approach.

Scaling Model for Cleavage Fracture

The model for characterizing constraint effects on fracture toughness is based on a local criterion for cleavage failure [*1*,*2*]. This model assumes that cleavage fracture is controlled by the volume of material at the crack tip that is subject to a high stress level; the larger the stress volume, the more likely cleavage will initiate from a critical microstructural feature such as a carbide or inclusion. This assumption is relatively general, e.g., it is not necessary to assume weakest-link fracture, nor is it necessary to obtain an independent measure of

the critical fracture stress. The model merely assumes that cleavage is controlled by the principal stress distribution near the crack tip.

Unlike other micromechanics models, the present methodology does not attempt to make absolute predictions of fracture toughness; rather, the results are *scaled* to a reference solution. The crack tip stress fields in a specimen of interest are compared to the limiting condition of small-scale yielding, where the plastic zone is small compared to length dimensions. A J-like parameter is defined from this comparison between the configuration of interest and the reference solution. This "small scale yielding J" (J_{ssy}) can be interpreted as follows:

1. An amplitude parameter that describes the principal stress distribution near the crack tip.
2. The effective driving force for cleavage.

A critical value of J_{ssy} represents the fracture toughness of an infinitely large specimen. The ratio J/J_{ssy} corresonds to the elevation in J_c due to constraint loss. (See the Appendix for further background on the definition and significance of J_{ssy}.)

Figure 1 shows a plot of J/J_{ssy} versus normalized specimen size for three-point bend specimens with $a/W = 0.05, 0.15, 0.50$ and $n = 10$, where n is the strain hardening exponent in the Ramberg-Osgood stress-strain equation

$$\frac{\epsilon}{\epsilon_0} = \frac{\sigma}{\sigma_0} + \alpha\left(\frac{\sigma}{\sigma_0}\right)^n \tag{4}$$

where ϵ is strain, σ is stress, σ_0 is a reference stress (yield strength in this case), $\epsilon_0 = \sigma_0/E$, and α is a fitting parameter. As the specimen size increases (or as J decreases), the

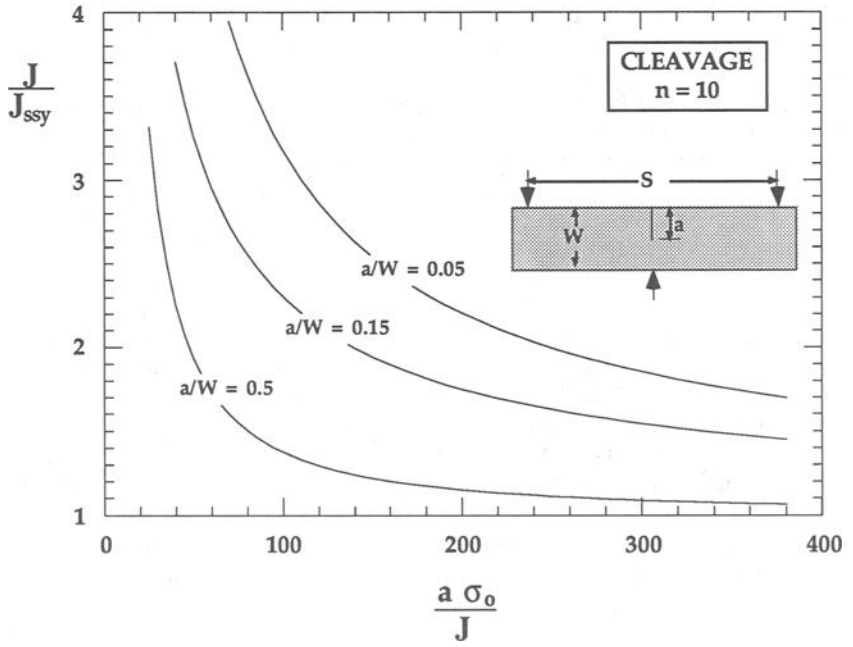

FIG. 1—*Effect of crack length and* a/W *on the* J/J_{ssy} *ratio for cleavage fracture in an SE(B) specimen.*

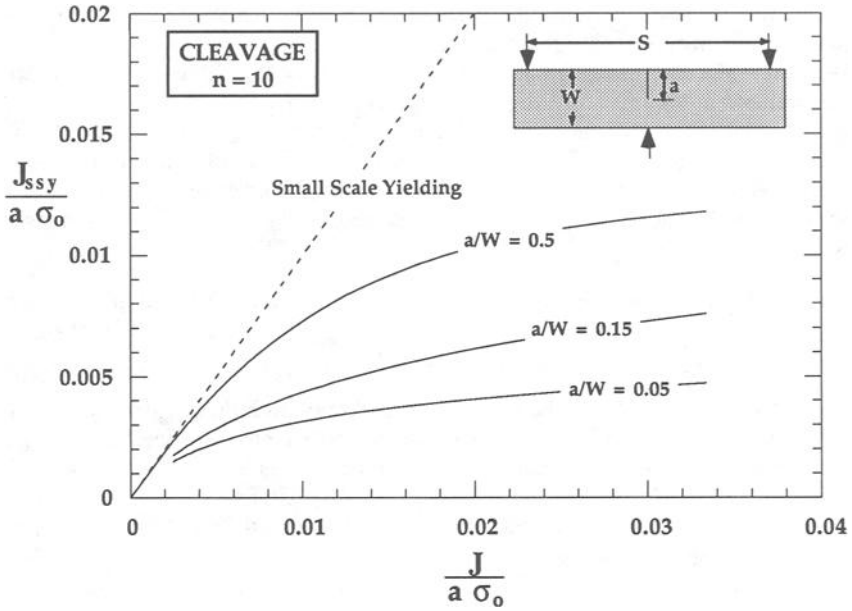

FIG. 2—*Comparison of effective and apparent driving force for cleavage fracture in an SE(B) specimen.*

J/J_{ssy} ratio approaches unity, as expected. For a given absolute crack length, deeply notched specimens ($a/W = 0.5$) are more highly constrained and exhibit lower toughness than specimens with shallow cracks. Figure 1 provides a graphic illustration of the size dependence of fracture toughness. For example, suppose that a specimen fails at $J_c = 200$ kPa m, but that the J/J_{ssy} ratio at failure was 2.0. This specimen would have failed at a J_c value of 100 kPa m had its dimensions been sufficiently large.

Figure 2 shows the results of Fig. 1 replotted in a different form. The *effective* driving force for cleavage fracture, J_{ssy}, is plotted against the *apparent* driving force for cleavage, J. The dashed line indicates the 1:1 trend, where $J = J_{ssy}$. (Note that the horizontal axis has an expanded scale.) At low loads (i.e., small J values), $J = J_{ssy}$ by definition. As load increases, however, constraint loss causes the effective driving force to increase at a slower rate than the applied J. Under large-scale yielding conditions, the curves become flat, indicating that further increases in J will have no effect on J_{ssy}. Thus, the driving force for cleavage saturates at a maximum value. If the material does not cleave prior to reaching the saturation value of J_{ssy}, cleavage is unlikely with subsequent loading.[3]

Figure 3 illustrates the effect of strain hardening on the J/J_{ssy} ratio in deeply notched bend specimens. The low hardening material ($n = 50$) exhibits the most sensitivity to specimen size. All three curves approach unity when the nondimensional quantity on the horizontal axis exceeds approximately 200. This plot is the source of the recommended size requirements in Eq 3; these requirements appear to be valid both for bend and compact specimens provided $a/W \geq 0.5$. Note that when the ratio $b\sigma_y/J = 25$ (the ASTM E 813 size limit in Eq 2), the J/J_{ssy} ratio exceeds 3.0 for $n = 10$, indicating a three-fold increase in toughness over the

[3] In such cases cleavage is possible only after ductile crack growth, where the crack tip "searches" for material that contains a critical cleavage nuclei. The stress volume, and therefore J_{ssy}, increase with crack growth. However, the present analysis considers only stationary cracks.

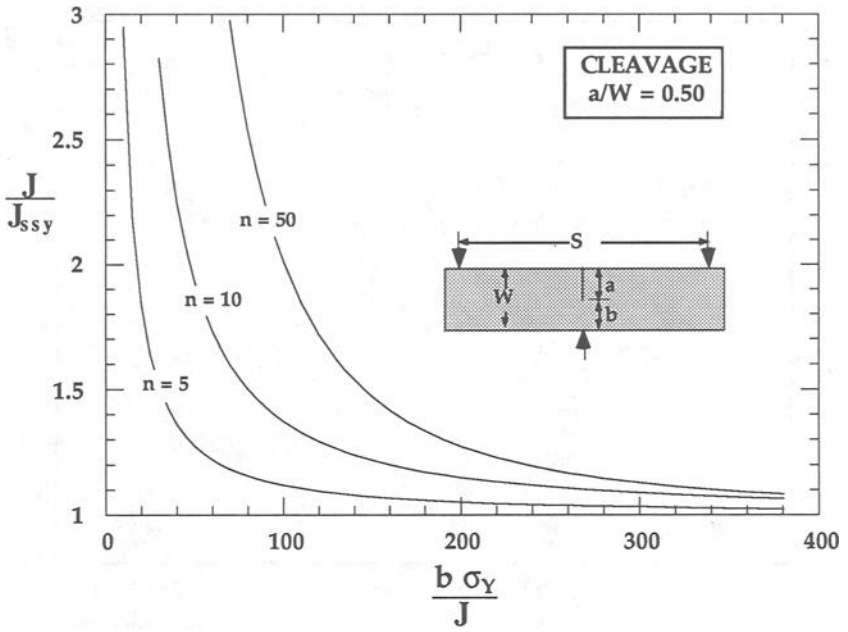

FIG. 3—J/J_{ssy} *for cleavage as a function of strain hardening,* J, *and flow stress.*

small-scale yielding limit. Thus, it is clear from Fig. 3 that the current size requirements for J_{IC} are inadequate when fracture is stress controlled.

The present methodology has been validated experimentally for a wide range of steels. Figure 4 illustrates the ability of the constraint model to quantify geometry effects on fracture toughness. This plot shows J_c data for an A 36 steel plate at two temperatures in the ductile-brittle transition region. At each temperature, the shallow notched specimens ($a/W = 0.15$) tend to have higher toughness than the deeply notched specimens. This geometry dependence disappears, however, when the data are corrected down to J_{ssy} values. An added benefit of this constraint correction is a reduction in data scatter. Referring to Fig. 2, we see that a small variability in J_{ssy} can be magnified when the data are plotted in terms of the applied J at failure.

Constraint Correction Equations

The curves in Fig. 3 have been fit to the following equation

$$\frac{J}{J_{ssy}} = 1 + \phi\left(\frac{J}{b\sigma_{YS}}\right)^{\gamma} \tag{5}$$

where ϕ and γ are constants that depend on the strain-hardening exponent. Table 1 lists ϕ and γ values for $n = 5$, 10, and 50. This equation can be expressed in terms of flow stress rather than yield strength by multiplying ϕ by $(\sigma_{YS}/\sigma_Y)^{\gamma}$. The following equations express ϕ and γ as a function of the Ramberg-Osgood exponent

$$\phi = 0.8425(n)^{2.262} \tag{6a}$$

$$\gamma = 1.126 + 0.01925n - 8.333 \times 10^{-5}(n)^2 \tag{6b}$$

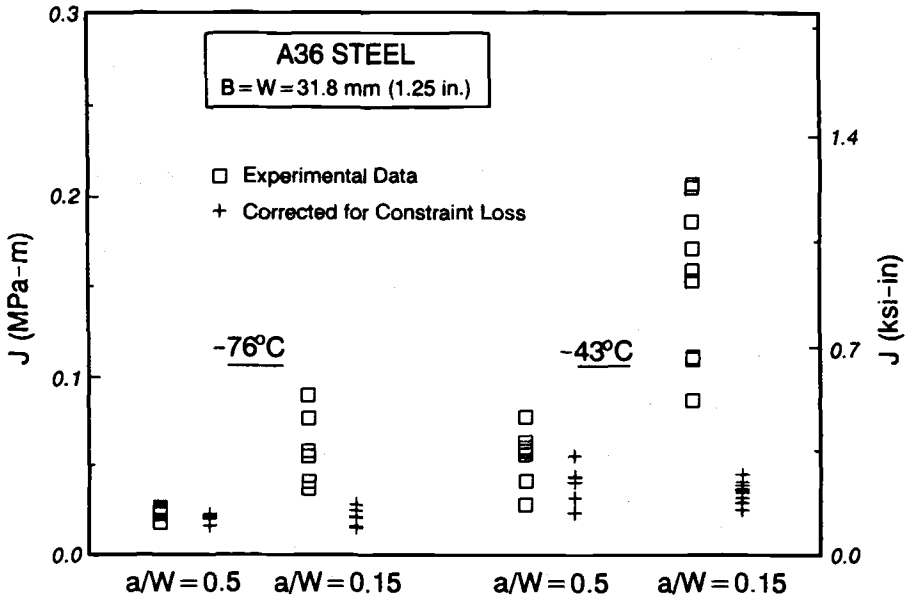

FIG. 4—*Comparison of* J_c *values for cleavage in A 36 steel, with* J_c *corrected for constraint loss* [1,2].

These equations are valid for $5 \leq n \leq 50$. Wallin [5] has also fit our results to an equation of the form of Eq 5, but his expressions for ϕ and γ are different from Eq 6.

Of course, the Ramberg-Osgood expression (Eq 4) is merely an idealization of flow behavior. Moreover, there are many instances where it is not possible to fit Eq 4 to a stress-strain curve because data for the entire curve are not available. In such cases, an approximate relationship between n and the tensile/yield ratio can be applied

$$\frac{\sigma_{TS}}{\sigma_{YS}} = \frac{\left(\frac{N}{0.002}\right)^N}{\exp(N)} \tag{7}$$

where $N = 1/n$. This expression was derived by solving for the tensile instability point in Eq 4 and converting true stress to engineering stress. Since the Ramberg-Osgood exponent appears in three places in Eq 7, an iterative solution for n is required.

TABLE 1—*Parameters for the constraint correction for three Ramberg-Osgood exponents.*

n	ϕ	γ
5	32.08	1.217
10	154.2	1.310
50	5867	1.882

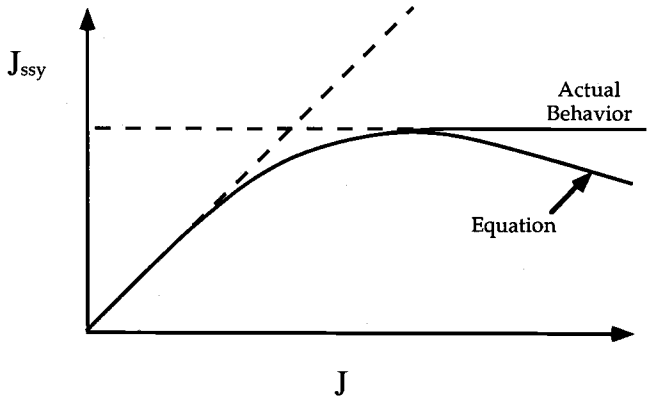

FIG. 5—*Schematic variation of the effective driving force for cleavage,* J_{ssy}, *with the apparent driving force,* J. *The effective driving force reaches a plateau, but the simple equation (Eq 5) exhibits a maximum and thus is not valid beyond the maximum point.*

Limitations of the Approach

Figure 2 indicates that the effective driving force for cleavage, J_{ssy}, reaches a plateau when J is large relative to ligament length and yield strength. The simple equation for J_{ssy} (Eq 5), however, exhibits a maximum, as Fig. 5 illustrates. Thus this equation is only valid up to its maximum. Figure 6 illustrates the valid range of Eq 5 as a function of strain-hardening exponent. The valid range is largest for high hardening materials (low n).

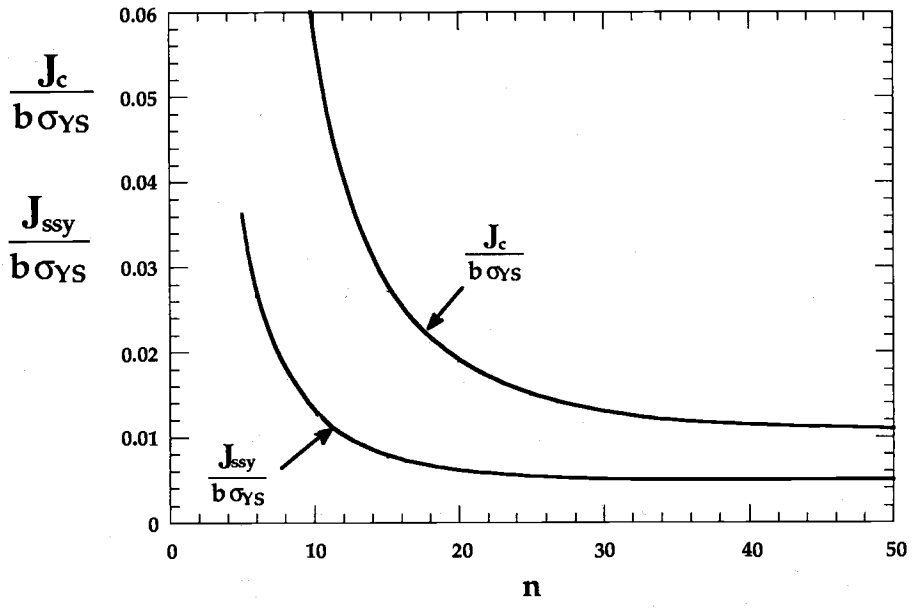

FIG. 6—*Nondimensionalized measuring capacity as a function of strain-hardening exponent. The limiting* J *and* J_{ssy} *values correspond to the plateau in* J_{ssy} *and the maximum in the simple equation (see Fig. 5).*

TABLE 2—*Measuring capacity for cleavage fracture in a 1T compact specimen, where* b = *25 mm. Assumed flow properties:* n = *10,* σ_{YS} = *450 MPa,* σ_{TS} = *550 MPa.*

	K_{JC}, MPa$\sqrt{\text{m}}$	
1T Compact Specimen	Measured	Corrected
Without correction	119	...
With correction	358	178

Even without the limitations of Eq 5, constraint corrections are not currently possible beyond the onset of the J_{ssy} plateau. If a specimen reaches this plateau without failing by cleavage, subsequent loading can produce cleavage only if the crack grows by ductile tearing, thereby increasing the stress volume and, in turn, increasing J_{ssy}. The present analysis considers only stationary cracks. Wallin [*5,6*] has considered the effect of crack growth on J_{ssy}, but he makes simple assumptions about the stress field in front of a growing crack. The authors are currently performing finite element analysis of growing cracks in an effort to extend the existing model into the upper transition region.

The aforementioned restrictions on the existing constraint correction impose an upper limit on the measuring capacity of laboratory specimens, that is, a test specimen is capable of quantifying cleavage fracture toughness only up to the plateau in J_{ssy}. Consider, for example, a material with $n = 10$, $\sigma_{YS} = 450$ MPa, and $\sigma_{TS} = 550$ MPa (typical properties for A 533 grade B steel). Table 2 lists the measuring capacity of a 1T compact specimen ($b = B = 25$ mm) made from this material. Fracture toughness is expressed in terms of K_{Jc}, the K equivalent of J_c, defined as

$$K_{Jc} = \sqrt{\frac{J_c E}{1 - \nu^2}} \tag{8}$$

The first row in Table 2 corresponds to the maximum toughness that meets the size requirements in Eq 3, while the second row lists the K equivalents of the J_c and critical J_{ssy} values at the plateau. Note that the constraint correction increases the measuring capacity of the specimen. The toughness values in Table 2 correspond roughly to the mid-transition region of a reactor pressure vessel steel. Table 3 lists the same information for a precracked Charpy specimen, with $b = 5$ mm. The measuring capacity is more limited in the smaller specimen. Without the constraint correction, the maximum K_{Jc} value that can be measured is 53 MPa$\sqrt{\text{m}}$, which is near the lower shelf. The largest corrected toughness that can be

TABLE 3—*Measuring capacity for cleavage fracture in a precracked Charpy specimen, where* b = *5 mm. Assumed flow properties:* n = *10,* σ_{YS} = *450 MPa,* σ_{TS} = *550 MPa.*

	K_{JC}, MPa$\sqrt{\text{m}}$	
Precracked Charpy Specimen	Measured	Corrected
Without correction	53	...
With correction	160	80

measured in the precracked Charpy specimen is 80 MPa$\sqrt{m}$. Thus, it is not possible to characterize toughness in the mid to upper transition region with specimens of this size.

The constraint corrections presented here are based on two-dimensional finite element analysis and consider only the effect of finite crack length and ligament effects. The effect of the thickness dimension is not explicitly considered here. Experimental data indicate that thickness is less important than in-plane effects [*4*]. Thickness does, however, influence the stress volume at the crack tip. The authors are currently performing three-dimensional finite element analysis to incorporate thickness effects.

Summary and Conclusions

A simple constraint correction was introduced that increases the cleavage fracture toughness measuring capacity of small specimens. Even with this correction, however, valid cleavage fracture toughness measurements are limited to the lower or mid-transition region, depending on the specimen size. Current research is aimed at extending this methodology to the upper transition region, where cleavage is preceded by stable tearing. The authors are also investigating three-dimensional constraint issues.

APPENDIX

Theoretical Basis of the Constraint Model

Under small-scale yielding conditions, the crack tip stresses and strains are uniquely characterized by J, and the onset of fracture is uniquely defined by a critical value of J, irrespective of the micromechanism of failure. When J dominance is lost, the stresses and strains no longer increase in proportion to one another, and critical J values are size dependent. The magnitude of this size dependence depends on the micromechanism of failure. For example, a material that fails when a critical strain is reached locally would exhibit a different fracture toughness size dependence from a material that fails at a critical local stress.

In order to quantify size effects on fracture toughness, one must assume a local failure criterion. In the case of cleavage fracture, a number of micromechanical models have recently been proposed, most based on weakest-link statistics. The weakest-link models assume that cleavage failure is controlled by the largest or most favorably oriented fracture-triggering particle. The actual trigger event involves a local Griffith instability of a microcrack which forms from a microstructural feature such as a carbide or inclusion; the Griffith energy balance is satisfied when a critical stress is reached in the vicinity of the microcrack. The size and location of the critical microstructural feature dictate the fracture toughness; thus cleavage toughness is subject to considerable scatter.

The Griffith instability criterion implies fracture at a critical normal stress near the tip of the crack; the statistical sampling nature of cleavage initiation (i.e., the probability of finding a critical microstructural feature near the crack tip) suggests that the volume of the process zone is also important. Thus, the probability of cleavage fracture in a cracked specimen can be expressed in the following general form

$$F = F\{V(\sigma_1)\} \tag{9}$$

where F is the failure probability, σ_1 is the maximum principal stress at a point, and $V(\sigma_1)$ is the cumulative volume sampled where the principal stress is $\geq\sigma_1$. Equation 9 is sufficiently general to apply to any fracture process controlled by maximum principal stress, not just weakest link failure. For a specimen subjected to plane strain conditions, $V = BA$, where

A is cumulative area on the x-y plane. (This article uses the conventional fracture mechanics coordinate axes, where x is the direction of crack propagation, y is normal to the crack plane, and z is parallel to the crack front.) For small-scale yielding, dimensional analysis shows that the principal stress ahead of the crack tip can be written as

$$\frac{\sigma_1}{\sigma_0} = f\left(\frac{J}{\sigma_0 r}, \theta\right) \tag{10}$$

where J is the applied J integral as defined by Rice [7], r is the radial distance from the crack tip, and θ is the angle from the crack plane. It can be shown that the HRR singularity [8,9] is a special case of Eq 10. When J dominance is lost, there is a relaxation in triaxiality; the principal stress at a fixed r and θ is less than the small-scale yielding value.

Equation 10 can be inverted to solve for the radius corresponding to a given stress and angle

$$r(\sigma_1/\sigma_0, \theta) = \frac{J}{\sigma_0} g(\sigma_1/\sigma_0, \theta) \tag{11}$$

Solving for the area inside a specific principal stress contour gives

$$A(\sigma_1/\sigma_0) = \frac{J^2}{\sigma_0^2} h(\sigma_1/\sigma_0) \tag{12}$$

where

$$h(\sigma_1/\sigma_0) = \frac{1}{2}\int_{-\pi}^{\pi} g^2(\sigma_1/\sigma_0, \theta) d\theta \tag{13}$$

Thus for a given stress, the area scales with J^2 in the case of small-scale yielding. Under large-scale yielding conditions, the specimen or structure experiences a loss in constraint, and the area inside a given principal stress contour (at a given J value) is less than predicted from small-scale yielding

$$A(\sigma_1/\sigma_0) = \Phi\frac{J^2}{\sigma_0^2} h(\sigma_1/\sigma_0) \tag{14}$$

where Φ is a constraint factor that is ≤ 1. Let us define an *effective J* in large-scale yielding that relates the area inside the principal stress contour to the small-scale yielding case

$$A(\sigma_1/\sigma_0) = \frac{(J_{ssy})^2}{\sigma_0^2} h(\sigma_1/\sigma_0) \tag{15}$$

where J_{ssy} is the effective small-scale yielding J, i.e., the value of J that would result in the area $A(\sigma_1/\sigma_0)$ if the structure were large relative to the plastic zone. Therefore, the ratio of the applied J to the effective J is given by

$$\frac{J}{J_{ssy}} = \sqrt{\frac{1}{\Phi}} \tag{16}$$

The small-scale yielding J value (J_{ssy}) can be viewed as *the effective driving force for cleavage,* while J is the *apparent* driving force.

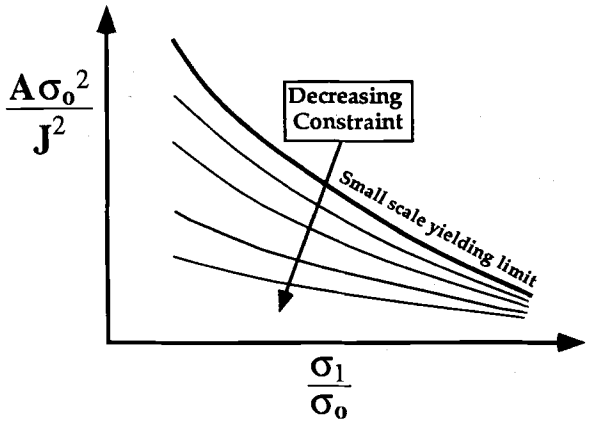

(a)

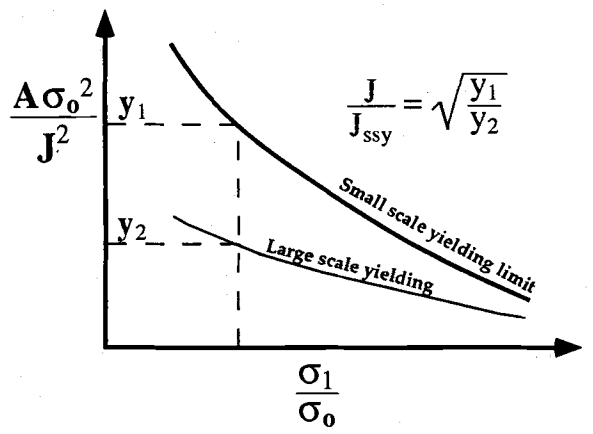

(b)

FIG. 7—*Procedure for determining the effective small-scale yielding* J *integral,* J_{ssy} *for cleavage.*

The procedure for determining J_{ssy} is illustrated schematically in Fig. 7. The dimensionless quantity $A\ \sigma_0^2/J^2$ is plotted against σ_1/σ_0 for both the small-scale yielding solution (i.e., infinite body) and a finite-size specimen. In the latter case, each value of J gives a different curve because ϕ varies during deformation; the small-scale yielding curve is invariant since $\phi = 1$. The ratio J/J_{ssy} is determined for a given J and σ_1 value through the ratio of $A\ \sigma_0^2/J^2$ values for small- and large-scale yielding, as illustrated in Fig. 7*b*.

References

[*1*] Anderson, T. L. and Dodds, R. H., Jr., "Specimen Size Requirements for Fracture Toughness Testing in the Ductile-Brittle Transition Region," *Journal of Testing and Evaluation,* Vol. 19, 1991, pp. 123–134.

[*2*] Dodds, R. H., Jr., Anderson, T. L., and Kirk, M. T., "A Framework to Correlate *a*/*W* Effects on Elastic-Plastic Fracture Toughness (J_c)," *International Journal of Fracture,* Vol. 48, 1991, pp. 1–22.

[3] Kirk, M. T., Koppenhoffer, K. C., and Shih, C. F., "Effect of Constraint on Specimen Dimensions Needed to Obtain Structurally Relevant Toughness Measurements," *Constraint Effects in Fracture,* STP 1171, American Society for Testing and Materials, Philadelphia, 1993, pp. 79–103.
[4] Kirk, M. T., unpublished work.
[5] Wallin, K., "Statistical Aspects of Constraint with Emphasis to Testing and Analysis of Laboratory Specimens in the Transition Region," *Constraint Effects in Fracture,* American Society for Testing and Materials, Philadelphia, 1993, pp. 264–288.
[6] Wallin, K., "The Effect of Ductile Tearing on Cleavage Fracture Probability in Fracture Toughness Testing," *Engineering Fracture Mechanics,* Vol. 32, 1989, pp. 523–531.
[7] Rice, J. R., "A Path Independent Integral and the Approximate Analysis of Strain Concentration by Notches and Cracks," *Journal of Applied Mechanics,* Vol. 35, 1968, pp. 379–386.
[8] Hutchinson, J. W., "Singular Behavior at the End of a Tensile Crack Tip in a Hardening Material," *Journal of the Mechanics and Physics of Solids,* Vol. 16, 1968, pp. 13–31.
[9] Rice, J. R. and Rosengren, G. F., "Plane Strain Deformation near a Crack Tip in a Power-Law Hardening Material," *Journal of the Mechanics and Physics of Solids,* Vol. 16, 1968, pp. 1–12.

DISCUSSION

Dr. M. P. Manahan,[1] *(written discussion)*—The constraint correction enables testing further into the transition region. How do the results of constraint correction for laboratory specimens compare with full section behavior?

T. L. Anderson and R. H. Dodds (authors' closure)—This depends on what is meant by full section behavior. The constraint correction predicts limiting toughness for an infinite body. In practical terms, this means that the structural dimensions and the crack size are $>>$ the plastic zone size. However, a structure that contains a *shallow* crack will *lose* constraint, particularly if the loading is predominantly membrane (as opposed to bending). In such cases, the critical J (or K) value in the structure may be higher than in the laboratory specimen, and the constraint-corrected value from the laboratory will be overly conservative when applied to the structure. Thus, in order to predict structural behavior, we must account for constraint loss in both the structure and specimen. Our early work focused on specimen geometries, but we are now considering structural geometries such as semi-elliptical surface cracks.

D. J. Alexander[2] *(written discussion)*—(1) Since all of your finite element analyses are done in plane strain, how can you justify your comment that thickness effects are second order effects? (2) Your finite element meshes are very fine near the crack tip, but quickly become much coarser. Is there any possibility that the coarseness of the mesh artificially restricts the growth of the plastic zone away from the crack tip and so suppresses the development of general yield in your specimens?

T. L. Anderson and R. H. Dodds (authors' closure)—(1) The comment on the relative unimportance of thickness is based in part on 3-D finite element results recently obtained at the California Institute of Technology. In addition, Kirk et al. [3] performed a series of tests in which they systematically varied both thickness and a/W; they observed that toughness was far more sensitive to crack length. (2) We have performed convergence studies which indicate that the mesh design is adequate to capture both the local crack tip stresses and the global plastic deformation. Note that although the mesh transitions from very small

[1] MPM Research and Consulting, 213 Teaberry Circle, State College, PA 16803.
[2] Oak Ridge National Laboratory, PO Box 2008, Oak Ridge, TN 37831-6151.

elements to fairly large elements, the transition in size between neighboring elements is relatively modest.

A. Kohyama[3] (*written discussion*)—What is your impact-tup geometry and how do you compensate or normalize the effect of tup geometry?

T. L. Anderson and R. H. Dodds (*authors' closure*)—The present analysis applies only to quasi-static loading of cracked specimens. The tup geometry is not a factor here because we were considering *slow* bending of precracked Charpy specimens. We are currently applying the methodology to dynamic loading, in which case the tup geometry may prove an important variable.

W. Schmitt[4] (*written discussion*)—In which way does your *J*-correction factor take into account stable tearing prior to cleavage (i.e., the changing stress-strain field from blunting to crack formation)?

T. L. Anderson and R. H. Dodds (*authors' closure*)—The constraint correction presented in this article applies only to stationary cracks. We have recently extended the model to the upper transition region, where ductile tearing precedes cleavage. The results will be published in the near future.

G. Lucas[5] (*written discussion*)—How sensitive is the mapping of J to J_{ssy} to the assumption of the magnitude σ_1 (threshold stress for change)/σ_0 (yield stress)?

T. L. Anderson and R. H. Dodds (*authors' closure*)—See Fig. 10 of Ref *1* (which was not included in this article due to space limitations). This figure illustrates that the ratio J/J_{ssy} is insensitive to σ_1/σ_0 up to roughly $a\sigma_0/J = 30$. The crack tip stress fields retain a self-similar character as long as the crack tip opening displacement (CTOD) is small relative to the crack length and ligament length. It is this self similarity which gives rise to a nearly constant J/J_{ssy} value over a range of σ_1/σ_0.

[3] University of Tokyo, Hongo Bunkyo-ku, Tokyo 113, Japan.
[4] Fraunhofer-Institut für Werkstoff Mechanik (IWM), Freiburg, Federal Republic of Germany.
[5] Department of Chemical and Nuclear Engineering, University of California, Santa Barbara, Santa Barbara, CA 93106.

Winfried Schmitt[1] *and Johann G. Blauel*[1]

Application of Micromechanical Material Models for the Evaluation of the Fracture Toughness of Primary Circuit Steel Components

REFERENCE: Schmitt, W. and Blauel, J. G., **"Application of Micromechanical Material Models for the Evaluation of the Fracture Toughness of Primary Circuit Steel Components,"** *Small Specimen Test Techniques Applied to Nuclear Reactor Vessel Thermal Annealing and Plant Life Extension, ASTM STP 1204,* W. R. Corwin, F. M. Haggag, and W. L. Server, Eds., American Society for Testing and Materials, Philadelphia, 1993, pp. 106–117.

ABSTRACT: The safety assessment of nuclear components requires that fracture mechanics material data or curves are available. These data must be measured with suitable specimens of the original material for the given condition, i.e., temperature and irradiation. Especially for reactor pressure vessel (RPV) weld material, fracture mechanics specimens are not available within the irradiation surveillance programs in sufficient number, or, if available, the performance of accurate fracture mechanics tests in hot cell facilities is extremely difficult.

New developments in the field of micromechanical material models taking into account the ductile damage process characterized by nucleation, growth, and coalescence of voids make it possible to determine micromechanical material parameters from tension tests and finite element analyses of notched and smooth specimens. If, in addition, a characteristic length, l_c, is considered, the ductile fracture resistance behavior of fracture mechanics specimens and, hence, J-resistance curves may be predicted.

Here, the modified Gurson model is applied to calculate a static J-resistance curve for irradiated weld material from the results of smooth static tension tests out of the irradiation surveillance program of a specific nuclear power plant. Since original material was not available in sufficient quantity for fracture mechanics tests, a verification program was conducted comprising tests and analyses of smooth tension specimens and side-grooved compact (CT) and wedge opening loading (WOL) X-type specimens of two unirradiated and one irradiated weld materials. In every case, the predicted resistance curves are in good agreement with the measured curves.

Following the successful evaluation of static material tests, the first experimental and numerical steps are presented towards the evaluation of dynamic J-R curves from the results of instrumented Charpy tests.

KEYWORDS: micromechanical material models, fracture toughness, J-resistance curves, steel, weld material, irradiation surveillance program, primary circuit, CT specimens, WOL-X-specimens, tension test, Charpy test

In order to complement the fracture toughness database for the pressure vessel of a specific light water nuclear power plant, the modified Gurson model for ductile fracture analysis has been applied to tension test data of irradiated weld material out of the surveillance program. This rather new method is based on developments by Needleman and Tvergaard

[1] Head of Department, Fraunhofer-Institut für Werkstoffmechanik (IWM), Freiburg, Federal Republic of Germany.

[*1*] on the basis of the yield condition suggested by Gurson [*2*]. In this material model the plastic flow is influenced by microscopic voids which are represented by a single damage parameter, the volume fraction of voids, f. Numerical and experimental investigations with this model [*3–5*] show that the development of microscopic damage and global plastic deformation are well described by the model.

Gurson introduced a plastic potential applicable to porous solids with the volume fraction of voids, f, given by

$$\phi = \frac{3\sigma'_{ij}\sigma'_{ij}}{2\sigma_m^2} + f \cosh\left(\frac{\sigma_{kk}}{2\sigma_m}\right) - (1 + f^2) = 0 \tag{1}$$

where σ_m is the flow stress of the material, σ_{ij} and σ'_{ij} are the components of the stress tensor and the deviator, respectively; Einstein's summation convention applies. If no voids are present, $f = 0$, the plastic potential (Eq 1) is identical with the well-known von Mises potential. For $f = 1$, that is, the material consists entirely of voids, all stress components have to vanish in order to satisfy Eq 1: the material loses its load-carrying capacity. For most of the materials investigated, the coalescence process starts at critical void volume fractions, f_c, much smaller than one.

The increase of the volume fraction of voids is caused by the nucleation of new voids and by the growth of existing voids. It is described by the following growth rate of f, $\dot{f}$

$$\dot{f} = \dot{f}_{\text{nucleation}} + \dot{f}_{\text{growth}} \tag{2}$$

$$\dot{f}_{\text{nucleation}} = B(\dot{\sigma}_m + \dot{\sigma}_{kk}/3) + D\dot{\epsilon}^p_m \tag{3}$$

$$\dot{f}_{\text{growth}} = (1 - f)\dot{\eta}^p_{kk} \tag{4}$$

where η^p_{ij} is the plastic part of the strain tensor.

The first term in Eq 3 models void nucleation controlled by the maximum normal stress at the boundary between second-phase particles and the matrix. The second term models void nucleation controlled by the equivalent plastic strain, ϵ^p_m. For the ductile materials of this study only strain-controlled void nucleation is considered, $B = 0$. Equation 4 is derived from the plastic incompressibility of the matrix material.

The Gurson model was implemented in the commercial finite element program ADINA. The finite element models of the fracture mechanics specimens consist of 440 isotropic plane strain elements with 1461 nodal points in the case of the CT-specimen (628 elements and 2155 nodes for the WOL-X specimen). A total number of 56 (80) time steps with full Newton equilibrium iterations were used. The assumption $B = 0$ ensures that the total stiffness matrix remains symmetric.

In the vicinity of stress or strain singularities, i.e. in the neighborhood of cracks, the critical void volume fraction would be exceeded even at negligibly small loads. Therefore, the numerical model must include a characteristic length, l_c, such that the process of coalescence is active only if f_c is exceeded at least over this distance. The characteristic length, l_c, of this study is evaluated by adjusting the size of the elements around the original crack tip in a numerical prediction of cracked (e.g., CT) specimens to fit the experimental results. With eight-noded quadratic elements and the 2 by 2-integration scheme, the typical element size is about 60 by 100 μm.

All parameters of the Gurson model have a physical meaning and must be evaluated for every material under consideration. For the prediction of the fracture toughness it is in many cases sufficient to enter best estimates for some of the parameters which are kept

constant throughout the analysis. For the ferritic base material, e.g., the initial volume fraction of voids has been identified with the volume fraction, determined from metallographic sectioning, of second-phase MnS particles capable of forming voids; according to Ref *6*, it is assumed that void nucleation follows a normal distribution. The material parameter, l_c, is related to the distance between the void-forming inclusions. This complete set of parameters is applied to predict the behavior of cracked specimens, thus yielding different *J*-resistance curves for different specimen geometries.

Within the irradiation surveillance program of the plant under investigation, not only were the usual tension and Charpy specimens included but also fracture mechanics specimens of the WOL-X type. All available specimens had been tested in the transition temperature range. Due to the relatively small specimen thickness of 25 mm, valid toughness values, K_{Ic}, according to the ASTM Test Method for Plane-Strain Fracture Toughness of Metallic Materials (E 399–81) were obtained only at low temperatures. At higher temperatures, initiation values of the *J*-integral, J_i, were determined using a potential-drop technique and were then converted into toughness values, K_{Ji}. Especially for the specimens tested at higher temperatures (i.e., 100°C and above), this testing and evaluation method turned out to be unreliable and over-conservative, requiring further investigation. Consequently, available test records of smooth tension specimens had to be used as a basis for the application of the modified Gurson model in order to obtain plant-specific fracture toughness values.

Validation Program

Although the method had successfully been applied in a number of cases for ferritic steels (base material), the extension to weld material and in particular to irradiated weld material implies additional problems because of material inhomogeneities and reduced accuracy of measurements in hot-cell facilities. Therefore, a validation program was conducted including two unirradiated and one irradiated weld materials typical for German RPVs.

Material 1 of the first program step is from a simulation weld used in a previous study to investigate the warm-prestress effect. Notched and smooth tension tests were performed and analyzed. Figure 1 shows the measured and calculated force versus displacement curves

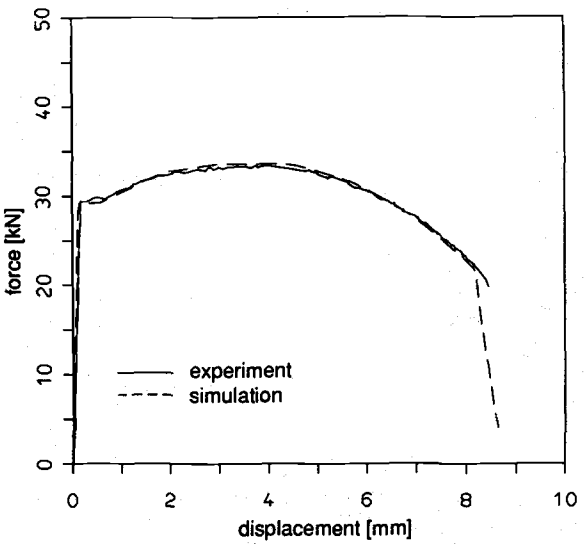

FIG. 1—*Material 1; smooth tension test: measured and calculated force versus displacement curves.*

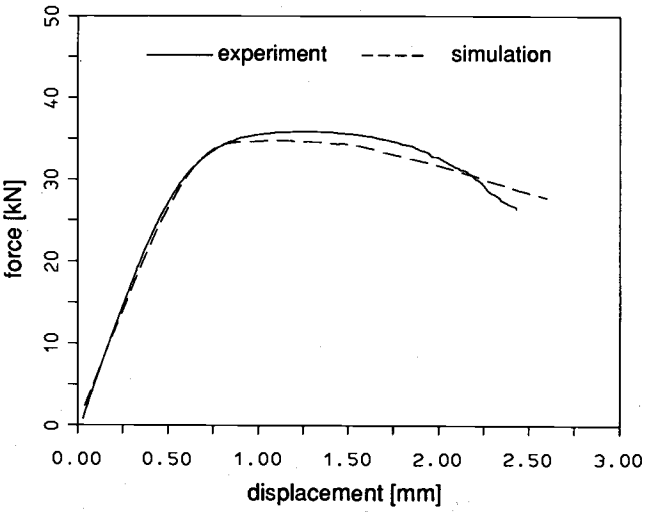

FIG. 2—*Material 1, compact specimen: measured and calculated force versus displacement curves.*

for the smooth specimen. From the finite element analysis the set of micromechanical material parameters, in particular a critical volume fraction of voids, $f_c = 0.045$, was determined. These parameters were used to predict the behavior of a compact specimen, Fig. 2. The calculated J-resistance curve is compared with the evaluation of two experiments in Fig. 3. Considering a substantial variation in the experiments, the agreement is satisfactory. The length in ligament direction of the near-tip elements was 80 μm.

Since the study of the irradiated weld material (Material 3, below) is complicated by the fact that the available fracture mechanics specimens are of the WOL-X type, a number of WOL-X specimens of Material 1 were included in the test program. The aim of these

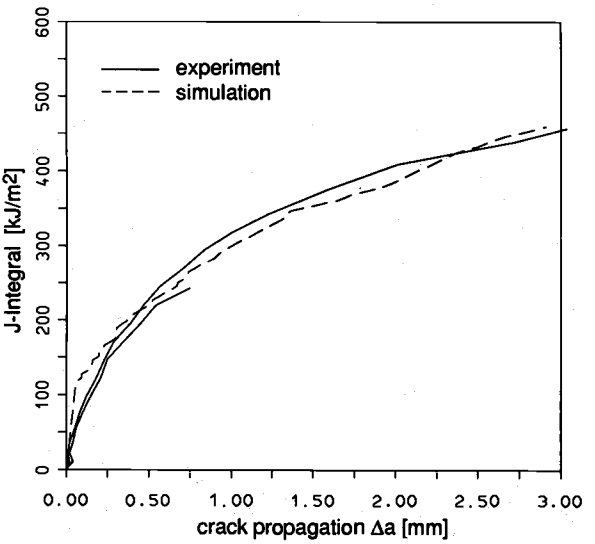

FIG. 3—*Material 1, compact specimen: measured (two experiments) and calculated J-resistance curves.*

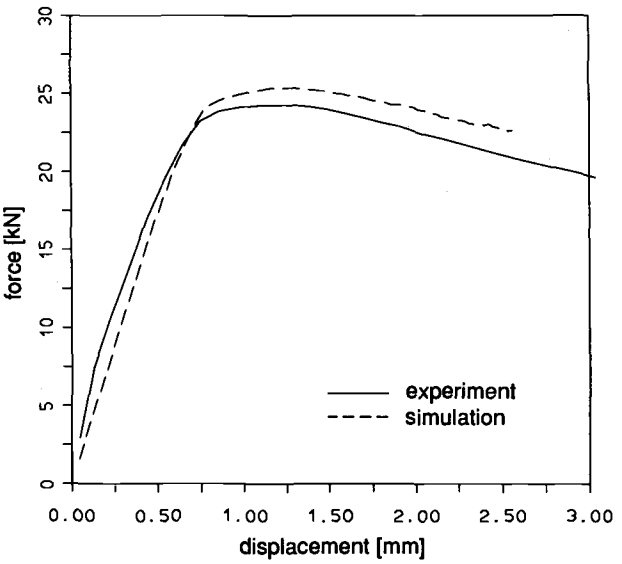

FIG. 4—*Material 1, WOL-X specimen: measured and calculated force versus displacement curves.*

additional tests was not only to check the numerical models employed, but also to optimize design of the loading grips for use in the hot cells. Finally, these tests gave an impression of the relatively large scatter to be expected from fracture mechanics tests with WOL-X specimens. Figure 4 compares the force-displacement diagram of one experiment with the numerical prediction: the predicted curve is in good qualitative agreement with the measured curve, but the calculated forces exceed the measured forces consistently by about 5%. The three measured *J*-resistance curves for one specimen size and the same material in Fig. 5

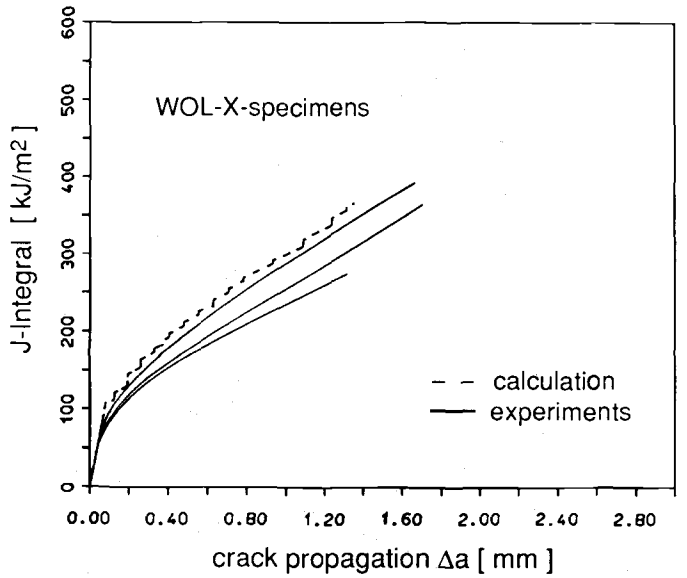

FIG. 5—*Material 1, WOL-X specimen: measured (three experiments) and calculated J-resistance curves.*

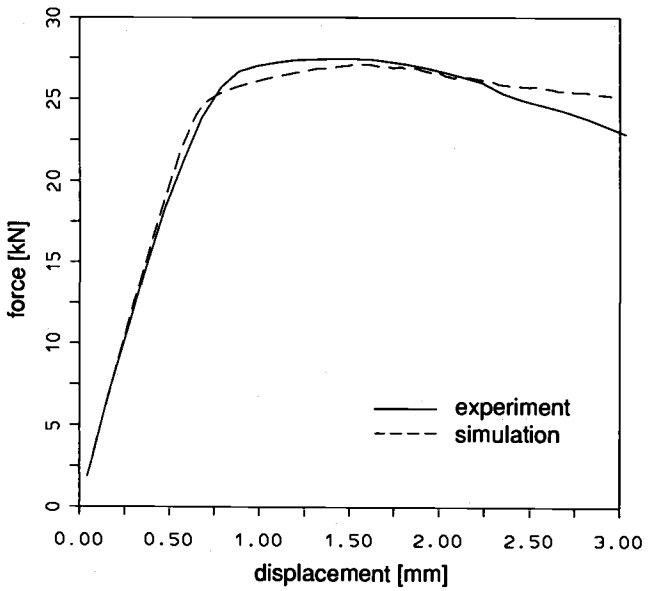

FIG. 6—*Material 2, WOL-X specimen: measured and calculated force versus displacement curves.*

show significant differences in the slopes. As could already be expected from Fig. 4, the curve which was predicted from the micromechanical material parameters forms an upper bound. The length in ligament direction of the near-tip elements was again 80 μm.

In the second step, unirradiated specimens out of the original weld material of the plant surveillance program were tested (Material 2). From the analysis of a smooth tension test, the critical volume fraction of voids, $f_c = 0.06$, was determined. The predicted force-displacement curve of a WOL-X specimen in Fig. 6 agrees well with the experimental curve. Figure 7 shows

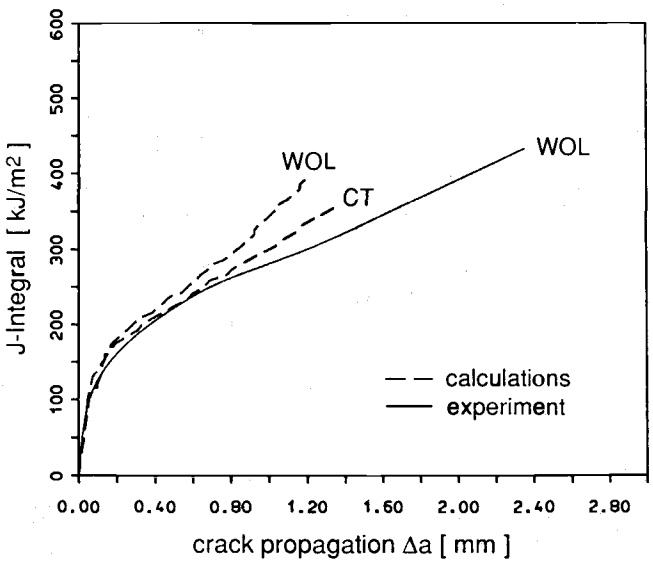

FIG. 7—*Material 2: measured (WOL-X) and calculated (CT and WOL-X) J-resistance curves.*

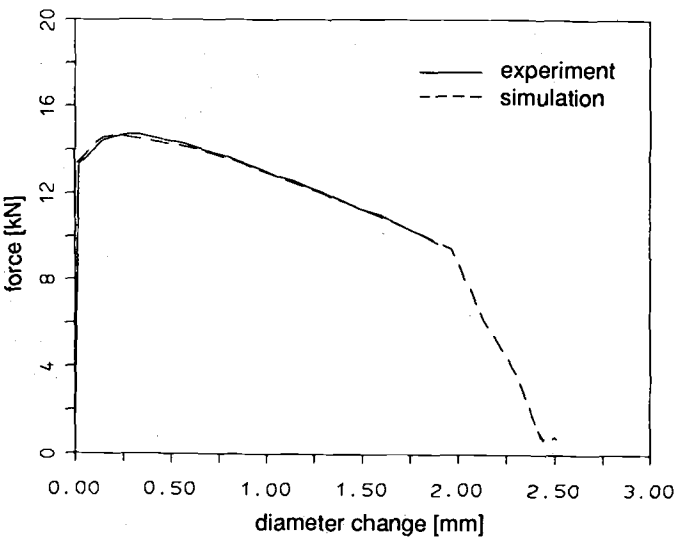

FIG. 8—*Material 3, smooth tension test: measured and calculated force versus displacement curves.*

good agreement also for the *J*-resistance curves, at least for small amounts of crack extension, Δa. The numerical simulation was also performed for a fictitious compact specimen. The resulting *J-R* curve also agrees very well with the other curves for small Δa. The length in ligament direction of the near-tip elements was now 64 μm, indicating a smaller value of l_c than for Material 1.

Finally, irradiated weld material (Material 3) out of the irradiation surveillance program of a different power plant was examined. The experiments were performed by SIEMENS/KWU in their hot-cell facilities [7]. Figure 8 shows the measured and calculated force versus diameter-change curves of a smooth tension specimen tested at room temperature. From this calculation the set of micromechanical material parameters of the material was determined. The critical volume fraction of voids was found to be $f_c = 0.004$. At 100°C, a fracture mechanics test was performed with a WOL-X specimen, yielding a force-displacement curve shown in Fig. 9 and a *J*-resistance curve shown in Fig. 10. The results of the numerical prediction using the micromechanical material parameters obtained from the tension test agree fairly well with the experimental results.

Summarizing the validation program, it may be concluded that the numerical models employed systematically overestimate the stiffness of WOL specimens, especially in the elastic-plastic regime, so that the calculated resistance curve in Fig. 10 lies above the measured curve. However, bearing in mind that the experimental evaluation scheme of *J*-resistance curves from WOL-type specimens is not very well established because of uncertainties concerning the stiffness of the loading system, that coincidence is acceptable. However, within the class of materials investigated, it was possible to extract relevant micromechanical material parameters from smooth tension tests. The characteristic material length, l_c, showed only small differences. If experiments with CT specimens could be performed, the agreement of prediction and experiment was usually very good, also quantitatively.

Evaluation of EOL Weld Material Properties

The micromechanical material parameters were extracted from the test record of a smooth tension specimen tested at 120°C. The specimen had seen a neutron flux of $1.7 \cdot 10^{19}$ n/cm^2,

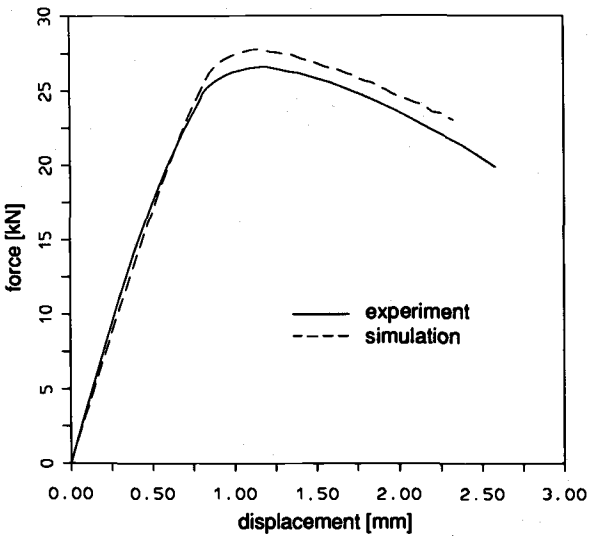

FIG. 9—*Material 3, WOL-X specimen: measured and calculated force versus displacement curves.*

representing end-of-life conditions. Figure 11 shows the force-displacement diagram of this test together with the result of the numerical simulation, yielding a critical volume fraction of voids, $f_c = 0.025$. In contrast to the former studies, no fracture mechanics test is available to define the characteristic material length, l_c. Since l_c is assumed to be closely related to the average spacing of void-forming inclusions which is not changed by neutron irradiation, the near-tip model employed for Material 2, i.e. the original weld material in the unirradiated state, was used.

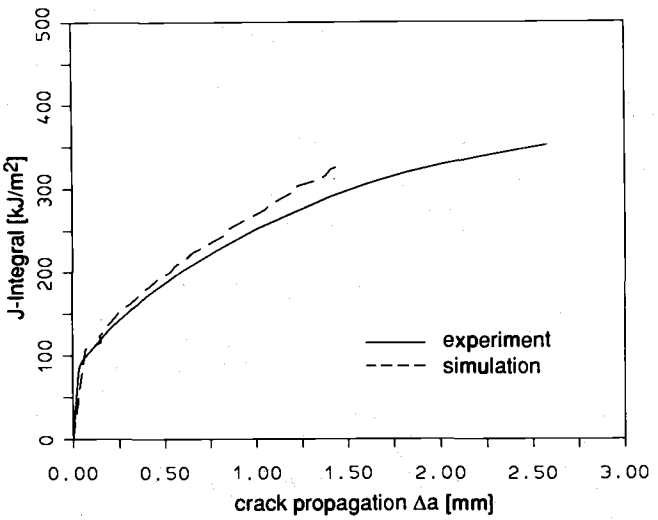

FIG. 10—*Material 3, WOL-X specimen: measured and calculated J-resistance curves.*

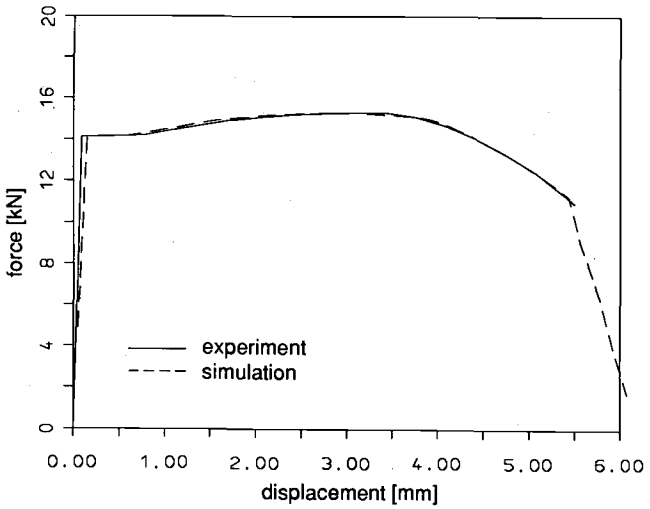

FIG. 11—*Original irradiated weld material, smooth tension test at 120°C: measured and calculated force versus displacement curves.*

Figure 12 shows the calculated J-resistance curve in comparison with an estimation according to Ref *8*, but using plant-specific material data. The calculated curve lies well above the conservative estimation and has an initiation value of J_i = 115 N/mm. As in the experimental program mentioned in the introduction, this initiation value was converted into a pseudo fracture toughness, K_{Ji} = 159 MPa$\sqrt{\text{m}}$. This value is plotted together with K_{Ji} values not rejected from the WOL-X experiments in Fig. 13. It extends the measured values to higher temperatures in a very reasonable way.

In order to evaluate the influence of a few model parameters, two additional calculations were made. First, the influence of the stress-strain curve was examined. Since the curves

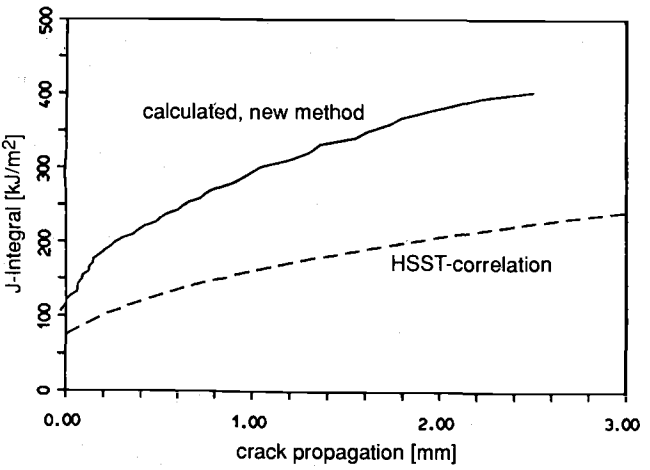

FIG. 12—*Original irradiated weld material: Calculated (CT) J-resistance curve compared with conservative approximation.*

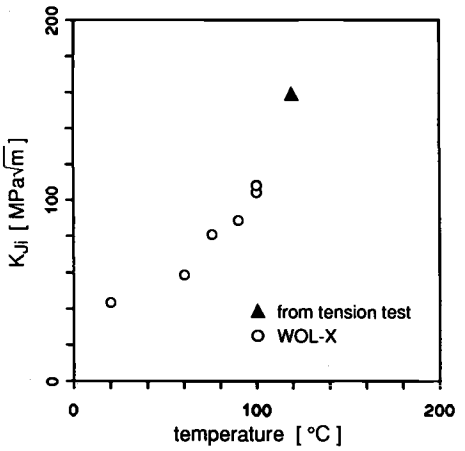

FIG. 13—*Original irradiated weld material:* K_{Ji} *value converted from the calculated resistance curve in Fig. 12, together with measured data at lower temperatures.*

available for different tests at 120°C do not show much variation, the original curve (Fig. 11) was arbitrarily changed so that the strain at fracture was reduced by 10%, representing a decrease in area reduction by about 30%. Although the decrease in the *J*-resistance curve in Fig. 14 is significant, the initiation value is practically unaffected.

Finally, the analysis was repeated using the characteristic material length, l_c, from (irradiated) Material 3. Again, the calculated resistance curve is lower than the original curve, Fig. 15, but in this case the initiation value also seems to be fairly insensitive to the choice of l_c.

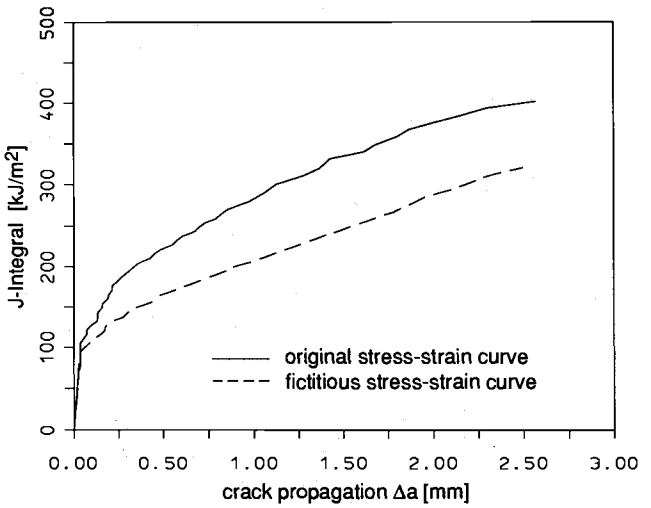

FIG. 14—*Original irradiated weld material, sensitivity study: influence of arbitrarily reduced fracture strain on the calculated* J*-resistance curve.*

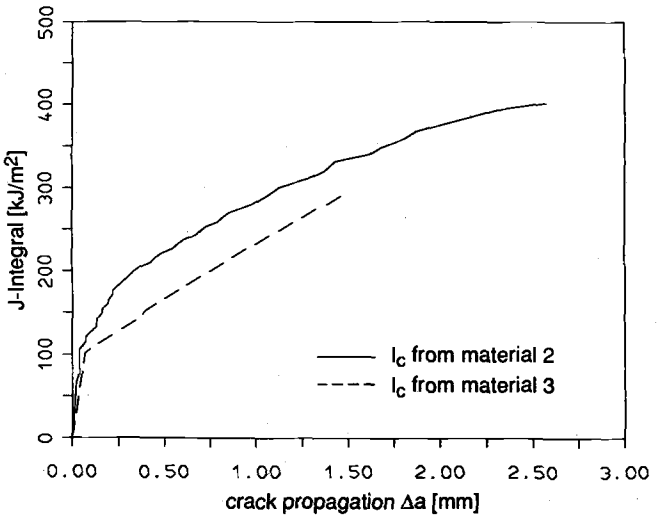

FIG. 15—*Original irradiated weld material, sensitivity study: influence of the characteristic material length,* l_c, *on the calculated J-resistance curve.*

Further Activities

The successful evaluation of the tension test gives rise to the hope that it will be possible to extract micromechanical material parameters in a similar way from instrumented Charpy V-notch tests. To achieve this goal, instrumented Charpy tests must reliably be modeled in finite element analyses taking into account the rather complicated loading situation and the strain rate sensitivity of the material.

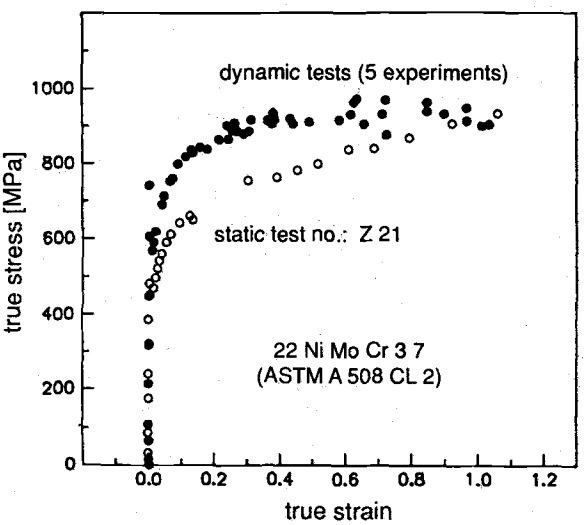

FIG. 16—*Ferritic base material: Experimental static and dynamic true-stress versus true-strain data, dynamic tests with initial strain rate of 40/s.*

As first steps in this direction, tension bars machined from a reactor pressure vessel steel, German designation 22 NiMoCr 37, equivalent to ASTM 508 Cl 2, have been loaded in a drop-weight tower at room temperature with initial strain of about 40/s, resulting in strain rates of up to 400/s in the necking part. The stresses have been measured with pairs of strain gages fixed on the bar. The deformation pattern including the necking process have been observed with a Cranz-Schardin high-speed camera throughout the whole loading history [9]. Figure 16 compares dynamic true stress versus true strain curves obtained from five experiments with a static curve of the same material. Two strain-rate-dependent material models are available to analyze these dynamic tests and will now be applied to the numerical simulation of the Charpy V-notch test.

References

[1] Needleman, A. and Tvergaard, V., "An Analysis of Ductile Rupture in Notched Bars," *Journal of the Mechanics and Physics of Solids,* Vol. 32, 1984, pp. 461–490.

[2] Gurson, A. L., "Continuum Theory of Ductile Rupture by Void Nucleation and Growth: Part I—Yield Criteria and Flow Rules for Porous Ductile Media," *Journal of Engineering Materials and Technology,* Vol. 99, 1977, pp. 2–15.

[3] Needleman, A. and Tvergaard, V., "An Analysis of Ductile Rupture Modes at a Crack Tip," *Journal of the Mechanics and Physics of Solids,* Vol. 35, 1987, pp. 151–183.

[4] Sun, D. Z., Siegele, D., Voss, B., and Schmitt, W., "Application of Local Damage Models to the Numerical Analysis of Ductile Rupture," *Fatigue and Fracture Engineering of Materials and Structures,* Vol. 12, 1988, pp. 201–212.

[5] Sun, D. Z., Kienzler, R., Voss, B., and Schmitt, W., "Application of Micromechanical Models to the Prediction of Ductile Fracture," *Fracture Mechanics: Twenty-Second Symposium (Volume II), ASTM STP 1131,* S. N. Atluri, J. C. Newman, Jr., I. S. Raju, and J. S. Epstein, Eds., American Society for Testing and Materials, Philadelphia, 1992, pp. 368–378.

[6] Chu, C. C. and Needleman, A., "Void Nucleation Effects in Biaxially Stretched Sheets," *Journal of Engineering Materials and Technology,* Vol. 102, 1980, pp. 249–256.

[7] Klausnitzer, E., private communication SIEMENS-AG, 1990.

[8] Merkle, J. G. and Johnson, R. E., "Example of Calculations Illustrating Methods for Analyzing Ductile Flaw Stability in Nuclear Pressure Vessels," Report NUREG-0939, Oak Ridge, TN, 1984.

[9] Böhme, W., Sun, D. Z., Schmitt, W., and Hönig, A., "Application of Micromechanical Material Models to the Evaluation of the Charpy Test," *Advances in Fracture/Damage Models of Engineering Problems, AMD Vol. 137,* American Society of Mechanical Engineers, New York, 1992, pp. 203–216.

T. Varga[1] *and D. H. Njo*[2]

On the Brittle-to-Ductile Transition Fracture Behavior

REFERENCE: Varga, T. and Njo, D. H., **"On the Brittle-to-Ductile Transition Fracture Behavior,"** *Small Specimen Test Techniques Applied to Nuclear Reactor Vessel Thermal Annealing and Plant Life Extension, ASTM STP 1204,* W. R. Corwin, F. M. Haggag, and W. L. Server, Eds., American Society for Testing and Materials, Philadelphia, 1993, pp. 118–129.

ABSTRACT: Brittle-to-ductile transition behavior is one important aspect in the material behavior of ferritic steels. Because of the many influencing parameters involved, the transition behavior is known to cause great difficulties in its theoretical treatment and modeling as well as in the development of a sufficiently reliable empirical correlation. In spite of this, some means have to be provided to treat or characterize brittle-to-ductile transition behavior in an appropriate or at least in an acceptable way, especially for integrity assessments of components.

In this paper, some basic considerations and treatments of brittle-to-ductile transition, as well as relevant influencing parameters and their effects, will be discussed. Also, experimental results will be presented and conclusions drawn and new aspects discussed that can have significant consequences in the application of structural integrity assessment methods.

KEYWORDS: fracture, transition behavior

Material behavior is one of the most important aspects in integrity assessments, especially when using fracture mechanics methods. Therefore, fracture mechanics concepts are differentiated by the different fracture behavior of the material, i.e., linear elastic (LEFM), elasto-plastic (EPFM), and ductile (tearing modulus). The dominating parameter in material behavior is temperature.

With respect to the characterization of material behavior, within the EPFM regime the brittle-to-ductile transition is the most difficult to accomplish. The main reasons for this will be described in paragraphs that follow.

The term "ductile-to-brittle transition temperature" or simply "transition temperature" is a somewhat arbitrarily defined temperature in the transition range where a change from a crystalline (cleavage) to a fibrous (shear)-appearing fracture can be observed. This is usually determined by means of Charpy V-notch impact bend specimens. Commonly used definitions are "transition temperature at 50% cleavage/fibrous fracture" or "transition temperature at 41 J (30 ft · lb) and 68 J (50 ft · lb) energy level, respectively."

Metals crystallizing in a body-centered cubic structure show a strong temperature and strain rate dependency in their brittle-to-ductile transition behavior. At low temperatures and high strain rates, the pronounced tendency is the brittle behavior, whereas at high temperatures and low strain rates, ductile behavior is dominant. Another significant influencing parameter is the constraint, which reduces the plastic deformation capability of the material.

[1] Institute for Testing and Research in Materials Technology (TVFA), University of Technology, A-1040 Vienna, Austria.

[2] Swiss Federal Nuclear Safety Inspectorate (HSK), CH-5232 Villigen-HSK, Switzerland.

With brittle behavior, unstable fracture directly follows crack initiation and is accompanied by none or very little plastic deformation, whereas with ductile behavior, the fracture, if it occurs, is preceded by crack initiation and stable crack growth, i.e., fracture will only be possible if additional work is available to further crack growth.

Unstable brittle (or cleavage) fracture behavior is initiated when the local stress concentration, such as at a notch or a crack tip, can no longer be accommodated by a local elastic/plastic deformation of the material, i.e., the local elastic/plastic deformation capability of the material is exceeded. Ductile fracture is caused by slipping that takes place mostly on sites with small inclusions by formation of voids followed by voids coalescence and slow tearing of the ligament under a sustained loading condition.

In the transition range, only limited plastic deformation can take place. Fracture will occur in a nonductile manner as described above at a location with high stress concentration as soon as plastic deformability at that location is exhausted. One important fact to be noted is that in the transition range, big scatter is always found in the required energy to break the specimens. This means that the fracture toughness will also show the same behavior.

Fracture mechanics methods are used widely for integrity assessments of components containing crack-like defects. Using the basic principle of fracture mechanics—that is, the interrelationship between crack size, load (stress), and fracture resistance of the material (the so-called FM triangle)—the critical condition for failure or fracture can be predicted. Before starting the assessment, however, several main aspects must be evaluated that directly or indirectly influence the FM analysis. The most important of these is the expected material behavior. In this respect, it is often forgotten that in the transition region material behavior is strongly strain rate and therefore also loading-rate dependent. At the same temperature, a specimen or part of a component will show different behavior under different loading conditions. It can show fully ductile behavior in quasi-static loading condition until fracture, but can exhibit a nonductile or brittle behavior under dynamic or impact load. In the transition region, triaxiality (constraint) effects in large/thick specimens or parts of components will cause reduction of the plastic deformation, i.e., reduce its ductility and show a decrease in the fracture toughness.

The Brittle-to-Ductile Transition Range

Using the commonly accepted representation of transition temperature of a ferritic steel by means of Charpy V-notch impact bend specimens, a so-called transition curve can be observed in Fig. 1. A similar but more pronounced behavior, i.e., steeper transition temperature curves and a narrower transition temperature range, can be observed when precracked Charpy-type specimens are used (see Fig. 1).

In Fig. 2, load deflection curves from instrumented precracked Charpy-type tests according to the ASK procedure [*1*] at different temperatures are shown. One can see the temperature dependency of the transition range with change (increase) of "fracture toughness." In the first loading phase, load and deflection increase almost linearly as a function of time. With linear elastic or brittle behavior, this is immediately followed by an unstable fracture, which can be seen as an almost vertical drop of the load in Fig. 2. With ductile material behavior, the fracture is preceded by plastic deformation, and until fracture a smoother curve can be observed similar to a tension test curve of a ductile material.

In a similar way, the strain/loading rate dependency of the transition range can be demonstrated; with higher loading rate, ferritic steels will "embrittle," i.e., will be less ductile. If no embrittlement can be observed with higher loading rate, then the increase of the yield strength caused by this higher loading rate must be reflected in the increase of the required energy-to-fracture of the specimen, i.e., the fracture toughness also will increase.

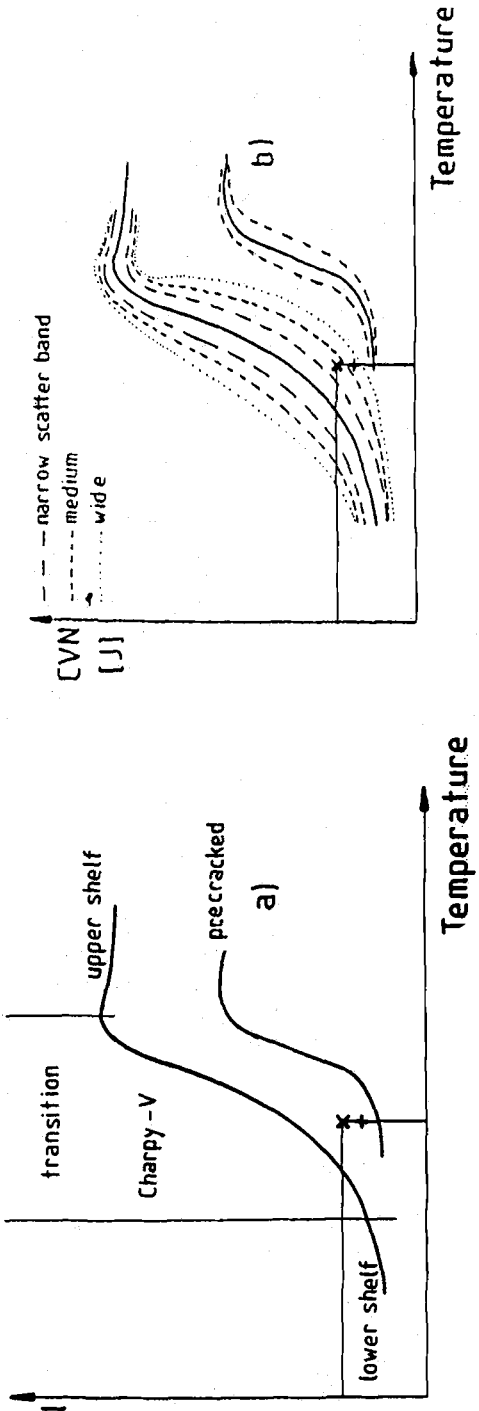

FIG. 1—*The brittle-to-ductile transition over temperature as measured by Charpy V specimen testing. The precracked Charpy-type specimen exhibits less ductility than the standardized Charpy V specimen:* (a) *mean value transition curves;* (b) *transition curves with scatter bands; precracked Charpy-type specimen testing shows less scattering.*

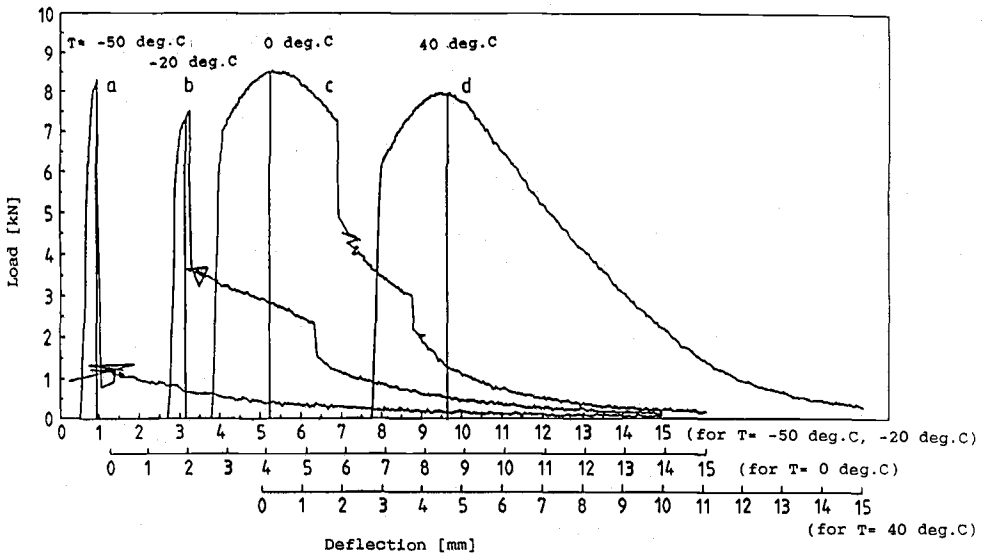

FIG. 2—*Load deflection diagrams for GMA weld metal, testing temperature −50 to +40°C, loading rate 0.1 m/s. All diagrams except that at +40°C exhibit single and multiple cleavage crack jumps followed by arrest.*

Based on theoretical considerations by Becker, Orowan, and Kochendörfer as described by Rühl [*2*] and experimental results by McGregor and Grossmann [*3*], Schnadt [*4*] used the relationship

$$\ln v = c_1 - \frac{c_2}{T}$$

to characterize the brittle-to-ductile transition behavior as well as its temperature and strain or loading rate dependency (v represents loading rate, c_1 and c_2 are material characteristics, and T is the absolute temperature).

Here Schnadt has represented the temperature and strain rate dependency of fracture toughness, using Charpy-type specimens containing a pressed sharp notch with a radius of 0.005 mm by means of so-called thermovectonic zones. Applying Schnadt's method, such a representation is given in Fig. 3, where parameters are shown such as the required energy for breaking the specimen (or the path-independent integral J), which is obtained from transition curves (Fig. 4) using precracked Charpy-type specimens at different loading rates of 5 and 0.1 m/s.

TABLE 1—*Chemical composition of the base metal and the solid welding wire.*

		wt%						
Material	Type	C	Si	Mn	P	S	Mo	Ni
Base metal	E 355 DD	0.16	0.37	1.41	0.016	0.026		0.007
Wire B/O	MnSi	0.07	0.96	1.54	0.007	0.019		

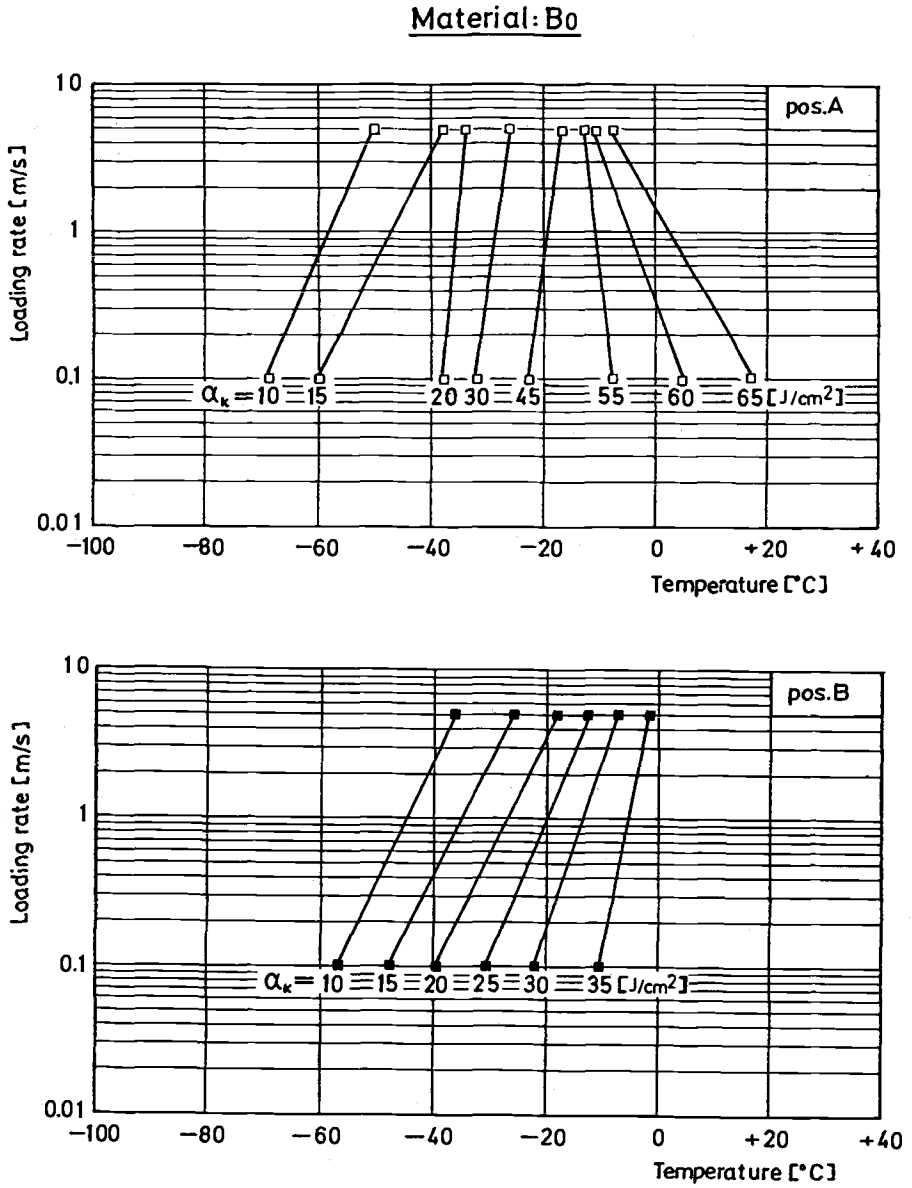

FIG. 3—*The loading rate and testing temperature dependence at different impact strength, a_k, levels. Pos. A represents the greatest possible amount of primary, coarse grain, whereas pos. B includes the highest proportion of secondary, fine grain in the fracture path.*

The general "accepted" rule that with increasing strain rate "embrittlement" will take place, which means that the originally obtained fracture toughness will only be attained at higher temperature with higher loading rate, is reflected in the lower part of the transition region. However, in the upper part of the transition region close to the upper shelf, where this "embrittlement" will no longer be effective, the inverse is observed. The originally

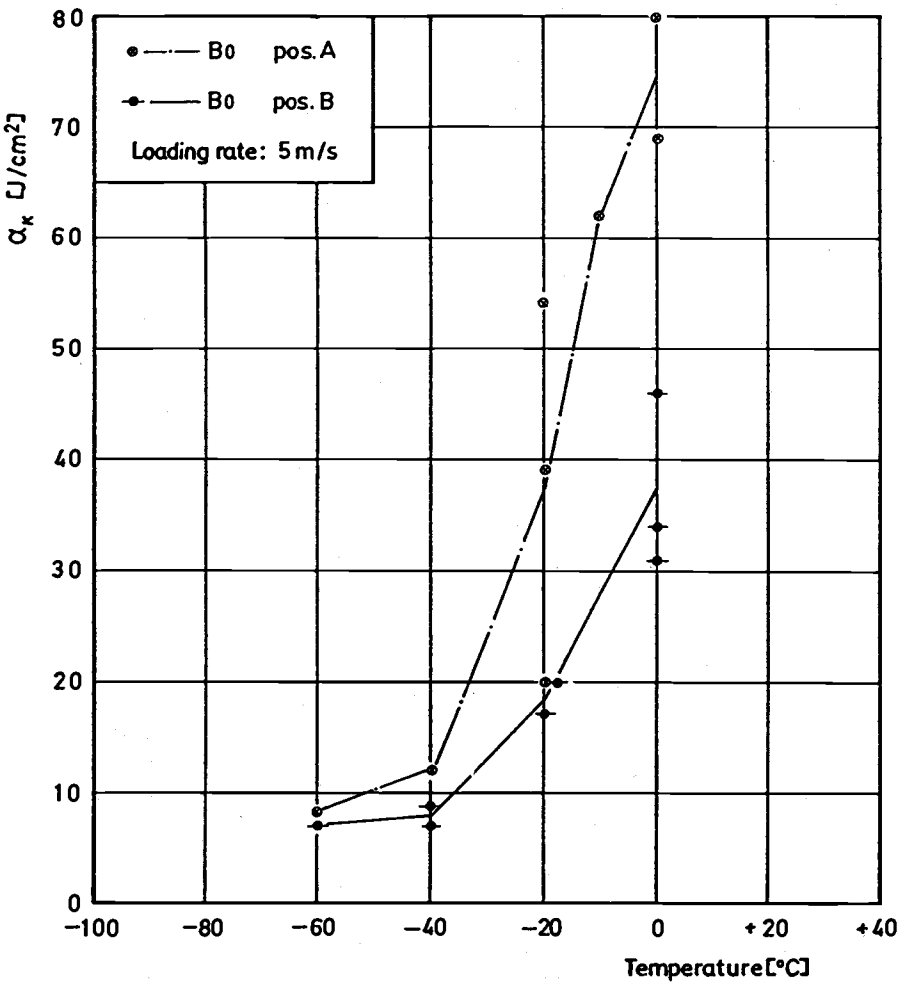

FIG. 4—*Typical mean transition curves as the result of testing precracked Charpy-type specimens, pos. A and B of weld metal using steel E 355 DD as base metal and wire B/O as consumable.*

obtained fracture toughness at a certain temperature can be attained at a lower temperature when higher loading rate is applied. This is shown in Fig. 3, where results from two different positions of MAG weld metal, see Table 1, are represented. It must be noted that the type of material, product form, and its microstructure also influence the parameters.

The instrumented precracked Charpy-type test used here (Fig. 5*a*) also allows the determination of the load at the time of crack arrest, if this occurs. This so-called "crack arrest load" (CAL) can be used in the development of a criterion for the determination of the arrestability of a running brittle (or cleavage) fracture. From this CAL (see Fig. 2) load deflection diagrams at −20 and 0°C, a crack arrest fracture toughness, K_{Ia}, can be derived. In addition to this, based on the crack tip opening (CTOD), an alternative K_{Ia} [similar to the ASTM Test Method for Determining the Plane-Strain Crack Arrest Fracture Toughness K_{Ia} of Ferritic Steels (E 1221)] can also be calculated.

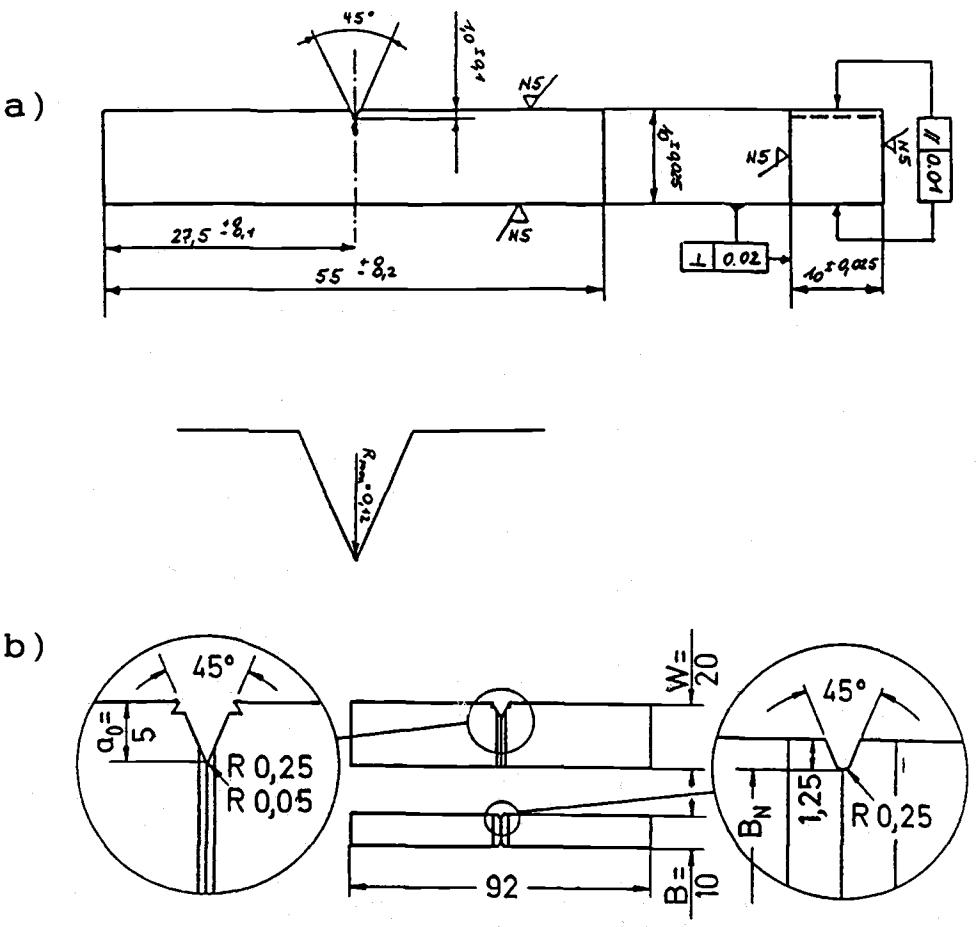

FIG. 5—*Three-point bend specimen geometries:* (a) *precracked Charpy-type specimen according to ASK AN 425 Rev. 1 (notch root radius reduced to 0.05 mm). Size of notch plus precrack 2.5 to 5.0 mm;* (b) *crack arrest specimen of* W = 2B, *three-point bending of larger ligament than with the Charpy specimen geometry.*

For many applications, e.g., integrity assessments, knowledge of the temperature above which ductile behavior of the component will prevail and therefore nonductile or brittle behavior can be disregarded, the so-defined "upper shelf temperature limit" (USTL) is very important. The "cleavage fracture length" (CFL), defined as the length of cleavage crack jump between initiation and arrest (Fig. 6) (in an instrumented precracked Charpy-type test), decreases with increasing temperature until as in our case both the CFL and the corresponding load drop disappear completely at 40°C. One way to determine this USTL, as can be seen from Fig. 2, is by plotting the "maximum attainable elastic load" and the "crack arrest load," with the corresponding temperature: The point of intersection of these two curves will give us this USTL. The application of this approach is shown in Fig. 7 for Ck 35 type of steel [5]. The accuracy of determination can be further improved by using more specimens and by statistical treatment of the results.

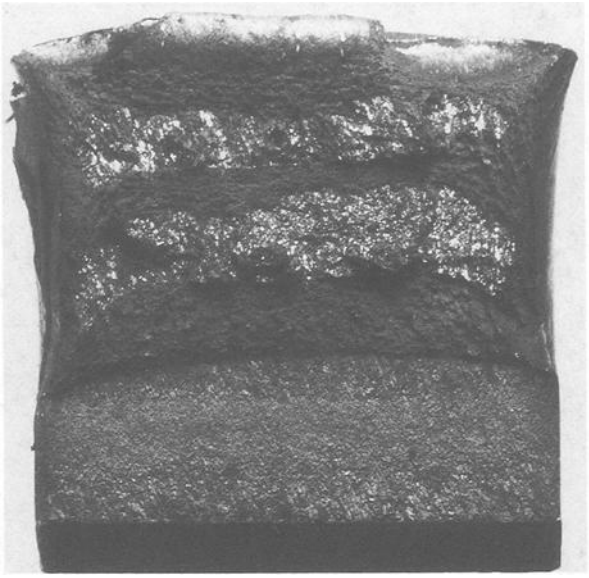

FIG. 6—*Fracture surface of precracked Charpy-type specimen. Two cleavage areas, reflecting the light (if appropriate grain separations are present), are visible here; these cause two jumps in crack propagation and result in load drops. In Fig. 2, the corresponding load deflection diagram at 0°C is shown.*

The Use of Fracture Mechanics Parameters Obtained from Small-Size Specimens

ASTM E 399 [Test Method for Plane-Strain Fracture Toughness of Metallic Materials] is presently the test standard that has worldwide acceptance for determination of a valid LEFM fracture toughness. The validity criteria regarding the specimen size, configuration, and preparation are given there. Other standards for LEFM as well as for EPFM applications exist, such as BS 5762 and ASTM E 1290 [Test Method for Crack-Tip Opening Displacement (CTOD) Fracture Toughness Measurement] for crack opening displacement (COD) and crack tip opening displacement (CTOD) testing, respectively, and ASTM E 813 [Test Method for J_{Ic}, a Measure of Fracture Toughness] and EGF P1-90 for ductile material testing. Here also similar validity criteria are stipulated. The general principle is that the specimen geometry (thickness) used to determine fracture toughness must show the same material behavior as the component being assessed. Thus the use of a full (component) thickness specimen is usually of primary importance. Experience has shown that the use of side grooves in "small" specimens can increase the range of applicability of these specimens because side grooves will increase triaxiality (constraint) and tend to give lower, more conservative toughness values. For the EPFM application, however, it should be ascertained that no intolerable amount of plastic deformation precedes fracture of specimens. This is more the concern of a J-type of test according to ASTM E 813 than with the COD-type test according to BS 5762, since COD tests usually show only little crack tip deformation differences due to specimen size effects up to initiation.

In the application of different FM concepts, different rules are presently used to determine fracture toughness or fracture resistance. In the LEFM concept, e.g., in the so-called 5% secant rule (ASTM E 399 paragraph 9.1.1 and 9.1.2), validity criteria have to be applied to qualify a K_{IC} test result. However, for COD and J-integral determination, no such criteria

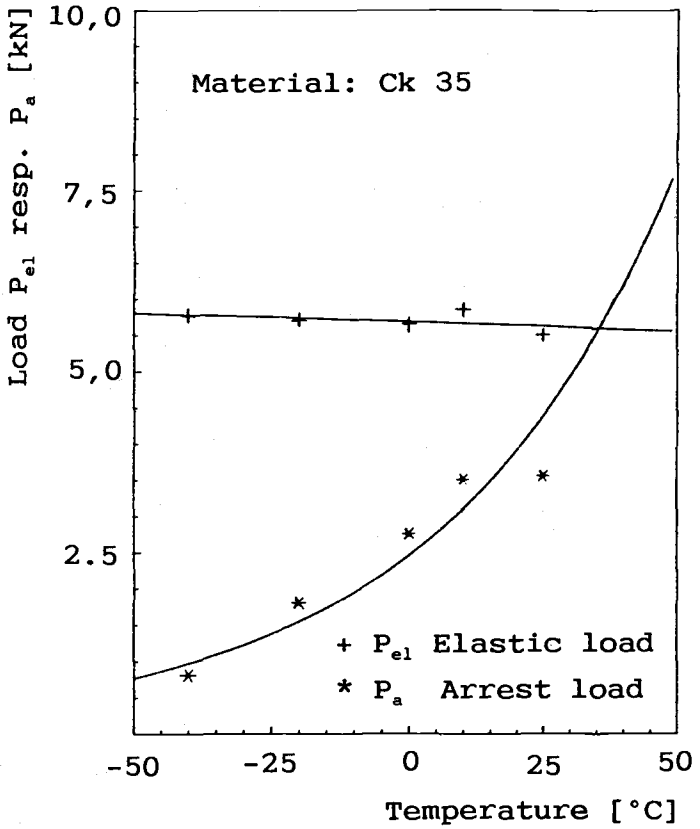

FIG. 7—*The maximum attainable elastic load and the crack arrest load (CAL) in function of temperature. The point of intersection of the two curves defines the upper shelf temperature limit (USTL) above which no crack jump, i.e., conversion ductile to brittle, exists.*

for a valid test exist; that is, should a crack remain stable (show a stable crack growth) or should a crack show an unstable cleavage behavior in order that the test result can be qualified as a valid COD or *J*-value?

The resistance (*R*)-curve approach is applied in the ductile region, mainly to make use of the observed phenomenon that with increasing crack length the required work for extending the crack also increases, i.e., the *J*-integral as defined increases with crack length. Because of the limited and much smaller expansion possibility of its plastic zone as well as the much lower triaxiality of the stress state in small specimens, their *R*-curves are shallower than those obtained with larger (thicker) specimens. From this aspect, the application of *R*-curves from small specimens for components with thicker sections is conservative. However, this is only true if it can be ascertained that the work (area under the load deflection curve) required to extend the crack stems mainly from the increase of the plastic zone and is not due mainly to deflection of the small specimen. Also, it must be shown that neither in small specimens nor in the thicker component sections can cleavage fracture occur. This is because if cleavage fracture occurs, the *R*-curve has a discontinuity and can no longer be used as defined. If such a behavior is to be expected in a component, especially in the transition region, the point of initiation or reinitiation cannot be determined or predicted in a deter-

ministic way. In such a case, the transferability of valid R-curves from small specimens to larger (thicker) parts of a component cannot be assured. Therefore, one important fact must be noted here: R-curves can only be applied correctly and sensibly if a mode conversion during crack extension from ductile-to-brittle fracture can be excluded.

Cases or boundary conditions may exist where crack initiation cannot be excluded or prevented, e.g., where one is unable to determine the weakest location, its material structure, and fracture resistance in a component. For a ductile region, usually the R-curve approach is applied and the cautions mentioned above should be taken into account. For the transition region with mixed-mode material behavior, unstable brittle (or cleavage) crack initiation may occur. In this case, integrity or safety of the component can only be shown if timely crack arrest will prevail. In the remaining ligament, the crack arrest fracture toughness becomes the only available material property to demonstrate safety.

The ASTM E 1221 standard gives a test method and procedure to determine a plane strain crack arrest toughness, K_{Ia}, using a compact crack arrest (CCA) specimen. As a supplement to this, a test method using small three-point bend specimens according to Fig. 5*b* was developed at TVFA [*6*]. Similar to the CCA specimen, the crack initiation starter is made of a notched brittle weld. If that instrumentation is used, it is possible to measure adequately and reliably an effective load at crack arrest and K_{Ia} can be determined, respectively calculated by using an appropriate calibration function, as in Fig. 8: δ represents crack mouth opening displacement, E' the modulus of elasticity [plane strain; $E' = E/(1 - \nu^2)$], a the crack length, and ν being Poisson's ratio (or according to ASTM E 1221 based on crack opening displacement). However, it has to be verified that the remaining ligament of the specimen effectively has the required load-carrying capability.

Crack arrest fracture toughness, K_{Ia}, test results within the ASTM round-robin test for the development of the E 1221 standard using CCA specimens and TVFA three-point bend-specimen test results on A 533 Gr. B Cl. 1 steel are shown in Fig. 9. It can be seen that all

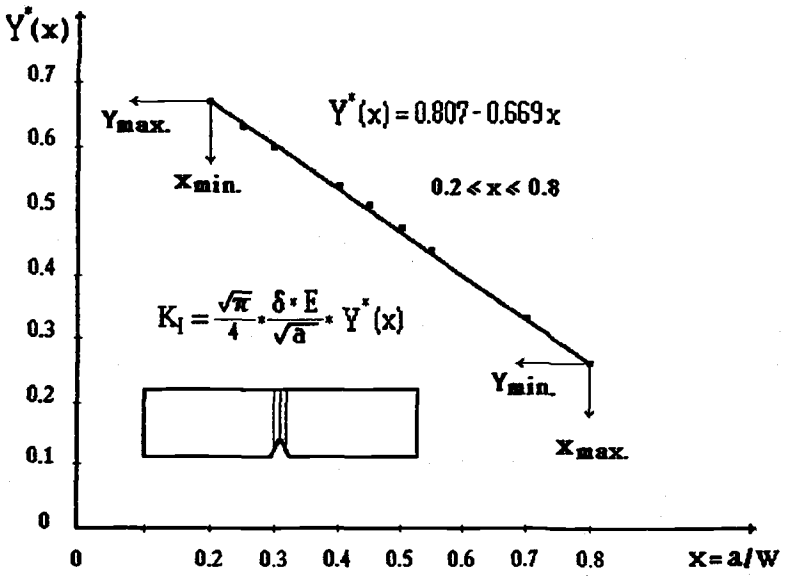

FIG. 8—*Geometry correction function as recommended for three-point bend specimens, crack arrest tests (decreasing* K_I *with increasing* a/W). Y'(x) *is the correction function for the three-point bend specimens that Nisitani et al. extended to* a/W = *0.8.*

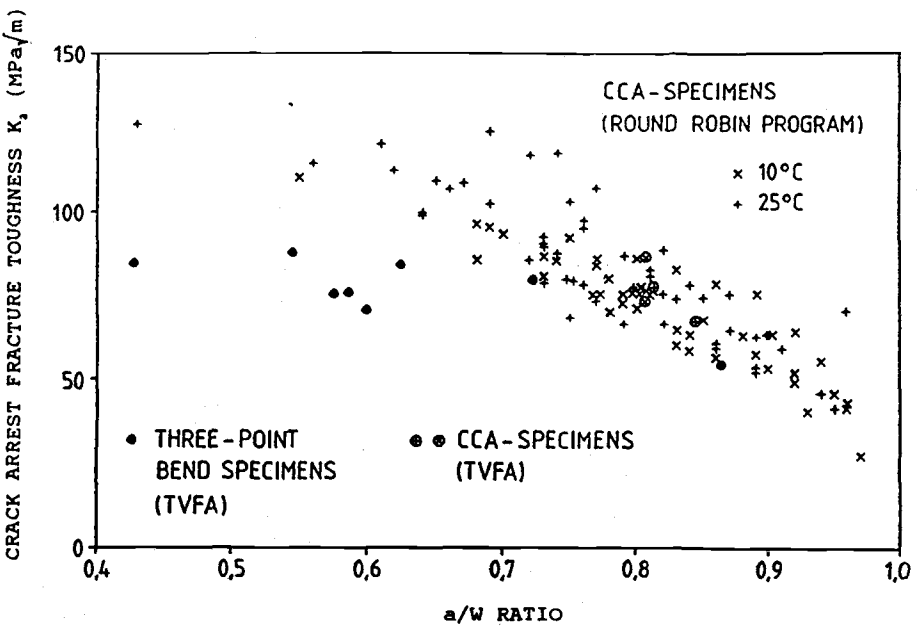

FIG. 9—*Crack arrest fracture toughness in function of* a/W *as measured on steel ASTM A 533 Gr. B Cl. 1 is the round robin before finalizing ASTM E 1221.*

K_{Ia}-values obtained above $a/W = 0.7$ are within the same scatter band. Below $a/W = 0.7$, the three-point bend specimens give more conservative results [6].

Final Remarks

In the application of fracture mechanics methods for integrity assessments, knowledge of expected material behavior in components to be assessed is of decisive importance. Problems arise when the expected material behavior lies in transition temperature regions, because in these cases mixed-mode behavior from brittle (cleavage) to ductile (fibrous) behavior can exist during the fracture process depending on environmental and loading conditions.

The use of the instrumented precracked Charpy-type (small-size) specimen test can aid in characterizing material fracture behavior better when using fracture mechanics methods. Loading rate and temperature effects as well as cleavage and crack arrest behavior can be readily investigated.

Also, a so-called upper shelf temperature limit (USTL) can be defined and used to aid in the characterization of expected material behavior, which is essential for *R*-curve applications.

The authors are indebted to R. Lechner, Dipl.-Ing., for his help in preparing the manuscript.

References

[1] Varga, T., Njo, D. H., and Prantl, G., "ASK Procedure for Instrumented Precracked Charpy-Type Tests," EPRI NP-2102-LD, Project 1757-1, CSNI No. 67, Proceedings, 1981, pp. 1-65–1-75 (ASK AN 425).

[2] Rühl, K., "Die Sprödbruchsicherheit von Strahlkonstruktionen," "The Brittle Fracture Safety of Steel Structures," Werner Verlag, Düsseldorf, 1959.
[3] McGregor, C. N. and Grossmann, N., "Dimensional Effects in Fracture," *Welding Journal*, Vol. 31, 1952, Welding Research Council, pp. 20–26.
[4] Schnadt, H., "A New Approach to the Solution of Brittle Fracture Problems in Modern Steel Construction," Paper Nr. 33, Selbstverlag, Zuerich-Oerlikon, 1962.
[5] Varga, T. and Loibnegger, F., "Some Temperature and Loading Rate Effects on the Ductile to Brittle Transition of Weld Metal," *Proceedings*, 20th Plenary Meeting of the European Structural Integrity Society, Task Group: Elastic-Plastic Fracture Mechanics, Vienna, 4–5 April, 1991.
[6] Varga, T. and Schneeweiss, G., "A New Method of Test Crack Arrest Toughness by Using Three-Point Bend Specimens," *Rapid Load Fracture Testing, ASTM STP 1130*, 1992.

David J. Alexander[1]

Fracture Toughness Measurements with Subsize Disk Compact Specimens

REFERENCE: Alexander, D. J., **"Fracture Toughness Measurements with Subsize Disk Compact Specimens,"** *Small Specimen Test Techniques Applied to Nuclear Reactor Vessel Thermal Annealing and Plant Life Extension, ASTM STP 1204,* W. R. Corwin, F. M. Haggag, and W. L. Server, Eds., American Society for Testing and Materials, Philadelphia, 1993, pp. 130–142.

ABSTRACT: Special fixtures and test methods have been developed for testing small disk compact specimens (12.5 mm in diameter by 4.6 mm thick). Both unloading compliance and potential drop methods have been used to monitor crack extension during the *J*-integral resistance (*J-R*) curve testing. Provisions have been made to allow the necessary probes and instrumentation to be installed remotely using manipulators for testing irradiated specimens in a hot cell. Laboratory trials showed that both unloading compliance and potential drop gave useful results. Both techniques gave similar data and predicted the final crack extension within allowable limits. The results from the small disk compact specimens were similar to results from conventional compact specimens 12.7 mm thick. However, the slopes of the *J-R* curves from the larger specimens were lower, suggesting that the smaller disk compact specimens may have lost some constraint due to their size. The testing shows that it should be possible to generate useful *J-R* curve fracture toughness data from the small disk compact specimens.

KEYWORDS: disk compact specimen, fracture toughness, irradiation effects, test methods, unloading compliance, potential drop, crack extension, *J*-integral resistance curves, *J-R* curves, clip gage

Candidate materials are being evaluated for the first-wall structure in the International Thermonuclear Experimental Reactor (ITER). Current estimates of the operating temperatures indicate that the structure will operate below about 300°C. One of the materials proposed for the first wall is type 316 stainless steel. Very little information is available on the effects of irradiation at these low temperatures on the mechanical properties of austenitic stainless steels, particularly the fracture toughness [*1*]. Therefore, work is under way at Oak Ridge National Laboratory (ORNL) to measure the effect of irradiation on the fracture toughness of a variety of austenitic stainless steels. This paper describes some of the techniques that have been developed for this testing and presents some preliminary results from unirradiated material and comparisons with larger conventional specimens.

The irradiations for these experiments are being conducted at the High Flux Isotope Reactor (HFIR) at ORNL due to the reactor availability and the high fluxes present in the HFIR target region. However, achieving the necessary low irradiation temperatures (60 and 300°C) placed severe restrictions on the specimen geometry. The gamma heating from the high-flux irradiation and the limited cooling available from the reactor cooling water required a very small specimen size to attain the lowest irradiation temperature. To use the HFIR

[1] Development staff member, Metals and Ceramics Division, Oak Ridge National Laboratory, Oak Ridge, TN 37831-6151.

target region efficiently, it was necessary to adopt a circular specimen geometry for the fracture toughness specimens. Therefore, the disk compact specimen geometry was chosen. This is an accepted specimen geometry for K_{Ic} measurements (ASTM Test Method for Plane-Strain Fracture Toughness of Metallic Materials, E 399-90), but is not yet included in the standards for J-integral-resistance (J-R) curve testing (ASTM Test Method for J_{Ic}, A Measure of Fracture Toughness, E 813-89, or ASTM Test Method for Determining J-R Curves, E 1152-87). These standards presently allow only conventional rectangular compact specimens or bend bars; however, the disk and rectangular compact specimens are very similar in geometry, and J-R data can be correctly determined from each if the appropriate compliance expressions are used. Preliminary experiments [2] indicated that useful data could be generated in the laboratory from small disk compact specimens.

The heat transfer calculations performed at ORNL and the size limitations imposed by the HFIR target region characteristics resulted in the selection of a specimen diameter and thickness of 12.5 and 4.63 mm (0.492 and 0.182 in.), respectively. This very small specimen size would demand special techniques for testing.

There are two conventional methods employed in J-R testing for monitoring crack growth during the test: unloading compliance and potential drop. Unloading compliance (UC) requires periodic partial unloadings of the specimen to determine the specimen compliance, from which the crack length and extension are calculated. This technique demands high accuracy for the measurement of the load-displacement data in order to determine the correct compliance values and hence crack extensions. The second method, potential drop (PD), imposes a constant current across the specimen and measures the changing resistance of the unbroken ligament as the crack extends. This resistance change is used to determine the crack length. Less accurate displacement measurements are necessary than with UC testing, as the displacement is used only to calculate the energy required for crack extension, and this calculation is less sensitive to the displacement measurement than are the compliance measurements necessary for UC determination of crack growth. UC measurements for irradiated specimens have been successfully done at ORNL, and much more experience had been accumulated in testing unirradiated material with UC than with PD. However, the small specimen size precluded the use of conventional displacement measuring methods available at ORNL, so it was decided to pursue both the UC and the PD techniques in case one of the methods proved to be impractical for remote testing in a hot cell.

Test Methods

The UC technique requires accurate measurement of the specimen displacements. The usual technique for measuring the displacements along the specimen load line is to fabricate the specimen with a cutout that allows a clip gage to be inserted between the loading pin holes to the load line, where it seats on knife edges fastened along the load line on the sides of the notch cutout. An example of the resultant specimen geometry is shown in Fig. 1 for a compact specimen 12.7 mm thick (0.5 in.) [designated 0.5 T C(T)]. However, the disk compact specimen is much smaller, with a thickness of only 4.6 mm (0.18 in.). [This disk compact specimen is thus designated 0.18 T DC(T)]. As a result, there is not sufficient room between the loading holes for a cutout to allow a clip gage to be inserted to the load line. Therefore, grooves were machined on the outer edge of the specimen above and below the loading holes (see Fig. 1) so that the load line displacement could still be measured directly, but outside the loading holes rather than in between them. The grooves had an included angle of 60°, with a depth of 0.5 mm (0.020 in.) and a root radius of 0.05 mm (0.002 in.). A robust and rugged yet highly accurate clip gage that could be handled by manipulators was designed. The gage included knife edges that would seat in the grooves. This clip gage,

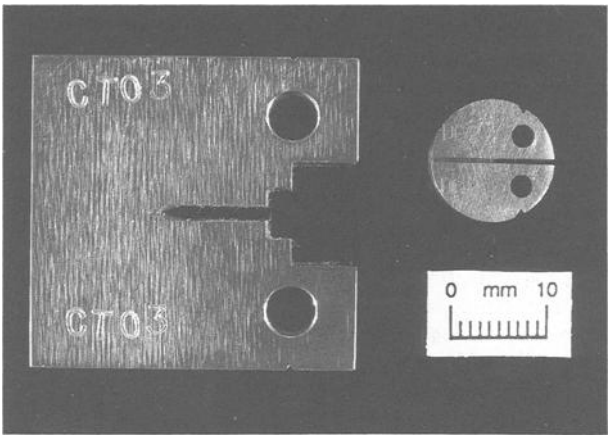

FIG. 1—*A comparison of a conventional ½ T compact specimen (left) and the 0.18 T disk compact specimen (right). Note the cutout in the compact specimen to allow a clip gage to be inserted to the load line between the loading holes. The disk compact has notches outside the loading holes for the outboard clip gage.*

termed an "outboard" gage since it was attached outside of the loading holes, contained a central flexural beam on which four strain gages were attached for a full-bridge measurement of the strains and hence the displacement. Figure 2 shows the outboard gage attached to one of the disk compact specimens.

There appeared to be only two drawbacks to the outboard gage: possible difficulties in using manipulators to remotely mount the gage on the specimens and possible damage to the gage if the specimen fractured suddenly during testing. Trials in the hot cells have shown that the gage can be handled with manipulators and the knife edges seated in the specimen

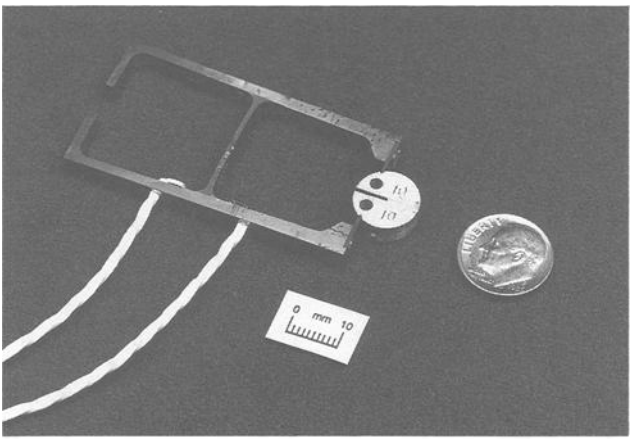

FIG. 2—*The outboard clip gage seated on the disk compact specimen. The central flexural beam has four strain gages for the measurement of the displacements. The back end of the gage will allow handling with a manipulator. The gap at the rear of the gage is designed to provide overtravel protection if the specimen fractures suddenly during testing.*

grooves. The problem of gage damage was addressed by providing overtravel stops on the back end of the gage. Hopefully, if the specimen did suddenly fracture and the servohydraulic test machine did not prevent a rapid separation of the grips and opening of the gage, the stops would prevent the central flexural beam from being permanently deformed and damaged. It was hoped that the knife edges would either slip out of the grooves or perhaps break off where they are attached to the gage arms, thus preventing damage to the gage.

The PD setup presented much greater difficulties. Four probes would have to be attached to each specimen: two for the constant current and two to monitor the changing voltage drop across the specimen ligament. Current input and output locations were chosen at the top and bottom of the specimen along the centerline, and the crack monitoring probes were located 15° above and below the crack plane, on the front edge of the specimen, where drilled and tapped holes could be located without damaging the loading holes. It was decided to forgo two additional probes for a reference measurement to reduce the number of connections that would have to be made in the hot cell. Instead, a second specimen would be connected in series with the test specimen, and the crack monitor signal from the dummy specimen would be used for a reference signal.

A PD calibration function was developed from measurements on thin aluminum mockups of the disk compact geometry. The specimen diameter was increased to 137.2 mm (5.4 in.) but the thickness was 3.2 mm (0.125 in.). Crack extension was simulated by slitting with a thin saw blade. The current and voltage readings were recorded at increments in the crack length to specimen width ratio (a/W) of about 0.05, for a/W values from 0.25 (the initial machined notch depth) to roughly 0.9. The voltage values were then normalized by the voltage value at a/W of 0.25 and fit with a third-order polynomial, given by

$$a/W = -0.261198 + 0.6237(V/V_0) - 0.118315(V/V_0)^2 + 0.008512(V/V_0)^3 \quad (1)$$

where a/W is the crack length, V is the measured voltage, and V_0 is the voltage for the specimen at a crack length of $a/W = 0.25$. This gave a correlation coefficient greater than 0.9999. During testing, an uncracked specimen would be used for the reference measurement to provide the value of the voltage at $a/W = 0.25$.

Attaching the probes would be simple in the laboratory, but much more difficult remotely in the hot cell. A fixture and special tools were designed to assist the manipulator operators in this task (Fig. 3). The specimen would be located in a special fixture to align the predrilled and tapped holes in the specimen with the threaded probes. The fixture would prevent the probes from being cross threaded. The initial prototype of the fixture was machined from clear plexiglass simply for expediency; however, it was realized that the transparency of the plastic was helpful in the assembly and desirable. The stainless steel probes were machined with hex heads, and a nutdriver would be used to attach them. The sequence of operations required to attach the probes is shown in Fig. 4. The top half of the fixture has been removed for clarity. The specimen would be placed in the central recess (Fig. 4*a*), and a thin piece of shim stock (omitted for clarity) would be inserted in the fixture slit and the specimen notch to properly align the specimen. The original proposal suggested that the probes be placed into the appropriate hole as shown in Fig. 4*b*, but it was realized that a better method would be to first load the probe into the shaft of the nutdriver, which was drilled out to allow the probe to slide into the nutdriver until the hex flats were engaged. The nutdriver would be inserted into the appropriate hole (Fig. 4*c*) and then rotated until the probe was secured. The process would be repeated until all four probes were attached (Fig. 4*d*). The specimen and probes would then be removed from the fixture (Fig. 4*e*). The final step would be to attach the proper leads to the probes (Fig. 4*f*). The leads would have fittings designed to slide onto the probes. The fittings on the leads were obtained by stripping the plastic

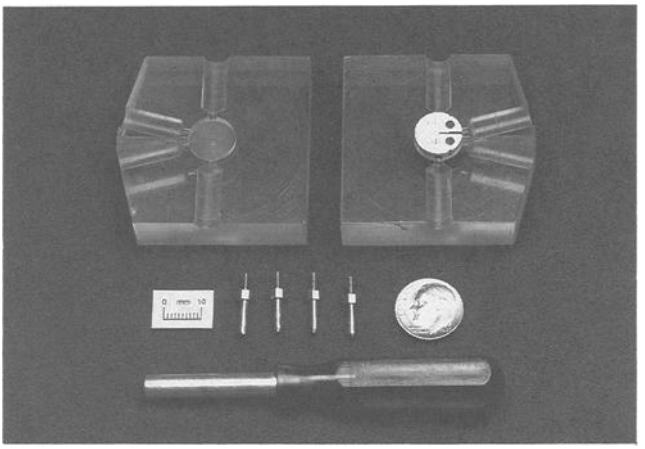

FIG. 3—*The fixtures, probes, and tools used for assembly of the potential drop setup.*

coating from female banana plugs and soldering the internal connector to the lead wires. The probe diameters matched the corresponding male banana plugs. This provided an effective electrical connection that could be assembled with manipulators.

The nutdriver for attaching the probes is shown in Fig. 5. To facilitate handling the nutdriver, cross pieces were added to the handle by drilling through two offset holes 90° apart near the end of the handle and pressing thin rods through these holes. These cross pieces prevent the nutdriver from rolling when it is laid down and also hold the handle of

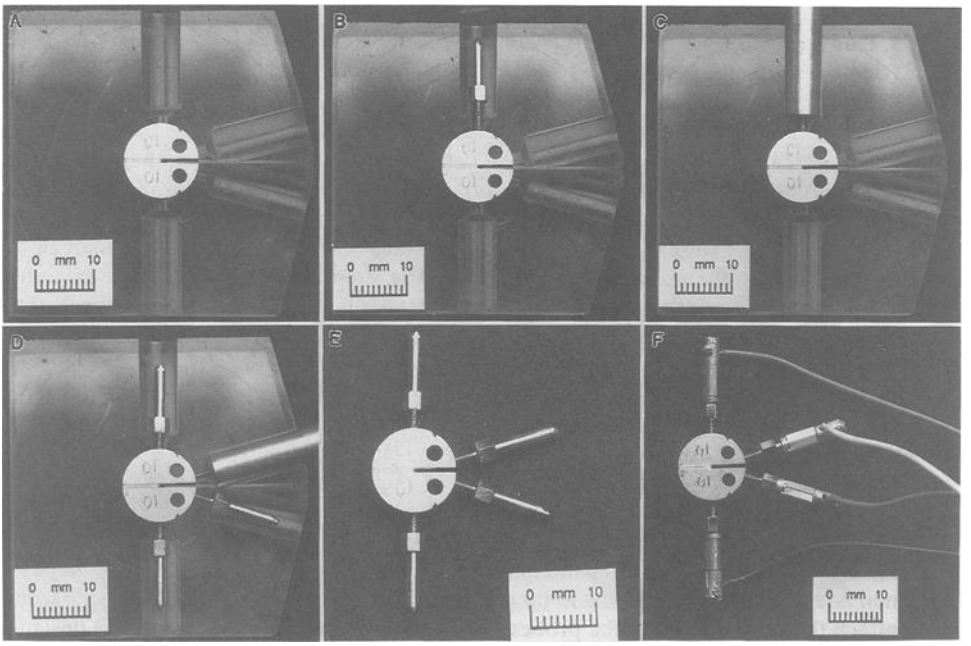

FIG. 4—*The sequence of operations required for the attachment of the potential drop probes to the disk compact specimen.*

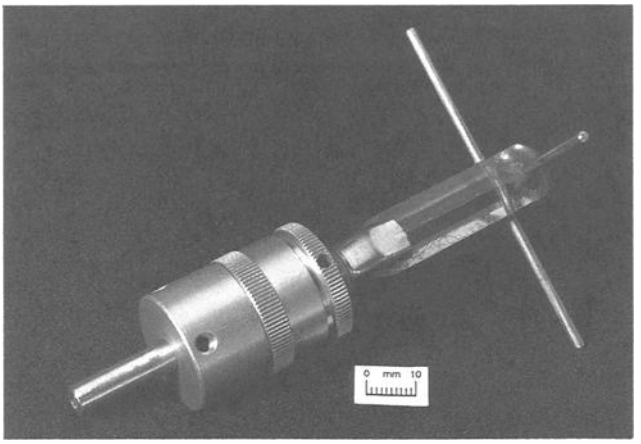

FIG. 5—*The modified nutdriver used for attaching the probes to the disk compact specimen. Note the cross pieces at the end of the handle and the slip coupling inserted on the shaft.*

the nutdriver up so that the manipulator can easily grasp the nutdriver. The primary function of the cross pieces is to allow the nutdriver to be rotated for screwing in the probes. An additional modification was the addition of a slip coupling with an adjustable torque setting on the shaft of the nutdriver (Fig. 5). The slip coupling was inserted by cutting the shaft of the nutdriver near the handle. A suitable torque level was determined by trial and error in the laboratory. The slip coupling would prevent inadvertent overtightening and twisting off of the fragile threaded probes as they were attached to the specimen. This would be very likely with the manipulators necessary for the attachment, as they do not transmit much "feel" back to the manipulator operator.

The completed assembly of the probes and clip gage on the specimen is shown in Fig. 6. This entire assembly would then be inserted into clevises for the fracture testing. The clevises

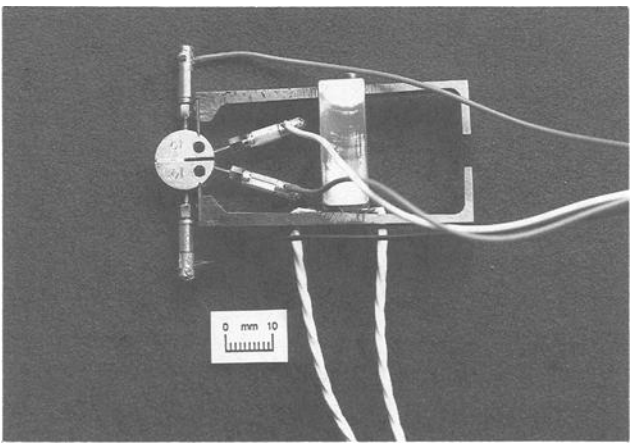

FIG. 6—*A view of the complete assembly showing the potential drop probes and lead wires and the unloading compliance clip gage. The clip gage has a protective shield mounted over the middle flexural member to protect the strain gages.*

would have a wider and deeper slot than normal to facilitate the insertion of the specimen assembly with manipulators. This would also reduce the likelihood of accidental contact of the leads with the legs of the clevises that would result in changes in the electrical signals or rubbing of the clip gage against the clevis that would distort the displacement measurements.

The disk compact specimen and the outboard clip gage have been successfully mounted in the load train of the servohydraulic test machine in the hot cell using manipulators. No additional fixturing was required to align the specimen assembly with the grips so that the loading pins could be inserted. The pins were made with one end tapered and an offset block on the other end for handling with the manipulator. The clip gage was first attached to the specimen and examined to be sure that the knife edges were seated in the grooves. The operator then grasped one arm of the clip gage with the manipulator and inserted the specimen in the load train. Inserting the pins through the loading holes was difficult, but was possible without needing special fixtures. No attempt has been made to attach the PD leads in the hot cell.

Laboratory Trials and Discussion of Results

Several trials have been conducted in the laboratory to compare the UC and PD techniques on the 0.18 T DC(T) specimens and to compare these results to UC data from 0.5 T C(T) specimens of the same material. Specimens of both geometries were machined from the same 14-mm-thick (0.55-in.) plate of annealed type 316 stainless steel from the National Fusion Reference Heat X15893. The specimens were oriented in the T-L orientation so that crack growth was in the rolling direction. All specimens were taken from the center of the plate thickness. The specimens were precracked at room temperature with a final maximum stress intensity of approximately 22 MPa$\sqrt{m}$ (20 ksi$\sqrt{in.}$). A chevron notch was used for both specimens to assist crack initiation and maintain crack front straightness during precracking. The DC(T) and C(T) specimens were precracked to nominal a/W values of 0.5 and 0.6, respectively. The specimens were then side grooved 10% of their thickness on each side (20% total) with an included angle of 45° and a root radius of 0.25 mm (0.010 in.) or 0.10 mm (0.004 in.) for the C(T) and DC(T) specimens, respectively. The side grooves would suppress the development of slant shear fracture.

All tests were conducted at room temperature, and the manufacturer's values of 260 and 560 MPa (38 and 81 ksi) were used for the yield and ultimate tensile strengths, respectively, in calculating the blunting lines for the data analyses. Values of 193 GPa (28 000 ksi) and 0.3 were assumed for the elastic modulus and Poisson's ratio, respectively. Tests were conducted in general accordance with E 813-89 and E 1152-87 using a computer-controlled testing and data acquisition system described elsewhere [*3*]. After completion of the test, the specimens were heat tinted to mark the final crack position by placing them on a hot plate and heating them until a noticeable color change was evident. The specimens were then cooled to room temperature and broken open. The initial and final crack lengths were measured with the aid of a measuring microscope, and the crack lengths were calculated by the nine-point average method.

An electrical isolation grip was used in the top of the loading train to insure that the test machine would not provide an alternate current path for the potential during the testing. Measurements of the potential showed that attaching the clip gage resulted in a slight shift (about 2%) in the apparent crack length calculated from the potential drop due to current traveling through the body of the clip gage. No correction was made for this small error.

A problem with the analysis of potential drop measurements is the determination of the initiation of crack growth. There may be significant changes in the potential drop signal

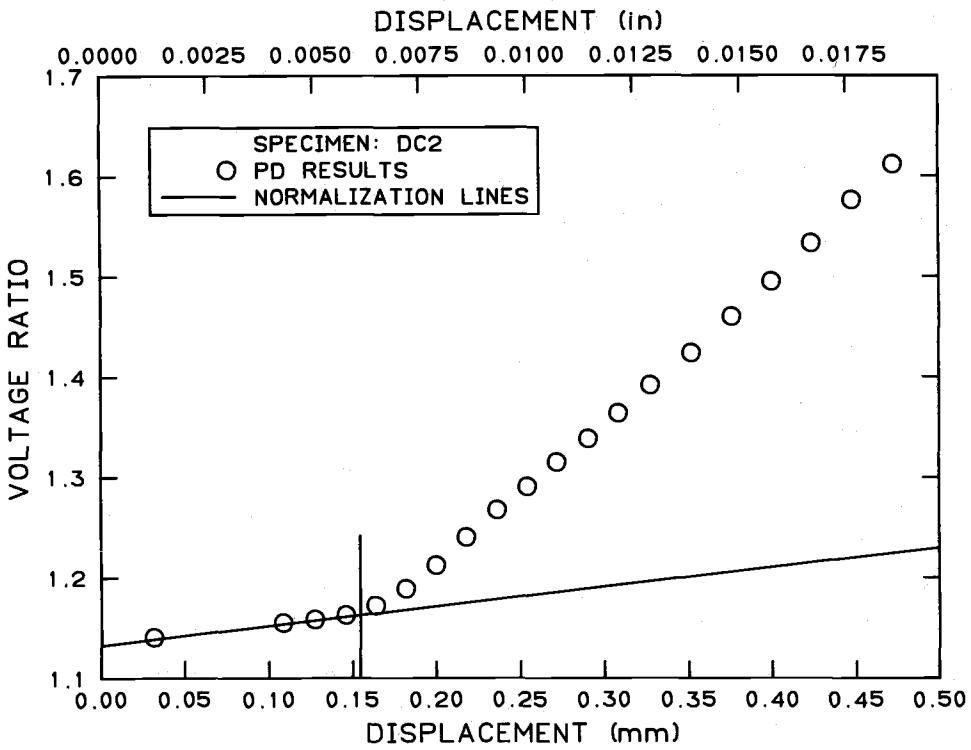

FIG. 7—*A plot of the voltage ratio versus the load line displacement for one of the disk compact specimens. The straight line is used to assist the selection of the point of initial deviation from linearity. The vertical line shows the point selected as the beginning of crack extension.*

prior to actual crack growth. In order to determine when crack growth begins, during the analysis routine the voltage ratio (the potential of the test specimen divided by the potential from the reference specimen) is plotted against the load line displacement. A typical example is shown in Fig. 7. There is an initial linear portion with a subsequent deviation from this linearity. This deviation from linearity is taken as the beginning of crack extension [*4–6*]. During the posttest analysis, the computer program allows the operator to interactively position a straight line through the data to assist in determining the initial deviation from linearity. The data prior to this point are assigned to the calculated blunting line, and crack extension is then calculated from this point on. As Fig. 7 shows, this material showed a sharp and distinct break, making the choice for the beginning of crack extension a simple one. The potential drop data shown in Fig. 7 are the average of sixty readings of the voltage taken during pauses in the test while the computer program performed calculations for the unloading compliance testing. Data were also taken continuously during the test and showed excellent agreement with the data taken during the pauses.

The UC and PD data gave very similar results for the DC(T) specimens. An example of the results is shown in Fig. 8. Both techniques show similar final crack extensions and predicted the measured final crack extension to within the 15% allowed by ASTM E 813-89. This excellent agreement between the two techniques provided further justification for the method used to determine the initiation of crack growth from the potential drop data.

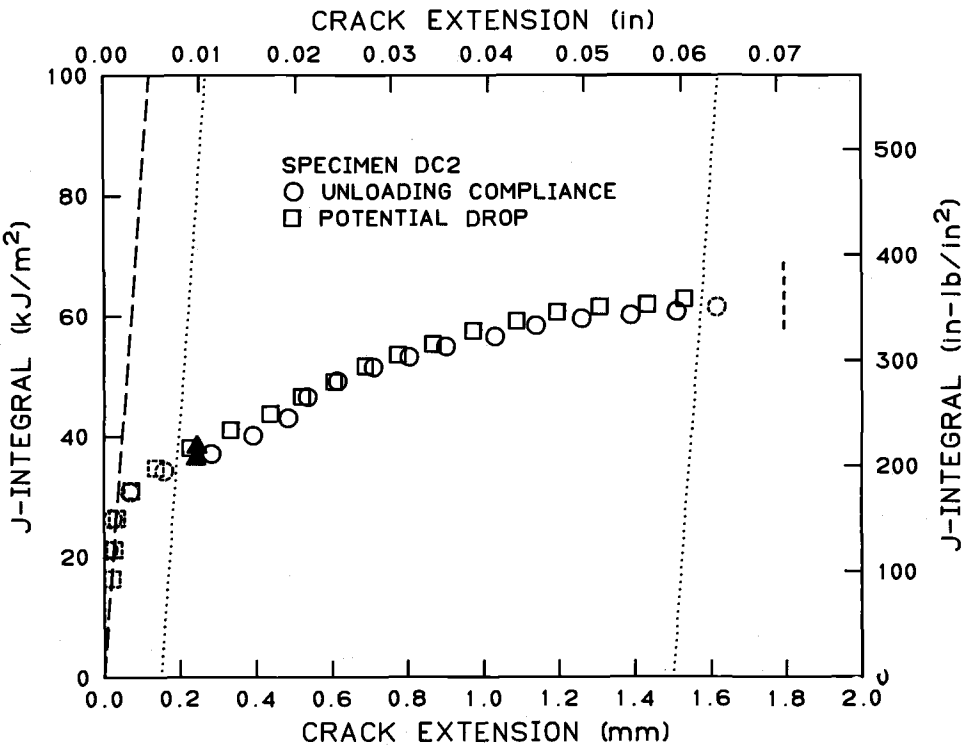

FIG. 8—*An example of the* J-R *curves from a disk compact specimen, showing excellent agreement between the data from unloading compliance and that from potential drop. Both methods predict the measured final crack extension (shown by the vertical dashed line) quite well. The solid triangles show the calculated critical* J *values.*

The load-displacement curves showed little or no hysteresis during the unload-load cycles until near the end of the test. The cause of this hysteresis late in the test is unclear. It may be caused by the knife edges contacting the sides of the grooves as the specimen opens or by rotation of the loading pins causing them to ride up the sides of the pin holes in the grips, although loading flats were provided in the clevises. Neither of these possibilities seems very likely as the specimens fractured without gross changes of geometry. Perhaps 90° grooves would be better than the 60° used for these specimens. This problem will be examined with additional testing, although it does not seem to have harmed the quality of the data.

The material tested showed some scatter in the toughness, as is shown in Fig. 9. These identical specimens show very different fracture behaviors. Specimen DC9 shows a greater J_{Ic} value and a higher *J-R* curve than does specimen DC2. The fracture toughness and tearing modulus values from all of the specimens tested are shown in Table 1. This table also includes the results from the 0.5 T C(T) specimens.

The thicker C(T) specimens gave results similar to the low toughness DC(T) specimens. In general, the J_{Ic} values were similar, but the *J-R* curves for the thicker specimens were flatter, giving lower values of the tearing modulus (see Table 1). A comparison of the results for the two specimens types is shown in Fig. 10.

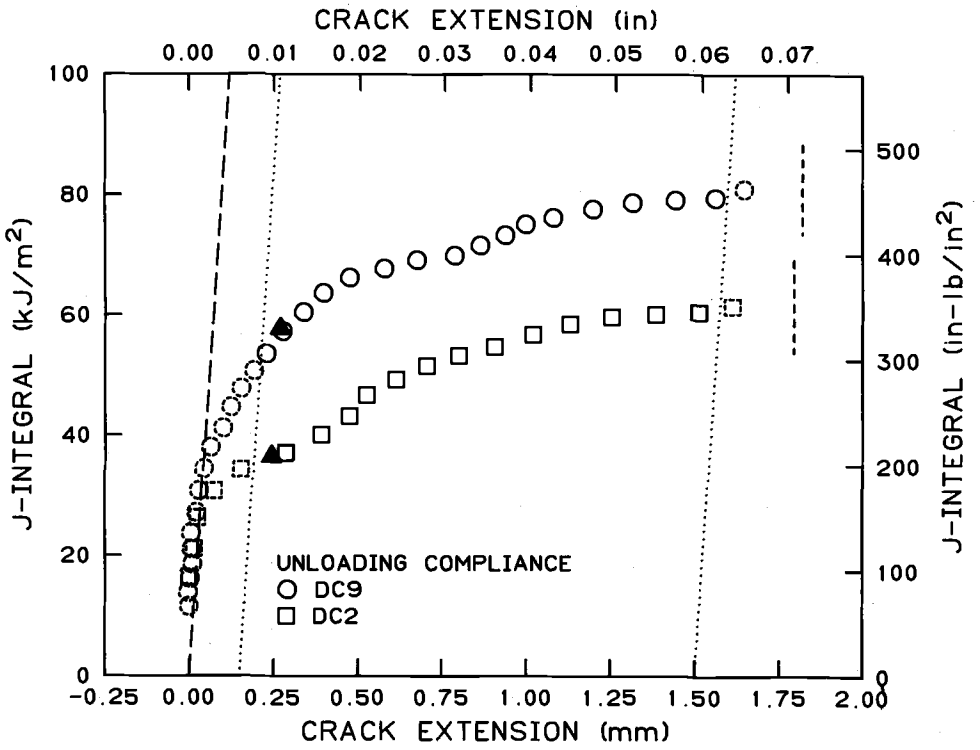

FIG. 9—J-R *curves obtained by the unloading compliance technique from two apparently identical disk compact specimens, showing that some scatter was observed from replicate tests. Both tests showed good agreement between measured and predicted crack extensions.*

The toughness values are surprisingly low for an annealed austenitic stainless steel. The tearing modulus values measured with the C(T) specimens are also very low. This low resistance to fracture resulted in very little distortion of the specimens. The fracture surfaces from two of the disk compact specimens are shown in Fig. 11. The low toughness resulted in very flat fracture surfaces and very little lateral contraction of the specimens ahead of

TABLE 1—*Fracture toughness results.*

Specimen Number	Specimen Type	Crack Extension Method[a]	J_Q		K_J		Tearing Modulus	Crack Extension Agreement,[b] %
			kJ/m²	in.-lb/in.²	MPa√m	ksi√in.		
DC5[c]	Disk compact	UC	63	356	110	100	15	−9.0
DC9	Disk compact	UC	58	329	106	96	22	−9.6
DC2	Disk compact	UC	36	207	84	76	24	−10.0
	Disk compact	PD	38	218	86	78	23	−14.8
DC16	Disk compact	UC	46	262	94	86	17	−13.4
	Disk compact	PD	44	254	93	84	21	−17.0
CT04	Compact	UC	36	203	83	75	10	−13.8
CT07	Compact	UC	34	196	81	74	18	−10.0

[a] UC = unloading compliance; PD = potential drop.
[b] Negative agreement indicates predicted crack extension was less than actual measured crack extension.
[c] Noticeable backup (apparent negative crack extension) reported at beginning of test.

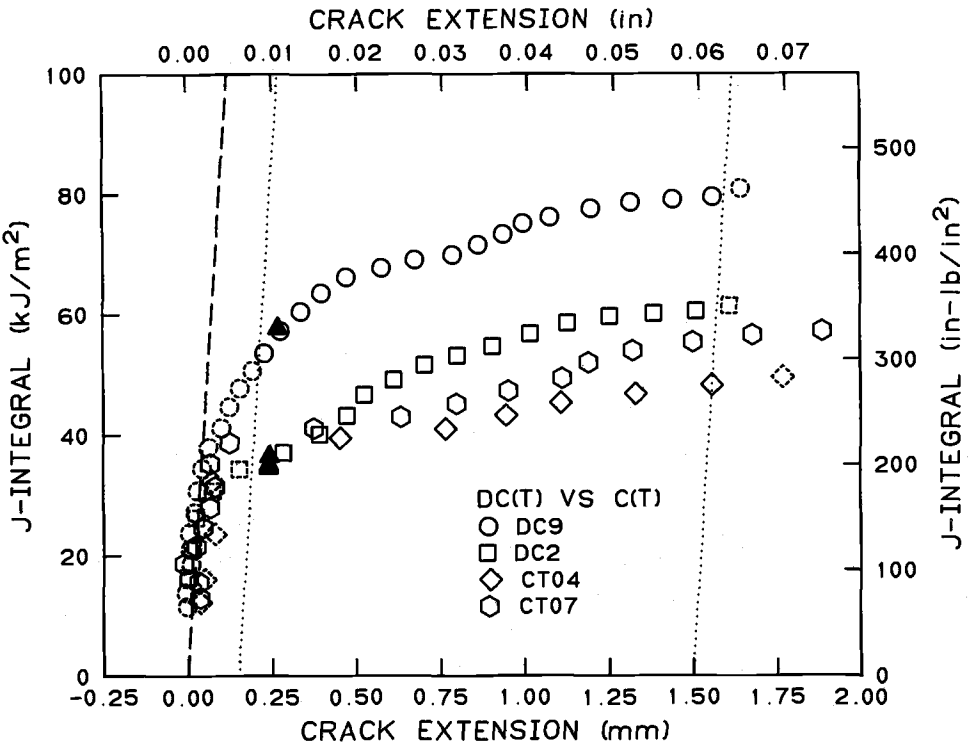

FIG. 10—*A comparison between the* J-R *curves obtained by unloading compliance from ½ T compact specimens and the 0.18 T disk compact specimens. The compact specimens gave similar* J_{IC} *values, but the* J-R *curves had lower slopes (lower tearing moduli).*

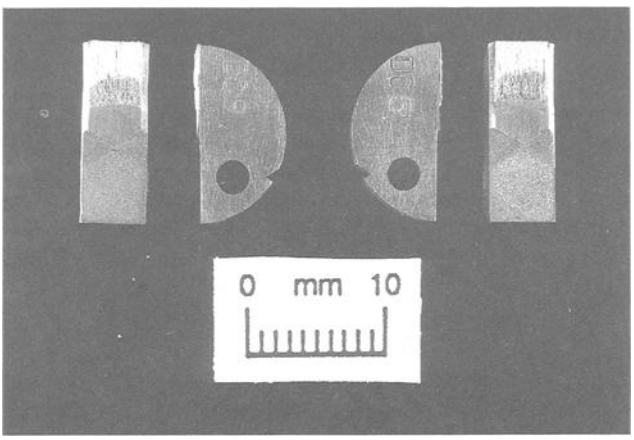

FIG. 11—*Fracture surfaces from two of the disk compact specimens. Note the chevron notch to assist in precracking, and the side grooves added after precracking was finished. The fracture surface shows that crack growth occurred with slight tunneling, but there was little distortion of the specimens' shape.*

the crack front. This lack of change in the specimen geometry may have helped the agreement between the different specimen types. The low toughness favors fracture rather than the growth of a large plastic zone. A large plastic zone would have relieved the stresses ahead of the crack tip and interacted more readily with the edges of the small disk compact than with those of the larger compact specimen for similar levels of stress intensity. Thus, the good agreement between these two specimen types may not extend to tougher materials. Further trials are planned with a tougher material. However, the good agreement between the two specimen types is very encouraging for the planned irradiation program, as the irradiation is expected to result in high strength and low toughness for the stainless steels. Thus the small disk compact specimen should provide useful data.

Conclusions

Special tools, fixtures, and instrumentation have been developed to permit both UC and PD measurements to be made on small disk compact specimens. The techniques are apparently suitable for remote operation with manipulators. Laboratory trials have shown that both methods give similar results. In addition, these results are in good agreement with results from UC testing of larger conventional compact specimens. These methods will be used to determine the effects of low-temperature irradiation on the fracture toughness of candidate stainless steel alloys for the first wall of a fusion reactor.

Acknowledgments

Research sponsored by the Office of Fusion Energy, U.S. Department of Energy, under contract DE-AC05-84OR21400 with Martin Marietta Energy Systems, Inc. The clip gage was designed and fabricated by John A. Shepic, Lakewood, CO 80228. The slip coupling was purchased from Winfred M. Berg, Inc., East Rockaway, NY 11518. We would like to thank L. J. Turner and A. E. Parker for helpful suggestions for modifications to assist handling with the manipulators. The fracture toughness testing was performed by R. L. Swain, and M. J. Swindeman and J. J. Henry, Jr., performed the potential drop calibration experiments with a system assembled by D. L. Thomas from the Instrumentation and Controls Division, ORNL. The manuscript was reviewed by R. W. Swindeman, D. E. McCabe, and R. K. Nanstad, and prepared by J. L. Bishop.

References

[1] Odette, G. R. and Lucas, G. E., "Effects of Low Temperature Neutron Irradiation on the Properties of 300 Series Stainless Steels," *Fusion Reactor Materials Semiannual Progress Report for Period Ending March 31, 1989,* DOE/ER-0313/6, DOE Office of Fusion Energy, p. 313.

[2] Elliot, C., Enmark, M., Lucas, G. E., Odette, G. R., and Rowcliffe, A. F., "Development of Disc Compact Tension Specimens and Test Techniques for HFIR Irradiations," *Fusion Reactor Materials Semiannual Progress Report for Period Ending September 30, 1990,* DOE/ER-0313/9, DOE Office of Fusion Energy, p. 7.

[3] Nanstad, R. K., Alexander, D. J., Swain, R. L., Hutton, J. T., and Thomas, D. L., "A Computer-Controlled Automated Test System for Fatigue and Fracture Testing," *Applications of Automation Technology to Fatigue and Fracture Testing, ASTM STP 1092,* A. A. Braun, N. E. Ashbaugh, and F. M. Smith, Eds., American Society for Testing and Materials, Philadelphia, 1990, p. 7.

[4] Lowes, J. M. and Fearnehough, G. D., "The Detection of Slow Crack Growth in Crack Opening Displacement Specimens Using an Electrical Potential Method," *Engineering Fracture Mechanics,* Vol. 3, 1971, pp. 103–108.

[5] Vassilaros, M. G. and Hackett, E. M., "J-Integral R-Curve Testing of High Strength Steels Utilizing the Direct-Current Potential Drop Method," *Fracture Mechanics: 15th Symposium, ASTM STP 833,* R. J. Sanford, Ed., American Society for Testing and Materials, Philadelphia, 1984, p. 535.

[6] Hackett, E. M., Kirk, M. T., and Hays, R. A., *An Evaluation of J-R Curve Testing of Nuclear Piping Materials Using the Direct-Current Potential Drop Technique*, NUREG/CR-4540, U.S. Nuclear Regulatory Commission, Washington, DC, August 1984.

DISCUSSION

F. H. Huang[1] (*written discussion*)—How do you calculate the crack extensions from potential outputs? Can you show potential outputs versus displacement curves? Do you use an electric potential calibration curve (a-v)?

D. J. Alexander (*author's closure*)—The crack extensions are calculated from the measured potential using Eq 1. As Fig. 7 shows, there are changes in potential at the beginning of the test. Data prior to the point chosen as the beginning of crack extension are forced to fit along the calculated blunting line. After this point, the potential determines the crack extension. During the posttest analysis the potential is multiplied by a factor to force agreement between the initial crack length measured from the fracture surface plus the crack extension due to blunting, and the crack length calculated from the potential at the point chosen to indicate the beginning of crack extension. This same factor is used for the remainder of the PD data. An example of the voltage-displacement curve is shown in Fig. 7. The continuous PD data agree very well with the discrete points shown in this figure.

M. L. Hamilton[2] (*written discussion*)—Do you expect any deleterious effect on the strain gages from the radiation field from the highly activated specimens irradiated in HFIR?

D. J. Alexander (*author's closure*)—We have tested many irradiated steel specimens in hot cells using similarly strain-gaged clip gages, and the gages have not been adversely affected by the irradiation levels. The stainless steel specimens will be irradiated to higher levels than the previous steel specimens, but will be much smaller. If the radiation damages the strain gages, we will have to replace the clip gage as necessary.

M. P. Manahan[3] (*written discussion*)—In your *J-R* curves, you plot EP measured data (which is measured prior to crack initiation) along the blunting line. Since the EP response prior to initiation is influenced by several factors other than crack tip blunting, would it not be better to discard the EP data prior to initiation and plot the initiation point at $\Delta a = 0$?

D. J. Alexander (*author's closure*)—In effect, we do discard the data prior to initiation; at least, we do not consider the (possibly) large changes in electric potential to be entirely due to crack extension. However, there must be crack blunting prior to actual crack extension, as the unloading compliance data shows, and therefore it seems more reasonable to allow for some apparent crack growth due to blunting by plotting the data along the blunting line rather than suggesting that there is no crack extension at all prior to initiation.

[1] Westinghouse Hanford Co., P.O. Box 1970, H5-67, Richland, WA 99352.
[2] PNL, Box 999 MS P8-15, Richland, WA 99352.
[3] MPM Research & Consulting, 213 Teaberry Circle, State College, PA 16803.

Marie Bernard,[1] *James W. Provan,*[2] *and Hulikal V. Lakshminarayana*[3]

On the Development of a Fracture Toughness Test Procedure Using a Notched Disk Specimen

REFERENCE: Bernard, M., Provan, J. W., and Lakshminarayana, H. V., **"On the Development of a Fracture Toughness Test Procedure Using a Notched Disk Specimen,"** *Small Specimen Test Techniques Applied to Nuclear Reactor Vessel Thermal Annealing and Plant Life Extension, ASTM STP 1204*, W. R. Corwin, F. M. Haggag, and W. L. Server, Eds., American Society for Testing and Materials, Philadelphia, 1993, pp. 143–161.

ABSTRACT: The research reported in this paper provides validation of a notched disk M(N) specimen geometry for both static and dynamic fracture toughness testing. More specifically, the work verifies the proposed procedure for the determination of the fracture toughness of materials most commonly used in plate-like configurations and extends its application to the dynamic case. The notched disk M(N) specimen has an axisymmetric notch machined on one of its faces, is clamped on its periphery, and is loaded axisymmetrically in a direction normal to its plane for both the precracking and loading-to-failure portions of the test. The advantage of this specimen geometry is that it is free from the adverse edge effects that exist in the standard C(T) specimen. Furthermore, a uniform plane strain state along the crack front induces a triaxial tensile stress and a small plastic zone. Finally, the specimens may be manufactured without difficulty.

Also reported in this paper are the findings of finite element analyses of both the 3-mm and 4-mm notch specimen geometries. Parametric studies emphasize the influence on the stress intensity factors of the notch location with respect to the clamped boundary. Stress intensity factors are evaluated for different crack lengths and orientations by the crack opening displacement method, the modified crack closure integral approach, and the virtual crack extension technique. The results, presented as normalized stress intensity factors, are essential for a reliable reduction of the test data.

Fracture toughness testing of an Al7075–T651 aluminum alloy was performed using 3-mm notch depth M(N) plate specimens. For dynamic fracture toughness testing, the 4-mm notch depth specimens, manufactured from polystyrene resins, were used.

Using the procedure fully detailed in the body of this paper, the static fracture toughness of Al7075–T651 was determined as K_{Ic} = 31.4 MPa $\sqrt{m}$, while the dynamic fracture toughnesses of polystyrene using the M(N) specimen geometry were between 0.73 and 0.99 MPa $\sqrt{m}$. These values indicate that the M(N) specimen geometry testing capabilities are substantiated.

KEYWORDS: notched disk specimen, plane strain, static and dynamic fracture toughness, Al7075–T651, polystyrene

In service failures, fractures are almost always produced in the presence of stress concentrators such as defects, inclusions, or cracks by applied stresses lower than the design

[1] Assistant professor, Mechanical Engineering, Ecole Polytechnique, PO Box 6079 Station A, Montreal, QC H3C 3A7 Canada.

[2] Professor and dean, Faculty of Engineering, P.O. Box 3055, Victoria, BC, Canada V8W 3P6.

[3] Visiting researcher, Mechanical Engineering, Ecole Polytechnique, PO Box 6079 Station A, Montreal, QC H3C 3A7.

stress. The situation is critical in large structures, commonly occurring in the nuclear power field, where plane strain states often exist. Indeed, the most important point emerging from the initial studies of fracture was that a lower limiting value of the fracture toughness, corresponding to plane strain, prevailed along the crack front. This critical stress intensity factor value, K_{Ic}, is the plane strain fracture toughness in Mode I. It is a measure of the resistance of a material to unstable fracture in the presence of a sharp crack under severe tensile constraint. Much effort has been directed towards the standardization of a test procedure for the experimental determination of the fracture toughness since K_{Ic} is an engineering design parameter that serves as a guide in relating quality, in terms of the size of flaws, cracks, and inclusions, to the load sustained by the component.

As is well known, ASTM Test Method for Plane-Strain Fracture Toughness of Metallic Materials (E 399) is designed around a mathematical analysis involving specimen dimensions, loading conditions, and their relationship to the stress introduced at the crack. The main ASTM E 399 requirements for an appropriate K_{Ic} measurement are: (1) specimens must have a sharp crack of length a; (2) the specimen thickness should be sufficient so that the shear lip contribution to the toughness may be neglected; (3) the crack tip plastic zone must be very much smaller than the crack length; (4) the elastic stress field should be evaluated at a very small distance, r, from the crack tip; and (5) the width, W, of the specimen ligament should be such that $0.45W < a < 0.55W$. Furthermore, the whole procedure consists of precracking a specimen whose dimensions are specified, loading it until it breaks, and then converting the failure load into the critical stress intensity value using a set of compliance tables where the variables are the load, the crack length, and the specimen thickness.

The drawbacks of the ASTM E 399 standard are centered around the fact that there is no advance assurance that a valid K_{Ic} will be determined in a particular test. Because of this, if the plane strain fracture toughness is routinely employed for quality control purposes, then the test program can be very expensive, time consuming, and inappropriate for production operations due to its high degree of sophistication, including the machining of specimens. Moreover, many materials have properties such as a high toughness combined with a low yield strength that make it difficult if not impossible to meet the prescribed K_{Ic} measurement conditions. Finally, it is clearly not possible to determine K_{Ic} if any dimension of the available raw material stock is insufficient to provide a specimen of the required size.

From the above considerations, it is seen that alternate test methods that are less complex, while being applicable to a wider variety of materials, are desirable. Different solutions have been proposed, such as the side-grooved C(T) specimen [*1*] and the short rod tests [*2,3*], but these do not completely solve the thickness effect problem when the fracture toughness is high.

In order to alleviate the limitations related to the thickness effect and to develop a technique that is simple to use and has an overall cost which does not make the price of the test prohibitive, a study of a novel plane strain fracture toughness specimen was undertaken [*4*].

The specimen geometry investigated is a notched disk M(N) specimen, illustrated in Fig. 1, having an axisymmetrical notch machined in one face. The specimen is clamped on its periphery and axisymmetrically and normally loaded for both precracking and fracture. The advantages of this specimen are:

1. It is free of all adverse edge effects.
2. A uniform plane strain state exists along the entire crack front.
3. It induces a high triaxial stress state at the crack tip.
4. The plastic zone is small.
5. It may be manufactured without difficulty.

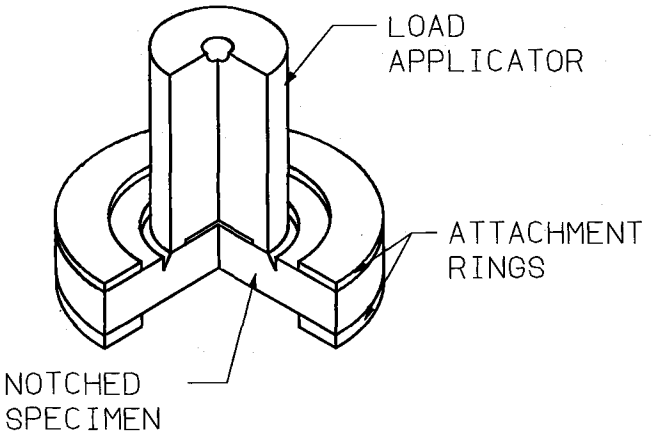

FIG. 1—*Details of the notched disk specimen.*

Its disadvantage is that it requires a larger load to fracture an M(N) specimen than the corresponding C(T) specimen.

The primary objective of this work is to validate this specimen geometry by stress analysis and fracture testing and to assess the applicability of the method to the determination of K_{Ic}.

The main steps in the development of the notched disk specimen geometry are:

1. The determination of the optimum notched configuration to obtain a high triaxial stress field at the notch tip and to induce a fatigue crack easily,
2. The rupture testing of precracked specimens to obtain the critical load,
3. An analysis of the precracked specimen stress field using finite element techniques, and
4. The determination of the specimen compliance to establish the fracture toughness value from the critical load.

The experimental investigations for both the static and dynamic situations are presented in the following two sections. The finite element modeling is described in the section that follows, where explicit formulae used for the evaluation of stress intensity factors, strain energy release rates, and the J-integral are presented. Numerical results are also presented from a parametric study involving two notch geometries, two notch depths, three notch locations, two crack orientations, and different crack lengths. In the final section, the results are reported as a validation of the notched disk specimen for both static and dynamic fracture toughness testing.

Static Testing

Procedure

The static notched disk fracture toughness measurement technique that was developed during the course of this investigation was applied to the determination of the fracture toughness of Al7075–T651 aluminum. The procedure used with the disk-shaped M(N) specimen follows essentially the same steps as in ASTM E 399, i.e., the specimen is subjected to repeated loading to start and develop a sharp crack prior to being statically loaded, with

a record being taken of the load at which fracture occurs. The specimens with notch depths of 3 and 4 mm were manufactured from an 11.1-mm (7/16-in.)-thick aluminum plate. For comparison purposes, the fracture toughness was also measured by strict adherence to the standard ASTM E 399 test. The M(N) and C(T) specimens were machined from alternating locations of the same Al7075–T651 plate, thereby ensuring that discrepancies resulting from variations in the material properties were kept to a minimum.

The fracture toughness tests were performed on a servohydraulic fatigue machine at room temperature. The specimens were clamped at r values between 26.0 and 38.5 mm in the steel holder, shown schematically in Fig. 2. The holder was fitted to the lower grip while the specimen was loaded through a self-aligning ball bearing plunger arrangement attached to the upper grip.

The fatigue precracking was accomplished at 2 Hz, applying a reversed compressive load under stroke control. The load-stroke curves indicated the presence and the extension of a

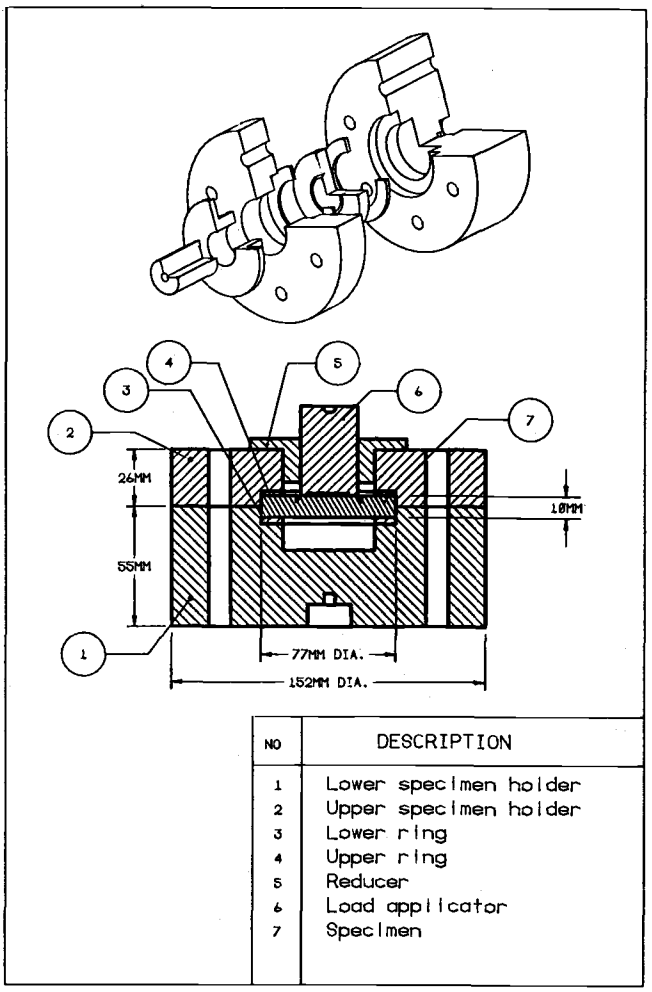

NO	DESCRIPTION
1	Lower specimen holder
2	Upper specimen holder
3	Lower ring
4	Upper ring
5	Reducer
6	Load applicator
7	Specimen

FIG. 2—*A schematic of the loading jig.*

crack by monitoring the maximum load behavior. The crack position following the fatigue precracking was marked by dyeing the crack surface with blue penetrant which readily penetrated the crack. Following this, the specimen was subjected to a slowly increased load until complete fracture occurred. The load corresponding to this fracture was evaluated from the maximum of the load-stroke curve without applying any correction, as per the ASTM E 399.

After rupture, four radial slices were cut at 90° intervals from the specimen to determine the crack orientation and length and were examined with a profile projector at a ×50 magnification. The study was completed by SEM observations of the fracture surface.

Results

Since direct optical observation of the crack length is not possible, the behavior of the compliance, while fatigue precracking the specimen, and the load, while subsequently monotonically increasing the load until fracture, were observed. During the fatigue precracking stage of the test, the cyclic load initially stabilizes after a short number of cycles. Subsequently, any observable decrease in the cyclic load amplitude that corresponds to an increase in the compliance is taken as an indication that a crack has begun to grow. All fatigue precracks were observed to grow uniformly in a radial direction at a constant angle, α, with respect to the normal of the M(N) specimen. After several tests, it was determined that a termination of the precracking period based on a decrease in the stabilized cyclic load equal to 15% gave good results.

After precracking, the specimens were loaded statically until rupture. In all cases, the load-stroke curves were similar to that illustrated in Fig. 3, indicating that the fracture occurred in a brittle, plane-strain manner. In contrast to the ASTM E 399 test procedure, the maximum load was easily ascertained for each specimen tested. From monotonic load-

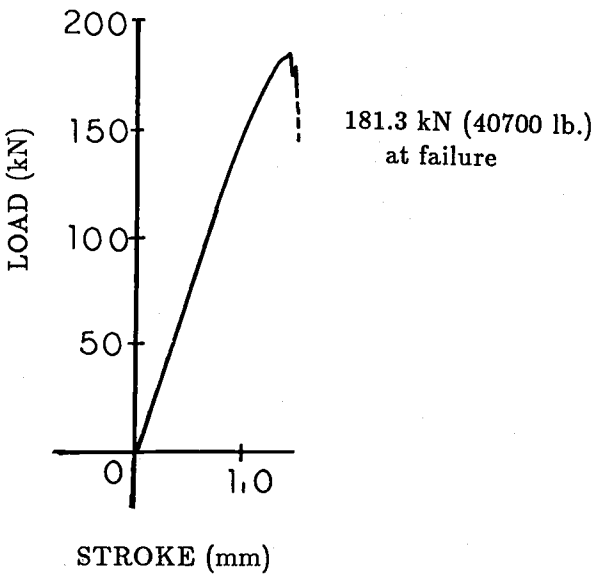

FIG. 3—*Load-stroke curve for 3-mm specimen.*

stroke curves similar to the one shown in Fig. 3, the fracture load sustained by a specimen was found in strict accordance with ASTM E 399.

Figure 4, which is typical, shows the crack path for both the precracking and final rupture stages for a 3-mm notched M(N) specimen. In all cases the crack orientations were the same, indicating that the crack propagated in the same mode. The dashed line in Fig. 4 indicates the projected extension of the fatigue precrack path, and the deviation from it indicates where the extension of the crack under static loading began.

The data collected from these tests, specifically the crack length and the load to fracture, were analyzed in conjunction with the finite element study to determine the fracture toughness, K_{Ic}, of the Al7075–T651. Furthermore, the specimens were subjected to a scanning electron microscope (SEM) study after rupture. All the classical features of fracture toughness testing were discernible with the obvious exception that no plane stress shear lips were present.

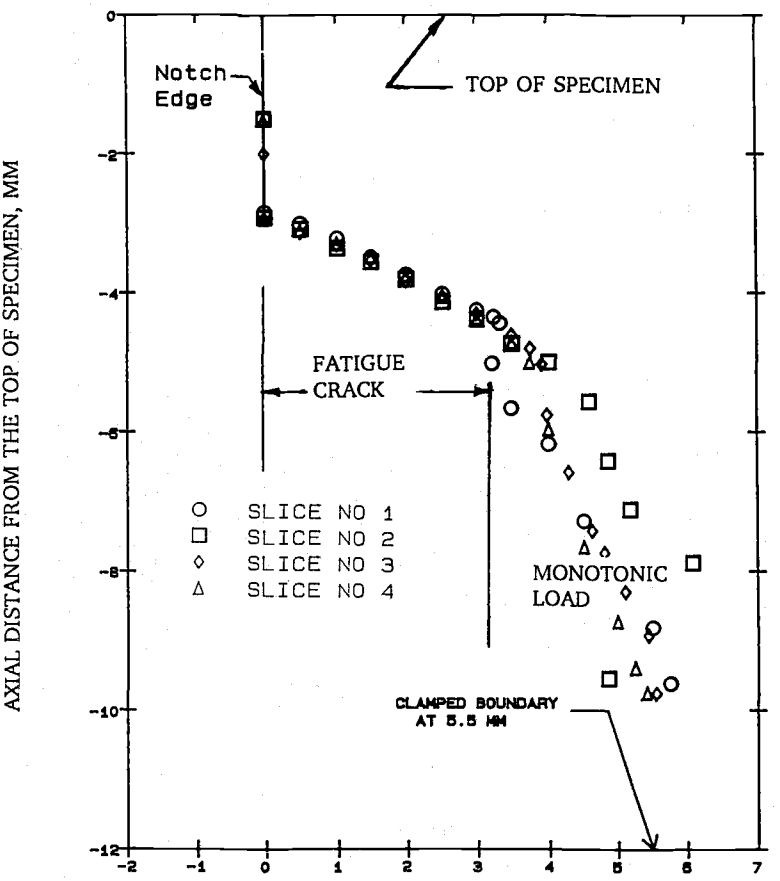

FIG. 4—*Crack orientations for 3-mm specimen.*

Discussion

In the procedure described above, the compliance behavior of the load was used as a reference point to decide when the precracking period should be terminated. Furthermore, during the rupture test, the control parameter was the stroke, which was slowly increased over a period that was typically 1.5 min, corresponding to a loading rate within the limits prescribed by ASTM E 399. The fatigue precracking upper limit load never exceeded 58% of the load at fracture for any crack length; this means that the stress intensity factor level during the stage of fatigue crack growth always conformed to the ASTM E 399 specification that establishes this limit at 60%. No offset procedure similar to the 5% secant method was applied to determine the load at rupture, the maximum load during the test being the value used for the estimation of K_{Ic}. Finally, it was noticed that the crack front length in the M(N) specimen is relatively more important (128.8 mm) at the beginning of precracking than in the C(T) specimen; this is reflected directly in the peak load value needed to break the specimen, which is high in comparison to the maximum applied to the companion ASTM E 399 C(T) specimen.

Dynamic Testing

The Specimen

Polystyrene (PS) was chosen for the dynamic testing portion of this investigation mainly because it is substantially different from the aluminum alloy used in the static tests, has good molding characteristics, gives specimens with superior optical properties, and is prone to brittle fracture. Early fracture studies using a standard specimen geometry were puzzling, [5], since notched specimens gave K_{Ic} values up to 4 MPa$\sqrt{m}$, i.e., substantially greater than for PMMA, to which it was known to be inferior. The explanation lay in the rather low craze stress of PS which resulted in it forming crazes, so that any attempt at notch sharpening using a wedging action produced craze bundles. This blunted the crack tip and increased the initiation value. Cracks with a single craze can be formed by fatiguing the specimen, by environmental crack growth, or by machining in a sharp notch with a very sharp fly cutter. For further information concerning the mechanisms as well as the kinetics associated with crack forming in polystyrene, the reader is referred to Ref [6].

The specimens were manufactured from PS resins placed in a mold being subjected to compression and heat in a Carver compression molding machine. The mold produced four specimens at a time having the dimensions of 10 mm in thickness and 60 mm in diameter. The temperature used was 108°C, 8° above the T_g of PS. The mold was inserted between two plates covered with aluminum foil, placed between the plates of the machine, and, when the temperature was set, compressed to a maximum of 68 MPa pressure. The axisymmetrical notch was machined with a fly cutter, and the sides of the specimens were smoothed so that the specimen conformed to the dimensions shown in Fig. 5.

The precracking of the specimens was carried out on the 4-mm notch depth specimens at room temperature (21°C) in a 10-tonne (22-kip) MTS servohydraulic fatigue machine. Before the specimen was mounted, oil was applied on its side surface, which enhanced the visual observation of any crack forming through the specimen. The specimen was clamped tightly in the jig to avoid any side movements, and then the jig was secured on the machine grip in a centered position. The machine was set in the load control and the load manually increased in an incremental manner. When a load value was reached that forced propagation of a crack, it was realized both visually and acoustically since there was a sharp noise generated by the formation of the crack. The length of the crack along with its shape was then observed. If there was enough clearance from the bottom of the specimen and the

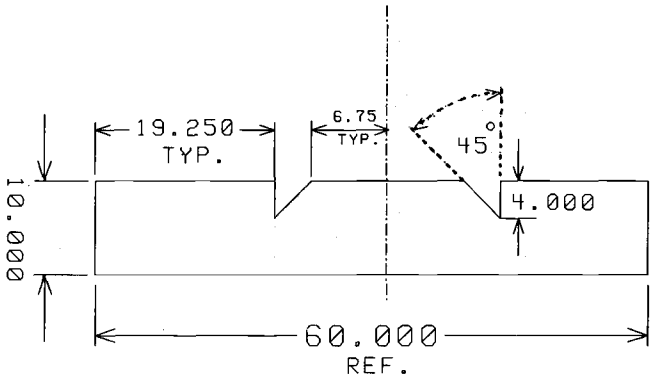

FIG. 5—*The polystyrene dynamic specimen.*

crack was not formed all around the notch, the above procedure was continued until a satisfactory crack was produced at a higher value of load. It is important to note that all the precracking was produced using static loading. The visual and acoustic "communication" of crack formation, along with the static loading, made the precracking operation rapid and easily controlled.

As shown in Table 1, most of the cracks in the different specimens initiated at approximately the same loads. Furthermore, the lengths of the cracks, which in all cases grew uniformly in a radial manner, are also listed. The 45° projection of the crack, starting from the bottom of the notch, was measured with a ×10 microscope and then converted to its actual length. The values given in Table 1 are averages of three values spaced 120° along the periphery of the specimen. The crack orientation was the same in all specimens, indicating that the crack propagated under the same Mode I conditions.

Impact Testing Apparatus

Impact tests have the advantage of being performed easily and rapidly and provide a relatively simple means of observing fracture phenomena of considerable practical impor-

TABLE 1—*PS experimental details and results.*

Specimen	Load for Crack Forming, kg	Crack Length, mm	Failure Load, kN	K_{Id}, MPa$\sqrt{m}$
D	541.00	6.33	5.40	0.95
E	428.50	5.76	...	...
F	577.75	5.88	5.62	0.98
G	595.25	6.38	4.15	0.73
H	545.00	6.33	4.86	0.86
I	544.25	6.40	5.62	0.99
J	669.25	6.55	...	...
K	419.25 up to 457.50	4.71	4.44	0.77
L	436.50 up to 525.00	6.02	4.68	0.82
M	410.50 up to 525.00	6.66	...	...

tance. In the present investigation, a Rheometrics Variable Speed Impact Tester (RVSIT) was used to obtain load-deflection data that allows for the evaluation of the dynamic fracture toughness of PS. The RVSIT is built around a linear-displacement, velocity-controlled, hydraulically driven mechanism. The system drives a penetrating rod to impact and puncture the flat notched-disk PS specimens. The tester is instrumented and fitted with a data acquisition system, which presents the data from the impact event in the form of load-deflection signals [7].

The crack length determined from the aforementioned precracking procedure is one of the parameters used in the fracture toughness equation developed in the next section. The other, as listed in Table 1, is the load at brittle fracture obtained from the RVSIT data acquisition system. At this stage, the estimates obtained from Specimens E, J, and M are excluded from further interpretation due to abnormal results. This abnormality was due to an inadequacy of the electronics, which combined with the inertia of the system made the data hard to interpret. The values obtained from the experiments are inserted into the fracture toughness equation, Eq 9, to evaluate the dynamic fracture toughness of PS using the M(N) specimen.

Finite Element Study

Finite Element Modeling

The numerical results reported in this paper were obtained using the general-purpose finite element (FE) analysis program ABAQUS. Figure 6 shows a typical finite element discretization of the notched disk specimen. The model incorporates two different types of elements, namely, singular (S) and regular (R). A locally refined mesh consisting of 16 singular elements around the crack tip is linked to a global mesh consisting of 122 regular elements. While the concept is appealing, the singular and regular element formulations must be compatible. The choice of the collapsed quadrilateral quarter point element as a singular element is essentially due to the availability of the eight-noded isoparametric quadrilateral axisymmetric solid element (CAX8R) and the multipoint constraint (MPC) facility in ABAQUS. Specifically, the CAX8R element becomes the singular element when: (1) the input data collapses a side and locates the side nodes at quarter points, and (2) the multiple nodes located at the crack tip are constrained to undergo the same displacements. This element displays the $1/\sqrt{r}$ singularity along all rays emanating from the crack tip, where r denotes radial distances measured from the crack tip. Both CAX8R and CAX6 (six-noded axisymmetric solid element) are used as regular elements. Inter-element displacement compatibility between the singular and regular elements is satisfied in this model. Finally, the length Δa of the singular elements used in the present study was such that $(\Delta a/a) \leq 0.01$, where a denotes the crack length.

The use of singular elements significantly improves convergence, accuracy, and computational efficiency of the finite element method for the analysis of cracked bodies. In particular, it enables the development of explicit formulae for the extraction of stress intensity factors, strain energy release rates, and the J-integral on the basis of a standard output provided by a commercial finite element software system.

SIF Evaluation using the COD Method

Figure 7 shows the details of finite element discretization around the crack tip. The crack opening displacement (COD) method [8] provides a convenient means of calculating both

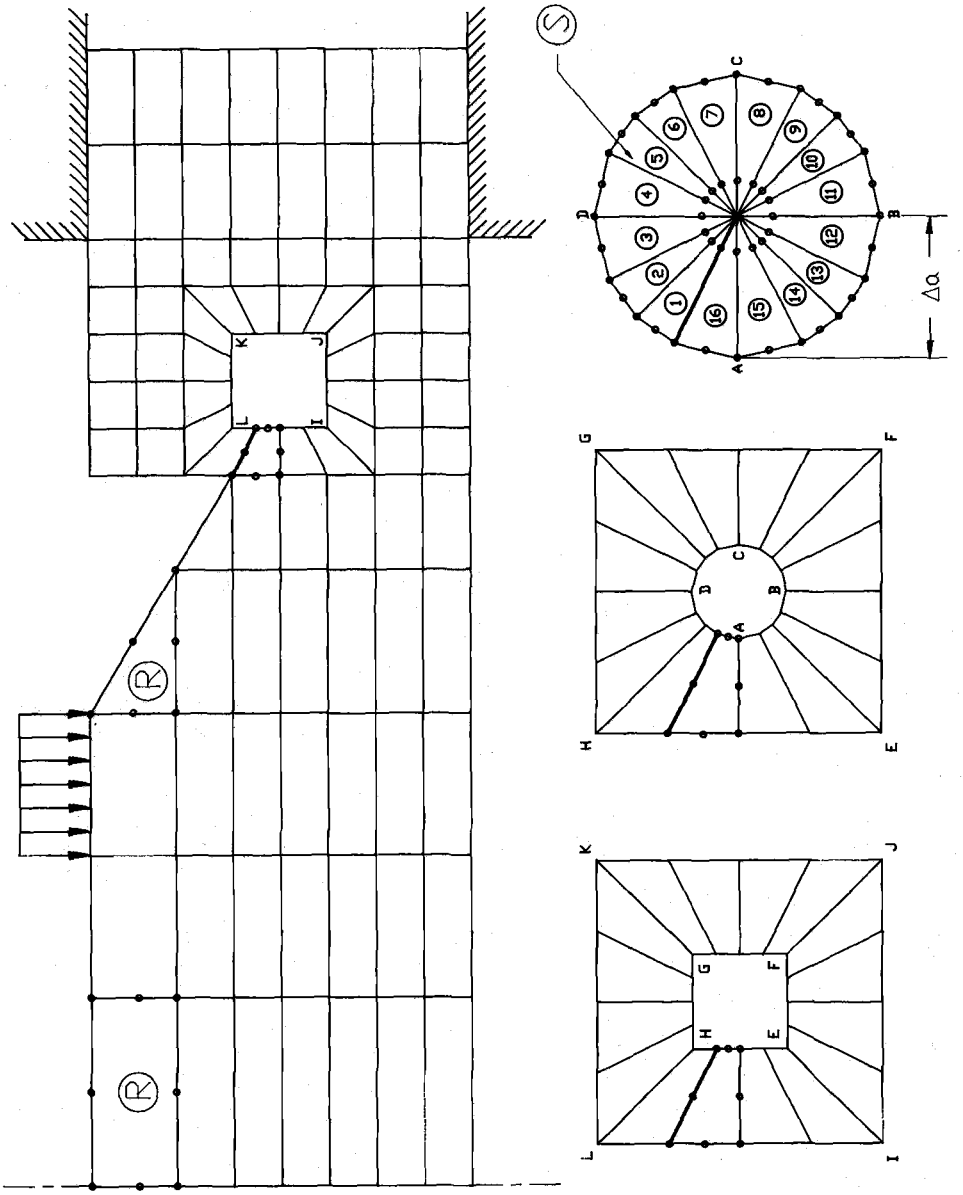

FIG. 6—*A typical finite element model of the specimen.*

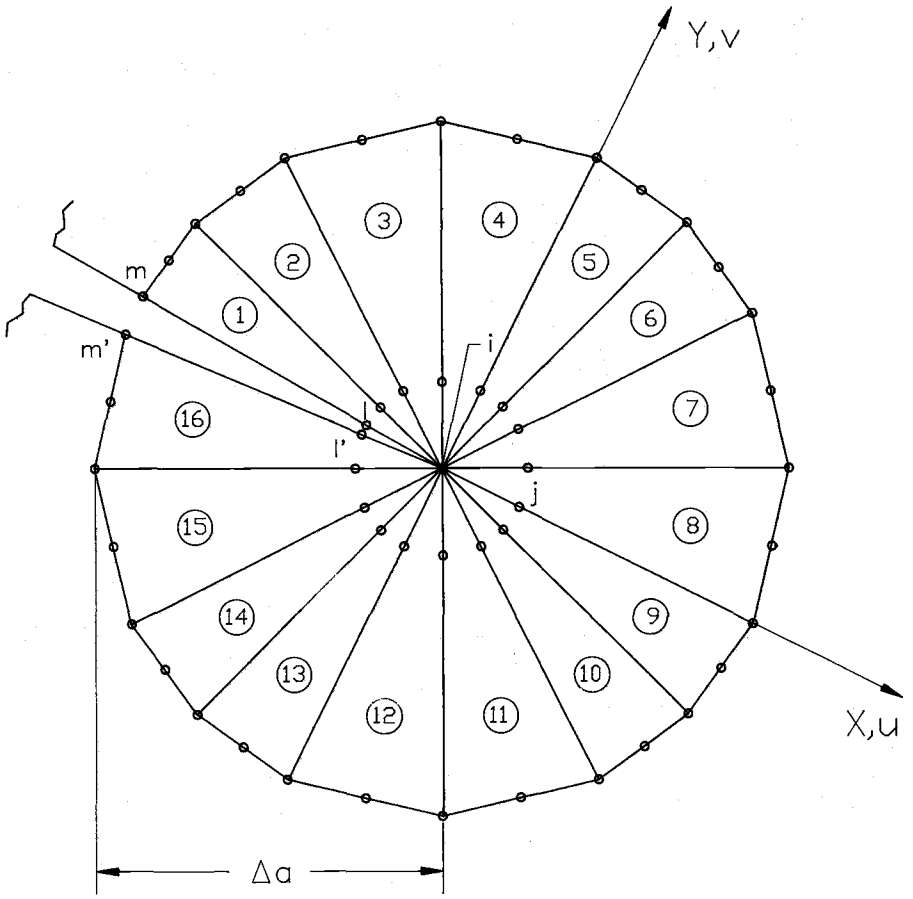

FIG. 7—*Finite element mesh around a crack tip.*

Mode I (K_I) and Mode II (K_{II}) components of the crack tip stress intensity factor (SIF). The SIF evaluation formulae used in the present study are

$$K_I = \frac{E}{(1+\nu)(\chi+1)}\left(\frac{1}{2\Delta a}\right)^{1/2}[4(v_l - v_{l'})(v_m - v_{m'})]$$
$$K_{II} = \frac{E}{(1+\nu)(\chi+1)}\left(\frac{1}{2\Delta a}\right)^{1/2}[4(u_l - u_{l'})(u_m - u_{m'})] \quad (1)$$

where E is Young's modulus, ν is Poisson's ratio, $\chi = 3 - 4\nu$ for plane strain or $(3 - \nu)/(1 + \nu)$ for plane stress, and $u_l, \ldots, u_{m'}, v_l, \ldots, v_{m'}$ denote the nodal displacements at l, l', m, and m', respectively.

The accuracy of the computed values of K_I and K_{II} can be improved by decreasing the length of the singular elements, by increasing the number of singular elements around the crack tip, and by changing the number and distribution of the regular elements.

G Evaluation Using the MCCI Approach

The modified crack closure integral (MCCI) approach [9] to the evaluation of the strain energy release rate (denoted by G) has the advantage of simultaneously delivering the Mode I (G_{I}) and Mode II (G_{II}) components. Referring to Fig. 7, the nodal forces at i and j and the nodal displacements at l, l', m, and m' are needed to compute G_{I} and G_{II}. These forces and displacements represent components that are normal and tangential to the crack plane. The nodal forces at i and j, denoted by F_{xi}, F_{yi}, F_{xj}, and F_{yj}, are taken as approximations for those unknown forces required to reverse and cancel the known nodal displacements, denoted by u_l, v_l, $u_{l'}$, $v_{l'}$, u_m, v_m, $u_{m'}$, and $v_{m'}$. Note that this approximation will only be exact in the limit $\Delta a \to 0$. However, numerical studies have confirmed that accurate G solutions are obtained even with a finite value for Δa and a coarse mesh. It is to be noted that forces F_{xi} and F_{yi} are calculated from elements 1 to 8 while forces F_{xj} and F_{yj} are computed from element 8 alone. The G evaluation formulae used in this study are:

$$
\begin{aligned}
G_{\mathrm{I}} &= \frac{1}{2\Delta a}\left[\frac{F_{yi}}{2\pi R_i}\{t_{11}(\overline{v_m} - \overline{v_{m'}}) + t_{12}(\overline{v_l} - \overline{v_{l'}})\}\right. \\
&\quad \left. + \frac{F_{yj}}{2\pi R_j}\{t_{21}(\overline{v_m} - \overline{v_{m'}}) + t_{22}(\overline{v_l} - \overline{v_{l'}})\}\right] \\
G_{\mathrm{II}} &= \frac{1}{2\Delta a}\left[\frac{F_{xi}}{2\pi R_i}\{t_{11}(\overline{u_m} - \overline{u_{m'}}) + t_{12}(\overline{u_l} - \overline{u_{l'}})\}\right. \\
&\quad \left. + \frac{F_{xj}}{2\pi R_j}\{t_{21}(\overline{u_m} - \overline{u_{m'}}) + t_{22}(\overline{u_l} - \overline{u_{l'}})\}\right]
\end{aligned}
\tag{2}
$$

where

$$
\begin{aligned}
&t_{11} = 6 - \frac{3\pi}{2};\ t_{12} = 6\pi - 20, \\
&t_{21} = \tfrac{1}{2};\ t_{22} = 1, \\
&\overline{v_m} = v_m - v_i;\ \overline{u_m} = u_m - u_i, \text{ etc.}
\end{aligned}
\tag{3}
$$

The accuracy of the computed values of G_{I} and G_{II} strongly depends on the value of Δa used in the computations. The value of Δa is determined by the length of the singular elements used around the crack tip. In the present case, G can be evaluated with good accuracy when $(\Delta a/a) \leq 0.01$.

J-Integral Evaluation Using VCE Technique

The virtual crack extension (VCE) technique provides a general procedure for J-integral evaluation using finite elements [10]. Using a compatible finite element model, the potential energy, π_p, of an elastic body may be calculated from

$$
\pi_p = \frac{1}{2}\{q\}^t[K]\{q\} - \{q\}^t\{F\} \tag{4}
$$

where $\{q\}$ is the vector of nodal displacements, $\{F\}$ is the vector of applied nodal forces, and $[K]$ is the elastic stiffness matrix. The finite element equations to be solved to get $\{q\}$ are given by

$$\frac{\partial \pi_p}{\partial q} = [K]\{q\} - \{F\} = 0 \tag{5}$$

The energy release rate for a crack of length a in the body is $\partial \pi_p / \partial a$, which is equal to the J-integral. By differentiating Eq 5, it follows that

$$J = -\frac{1}{2}\{q\}^t \frac{\partial K}{\partial a}\{q\} + \{q\}^t \frac{\partial F}{\partial a} - \frac{\partial}{\partial a}\{q\}^t(K_q - F) \tag{6}$$

which, in view of Eq 5, reduces to

$$J = -\frac{1}{2}\{q\}^t \frac{\partial K}{\partial a}\{q\} + \{q\}^t \frac{\partial F}{\partial a} \tag{7}$$

The derivatives in Eq 7 are approximated by

$$\frac{\partial K}{\partial a} = \frac{1}{\Delta a}[K|_{a+\Delta a} - K|_a], \frac{\partial F}{\partial a} = \frac{1}{\Delta a}[F|_{a+\Delta a} - F|_a] \tag{8}$$

Equations 7 and 8 provide a simple means of evaluating the J-integral using the results of a single finite element analysis. The technique is generally known as the method of virtual crack extension (VCE) [*11*]. There are also various refinements of the VCE technique. In this connection, reference may be made to Refs *12–14*. The VCE technique has been implemented in ABAQUS for J-integral evaluations. Very accurate solutions have been obtained using quadratic isoparametric elements for the far field and quarter point elements around the crack tip. There is no need for the analyst to specify Δa. Any number of crack tips may be evaluated in a single analysis. The user, however, must specify the node set forming each crack tip and the number of contours. Note that each contour is now an element set. To be useful, it must consist of a ring of elements completely surrounding the crack from one face to the opposite face. ABAQUS is programmed to find the element set that forms each ring from the node set.

Since the J-integral should be path independent, path dependence of the computed values of J may be taken as an indication of solution accuracy. The procedure for J-integral evaluation implemented at ABAQUS is particularly attractive because it is simple to use, adds little to the cost of conventional analysis, and provides excellent accuracy. However, the use of singular elements in the crack tip zone and proper mesh refinement in the vicinity of the crack tip are essential for high accuracy.

Numerical Results and Discussion

The three specimen configurations shown in Fig. 8 were studied in detail. The associated parameters are given in Table 2. Numerical results obtained for each are presented and discussed below.

Specimen A—Normalized values of K_I, K_{II}, G_I, G_{II}, and J are presented in Table 3 for three different crack lengths. These results show that the value of E^*J obtained using the

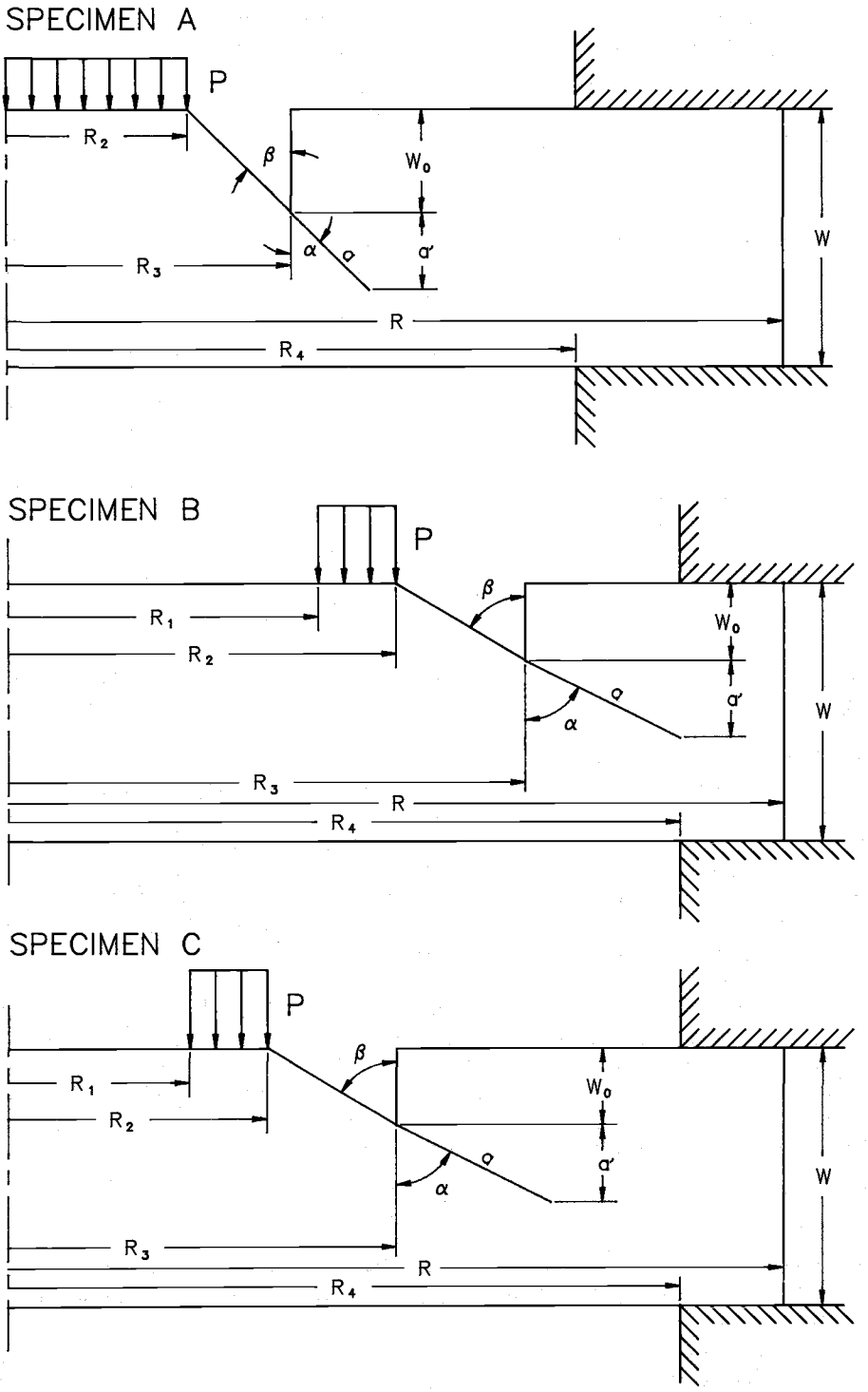

FIG. 8—*Specimen configurations considered in the study.*

TABLE 2—*Geometric details of test specimens shown in Fig. 8.*

Parameter	Specimen A	Specimen B	Specimen C
R_1, mm	0.0	12.5	7.0
R_2, mm	7.0	15.0	10.0
R_3, mm	11.0	20.0	15.0
R_4, mm	22.0	26.0	26.0
R, mm	30.0	30.0	30.0
W_o, mm	4.0	3.0	3.0
W, mm	10.0	10.0	10.0
β, °	45.0	60.0	60.0
α, °	45.0	63.4	63.4

VCE technique is in excellent agreement with the value of $K_I^2 + K_{II}^2$ given by the COD method. The J-integral evaluated on Contour 1 is in very good agreement with the value of $G(=G_I + G_{II})$ obtained using the MCCI approach. Computed values of $\sqrt{E^*G_I}$ and $\sqrt{E^*G_{II}}$ are also in good agreement with the values of K_I and K_{II}.

The results presented are reliable and accurate to within 2%. Furthermore, the notch location and crack orientation are such that the ratio K_I/K_{II} varies between 1.76 and 1.24 over the range of crack lengths studied. Consequently, the fracture is under mixed mode and the precrack may not propagate in its own plane.

Specimen B—Normalized stress intensity factors K_I and K_{II}, strain energy release rates G_I and G_{II}, and the J-integral are given in Table 4 for a crack of length $a'/W = 0.2$. The value of E^*J obtained using the VCE technique is in excellent agreement with the value of $K_I^2 + K_{II}^2$ obtained using the COD method. The computed value of J on Contour 1, involving a ring of singular elements only, is in excellent agreement with the value of $G(= G_I + G_{II})$ obtained using the MCCI approach. However, the J-integral values obtained using Contours 2, 3, and 4, which include the first, second, and third rings of regular elements, respectively, are indeed path independent to within 1%, but deviate considerably (up to 15%) from those obtained using Contour 1. The values of $\sqrt{E^*G_I}$ and $\sqrt{E^*G_{II}}$ obtained using the MCCI approach are also in very good agreement with the values for K_I and K_{II} obtained using the COD method. It is therefore fair to conclude that the FE model chosen and the assumed crack extension, Δa, are capable of providing accurate and reliable solutions to the problem at hand.

TABLE 3—*Comparison of numerical solutions—specimen A.*[a]

Crack Length, $\frac{a'}{W}$	Stress Intensity Factors		Energy Release Rates		J-Integral
	$\frac{K_I}{K_o}$	$\frac{K_{II}}{K_o}$	$\frac{\sqrt{E^*G_I}}{K_I}$	$\frac{\sqrt{E^*G_{II}}}{K_{II}}$	$\frac{E^*J}{(K_I^2 + K_{II}^2)}$
0.1	0.1562	0.0889	1.0047	0.9877	0.9964
0.4	0.5795	0.3725	1.0003	0.9797	1.0017
0.5	0.8354	0.6662	1.0129	0.9905	1.0049

[a] $K_o = P/(R_3\sqrt{\pi a})$; $P = p\pi(R_2^2 - R_1^2)$; $p = 1$ kgf/mm^2; $E^* = E/(1 - \nu^2)$; $E = 350$ kgf/mm^2; $\nu = 0.3$.

TABLE 4—*Comparison of numerical solutions—specimen B.*[a]

Crack Length, $\frac{a'}{W}$	Stress Intensity Factors		Energy Release Rates		*J*-Integral,
	$\frac{K_I}{K_o}$	$\frac{K_{II}}{K_o}$	$\frac{\sqrt{E^*G_I}}{K_I}$	$\frac{\sqrt{E^*G_{II}}}{K_{II}}$	$\frac{E^*J}{(K_I^2 + K_{II}^2)}$
0.2	0.4463	0.0608	1.0015	1.0245	1.0026

[a] $K_o = P/(R_3\sqrt{\pi a})$; $P = p\pi(R_2^2 - R_1^2)$; $p = 1$ kgf/mm^2; $E^* = E/(1 - \nu^2)$; $E = 7\,000$ kgf/mm^2; $\nu = 0.3$.

The particular crack orientation is such that the ratio $K_I/K_{II} = 7.34$. Consequently, the fracture is partially mixed mode and crack growth may or may not be self-similar. Furthermore, the notch location is such that the crack tip stress field interferes with the clamped boundary for further increases in crack length.

Specimen C—The geometric details for this specimen (Fig. 8) are given in Table 5. Normalized stress intensity factors, strain energy release rates, and *J*-integral values are given in Table 5 for five different crack lengths. It is interesting to note that the value of E^*J is in excellent agreement with $K_I^2 + K_{II}^2$ and that J also agrees very well with the value for $G(= G_I + G_{II})$. The values of $\sqrt{E^*G_I}$ and $\sqrt{E^*G_{II}}$ compare very well with K_I and K_{II}.

Therefore, these results form a set of numerically accurate stress intensity factor solutions. As shown in Fig. 9, the variation of K_I with crack length is linear over a wide range, while K_{II} remains almost constant. For all crack lengths considered, the ratio K_I/K_{II} is greater than 14.

SIF Expression for the M(N) Notched-Disk Specimen Geometry C

In order to reduce the test data, a calibration formula is needed for K_I as a function of geometry, applied load, and crack length. Such a formula, determined from the FE analysis and valid over the useful range of crack lengths for specimen geometries similar to that of Specimen C, is given by

$$K_I = \frac{P}{R_3\sqrt{\pi a}}\left\{0.03 + 2.1445\left(\frac{a'}{W}\right)\right\} \text{ for } 0.1 \le \left(\frac{a'}{W}\right) \le 0.4 \tag{9}$$

TABLE 5—*Comparison of numerical solutions—specimen C.*[a]

Crack Length, $\frac{a'}{W}$	Stress Intensity Factors		Energy Release Rates		*J*-Integral, $\frac{E^*J}{(K_I^2 + K_{II}^2)}$	SIF Ratio, $\frac{K_I}{K_{II}}$
	$\frac{K_I}{K_o}$	$\frac{K_{II}}{K_o}$	$\frac{\sqrt{E^*G_I}}{K_I}$	$\frac{\sqrt{E^*G_{II}}}{K_{II}}$		
0.1	0.2423	0.0171	0.2425	0.0178	1.0007	14.15
0.2	0.4590	0.0325	0.4590	0.0341	0.9996	14.12
0.3	0.6712	0.0180	0.6714	0.0206	0.9991	37.26
0.4	0.8501	0.0206	0.8500	0.0171	0.9987	41.18
0.5	0.8053	0.0246	1.0029	0.1346	1.0091	32.71

[a] $K_o = P/(R_3\sqrt{\pi a})$; $P = p\pi(R_2^2 - R_1^2)$; $p = 1$ kgf/mm^2; $E^* = E/(1 - \nu^2)$; $E = 7\,000$ kgf/mm^2; $\nu = 0.3$.

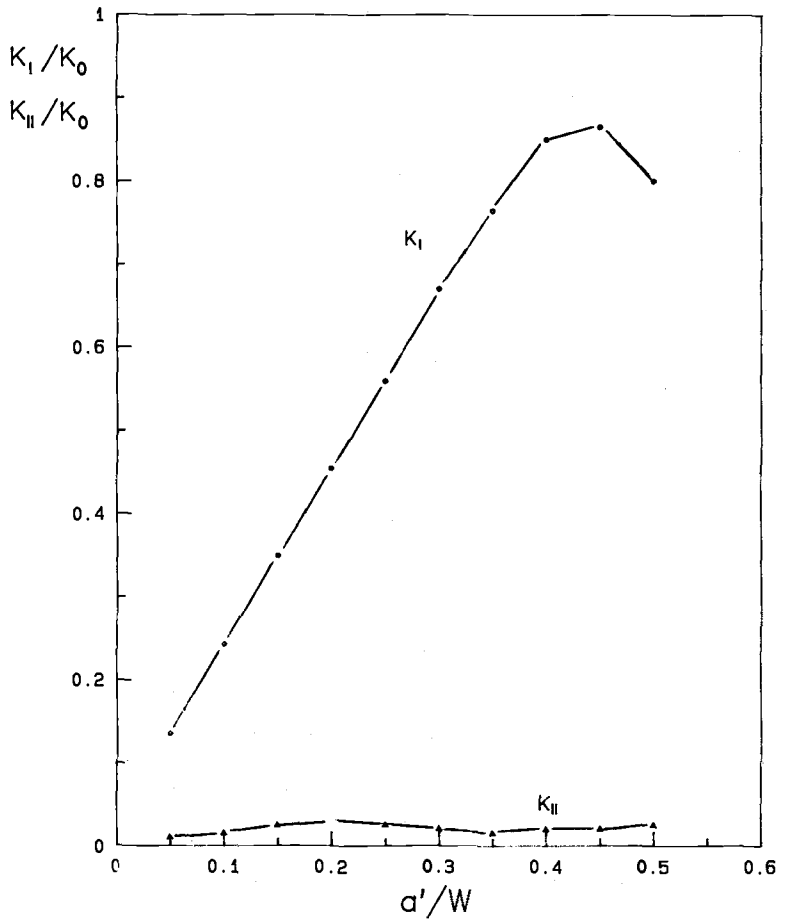

FIG. 9—*Normalized stress intensity factors for Specimen C.*

It should be noted, however, that this formula applies only in situations where the crack orientation is maintained.

Discussion

Finite element modeling using singular and regular quadratic isoparametric elements and the formulae for the determination of mixed mode stress intensity factors and strain energy release rates used in this study offer a powerful tool for practical applications since commercial finite element analysis codes can be employed without any modification. The parametric studies cannot be considered complete. There is still a need to consider other crack orientations in Specimen C to assess the direction of precrack initiation. There is also a need to study the specimen size requirements to ensure elastic plane-strain behavior. In establishing the specimen size required for valid K_{Ic} tests, the specimen dimensions should be large enough compared with the crack tip plastic zone size. Among the various finite element analyses to determine plastic zone shape and size, the work reported in Ref *15* is well known.

Static and Dynamic Fracture Toughnesses

The results presented in this section demonstrate the potential of the M(N) notched disk-shaped specimen (Specimen C in particular) for the determination of plane strain fracture toughness. Calibration formulae similar to Eq 9 for K_{Ic} and K_{Id} (obtained in this study) are crucial to the widespread use of this test.

Evaluation of K_{Ic} of Al7075–T651 Aluminum Using the M(N) Specimen

Applying a calibration formula similar to Eq 9, which was reported in Ref *4*, to evaluate the fracture toughness, K_{Ic}, a value of

$$K_{Ic} = 31.4 \text{ MPa}\sqrt{\text{m}} \tag{10}$$

was established. This result, determined with the M(N) specimen, is in good agreement with the value of 27.1 MPa$\sqrt{\text{mm}}$ that was obtained with C(T) specimens tested in strict accordance with ASTM E 399. Other values reported in the literature are 30 MPa$\sqrt{\text{m}}$ [*16*] and 32 MPa$\sqrt{\text{m}}$ [*17*] for specimens of the L-T crack configuration. In the M(N) specimen there is no such preferred orientation, the crack front being circular.

The M(N) specimen geometry was studied in the present work to alleviate the drawbacks and limitations of the existing ASTM E 399 procedure. Tests on the Al7075–T651 precracked specimens have shown that the crack fails under Mode I conditions. Using the specimen calibration that was established by a finite element method and the rupture test results, the Al7075–T651 plane strain fracture toughness was successfully determined.

Although the outcome of the research has not been presented as a new standard method, it has nevertheless good prospects for further development. The specimen has the advantages of ensuring a plane strain state over the entire crack front and of being easy to manufacture.

Evaluation of K_{Id} for PS Using the M(N) Specimen

The equation for the evaluation of K_{Id} as established in the previous section was applied to the dynamic situation under consideration in this investigation. Using the results listed in Table 1, i.e., the fracture load, P, and the precrack length, a, the last column in Table 1 displays the values of K_{Id}. All the values are between 0.77 and 0.99 MPa$\sqrt{\text{m}}$ and, hence, the dynamic fracture toughness of PS, taken as the average of these values, is

$$K_{Id} = 0.87 \text{ MPa}\sqrt{\text{m}} \tag{11}$$

Reference *5* reports K_{Ic} values for PS recorded at 20°C as ranging from 0.7 to 1.1 MPa$\sqrt{\text{m}}$, while the value recorded by Ref *6* is 1.1 MPa$\sqrt{\text{m}}$. Other references discuss the fracture of plastics, but there are no values reported in terms of K_{Ic}, except in Ref *18*, where a value of 1.0 MPa$\sqrt{\text{m}}$ is reported. All of the values obtained in this work, as well as the average fracture toughness given in Eq 11, fall within the range of the data reported in Ref *5*. Furthermore, as the calculations of the dynamic fracture toughness for the individual specimens show, the equation developed for the determination of the dynamic fracture toughness using the M(N) specimen geometry is not sensitive to crack variations, while it is sensitive to load variations. This is emphasized by the similar fracture toughness values calculated for the same fracture load for specimens K and G, while their respective crack lengths varied by approximately 1.2 mm or 26.1%.

The M(N) specimen geometry used here was, in principle, the same as in the static case, except for the radius being 15.5 mm for the aluminum specimens and 6.75 mm for the PS

specimens. This indicates that the testing capabilities of the M(N) geometry are not dependent solely on specific dimensions. This is encouraging and further validates the M(N) specimen geometry testing method for the determination of both static and dynamic fracture toughnesses. However, only after a considerable amount of analytical and numerical study, coupled with experimental verification, will an ASTM standardized test procedure using the M(N) specimen for plane strain fracture toughness testing be established.

References

[1] Masanori, K., Satya, N. A., and Hiroshi, M., "Studies on Size Effects and Crack Growth of Side-Grooved C(T) Specimens," *Fracture Mechanics: Sixteenth Symposium, ASTM STP 868,* American Society for Testing and Materials, Philadelphia, 1985, pp. 251–278.

[2] Barker, L. M., "A Simplified Method for Measuring Plane Strain Fracture Toughness," *Engineering Fracture Mechanics,* Vol. 9, 1977, pp. 361–369.

[3] Biner, S. B., Barnby, J. T., and Elwell, D. W. J., "On the Use of Short-Rod/Bar Test Specimens to Determine the Fracture Toughness of Metallic Materials," *International Journal of Fracture,* Vol. 26, 1984, pp. 3–16.

[4] Bernard, M., "The Development of a New Fracture Toughness Procedure," Ph.D. thesis, McGill University, Montreal, 1988.

[5] Williams, J. G., *Fracture Mechanics of Polymers,* Halsted Press, New York, 1984.

[6] Kinloch, A. J. and Young, R. J., *Fracture Behaviour of Polymers,* Applied Science, Essex, England, 1983.

[7] Kamal, M. R., Samak, Q., Provan, J. W., and Ahmad, V., "Evaluation of a Variable Speed Impact Tester for Analysis and Impact Behaviour of Plastics and Composites," *Instrumented Impact Testing of Plastics and Composite Materials, ASTM STP 936,* S. L. Kessler, G. C. Adams, S. B. Driscoll, and D. R. Ireland, Eds., American Society for Testing and Materials, Philadelphia, 1987, pp. 58–80.

[8] Cook, R. D., Malkus, D. S., and Plesha, M. E., *Concepts and Applications of Finite Element Analysis,* John Wiley & Sons, New York, 1989.

[9] Raju, I. S., "Calculation of Strain Energy Release Rates with Higher Order and Singular Finite Elements," *Engineering Fracture Mechanics,* Vol. 28, 1987, pp. 251–274.

[10] Parks, D. M., "Virtual Crack Extension: A General Finite Element Technique for *J*-Integral Evaluation," *Numerical Methods in Fracture Mechanics,* A. R. Luxmore and O. R. J. Owen, Eds., University of Wales, Swansea, 1978.

[11] Hellen, T. K., "On the Method of Virtual Crack Extensions," *International Journal for Numerical Methods in Engineering,* Vol. 9, 1975, pp. 187–207.

[12] Haber, R. B. and Koh, H. M., "Explicit Expressions for Energy Release Rates using Virtual Crack Extensions," *International Journal for Numerical Methods in Engineering,* Vol. 21, 1985, pp. 301–315.

[13] Lin, S. C. and Abel, J. F., "Variational Approach for a New Direct Integration Form of the Virtual Crack Extension Method," *International Journal for Numerical Methods in Engineering,* Vol. 38, 1988, pp. 217–235.

[14] de Lorenzi, H. G., "On the Energy Release Rates and the *J*-Integral for 3-D Crack Configurations," *International Journal of Fracture,* Vol. 19, 1982, pp. 183–193.

[15] Levy, N., Marcal, P. V., Ostergren, W. J., and Rice, J. R., "Small Scale Yielding Near a Crack in Plane Strain: A Finite Element Analysis," *International Journal of Fracture,* Vol. 1, 1971, pp. 143–156.

[16] Pook, L. P. and Smith, R. A., "Theoretical Background to Elastic Fracture Mechanics," *Fracture Mechanics Current Status, Future Prospects,* Conference preceedings held at Cambridge University, 1979, pp. 29–39.

[17] Kaufman, J. G., "Experience in Plane-Strain Fracture Toughness Testing per ASTM Method E 399," *Developments in Fracture Mechanics Test Methods Standardization, ASTM STP 632,* American Society for Testing and Materials, Philadelphia, 1977, pp. 3–24.

[18] *Polymers: An Encyclopedic Sourcebook of Engineering Properties,* John Wiley & Sons, New York, 1987.

Anthony N. Sinclair,[1] *Olev Lepik,*[2] *Michael Gabbani,*[3] *Biswajit Mukherjee,*[2] *and Eric Albertini*[4]

Assessment of Fracture Toughness by a Punch Test with Miniature Specimens

REFERENCE: Sinclair, A. N., Lepik, O., Gabbani, M., Mukherjee, B., and Albertini, E., **"Assessment of Fracture Toughness by a Punch Test with Miniature Specimens,"** *Small Specimen Test Techniques Applied to Nuclear Reactor Vessel Thermal Annealing and Plant Life Extension, ASTM STP 1204,* W. R. Corwin, F. M. Haggag, and W. L. Server, Eds., American Society for Testing and Materials, Philadelphia, 1993, pp. 162–181.

ABSTRACT: A series of punch test measurements was performed on a broad set of engineering alloys to establish the correlation between J_{IC} and the equivalent plastic strain, ε_f, at the point of fracture. The punch test has a strong advantage over conventional methods for measuring material toughness because it requires only small coupons of material that can be removed from in-service structures. Tests were performed at both room and elevated temperatures in both weakly and strongly anisotropic materials. Results of the program indicated that the simple linear correlation between J_{IC} and ε_f predicted by the theory is too simple to describe such a complex phenomenon as ductile fracture. Furthermore, difficulties were discovered in the testing of strongly anisotropic materials that allow for toughness measurements only on those planes with relatively weak crack growth resistance. A modified punch test apparatus is proposed to address this problem.

KEYWORDS: punch test, elastic plastic fracture mechanics, fracture toughness, plastic strain

The existence of some form of qualitative relationship between material ductility and toughness has long been recognized. One demonstration of such a relationship is the Charpy V-Notch test, frequently used to establish the approximate nil-ductility transition temperature (NDTT) in ferritic steels. Cleavage or brittle fracture occurring below the NDTT is considered a stress-induced phenomenon, i.e., it occurs when the stress intensity reaches a critical value. By contrast, at temperatures well above the NDTT where plastic flow occurs relatively easily, a strain-induced fracture process can be considered dominant; it is usually associated with growth and coalescence of voids leaving dimpled fracture surfaces. Over an intermediate temperature range, evidence of both stress- and strain-induced fracture processes is apparent.

Confining attention to the upper shelf region above the NDTT, the arguments in the foregoing paragraph would suggest that straight-forward measurements of yield strain or reduction in the cross-sectional area in a uniaxial tension test might be correlated with J_{IC}. ASTM Test Method for J_{IC}, a Measure of Fracture Toughness (E 813-89) requires large

[1] Associate professor, Department of Mechanical Engineering, University of Toronto, Canada M5S-1A4.

[2] Research engineer, Ontario Hydro, 800 Kipling Ave., Toronto, Canada M8Z-5S4.

[3] Research engineer, Atomic Energy of Canada Limited, Sheridan Park, Mississauga, Ontario, Canada.

[4] Student, Department of Mechanical Engineering, University of Toronto, Canada M5S-1A4.

specimens, expensive machining, a lengthy test on sophisticated loadframes, followed by a considerable amount of computation. An algorithm for estimating J_{IC} from simple strain measurements on small specimens would offer the following advantages:

1. The cost of manufacturing specimens would be greatly reduced.
2. Less material would be required for each test. In the case of inspecting an in-service structure, specimens could be removed from a noncritical location without compromising the structure's integrity.
3. In the case of toughness measurements on a thin component such as a turbine disk or thin-walled tube, compact tension specimens can be machined with a thickness close to that of the engineering component in question. Values of J_Q obtained from such specimens would be representative of the expected behavior of the component, whose thin wall would not induce plane strain conditions. However, these values of J_Q could not readily be compared with any valid J_{IC} values for that material. A test method to obtain J_{IC} from a subsized specimen would be required to meet this objective.
4. Less sophisticated equipment would be required for the test, and the test duration would be substantially less than that required for a measurement of J_{IC} according to the ASTM E 813 standard.
5. The low expense of the test would permit large numbers of samples to be inspected. This would be particularly welcome in cases where there is considerable scatter of the data or when samples from a large number of heats or locations on a component require testing.
6. Evaluation of localized variations in toughness could be performed. This would be particularly useful in evaluating through-thickness variations of J_{IC} of pressurized components or in assessing localized effects of radiation embrittlement.

Objective

The particular procedure to be investigated in this study is called a "small punch," "bulge," or "ball punch" test. Specific objectives of the investigation are as follows:

1. Review the theory for predicting material toughness and plastic flow properties through punch testing.
2. Construct a small punch testing apparatus capable of conducting tests at up to 500°C.
3. Test several structural alloys with the punch test apparatus. Assess the accuracy and repeatability with which measurements can be made. The repeatability will be assessed by statistical analysis of many measurements performed under the same test conditions; the accuracy of an individual measurement can be estimated by quantifying the sources of error in a measurement.
4. Investigate the correlation between values of equivalent plastic strain of the specimens and the values of J_{IC} measured according to ASTM E 813.
5. Evaluate the accuracy and range of applicability of the punch test for estimating toughness of engineering materials. Propose modifications to the test apparatus or test procedure to address problems posed by strongly anisotropic materials.

Theory

Many researchers have attempted to extract information related to material toughness or ductility by the use of small-punch or related types of tests. Misawa et al. [*1*,*2*] conducted punch tests on miniature samples (ranging down to sizes as small as TEM disks) of ferritic

steels in an attempt to find their NDTT as a function of radiation damage. The small specimen size was essentially due to the localized character of the radiation damage and the need to insert the specimens into a small test reactor. A steel ball with a diameter on the order of 1 to 2.5 mm was pushed at a controlled speed into the small sheet specimen that was clamped at its edges. The area under the load-deflection curve at the point of crack initiation was then compared with Charpy data. Misawa developed an empirical correlation between the punch test results and Charpy estimates of the NDTT; of equal interest were two observations of Misawa that have implications for the current project:

1. Punch test data taken above the transition temperature tended to be highly repeatable. These data were dominated by the plastic flow properties of the material. Below the NDTT, however, a number of "premature" failures occurred due to brittle or semi-brittle fracture. Statistical analysis of this low-temperature data was far more challenging.
2. Heterogeneities in the material contributed greatly to scatter, as an inclusion could penetrate a considerable portion of the specimen thickness. This would indicate that the punch test may be ill-suited to characterize materials with large inclusions.

Unlike Misawa, who was primarily interested in finding the NDTT, Pandey and Banjeree [*3*] sought numerical estimates of J_{IC} from ductility measurements on tension specimens. These authors conducted a series of tension tests, J_{IC} measurements, and ductility tests on two carbon steels, one a standard ship-building steel, and the other a Mn-V steel in which vanadium carbide particles in the ferrite matrix result in increased yield strength. Their work was developed on the premise that fracture by void growth and coalescence is initiated when the strain reaches a critical value; this value is dependent on geometry and lateral constraint at the initiation location. For complex loading geometries, the critical parameter would be the equivalent (plastic) fracture strain, ε_f, which is a function of the three principal strains. The authors' goal was to correlate the critical crack-opening displacement δ_t at fracture, the fracture strain ε_f in fracture toughness specimens, and the critical strain zone size X_f about the crack tip in which the strain is greater than or equal to ε_f. To this end, the strain profile ahead of a crack tip was taken from the small-scale yielding solution of Rice and Johnson [*4*]

$$\varepsilon_f = C_1\delta_t/X_f \tag{1}$$

where the crack tip opening displacement, δ_t, at the point of fracture is given by

$$\delta_t = C_2 J_{IC}/\sigma_{ys} \tag{2}$$

and both C_1 and C_2 are constants. Combining these two equations gives

$$J_{IC} = C_3 \varepsilon_f X_f \sigma_{ys} \tag{3}$$

Equation 3 suggests a linear relationship between J_{IC} and the equivalent fracture strain within the range of applicability of Eqs 1 and 2. The value of C_3 can be shown to be a function of the strain-hardening exponent, n, thereby providing one limiting guideline as to the range of materials that would correspond to a single value of C_3. Although this parameter is also dependent on specimen geometry, its value could be established empirically in a series of tests.

Certain problems, however, remain. One such problem is the value for the critical strain zone size, X_f. Pandey and Banjeree [3] found X_f to be about three to ten times the inter-inclusion spacing for the largest inclusions, suggesting to them that coalescence of several voids is required for a crack to advance. No objective, consistent method has yet been established for selection of an appropriate value for this parameter; there is little reason to expect that a single value would be applicable over a broad class of alloys. Even for a single alloy, the observation that the critical strain zone size X_f generally increases with temperature while yield stress shows the opposite trend has led to a modified version of Eq. 3

$$J_{IC} = C_3' \varepsilon_f \tag{4}$$

Despite the attraction of the simple form of Eq 4, its range of applicability for various alloys and temperatures has not been established. In particular, values of X_f and yield stress are normally interrelated with ε_f such that the purported linear relationship between toughness and fracture strain of Eq 4 is difficult to justify on theoretical grounds.

Dooley et al. [5] also compared fracture strain in uniaxial tension specimens against fracture strain in bulge test specimens; the existence of such a relationship forms the basis of Eq 2. Their work is interesting in that a wide variety of materials were tested—copper, brass, mild steel, and stainless steel in various metallurgical conditions. They evaluated a fracture parameter dependent only on the principal stresses, as suggested by Ghosh [6]. The authors found that when this parameter reaches a critical value labeled K_{cr} (which in turn is microstructure dependent), the specimen fractures regardless of its geometry or loading configuration. This result indicates that equivalent information regarding a material's ductility can be extracted from a variety of specimen sizes, shapes, or loading geometries. Pursuing the concept that fracture by void growth and coalesence is strain-controlled phenomenon, these results imply that the fracture strain data extracted from a small punch test might be correlated to fracture toughness.

Ritchie et al. [7] also arrived at Eq 3 in their studies of SA 533B pressure vessel steel using circumferentially notched tension specimens. They suggested that the characteristic length, X_f, is a small multiple of the interparticle spacing. Ritchie pointed out that the selection of the X_f value should depend on material temperature. At low temperatures, below the NDTT, the grain size would be the crucial parameter, as a critical fracture event might be the progression of a crack through the next grain boundary or the cracking of grain boundary carbide. At upper shelf temperatures, however, where fracture is caused by the linking of voids nucleated at (sulphide) inclusions, the inter-inclusion spacing would be a lower bound for X_f.

Ritchie et al. [7] pursued these ideas to infer details of the fracture mechanism. Their calculations and measurements indicated that for the SA 533B steel, X_f was approximately six or seven times the inter-inclusion spacing, suggesting that ductile fracture consisted of the coalescence of several voids ahead of a crack tip. By contrast, for SA 302B steel, X_f was found to be roughly equal to a single inter-inclusion spacing, indicative of a fracture mechanism in which a single void nucleating ahead of the crack tip eventually grows into the crack. The authors noted that estimates of ε_f should ideally be obtained from deeply notched tension specimens in order to emulate the stress conditions seen at the crack tip.

A certain inconsistency can be detected in some of the ideas of Ritchie and other authors. Although the theory is based on the idea of a strain-controlled failure, reference is made to principles of linear elastic fracture mechanics. In many cases, the actual fracture mechanism is a combination of elastic and plastic phenomena.

Haggag et al. [*8*] and Lucas et al. [*9*] attempted to extract various pieces of information from shear punch test data: yield strength, ultimate tensile strength, work-hardening exponent, and reduction in area. Their test rig was somewhat similar to that employed in the current project, which is shown in Fig. 1; however, a flat cylindrical punch was used instead of the spherical ball employed in the current study. It was noted [*8,9*] that the load-displacement curve obtained in a shear punch test was similar to that in a uniaxial tension test: a region of elastic loading, followed by a nonlinear increase of load with displacement, a load maximum, and, finally, a decrease in load to failure. The authors therefore attempted to find empirical formulas to give σ_{ys}, ultimate tensile strength σ_{UTS}, and strain-hardening exponent n on the argument that a shear punch test is inherently similar to a tension test and should therefore reveal the same information. Haggag et al. used Eq 3 to estimate fracture toughness, but offered no new insights as to its origin or range of applicability.

Bayoumi and Bassim [*10*] attempted to address the problem of both elastic and plastic mechanisms in the fracture process. They sought an analytical relationship between J_{IC} and bulge ductility at both low temperature (linear elastic region) and in the elastic plastic regime at high temperature. Their elastic plastic analysis was identical to that given by Eqs 1 through 4 above; their experiments indicated that the values for J_{IC} obtained from Eq 4 were more accurate than those obtained from Eq 3 in describing the temperature dependence of fracture behavior for Type 1045 steel in the elastic-plastic region. For this material, they found the characteristic length, X_f, to be on the order of three to four times the size of a pearlite colony. However, their analysis strongly suggests that the critical strain zone size would tend to vary significantly among various metal alloys such that Eqs 3 or 4 should not be expected to be generally valid for a single value of the proportionality constant.

Bayoumi and Bassim's work is significant in that they spanned a large temperature range in both their analysis and experiments. At low temperatures, their experiments indicated a nonlinear relationship between J_{IC} and fracture strain. In fact, at low temperatures where elastic effects are dominant, J is equivalent to G, which in turn is proportional to the surface energy, γ, required per unit area of crack growth. As this energy is proportional to the square of the strain (linear theory), it is expected that J_{IC} will be proportional to ε_f^2. Although Bayoumi and Bassim did see evidence of this trend, experimental results were somewhat complicated by the presence of both elastic and plastic deformation mechanisms.

Mao et al. [*11–13*] carried out a series of experimental studies on various carbon steel, stainless steel, and copper alloys to explore the relationship between bulge ductility and toughness. The bulge ductility of the punch specimen was determined from the equivalent strain at fracture ε_f, assuming incompressible plastic deformation. In cylindrical coordinates representing normal strains in the radial, circumferential, and through-thickness directions by ε_r, ε_θ, and ε_t, respectively, it can be assumed that radial and circumferential strains are equal. The von Mises formulation then gives

$$\varepsilon_f = (2/3)^{1/2} (\varepsilon_t^2 + \varepsilon_r^2 + \varepsilon_\theta^2)^{1/2} = \ln (t_0/t) \tag{5}$$

where t_0 and t are initial and final thicknesses, respectively, of the specimen adjacent to the area of failure. Mao's experimental results are in agreement with the theory outlined in the preceding paragraphs: For ductile materials, J_{IC} was found to be approximately linearly dependent on equivalent fracture strain, as suggested by Eq 4. For the less ductile materials and at low temperature where it is expected that the fracture mechanism is dominated by elastic stress-controlled phenomena, there is a sharp departure from linearity [*10,13*].

An interesting note on Mao's work is that he found Eq 4 to be applicable to a wide range of steel and copper alloys. As little material data were provided, it is not clear whether the product $\sigma_{ys}X_f$ varied significantly among the materials tested.

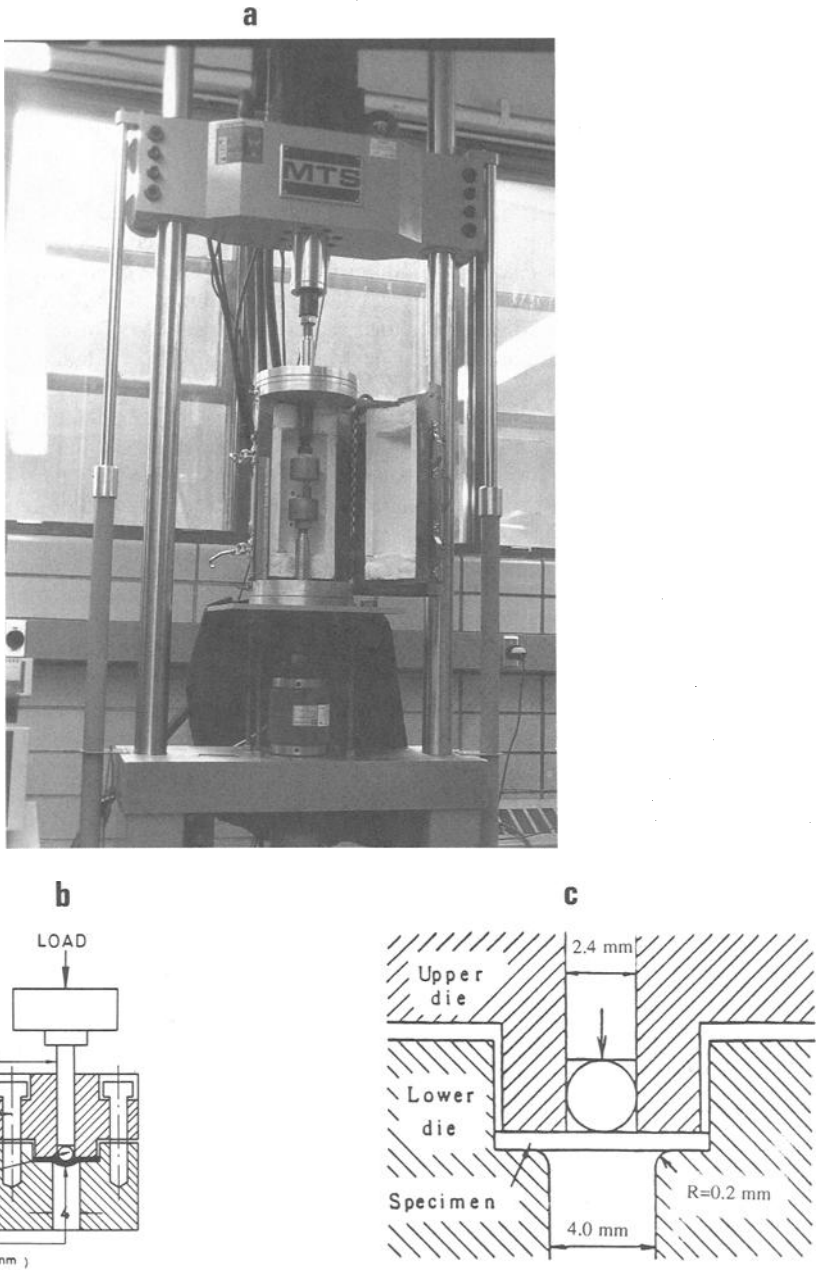

FIG. 1—*Punch test apparatus:* (a) *system mounted inside a hydraulic loadframe oven;* (b) *assembled punch test apparatus;* (c) *details of loading configuration.* (*Figures* 1b *and* 1c *were adapted from Ref* 20 *and* 13, *respectively.*)

Experiment

Punch Test

A punch test apparatus was constructed following the design of Mao et al. [*11–13*]. The components of the system are shown in Fig. 1; high-temperature tests are easily accommodated by the use of an oven, although the minimum duration of a single test at 250°C is approximately 45 min due to time required for temperature stabilization. An electronic controller and heating coil maintain the temperature to within ±3°C of the setpoint, as measured by a thermocouple [*14*]. A coupon of material, 1 cm by 1 cm by 0.5 mm, is anchored along its edges and supported underneath over its entire cross-sectional area except for a central portion 4 mm in diameter. A ball bearing 2.4 mm in diameter is slowly forced down a set of guides by a loadframe into the center of the specimen. This causes the specimen to develop a central bulge, illustrated in the cross-sectional view of a failed specimen in Fig. 2. Material in the bulging portion of the specimen becomes thinned due to plastic flow. Eventually cracks form in the specimen; in the ideal case, the cracks will form a circular pattern along the contour of material that has undergone the most thinning. Initiation of such cracks is readily apparent on a load-displacement plot due to a marked decrease in load. The test is then stopped and the specimen removed for examination.

The specimen thickness, t, shows the largest reduction in the area adjacent to the crack, as shown in Fig. 2. The maximum thickness reduction is measured by a dial gage, and then the equivalent plastic strain at fracture, ε_f, is determined from Eq 5. As noted by several authors, including Mao et al. [*11–13*], an empirical relationship can be developed between the thickness reduction and the deflection of the specimen at the point of fracture; this relationship can be used to avoid the tedious procedure of measuring the thickness of the specimen with a dial gage. Such an empirical relationship was not used in this test program, however, as it would have unnecessarily introduced an additional source of uncertainty.

For each test condition, a minimum of twelve punch tests were performed in order to get an estimate of the uniformity of results. For those specimens in which the standard deviation of ε_f was greater than 5%, the number of tests was increased to a maximum of 20.

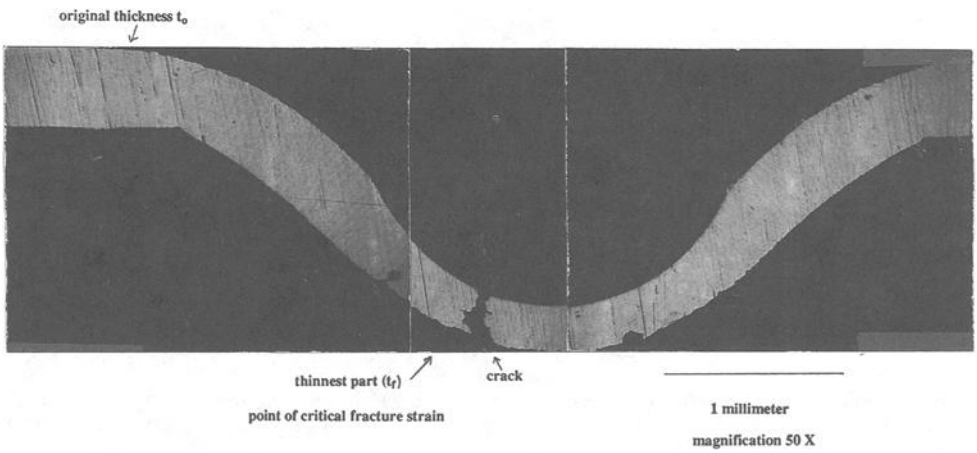

FIG. 2—*Cutaway section of deformed SA-106 Grade B steel specimen, cut in RC plane. Central section bulge was caused by steel ball of punch apparatus. Original specimen thickness* t_0 *(approx 0.5 mm) and point of maximum effective plastic strain (with final thickness* t_f*) are marked. Crack initiation occurred adjacent to area of maximum plastic strain. Inclusion stringers are perpendicular to plane of specimen.*

Full-Scale Destructive Tests

In order to test the linear relationship between J_{IC} and ε_f indicated by Eqs 3 or 4, each set of punch tests on a given material was complemented by the following destructive tests:

1. Either two or three full-sized compact tension (CT) specimens were tested with the aim of obtaining a value of J_{IC} according to ASTM E 813–89. Several test materials repeatedly led to values J_Q for apparent fracture toughness that did not meet the standard's validity criteria. This was due to factors such as inadequate thickness of compact tension specimens or anomalous crack propagation behavior. Such cases are noted in the section on results.
2. Tension tests were performed on each test material to determine the yield strength. For some materials such as the Zr-2.5% Nb alloy, miniature tension specimens were used; however, it is believed that these give an accurate measure of yield stress. Values for the ultimate tensile strength σ_{UTS} and Young's modulus E were also obtained in order to characterize each test material, although the theoretical correlations of Eqs 3 and 4 between J_{IC} and ε_f are not directly dependent on these two material properties.

Test Materials

Tests were conducted on a wide variety of engineering alloys, listed in Table 1. Five heats of the nuclear grade steel SA 106 Grade B were included to complement a recent series of fracture toughness tests in a comprehensive leak-before-break assessment program [*15*]. For the first three material heats, values of J_{IC} were obtained in the L-C orientation; for the two remaining heats, C-L values of J_{IC} were obtained. (The notation used to designate specimen orientation for both standard CT and punch test specimens is described in Table 1.) All tests on the CT specimens were performed at room temperature except for one of the heats tested in the L-C orientation, which was conducted at 250°C. Three compact tension specimens were used for each test condition; specimens of both 2.54 and 3.18 cm thickness were used and were side grooved to a total thickness reduction of 20%.

Yield stress measurements using two specimens for each heat were performed along the axis perpendicular to the crack face. Both punch tests and yield stress evaluations were conducted at the same temperature as that of the corresponding J_{IC} measurements.

The purpose of the single set of elevated temperature tests was to confirm that the punch test is not restricted to a laboratory environment. The only minor stumbling block posed by the high temperature was a considerable lengthening of the punch test duration to accommodate heat-up and cool-down time for the oven. The test temperature of 250°C corresponded to the temperature at which a minimum in crack growth resistance was observed for this particular steel.

A major problem in the punch tests for strongly anisotropic materials was the selection of the plane in which the punch specimen should be cut to correspond to J_{IC} measurements. The two planar axes of each series of punch specimens is listed in Table 1. Ideally, the punch specimen should be oriented such that a crack is forced to initiate in the same plane as in the corresponding CT specimen. However, although the crack plane and direction of crack growth are strictly controlled by the configuration and loading geometry of a CT specimen, such control is not present in a punch specimen. This is a major limitation in the use of the punch test to analyze strongly anisotropic materials.

Heat-treatable 4340 carbon steel specimens were included in the program to generate data corresponding to the higher strength steels. A number of different tempers of this steel were produced. Other carbon steels that were tested include A516 Grade 70 mild steel and ASTM A 808 carbon plate steel; the latter was tested in two orientations and at two temperatures,

TABLE 1—*Test materials and results.*

Test Series	Material	Temperature, °C	σ_{ys}, MPa	σ_{UTS}, MPa	E, MPa	Plane of Punch Specimen	ε_f	J_Q $(kN/m)^a$
A1	SA 106 Grade B	21	228	510	183	CL[b]	0.53 ± 0.12	172 (L-C)[c]
A2	SA 106 Grade B	21	320	532	192	CL	0.54 ± 0.09	236 (L-C)
A3	SA 106 Grade B	250	220	508	183	CL	0.68 ± 0.06	143 (L-C)
A4	SA 106 Grade B	21	324	529	192	RC	0.55 ± 0.08	124 (C-L)
A5	SA 106 Grade B	21	311	562	192	RC	0.56 ± 0.06	99 (C-L)
B1	4340 steel[d]	21	655	855	204	LC	0.42 ± 0.02	108 (C-R)
B2	4340 steel[d]	250	620	941	198	LC	0.53 ± 0.02	94 (C-R)
C1	4340 steel[e]	21	774	855	210	LC	0.45 ± 0.15	56 (C-R)
D1	A808 plate steel	21	414	488	227	SL	0.79 ± 0.04	116 (T-L)
D2	A808 plate steel	250	285	483	189	SL	0.72 ± 0.06	94 (T-L)
D3	A808 plate steel	21	408	475	227	ST	0.82 ± 0.01	129 (L-T)
D4	A808 plate steel	250	268	464	195	ST	0.78 ± 0.04	110 (L-T)
E1	A516 Grade 70	21	348	518	205	SL	0.71 ± 0.08	506 (L-T)
F1	Zr-2.5% Nb	21	790	817	97	CL	0.47 ± 0.01	39 (C-L)
G1	Al 6061-T651	21	276	310	70	LT	0.75 ± 0.02	11.2 (L-T)[f]
H1	Ti 6-2-4-2	21	959	1 062	125	LR	0.40 ± 0.02	20 (C-R)[f]

[a] Only test series "A" strictly satisfied ASTM E 813 criteria for a valid J_{IC} test. Details supplied in text.

[b] Plane of punch specimen is defined in terms of its two principal axes, e.g., CL. Note that this does not uniquely define the plane of the crack.

[c] Conventional notation for designating orientation of compact tension specimen, e.g., C-L: First letter "C" represents vector perpendicular to crack plane, and second letter "L" idicates direction of crack propagation.

[d] Tempered at 1325°C.

[e] Tempered at 1250°C.

[f] Estimate of J_{IC} based on K_{IC}.

as listed in Table 1. These two steels were selected in an effort to gather data for materials that do not exhibit such strongly anisotropic behavior as the SA 106 Grade B steel. A portion of these tests were performed at elevated temperatures as shown in Table 1; this had the effect of producing useful data for "new" test materials with markedly different flow properties from their room temperature counterparts.

Zirconium alloy Zr-2.5% Nb pressure tube material was included in this study because it is used as a primary pressure boundary material in Canadian Deuterium Uranium (CANDU) pressurized heavy water reactors; the punch test was seen as a possible avenue to monitor the radiation-induced hardening or hydride-induced embrittlement (with accompanying reduced toughness) of this material. It is noted that the pressure tube wall thickness of only 4.1 mm is not sufficiently large to permit valid measurements of J_{IC} according to current ASTM standards. Two other more common nonsteel alloys were also evaluated: Al 6061-T6 and Ti 6-2-4-2.

Preliminary Tests on SA 106 Grade B Steel

This steel possessed high ductility that makes it well-suited for use in primary coolant piping in nuclear power plants. The drawing process used during fabrication produces an anisotropic structure in which MnS inclusions are stretched out in the axial direction, some reaching lengths of several hundred microns as shown in Fig. 3. An extensive series of J_{IC} measurements according to ASTM E 813 have shown that this material is significantly tougher with respect to crack propagation in the L-C orientation, where the crack cuts across inclusions, than the C-L orientation, where the inclusions lie in the crack plane [*15,16*].

In a preliminary set of tests on SA 106 Grade B, punch specimens were machined on each of the three principle planes from several heats of material. Punch tests were then performed at room temperature on these specimens and the following points noted:

1. For punch specimens machined in the radial-circumferential plane, the inclusion orientation was perpendicular to the specimen plane. Cracks induced by the punch mech-

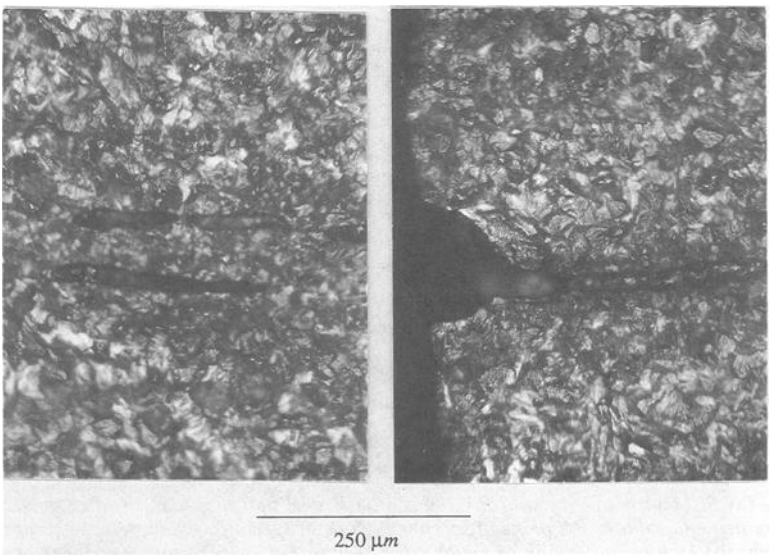

FIG. 3—*Magnified view of inclusions in etched SA 106 Grade B steel specimen.*

anism tended to follow an approximately circular path on each specimen, along the contour of the maximum plastic strain energy density (Fig. 4). Due to its circular path, the crack did not lie in a single plane, but in effect encompassed all planes perpendicular to the specimen, i.e., all planes parallel to the longitudinal direction. This implies that in general none of the crack surface cut through the inclusions.

In a practical application of the punch test to evaluate fracture toughness, it would be highly undesirable to require detailed microanalysis to ascertain details of the crack initiation mechanism. However, without such an analysis, it would be unclear whether the results for these specimens were indicative of C-L, C-R, R-C, or R-L toughness. The fact that cracks were repeatedly observed on all failed specimens in roughly circular

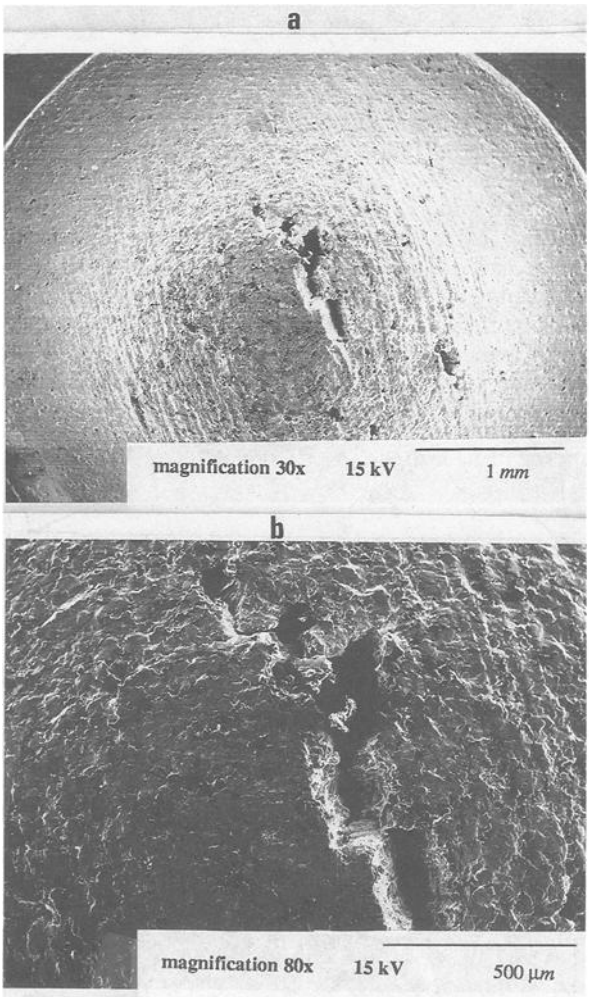

FIG. 4—(a) *SEM view of cracks in SA 106 Grade B steel punch specimens after failure. Inclusion stringers are perpendicular to RC plane of specimen. Zone of specimen failure follows an approximately circular path;* (b) *high magnification of major crack seen in Fig. 4*a. *Fracture mode was predominantly ductile.*

patterns would indicate that for this material, all crack planes parallel to the longitudinal direction have somewhat similar toughness; this conclusion is supported by previous studies [*16*]. The standard deviation in the value of ε_f, calculated from Eq 5, was of the order of 10 to 15%.

2. For punch specimens machined in the longitudinal-circumferential plane, the MnS inclusions were parallel to the specimen plane. Specimen failure typically occurred by a series of straight, parallel cracks aligned with the inclusions, often with one crack being dominant, as illustrated by Fig. 5. The corresponding strain at fracture ε_f should then be indicative of toughness in the C-R or C-L orientation, and therefore results similar to those for specimens cut in the radial-circumferential plane would be expected. Although this was generally the case, the presence of large inclusions in the specimen plane would occasionally lead to a "premature" specimen failure. Although such fail-

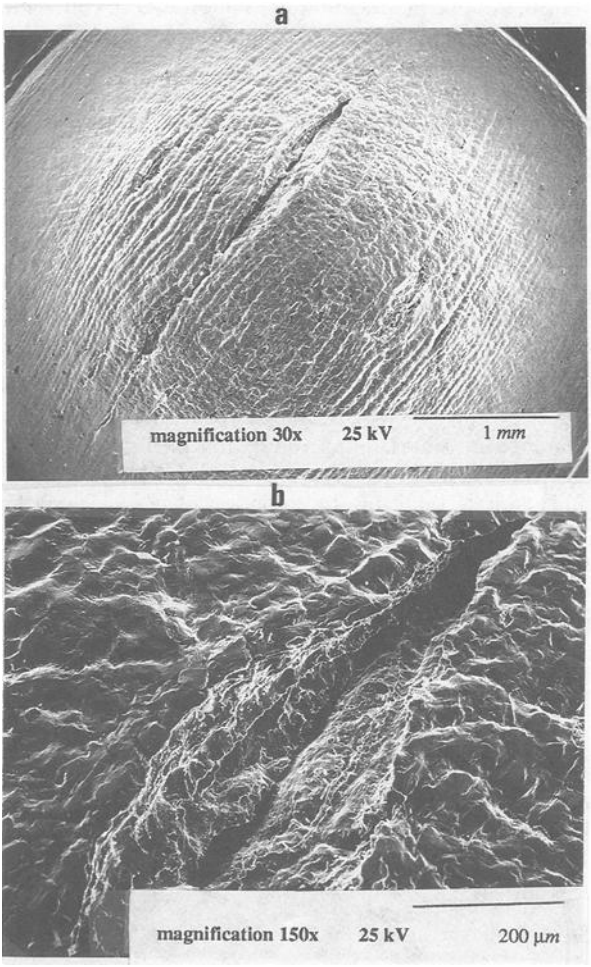

FIG. 5—(a) *SEM view of cracks in SA 106 Grade B steel punch specimens after failure. Inclusion stringers are parallel to CL plane of specimen. Note orientation of cracks parallel to those of inclusions.* (b) *High magnification of major crack seen in Fig. 5*a.

ures might feature large-scale plastic deformation on an extremely localized level, this was not discernible with the dial gage used to measure the extent of specimen thinning adjacent to the crack. Values obtained for ε_f were up to 40% lower than the average when premature failure took place, thereby depressing the average value of ε_f and measurably increasing the standard deviation to the order of 15 to 25%. It is noted that it was not possible to induce cracks to initiate in the relatively tough L-C or L-R orientations—the orientations that are of concern in leak-before-break studies of guillotine-type pipe failure.

3. Punch specimens machined in the longitudinal-radial plane gave very similar results to those described in Item 2 above. Failure occurred by a series of parallel cracks aligned with the inclusions, with a large inclusion occasionally inducing early failure. The test results would be indicative of toughness in the R-C or R-L direction; again, no information is obtained regarding the L-C or L-R orientations.

The implications of the above points are quite important. In conducting integrity assessments of engineering components, fracture properties are required for postulated crack orientations for which the applied load is expected to be highest or the consequences of failure would be the most severe. Unlike the compact tension specimen in which both the crack plane and direction of crack growth can be imposed, the punch specimen used in this study will always develop cracks on the weakest plane that is perpendicular to the specimen plane.

It is also noted that even for a single specified crack plane it is not possible to definitively label the direction of crack growth with a punch specimen; there is some ambiguity as to whether the crack is propagating through the thickness or along the plane of the specimen. This further complicates efforts to correlate results of punch tests with standard J_{IC} measurements.

It is proposed that one method to address this problem is to redesign the punch test such that more control over the direction of crack propagation would be available. A proposed design, shown in Fig. 6, would require a rectangular sheet specimen on the order of 1 by 2 cm. The sheet is clamped in a horizontal orientation on its two longer sides, and a thin horizontal rod is forced down into the specimen, causing a long bulge or "trench" to form. The specimen would ultimately fail by the initiation of cracks along lines parallel to the horizontal rod. By appropriate selection of the orientation in which specimens are machined, better control would be gained over the plane of crack growth. Note that proper clamping of the specimen would be more difficult with this new test design, as comparatively large loads would be required to induce specimen failure.

An alternative approach would be to retain the design shown in Fig. 1, but use a punch with an elliptical contact area. By appropriate alignment of the ellipse on the specimen, cracks could be induced to initiate along any desired orientation. One major drawback to this design is that the modeling and analysis of experimental results would be considerably more complicated than for the circular punch or for the design of Fig. 6. Descriptions of both three-point and four-point bend tests that would also address the orientation problem are given in an extensive review of small specimen test techniques by Lucas [*17*].

Results of Test Program

SA 106 Grade B Steel

Values of J_{IC} for each of the five specimen heats were obtained as an average of three measurements on compact tension specimens. All specimens were of sufficient thickness to give valid test results, according to ASTM E 813. Results are given in Table 1.

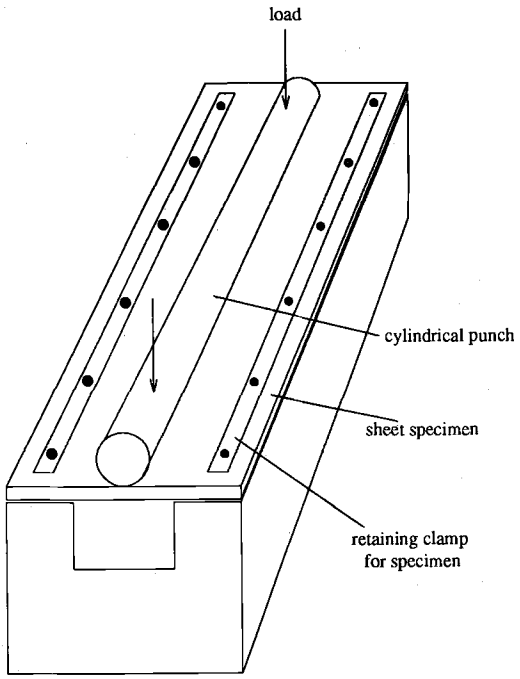

FIG. 6—*Proposed punch-testing apparatus designed to force cracks to grow on a single plane.*

For the four room-temperature sets of data, the punch specimens were oriented in either the radial-circumferential or circumferential-longitudinal planes, as indicated in Table 1. As described in the previous section, the orientation of the punch specimens had little effect on the resulting values of ε_f, although the first set had the lower standard deviation. Metallographical examination of the failure area showed predominantly ductile fracture, with some indications of cleavage along inclusions.

The one set of data collected at 250°C showed a markedly larger value of ε_f than the room temperature specimens despite the fact that J_{IC} for this material is actually lower at the elevated temperature. The low standard deviation in the values of ε_f at elevated temperature suggests that the presence of inclusions played a more minor role in inducing premature failure at high temperature. The relatively high ε_f value is quantitatively consistent with the high value of σ_{UTS}/σ_{ys} for this material at 250°C. These observations offer further evidence that the linear relationship between J_{IC} and ε_f indicated by Eq 4 may be inadequate to model the complex mechanism of ductile fracture.

4340 Heat-Treatable Steel

Three series of tests were conducted on this material, two at room temperature and one at 250°C (Series B1, C1, and B2 as shown in Table 1). Problems in attaining valid measurements of J_{IC} in destructive tests are believed to be due to the choice of C-R orientation; an L-C orientation might have inhibited the crack jumping noted in some of the tests. Additional problems that resulted in an uneven crack front also invalidated some of the toughness measurements according to ASTM E 813. Despite such difficulties, the values obtained for apparent toughness, J_Q, shown in Table 1 were repeatable within 10 to 15%.

MnS inclusions in the plane of the punch-test specimens may have contributed to some of the scatter noted in the measured values of ε_f. Cracks were not generally circular on the failed specimens, but instead often tended to be aligned with the direction of the inclusion stringers. Microanalysis of failed specimens, however, indicated that the largest inclusions never accounted for more than a few percent of the total wall thickness.

A808 Plate Steel

This steel was selected for study because of its lack of inclusion stringers. Small MnS inclusions as observed by optical microscopy were globular in shape; no significant features in the microstructure were observed that would suggest substantially different crack propagation mechanisms in the L-T as opposed to the T-L orientation. As indicated in the summary of results in Table 1, however, both the punch test and fracture toughness measurements indicated a small but distinct anisotropic nature to the toughness of this material.

It is noted from Table 1 that strictly valid estimates of J_{IC} were not attainable for this material, both at 21°C and 250°C. This was due to an uneven extension of the crack across its width and was believed to be caused by a slight gradient of material properties across the thickness of the plate.

A516 Grade 70 Mild Steel

Measurements of J_{IC} for this steel, conducted in the L-T orientation, gave the relatively large average value of 506 kN/m. This crack orientation would cut across the small inclusion stringers observed by optical microscopy. As noted earlier, the punch test conducted on specimens oriented in the SL plane would tend to produce data corresponding only to fracture in a plane parallel to the inclusions and would therefore not correspond directly to the fracture toughness measurements. Examination of failed punch specimens revealed large elongated dimples, indicative of ductile fracture. SEM examination showed no evidence of inclusions on the crack faces, although any inclusions might have been displaced when the crack opened up.

Zr-2.5% Nb

Because this material was available in the form of tubing with a wall thickness of 4.1 mm, it was not possible to manufacture specimens leading to valid J_{IC} values in accordance with ASTM E 813. The values of J_Q given in Table 1 therefore are indicative of a mixed plane stress/plane strain fracture mode. As indicated earlier, this is one of the motivations for development of a reliable punch test, but the lack of strictly valid J_{IC} data severely hampers an assessment of the punch test's value.

Scanning electron microscope observation of the fracture surfaces on the punch-test specimens confirmed that the failure mode involved considerable ductile shear along one main circular crack; however, the high strength of this material led to measurably smaller dimples than were observed for the SA 106 Grade B specimens, with some evidence of a mixed ductile/brittle fracture mode. Punch test results were extremely uniform, as indicated by the small standard deviation in the measured value of ε_f. This was consistent with the lack of any significant inclusions observed by optical or SEM microscopy.

Al 6061-T6 and Ti 6-2-4-2

These two alloys were both tested at room temperature. Both displayed relatively small variations in the values of ε_f in the punch test. Both types of materials failed via one main

circular crack, indicating minimal dependence of toughness for crack planes perpendicular to the punch-test specimen; optical microscopy showed no evidence of significant inclusions. While the Al 6061 fracture surfaces showed considerable evidence of ductility, a mixed mode of fracture was seen in the Ti-6-2-4-2 specimens due to the high strength of this alloy.

Analysis

Figure 7*a* shows a plot of J_{IC} (or J_Q) plotted against $\varepsilon_f\sigma_{ys}$ for all test materials to test for the linear correlation indicated by Eq 3. Note that the parameter X_f is not included in the

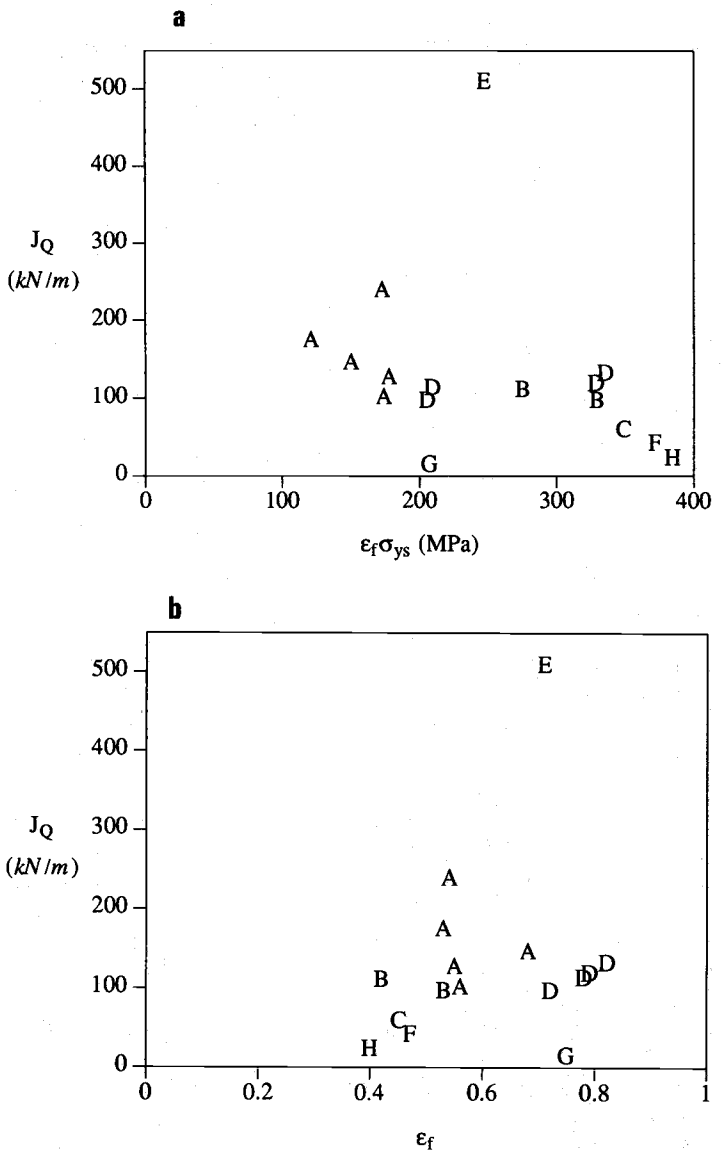

FIG. 7—(a) *Correlation of* $\varepsilon_f\sigma_{ys}$ *with* J_{IC}; (b) *Correlation of* ε_f *with* J_{IC}.

abscissa, consistent with the assumption that this parameter is a constant. As suggested earlier, this assumption is a major limitation to the current work, but there would normally be no method available to obtain a good estimate for X_f in any practical application of the punch test.

Figure 7*b* shows J_{IC} (or J_Q) plotted against ε_f in accordance with the more simple model of Eq 4 used by Bayoumi and Bassim [*10*], Mao et al. [*13*], and others. Neither Figs. 7*a* nor 7*b* indicate a linear relationship as predicted by Eq 3 or 4. Several reasons are readily apparent based on the points noted earlier:

1. Strictly valid estimates for J_{IC} were not attainable for several of the test materials. For certain materials, such as the A516 Grade 70 steel, this problem was clearly dominant in testing for a linear correlation between J_{IC} and ε_f. However, if only the data for which valid (or close to valid as defined by ASTM E 813) estimates of J_{IC} are retained, it is clear that a linear relationship between toughness and fracture strain is still not present. Fundamental problems, as outlined in Items 2 through 4 below, need to be addressed.
2. Both Eqs 3 and 4 are based on the assumptions of a strain-controlled ductile tearing process. Evidence of cleavage facets on the crack surfaces of some specimens and the role of inclusions would tend to invalidate these assumptions.
3. Strongly anisotropic materials could not be accommodated by the current design of the punch apparatus, as it allowed minimal control of the crack orientation. This inhibited the collection of punch test data on the relatively tougher plane of crack growth in an anisotropic material.
4. The relationship among the parameters ε_f, δ_t, and X_f given by Eq 1 is a model to be applied to perturbations of a material's properties from some reference condition. It should not be expected to be reliable over such a broad class of alloys as considered in this test program without appropriate variations in the proportionality constant. This conclusion is supported by Figs. 7*a* and 7*b*, where it is seen that the nonsteel alloys exhibit markedly different correlations between ε_f and J_{IC} than do the steel alloys.

Consistent with Item 4, very recent efforts to use the punch test as an indicator of material toughness and degradation have been generally confined to a single alloy, in particular the evaluation of the NDTT [*18–20*]. In such cases, the punch test has been found to be a useful tool when large specimens are inappropriate for toughness assessment.

Conclusions

1. An experimental program with a wide range of metal alloys has found no evidence of a consistent linear relationship between J_{IC} (or J_Q) and equivalent plastic strain as measured in a punch test.
2. The punch test suffers from a lack of control of the orientation of the failure plane; this can inhibit the use of a punch test to attain toughness data on the plane of interest. A modified punch apparatus was proposed to address this problem; challenges posed by this modified design are the relatively large loads required and clamping considerations.
3. The theoretical background for correlating J_{IC} with ε_f is based on many simplifying assumptions regarding the deformation and fracture processes. This would indicate that the punch test should be confined to a very narrow class of materials (or a single material)

within which perturbations in values of J_{IC} might be correlated with perturbations in values of ε_f or $\varepsilon_f \sigma_{ys}$.

References

[1] Misawa, T., Adachi, T., Saito, M., and Hamaguchi, Y., "Small Punch Tests for Evaluating Ductile-Brittle Transition Behavior of Irradiated Ferritic Steels," *Journal of Nuclear Materials,* Vol. 150, 1987, pp. 194–202.

[2] Misawa, T. and Hamaguchi, Y., "The Mechanism of Fracture," *Proceedings,* International Conference on Fatigue, Corrosion Cracking, Fracture Mechanics and Failure Analysis, Salt Lake City, 2–6 Dec. 1985, ASM, Metals Park, OH, pp. 521–527.

[3] Pandey, R. K. and Banjeree, S., "Strain Induced Failure in Low Strength Steels," *Engineering Fracture Mechanics,* Vol. 10, 1978, pp. 817–829.

[4] Rice, J. R. and Johnson, M. A., "The Role of Large Crack Tip Geometry Changes in Plane Strain Fracture," *Inelastic Behavior of Solids,* M. F. Kanninen et al., Eds., McGraw Hill, New York, 1970.

[5] Dooley, M., Lucas, G. E., and Sheckherd, J. W., "Small Scale Ductility Tests," *Journal of Nuclear Materials,* Vols. 103 and 104, 1981, pp. 1533–1538.

[6] Ghosh, A. K., *Metallurgical Transactions,* Vol. 7A, 1976, p. 523.

[7] Ritchie, R. O., Server, W. L., and Wullaert, R. A., "Critical Fracture Stress and Fracture Strain Models for the Prediction of Lower and Upper Shelf Toughness in Nuclear Pressure Vessel Steels," *Metallurgical Transactions A,* Vol. 10A, 1979, pp. 1557–1570.

[8] Haggag, F. M., Server, W. L., Lucas, G. E., Odette, G. R., and Sheckherd, J. W., "The Use of Miniaturized Tests to Predict Flow Properties and Estimate Fracture Toughness in Deformed Steel Plates," *Journal of Testing and Evaluation,* Vol. 18, No. 1, 1990, pp. 62–69.

[9] Lucas, G. E., Sheckherd, J. W., Odette, G. R., and Panchandeeswaran, S., "Shear Punch Tests for Mechanical Property Measurements in TEM Disc-Sized Specimens," *Journal of Nuclear Materials,* Vols. 122 and 123, 1984, pp. 429–434.

[10] Bayoumi, M. R. and Bassim, M. N., "Study of the Relationship Between Fracture Toughness (J_{IC}) and Bulge Ductility," *International Journal of Fracture,* Vol. 23, 1983, pp. 71–79.

[11] Mao, X., Shoji, T., and Takahashi, H., "Development of a Miniaturized Specimen Technique for Fracture Toughness J_{IC} Measurement," *Journal of Testing and Evaluation,* Vol. 16, No. 2, 1988, pp. 229–241.

[12] Mao, X. and Takahashi, H., "Development of a Further-Miniaturized Specimen of 3 mm Diameter for TEM Disk Small Punch Tests," *Journal of Nuclear Materials,* Vol. 150, 1987, pp. 42–52.

[13] Mao, X., Shoji, T., and Takahashi, H., "Characterization of Fracture Behavior in Small Punch Test by Combined Recrystallization-Etch Method and Rigid Plastic Analysis," *Journal of Testing and Evaluation,* Vol. 15, No. 1, 1987, pp. 30–37.

[14] Sinclair, A. N. and Gabbani, M., "Determination of Fracture Toughness from Measurements on Undersized Specimens," Interim contract report to Ontario Hydro Research, Toronto, February 1990.

[15] Mukherjee, B. and Carpenter, D., "Darlington Leak Before Break Material Test Program *J*-Resistance Curves," Technical Report 87-232-K, Ontario Hydro, Toronto, 1987.

[16] Venter, R. D., McCammond, D., Sinclair, A. N., and Gilbert, K. R., "Application of Elastic Plastic Fracture Mechanics to Nuclear Grade Piping Steels," *Proceedings,* Ninth Symposium on Engineering Applications of Mechanics, University of Western Ontario, 1988, pp. 58–65.

[17] Lucas, G. E., "Review of Small Specimen Test Techniques for Irradiation Testing," *Metallurgical Transactions A,* Vol. 21A, No. 5, 1990, pp. 1105–1119.

[18] Joo, Y., Hashida, T., and Takahashi, H., "Determination of Ductile-Brittle Transition Temperature (DBTT) in Dynamic Small Punch Test," *JTEVA,* Vol. 20, No. 1, 1992, pp. 6–14.

[19] Foulds, J. R., Jewett, C. W., and Viswanathan, R., "Miniature Specimen Test Technique for FATT," *Proceedings,* Steam Turbine/Generator Workshop, Charlotte, 1991.

[20] Takahashi, H., Shoji, T., Mao, X., Hamaguchi, Y., Misawa, T., Saito, M., Oku, T., Kodair, T., Fukaya, K., Nishi, H., and Suzuki, M., "Recommended Practice for Small Punch (SP) Testing of Metallic Materials," Technical Report JAERI-M 88-173, 1988.

DISCUSSION

S. G. Dryck[1] *(written discussion)*—Workers have shown that fracture strain is a function of stress triaxiality. Do you consider that the lack of correlation between J_{IC} and ε_f may in part be due to the intrinsic low triaxiality of the shear punch test?

A. N. Sinclair et al. (authors' closure)—In order to properly address this question, it is necessary to remove the highly nonisotropic specimens from the analysis, as the effects of inclusions were clearly dominant in the distortion of their results. This proves to be very difficult, as even relatively small inclusions tend to have a significant effect in such thin specimens. It is therefore not feasible to answer your question based on the experimental results of this project.

As you point out, the punch test features a two-dimensional stress field as compared to a three-dimensional field in a thick compact tension specimen used for measuring J_{IC}. In the model used in this study, it was assumed that this difference is accounted for by the von Mises formulation for equivalent stress, together with the assumption of incompressible plastic flow. I would agree that there is a danger of inherent inaccuracy in using such a model to infer the value of plane strain toughness based on a two-dimensional test configuration.

G. Lucas[2] *(written discussion)*—The lack of a correlation between J_{IC} and ε_f notwithstanding, have you looked at scoring or notching the disk specimens to force a crack across inclusions in your more anisotropic specimens?

A. N. Sinclair et al. (authors' closure)—A notch or surface score across the axis of the inclusions would certainly induce cracks to initiate in the "tough" direction in some anisotropic specimens. In theory, the information gained from such a test could lead to an estimate for J_{IC}. Such an approach is not being pursued in this study, however, because it would be necessary to have an accurate measurement of the score profile in order to analyze the equivalent strain at fracture; our objective is to develop a relatively inexpensive, quick test method that requires a minimum of experimental measurements. Clearly, the theoretical correlation between J_{IC} and ε_f becomes much more complicated once the surface condition of the specimen is altered.

Your question does illustrate one of the weaknesses of the simple theoretical correlations given in Eqs 3 or 4 for these thin specimens. The punch test is based on an assumption of elastic-plastic fracture, with plastic strain being much larger than elastic strain. In specimens with elongated inclusions, however, such as the SA 106 Grade B, an examination of the fracture surface clearly showed that this assumption can be violated. A single inclusion can be sufficiently prominent that it is no longer appropriate to consider a thin specimen as being homogeneous. The situation would be further complicated by the introduction of a stress concentration factor induced by surface notching.

W. R. Corwin[3] *(written discussion)*—The limitation of not being able to induce fracture in the LT (strong) orientation can possibly be overcome by using an elongated punch and support geometry. This is common practice in testing the drawability of sheet metal where biaxiality ratios of 1:2 and higher are readily achieved by such a technique. Obviously, the

[1] ARA Technology, Harwell Technology, Oxon OX11 ORA, England.
[2] Chemical/Nuclear Engineering, UCSB, Santa Barbara, CA 93106.
[3] ORNL, Oak Ridge, TN.

effect of nonisotropic loading would need to be included in any analysis of such an experiment.

A. N. Sinclair et al. (authors' closure)—Your suggestion of an elongated specimen has been considered, as shown in Fig. 6. By using a sufficiently large length-to-width ratio, it is suggested that the problem would be two-dimensional in nature, thereby easing the mathematical modeling of the deformation. One problem anticipated in the geometry of Fig. 6, however, is that relatively large forces would be needed to induce crack initiation. Such forces would tend to rip the specimen out of its clamp; there might also be a tendency for cracks to initiate immediately adjacent to the clamped area, where their analysis would be very difficult.

I believe that your specific suggestion may be a compromise between the configurations of Figs. 1 and 6, i.e., an oval-shaped punch for which the forces required might not be excessive. As you point out, however, the analysis would be difficult.

We are currently investigating an idea that is similar to the elongated cylindrical punch of Fig. 6, but using a specimen that has been symmetrically thinned (tapered) in the central area under the punch. This geometry will slightly increase the effort at analysis over that required for a flat specimen, but the problem will still be only two-dimensional. The tapered geometry will force the crack to grow in the central area of the specimen.

Frank H. Huang[1]

Fracture Toughness Evaluation for Zircaloy-2 Pressure Tubes with the Electric-Potential Method

REFERENCE: Huang, F. H., **"Fracture Toughness Evaluation for Zircaloy-2 Pressure Tubes with the Electric-Potential Method,"** *Small Specimen Test Techniques Applied to Nuclear Reactor Vessel Thermal Annealing and Plant Life Extension, ASTM STP 1204,* W. R. Corwin, F. M. Haggag, and W. L. Server, Eds., American Society for Testing and Materials, Philadelphia, 1993, pp. 182–198.

ABSTRACT: Zircaloy is commonly used for the cladding or pressure tubes in commercial nuclear reactors because of its strength, corrosion resistance, and low absorption of thermal neutrons. Fracture toughness test techniques using small samples fabricated from archival materials from the N Reactor pressure tubes of Zircaloy-2 were developed to study the factors affecting tube fracture toughness. Compact tension specimen thickness was limited by the wall thickness (7 mm) of the tubes. Specimens (5 mm thick) were prepared for fracture toughness testing, and results were analyzed using the *J*-integral approach. To reduce the high cost of irradiated specimen testing and to more easily precrack specimens remotely, single-specimen potential drop techniques were employed to evaluate the fracture toughness of Zircaloy-2.

The initiation fracture toughness was determined from *J-R* curves, which were constructed by plotting values of *J* as a function of crack extension computed from the electric-potential calibration curve. The *J-R* curves obtained from the calibration curve equation fit the initial portion of the blunting line and heat-tint data.

Results showed that at room temperature, the toughness of unirradiated N Reactor pressure Tube 1054 was the lowest and that of Tube 2755 was the highest. As the temperature was increased the fracture toughness decreased slightly, while the tearing modulus increased with temperature. The fracture resistance in the circumferential orientation was inferior to that for the longitudinal orientation. The effects of neutron fluence and hydrogen content on the fracture toughness of N Reactor pressure tubes were evaluated. Neutron irradiation substantially degraded fracture toughness. Increasing fluence decreased the fracture toughness of the alloy. Hydrogen also decreased fracture toughness, but this effect was insignificant for the pressure tubes tested.

KEYWORDS: pressure tube, neutron fluence, fracture toughness, hydrogen, orientation, reactor, Zircaloy-2, electric potential

Zirconium absorbs very few thermal neutrons. One of its principal alloys, Zircaloy-2, is widely used as nuclear structural and cladding material for water-cooled reactors. The Hanford Site's N Reactor contains 1003 horizontal fuel channels which consist of cold-worked Zircaloy-2 pressure tubes inside a graphite matrix. None of these pressure tubes have been known to develop cracks or leaks since the startup of the N Reactor in 1963. However, earlier investigations [*1*] have revealed that the fracture toughness of the materials has decreased considerably after irradiation, and it is important to understand the effects of the

[1] Principal scientist, Westinghouse Hanford Co., P.O. Box 1970, Richland, WA 99352.

in-service environment on the tube integrity of Zircaloy-2. A surveillance program was established in which tubes were periodically removed for extensive examination and testing.

The peak fluence of removed tubes was 6.3×10^{21} n/cm^2 ($E > 1.0$ MeV). Test results of these irradiated tubes will provide high fluence data for a comparison with the earlier observation that a saturation in toughness degradation was reached at low exposures. It is speculated that irradiation embrittlement may not saturate but will continue at higher neutron exposure levels. This speculation is based on the fact that the fracture behavior of Zircaloy-2 is affected by not only neutron irradiation but also directional hydride and deformation modes. Localized embrittlement occurs when hydrides form normal to the applied stress direction through rapid hydrogen diffusion. This delayed hydride cracking (DHC) is enhanced by the presence of cracks because hydrogen diffuses up the crack-tip stress gradient. Experimental results showed that irradiation could increase DHC crack growth rates 35 to 50 times over that of unirradiated material at a given temperature [*2*]. The fracture responses of this anisotropic material are even more complicated by the twinning and slip, which contribute to the deformation in the plastic zone at the crack tip and influence the fracture resistance. The assessments of brittle frac[illegible]99 potential for reactor core components are therefore necessary to ensure structural soundness and thus extend the plant life.

Fracture toughness testing was conducted on unirradiated pressure tubes of Zircaloy-2 at elevated temperatures. Because the thickness of the test specimen was limited by the thickness (7 mm) of the tube, subsized specimen test techniques were developed with compact tension samples taken from archived N Reactor pressure tubes. These unirradiated small specimens were expected to exhibit stable tearing behavior, and the test results were thus analyzed by the *J*-integral approach. Specimens were fabricated with a notch in the axial (C-L) as well as the circumferential (L-C) orientations to investigate the effect of flaw orientation on fracture toughness. To minimize the number of specimens required for the evaluation of J_{Ic} at various temperatures, the single specimen electric-potential method was used [*3*]. An empirical equation describing the relationship between electric potential and crack extension was used to produce *J-R* curves for J_{Ic} determination.

The objectives of this work were to develop in-cell test techniques for testing compact tension specimens of irradiated Zircaloy-2 and to investigate the effect of neutron fluence on the fracture toughness of N Reactor pressure tubes.

Experimental Procedure

Specimen Preparation

Compact tension specimens were fabricated from unirradiated Zircaloy-2 pressure tubes 1054, 2755, and 2566 and irradiated tube 3053. Tube 1054, supplied by Chass Brass and Copper Company, was fabricated to 18% cold-worked condition. Tubes 2755, 2566, and 3053 were produced by the Harvey Aluminum Company from single extrusions of Zircaloy-2 with 28, 28, and 18% cold work, respectively. Both unirradiated and irradiated specimens were cut from the inner part of each tube so that the high hydrogen layer along the inner diameter of irradiated tubes was intact in the notch plane. The two orientations of compact tension specimens, axial (C-L) and circumferential (L-C) orientations, are shown in Fig. 1*a*. Details of the specimen dimensions, as recommended in ASTM Test Method for Plane-Strain Fracture Toughness of Metallic Materials (E 399), are shown in Fig. 1*b*.

Four Zircaloy-2 electrodes were welded to each specimen to facilitate the connection of electric leads in the hot cell. The optimized locations for the current leads and potential probes are shown in Fig. 2. The specimens were prepared for in-cell testing. The single-

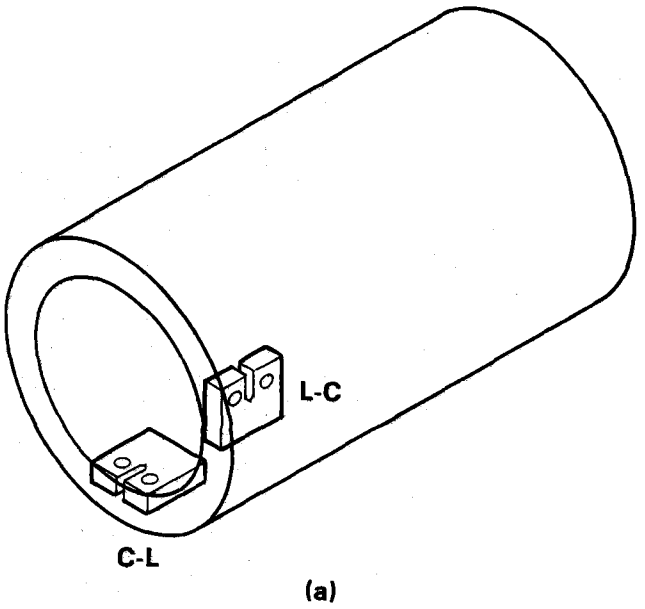

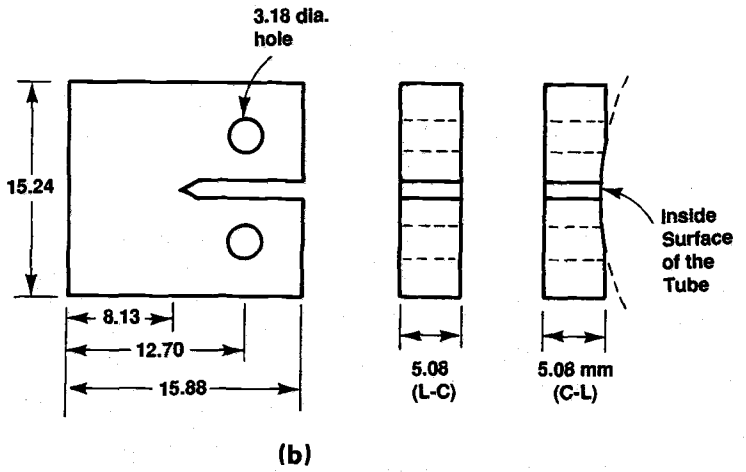

FIG. 1—(a) *Orientation of fracture toughness specimen fabricated from Zircaloy-2 tube;* (b) *Compact tension specimen dimensions (in mm).*

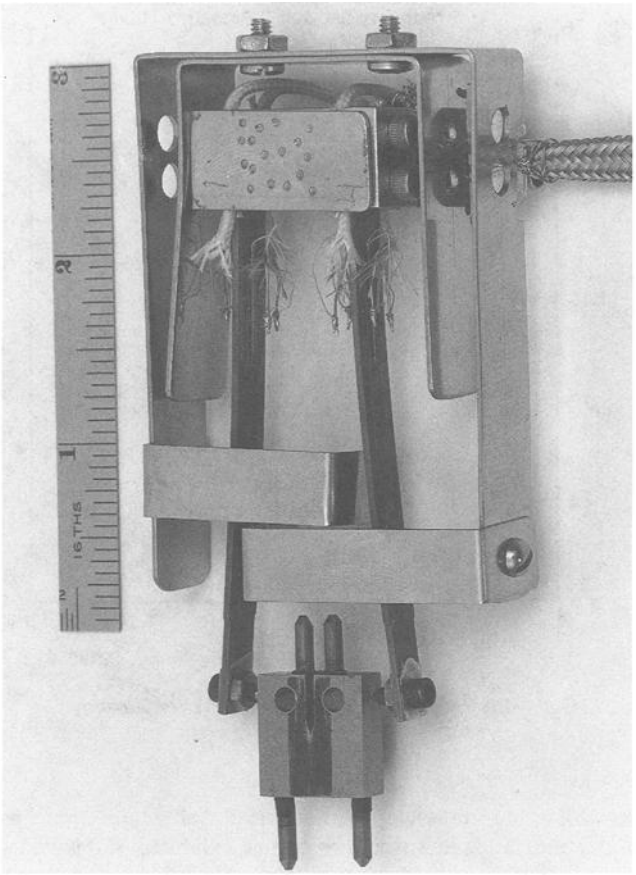

FIG. 2—*Clip gage attached to a compact tension specimen with four electrodes.*

specimen electric-potential method was used to evaluate the values of J_{Ic} at various temperatures.

Test Procedure

Unirradiated Specimen—Fracture toughness tests were performed at 32, 177, and 260°C in accordance with the test procedure outlined in ASTM Test Method for J_{Ic}, a Measure of Fracture Toughness (E 813-81). Before testing, each specimen was fatigue precracked with the electric-potential technique to monitor the crack extension, which was in the range of 1.8 to 2.3 mm. The test specimen assembly was electrically insulated by ceramic spacers placed in the couplings of the pull rods [*3*].

An electrical-resistant clip gage was mounted on the top and bottom surfaces of the specimen along the loadline to measure displacements. During the test, the load, potential output, loadline displacement, and the ram displacement at a speed of 0.42 mm/min were continuously recorded. After the test was completed, each cracked specimen was heat tinted at 315°C to reveal the crack extension. Results were analyzed for the values of initiation

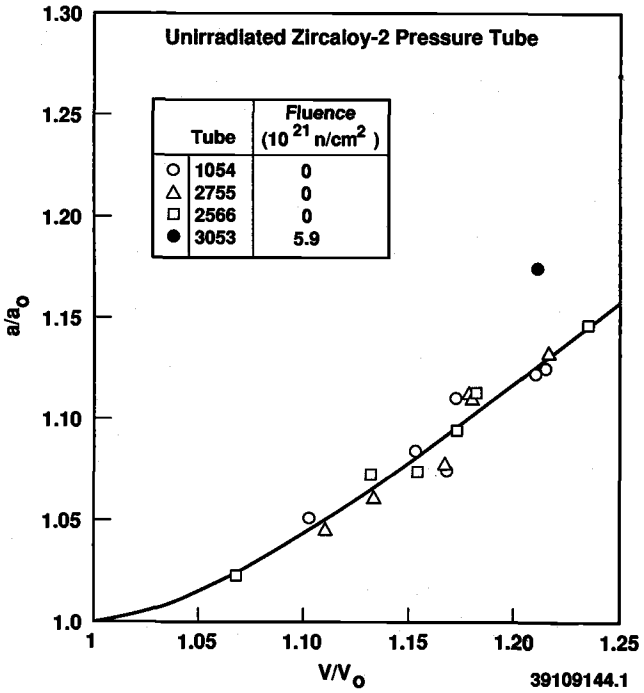

FIG. 3—*Electric-potential calibration curve for Zircaloy-2.*

fracture toughness with either linear elastic or elastic plastic fracture mechanics techniques. Because most of the unirradiated specimens tested exhibited stable tearing behavior, a continuous *J-R* curve was constructed by calculating crack extension through the electric-potential calibration curve shown in Fig. 3. The normalized crack length (a/a_0) versus the normalized potential output (V/V_0) calibration curve is expressed in the form of a hyperbolic tangent (tan$h$) [*4*]

$$a/a_0 = (X_0 - 1) \tanh [(V/V_0 - 1)/(V^*/V_0 - 1)] + \beta(V/V_0 - 1) + 1 \qquad (1)$$

where X_0 and β are determined from the linear least-squares fit to the heat-tint data.

Based on the data given in Fig. 3, X_0 and β are found to be 0.9623 and 0.7733, respectively. The potential output at the neighborhood of crack initiation is V^*. The value of V^*/V_0 can be estimated from the potential output records and crack extension data including the blunting line. It was found that with $V^*/V_0 = 1.075$, Eq 1 satisfactorily described the crack extension-potential output data obtained from compact tension specimens of Zircaloy-2 (Fig. 3).

The J_{Ic} value is evaluated at the intersection of a least-squares regression line through the portion of the *J-R* curve with the 0.15-mm offset and the blunting line given by $J = 2\sigma_f \Delta a$, where σ_f is the flow stress and is equal to $1/2(\sigma_{ys} + \sigma_{uts})$. Equivalent plane strain fracture toughness was computed from J_{Ic} values using the following equation: $K_{Ic} = \sqrt{J_{Ic}E}$, where E is Young's modulus. The value of plane strain fracture toughness is termed as K_c rather than K_{Ic} if the K_{Ic} test is invalid.

Irradiated Specimen—Because the goal of the fracture toughness testing was to evaluate the postirradiation toughness of Zircaloy-2 pressure tubes, the test procedure was established for unirradiated specimens as well as irradiated specimens. However, the electric-potential calibration for fatigue-cracked specimens of Zircaloy-2 was found not to be applicable to irradiated specimens. As shown in Fig. 3, the potential drop in an irradiated specimen is less sensitive to crack extension than in unirradiated specimens. The potential output may be affected by the hydrides present on the rough crack surfaces.

Irradiated specimens of Zircaloy-2 tend to fail by unstable fracture. The crack extension in these specimens is either undefined or too long and difficult to relate to the final potential output. During the early stage of loading, the electric potential increases linearly, then rises rapidly when the crack is initiated. In most cases, the point of initiation was readily apparent from the electric-potential record. Therefore, the J_{Ic} toughness was obtained on the basis of the area under the load-displacement curve up to the point of deviation from the linear region of the electric-potential curve.

Results

Fracture Behavior

Unirradiated specimens of Zircaloy-2 may fail by stable tearing or unstable fracture with little apparent plastic deformation. Typical load and potential output records for samples cut from irradiated tubes are shown in Fig. 4. The load increases nonlinearly to the maximum

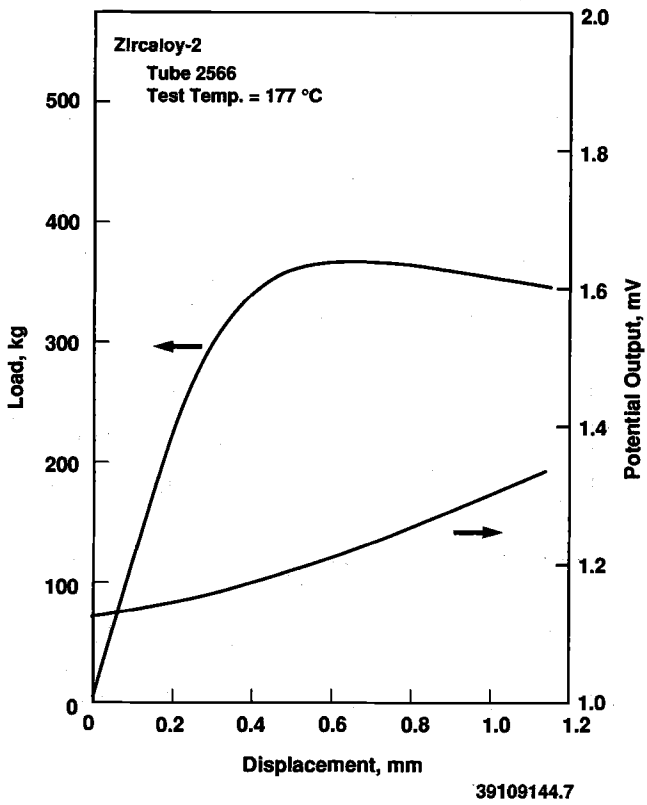

FIG. 4—*Load and electric-potential records for stable tearing behavior.*

load and then gradually decreases while the potential output smoothly increases with displacement. Unirradiated Tubes 2755 and 2566 displayed such crack growth behavior. At room temperature, a sample cut from Tube 1054 exhibited an unstable fracture as shown in Fig. 5. In this type of fracture, the load increases nonlinearly before a sudden load drop occurs. The fracture behavior commonly seen in irradiated Zircaloy-2 is shown in Fig. 6, where stable tearing followed by unstable fracture is illustrated; the potential output from the specimens surges when the cracking in the specimen begins. Some irradiated specimens exhibited either an unstable fracture or stable tearing.

Fracture Toughness Values

Through the use of the electric-potential calibration curve (Eq 1), the crack extensions were calculated from potential output records to construct *J-R* curves. Figure 7 shows the *J-R* curves for unirradiated specimens with various crack lengths. Also plotted in this figure are the final heat-tinted Δa values for each specimen represented by the solid symbol. Values of K_c are evaluated from these *J-R* curves and are listed in Table 1 for unirradiated samples. The tearing modulus (T) was computed from the following equation: $T = (E/\sigma_f^2)(dJ/da)$, where dJ/da is the slope of the *J-R* curve.

There were twelve specimens fabricated from N Reactor pressure tube 3053. The specimen thickness and the irradiation and test conditions are given in Table 2. Only three tests on

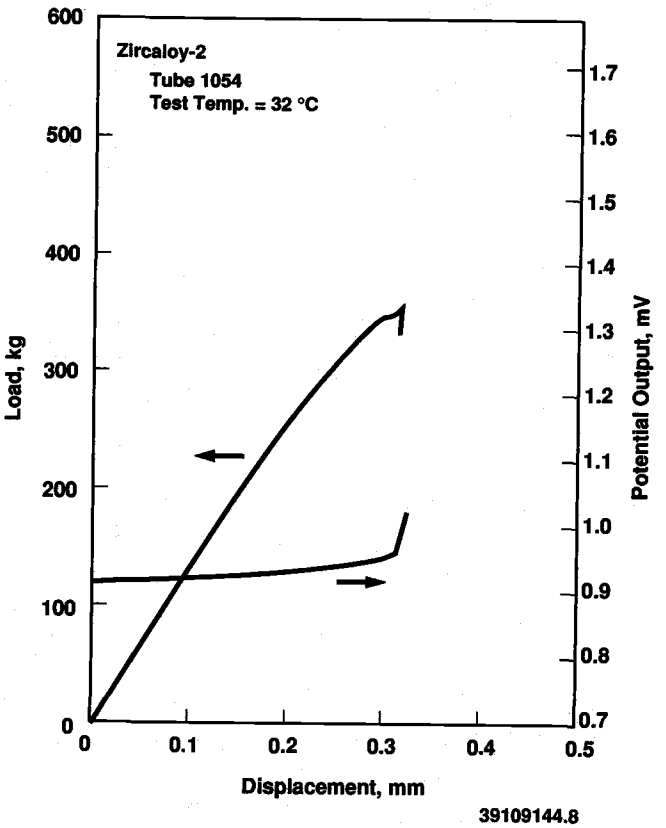

FIG. 5—*Load and electric-potential records for unstable fracture behavior.*

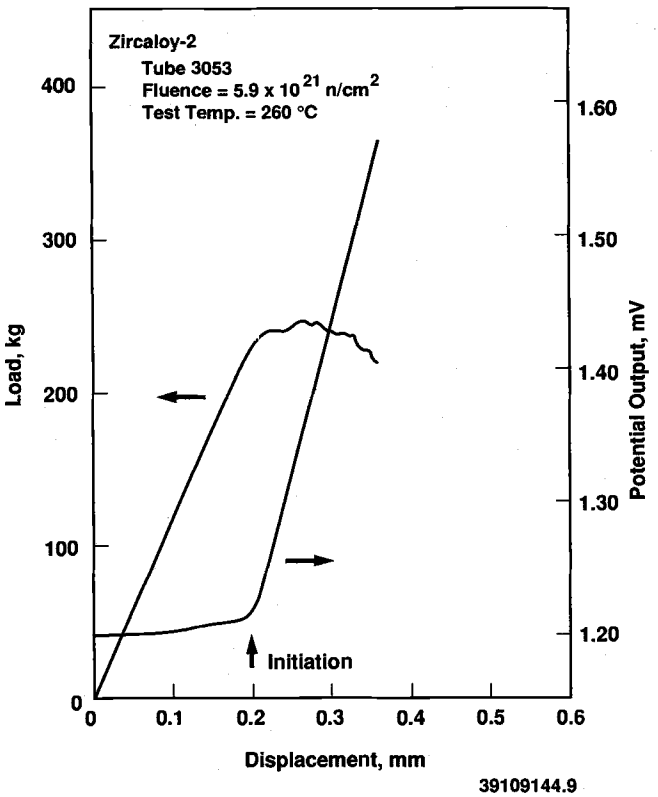

FIG. 6—*Load and electric-potential records for stable tearing/unstable fracture behavior.*

irradiated specimens yielded valid K_{Ic} values. Elastic-plastic fracture mechanics techniques were used to characterize the fracture toughness of the remaining irradiated specimens. Because there was no appropriate electric-potential calibration curve for irradiated specimens, the construction of *J-R* curves was precluded. The value of J_{Ic} was obtained on the basis of the crack growth initiation point apparently determined from the electric-potential curve (see Fig. 6). Table 2 compiles the equivalent K_c values of irradiated specimens.

Temperature and Fluence Dependence

The temperature dependence of the fracture toughness for unirradiated Zircaloy-2 pressure tubes is shown in Fig. 8. At room temperature, Tube 1054 failed by unstable fracture. The fracture behavior evolved into a mixed mode of stable tearing and unstable fracture and then stable tearing as the temperature was increased to 177°C or higher. Specimens taken from Tubes 2755 and 2566 exhibited stable tearing at room temperature or higher. In comparison, the temperature at which the ductile-brittle transition occurs in Tube 1054 is higher than those for Tubes 2755 and 2566. These two tubes would fail by brittle fracture at temperatures below room temperature. The tearing modulus is plotted in Fig. 9 in terms of temperature. The trend, clearly indicated by this figure, is that the tearing resistance of Zircaloy-2 increases with increasing temperature.

Neutron irradiation can markedly degrade the fracture toughness of Zircaloy-2. Figures 8 and 10 show that the fracture toughness of the alloy is significantly reduced by a fluence

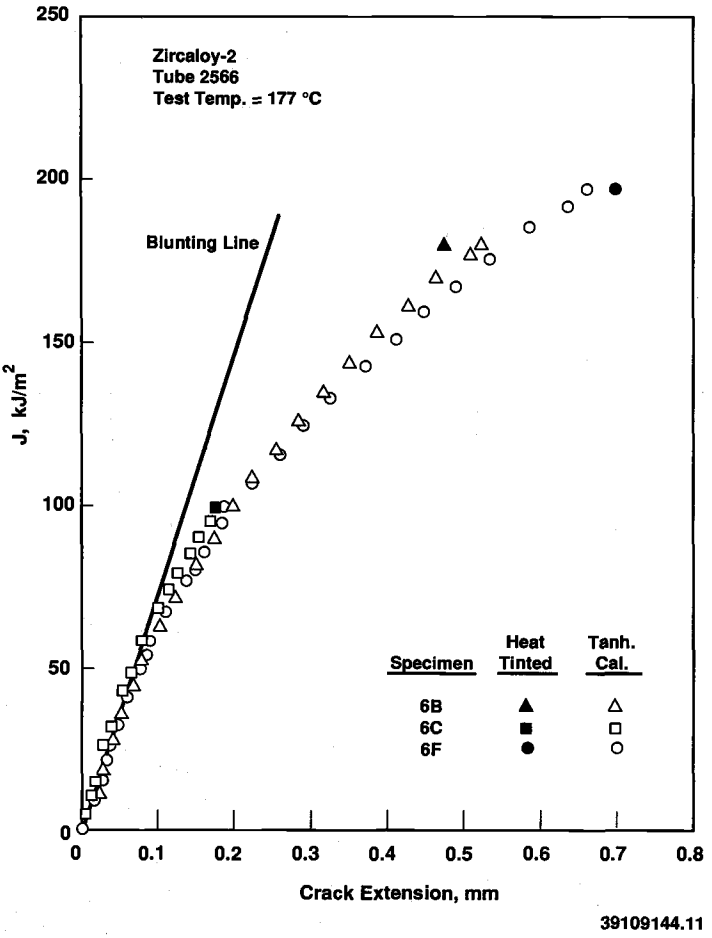

FIG. 7—*The* J-R *curves obtained via an electric-potential calibration curve for unirradiated Zircaloy-2 tested at 177°C.*

of 6×10^{21} n/cm^2 ($E > 1.0$ MeV). The irradiated specimens failed by unstable fracture at room temperature and by stable tearing at 260°C.

Effects of Orientation and Hydrogen

The effect of orientation on the fracture behavior of Zircaloy-2 tubing is illustrated in Fig. 11. The fracture resistance in the L-C (circumferential) orientation was inferior to that for the C-L (longitudinal) orientation. Temperature has a stronger influence in raising the fracture toughness in the C-L orientation than in the L-C orientation. The lower fracture toughness in the L-C orientation is believed to be associated with the higher yield strength in this orientation because of crystalline anisotropy.

Two thinner specimens with a thickness of 2.54 mm were tested to investigate the effect of hydrogen on the fracture toughness of Zircaloy-2. Figure 12 shows the hydrogen concentration in relation to the tube wall thickness of Tube 3053. Hydrogen content gradually

TABLE 1—*Fracture toughness of unirradiated Zircaloy-2 pressure tube.*

Specimen ID	Tube	Crack Orientation	Test Temperature, °C	K_c, MPa$\sqrt{m}$	Tearing Modulus	Fracture Mode
4A	1054	C-L	32	58.0	···	Unstable fracture
4B	1054	C-L	177	89.2	89	Stable tearing
4E	1054	C-L	177	85.5	76	Stable tearing
4C	1054	C-L	260	86.1	114	Stable tearing
3047	1054	L-C	32	44.2	14	Stable tearing
3046	1054	L-C	177	56.7	31	Stable tearing
5A	2755	C-L	32	99.5	35	Stable tearing
5E	2755	C-L	32	98.2	36	Stable tearing
5D	2755	C-L	177	95.0	120	Stable tearing
5F	2755	C-L	177	95.0	110	Stable tearing
5C	2755	C-L	260	85.5	139	Stable tearing
6A	2566	C-L	32	87.5	60	Stable tearing
6E	2566	C-L	32	94.5	71	Stable tearing
6B	2566	C-L	177	88.0	116	Stable tearing
6F	2566	C-L	177	89.0	102	Stable tearing
6D	2566	C-L	260	86.1	170	Stable tearing

increased from the outer surface to near the inner surface where a sharp increase was observed at the inner surface. The specimen taken from the inner diameter region has higher hydrogen content (302 ppm) than the one taken from the outer diameter region (22 ppm). Results showed that these two specimens had comparable fracture toughness values, an indication that the hydrogen gradient had little effect on the overall fracture resistance.

In addition to the above variables (fluence, test temperature, hydrogen concentration, and notch orientation) that have an effect on the fracture toughness of Zircaloy-2, test results also differ by tube manufacturer and tube-to-tube variation in tubes manufactured by the same supplier. Because only one or two specimens cut from each tube were tested in this work, the significance of the tube-to-tube variables will be analyzed by a statistical analysis when enough data are available.

TABLE 2—*Fracture toughness of N Reactor pressure Tube 3053 (C-L orientation).*

Specimen ID	Specimen Thickness, mm	Test Temperature, °C	Fluence, 10^{21} n/cm^2	K_{Ic}, MPa$\sqrt{m}$	K_c, MPa$\sqrt{m}$	Fracture Mode
U4A1	5.08	32	0	···	79.9	Stable tearing
U4A3	5.08	177	0	···	68.1	Stable tearing
U4A5	5.08	260	0	···	68.4	Stable tearing
7X3A1	5.08	32	1.2	31.1	···	Unstable fracture
3R1A2	5.08	32	3.3	···	42.6	Stable/unstable fracture
T-3A1	5.08	32	5.9	23.9	···	Unstable fracture
T3D2B	2.54 inner	177	5.9	···	35.5	Stable tearing
T-2J	2.54 outer	177	5.9	···	39.6	Stable tearing
T-3A2	5.08	177	5.9	···	36.0	Stable/unstable fracture
T-2F	5.08	260	5.9	···	34.4	Stable/unstable fracture
T-2C	5.08	260	5.9	···	36.1	Stable/unstable fracture
3S1A3	5.08	32	6.3	33.3	···	Unstable fracture

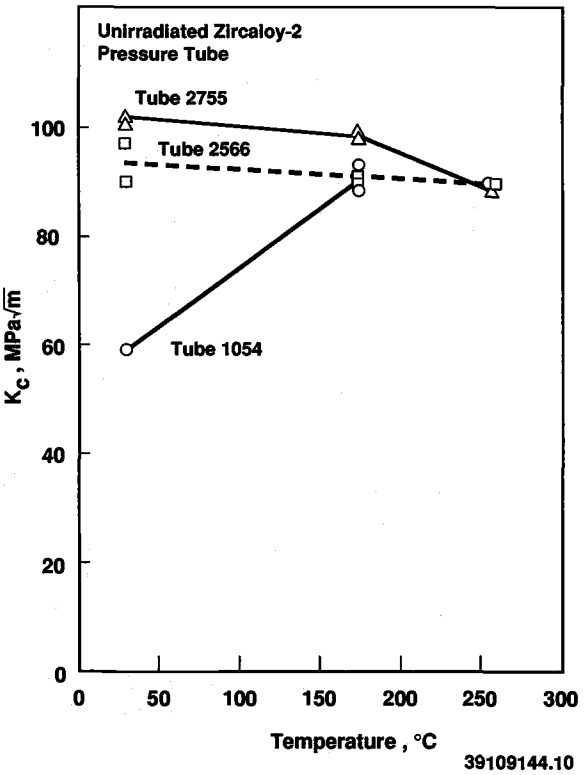

FIG. 8—*Temperature dependence of* K_c *for unirradiated Zircaloy-2 pressure tubes.*

Discussion

Specimen Thickness Requirement

There are specimen thickness limitations for which the values of K_{Ic} or J_{Ic} can be determined under conditions of "plane strain." Irradiated specimens 7X3A1, T-3A1, and 3S1A3 exhibiting an unstable fracture satisfied the specimen size and validity requirements recommended by ASTM Standard E 399. These requirements are

$$a,\ W - a,\ B > 2.5(K_Q/\sigma_{ys})^2 \tag{2}$$

$$P_{max}/P_Q < 1.1 \tag{3}$$

where

a = crack length,
W = specimen width,
B = specimen thickness, and
P_{max} = maximum load.

The test results of the remaining irradiated specimens and unirradiated specimens were analyzed for J_{Ic} values. According to ASTM E 813, the minimum specimen thickness required

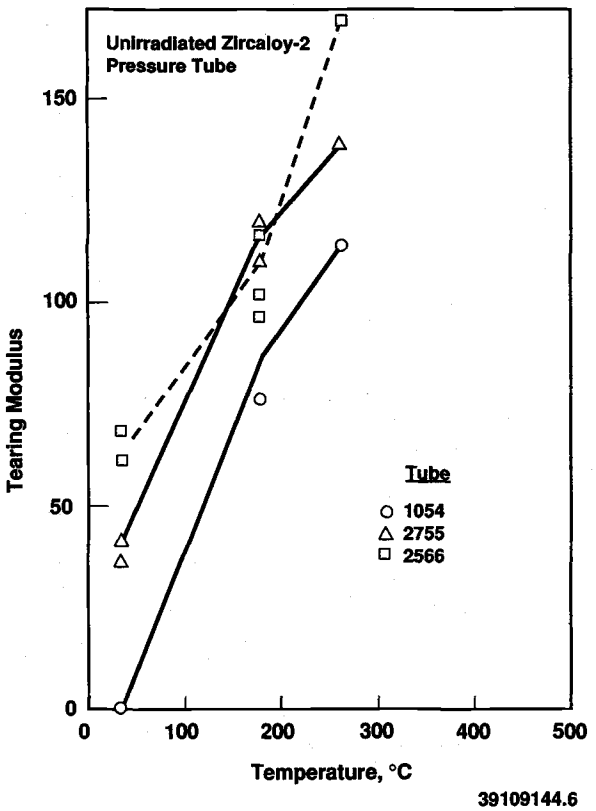

FIG. 9—*Temperature dependence of tearing modulus for unirradiated Zircaloy-2 pressure tubes.*

for valid J_{Ic} tests is $25J_{Ic}/\sigma_{ys}$. The minimum thickness B^J_{min} for each test temperature is listed in Table 3. Only at room temperature do the 5.08-mm-thick specimens of unirradiated Zircaloy-2 pressure tubes used in this work meet the specimen thickness requirement. As the temperature is increased, the value of J_{Ic} increases while the yield stress decreases; the B^J_{min} increases and becomes larger than the specimen thickness of 5.08 mm. For irradiated specimens, the minimum thickness is about 0.7 mm. Therefore, either a 5.08-mm- or 2.54-mm-thick specimen of irradiated Zircaloy-2 (listed in Table 2) satisfies the requirements for valid J_{Ic} tests.

Electric-Potential Calibration

In establishing the experimental electric-potential calibration, there are two questions which need to be answered: (1) Are the specimens used to generate the potential drop and crack length data the same specimens used for fracture toughness tests? (2) How are the potential outputs related to the crack length in terms of specimen initial conditions (W or a_0)? Because theoretical calibration was formulated in an expression of V/V_0 versus a/W [*5*], experimental calibration had generally been established in the same relationship. However, evidence showed that experimental and theoretical calibrations were not in agreement [*6*].

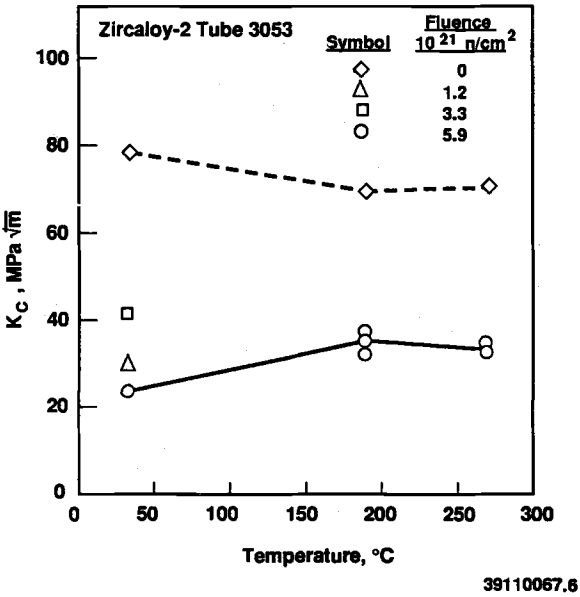

FIG. 10—*Temperature dependence of* K_c *for irradiated Zircaloy-2 pressure tubes.*

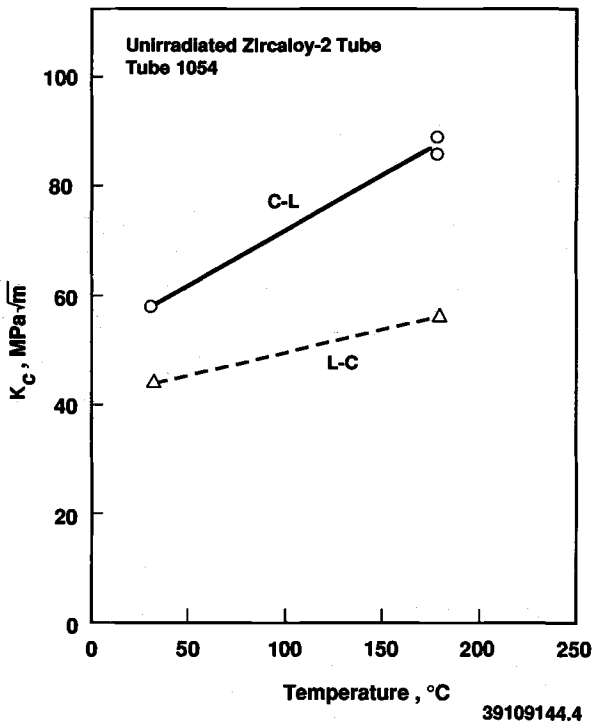

FIG. 11—*Temperature dependence of* K_c *for unirradiated Zircaloy-2 with different notch orientations.*

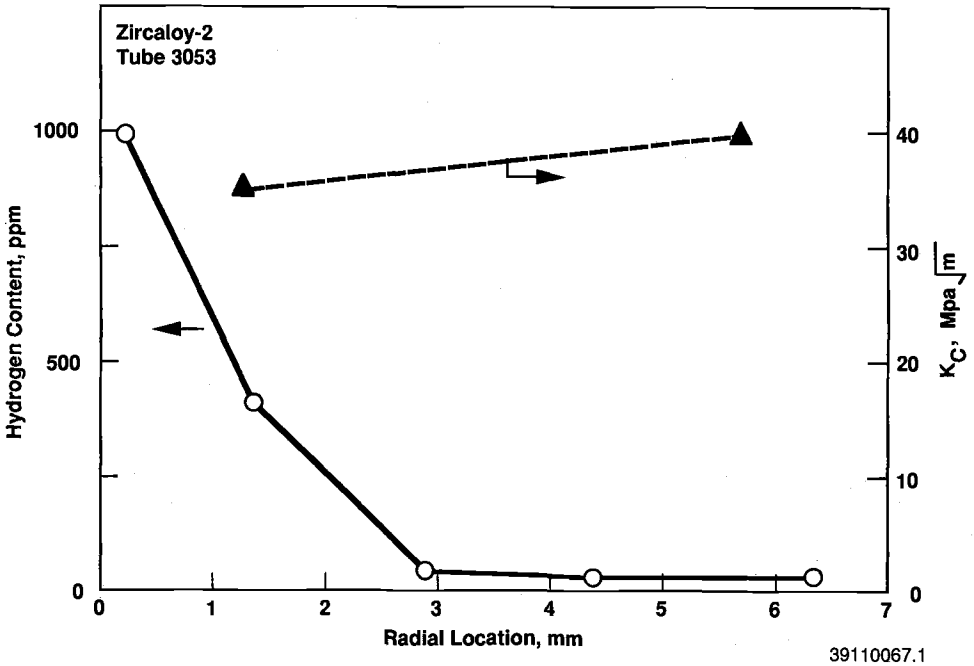

FIG. 12—*Radial distribution of hydrogen in Zircaloy-2 Tube 3053 at 9.16 m from the upstream inlet rolled joint end of the tube.*

In this work, the final potential output and heat tinted Δa of each tested specimen were used to establish the electric-potential calibration. Because the widths of all specimens are identical, but the initial crack lengths are not, the results are plotted in the form of a non-dimensional ratio (a/a_0 versus V/V_0) in Fig. 3. The near linearity of this plot makes the description of the *V-a* relationship simple and accurate. However, this nearly straight line calibration curve has to be extrapolated through the starting point ($a/a_0 = V/V_0 = 1$). Near the blunting region precisely where the J_{Ic} values are determined, the cracks are small and difficult to accurately measure.

A polynomial equation can be used to represent the stable crack growth and blunting behavior, but data fitting for this equation is poor. To better describe the behavior exhibited in these two regions, a bilinear form with the smooth joint point, near where the crack began, was used. Equation 1, expressed in a hyperbolic tangent form, consists of two linear segments: $a/a_0 = X_0 + \beta(V/V_0 - 1)$ and $a/a_0 = (X_0 - 1)(V/V_0 - 1)/(V^*/V_0 - 1) +$

TABLE 3—*Minimum specimen thickness required for valid* J_{Ic}.

Specimen	Test Temperature, °C	B^J_{min}, mm
Unirradiated	32	1.9–5.6
Unirradiated	177	5.6–7.1
Unirradiated	260	7.2
Irradiated	32–260	0.7

$\beta(V/V_0 - 1)$ for the stable crack growth and blunting region, respectively. At $V = V^*$, these two equations are equal. In the blunting region, the value of J is linearly related to V. With the slope of J versus V curve equal to S, V^* is easily estimated to be $[(X_0 - 1)/(S/2\sigma_f a_0 - \beta) + 1]V_0$. Figure 7 shows that Eq 1 is capable of producing satisfactory J-R curves that fit both the blunting line and experimental data. On the basis of these J-R curves, reasonably accurate values of J_c are determined.

Irradiation Effect

A comparison between Figs. 8 and 10 clearly shows that irradiation significantly decreases the fracture toughness of Zircaloy-2. The data trend is clear as seen in Fig. 13, where the

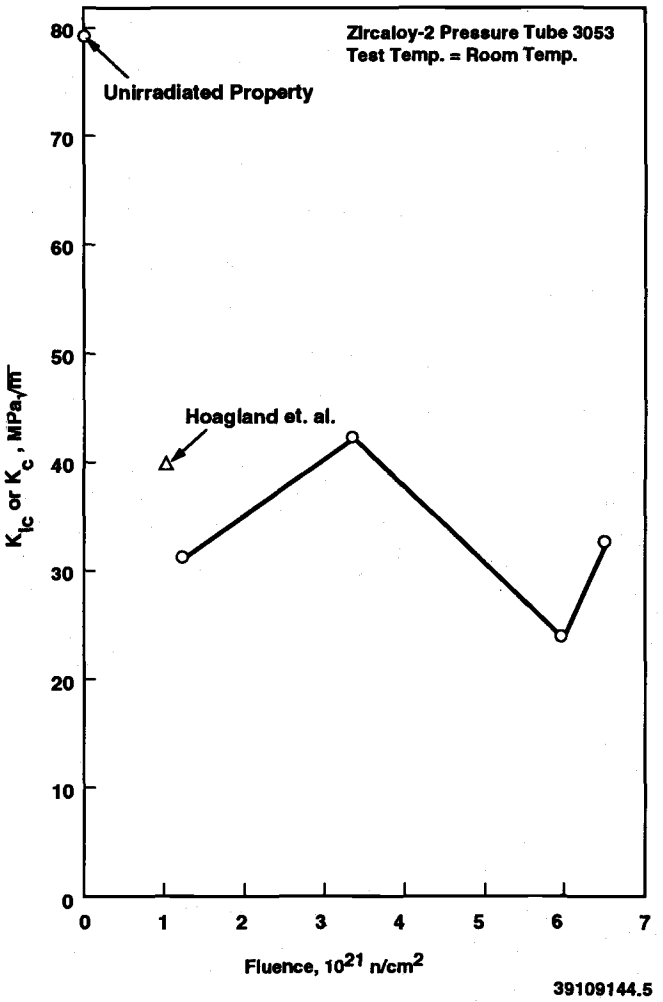

FIG. 13—*Fluence dependence of* K_{Ic} *or* K_c *for irradiated Zircaloy-2 tested at room temperature.*

room temperature fracture toughness is shown to decrease with increasing fluence. The data obtained from the N Reactor pressure tubes appear to be in agreement with earlier results [*1*]. More data are needed to conclude whether the fracture toughness degradation saturates at this fluence level of 6×10^{21} n/cm^2 ($E > 1.0$ MeV).

Zircaloy-2 is a hexagonal closed-packed (HCP) metal. Like face-centered cubic (FCC) metals, Zircaloy-2 is nominally ductile metal although generally less ductile than FCC metals. The radiation embrittlement in these two kinds of metals is characterized by dimple rupture undergoing a premature onset of plastic instability. Highly irradiated FCC metals such as austenitic steels fail by channel fracture. Because the slip system in HCP materials are limited, only highly textured Zircaloy displays deformation bands that are a result of dislocation channeling [*7*]. Consequently, irradiation damage on a much finer scale, not dislocation channeling, degrades the fracture toughness of Zircaloy-2.

Another important factor contributing to the toughness degradation is the presence of zirconium hydride (ZrH_2) which occurs during reactor service. These brittle precipitates of hydride, with K_{Ic} values of 1 to 3 MPa$\sqrt{m}$ [*8*], severely reduce cracking resistance when the hydride platelet normal is parallel to the applied stress. Hydride formation provides sites for easy crack nucleation driven by either irradiation hardening or the interaction of radiation-induced deformation bands. However, hydrogen effects on toughness degradation in Zircaloy-2 were not significant. Experimental evidences showed that irradiation reduced substantially the fracture toughness of Zircaloy-2 containing up to 100 ppm hydrogen [*1*]. This finding is consistent with the present results showing little difference in through-wall toughness even with a large hydrogen gradient.

Conclusion

Fracture toughness testing was performed on Zircaloy-2 pressure tubes with a single subsized-specimen method. The electric-potential techniques are suitable for the specimen size and testing system used in this work for J_{Ic} determination. All unirradiated specimens, except for one tested at room temperature, fractured by stable tearing. Irradiated specimens failed in two additional types of fracture behavior: unstable fracture and stable tearing followed by unstable fracture. Specimens exhibiting unstable fracture may yield valid K_{Ic} values. Results of other specimens were analyzed by elastic-plastic fracture mechanics techniques. An electric-potential calibration curve in the form of a hyperbolic tangent fits the data of potential output versus crack extension well and was used to construct *J-R* curves for unirradiated specimens. For irradiated specimens, the values of J_{Ic} toughness could only be determined from the point of crack initiation indicated by the electric-potential curves.

The preirradiation fracture toughness of Zircaloy-2 slightly decreased while the tearing modulus significantly increased with temperature. After irradiation, the fracture toughness markedly decreased and appeared to decrease further with increasing fluence. The orientation of a crack in the specimen can affect the fracture resistance because Zircaloy-2 is anisotropic. In general, both irradiation and hydrogen degrade the postirradiation fracture toughness of Zircaloy-2. In this work, results showed that radiation caused the most significant decrease in fracture toughness, and hydrogen caused the least.

Acknowledgment

This paper is based on work performed under U.S. Department of Energy Contract DE-AC06-87RL10930 with Westinghouse Hanford Company, a subsidiary of Westinghouse Elec-

tric Corporation. The author wishes to thank K. V. Scott and D. J. Trimble for their efforts in the initiation and development of this program, and W. J. Mills for his assistance in performing this investigation.

References

[1] Hoagland, R. G. and Rowe, R. G., "Fracture of Irradiated Zircaloy-2," *Journal of Nuclear Materials,* Vol. 30, 1969, pp. 179–195.

[2] Huang, F. H. and Mills, W. J., "Delayed Hydride Cracking Behavior for Zircaloy-2 Tubing," *Metallurgical Transaction,* Vol. 22A, 1991, pp. 2049–2060.

[3] Huang, F. H., "J_{Ic} Measurements on Single Subsized Specimens of Ferritic Alloys," *Journal of Testing and Evaluation,* Vol. 13, No. 4, 1985, pp. 257–264.

[4] Huang, F. H., "Fracture Toughness of Aged Stainless-Steel Primary Piping Welds Evaluated by Multiple- and Single-Specimen Method," WHC-SA-1087-FP, Westinghouse Hanford Company, Richland, WA, 1991.

[5] Johnson, H. H., *Materials Research and Standards,* Vol. 5, 1965, pp. 442–445.

[6] Vassilaros, M. G. and Hackett, E. M., "J-Integral R-Curve Testing of High Strength Steels Utilizing the Direct-Current Potential Drop Method," *Fracture Mechanics, ASTM STP 883,* American Society for Testing and Materials, Philadelphia, 1984, pp. 535–552.

[7] Rosenbaum, H. S., Rieger, G. F., and Lee, D., "Localized Deformation and Fracture in Neutron Irradiated Zircaloy-2," *Metallurgical Transactions,* Vol. 5, 1974, pp. 1867–1874.

[8] Simpson, L. A. and Cann, C. D., "Fracture Toughness of Zirconium Hydride and Its Influence on the Crack Resistance of Zirconium Alloys," *Journal of Nuclear Materials,* Vol. 87, 1979, pp. 303–316.

Michael P. Manahan, Sr.[1]

Miniaturized Fracture Toughness Testing During the Plant Life Extension Period

REFERENCE: Manahan, M. P., **"Miniaturized Fracture Toughness Testing During the Plant Life Extension Period,"** *Small Specimen Test Techniques Applied to Nuclear Reactor Vessel Thermal Annealing and Plant Life Extension, ASTM STP 1204,* W. R. Corwin, F. M. Haggag, and W. L. Server, Eds., American Society for Testing and Materials, Philadelphia, 1993, pp. 199–213.

ABSTRACT: It is desirable to obtain plane strain fracture toughness data in support of plant refurbishment and plant life extension (PLEX) efforts. These data may be needed for pressurized thermal shock (PTS) analyses, low upper shelf energy analyses, and to verify shifts in the K_{IR} curve. A major impediment to the development of plant-specific fracture toughness data is the specimen size requirement and the fact that many surveillance capsule programs do not include fracture toughness specimens.

A new test has been developed to resolve these difficulties. An experimental modification, referred to as stress field modification, enables testing using specimens substantially thinner than those currently required by ASTM. Examination of the stress field modified specimen fracture surface demonstrates that plane strain conditions were achieved in the miniature specimens. The miniature specimens were machined from a nuclear-grade ASTM A508 steel used in the Oak Ridge National Laboratory pressurized thermal shock study. The miniature specimen data lie within the experimental scatter of the 6-in. (15.24 cm) vessel data. The development of this new fracture test enables plane strain testing of materials from surveillance programs (broken Charpy specimens) and from material cut from in-service components.

KEYWORDS: miniature specimens, fracture toughness, plane strain, stress field modification, *J*-Integral, finite element

In order to calculate pressure-temperature (P-T) operating limits, it is necessary to determine the temperature dependence of the lower bound to static and dynamic fracture toughness for the limiting beltline material. As stated in the ASME code, Section XI, Article A-4400, it is intended that plant-specific fracture toughness data be determined directly in the surveillance program. In particular, the ASME code states, "Radiation induced changes in fracture toughness should be determined from surveillance specimens of the actual material and product form, irradiated according to the surveillance techniques of ASTM E 185, Standard Recommended Practice for Effects of High-Energy Irradiation on the Mechanical Properties of Metallic Materials." Since most surveillance programs do not include fracture toughness specimens, the effects of neutron irradiation are considered for both K_{IA} and K_{IC} by shifting the reference nil ductility temperature (RT_{NDT}) as a function of irradiation using

[1] President, MPM Research & Consulting, 915 Pike Street, Lemont, PA 16851; Adjunct professor of nuclear engineering, The Pennsylvania State University, 231 Sackett Building, University Park, PA 16802.

[2] The techniques described in this paper are protected by U.S. Patent No. 4,885,027, entitled "Determining Plane-Strain Fracture Toughness and the J-Integral for Solid Materials Using Stress-Field-Modified Miniature Specimens."

trend curves. In particular, Regulatory Guide 1.99 (Revision 2) [RG 1.99(2)][3] is used to determine the Charpy shift at the 41-J level (ΔT_{41}) due to neutron damage. In cases where two or more credible surveillance data are available, the Regulatory Guide provides a procedure for combining the measured data with the generic model to predict the Charpy shift fluence dependence. As stated in ASME Section III, Article A-4400, this approach is intended to be extremely conservative: "These curves (the shifted K_{IA} and K_{IC} curves) are intended to be very conservative since the recommended procedure is to determine the irradiation effects from surveillance specimens of the actual material and product form in question." The curves referred to are the shifted ASME K_{IA} and K_{IC} reference curves. Further, as stated in article A-4200, these unirradiated curves are intended to be very conservative as well: "The curves in Fig. A-4200-I are intended to be very conservative since the recommended procedure is to determine the material fracture toughness from specimens of the actual material and product form in question." In addition, the shift in fracture toughness data due to irradiation of a pressure vessel steel, measured in accordance with ASTM Test Method for J_{IC}, a Measure of Fracture Toughness (E 813), does not compare well with the K_{IR} curve when shifted by the measured Charpy 40 J transition temperature shift [*1*]. In response to these concerns and to the need within the nuclear industry's plant life extension (PLEX) program for in-service materials data, a new approach to plane strain fracture toughness testing has been developed. The theoretical framework and initial benchmark data are presented in this paper. The approach described has been applied to determine static plane strain fracture toughness data using specimens substantially thinner than those required by ASTM. As shown in the ASME code, dynamic fracture toughness data are significantly more conservative than static data. However, analysis of the data and equations presented in Ref *2* reveals that static data can be used to represent crack arrest data for SA-533 Grade B Class 1, SA-508 Class 2, and SA-508 Class 3 steel by

1. Fitting the lower bound to the measured static fracture toughness data.
2. Decreasing the lower bound static fracture toughness data by ~10 MPa $\sqrt{m}$.
3. Translating the lower bound fit 24°C to the right.

Thus, data obtained using the static testing approach described herein can be mapped into dynamic data by using the procedure described above. In addition, the results of on-going research suggest that the stress field modification technique can be adapted for dynamic testing to enable direct K_{IA} measurement in the future [*2a*].

Theory

Current static fracture toughness test procedures require a minimum specimen thickness to ensure plane-strain conditions are simulated in laboratory specimens. In particular, the critical fracture toughness testing parameters prescribed in ASTM E 399 [*3*] require

$$B, a_0 > 2.5 \left(\frac{K_{IC}}{\sigma_{ys}}\right)^2 \tag{1}$$

and ASTM E 813 [*4*] requires

$$B, b_0 > 25 \frac{J_{IC}}{\sigma_y} \tag{2}$$

[3] Regulatory Guide 1.99 Revision 2, "Radiation, Embrittlement of Reactor Vessel Materials," May 1988.

where

B = specimen thickness,
b_0 = uncracked ligament length,
a_0 = initial crack length,
σ_{ys} = 0.2% offset yield strength, and
σ_y = effective yield strength.

References *3* and *4* semi-empirical relationships were determined by ASTM committees using experimental data. The *J*-integral procedure enables testing with samples thinner than ASTM E 399 specimens by about a factor of 20. Reference *5* has clearly demonstrated that testing using the *J*-integral procedure yields data identical to that obtained using the Ref *3* procedures over the temperature range of validity for that procedure.

This paper reports on a new concept for fracture toughness testing. As shown schematically in Fig. 1, the new test is applicable in the region indicated, where plane stress data would be obtained using conventional methods. The basic idea is to modify the stress field in the vicinity of the crack tip to produce plane-strain conditions. The stress field modification approach uses material that is integrally machined or may be welded on the specimen sides to produce the needed through thickness material constraint to achieve plane strain conditions. This approach enables testing of very thin specimens. At present, the lower limit on thickness has not been determined. However, the early benchmark experiments have focused on the Charpy specimen thickness for application to surveillance capsule testing. It is likely that specimens with dimensions on the order of the plastic zone size, which is a

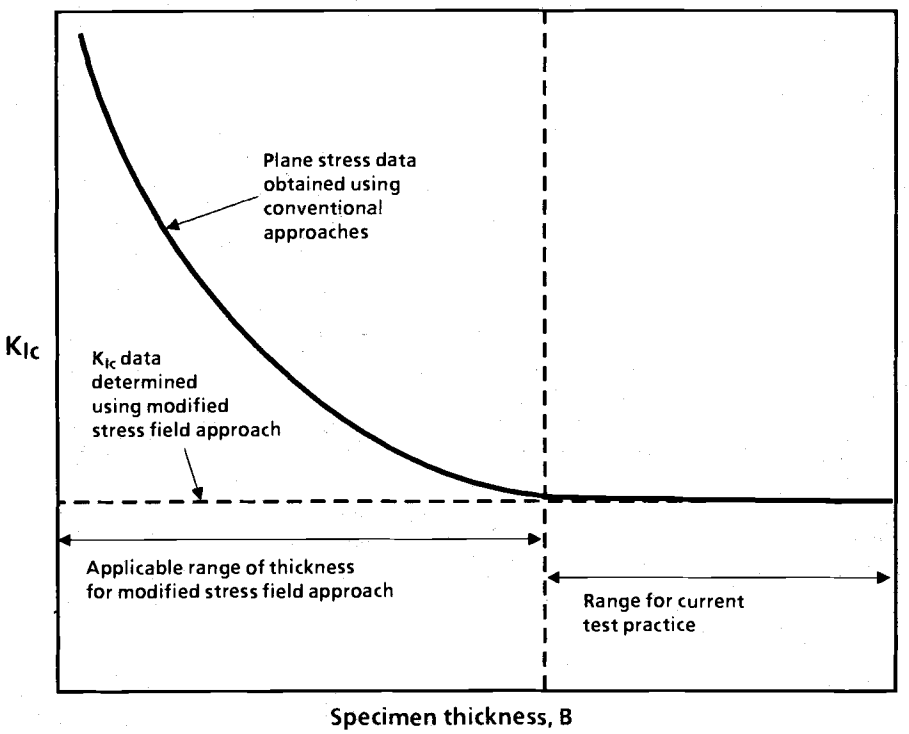

FIG. 1—*Schematic representation of the applicable range of specimen thickness* (B) *for the modified stress field approach.*

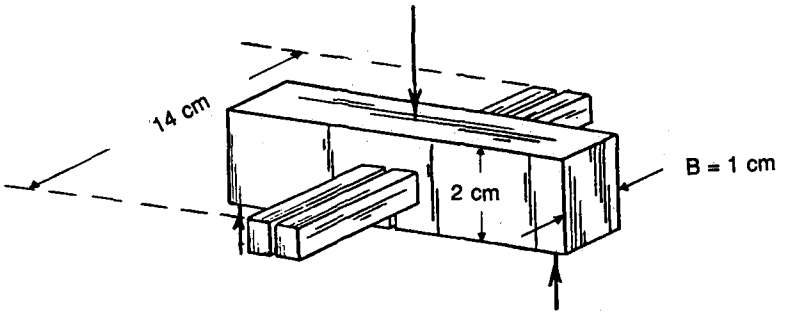

FIG. 2—*Miniaturized fracture toughness specimen design.*

function of test temperature, can be used. For pressure vessel steels, specimens with thicknesses on the order of 0.5 cm represent a practical lower bound.

There are several experimental procedures that can be used to modify the stress field. In the current study, side-constraint arms were integrally machined to simulate welded arms attached to pressure vessel surveillance specimens. Future studies will focus on solving problems associated with welding the side-constraint arms in place. The size of the arms and placement on the specimen are critical parameters in successful miniature specimen testing. Figure 2 shows the specimen design. Further details concerning specimen design are presented in Ref *6*.

In order to determine the critical experimental parameters and to validate the basic approach, two- and three-dimensional finite-element model (FEM) analyses were performed. Hence, the benchmark solution is a two-dimensional plane-strain analysis of the miniature three-point bend specimen. To validate the approach, a three-dimensional finite-element analysis of the three-point bend specimen was performed, in which the side-constraint arm was modeled so that the out-of-plane displacements on the surface are prohibited. Thus, an approximated local plane-strain condition that retains a triaxial stress state at the crack tip is achieved in the miniature specimen.

Elastic FEM Solutions

The reference formulae from the load-point displacement, the crack mouth opening, and the opening mode stress-intensity factor were reported in Ref *7* along with a comparison of the finite-element elastic solution. The key results are presented in Table 1.

The displacement solutions for the two-dimensional and the three-dimensional analyses agreed well. These solutions also agreed with the analytical load-point displacement data. The *J*-integral calculated using the two-dimensional contour integral and the virtual crack-extension (VCE) method both agreed with the analytical data to within a few percent. The approximate *J* estimated from the load versus displacement results, however, yielded data 12% higher than the analytical value. The accuracy of the approximated *J* is improved as the plastic deformation increases. These results are discussed further below.

Inelastic FEM Solutions

Reference *7* also shows the accuracy of the *J*-integral calculation in terms of its path independence for the two-dimensional analysis. Good agreement between the *J*-integral data and the virtual crack-extension data were observed.

TABLE 1—*Verification of the elastic FEM solutions at an elastic loading of P/B = 14 000 lb/in. (250 kg/cm).*

	Reference Equations	Two-Dimensional Plane Strain	% Variance from Reference Equation	Three-Dimensional With Side-Constraint	% Variation from Reference Equation
Load-Point Displacement, in. (cm)	1.770×10^{-3} (4.50×10^{-3})	1.808×10^{-3} (4.59×10^{-3})	+2.15	1.808×10^{-3} (4.59×10^{-3})	+2.15
Crack Mouth Opening Displacement, in. (cm)	1.065×10^{-3} (2.71×10^{-3})	1.053×10^{-3} (2.67×10^{-3})	−1.13	1.087×10^{-3} (2.76×10^{-3})	+2.07
J, lb/in. (kJ/m^2)	5.88 (1.03) $\left(J = \frac{K_1^2}{E'}\right)$	5.77 (1.01)	−1.87	6.623 (1.16) $\left(J = \frac{2W_i}{B(W - a)}\right)$	+12.6

Figure 3 is a plot of the load-versus-load-line displacement for the two-dimensional plane-strain analysis and the three-dimensional analysis. As anticipated, the constrained three-dimensional results are slightly softer than the two-dimensional plane-strain results, but the three-dimensional constrained data are very close to the plane-strain conditions. This result indicates that approximate plane-strain conditions were achieved using the side-constraint technique. On the other hand, the unconstrained three-dimensional results are about 12% lower in load, showing this case is rather close to the two-dimensional plane-stress conditions.

The three-dimensional finite-element data are compared with the contour J and VCE J for the two-dimensional analyses in Figs. 4 and 5. The results in these two figures show that the approximate formula for J for the constrained three-dimensional model agrees well with the rigorous plane-strain J data. Both of these curves agree well with the side-constraint data.

In addition to verifying the side constraint theory using the integral parameters discussed above, the crack tip region stress contour data were also evaluated. A comparison of the stress contour data for the case with side constraint and without indicates that the zone of

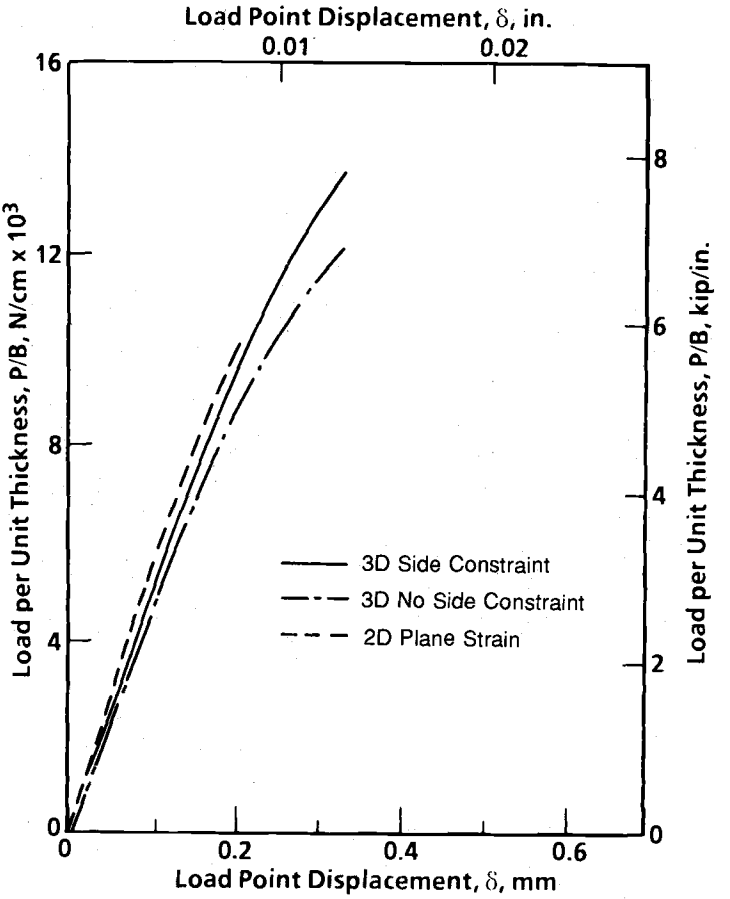

FIG. 3—*Load per unit thickness versus load-point displacement for two- and three-dimensional finite-element analyses.*

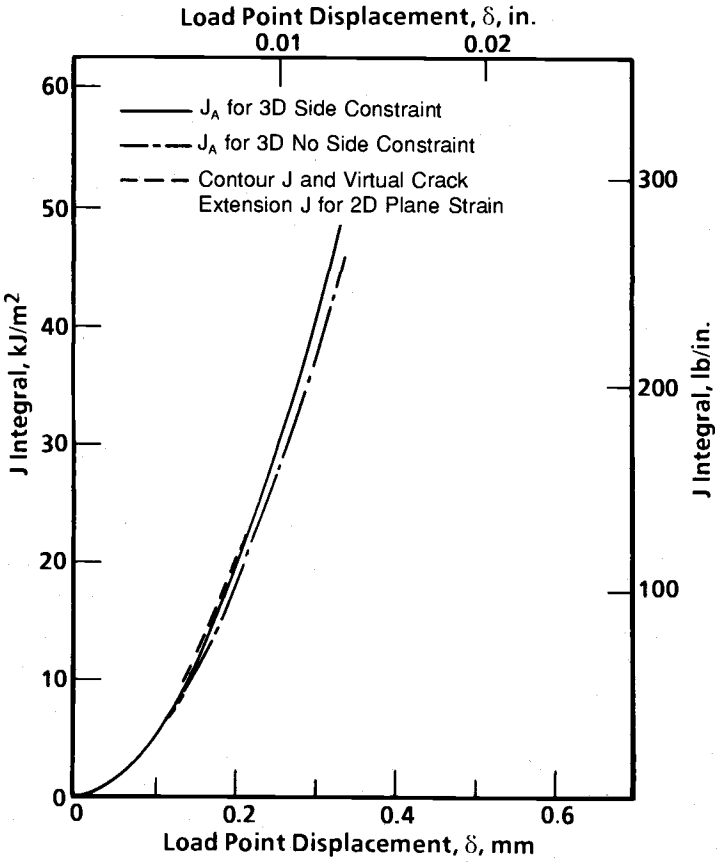

FIG. 4—*J-integral versus load-point displacement for two- and three-dimensional finite-element analyses.*

intense plastic flow in the vicinity of the crack tip is smaller for the side-constraint case. This result is expected since material constraint enhances triaxiality and thus prevents yielding by increasing the hydrostatic stress. This will reduce the plastic zone size [*8*].

Miniaturized Fracture Toughness Experiment

The test results are provided in Table 2 and Fig. 6. The specimens labeled "SC-#" are the side constraint arm tests, and these data are shown in Fig. 6. The specimens labeled "NA-#" are the "no arm" conventional specimen tests, and these data have not been included in Fig. 6 to avoid confusion. The "NA-#" tests fell within the uncertainty bands for the ORNL 0.4T data shown in Fig. 6. As indicated in Table 2, all calculations were performed in accordance with ASTM procedures. Whether ASTM E 813 or ASTM E 399 calculative methodologies were followed, the width of the crack plane (1.02 cm) was used as the specimen thickness in the mechanics equations. All other parameters have their usual definition. The electric potential method was used to detect crack initiation. The probes were attached to the specimen surface on opposite sides of the notch and spaced approximately 0.2 cm from the edge of the notch. Initiation was determined by intersecting the

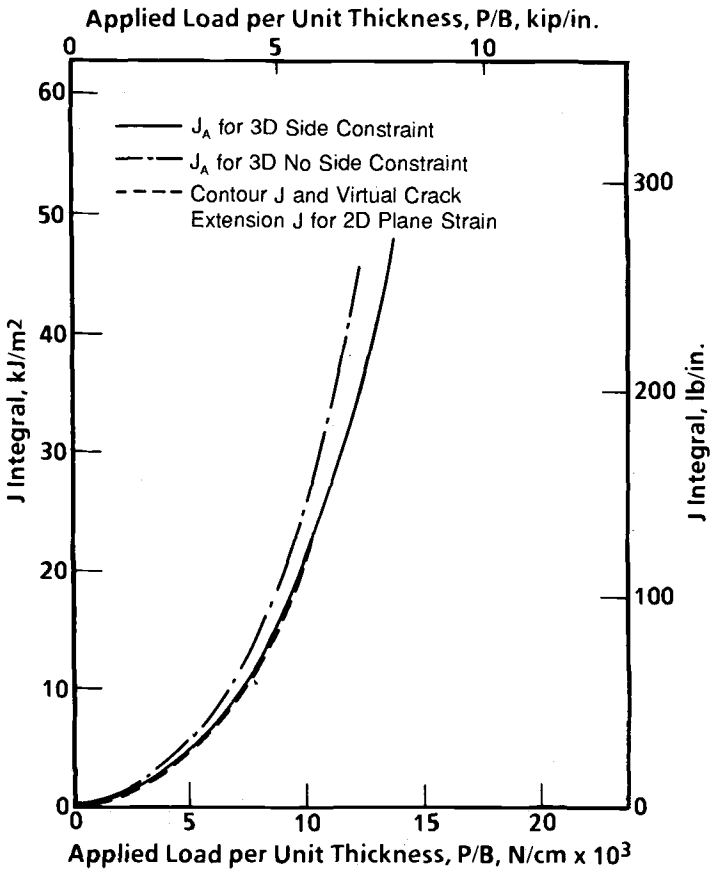

FIG. 5—*J-integral versus applied load per unit thickness for two- and three-dimensional finite-element analyses.*

baseline voltage versus loadline displacement slope with the linear slope associated with crack propagation.

Specimen NA-1 was run first at 80°C. Since ductile tearing was observed, we were concerned that this may be the fracture mode in the thick section material at that temperature. Therefore, a decision was made to run the next tests at 27°C. Specimens NA-2 and SC-3 were run next. Specimen SC-3 came close to satisfying all of the ASTM E 399 requirements. However, when Specimen NA-4 was run and it was discovered that cleavage occurred in this specimen after a very small amount of stable crack growth, we decided that a more conclusive demonstration of the success of the modified stress field approach would be obtained at 55°C. This test temperature was chosen because the specimens of the same thickness without stress field modification clearly yield K_{IC} data which are above the upper scatter band of the full thickness vessel.

Specimen NA-3 was tested at 55°C and exhibited cleavage after a large amount of ductile tearing. Specimen SC-1 was also tested at 55°C and cleavage occurred after a very small amount (0.76 mm) of stable crack growth. This specimen satisfied all of the ASTM E 399 requirements and yielded a K_{IC} value well within the scatter band of the thick section (6T vessel) data. The load versus load-point displacement data from Specimens NA-3 and SC-

TABLE 2—*Modified stress field fracture toughness data summary.*

Specimen ID	Test Temperature, °C (°F)	J_{Ic},[a] kJ/m² (in.-lb/in.²)	K_{Ic},[a] MPa$\sqrt{m}$ (ksi$\sqrt{in.}$)	K_{Ic},[b] MPa$\sqrt{m}$ (ksi$\sqrt{in.}$)	Thickness Requirement B, mm (in.)		ASTM Validity Requirements Satisfied		Fracture Mode	Ductile Crack Length, mm (in.)
					E 813	E 399	E 813	E 399		
NA-2	27 (80)	176.1 (1006)	190 (172.9)	...	5.8 (0.23)	n/a	yes	no	Ductile, terminated by cleavage	~1.6 (~0.064)
NA-4	27 (80)	126.0 (720)	161 (146.5)	...	4.3 (0.17)	...	yes	no	Cleavage after very short ductile crack	~0.5 (~0.02)
SC-3	27 (80)	162.8 (930)	183 (166.6)	88 (80.1)	5.3 (0.21)	40.6 (1.6)	yes	no[c]	Cleavage after short ductile crack	~0.5 (~0.02)
NA-3	55 (130)	266.5 (1523)	235 (213.9)	...	9.1 (0.36)	n/a	yes	no	Ductile terminated by cleavage	~6.4 (~0.25)
NA-5	55 (130)	205.3 (1173)	206 (187.5)	...	7.1 (0.28)	n/a	yes	no	Ductile	Entire ligament
SC-1	55 (130)	n/a	n/a	91 (82.8)	n/a	45.7 (1.8)	n/a	yes	Cleavage after very short ductile crack	~0.8 (~0.03)
SC-2	55 (130)	n/a	n/a	79	n/a	33.02 (1.3)	n/a	no	Cleavage after very short ductile crack	~0.8 (~0.03)
NA-1	80 (175)	249.4 (1425)	226 (205.7)	...	8.9 (0.35)	...	yes	no	Ductile	Entire ligament

[a] Determined in accordance with ASTM E 813 with initiation detected using electric potential.
[b] Determined in accordance with ASTM E 399.
[c] As a result of slippage of the COD gage, the P_{max}/P_Q requirement could not be accurately checked. The equivalent specimen thickness is 0.9 in., which does not satisfy the E 399.

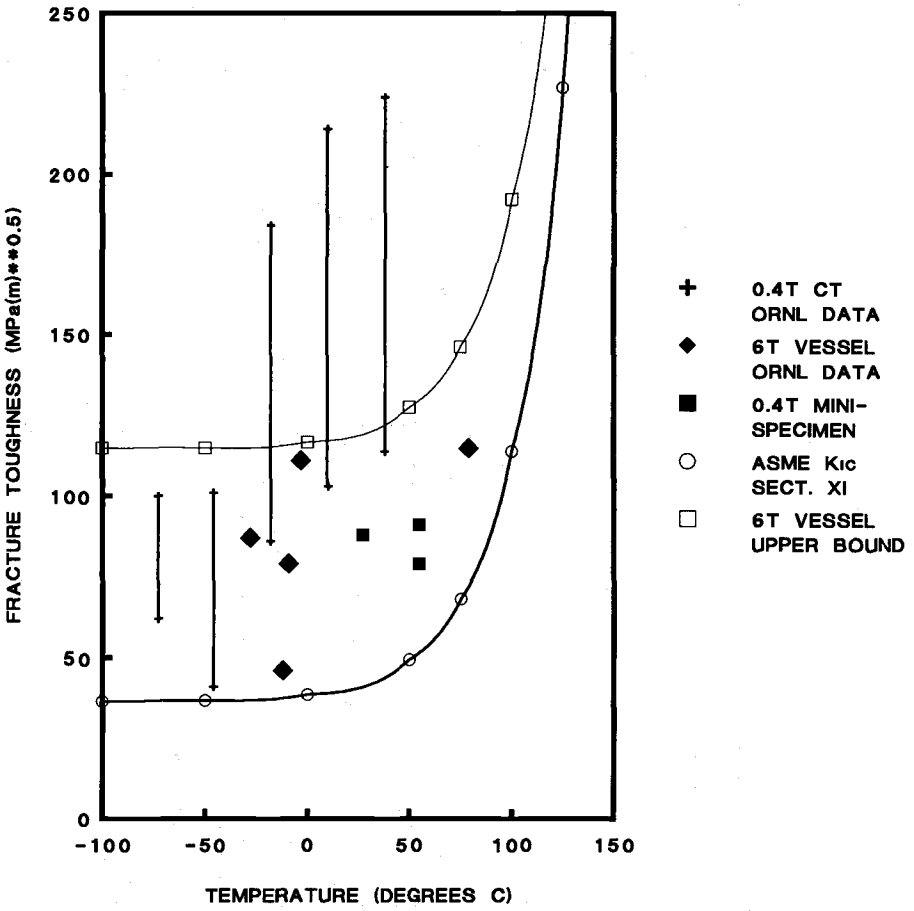

FIG. 6—*Modified stress field data compared with ORNL thick-section test results for TSE-5 and TSE-6 material.*

1 are given in Figs. 7 and 8, respectively. These data demonstrate the efficacy of the stress field modification in producing plane-strain conditions in thin specimens. Reproducibility experiments were conducted at 55°C, as shown in Fig. 6, and Specimen NA-5 yielded a high K_{JC} value and the fracture mode was entirely ductile. Specimen SC-2, like SC-1, exhibited cleavage shortly after peak load. Although this specimen did not satisfy the ASTM E 399 P_{max}/P_Q requirement, the fracture toughness data are consistent with the 6T vessel behavior.

The fracture surfaces of all the specimens tested were examined to verify the mode of fracture. Figure 9 shows the fracture surface for Specimen NA-3. Notice the large amount of stable crack growth which is terminated by cleavage. The fracture surface for the stress field-modified Specimen SC-2, tested at the same temperatures as NA-3, is given in Fig. 10. In this specimen, the fracture surface is almost entirely cleavage fracture, the exception being an initial 0.8 mm of stable crack growth. Thus, Figs. 6 through 10, the data presented in Table 2, and the results from the finite-element analysis, show that the stress field modification approach can yield data comparable to that obtained for thick section behavior (6T vessel). As shown in Fig. 6, the minaturized fracture toughness specimen data are within

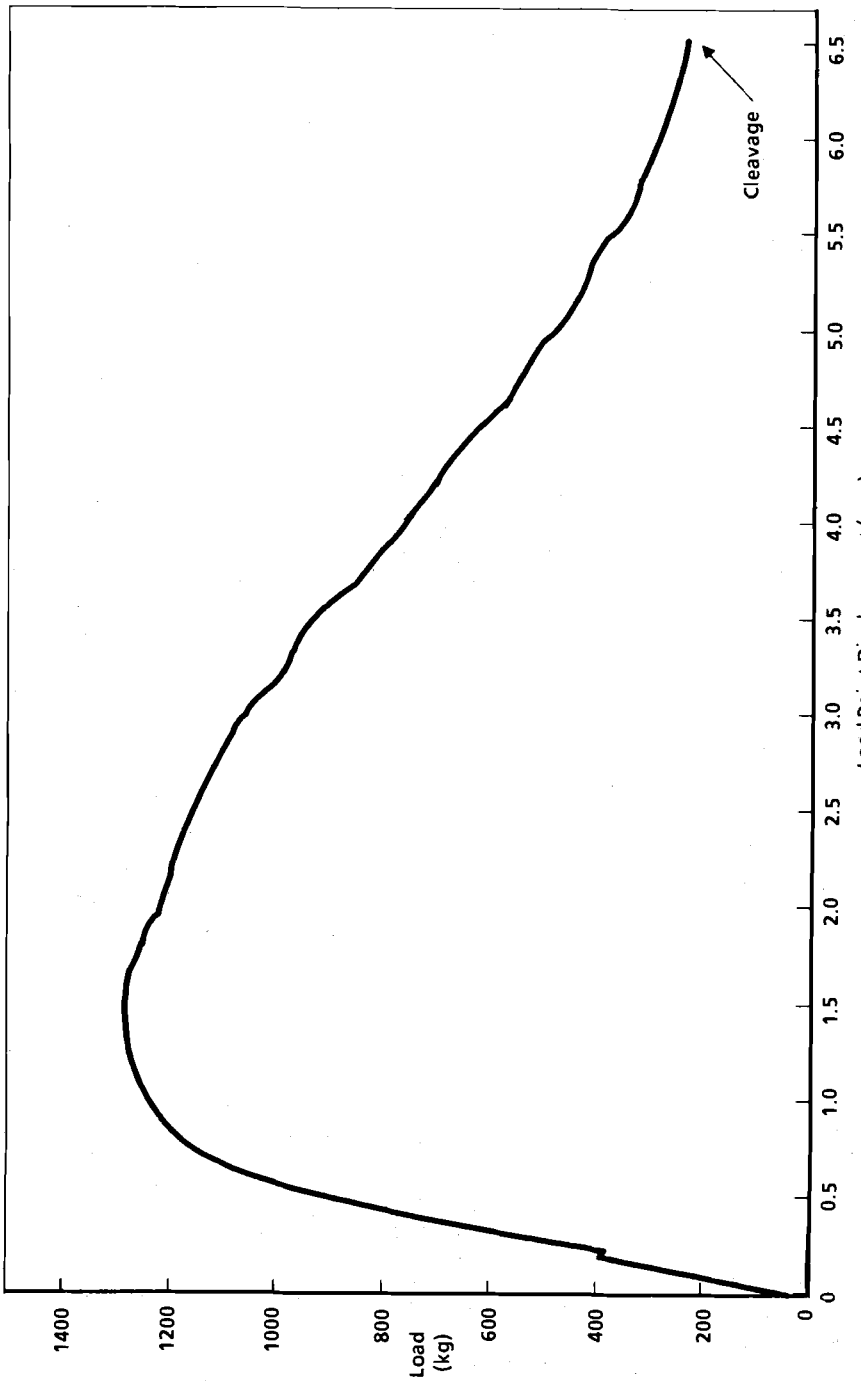

FIG. 7—*Load versus load-point displacement for Specimen NA-3.*

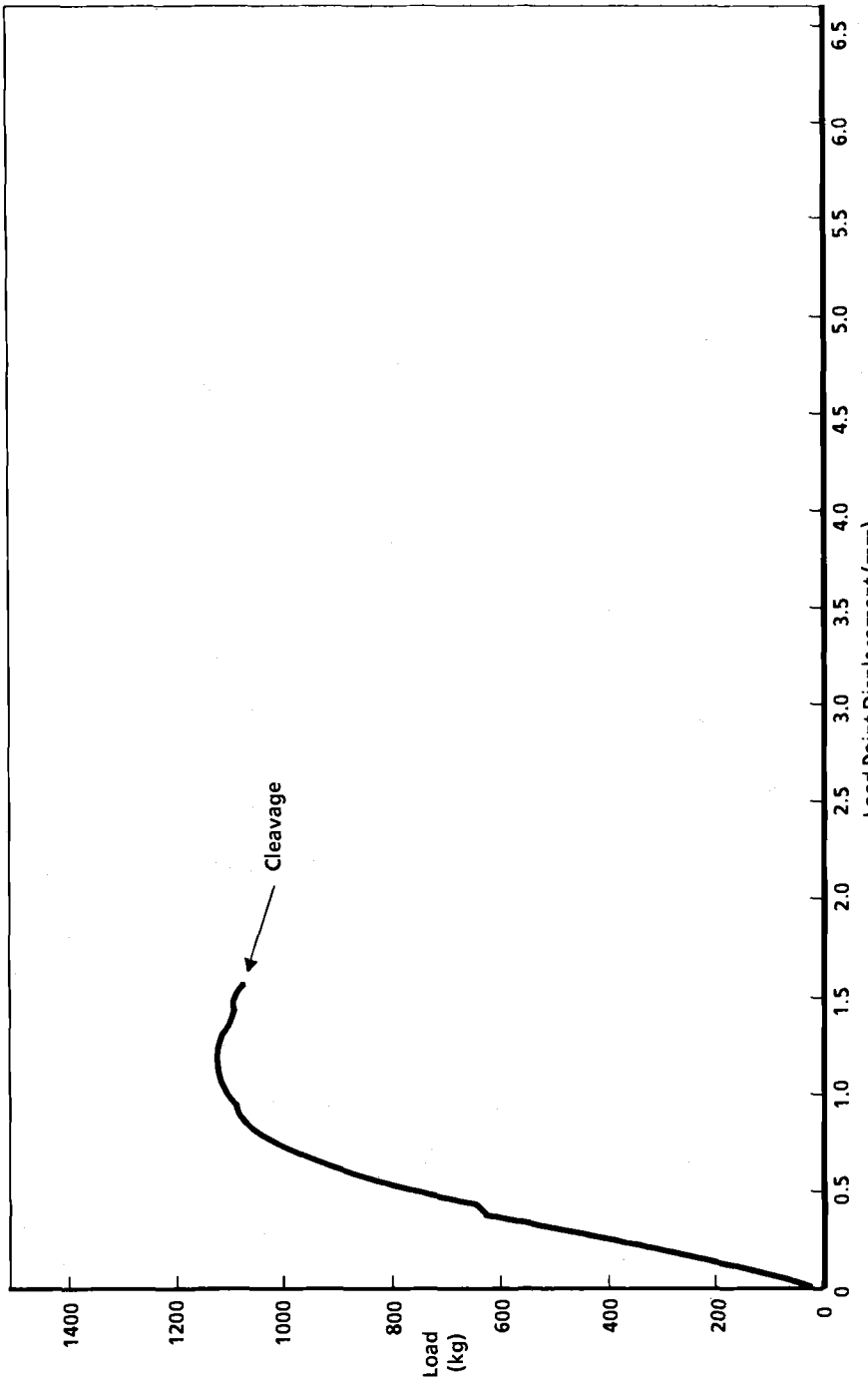

FIG. 8—*Load versus load-point displacement for Specimen SC-1.*

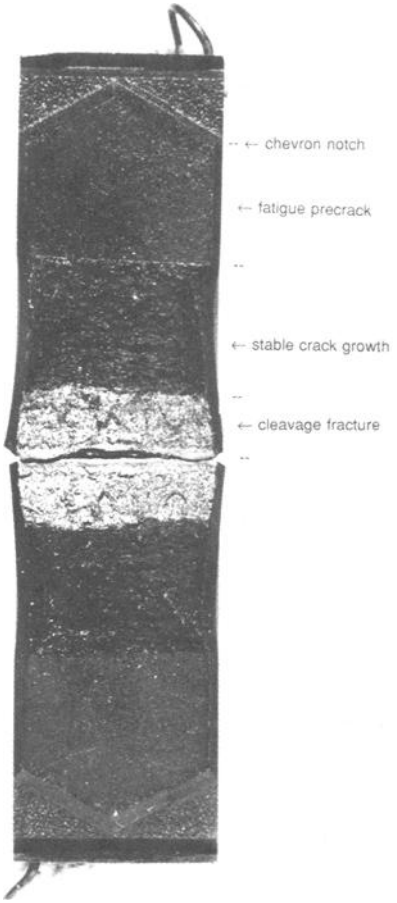

FIG. 9—*Fracture surface for Specimens NA-3 (tested at 55°C) showing predominant ductile fracture (specimen thickness = 1 cm).*

the experimental scatter of the 6T vessel data. Additional testing in the future is needed to fully characterize the uncertainty associated with miniature specimen fracture toughness testing.

Summary and Conclusions

The validity of the modified stress field theory in producing plane strain conditions in very thin specimens has been experimentally and analytically demonstrated for an ASTM A508 pressure vessel steel. The basic concept is that the small zone of intense stress in the vicinity of the crack tip controls initiation. Specimen design can achieve a modification of this field to yield plane-strain behavior in specimens which would otherwise fracture in plane stress. This approach enables testing specimens which are much thinner than those allowed by current test practices.

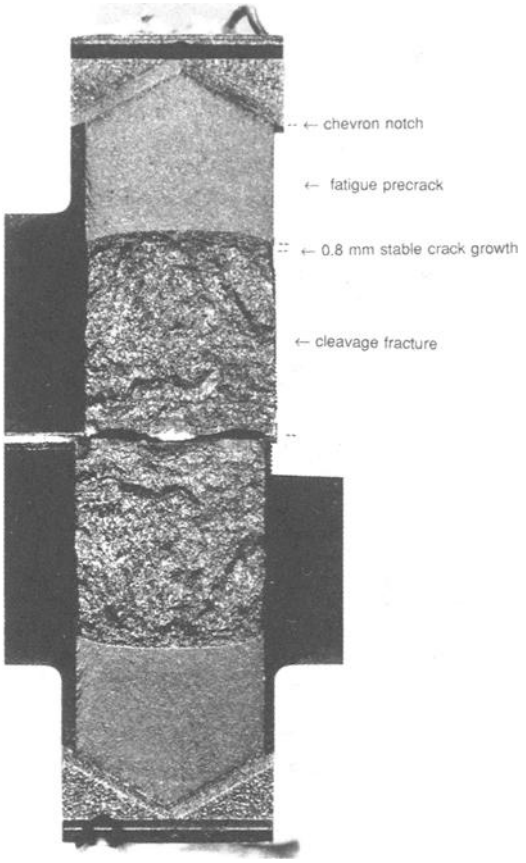

FIG. 10—*Fracture surface for Specimen SC-2 (tested at 55°C) showing predominant brittle fracture (specimen thickness = 1 cm).*

References

[*1*] Manahan, M. P., "A Comparison of Fracture Toughness Data on a Pressure Vessel with the ASME K_{IR} Curve," *Proceedings,* Seventh ASTM-EURATOM Symposium on Reactor Dosimetry, Strasbourg, France, August 1990, to be published in the conference proceedings.

[*2*] Welding Research Council, Bulletin 175, "PVRC Recommendations on Toughness Requirements for Ferritic Materials," WRC, August 1972.

[*2a*] Manahan, M. P., "Miniaturized Dynamic Fracture Toughness Measurement," patent application in preparation, 1992.

[*3*] ASTM Standard E 399, Plane-Strain Fracture Toughness of Metallic Materials, American Society for Testing and Materials, Philadelphia, PA.

[*4*] ASTM Standard E 813, Test Method for J_{IC}, A Measure of Fracture Toughness, American Society for Testing and Materials, Philadelphia, PA.

[*5*] Logsdon, W. A., "Elastic-Plastic (J_{IC}) Fracture Toughness Values: Their Experimental Determination and Comparison with Conventional Linear Elastic (K_{IC}) Fracture Toughness Values for Five Materials," *Mechanics of Crack Growth, STP 590,* American Society for Testing and Materials, Philadelphia, 1976, pp. 43–60.

[6] Manahan, M. P., "Plane-Strain Fracture Toughness Determination Using Stress Field Modified Miniature Specimens," submitted to the *International Journal of Fracture*, 1991.
[7] Manahan, M. P. and Nakagaki, M., "Modified Stress-Field Fracture-Toughness Theory Validation," submitted to the *International Journal of Fracture*, 1991.
[8] Broek, D., *Elementary Engineering Fracture Mechanics*, 4th ed., Martinus Nyhoff Publishers, 1986.

DISCUSSION

T. Sinclair[1] (*written discussion*)—How can you be certain that the welding operation does not lead to a change in toughness value on the specimen surface or lead to an uneven residual stress field in the specimen?

M. Manahan (*author's closure*)—A welding technique should be chosen which does not produce a large heat-affected zone. The laser welding approach has been chosen for further development because the HAZ is highly localized and there are several process parameters which can be adjusted. After welding, light microscopy and microhardness measurements can be made to characterize the extent of the HAZ.

R. Odette[2] (*written discussion*)—Explain how this specimen is different than very deep sidegrooves.

M. Manahan (*author's closure*)—Sidegrooves have been used in the past to constrain fracture to a plane and to straighten the crack front. Sidegrooves are not sufficient to achieve plane strain. The side constraint arms reported in my paper yield plane-strain conditions.

F. M. Haggag[3] (*written discussion*)—What is (if any) the requirement for material choice for use as constraint side arms in your test?

M. Manahan (*author's closure*)—The side constraint arm material must be compatible, in terms of weldability, with the material being tested.

[1] Mechanical Engineering Dept., University of Toronto, Canada.
[2] University of California at Santa Barbara.
[3] Oak Ridge National Laboratory, Oak Ridge, TN.

Novel Bend and Punch Testing Techniques

Masahide Suzuki,[1] *Motokuni Eto,*[1] *Yutaka Nishiyama,*[1]
Kiyoshi Fukaya,[1] *and Takanori Isozaki*[1]

Estimation of Toughness Degradation by Microhardness and Small Punch Tests

REFERENCE: Suzuki, M., Eto, M., Nishiyama, Y., Fukaya, K., and Isozaki, T., **"Estimation of Toughness Degradation by Microhardness and Small Punch Tests,"** *Small Specimen Test Techniques Applied to Nuclear Reactor Vessel Thermal Annealing and Plant Life Extension, ASTM STP 1204,* W. R. Corwin, F. M. Haggag, and W. L. Server, Eds., American Society for Testing and Materials, Philadelphia, 1993, pp. 217–227.

ABSTRACT: Microhardness and small punch (SP) tests were conducted to improve the reliability of evaluating the ductile-to-brittle transition temperature (DBTT) shift caused by aging (thermal aging, neutron irradiation, cold rolling) using several model alloys (Fe-0.15C alloys and 2¼Cr-1Mo steels). Although evaluation of DBTT by the SP test was good overall, intergranular brittleness could not be detected by SP-DBTT measurement only. By combining other measurements like fractographic observation, however, material degradation can be better evaluated.

KEYWORDS: small punch test, Fe-0.15C alloy, 2¼Cr-1Mo steel, DBTT, microhardness, intergranular fracture, neutron irradiation, temper embrittlement, transgranular fracture, fractography

Small specimen techniques are used to evaluate the radiation response of materials for fusion and fission reactors. The latter case arises from the necessity for improving availability of surveillance specimens. However, fracture-related properties like fracture toughness, ductile-to-brittle transition temperature (DBTT), and so on are difficult to measure with small specimens or a limited number of specimens. As these properties are key factors for assessing the structural integrity of nuclear reactor components, it is essential that small specimen techniques for toughness evaluation be developed. Hardness and bulge tests have methodological advantages because they possess a certain flexibility from the standpoint of miniaturization. The former is well known to relate well to tensile strength. As an example of the latter method, the small punch (SP) test is being developed to evaluate fracture-related properties such as the DBTT [*1–7*].

In the SP test, DBTT determination is based on the temperature dependence of an SP-related parameter. The SP energy parameter, which is defined as energy consumed during the test before the onset of macrocracking, is often used. The DBTT determined from the SP test (SP-DBTT) has been shown to correlate well with the DBTT determined from Charpy impact tests [*1–3*]. However, further study is needed to determine its sensitivity in detecting and evaluating degradation corresponding to various material degradation modes.

In the present paper, an improved method of DBTT assessment using SP and microhardness tests is presented.

[1] Japan Atomic Energy Research Institute, Tokai-mura, Ibaraki-ken, 319-11 Japan.

Experimental Procedure

Materials

The materials used in the present experiment were two kinds of Fe-C alloys with different heat treatments (Materials C and D) and two kinds of 2¼Cr-1Mo steels (Material NT: normalized and tempered; Material AN: annealed). Chemical compositions and heat treatments are shown in Tables 1 and 2. Experiments were also conducted using the NT 2¼Cr-1Mo steels in the thermally aged, neutron-irradiated, and cold-worked conditions. Thermal aging was conducted at 723 K for 50 000 h. Neutron irradiation was conducted in the Japan Research Reactor-2 (JRR-2) at 573 K to a fluence of 2×10^{23} n/m^2 ($E > 1$ MeV).

Microhardness and Small Punch Tests

Microhardness tests with a maximum applied load of 0.98 N (100 g_f) were conducted from room temperature to 160 K. During the test, applied load and indentation depth were measured to evaluate additional hardness-related properties described later.

SP tests were performed in the temperature range from 77 to 300 K. Specimens for the SP test were 10 by 10 mm^2 coupons with a 0.5-mm thickness. The SP test method and apparatus are described elsewhere [*4,5*]. A hard steel ball with a 2.4-mm diameter was used for punching. All SP tests were performed at a crosshead speed of 8.3×10^{-3} mm/s.

Results and Discussion

Temperature Dependence of Microhardness-Related Properties

Hardness-related properties can be evaluated well by analyzing the load versus indentation depth relationship [*8*]. For example, the relationship obtained during loading can be expressed as

$$L/d = A_0 + A_1 \cdot d \tag{1}$$

where L is load, d is indentation depth, and A_0 and A_1 are constants. Suzuki et al. showed that the constant A_1 has a linear relationship with yield or tensile strength [*8*]. Although various attempts were made to detect the temperature dependence of a certain microhardness-related parameter which could be correlated with ductile-to-brittle transition behavior, none of these parameters could be correlated with a fracture-related property like DBTT in the present experiment. Figure 1 shows A_1 as a function of test temperature for NT 2¼Cr-1Mo steels in the as-received and 80% cold-worked condition. As the test temperature decreases, A_1 for both materials increased in a similar manner.

TABLE 1—*Chemical composition of the materials used.*

Alloy		C	Si	Mn	P	S	Ni	Cr	Cu	Mo
Fe-0.15C	C	0.144	0.02	<0.01	0.032	0.003	<0.01	<0.01	<0.01	<0.01
Fe-0.15C	D	0.152	0.02	<0.01	0.032	0.003	<0.01	<0.01	<0.01	<0.01
2¼Cr-1Mo	NT	0.14	0.08	0.54	0.009	0.009	0.12	2.36	0.09	1.04
2¼Cr-1Mo	AN	0.13	0.07	0.52	0.009	0.009	0.12	2.32	0.09	1.03

TABLE 2—*Heat treatment conditions of the materials used.*

Designation	Treatment Type	Details
NT	Normalized and tempered	Austenized at 1173/1198 K for 5 h, quenching Tempered at 913/933 K for 6 h, air cooled, PWHT
AN	Annealed	Austenized at 1173/1198 K for 5 h, cooled at a rate of 60 K/h, PWHT[a]
C	Annealed	Austenized at 1153 K for 1 h, 100 K/h furnace cooling
D	Quenched and tempered	Austenized at 1153 K for 1 h, water quenching, tempered at 913 K for 1 h, air cooling

[a] 950/963 K for 22 h.

Temperature Dependence of SP-Related Properties

Figure 2 shows SP-related properties (SP_{energy}, δ^*, P_{max}) of the Fe-0.15C alloys (Materials C and D) as a function of test temperature. Here, δ^* is the maximum deflection at the onset of macrocracking, and P_{max} is the maximum load during the test (for a detailed definition, see Ref 5). P_{max} is normalized by t_0^2 (t_0 is the initial specimen thickness). As the test temperature decreases, all these SP-related values show a sudden decrease at a certain temperature. This temperature is thought to correspond to the point where ductile-to-brittle transition occurs. There is no difference in temperature at the point where this sudden drop occurs among these properties. Therefore, as maximum load can be measured most easily and with less scatter, P_{max} was used here as the parameter to determine DBTT.

Factors Affecting the Temperature Dependence of P_{max}

Effect of Microstructure—Differences in microstructure can give rise to clear differences in the P_{max} versus test temperature relationship. In Fig. 2, a clear difference is seen for Fe-0.15C alloys having a different microstructure (Materials C and D), where the microstructure

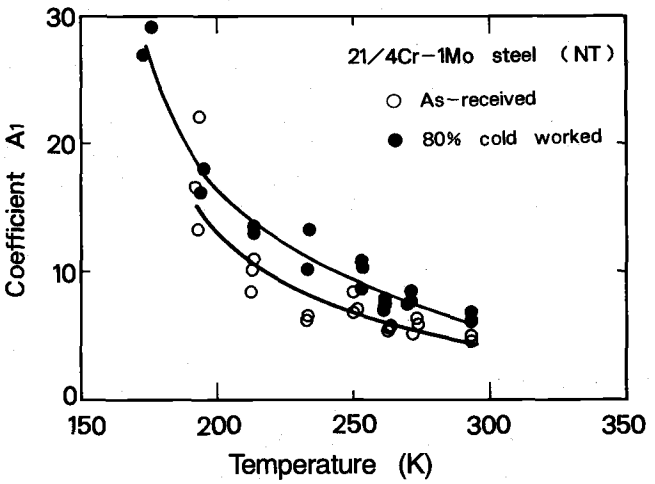

FIG. 1—*Microhardness-related property (coefficient* A_1*) as a function of test temperature for the NT 2¼Cr-1Mo steel, as-received and 80% cold worked.*

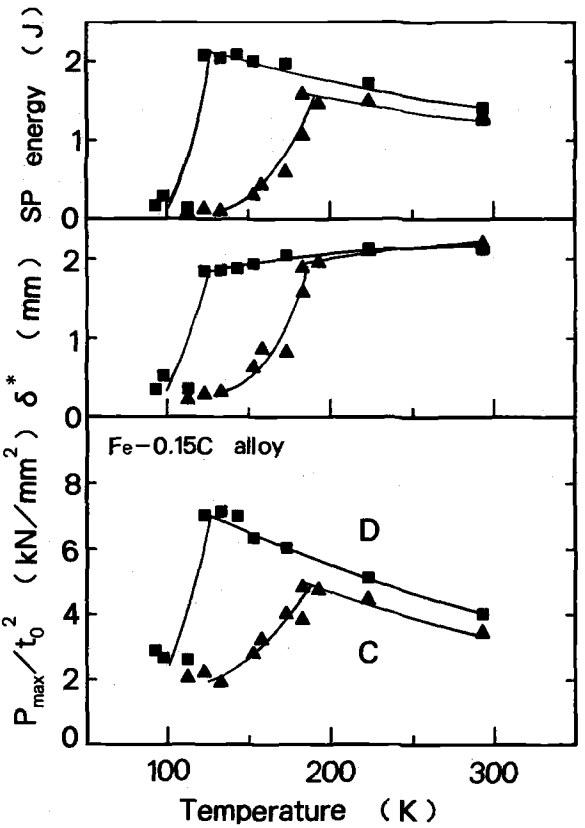

FIG. 2—*SP-related properties (SP_{energy}, δ*, and P_{max}) as a function of test temperature.*

is ferrite plus pearlite for Material C and bainite for Material D. Another example is also seen in Fig. 3, where P_{max} versus test temperature for the 2¼Cr-1Mo steels having different heat treatments is shown. The microstructure is ferrite plus pearlite for Material AN (annealed) and bainite with a small amount of proeutectoid ferrite for material NT (normalized and tempered). Consequently, SP-DBTT is also very sensitive to microstructure. Figure 4 shows the relationship between SP-DBTT and Charpy DBTT. The former is tentatively determined to be a temperature corresponding to half the maximum P_{max}, and the latter is evaluated in terms of 68 J absorbed energy. SP-DBTT is often correlated with Charpy DBTT by the following equation

$$\text{SP-DBTT} = \alpha * \text{Charpy DBTT} \tag{2}$$

where α is the correlation coefficient.

Using the materials with different microstructures (ferrite, pearlite), an α of approximately 0.4 was obtained.

Effect of Hardening (Cold Rolling and Neutron Irradiation)—In general, the shift of DBTT caused by hardening can be explained by the so-called Ludwig-Davidenkov relationship [*9*]; the relationship predicts that an increase in yield stress from fabrication history or radiation hardening results in a DBTT shift. In Fig. 5, P_{max}/t_0^2 is shown as a function of test temperature

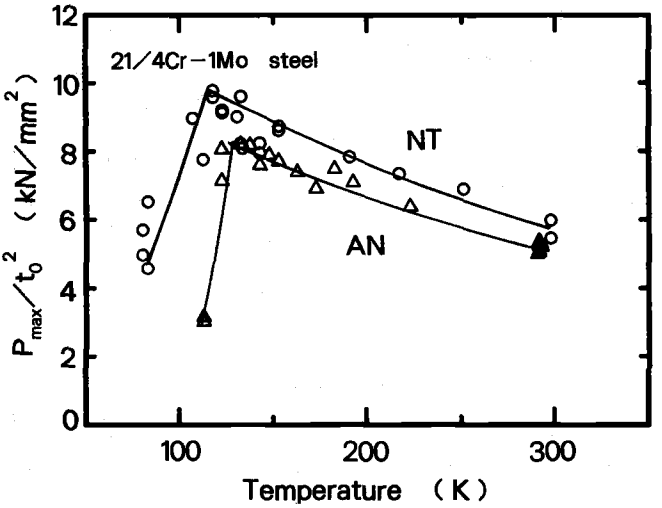

FIG. 3—P_{max}/t_0^2 *as a function of the SP test temperature for the NT and AN 2¼Cr-1Mo steels.*

for NT 2¼Cr-1Mo steels in the as-received, 20% cold-worked, and 50% cold-worked condition. The temperature at which P_{max} showed a sudden drop was more than 50 K higher for the 50% cold-worked material. (SP-DBTT in terms of half the maximum P_{max} could not be determined owing to the unusual temperature dependence of this material, i.e., P_{max} did not reach half the maximum P_{max}.) An interesting feature of the temperature dependence of P_{max} for cold-worked materials is that the difference in P_{max} among materials becomes less as temperature decreases. That is, $\Delta P_{max} = P_{max}$ (cold-worked) $- P_{max}$ (as-received) is largest at room temperature and tends to be very small as the SP test temperature decreases.

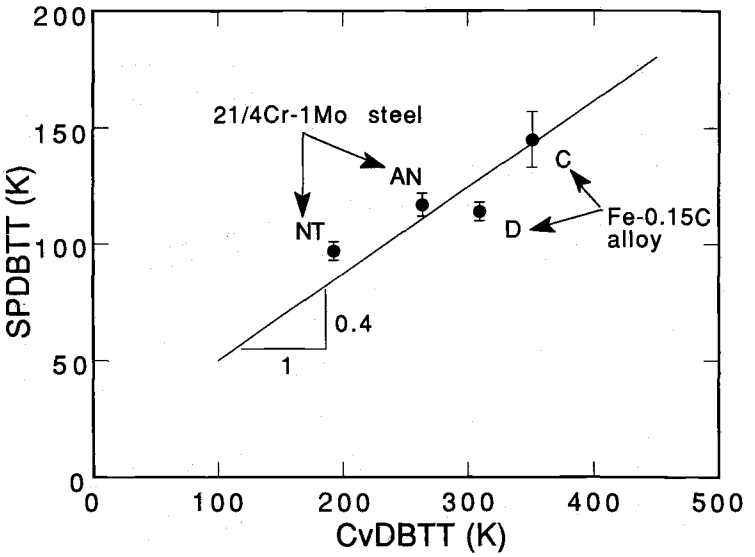

FIG. 4—*The relationship between SP DBTT and Charpy DBTT for 2¼Cr-1Mo steels and Fe-0.15C alloys.*

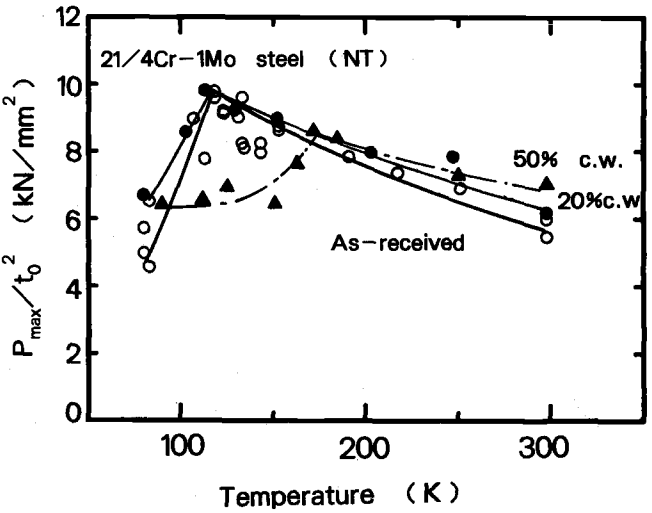

FIG. 5—P_{max}/t_0^2 *as a function of the SP test temperature for the NT 2¼Cr-1Mo steels after 20 and 50% cold working.*

This tendency also holds true for neutron-irradiated materials as shown in Fig. 6, where P_{max} for the NT 2¼Cr-1Mo steel before and after irradiation is shown as a function of test temperature. This tendency is in clear contrast to the case where two materials have different microstructure as a result of different heat treatments, where, for example, $\Delta P_{max} = P_{max}(NT) - P_{max}(AN)$ is almost constant over the entire temperature range down to the low temperature (see Figs. 2 and 3).

Effect of Intergranular Brittleness—The DBTT also increases as a result of intergranular brittleness. A typical example of this case is temper embrittlement, which is seen in low-

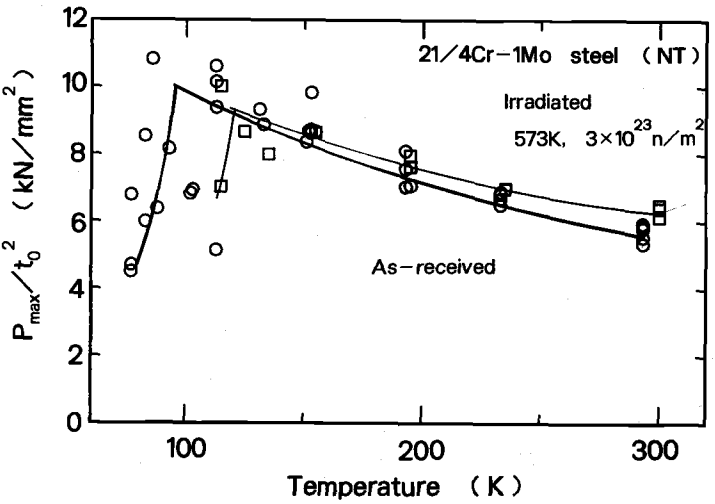

FIG. 6—P_{max}/t_0^2 *as a function of the SP test temperature for the NT 2¼Cr-1Mo steel before and after neutron irradiation at 573 K to the fluence of* 3×10^{23} *n/m*^{2} (E > 1 *MeV).*

TABLE 3—*Charpy-related properties of the NT 2¼Cr-1Mo steel before and after 50 000 h aging at 723 K.*

NT 2¼Cr-1Mo	Charpy-Related Properties		
	vTr_{50}, K[a]	FATT, K[b]	FIF, %[c]
As received	193	215	0
723 K × 50 000 h aged	234	273	22

[a] 68 J absorbed energy transition temperature.
[b] 50% fibrosity transition temperature.
[c] Fraction of intergranular fracture at lower shelf region.

alloy steels when they are exposed to the temperature range from ~673 to ~823 K. NT 2¼Cr-1Mo steel also becomes temper embrittled after long-term thermal aging. Table 3 shows the DBTT measured by 68 J absorbed energy, fracture appearance transition temperature (FATT), and the fraction of intergranular fracture for NT 2¼Cr-1Mo steel tested by Charpy impact testing before and after 50 000 h thermal aging. After 50 000 h of thermal aging at 723 K, the DBTT increased about 40 K, and this shift is accompanied by an increase in the fraction of intergranular fracture. In Fig. 7, P_{max} is shown as a function of test temperature for the as-received and thermally aged material. It should be noted that, despite the fact that the Charpy DBTT increased, there was no clear difference in SP-related properties. Hence, the SP test alone can fail to detect the material degradation caused by intergranular brittleness.

Observation of Fracture Surface for SP Specimen—The fracture surface of the SP specimens was observed by scanning electron microscopy (SEM). It was ascertained that as the test temperature decreased, the fracture mode changed from the ductile fracture to the brittle fracture mode. Figure 8 shows the fraction of ductile fracture as a function of test temperature for materials already described. The temperature dependence of the fraction of ductile fracture is coincident with that of P_{max}. This fact means that degradation of NT 2¼Cr-1Mo steels caused by thermal aging (723 K × 50 000 h) could not be detected using this parameter,

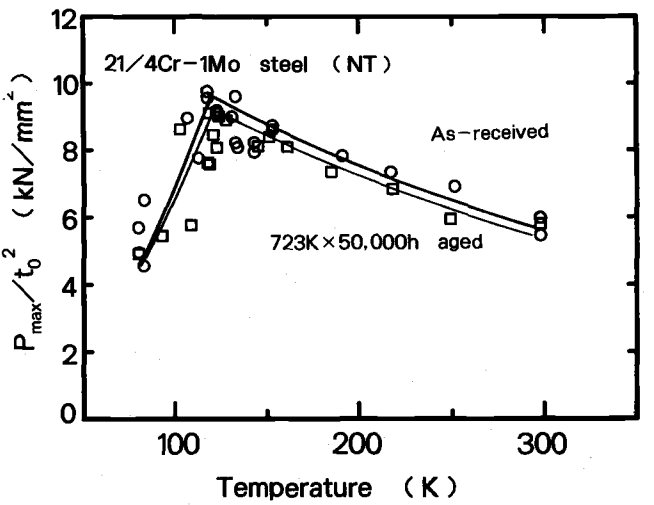

FIG. 7—P_{max}/t_0^2 *as a function of the SP test temperature for the NT 2¼Cr-1Mo steel before and after thermal aging at 723 K for 50 000 h.*

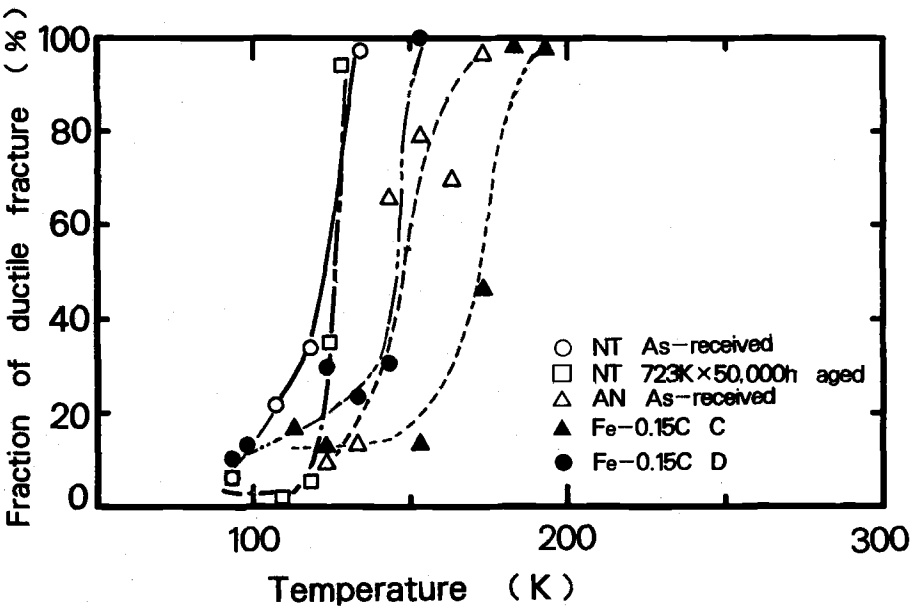

FIG. 8—*Fraction of the ductile fracture as a function of the SP test temperature for 2¼Cr-1Mo steels and Fe-0.15C alloys.*

either. However, from careful observation, the point where the fraction of ductile fracture begins to increase was higher for the aged material. Furthermore, in the fractographic examination, it was observed that the fracture appearance was greatly changed in this temperature region. Figure 9 shows the scanning electron micrographs of the SP specimen after testing (Fig. 9*A*) and its typical fracture surface appearance (Figs. 9*B* through 9*D*) for the NT 2¼Cr-1Mo steel after thermal aging (723 K × 50 000 h) at a test temperature of 118 K (transition region). As shown in Figs. 9*B* through 9*D*, intergranular fracture was clearly seen for this material. By contrast, only a small fraction of intergranular fracture was observed in the as-received material. Fracture appearance is summarized in Fig. 10 for NT 2¼Cr-1Mo steels before and after thermal aging. Here, the fractions of intergranular (IG), transgranular cleavage (C), and ductile (D) fracture were determined based on about 10 to 20 SEM photographs taken at a magnification of × 1000. The fraction of occurrence of intergranular fracture was larger than that of the corresponding Charpy specimens, possibly due to the biaxial stress state in the SP specimen.

Reliable Detection of Material Degradation by SP Tests

Although a clear relationship is seen between Charpy DBTT and SP-DBTT from experiments using materials of different microstructures, whether this correlation is valid for evaluating material degradation is still open to question. Deformation behavior during the SP test can be divided into four regions [*1*]: I. elastic bending, II. plastic bending, III. plastic membrane stretching, and IV. plastic instability. As test temperature decreases, the region at which fracture occurs changes from Region IV to Region II via Region III. Material degradation can affect the balance among these deformation regions. One example was shown in the temperature dependence of P_{max}. P_{max} is constituted by four components corresponding to the four deformation modes

$$P_{max} = P_{I} + P_{II} + P_{III} + P_{IV} \quad (3)$$

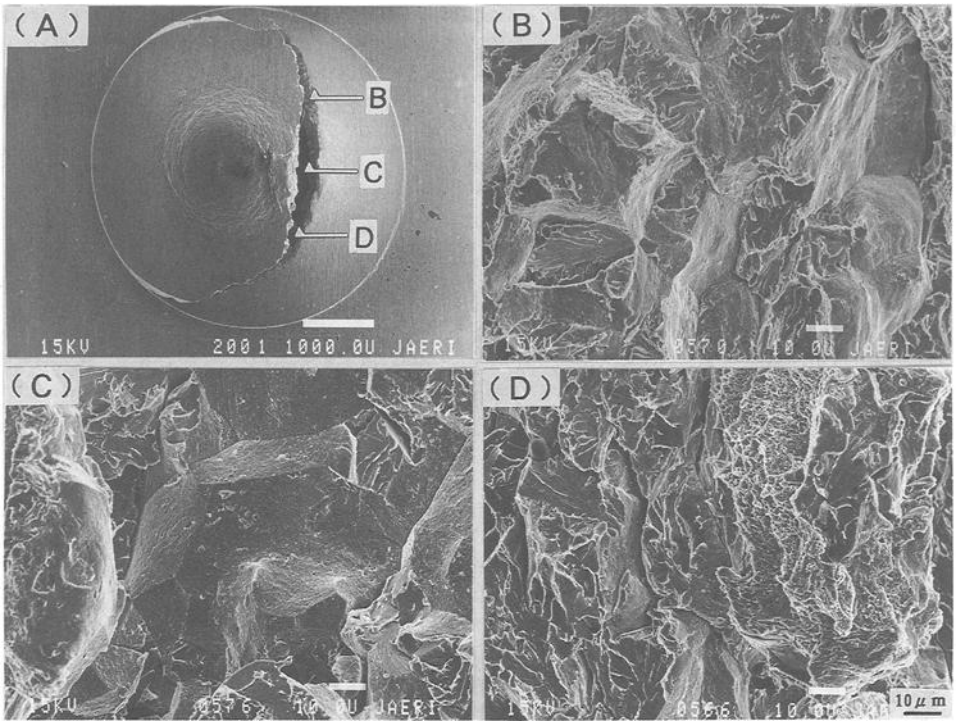

FIG. 9—*Scanning electron micrographs of the SP specimen after the test* (A) *and its typical fracture surface, corresponding to location* B, C, *and* D (B-D) *for 2¼Cr-1Mo steel thermally aged at 723 K for 50 000 h. The SP test was conducted at 118 K.*

Although hardened material showed larger P_{I}, as cold working or neutron irradiation reduces plasticity (elongation), reductions in the constituents of P_{II}, P_{III}, or P_{IV} make the total increment (ΔP_{max}) smaller as the temperature lowers (it can be negative). It is apparent that there will be no clear relationship between P_{max} in the SP test and ultimate tensile strength in the tension test when the entire test temperature region is considered. Therefore, for

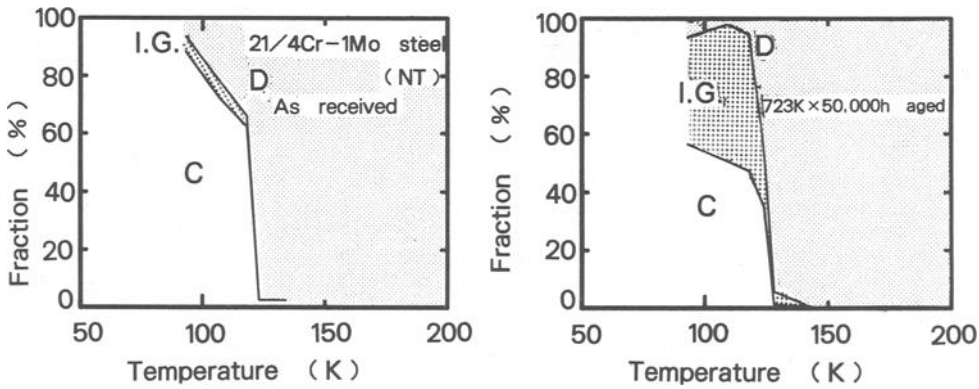

FIG. 10—*Fraction of intergranular, transgranular cleavage, and ductile fracture in the SP fracture surface as a function of SP test temperature for NT 2¼Cr-1Mo steel before and after thermal aging at 723 K for 50 000 h.*

obtaining tensile-related properties, hardness still possesses an advantage over the SP test. Likewise, for tensile properties, the SP-Charpy DBTT correlation has limitations. As shown for thermal-aged NT 2¼Cr-1Mo steel, mere execution of the SP test could not detect the DBTT shift. Fractographic observation was absolutely necessary, by which the change of the fracture mode could be detected. However, the fact that neutron irradiation or hardening-induced DBTT shifts can be detected by the SP test is encouraging for the application of the SP test to the material degradation evaluation in nuclear reactor components. Reliability in DBTT determination could improve by incorporating a statistical analysis [*10*].

Conclusion

Microhardness and SP tests were conducted to improve the reliability of evaluating the DBTT shift caused by aging or irradiation. Several model alloys were used (Fe-0.15C alloys and 2¼Cr-1Mo steels), and one also received thermal aging, neutron irradiation, and cold-working treatments. The principal conclusions are:

1. The maximum load during the SP test (P_{max}) can be used as a parameter to determine the DBTT.
2. The SP-DBTT is sensitive to microstructural change (ferrite, pearlite). In this case, the SP-DBTT–Charpy DBTT correlation coefficient is about 0.4.
3. The SP-DBTT shift owing to hardening (cold working and neutron irradiation) can be detected by the temperature dependence of P_{max}, although $\Delta P_{max} = P_{max}$ (cold-worked or irradiated) $- P_{max}$ (as received) is largest at room temperature and tends to be very small as the SP test temperature decreases.
4. Temper embrittlement of 2¼Cr-1Mo steel could not be detected by SP-DBTT measurement. In this case, fractographic observation revealed a change of fracture mode from transgranular to intergranular type.
5. Microhardness-related parameters could not be correlated with ductile-to-brittle transition behavior. However, it is still useful in assessing material degradation because it possesses an advantage for obtaining tensile-related properties over the SP test in the entire temperature region.

Acknowledgments

The authors would like to express their sincere gratitude to Professors H. Takahashi of Tohoku University and T. Misawa of the Muroran Institute of Technology for valuable advice. Dr. S. Jitsukawa of JAERI is also acknowledged for valuable discussion and comments.

References

[*1*] Baik, J. M., Kameda, J., and Buck, O., "Development of Small Punch Tests for Ductile-Brittle Transition Temperature Measurement of Temper-Embrittled Ni-Cr Steels," *The Use of Small Scale Specimens for Testing Irradiated Materials, ASTM STP 888,* W. R. Corwin and G. E. Lucas, Eds., American Society for Testing and Materials, Philadelphia, 1986, pp. 92–111.

[*2*] Misawa, T., Adachi, T., Saito, M., and Hamaguchi, Y., "Small Punch Tests for Evaluating Ductile-Brittle Transition Behavior of Irradiated Ferritic Steels," *Journal of Nuclear Materials,* Vol. 150, 1987, pp. 194–202.

[*3*] Matsushita, T., Saucedo, M. L., Yotsutsuji, M., Shoji, T., and Takahashi, H., "Correlation between a Charpy V-Notch Impact Test and a Small Punch Test in Ductile-Brittle Fracture Mode Transition Behavior," *Transactions, Japan Society of Mechanical Engineers,* Vol. 55–515, 1989, pp. 1619–1622 (in Japanese).

[4] Mao, X., Shoji, T., and Takahashi, H., "Characterization of Fracture Behavior in Small Punch Test by Combined Recrystallization-Etch Method and Rigid Plastic Analysis," *Journal of Testing and Evaluation*, Vol. 15, 1987, pp. 30–37.

[5] Takahashi, H., Shoji, T., Mao, X., Hamaguchi, Y., Misawa, T., Saito, M., Oku, T., Kodaira, T., Fukaya, K., Nishi, H., and Suzuki, M., "Recommended Practice for Small Punch (SP) Testing of Metallic Materials," Draft, JAERI-M Report 88–172, 1988.

[6] Suzuki, M., Eto, M., Fukaya, K., Nishiyama, Y., Kodaira, T., Oku, T., Adachi, M., Umino, U., Takahashi, I., Misawa, T., and Hamaguchi, Y., "Evaluation of Toughness Degradation by Small Punch (SP) Tests for Neutron Irradiated 2¼Cr-1Mo Steel," *Journal of Nuclear Materials*, Vol. 179–181, 1991, pp. 441–444.

[7] Suzuki, M., Eto, M., Nishiyama, Y., Fukaya, K., Saito, M., and Misawa, T., *Journal of Nuclear Materials*, Vol. 191–194, 1992, pp. 1023–1027.

[8] Inamura, M. and Suzuki, T., in *Seisan-kenkyu*, Vol. 42, No. 257, 1990 (in Japanese).

[9] Finnie, I. and Mayville, R. A., "Historical Aspects in Our Understanding of the Ductile-Brittle Transition in Steels," *Transactions of the ASME*, American Society of Mechanical Engineers, Vol. 112, January 1990, pp. 56–60.

[10] Misawa, T., Suzuki, K., Saito, M., and Hamaguchi, Y., "Determination of the Minimum Quantity of Irradiated Ferritic Steel Specimens for Small Punch DBTT Testing," *Journal of Nuclear Materials*, Vol. 179–181, 1991, pp. 421–424.

Takeo Iwai,[1] *Hiroshi Kawanishi,*[1] *Yoshio Arai,*[1] *Yoshiaki Kato,*[1] *Naoto Sekimura,*[2] *and Shiori Ishino*[1]

Hardening Characteristics of Ion-Irradiated Iron-Based Model Alloys

REFERENCE: Iwai, T., Kawanishi, H., Arai, Y., Kato, Y., Sekimura, N., and Ishino, S., **"Hardening Characteristics of Ion-Irradiated Iron-Based Model Alloys,"** *Small Specimen Test Techniques Applied to Nuclear Reactor Vessel Thermal Annealing and Plant Life Extension, ASTM STP 1204,* W. R. Corwin, F. M. Haggag, and W. L. Server, Eds., American Society for Testing and Materials, Philadelphia, 1993, pp. 228–240.

ABSTRACT: Fe-C-Cu, Fe-C-Ni, and Fe-C-Cu-Ni model alloys were prepared in order to investigate the effects of copper and nickel on radiation embrittlement. They were irradiated with 4 MeV Ni^{3+} ions at 563 K to introduce displacement damage, followed by a micro-Vickers hardness test employing low load (0.5 g). It was observed that greater hardening occurred for samples of larger copper content, and that hardening of the samples containing both copper and nickel was greater than hardening of the ones containing copper or nickel solely for samples irradiated to 10^{-2} and 10^{-1} dpa. Increased hardness after annealing occurred for Fe-0.1C-0.2Cu and Fe-0.1C-0.4Cu. Small defect clusters of approximately 3 nm in diameter were observed by transmission electron microscopy (TEM) of the irradiated Fe-0.1C and Fe-0.1C-0.4Cu samples, which cause hardening.

KEYWORDS: radiation hardening, heavy ion irradiation, micro-Vickers hardness test, isochronal annealing, defect clusters

The nuclear reactor pressure vessel (RPV) is the most important component for evaluation of plant life because it needs complete integrity. It is well known that low-alloy steels for RPVs are embrittled by neutron irradiation, and it is necessary for the estimation of plant life to predict embrittlement accurately. Nowadays, empirical methods are employed for the evaluation of embrittlement, but mechanistic modeling is needed for the prediction of embrittlement after several decades of irradiation, for which no empirical data are available. It is also needed for estimating how long recently improved materials will be safely usable. However, mechanisms of embrittlement are not well understood. Data analyses of mechanical property tests after the surveillance and material test reactor (MTR) irradiations have revealed that a residual level of copper enhances embrittlement [*1,2*]. It is known that nickel, which is an alloying element of RPV steels, has an effect on embrittlement [*1,3*]. Various microanalytical methods such as transmission electron microscopy (TEM), positron annihilation (PA), small angle neutron scattering (SANS), and atom probe field ion microscopy (APFIM) have been applied to the study of embrittlement mechanisms [*4*]. Production of copper-rich precipitates and matrix defects have been reported as dominant

[1] Department of Quantum Engineering and Systems Science, University of Tokyo, 7-3-1 Hongo, Bunkyo-ku, Tokyo 113, Japan.
[2] Nuclear Engineering Research Laboratory, University of Tokyo, Tokai-mura, Naka-gun, Ibaraki-ken, 319-11, Japan.

mechanisms from these methods [*1*,*4*], and more study is required to obtain knowledge about their nature and the processes of their formation, growth, and annihilation.

Radiation embrittlement of nuclear reactor pressure vessel steels is a function of many factors such as neutron fluence, neutron flux, neutron energy spectrum, irradiation temperature, chemical composition, microstructure, etc. Irradiation experiments in which these factors are separated are desirable for better understanding of the mechanisms. However, it is difficult to separate these factors due to the complexity of the chemical composition of steels and the difficulty in neutron irradiation at different fluxes under the same spectrum. We think that ion irradiation has the advantage of relatively easy control of irradiation conditions such as damage rate and irradiation temperature and that it is useful for the fundamental study of radiation embrittlement. Low radioactivity of ion-irradiated samples is another advantage, which makes handling of the specimens easy. So we applied ion irradiation to the study of embrittlement mechanisms. Fe-C-Cu, Fe-C-Ni, and Fe-C-Cu-Ni model alloys were prepared in order to simplify the effect of the elements of copper and nickel. In this study, irradiation was carried out with varied fluence and fixed flux and temperature as the first stage of experiments.

Experimental

In this study we used micro-Vickers hardness as a measure which gives information on internal phenomena. Because the damaged region of samples irradiated with energetic heavy ions is limited to a thin surface layer, low load (0.5 g) was employed so that the diamond indentor does not penetrate too deeply. According to previous studies [*5*], the shift of ductile-brittle transition temperature (DBTT) caused by neutron irradiation is generally proportional to the hardness increase. Therefore, it is important to investigate the hardening mechanisms using microstructural and microchemical methods. We attempted to apply TEM techniques to interpreting the hardness data.

Model Alloys

The chemical compositions of the model alloys investigated in this study are shown in Table 1. It is well known that carbon has a great effect on vacancy mobility in iron. Therefore, it is probable for carbon to have an effect on embrittlement of RPV. So we added copper and/or nickel to Fe-0.1 wt%C (Fe-0.1C). The copper contents were 0.1, 0.2, and 0.4 wt%

TABLE 1—*Chemical compositions (wt%) of the model alloys investigated.*

	C	Cu	Ni	O, ppm
Fe	<0.01	<0.01	<0.01	24
Fe-0.1C	0.10	<0.01	<0.01	7
Fe-0.1C-0.1Cu	0.09	0.11	<0.01	8
Fe-0.1C-0.2Cu	0.10	0.20	<0.01	8
Fe-0.1C-0.4Cu	0.10	0.38	<0.01	6
Fe-0.1C-0.7Ni	0.11	<0.01	0.72	9
Fe-0.1C-0.1Cu-0.7Ni	0.09	0.11	0.72	10

NOTE: Fe = balance; other elements: Si, Mn, Cr, Mo, V < 0.01; P, S, Sn, As < 0.003; Al, Ti, Nb, Co < 0.005.

(Fe-0.1C-0.1Cu, Fe-0.1C-0.2Cu, and Fe-0.1C-0.4Cu, respectively). Nickel of 0.7 wt% was added to Fe-0.1C and Fe-0.1C-0.1Cu (Fe-0.1C-0.7Ni and Fe-0.1C-0.1Cu-0.7Ni, respectively). Model alloys are called in their nominal value of chemical composition below.

All the model alloys were melted by high frequency induction heating in vacuum, hot-rolled, and then cold-rolled to 0.2 mm in thickness. The final reduction ratio is 2.5 for each alloy. They were mechanically polished, punched out in the form of TEM disks 3 mm in diameter, annealed in vacuum using recrystallization annealing of 1130 K-0.5h followed by solution annealing of 1023 K-1h, and then furnace cooled. Each of them except Fe has ferrite-pearlite structure, and the grain size of ferrite was 10 to 50 μm. They were electropolished finally using a 900 mL acetic acid-100 mL perchloric acid-0.5 g chromium trioxide (CrO_3) electrolyte.

Ion Irradiation

In order to introduce displacement damage, the specimens mentioned above were irradiated with Ni^{3+} ions, which were accelerated to 4 MeV by the Tandetron accelerator at the High Fluence Irradiation Facility, University of Tokyo (HIT Facility). Ion flux and irradiation temperature were fixed, and irradiation time was varied in the range of 10 to 10^4 s. Irradiation temperature was kept at 563 K, which is the normal temperature for RPV steels in service. According to the damage profile calculated by the EDEP-1 code [*6*], the damaged layer is about 1 μm thick and the damage peak is 0.8 μm deep from the surface (Fig. 1). Displacement per atom (dpa) at the damage peak is used as a scaling parameter for the irradiation dose. The damage rate at the damage peak is controlled to have a value of 10^{-4} dpa/s in this case, greater by seven orders of magnitude than that in RPVs. This can make the radiation-induced change enhanced or suppressed by the accelerated irradiation [*7*]. Specimens were irradiated to 0.001, 0.01, 0.1, and 1 dpa at the damage peak in order

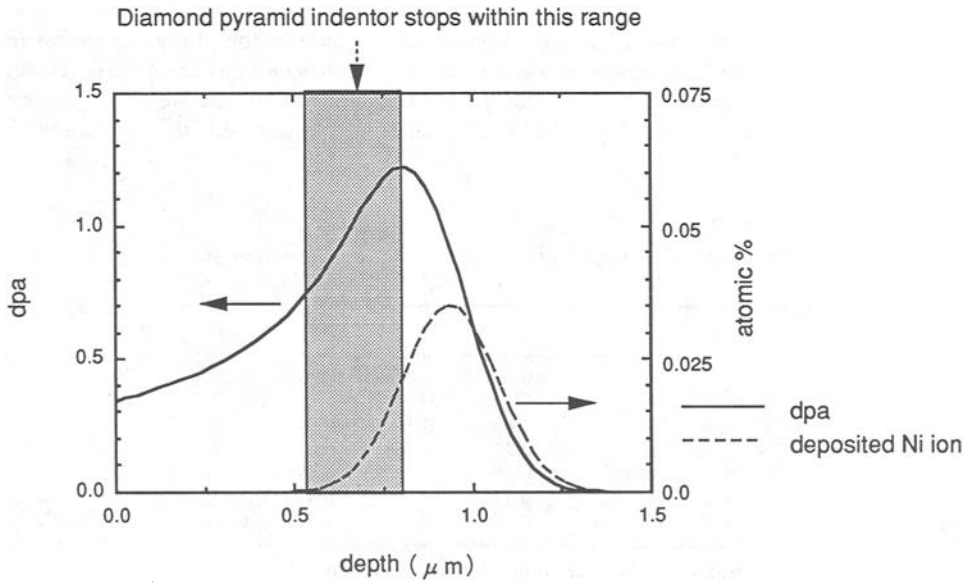

FIG. 1—*Damage profile and range distribution for Fe irradiated with 4 MeV Ni^{3+} to 10^{19} m^{-2}.*

to obtain data in the wide range of dose, while the maximum end-of-life neutron dose at the belt line of a four-loop PWR pressure vessel will be 2.3×10^{23} n/m^2 [*8*], which approximately corresponds to 3.9×10^{-2} dpa.

Micro-Vickers Hardness Test Employing Low Load

A micro-Vickers hardness test was carried out to obtain data about radiation hardening caused by ion irradiation in room atmosphere at room temperature. As the damage region is only within the surface layer of about 1 μm in thickness, micro-Vickers hardness tests employing low load (0.5 g) were carried out so that the tip of the diamond indentor stopped within the damage region. The depth of indentation is 0.57 μm for the hardest sample and 0.81 μm for the softest one in this study (Fig. 1). The grain sizes of specimens are larger than the diagonal of the diamond traces, so the effect of grain boundaries on hardness is avoided when the center region of a grain is indented. Vickers hardness numbers (HV) were determined as the mean value of five or more different grains.

Isochronal annealing after irradiation was done to measure the hardness change of specimens irradiated to 1 dpa at 563 K. Each annealing step was performed in a vacuum better than 10^{-4} Pa during 4 h. The duration of 4 h was chosen to keep the heating and cooling periods short [*9,10*].

Transmission Electron Microscopy (TEM)

TEM observations were carried out for irradiated Fe-0.1C and Fe-0.1C-0.4Cu to obtain information about the microstructural evolution caused by ion irradiation. Thin foils of the damage peak region were prepared from irradiated samples. Controlled electropolishing was done to polish out the layer from the irradiated surface to the damage peak region followed by back-thinning using Tenupol-3 to make a hole. The electrolyte used was 900 mL acetic acid-100 mL perchloric acid-0.5 g CrO_3, and the polishing voltage during back-thinning was 35 V. There was difficulty making a round hole because carbide could fall out, creating corrugated holes. This added another difficulty to the TEM observation in addition to the magnetic field caused by ferromagnetic ferrite samples.

Results

Hardening of As-Irradiated Specimens

Radiation hardening caused by heavy ion irradiation was detectable by the micro-Vickers hardness test. Figure 2 shows the dependence of irradiation hardening on dose. The hardness change on the ordinate is the difference between the hardness number of the irradiated area and unirradiated area in the same specimen so that the effect of thermal history is eliminated. The hardness value of an irradiated sample is an average over the damaged layer. As ion energy was constant, damage profile in the depth direction is probably similar in shape for all dpa levels. So the ΔHV is a relative value, but it represents the characteristics of hardening caused by ion irradiation. When the standard deviation of ΔHV ($\sigma\{\Delta HV\}$) is defined as $\sigma\{\Delta HV\} = [(\sigma\{HV_{irr}\})^2 + (\sigma\{HV_{unirr}\})^2]^{1/2}$, the mean value of $\sigma\{\Delta HV\}$ is 7.1 (where HV_{irr} and HV_{unirr} are the Vickers hardness numbers measured at the irradiated area and the unirradiated area on a specimen, respectively).

The hardening of each specimen increases with increasing dose. Hardening of Fe-0.1C-0.4Cu and Fe-0.1C-0.1Cu-0.7Ni is relatively greater than that of the other alloys except at

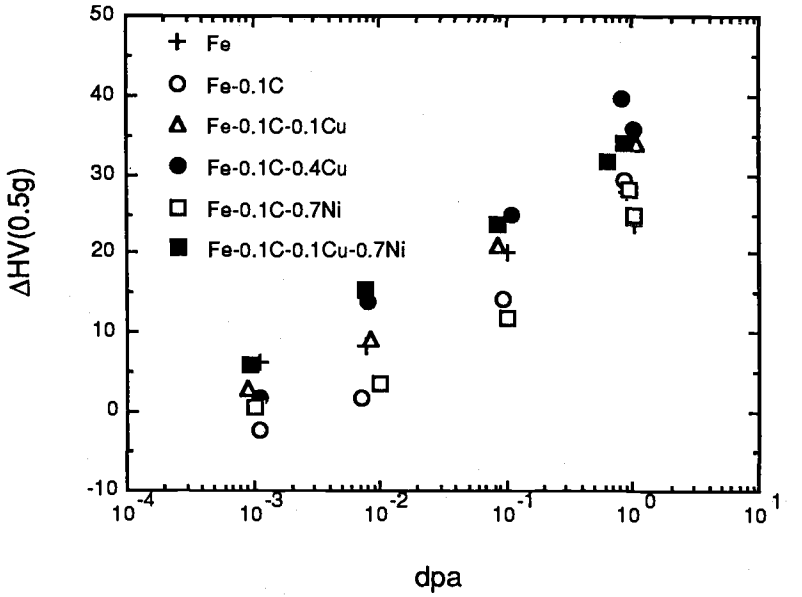

FIG. 2—*Dependence of radiation hardening caused by ion irradiation on dose.*

10^{-3} dpa, at which all data are within ±5 of zero. At doses higher than 10^{-3} dpa, larger copper content enhanced hardening. Fe-0.1C and Fe-0.1C-0.7Ni have a similar hardening trend, and the hardening of the two alloys is lower than Fe at 10^{-2} and 10^{-1} dpa. With respect to nickel content, there is no or little effect of nickel content for the alloys without copper. However, nickel has an effect for alloys containing 0.1 wt% copper.

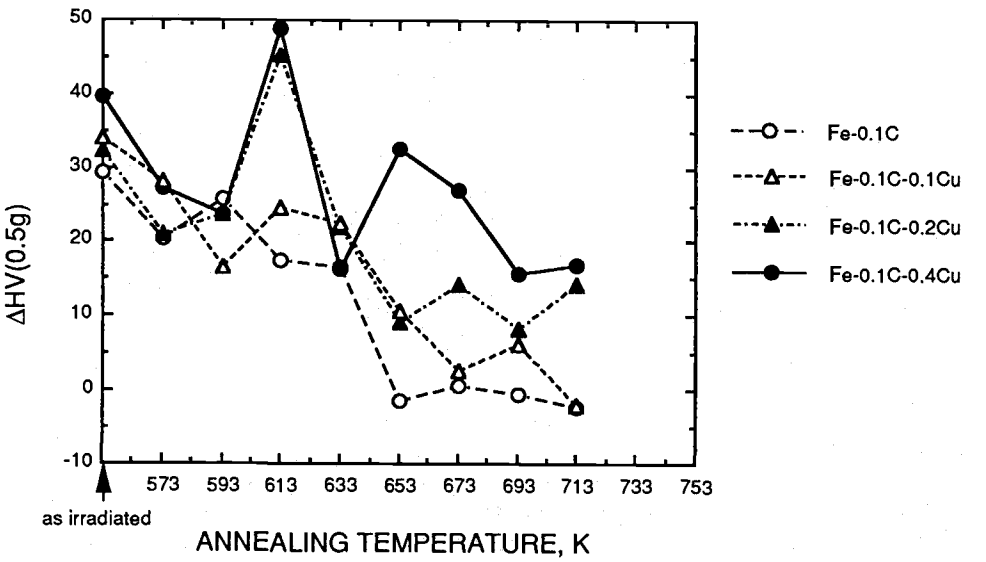

FIG. 3—*Recovery process of radiation hardening of Fe-C-Cu in isochronal annealing for 4 h.*

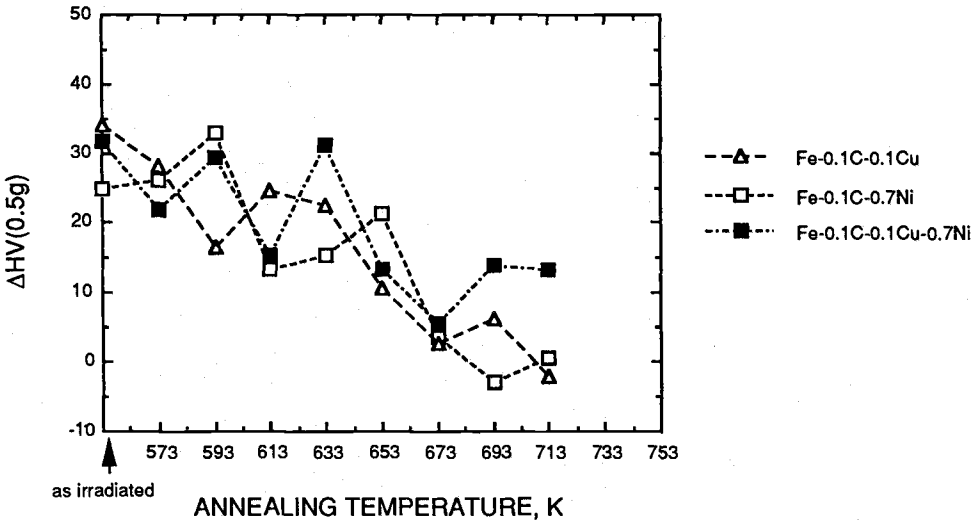

FIG. 4—*Recovery process of radiation hardening of Fe-C-Ni and Fe-C-Cu-Ni in isochronal annealing for 4 h.*

Hardness Measurement of Isochronal Annealed Specimens

Figures 3 and 4 show the ΔHV change as a function of temperature in isochronal annealing for 4 h for Fe-0.1C, Fe-0.1C-0.1Cu, Fe-0.1C-0.2Cu and Fe-0.1C-0.4Cu, and for Fe-0.1C-0.1Cu, Fe-0.1C-0.7Ni, and Fe-0.1C-0.1Cu-0.7Ni, respectively. A hardness change in HV (0.5 g) on the ordinate is defined as the difference between the hardness number of irradiated and unirradiated areas in the same annealed samples. This value contains uncertainty of ±5 in HV (0.5 g) as mentioned above.

In Fig. 3 the hardening of Fe-0.1C and Fe-0.1C-0.1Cu is gradually recovered and after 673 K annealing it seems to be recovered completely. Significant hardening was observed for Fe-0.1C-0.2Cu and Fe-0.1C-0.4Cu after annealing at 613 K. Hardening of Fe-0.1C-0.2Cu and Fe-0.1C-0.4Cu was not recovered completely even after annealing at 713 K.

In Fig. 4 hardening of Fe-0.1C-0.7Ni seems to be recovered after 673 K annealing. Hardening of Fe-0.1C-0.1Cu-0.7Ni would not be completely recovered after annealing at 713 K, while that of Fe-0.1C-0.7Ni seems to be completely recovered after the annealing. Further hardening caused by annealing after irradiation was not observed in Fig. 4.

TEM Observations of Irradiated Specimens

TEM observation of Fe-0.1C and Fe-0.1C-0.4Cu irradiated to 0.01, 0.1, 1 dpa, and Fe-0.1C-0.2Cu irradiated to 1 dpa was carried out using a JEM-200CX electron microscope. Figure 5 shows the dark field image of Fe-0.1C-0.2Cu irradiated to 1 dpa at 563 K (**g** = 1 1 0). It is a typical example of the dark field image of ion-irradiated specimens. Other specimens showed similar images. White spots of small defect clusters were observed whose number density against dose are shown for Fe-0.1C and Fe-0.1C-0.4Cu in Fig. 6. Figures 7 and 8 show the size distribution of observed defect clusters for Fe-0.1C and Fe-0.1C-0.4Cu, respectively. Number density of visible defect clusters increases, and larger defect clusters are formed in both cases as dose increases. Because of difficulties in observation mentioned

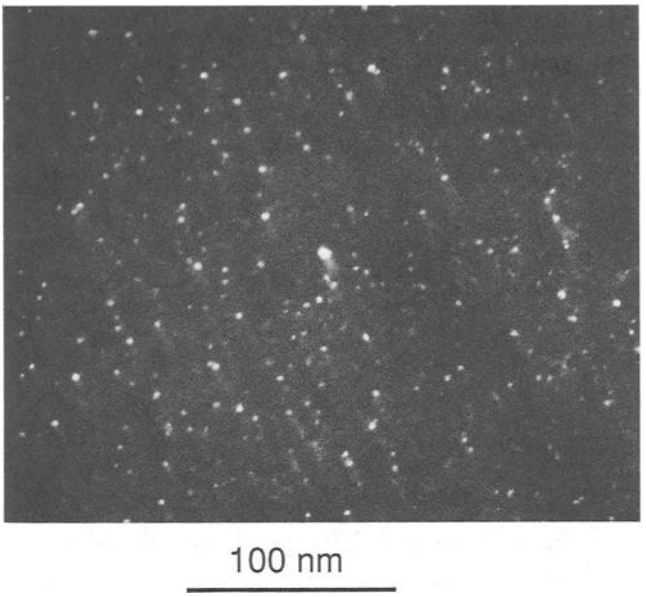

FIG. 5—*Typical example of dark field image of Fe-0.1C-0.2Cu irradiated to 1 dpa at 563 K,* $\mathbf{g} = 110$. *This is typical of our irradiated samples.*

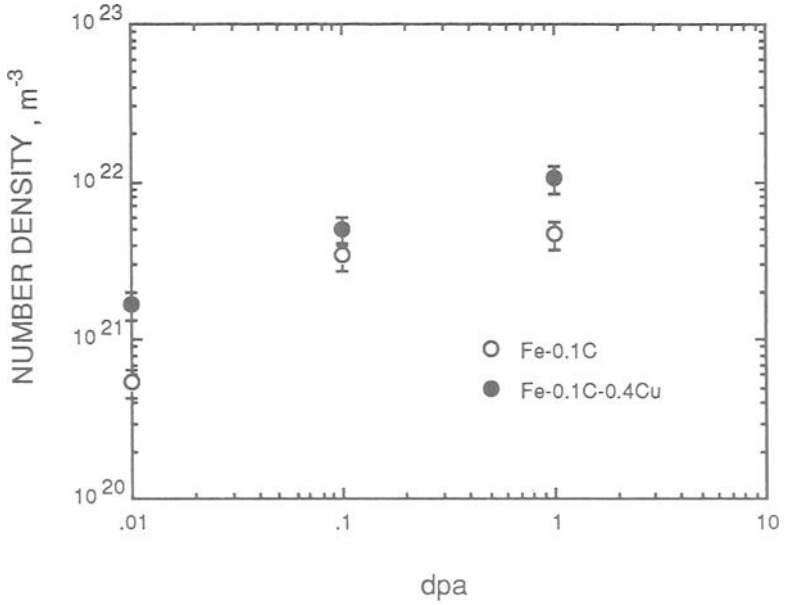

FIG. 6—*The dose dependence of number density of defect clusters observed in irradiated Fe-0.1C and Fe-0.1C-0.4Cu.*

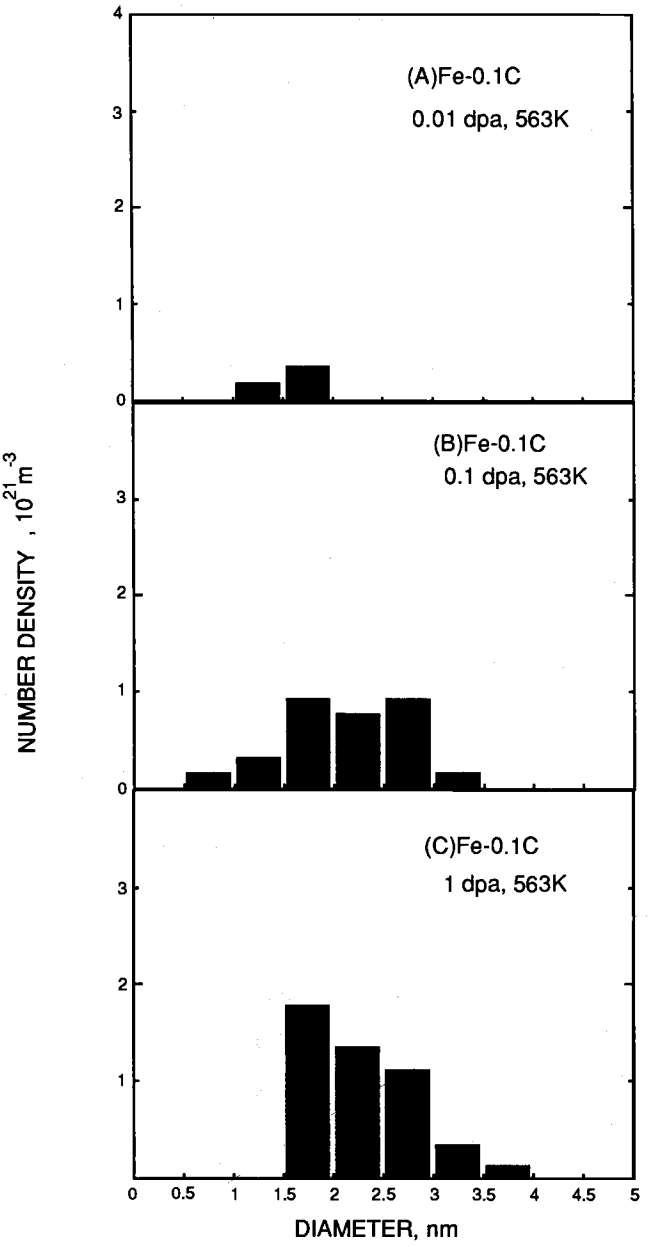

FIG. 7—*Size distribution of clusters observed in Fe-0.1C irradiated to* A *0.01 dpa;* B *0.1 dpa;* C *1 dpa.*

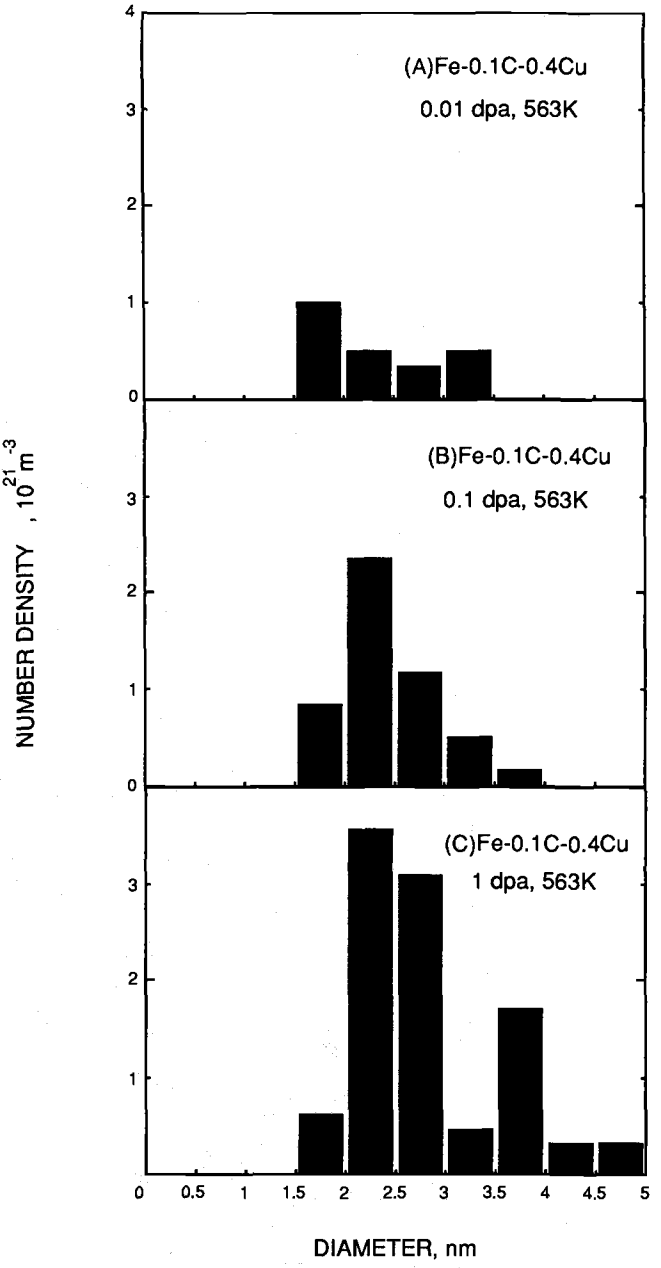

FIG. 8—*Size distribution of clusters observed in Fe-0.1C-0.4Cu irradiated to* A *0.01 dpa;* B *0.1 dpa;* C *1 dpa.*

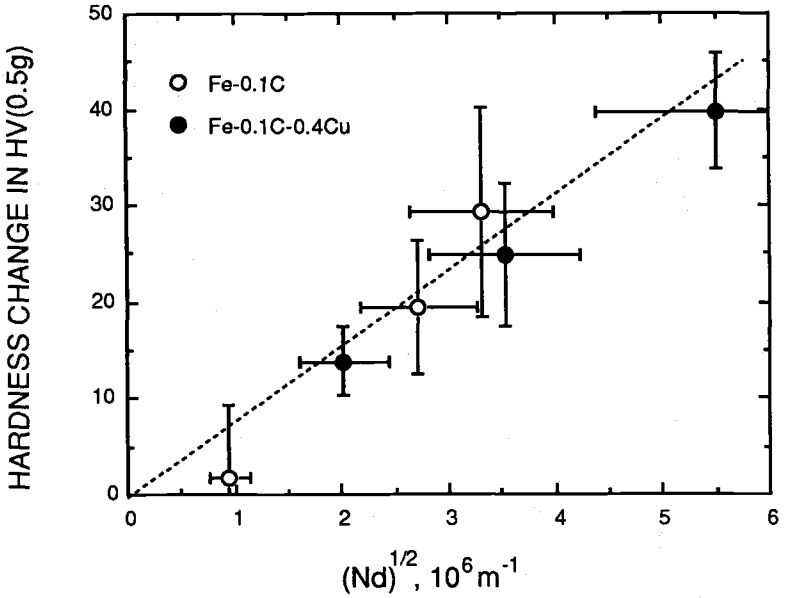

FIG. 9—*Relationship between radiation hardening and* $(Nd)^{1/2}$.

previously, it is probable for clusters of small diameter not to be detected. This may be the reason why the size distribution is not symmetric.

According to previous studies [*11*], when defect clusters act as barriers to the movement of dislocations, the hardness increase can be represented as follows

$$\Delta HV = K\alpha Gb(Nd)^{1/2} \tag{1}$$

where

K = constant,
α = strength parameter for the obstacle ($0 < \alpha < 1$),
G = shear modulus,
b = Burgers vector,
N = number density of clusters, and
d = diameter of clusters.

As K, α, G, and b are constant, ΔHV is proportional to $(Nd)^{1/2}$ when defect clusters cause hardening. Figure 9 shows the relationship between $(Nd)^{1/2}$ and ΔHV for Fe-0.1C and Fe-0.1C-0.4Cu, where the error bars on the X axis are 20% and come from uncertainty in the thickness of observed foils and the thickness of polished layers, and the error bars on the Y axis are the standard deviation of the hardness number. As shown in Fig. 9, there is good proportionality between $(Nd)^{1/2}$ and ΔHV. Therefore, radiation hardening may probably be caused by the observed defect clusters and their smaller, unobservable counterparts.

Discussion

In this study, we attempt to apply ion irradiation to the study of embrittlement mechanisms of RPVs. In spite of the large difference between neutron and ion irradiation regarding dose rate and damage profile, ion irradiation data have some trends similar to neutron irradiation from the viewpoint of copper content dependence of hardening or the combined effect of copper and nickel (Fig. 2). This may justify application of ion irradiation to the study of embrittlement mechanisms in neutron-irradiated steel. So ion irradiation experiments concerning the dose rate effect or the irradiation temperature effect may be promising for fundamental understanding of the hardening mechanisms.

Observed defect clusters would cause hardening, but we could not acquire credible evidence to determine their nature, i.e., interstitial type or vacancy type. At this irradiation temperature the mobility of vacancies is not so large; the defect clusters are more likely to be of the interstitial type [*12*]. The following is based on the assumption that the observed defect clusters are of the interstitial type. During irradiation a copper atom may have served as a heterogeneous nucleation site of an interstitial cluster, and the number density of interstitial clusters may have been enhanced compared with the alloy without copper (Fig. 6). On the other hand, Smidt et al. [*13*] have reported that higher binding energy exists between vacancies and copper atoms than between vacancies and other elements such as nickel or vanadium. Then it is possible to form copper-carbon-vacancy complexes during irradiation, considering a carbon atom is rapidly trapped by a vacancy. In brief, copper atoms may simultaneously serve as the nucleation sites for interstitial clusters and form copper-carbon-vacancy complexes for Fe-0.1C-0.4Cu during irradiation. Fairly good correlation between $(Nd)^{1/2}$ and ΔHV (Fig. 9) presumes that radiation hardening was caused mainly by observed interstitial clusters and the contribution of copper-carbon-vacancy to hardening was small compared to that of the interstitial clusters.

A significant hardening due to a post-irradiation anneal at 613 K for only Fe-0.1C-0.2Cu and Fe-0.1C-0.4Cu was observed as seen in Fig. 3. Similar hardening due to post-irradiation anneal has been observed in neutron-irradiated model alloys: Takaku et al. [*14*] irradiated Fe, Fe-0.1Cu, and Fe-0.3Cu in the Japanese Material Testing Reactor (JMTR) at 523 K to 5×10^{18} n/cm^2. Data on isochronal annealing after the irradiation showed hardening after 573 K annealing for Fe-0.1Cu and Fe-0.3Cu similar to the present work. They indicated that the phenomenon is possibly due to the formation of complex defects such as Cu-C-V or Cu-N-V (V: irradiation defects) in the matrix. In this ion irradiation experiment Cu-C-vacancy complexes may have been produced during irradiation and have remained after irradiation. In the isochronal annealing experiment Cu-C-vacancy may have enough mobility to form clusters during 613 K annealing and caused hardening. Above 623 K, release of carbon atoms from the traps and the corresponding recovery of hardening has been reported as evidence for defect annihilation by Takahashi et al. [*15*] from the internal friction measurement of neutron-irradiated Fe-C-Cu alloys. So the recovery of hardening for Fe-0.1C-0.2Cu and Fe-0.1C-0.4Cu at 633 K may be caused by annihilation of vacancies from the Cu-C-V clusters. The annihilation of vacancies and the release of carbon possibly resulted in the production of copper clusters from Cu-C-V clusters and incomplete recovery of hardening for Fe-0.1C-0.2Cu and Fe-0.1C-0.4Cu after 713 K annealing.

Conclusions

In order to obtain fundamental knowledge about radiation embrittlement of RPV steels, ion irradiation techniques were applied. The micro-Vickers hardness test successfully de-

tected relative hardening caused by ion irradiation. Hardening increased with dose for each specimen and was attributed to clusters observed by TEM; larger copper content enhanced hardening. The proportionality between ΔHV and $(Nd)^{1/2}$ indicated hardening caused by defect clusters for Fe-0.1C and Fe-0.1C-0.4Cu. Hardening of materials containing both copper and nickel was greater than the sum of the hardening of materials containing the same level of copper or nickel alone. Further hardening was observed after 613 K-4h, annealing and hardening was not recovered completely after 713 K-4h annealing in irradiated Fe-0.1C-0.2Cu and Fe-0.1C-0.4Cu. The effect of copper on these phenomena may be explained by the heterogeneous nucleation of defect clusters enhanced by copper and the formation of copper-carbon-vacancy complexes during irradiation and copper cluster formation during isochronal annealing at above 613 K.

References

[1] Odette, G. R. and Lucas, G. E., "Irradiation Embrittlement of Reactor Pressure Vessel Steels: Mechanisms, Models, and Data Correlations," *Radiation Embrittlement of Nuclear Reactor Pressure Vessel Steels: An International Review (Second Volume), ASTM STP 909*, L. E. Steele, Ed., American Society for Testing and Materials, Philadelphia, 1986, pp. 206–241.

[2] Fisher, S. B. and Buswell, J. T., "A Model for PWR Pressure Vessel Embrittlement," *International Journal of Pressure Vessels and Piping*, Vol. 27, 1987, pp. 91–135.

[3] Odette, G. R. and Lucas, G. E., "The Effect of Nickel on Irradiation Hardening of Pressure Vessel Steels," *Effects of Radiation on Materials: 14th International Symposium (Volume 2), ASTM STP 1046*, N. H. Packan, R. E. Stoller, and A. S. Kumar, Eds., American Society for Testing and Materials, Philadelphia, 1990, pp. 323–347.

[4] Phythian, W. J., English, C. A., and Buswell, J. T., "The Microstructural and Microchemical Examination of Reactor Pressure Vessel Steels," *Proceedings*, Fifth International Symposium on Environmental Degradation of Materials in Nuclear Reactor Systems-Water Reactors, American Nuclear Society, La Grange Park, IL, 1991, pp. 27–38.

[5] Mancuso, J. F., Spitznagel, J. A., Shogan, R. P., and Holland, J. R., "Correlation Between Microhardness, Tensile Properties, and Notch Ductility of Irradiated Ferritic Steels," *Effects of Radiation on Materials: Tenth Conference, ASTM STP 725*, D. Kramer, H. R. Brager, and J. S. Perrin, Eds., American Society for Testing and Materials, Philadelphia, 1981, pp. 38–48.

[6] Davisson, C. M. and Manning, I., "Adaptation of a Program for Depth Distribution of Energy Deposition by Ion Bombardment: Better Stopping Powers," *Computer Physics Communications*, Vol. 42, 1986, pp. 137–147.

[7] Kiritani, M., "Radiation Rate Dependence of Microstructure Evolution," *Journal of Nuclear Materials*, Vol. 169, 1989, pp. 89–94.

[8] Davies, L. M. and Ingham, T., "Overview of Studies in the United Kingdom on Neutron Irradiation Embrittlement of Pressure Vessel Steels," *Radiation Embrittlement of Nuclear Reactor Pressure Vessel Steels: An International Review (Second Volume), ASTM STP 909*, L. E. Steele, Ed., American Society for Testing and Materials, Philadelphia, 1986, pp. 13–33.

[9] Pachur, D., "Radiation Annealing Mechanisms of Low-alloy Reactor Pressure Vessel Steels Dependent on Irradiation Temperature and Neutron Fluence," *Nuclear Technology*, Vol. 59, December 1982, pp. 463–475.

[10] Gil, C. L., De Lima, A. P., De Campos, N. A., Fernandes, J. V., Kögel, G., Sperr, P., and Pachur, D., "Neutron-irradiated Reactor Pressure Vessel Steels Investigated by Positron Annihilation," *Journal of Nuclear Materials*, Vol. 161, 1989, pp. 1–12.

[11] Smidt, F. A. Jr., "Correlation of Microstructure and Strength During Stage 3 Annealing of Irradiated Vanadium," *Radiation Effects*, Vol. 10, 1971, pp. 205–214.

[12] Yoshida, N., Heinisch, H. L., Muroga, T., Araki, K., and Kiritani, M., "Microstructure-Tensile Property Correlation of 316 SS in Low-Dose Neutron Irradiations," *Journal of Nuclear Materials*, Vol. 179–181, 1991, pp. 1078–1082.

[13] Smidt, F. A. Jr. and Watson, H. E., "Effect of Residual Element on Radiation Strengthening in

Iron Alloys, Pressure Vessel Steels, and Welds," *Metallurgical Transactions,* Vol. 3, August 1972, pp. 2065–2073.

[*14*] Takaku, H., Tokiwai, M., Kayano, H., Higashiguchi, Y., Narui, M., Suzuki, Y., and Matsuyama, K., "The Improvement of Irradiation-Enhanced Copper Embrittlement in Fe-Cu Alloys," *Journal of Nuclear Materials,* Vol. 80, 1979, pp. 57–68.

[15] Takahashi, J. and Yamane, T., "Hardening and Recovery of Neutron-Irradiated Fe-Cu-C Alloy," *Journal of Nuclear Science and Technology,* Vol. 12, October 1975, pp. 634–636.

Motokuni Eto,[1] *Hideaki Takahashi,*[2] *Toshihei Misawa,*[3] *Masahide Suzuki,*[1] *Yutaka Nishiyama,*[1] *Kiyoshi Fukaya,*[1] *and Shiro Jitsukawa*[1]

Development of a Miniaturized Bulge Test (Small Punch Test) for Post-Irradiation Mechanical Property Evaluation

REFERENCE: Eto, M., Takahashi, H., Misawa, T., Suzuki, M., Nishiyama, Y., Fukaya, K., and Jitsukawa, S., " **Development of a Miniaturized Bulge Test (Small Punch Test) for Post-Irradiation Mechanical Property Evaluation,"** *Small Specimen Test Techniques Applied to Nuclear Reactor Vessel Thermal Annealing and Plant Life Extension, ASTM STP 1204,* W. R. Corwin, F. M. Haggag, and W. L. Server, Eds., American Society for Testing and Materials, Philadelphia, 1993, pp. 241–255.

ABSTRACT: To examine the effectiveness of the small punch test for evaluating strength and toughness of irradiated ferritic steels, detailed procedures are described aiming at standardization of the test. The statistical approach to analysis of the SP energy as a function of temperature for evaluation of DBTT was also reviewed. The method was then applied to neutron-irradiated ferritic steels, which included F-82, F-82H, HT-9, and 2¼Cr-1Mo steel. Fluence and irradiation temperatures ranged from 2 to 12 × 10^{23} n/m^2 ($E \geq 1$ MeV) and from 573 to 673 K, respectively. Comparison of parameters obtained from the small punch test with the properties measured by the conventional method indicated that: (*a*) the 0.2% offset stress and the ultimate tensile strength at room temperature can be correlated well with the parameters, $P_y/(t_0)^2$ and $P_{max}/(t_0)^2$, respectively. Here, P_y and P_{max} are the loads corresponding to the yield and the maximum, and t_0 is the initial thickness of a specimen; (*b*) fracture toughness, J_{IC}, can be evaluated using equivalent fracture strain, $\bar{\varepsilon}_{qf}$, and the previously established relationship between these values; and (*c*) DBTT measured by a Charpy test can be predicted from the results of temperature dependence of SP energy determined from the area under the load-deflection curve using a statistical analysis based on a Weibull distribution.

KEYWORDS: small specimen test technique, SP test, ferritic steel, irradiation, strength, toughness, DBTT

Among various small specimen test techniques (SSTT), the miniaturized bulge test (SP test) is of no less importance than other methods such as the tension test. There have been a number of investigations on the evaluation of strength and toughness of various alloys using the SP test method [*1–4*]. However, the details of the method employed by individual researchers have differed somewhat from one to the other: specimen size, punching ball or rod, setup of specimen, etc.

In this paper we describe the basics of our testing procedure, which was aimed at standardization of the technique. Then, the results obtained when the method was applied to unirradiated ferritic and austenitic steels are presented to indicate if the test procedure is

[1] Department of High Temperature Engineering, Japan Atomic Energy Research Institute, Tokai-mura, Ibaraki-ken 319-11, Japan.
[2] Faculty of Engineering, Tohoku University, Aza-Aoba, Aramaki, Aobaku, Sendai 980, Japan.
[3] Faculty of Engineering, Muroran Institute of Technology, Mizumoto-cho 27-1, Muroran 050, Japan.

effective for evaluating the strength and toughness of these materials. As to the ductile-to-brittle transition temperature (DBTT), a statistical method to analyze a limited number of data points has already been proposed by Misawa et al. [5]. Their method will be described so that the applicability of their method to irradiated materials can be discussed. Although results obtained by a number of researchers indicate that the SP test can be utilized to evaluate mechanical properties of metallic materials, relatively few investigations have dealt with irradiated specimens.

Since one of the advantages of the SP test would be its applicability to irradiated materials, it is important to accumulate data on irradiated materials to confirm the effectiveness of the test as an SSTT. To do this, the SP test was carried out on neutron-irradiated ferritic steels and the results discussed focusing on its effectiveness and how it can be standardized.

The paper involves cooperation among the Japan Atomic Energy Research Institute, Tohoku University, and the Muroran Institute of Technology in the development of the technique.

Basics of the SP Test

Outline of the Test

Figure 1 shows a schematic of the specimens and the set up for the SP test [3]. Three kinds of coupon-type specimens are used: (1) 10 by 10 by 0.5 mm, (2) 10 by 10 by 0.25 mm, and (3) 3 mm in diameter by 0.25 mm in thickness (TEM disk). Specimens differing in thickness were used to examine the effect of specimen thickness on the result of the small punch test. Steel balls of different size for loading fixtures are employed, i.e., 2.4 and 1 mm in diameter.

The two parameters which correspond to fracture toughness can be obtained from the load-deflection curve: (1) SP energy is calculated from the area under the load-deflection curve; (2) the equivalent fracture strain, $\bar{\epsilon}_{qf}$, is calculated from the maximum deflection at fracture, δ^*. The SPDBTT can be derived from the result of the SP energy-test temperature relationship.

J_{ICSP} can be esimated from the empirical correlation curve between equivalent fracture strain and J_{IC}. Here, J_{ICSP} represents the J_{IC} value estimated as a result of the SP test.

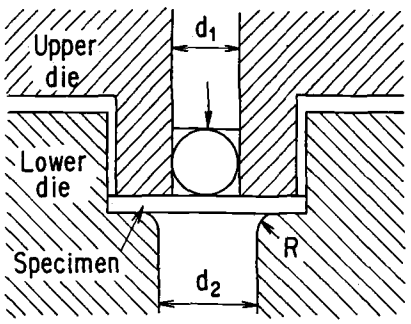

	Small (10 x 10)	TEM disk (ϕ3)
t_0	0.50 0.25	0.25
d_1	2.4	1.0
d_2	4.0	1.5
R	0.2	0.2
Steel ball	ϕ2.4	ϕ1

: mm

$$d_2 \geq d_1 + 2t_0$$

FIG. 1—*Schematic of the setup for the SP test.*

Test Method

Apparatus—A screw-driven testing machine is used for loading compressively the fixture shown in Fig. 1. The load is measured with an accuracy of 1%. Steel balls for loading should have a hardness number of HRC62 to HRC67. The lower die in contact with the specimen should have a smooth surface, e.g., $R_{max} = 3.2\ S$. Here, R_{max} and S are defined in the Japanese Industrial Standard JIS B 0601. The above value means that the maximum amplitude of roughness is smaller than 3.2 μm over any given distance of 0.8 mm on a surface. Holes machined adjacent to the space for mounting a specimen in the lower die are required to facilitate the handling of the specimen.

Deflection was measured from the displacement of the crosshead, to which a dial gage was attached. For irradiated specimens, the deflection was also measured using a clip gage, which was connected to a push rod in contact with the back surface of a specimen. A schematic of this case is shown in Fig. 2. An accuracy within ±1% should be achieved whichever method is used.

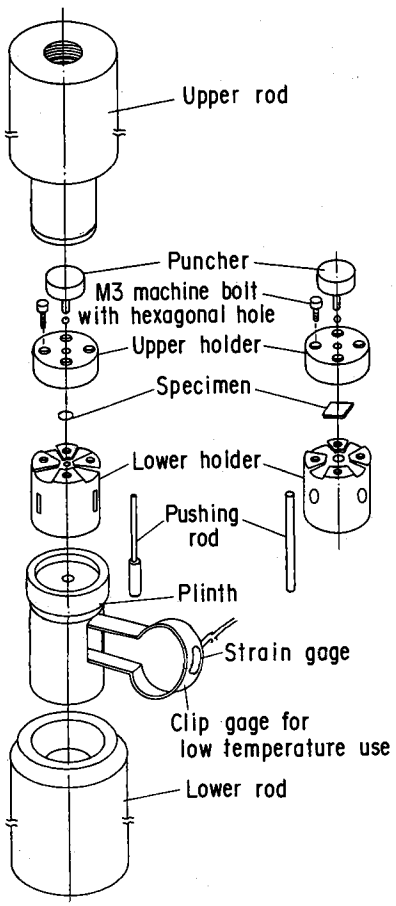

FIG. 2—*Schematic for the apparatus for the SP test on irradiated materials.*

Temperature control during the test was within 2°C. For the low-temperature test in this paper, liquid nitrogen and an appropriate sheathed heater wound around the specimen holder beneath the specimen or a constant temperature chamber with gas evaporating from liquid nitrogen was used. The latter system was used for irradiated specimens. In both cases the temperature of the whole loading fixture was maintained at each test temperature.

Specimen surfaces should be as smooth and flat as possible. Specimens were polished mechanically or electrochemically. For the mechanical polish, No. 1200 emery paper was used, and, in most cases, a buff was also used for polishing. No additional polishing was made after the irradiation. Since the specimens were irradiated in capsules filled with helium and stored in oil until the testing started, practically no corrosion products nor debris were observed on the specimen surface.

Procedure—Specimens were placed at the center of the fixture, and bolts were used to clamp the specimen. The clamping torque ranged from 0.5 to 1.0 N-m. Crosshead speed was 0.5 mm/min.

Calculation and Interpretation of Results

Evaluation of Equivalent Fracture Strain $\bar{\epsilon}_{qf}$ and Estimation of J_{ICSP}—The maximum deflection at fracture δ^* is defined as one at the fracture load, P_F, beyond which the load decreases with a sudden drop. A typical load-deflection curve is shown in Fig. 3. $\bar{\epsilon}_{qf}$ is calculated using the following rational equation.

$$\bar{\epsilon}_{qf} = \ln (t_0/t^*) \tag{1}$$

$$= \beta(\delta^*/t_0)^2 \tag{2}$$

where t_0 is the initial thickness of the specimen, t^* is the minimum thickness of the fractured specimen, and β is a constant. Values of 0.09 and 0.043 were chosen for ferritic and austenitic

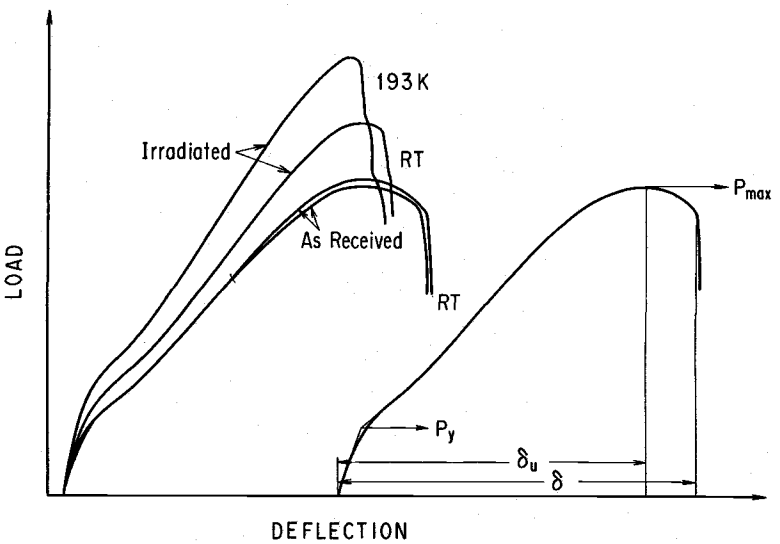

FIG. 3—*Typical examples for the load-deflection curve obtained by the SP test.*

steels, respectively, as determined from the results obtained in the previous experiments [4]. J_{IC} can be estimated by a correlation between $\bar{\epsilon}_{qf}$ and J_{IC} obtained for various alloys, which will be described below [3,4,6].

Evaluation of SP Energy and SPDBTT—SP energy is estimated from the area under the load-deflection curve up to the fracture load or maximum deflection. Either a roller planimeter or numerical integration method is employed for the estimation.

SPDBTT is defined by the temperature at the energy level of $(SP_{max} + SP_{min})/2$ where SP_{max} and SP_{min} are energies at the upper and lower shelves, respectively. In the present experiment the upper shelf energy was not constant, so the maximum value of SP energy was chosen as SP_{max}. For SP_{min}, SP energy at 50 K was taken by extrapolating the data points in the transition regime as done in Ref 5.

Dependence of SP energy on the thickness of specimens was extensively examined at JAERI. Figure 4 shows an example of the results obtained on 10 by 10-mm coupon specimens of the forged 2¼Cr-1Mo steel irradiated at 673 K to a fluence of 4×10^{23} n/m^2 ($E \geq 1$ MeV). It is seen that the SP energy is a reproducible measure as long as the specimen thickness is properly evaluated. The results shown here could be taken into account when one has to machine SP specimens from irradiated Charpy specimens. The thickness variation is often rather large in cases where the handling of specimens in the hot cell is difficult.

Determination of SPDBTT by Statistical Analysis—Since, in general, a limited number of irradiated specimens are available and scatter is large for SP energy because of the unavoidable microstructural heterogeneity for the SP test, a statistical approach is desired for the determination of SPDBTT. This should be investigated further, e.g., with regard to the possibility of application of the SP test to the weld. We employed the statistical analysis proposed by Misawa et al. [5]. Figure 5 is a typical example of an SP energy-temperature

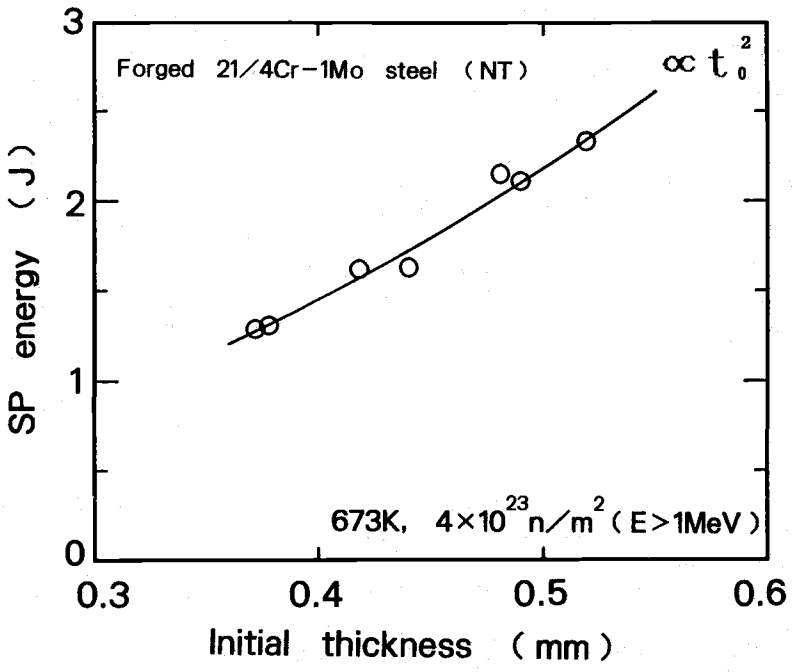

FIG. 4—*Dependence of SP energy on the thickness of the specimen.*

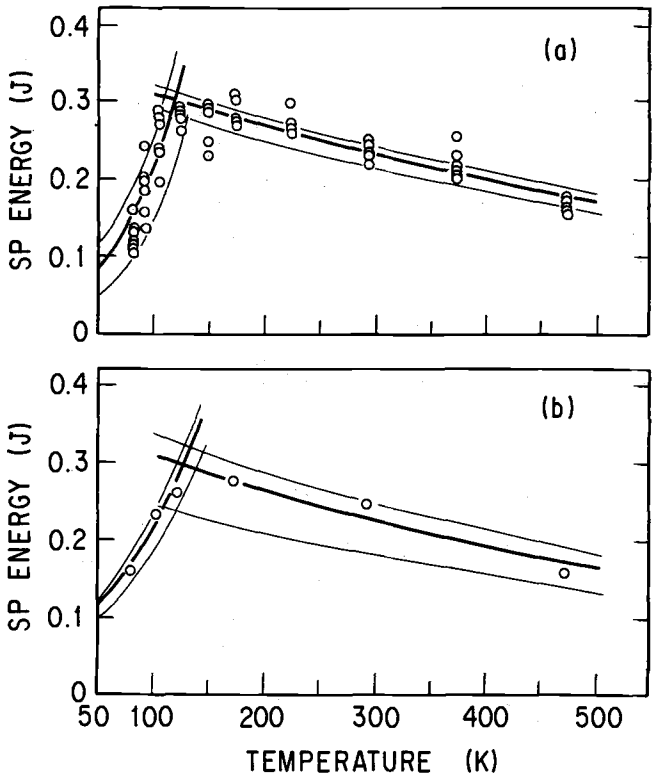

FIG. 5—*Examples of the temperature dependence of SP energy based on the data-partitioning method for the TEM disk specimens of F-82* [5]*:* (a) *every six data at ten test temperatures,* (b) *a single datum at six test temperatures. The middle solid lines show the estimated* E_0 *in the two separated regions. The lower and higher thin lines represents 5 and 95% failure probability, respectively.*

curve for F-82 ferritic steel obtained by them, which is shown to summarize the statistical analysis. In this case, SPDBTT is defined as the temperature corresponding to the middle energy between the energy at the intersection of the two fitting curves and that at 50 K.

The statistical analysis is carried out by the data-partitioning method on the basis that the SP energy is to be expressed by the Weibull distribution. The Weibull distribution parameters, m and E_0, are determined from the Weibull plot gradient, and the energy corresponding to a cumulative distribution of 63.2% by using the least squares method, i.e.,

$$F(x) = 1 - \exp[-(x/E_0)^m] \tag{3}$$

All the data points obtained are used for analysis. Figure 5*a* is an example. SPDBTT, defined above, is nearly equal to that estimated by the standard method where a curve for mean energy, μ, in the Weibull plot at each temperature is evaluated. Next, three data points at each temperature, then two, and then one chosen randomly are analyzed using the fitting procedure. Figure 5*b* is the result of an extreme case where only six data points were used for the analysis.

Table 1 summarizes the results of statistical analysis done by Misawa et al. for F-82H, HT-9, and F-82 ferritic steels. It is indicated in this table that the scatter of estimated SPDBTT

increases as the number of data points sampled for the analysis decreases. However, for the F-82 and F-82H steels, even a set of one data point at each temperature gives an SPDBTT within an error of ±5 K. To determine SPDBTT for HT-9 steel, more data are necessary to assure the above accuracy.

Necessary Minimum Number of Specimens for SPDBTT Measurement—The minimum number of irradiated specimens to determine SPDBTT can be estimated in the following way. First, six unirradiated specimens are tested at room temperature. The shape parameter, m, is determined from the gradient of the measured Weibull plot of SP energy. If m is greater than or equal to 18, a reliable SPDBTT can be estimated using ten specimens because the material is believed to have a fairly homogeneous microstructure. If m is smaller than 18, more specimens are necessary for SPDBTT to be reliably determined.

In reality, to estimate the reliability of SPDBTT for irradiated specimens, we need a value of m for irradiated specimens, m'. However, m' is very difficult to obtain, so we assume $m = m'$ for the first approximation.

Application of SP Test to Neutron-Irradiated Ferritic Steels

The technique summarized in the previous section was applied to several irradiated ferritic steels to examine the effectiveness of the method and to accumulate SP test data for further discussion.

Materials, Specimens, and Test Method

Four ferritic steels were tested: 2¼Cr-1Mo steel (Cr-Mo steel, hereafter), F-82, F-82H, and HT-9. Chemical compositions are shown in Tables 2*a* and 2*b*. Both specimens of the 10 by 10 by 0.5 mm and TEM disk type were used for the Cr-Mo steel, whereas only the latter was used for the other materials. Specimens were prepared and SP tested according to the procedure described above.

Conventional tests for comparison with the SP test results were done on standard or common specimens. The gage section of tension specimens was 4 mm in diameter and 22 mm in length. J_{IC} was calculated using disk-shaped compact tension (DCT) specimens 10 mm in thickness and 27 mm in diameter, which were tested following the procedure designated in the ASTM Test Method for J_{IC}, a Measure of Fracture Toughness (E 813–81). Specimens of this type were used to be accommodated effectively in an irradiation capsule. Details of the results on these specimens, including those on the effect of specimen thickness and the difference observed between ASTM E 813–81 and ASTM E 813–89, are published elsewhere [7].

The microstructure of Cr-Mo steel consists mainly of bainite with a small amount of pre-eutectoid ferrite. The other steels consist of tempered martensite, and the HT-9 contains 1% δ-ferrite.

Neutron Irradiations

Irradiations were performed in JRR-2 at JAERI. Irradition conditions are given in Table 3.

Results and Discussion

Correlation of SP Parameters with the Tensile Properties—Figures 6*a* through 6*d* show results of several trials for correlating SP-related parameters with tensile properties of Cr-

TABLE 1—*Estimates of the DBTT by TEM disk-specimen SP tests for F-82, F-82H, and HT-9 ferritic steels.*

Alloy	DBTT, K, Standard Method (μ Line)	Iteration	Data Partitioning Method: DBTT, K, at Ten Test Temperatures: All Data (60)[a]	Three Data (30)[a]	Two Data (20)[a]	One Datum (10)[a]	DBTT, K, at Six Test Temperatures: One Datum (6)[a]
F-82	93	1	94	94	93	97	97
F-82	93	2	94	94	93	94	100
F-82	93	3	94	97	94	98	96
F-82H	109	1	107	113	108	107	105
F-82H	109	2	107	108	108	108	114
F-82H	109	3	107	109	106	105	107
HT-9	156	1	154	157	159	170	137
HT-9	156	2	154	161	169	166	163
HT-9	156	3	154	161	162	149	145

[a] The value in parentheses shows the total number of specimens used for small-punch DBTT estimation.

TABLE 2*a*—*Chemical composition (wt%) of the materials used in the present experiment.*

Alloy	C	Si	Mn	P	S	Ni	Cr	Mo	W	V	Ta	Ti	B	Total, Al	Total, N	Cu	Co
Cr-Mo A	0.14	0.08	0.54	0.09	0.09	0.12	2.36	1.04								0.09	0.012
Cr-Mo B	0.12	0.30	0.53	0.008	0.003	0.13	2.27	1.02								···	···
F-82	0.100	0.17	0.49	0.003	0.002	0.005	7.52	Trace	2.19	0.19	···	0.005	0.0035	0.01	0.0018	···	···
F-82H	0.093	0.09	0.49	0.005	0.001	0.01	7.65	Trace	1.98	0.18	0.038	0.005	0.0034	0.01	0.0019	···	···
HT-9	0.188	0.22	0.48	0.018	0.001	0.59	12.01	1.01	0.51	0.29	···	0.005	···	0.02	0.0022	···	···

TABLE 2*b*—*Heat treatment conditions of the materials used in the present experiment.*

Alloy	Normalizing	Tempering	Microstructure	PWHT
Cr-Mo A	1 183 K × 5 h	923 K × 6 h	Bainite plus pre-eutectoid ferrite	958 K × 22 h
Cr-Mo B	1 203 K × 6 h	945 K × 8 h	Bainite plus pre-eutectoid ferrite	968 K × 20 h
F-82	1 183 K × 0.5 h	983 K × 2 h	Tempered martensite	
F-82H	1 313 K × 0.5 h	1 013 K × 2 h	Tempered martensite	
HT-9	1 313 K × 0.5 h	1 033 K × 2 h	Tempered martensite plus δ-ferrite	

TABLE 3—*Irradiation conditions.*

Material	Fluence, 10^{23} n/m^2, $E > 1$ MeV	Temperature, K
Cr-Mo, A	2	573
Cr-Mo, Aged A	3	673
Cr-Mo, B	4	673
F-82, F-82H, HT-9	12	600

Mo steels. Both SP and conventional tests were done at room temperature. One can see that the parameters, $P_y/(t_0)^2$ and $P_{max}/(t_0)^2$, correlate well with 0.2% offset stress and ultimate tensile strength, respectively. However, as for total elongation, only a qualitative tendency common to each material was observed with the parameter δ^*/t_0. For room temperature tensile properties of F-82, F-82H, and HT-9, correlations similar to those for the Cr-Mo steel were observed.

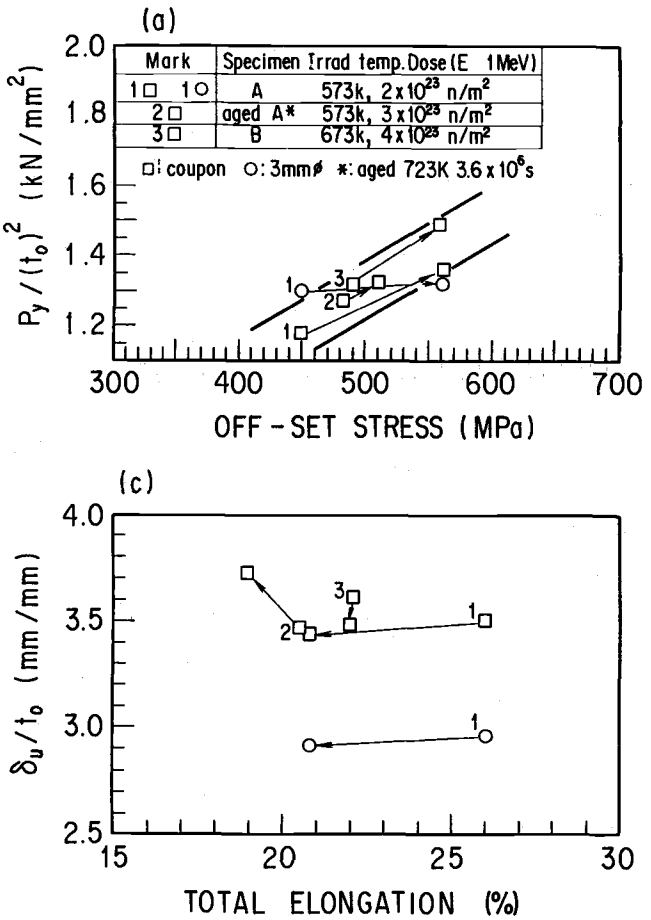

FIG. 6—*Strength parameter correlation for:* (a) *the 0.2% offset stress,* (b) *ultimate tensile strength, and* (c, d) *total elongation.*

However, it seemed that the parameters obtained for the SP test at low temperatures could not be correlated well with tensile properties. The cause for this is not clear at present. The experimental difficulties at the lower temperatures, including the possibility of the inclination of the specimen during the test, might be a cause.

Evaluation of Fracture Toughness—$\bar{\epsilon}_{qf}$ was calculated using Eq 1 or 2. It has not yet been confirmed that β and the exponent in Eq 2 remain unchanged after irradiation. J_{IC} obtained from the DCT test versus $\bar{\epsilon}_{qf}$ calculated from Eqs 1 or 2 is plotted in Fig. 7. The value of $\bar{\epsilon}_{qf}$ after irradiation is an average for two or three test runs. Most data points for irradiated specimens seem to obey the relationship proposed by Takahashi et al. [*4*]. For HT-9, however, $\bar{\epsilon}_{qf}$ calculated by Eq 1 was higher, whereas that calculated by Eq 2 was lower. Changes caused by irradiation are indicated by the arrows. The J_{IC} of HT-9 was not estimated after irradiation because of its elastic characteristics. The cause for this is not clear, but one possibility is that the constants in Eq 2 might change after irradiation. Thus, it is recommended that when the fracture toughness is evaluated from the results of an SP test, the thickness of the irradiated specimens after fracture is also measured.

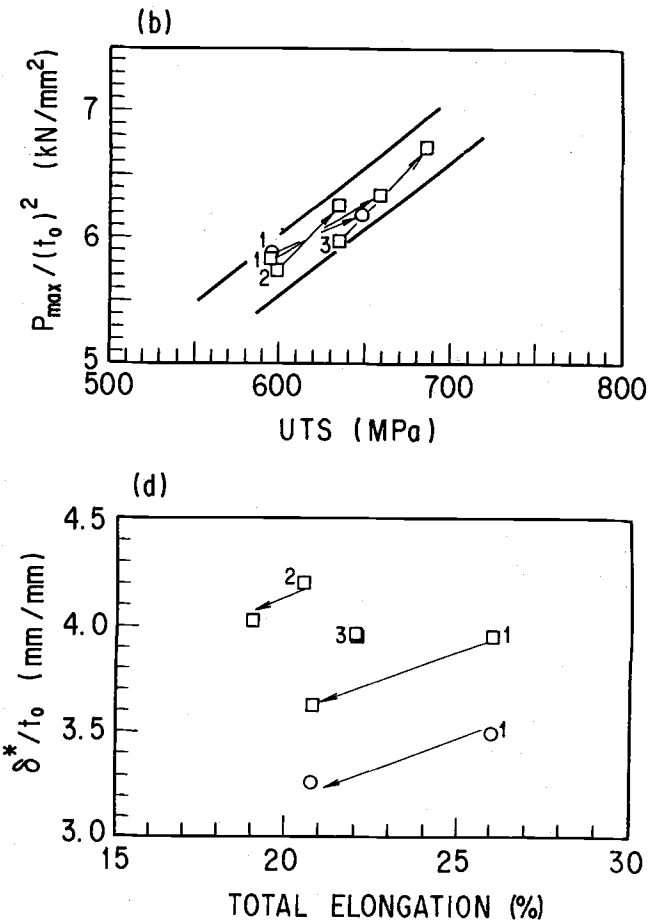

FIG. 6—*Continued.*

As reported in Ref *8*, values of $\bar{\epsilon}_{qf}$ for irradiated Cr-Mo steel were somewhat higher than expected from the relationship shown in Fig. 7. To determine the cause of this, more data should be accumulated. It should be mentioned that one must be very cautious about the application of the result of the SP test to the estimation of fracture toughness of irradiated materials.

Evaluation of SPDBTT—It is well known that SP energy falls drastically corresponding to the ductile-brittle transition of the material. SP energy was analytically related with the ductile-brittle transition behavior by several researchers [*3,9*]. The transition temperature (SPDBTT) is approximately linearly correlated with DBTT measured by a Charpy test

$$\text{SPDBTT} = \alpha \times \text{CVN-DBTT} \tag{4}$$

where α is the correlation coefficient ranging from 0.35 to 0.45 [*9–11*]. Here, each DBTT is represented in K.

In the present experiment on the ferritic steels other than Cr-Mo, only five to six irradiated specimens were tested at temperatures from 113 to 300 K so that the statistical analysis described in the previous section was applied to the data points. The results on the F-82H alloy are shown in Fig. 8. SPDBTTs were determined using the same distribution parameters obtained for the unirradiated specimens.

The CVN-DBTT shift predicted by SP tests are plotted in Fig. 9 against the increase in 0.2% offset stress. The CVN-DBTT shift was estimated assuming $\alpha = 0.4$ in Eq 4. The line mentioned in Ref *12*, which represents $\Delta T/\Delta\sigma_{0.2} = 5$ K/10 MPa, is shown in the figure

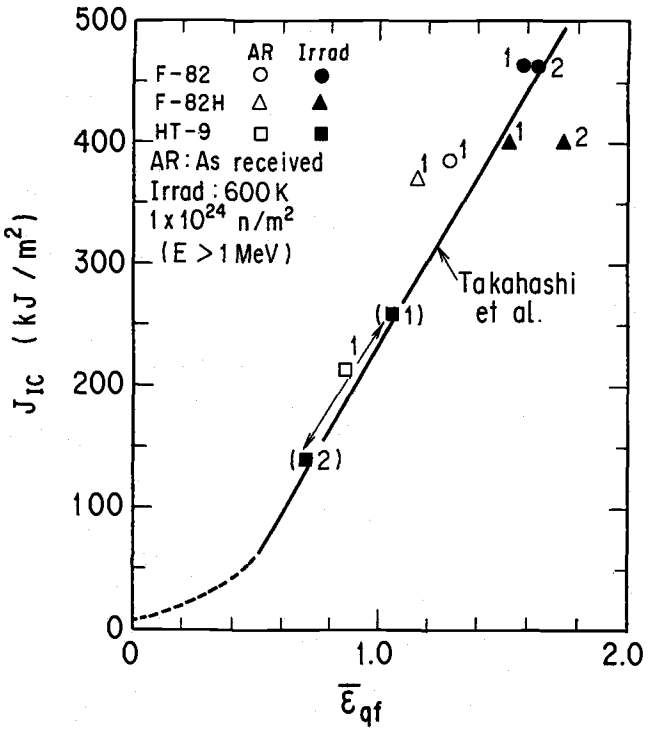

FIG. 7—*Correlation between the fracture toughness and equivalent fracture strain for ferritic steels.*

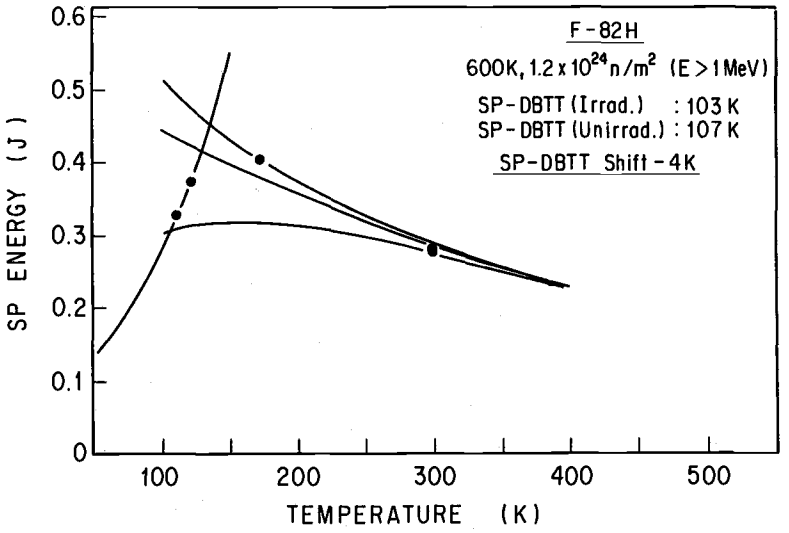

FIG. 8—*An example of the results on SP energy as a function of temperature for F-82H.*

for comparison. It is seen that the estimation of DBTT of irradiated HT-9 alloy is also difficult. However, the results on the other materials seem reasonable. The results indicate that the CVN-DBTT shift can be evaluated from that of the SPDBTT and that as many as 20 specimens would be desirable to assure reliability of evaluation.

Data on the Charpy impact test of irradiated HT-9 steel were obtained by Vitek et al. [*13*]. The lower fluence in their paper is 0.86×10^{24} n/m^2 and the temperature is 573 K, in comparison with 1.2×10^{24} and 600 K in the present study. The DBTT shift obtained by them seems to be less than 20 K, which gives a data point still lower than the line in Fig. 9.

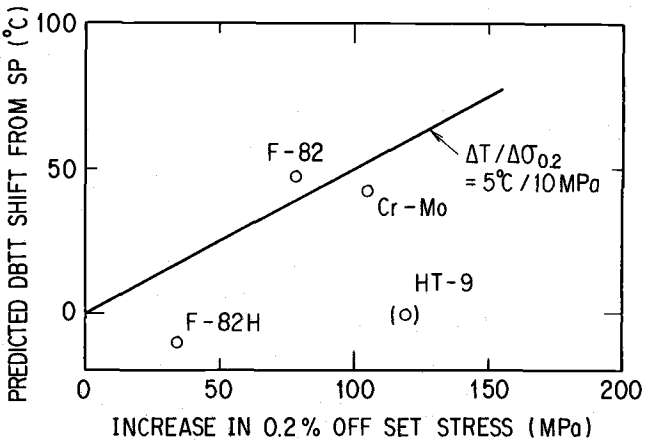

FIG. 9—*Charpy DBTT shift estimated from SP test results plotted as a function of change in 0.2% offset stress for several ferritic steels.*

Conclusions

Detailed procedures of the SP test including the apparatus, the definition of SP-related parameters, and the interpretation of results were presented, aiming at its standardization. A statistical approach to analyze the results on SP energy of a limited number of specimens was also reviewed for application of the method to irradiated ferritic steels.

Neutron-irradiated F-82, F-82H, HT-9, and 2¼Cr-1Mo ferritic steels were tested in the proposed way at temperatures from 100 to 300 K. Irradiation conditions were 2 to 12 × 10^{23} n/m^2 ($E > 1$ MeV) at temperatures from 573 to 673 K.

The main conclusions are:

1. The 0.2% offset stress and the ultimate tensile strength of these materials at room temperature can be evaluated from SP-related parameters such as $P_y/(t_0)^2$ and $P_{max}(t_0)^2$ obtained from the SP test at room temperature.
2. Fracture toughness can be evaluated in principle using the relationship established previously between J_{IC} and the equivalent fracture strain, $\bar{\epsilon}_{qf}$, on various materials, though there were discrepancies observed for HT-9 and 2¼Cr-1Mo steel.
3. The DBTT measured by a Charpy test may be estimated from the results on the temperature dependence of SP energy, i.e., SPDBTT obtained from five or six specimens. However, the number of specimens necessary for the more reliable prediction would be larger, especially for the materials with a heterogeneous microstructure.

References

[1] Baik, J. M., Kameda, J., and Buck, O., "Small Punch Test Evaluation of Intergranular Embrittlement of an Alloy Steel," *Scripta Metallurgica*, Vol. 17, No. 12, pp. 1443–1447.

[2] Baik, J. M., Kameda, J., and Buck, O., "Development of Small Punch Tests for Ductile-Brittle Transition Temperature Measurement of Temper Embrittled Ni-Cr Steels," *The Use of Small-Scale Specimens for Testing Irradiated Materials, ASTM STP 888*, W. R. Corwin and G. E. Lucas, Eds., American Society for Testing and Materials, Philadelphia, 1986, pp. 92–111.

[3] Mao, X., Shoji, S., and Takahashi, H., "Characterization of Fracture Behavior for Small Punch Test by Combined Recrystallization Etch Method and Rigid Plastic Analysis," *Journal of Testing and Evaluation*, JTEVA, Vol. 15, No. 1, 1987, pp. 30–37.

[4] Takahashi, H., Shoji, T., Mao, X., Hamaguchi, Y., Misawa, T., Saito, M., Oku, T., Kodaira, T., Fukaya, K., Nishi, H., and Suzuki, M., "Recommended Practice for Small Punch (SP) Testing of Metallic Materials (Draft)," JAERI-M Report 88-172, Japan Atomic Energy Research Institute, September 1988.

[5] Misawa, T., Suzuki, K., Saito, M., and Hamaguchi, Y., "Determination of the Minimum Quantity of Irradiated Ferritic Steels Specimens for Small Punch DBTT Testing," *Journal of Nuclear Materials*, Vol. 179-181, 1991, pp. 421–424.

[6] Ghosh, A. K. and Hecker, S. S., "Failure in Thin Sheets Stretched over Rigid Punches," *Metallurgical Transactions*, Vol. 6A, 1975, pp. 1065–1074.

[7] Nishiyama, Y., Fukaya, K., Suzuki, M., Kodaira, T., and Oku, T., "Evaluation of Irradiation Embrittlement of 2¼Cr-1Mo Steel in Terms of Elastic-Plastic Fracture Toughness," *Effects of Radiation on Materials: 15th International Symposium, ASTM STP 1125*, R. E. Stoller, A. S. Kumer, and D. S. Gelles, Eds., American Society for Testing and Materials, Philadelphia, 1992.

[8] Suzuki, M., Eto, M., Fukaya, K., Nishiyama, Y., Kodaira, T., Oku, T., Adachi, M., Umino, A., Takahashi, H., Misawa, T., and Hamaguchi, Y., "Evaluation of Toughness Degradation by Small Punch (SP) Tests for Neutron-Irradiated 2¼Cr-1Mo Steel," *Journal of Nuclear Materials*, Vol. 179-181, 1991, pp. 441–444.

[9] Kameda, J., "A Kinetic Model for Ductile-Brittle Fracture Mode Transition Behavior," *Acta Metallurgica*, Vol. 34, No. 12, 1986, pp. 2391–2398.

[10] Misawa, T., Adachi, T., Saito, M., and Hamaguchi, Y., "Small Punch Tests for Evaluating Ductile-Brittle Transition Behavior of Irradiated Ferritic Steels," *Journal of Nuclear Materials*, Vol. 150, No. 1, 1987, pp. 194–202.

[11] Matsushita, T., Saucedo, M. L., Joo, Y. H., and Shoji, T., "DBTT Estimation of Ferritic Low

Alloy Steels in Service Plant by Means of Small Punch Test," *Proceedings,* KSME/JSME Joint Conference, Fracture and Strength '90, 6–7 July, 1990, Seoul, Korea.

[*12*] Odette, G. R., Lombrozo, P., and Wullaert, R. A., "Relationship Between Irradiation Hardening and Embrittlement of Pressure Vessel Steels," *Effects of Radiation on Material: 12th International Symposium, ASTM STP 870,* F. A. Garner and J. S. Perrin, Eds., American Society for Testing and Materials, Philadelphia, 1985, pp. 840–860.

[*13*] Vitek, J. M., Corwin, W. R., Klueh, R. L., and Hawthorne, J. R., "On the Saturation of the DBTT Shift of Irradiated 12Cr-1Mo VW with Increasing Fluence," *Journal of Nuclear Materials,* Vol. 141-143, Part B, 1986, pp. 948–953.

Shigetomo Nunomura,[1] *Tohoru Nishijima,*[2] *Yakichi Higo,*[1] *and Akimichi Hishinuma*[3]

Evaluation of Tensile Properties Using a TEM Disk-Size Specimen

REFERENCE: Nunomura, S., Nishijima, T., Higo, Y., and Hishinuma, A., **"Evaluation of Tensile Properties Using a TEM Disk-Size Specimen,"** *Small Specimen Test Techniques Applied to Nuclear Reactor Vessel Thermal Annealing and Plant Life Extension, ASTM STP 1204,* W. R. Corwin, F. M. Haggag, and W. L. Server, Eds., American Society for Testing and Materials, Philadelphia, 1993, pp. 256–266.

ABSTRACT: Attempting to miniaturize mechanical specimens is certainly not new. In fusion reactor material development, limited space in the test reactor and the dose to personnel in the post-irradiation state dictates that the specimen size be reduced without reducing the accuracy of the test. A four-point bend test on TEM disk specimens (0.3 mm in thickness and 3 mm in diameter) was carried out to evaluate tension test parameters. The bending load-deflection records obtained from the miniature specimen were interpreted with a large-scale deflection bending analysis. The tensile yield strength and the ultimate tensile strength of both a 316L-type stainless steel and a 7075 T6 aluminum (Al) alloy obtained from the miniature four-point bend test agreed well with standard tension test results. A gripping system for tension testing of the TEM-size specimens was also developed. The ultimate tensile strength results of two stainless steels agreed well with those obtained from standard-size specimens; however, the tensile yield strength could not be determined.

KEYWORDS: small specimen, tensile properties, bend test, small tension test, fusion reactor materials

The following advantages are evident if a material can be examined using a small-size specimen. First, the restriction concerning the size of the test material is released. Specimens can be extracted from a small piece of the structure following catastrophic failure. Distribution of mechanical properties in a minute part as well as distribution of the chemical composition can be examined employing an electron probe microanalyzer (EMX). Since the weight of a material for specimen fabrication decreases, the cost of materials is reduced. Reduction of manufacturing cost of the specimen is also expected. The cost of test equipment is reduced with the subsequent decrease in test load parameters. In addition, where there is concern about pollution from radioactive materials, the risk is dramatically reduced in proportion to the weight of the specimen.

Prior to designing a structure, detailed data of material characteristics are necessary. Material testing is performed to obtain properties data, particularly concerning mechanical properties. If the mechanical properties are linearly related to specimen size, experimental

[1] Professor, Precision and Intelligence Laboratory, Tokyo Institute of Technology, Nagatsuta, Midori-ku, Yokohama, Japan 227.

[2] Former graduate student, Tokyo Institute of Technology, Nagatsuta, Midori-ku, Yokohama, Japan 227.

[3] Principal researcher, Department of Fuels and Materials Research, Japan Atomic Energy Research Institute, Tokai-mura, Ibaraki-ken, Japan 319-11.

data from miniaturized specimens may easily be converted into values for standard-size specimens. However, in engineering standards, the dimension and shape of the specimen are defined in detail since most mechanical properties do not depend on the size of the structure in a simple manner. Some properties change discontinuously with specimen-size change, and therefore the actual component size must be tested unless a law for the conversion is established. Fracture toughness is an example, where the safety of a structure cannot be confirmed by using a reduced scale model except under special circumstances. Therefore, the potential for using miniaturized specimens is dependent on whether or not a conversion rule is established. Some conversion rules provide only approximate values, which affect the accuracy of the evaluation [*1*].

In a miniaturized specimen the measured length will be small, and therefore errors are easily introduced. As a result, the accuracy of the evaluation is decreased. To compensate for accuracy losses from using miniaturized specimens, a high precision of the loading and measuring systems is required, although this suppresses the advantage in decreasing the cost of testing.

The mechanical properties of a structural material are strongly dependent on grain size and grain structure. Manufacturing miniature specimens may change the relative effect of the crystal boundary. Though the evaluation of mechanical characteristics by using miniaturized specimens has many merits, it has not been adopted for general test procedures because of the above-mentioned disadvantages. Its use is minimal and limited only to special circumstances.

In evaluating and developing nuclear fusion first wall material, the specimen size should be as small as possible because of the limited volume for irradiating specimens, the high cost of irradiating specimens, and the difficulty in handling irradiated material.

Therefore, employing a miniaturized specimen technique is extremely desirable. However, the results obtained from miniaturized specimens must be equivalent to those obtained using standard-size specimens. In addition, accurate nuclear reactor material characteristics are of prime importance. Unfortunately, there has been no advancement in improving the testing technique in recent years. Use of miniaturized specimens has, however, been adopted for the development of gradient function material, which is a newly developed material [*2*].

The specimen size adopted to evaluate the first wall material characteristics has been a TEM disk, 3 mmϕ by 3 mm (Fig. 1). The disk-bending test, the disk-punching test, and the

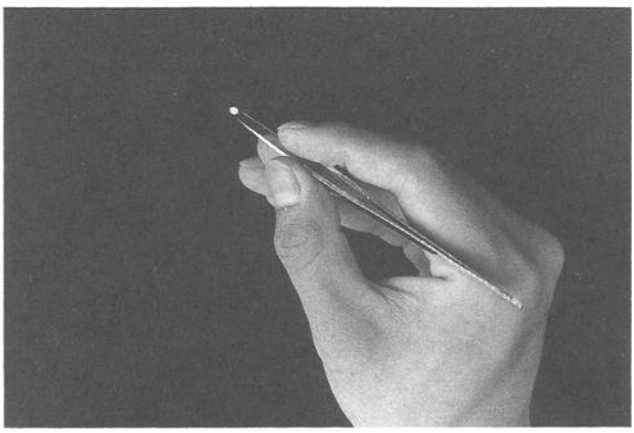

FIG. 1—*TEM disk-size specimen.*

micro-hardness test have been performed using this specimen [*3,4*], but they do not provide the stress-strain relationship which represents the essence of the mechanical characteristics of the material. Detailed information of the stress-strain relationship is earnestly required in designing the furnace. The tension test provides the tensile properties directly, but the test machine has difficulty gripping the TEM disk. Gripless-type specimens are desired for a test done in the hot laboratory, where manipulator operations are required. The authors developed a method evaluating the stress-strain relationship by a combination of miniaturized four-point bend test and numerical analysis. It is known that the bend test alone does not provide a knowledge of reliable mechanical properties.

The authors have developed a new type of gripping system for tension-tension fatigue testing of TEM-size specimens [*5*]. Tensile properties were also determined employing this equipment in two stainless steels. The .small tension test seems inferior to the analytical bend test, which is easy to perform and produces accurate results for irradiated materials.

Experimental Procedure

The materials used in the present work were a modified 316 austenitic stainless steel and a 7075 T6 aluminum alloy. The chemical compositions are listed in Table 1 for both materials. The steel, which had been rolled in various reductions, was supplied by the Japan Atomic Power Research Institutes in the form of TEM disks.

Since the disk shape, stress, and moment change with distance from the loading point due to sectional area alteration in four-point bending, an accurate stress analysis becomes difficult. Therefore, a bar-like specimen was used in the present work.

For the test apparatus, tool alloy rods 0.3 mm in diameter were used for the loading pins, with intervals between the outer and inner pins equal to 2.2 and 0.8 mm, respectively. Standard-size tension specimens were also used in comparative tests. Details of the small tension test are described in Ref *5*.

Evaluation

True Stress—True Strain Relationship

The true stress–true strain relationship cannot be deduced analytically from the load deflection record of three- or four-point bend tests where the material has been plastically deformed.

In this evaluation a true stress–true strain relation $\sigma(\epsilon)$ was assumed, and the corresponding bending load/deflection curve was deduced numerically as shown in the following sections. The curve was compared with that obtained experimentally, and the assumed relation $\sigma(\epsilon)$ was adjusted for the next calculation. If the calculated load/deflection curve was within

TABLE 1—*Chemical composition of material tested (wt%).*

Alloy	C	Cr	Ni	Mo	Ti	Fe			
316Mod	0.04	14.0	16.0	2.5	0.25	bal.			
Alloy	Cu	Fe	Si	Mg	Mn	Zn	Cr	Ti	Al
7075	1.49	0.17	0.08	2.65	0.02	5.46	0.25	0.01	bal.

an acceptable tolerance band, based on the experimentally determined load/deflection curve, then the original assumption was assumed correct.

Moment-Curvature Relationship

The equilibrium equations of the force and the moment in the bending bar are given in the form of the following integrals

$$\int \sigma(1 - \nu \cdot \epsilon) \exp(\epsilon)\, d\epsilon = 0 \tag{1}$$

$$\int \sigma(1 - \nu \cdot \epsilon)\{\exp(\epsilon) - 1\} \exp(\epsilon)\, d\epsilon = M \frac{\kappa^2}{B_0} \tag{2}$$

where σ is the true stress, ϵ is the true strain, ν is Poisson's ratio, M is the moment, κ is the curvature, and B_0 is the initial width of the bar. Since both the upper and lower bounds of the integral are a function of κ, Eqs 1 and 2 are differentiated with respect to κ, applying Leibnitz's rule.

$$\sigma_t \exp(\epsilon_t) \frac{d\epsilon_t}{d\kappa} - \sigma_c \exp(-\epsilon_c) \frac{d\epsilon_c}{d\kappa} = 0 \tag{3}$$

$$\sigma_t\{\exp(2\epsilon_t) - \exp(\epsilon_t)\} \frac{d\epsilon_t}{d\kappa}$$

$$-\sigma_c\{\exp(2\epsilon_c) - \exp(-\epsilon_c)\} \frac{d\epsilon_c}{d\kappa} = \frac{\kappa}{B_0\left(2M + \kappa \dfrac{dM}{d\kappa}\right)} \tag{4}$$

where σ_t and σ_c are the true tensile and the true compressive stresses, respectively, ϵ_t and ϵ_c are the true tensile and the true compressive strains, respectively, and H is the thickness. Equation 3 is given in the following form of differential equation

$$\frac{d\epsilon_t}{d\epsilon_c} = \frac{\sigma_c (1 + \nu\epsilon_c)}{\sigma_t (1 - \nu\epsilon_t)} \exp(-\epsilon_c - \epsilon_t) \tag{5}$$

$\epsilon_t - \kappa$ and $\epsilon_c - \kappa$ quantities are given by numerical integration using the Runge-Kutta's method.

The curvature κ may also be expressed as follows

$$\kappa = \{\exp(\epsilon_t) - \exp(-\epsilon_c)\}/H \tag{6}$$

Equation 4 may also be given in the following form of differential equation

$$\frac{dM}{d\kappa} = \frac{B_0}{\kappa^2}\left[\sigma_t (1 - \nu\epsilon_t)\{\exp(2\epsilon_t) - \exp(\epsilon_t)\} \frac{d\epsilon_t}{d\kappa}\right.$$

$$\left. -\sigma_t (1 + \nu\epsilon_c)\{\exp(-2\epsilon_c) - \exp(\epsilon_c)\} \frac{d\epsilon_c}{d\kappa}\right] - \frac{2M}{\kappa} \tag{7}$$

The M-κ relation is also given by numerical integration using Runge-Kutta's method. When integrating Eq 7, $\epsilon_t - \kappa$, $\epsilon_c - \kappa$, $d\epsilon_t/d\kappa - \kappa$, and $d\epsilon_c/d\kappa - \kappa$ relations obtained above are used.

Load-Deflection Relationship

The load applied to a large deformed bar can be deduced from the M-κ relationship after due consideration of the effect of friction between the loading pin and the specimen and on the loading vector change.

Assuming the friction coefficient is μ and the friction angle $\omega = \arctan\mu$, the relationship between the load P and the moment M of the deformed bar may be written as follows [*6*,*7*]

$$M = \frac{P}{2}\left(x + \frac{H}{2}\sin\theta_a\right) + \frac{P}{2}\tan(\theta_a - \omega)\left(y - \frac{H}{2}\cos\theta_a\right)$$

$$\left\{0 \le x \le a - \left(r + \frac{H}{2}\right)\sin\theta_a - \left(r + \frac{H}{2}\right)\cos\theta_a\right\} \tag{8}$$

$$M = \frac{P}{2}\left\{a - \left(r + \frac{H}{2}\right)(\sin\theta_a + \sin\theta_c)\right\} + \frac{P}{2}\tan(\theta_a - \omega)\left(y - \frac{H}{2}\cos\theta_a\right)$$

$$- \frac{P}{2}\tan(\theta_c + \omega)\left(y - y_c + \frac{H}{2}\cos\theta_c\right)\left\{a - \left(r + \frac{H}{2}\right)\sin\theta_a - \left(r + \frac{H}{2}\right)\cos\theta_a\right.$$

$$\left. < x \le 1 - \left(r + \frac{H}{2}\right)\sin\theta_a\right\} \tag{9}$$

where θ_a and θ_c are angles between the bar axis and x-axis at the outer pin and the inner pin, respectively (Fig. 2) and are also equal to dy/dx in Eq 10. The curvature κ may be

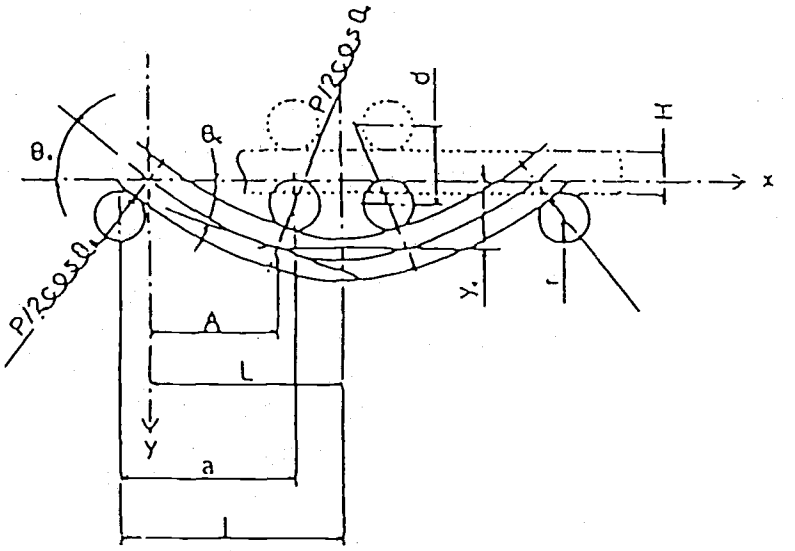

FIG. 2—*Four-point bend test.*

written as follows and may be solved numerically

$$\kappa = \frac{\frac{d^2y}{dx^2}}{\left\{\left(1 + \frac{dy}{dx}\right)^2\right\}^{3/2}} \tag{10}$$

where y is the deflection at x.

Young's Modulus, Yield Strength, and Tensile Strength

Yield strength and Young's modulus may be directly read from the true stress–true strain curve. The tensile strength can be obtained as follows. In the tension specimen, the load is the product of the true stress and area of specimen cross section

$$P = \sigma A$$

$$dP = \sigma dA + A d\sigma$$

Tensile strength is the stress where the load P is maximum.

$$dP = 0$$

$$\frac{dA}{A} = -\frac{d\sigma}{\sigma} \tag{11}$$

During plastic deformation, the volume of specimen is held constant.

$$V = LA$$

$$dV = LdA + AdL = 0$$

$$\frac{dA}{A} = -\frac{dL}{L} = -d\epsilon \tag{12}$$

Substituting Eq 11 into Eq 12

$$\frac{d\sigma}{d\epsilon} = \sigma$$

That is, the value of σ which agrees with the gradient of the true stress–true strain curve is the "true" tensile strength and is converted into the nominal tensile stress σ_n using the following relationship

$$\sigma_n = \frac{\sigma}{\exp(\epsilon_n)}$$

Ductility

The elongation and the local contraction are often used for engineering measures of the ductility of the material. In the common bend test, however, such parameters are not

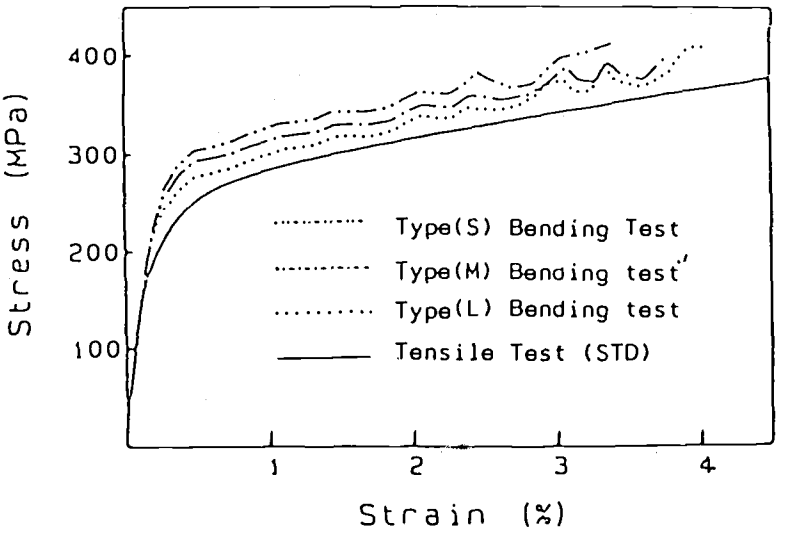

FIG. 3—*Calculated true stress–true strain curves.*

available. Inspection of them, the uniform elongation, the elongation at the maximum load, and the absorbed energy up to the maximum load were obtained from the resultant true stress–true strain relationship.

Results and Discussion

To confirm the analysis, three different geometrical stainless steel specimens were employed: (L) 180 by 32 by 6, (M) 90 by 16 by 3, and (S) 45 by 8 by 1.5 (mm). Figure 3 shows the true stress–true strain curves deduced from a standard scale four-point bend test (as-

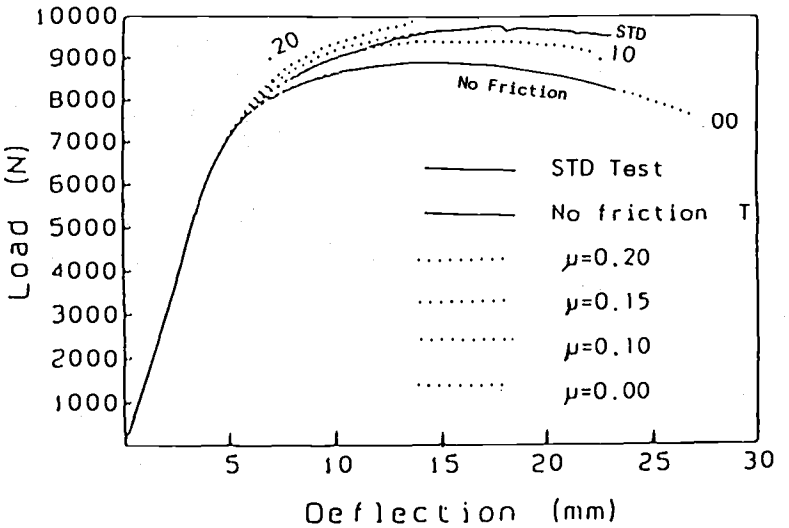

FIG. 4—*Effect of friction in the bend test.*

suming the friction coefficient equals zero) compared with that from the tension test using the same material. From the first approximation, the deduced curves agree with those obtained experimentally. There is a small effect of specimen size, however, because the curve from the larger specimen showed better agreement.

The difference vanished when the assumed frictional coefficient was 0.20, and thus in subsequent calculations this value was used for the deduction from the bend test record of the TEM disk specimen (Fig. 4).

Figure 5 shows an example of the load curves obtained from the miniaturized bend test. The scatter in the curves was attributed to the variation in specimen size, and the subsequent scatter in the true stress–true strain curve was less than that in the load curves. Figure 6 shows the true stress–true strain curves for the modified stainless steel where $\mu = 0.2$ was assumed. Table 2 shows the 0.2% proof stress and the tensile strength of the steel obtained

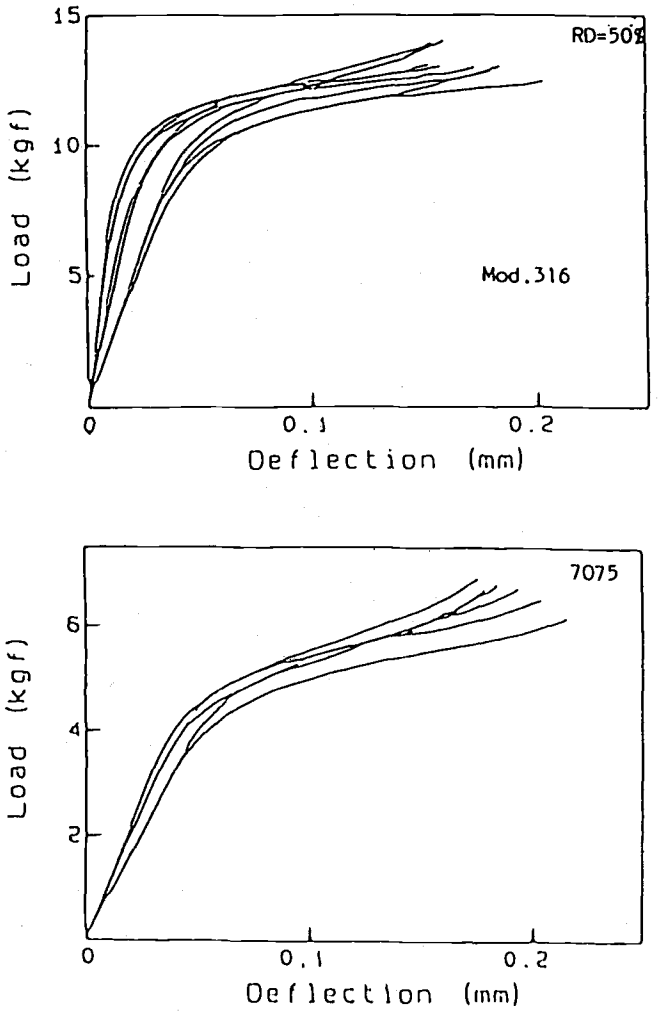

FIG. 5—*Load-deflection curves by the miniature specimen bend test.*

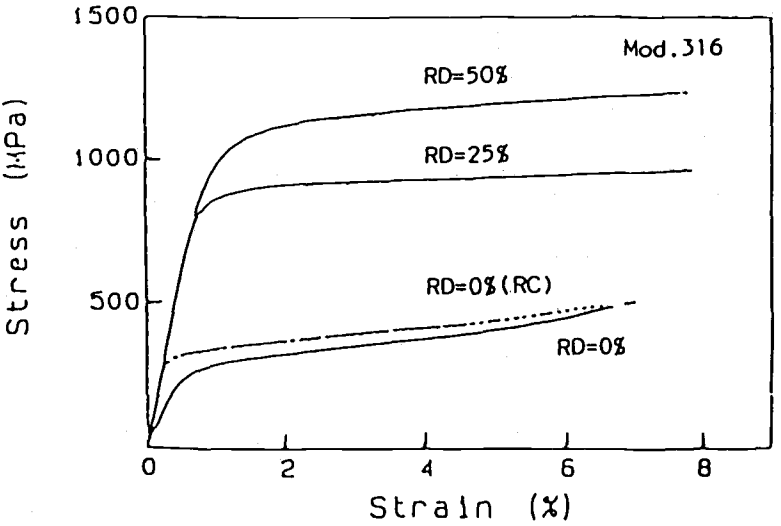

FIG. 6—*True stress–strain curves of the modified 316 stainless steel.*

from the miniaturized four-point bend test and the regular tension test. They were deduced under the assumption of both "no friction" and a value of $\mu = 0.2$. Deduced 0.2% proof stresses using a value of $\mu = 0.2$ did agree surprisingly with regular tension tests. Except for the 0% reduction steel, errors in the tensile strength remained less than 5%. The reason for the larger error in the tensile strength of the 0% reduction steel was investigated according to the following conditions: (1) local deformation of both the specimen and loading pins, (2) microstructural effect of the material, and (3) calculation errors due to large plastic deformation. The effect of the local deformation in the specimen and in the device seems negligible according to the hardness data analysis. As for the polycrystal material, more than three grains in the slipping direction are required [*8*]. When the grain size of the steel tested was about 100 μm, there were more than three grains existing in the smallest specimen section. The true strain deduced from the bend load record was less than 5%, and the true strain at the estimated maximum load was more than 20%. For precise extrapolation, the load record incorporating larger plastic deformation may be required.

Figure 7 shows stress-strain diagrams from miniature tension tests for a SUS316L stainless steel. Although the shape of each plot was not identical, their ultimate strengths showed

TABLE 2—*Tensile properties obtained by the micro-size bend test and the regular-size tension test in a 316L-type stainless steel and a 7075-T6 Al alloy (MPa).*

Materials Specimen	rd	0.2% Proof Strength		Tensile Strength	
		Micro	Regular	Micro	Regular
316L	0%	232	237	274	526
	25%	721	733	798	761
	50%	900	902	1012	979
7075-T6		450	461	490	530

NOTE: rd = reduction by cold rolling.

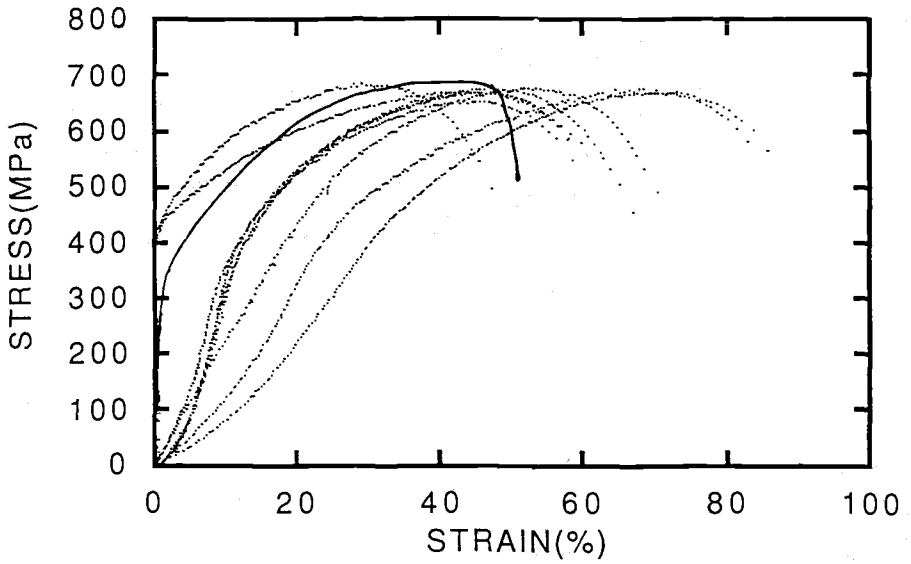

FIG. 7—*Stress-strain diagrams from miniature tension tests for a SUS316L stainless steel. The solid line represents a regular-size tension test result.*

good correspondence. The solid line in Fig. 7 represents the stress-strain diagram from a regular-sized specimen of the same steel. Since measurement in the early stages of displacement is unsuccessful, the tensile yield strength and the elongation were not evaluated. The displacement-measuring system is being improved. Figure 8 also shows stress-strain diagrams from miniature tension tests for a SUS304 stainless steel.

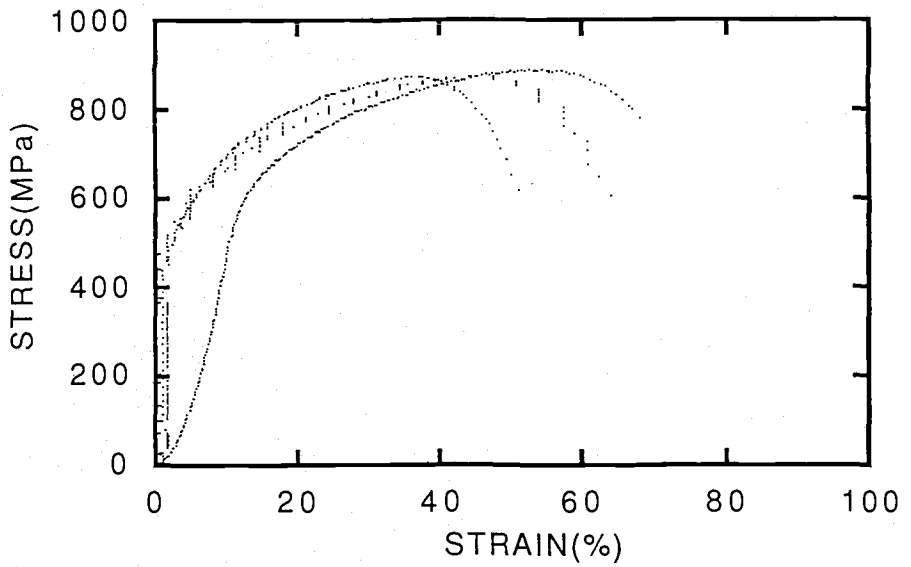

FIG. 8—*Stress-N strain diagrams from miniature tension tests for a SUS304 stainless steel.*

Conclusion

The experimentally obtained bending load-deflection records from TEM disk-type miniature specimens were interpreted following the development of a large-scale deflection bending analysis. The effect of friction in the device was small, but for precise evaluation a friction coefficient of 0.20 should be incorporated into the analysis. The tensile yield strength of a 316L-type stainless steel and a 7075-T6 Al alloy deduced from the miniature four-point bend test agreed well with the standard specimen tension test. Except for the most ductile steel, errors in the experimentally obtained tensile strength remained less than 5%.

References

[1] Igata, N., Miyahara, K., Uda, T., and Asada, S., "Effects of Specimen Thickness and Grain Size on the Mechanical Properties of Types 304 and 316 Austenitic Steel," *The Use of Small-Scale Specimens for Testing Irradiated Materials, ASTM STP 888,* American Society for Testing and Materials, Philadelphia, 1986, p. 161.

[2] Saito, M. and Takahashi, H., "Development of Small Punch Test Procedure for FGM Fabrication," *Proceedings,* 1st International Symposium on FGM (FGM90), JSM, Sendai, Japan, 1990, p. 297.

[3] Corwin, W. R. and Lucas, G. E., Eds., in *The Use of Small-Scale Specimens for Testing Irradiated Materials, ASTM STP 888,* American Society for Testing and Materials, Philadelphia, 1986.

[4] Lucas, G. E., Odette, G. R., and Sheckherd, "Shear Punch and Microhardness Tests for Strength and Ductility Measurements," *The Use of Small-Scale Specimens for Testing Irradiated Material, ASTM STP 888,* W. R. Corwin and G. E. Lucas, Editors, American Society for Testing and Materials, Philadelphia, 1986, pp. 112–140.

[5] Nunomura, S., Noguchi, S., Okamura, Y., Kumai, S., and Jitsukawa, S., "Two Micro Fatigue Test Methods for Irradiated Materials," this publication, pp. 275–288.

[6] Ohtsuki, A., "An Analysis on a Large Scale Deflection in Beam," *Journal of NDT (Japan),* Vol. 34, 1985, p. 453.

[7] Ohtsuki, A., "Large Scale Deflection Analysis Concerning the Friction," *Journal of the Japan Society of Mechanical Engineers,* Vol. 51, 1985, p. 2209.

Gopal R. Rao[1] *and Bryan A. Chin*[2]

Development of a Miniature-Disk Bending Fatigue Specimen

REFERENCE: Rao, G. R. and Chin, B. A., **"Development of a Miniature-Disk Bending Fatigue Specimen,"** *Small Specimen Test Techniques Applied to Nuclear Reactor Vessel Thermal Annealing and Plant Life Extension, ASTM STP 1204,* W. R. Corwin, F. M. Haggag, and W. L. Server, Eds., American Society for Testing and Materials, Philadelphia, 1993, pp. 267–274.

ABSTRACT: A miniature-disk bending fatigue specimen was earlier developed for testing materials to be used for fusion reactor applications. The specimen is based on a 3-mm-diameter transmission electron microscope disk. A second larger rectangular specimen was also developed, with dimensions of 30.16 by 4.76 by 0.76 mm. The specimens, made from annealed type 316 stainless steel, were tested using a specialized bending fatigue machine at temperatures of 25, 550, and 650°C. In the current study, the results are compared against standard full-size specimen results.

Strain ranges were calculated using an analytical technique based on specimen geometry and material properties. For the rectangular specimen, strains were also measured using strain gauges attached to the gauge region. The calculated strains were then modified using a calibration factor based on the measurement. The rectangular specimen results were in good agreement with ASTM full-size specimen results. The miniature-disk specimen data fell below the other results, indicating that the analytical technique underestimates strain values. No clear temperature dependence was evident for the miniature-disk specimen, unlike larger specimens which show a degradation of fatigue properties with increasing temperature. The miniature-disk specimen results also show a greater scatter about the best-fit curve, which was attributed to greater sensitivity to misalignment.

KEYWORDS: miniaturized specimen technology, fatigue, stainless steel, fusion

Miniaturized specimen technology (MST) is of significance in the nuclear industry and has been utilized in the past for developing, testing, and monitoring materials used in or proposed for nuclear power generation systems. The current fusion materials program has further added to the interest in the development of small-scale specimens due to the limited irradiation volume available in existing and proposed neutron irradiation facilities capable of simulating fusion reactor conditions [*1*]. Fluence gradients in irradiated specimens, gamma heating, availability of materials, and concerns regarding radiation exposure to personnel are other factors that make MST attractive [*1,2*].

Currently envisioned fusion reactors will operate in a cyclic mode. Therefore, thermal fatigue becomes an important factor, and determination of cyclic properties of materials in an irradiated condition become important for the design of first wall and blanket materials. At Auburn University, two small-scale bending fatigue specimens have been developed for

[1] Post-doctoral fellow, Oak Ridge National Laboratory, Metals and Ceramics Division, P.O. Box 2008, Building 5500, M.S. 6376, Oak Ridge, TN 37831.

[2] Professor and chairman, Materials Engineering Program, Auburn University, 201 Ross Hall, Auburn, AL 36849.

this purpose. Earlier papers have described the development of the specimens and compared results with accepted larger sub-size axial fatigue specimens [*3,4*]. It was shown that good agreement existed between the fatigue data for the two specimens. In this paper, fatigue test results obtained for the smaller of the two specimens, the miniature-disk specimen, are compared with those obtained from the full-size and the other subsize specimen.

Experimental

Specimen

The specimen developed is termed the miniature-disk specimen and is shown in Fig. 1. It is basically a 3-mm transmission electron microscope disk with two circular notches of radius 1.5 mm each, cut from the disk to form the gauge region. The specimens were made from type 316 stainless steel of reference heat 8092297 obtained from Oak Ridge National Laboratory. All specimens were fabricated from the same batch of material. The specimens were fabricated from 0.254-mm-thick sheets using the electric discharge machining technique. This technique produces one of the smallest depths of surface damage among the various metal-cutting techniques available [*5*].

Along with the miniature-disk specimen, a second specimen, termed the rectangular specimen, with dimensions of 30.16 by 4.76 by 0.76 mm, was also developed and is shown in Fig. 2. Results obtained using the rectangular specimen were compared with the miniature-disk specimen results [*3,4*]. All specimens were subjected to a vacuum anneal at 1050°C for 1 h. The specimens were electrolytically polished using a 95% ethanol-5% perchloric acid electrolyte at 0°C to remove surface damage produced during fabrication.

Fatigue Test Machine

A specialized bending fatigue machine was developed for testing both specimens. The specimens are tested in a cantilever beam configuration with one end fixed and load applied to the free end. The load is applied by means of an eccentric cam which enables changing the deflection and hence the load on the specimen. The load is detected using a load cell consisting of four strain gauges connected to the end of the cantilevered specimen holder arm in a Wheatstone bridge network. The output of this bridge is calibrated in terms of

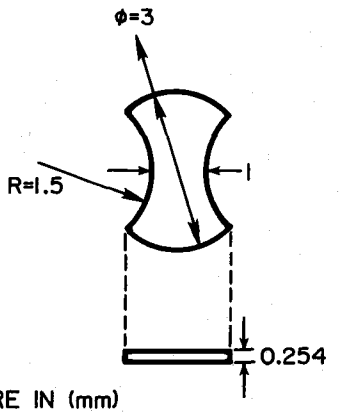

FIG. 1—*The miniature-disk specimen whose dimensions are based on those of a transmission electron microscope disk.*

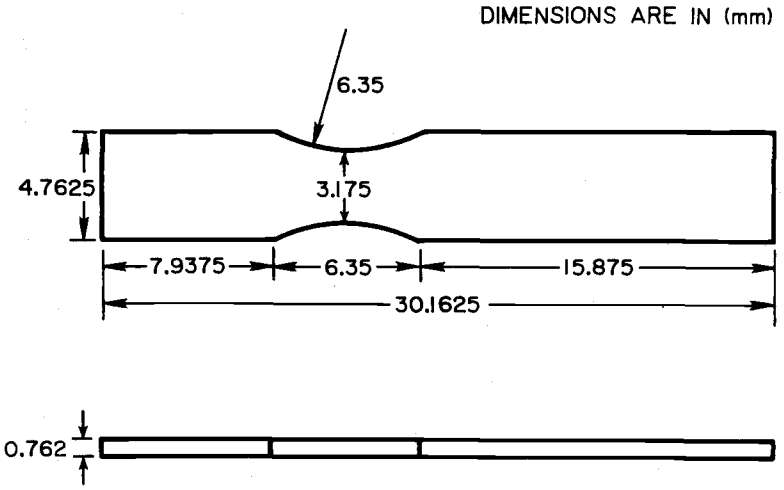

FIG. 2—*The rectangular specimen.*

applied load. The output of the load cell is conditioned by a control box before being monitored on an oscilloscope. Both cyclic load and input deflection can be monitored simultaneously.

The control box is used to terminate the test when the load decays to a pre-specified value, which in this study was 80% of the original load. The elevated temperature tests were performed using a stainless steel furnace enclosure around the specimen containing an electric heater coil, which is attached to a temperature controller. The temperature of the specimen is monitored by a thermocouple located at the center of the specimen gauge region which continually feeds temperature information back to the controller. An argon atmosphere is maintained within the furnace. Additional information concerning the test setup may be obtained from Ref *6*.

Results and Discussion

The fatigue data for the miniature-disk specimen are plotted in terms of total strain as a function of failure cycles in Fig. 3. Strain ranges were calculated using the specimen geometry and material properties [*6*]. The total strain range was calculated for the cross section of maximum stress where the fatigue crack formed. The results indicate no specific temperature effect. The results were analyzed in terms of a simple power law relation containing two components for the elastic and plastic regimes of the total strain range

$$\Delta\epsilon = AN^{-\alpha} + BN^{-\beta} \tag{1}$$

The results are shown in Table 1. The exponents α and β were assigned values of 0.12 and 0.5 for comparison with fatigue results obtained by Liu and Grossbeck, who used these values for the exponents in their analysis [*7,8*].

The results for the rectangular specimen are also shown in Fig. 3 for the three temperatures investigated. For the rectangular specimens, strain ranges were both calculated (using the same analytical technique used for the miniature-disk specimen) and measured using strain gauges attached to the gauge region. The analytical technique was found to underestimate

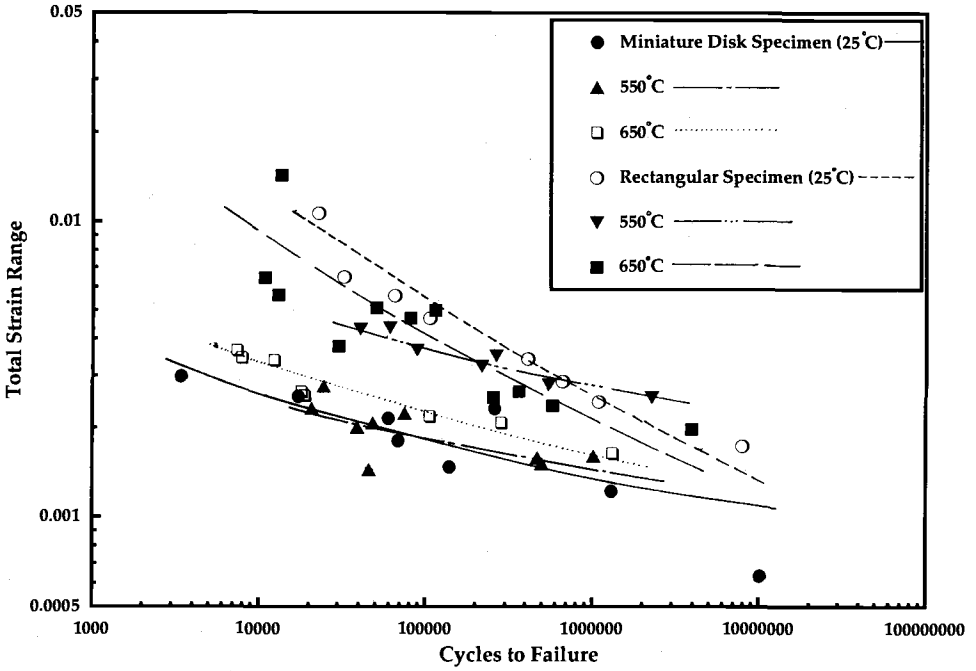

FIG. 3—*Fatigue results for the miniature-disk specimen compared with the rectangular specimen results at 25, 550, and 650°C.*

strain ranges. To correct for this difference, all calculated strains were modified by a calibration factor determined by the actual measurement, which was a function of the strain range, and the results are shown in Fig. 3. The results of a least squares regression of the data to fit Eq 1 are shown in Table 1. In this case, there is a clear degradation of fatigue properties with increasing test temperatures, with the 650°C results falling below the room temperature and 550°C results.

The room temperature data are compared in Fig. 4 with results reported by Jaske and Frey using standard ASTM full-size axial fatigue specimens [9]. The material tested by Jaske

TABLE 1—*Comparison of power law exponents and constants in Eq 1 for the miniature disk and rectangular specimens.*

Data	Temperature, °C	A	α	B	β
Disk	25	0.0072	−0.12	0.02	−0.5
Rectangular	25	0.007	−0.12	1.07	−0.5
Disk	550	0.007	−0.12	0.044	−0.5
Rectangular	550	0.014	−0.12	0.11	−0.5
Axial (ORNL)[a]	550	0.016	−0.12	0.66	−0.5
Disk	650	0.008	−0.12	0.06	−0.5
Rectangular	650	0.009	−0.12	0.6	−0.5
Axial (ORNL)[b]	650	0.014	−0.12	0.54	−0.5

[a] Ref 7.
[b] Ref 8.

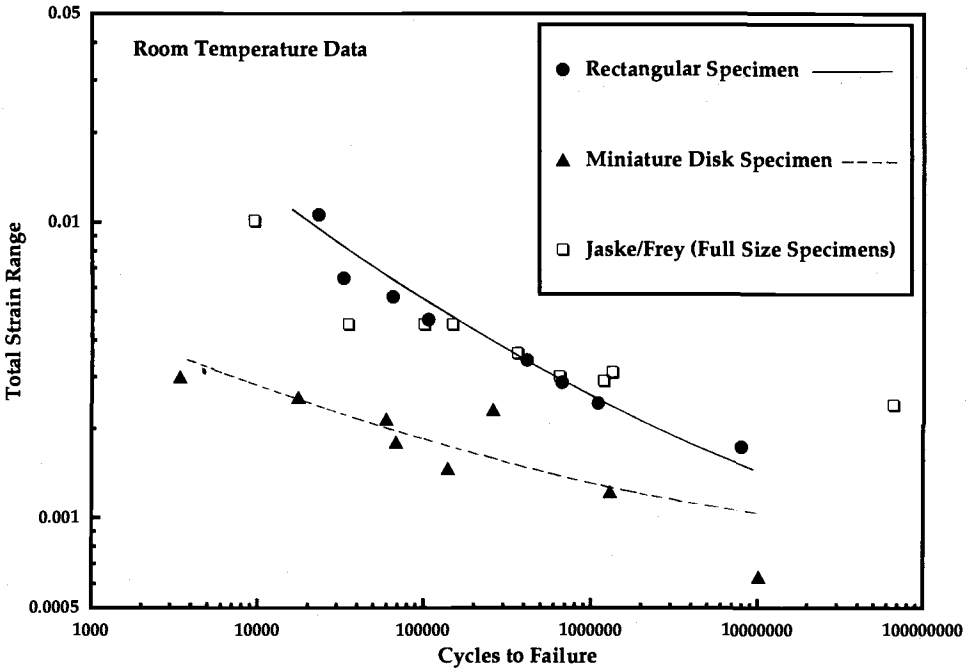

FIG. 4—*Room temperature results for the miniature-disk specimen compared with rectangular and ASTM full-size specimen results for annealed type 316 stainless steel.*

and Frey was annealed type 316 stainless steel, which is the same condition used in this study. It can be seen that the corrected strain range values for the rectangular specimen are in good agreement with the full-size specimen results. However, results for the miniature-disk specimen lie below the full-size specimen data, indicating that the analytical technique used in this study underestimates strain values.

Figure 5 similarly compares the elevated temperature results obtained for the miniature-disk and rectangular specimens with full-size specimens using annealed type 316 stainless steel tested at 550°C [*9*] and 650°C [*10*]. The figure also shows data reported by Liu and Grossbeck using subsize axial fatigue specimens which are half the size of a standard ASTM E 606 [ASTM Recommended Practice for Constant-Amplitude Low-Cycle Fatigue Testing] hourglass specimen with an identical geometry. They used 20% cold-worked type 316 stainless steel, which accounted for their data points lying above the annealed full-size specimen data [*7,8*]. Liu and Grossbeck have analyzed their data using Eq 1, and the results are shown in Table 1.

Jaske and Frey found that their data at different temperatures could be approximated by the relation

$$\Delta\epsilon = AN_f^{-a} + \Delta\epsilon_L \tag{2}$$

where the values of A, a, and $\Delta\epsilon_L$ were functions of temperature [*9*]. The data from this study were also analyzed using Eq 2, and the results obtained using a least squares regression are given in Table 2. As can be seen from Table 2 and Fig. 5, the elevated temperature data for the rectangular specimen are also in good agreement with the data reported by

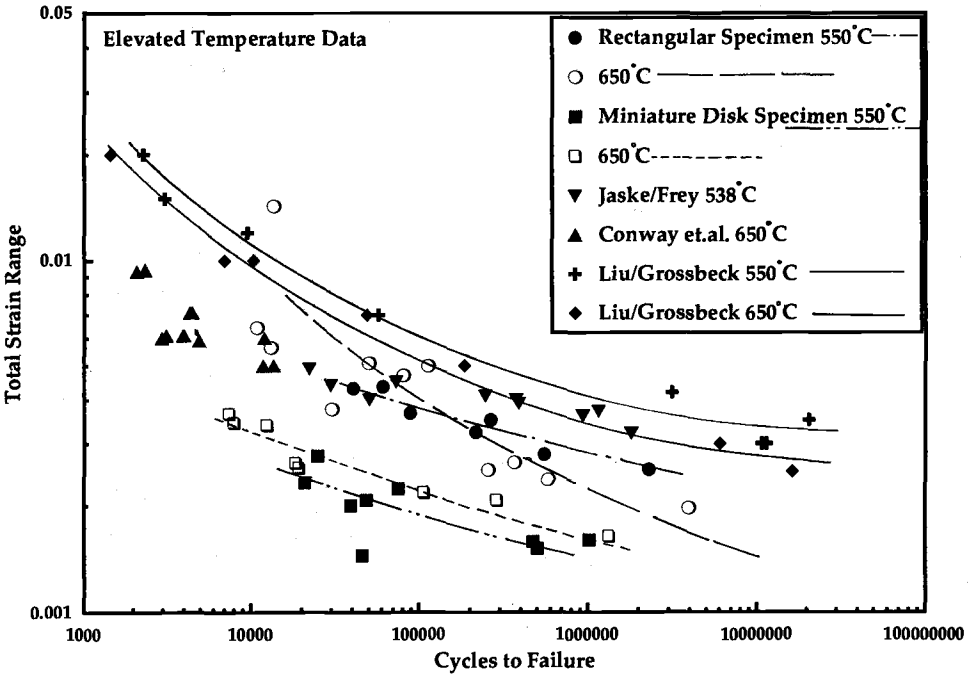

FIG. 5—*Elevated temperature data for the miniature-disk specimen compared with rectangular specimen and ASTM full-size specimen results.*

Jaske and Frey and Conway et al. for the full-size specimens. The data for the miniature-disk specimen again fall below the other results.

It is clear from the above discussion that the analytical technique used to calculate strain ranges underestimates the actual strain range values as seen for the rectangular specimen. While there was good agreement between the miniature-disk specimen data and the rec-

TABLE 2—*Comparison of constants in Eq 2 for the miniature-disk and rectangular specimens with full-size specimen results.*

Data	Temperature, °C	A	a	$\Delta\epsilon_L$[b]
Miniature disk	25	0.014	0.21	0.00277
Rectangular	25	6.65	0.672	0.0017
Full size[a]	20–25	3.4445	0.687	0.00277
Miniature disk	550	1.83	0.75	0.00144
Rectangular	550	0.81	0.57	0.00253
Full size[a]	538–566	1.521	0.691	0.00338
Miniature disk	650	0.284	0.56	0.00164
Rectangular	650	1.03	0.54	0.00197
Full size[a]	625–650	0.278	0.502	0.0025

[a] Ref 9.

[b] $\Delta\epsilon_L$ represents the asymptotic limit as N_f approaches infinity and provides an approximation of the almost horizontal trend of the fatigue curves at low strains.

tangular specimen data when the analytical technique was used for strain measurement, additional refinements are required in the calculations for strain values. The good agreement between real strain values for the rectangular specimens with the full-size specimen data indicates that, with modifications in the strain calculation technique, the two bending fatigue specimens may be used to scope fatigue properties of irradiated materials. Efforts are under way to attach miniature strain gauges to the miniature-disk specimen to measure actual strain values. An alternate technique, moire fringes, is also being pursued. Finite element methods are also under consideration for strain calculations.

It was seen earlier that the miniature-disk specimen did not show a clear temperature dependence as seen for the larger specimens. This separately indicates the necessity for refining the method for determining strain values. Moreover, the miniature-disk specimen results show a greater scatter about the best fit curve as compared to the rectangular specimen. This can be attributed to slight misalignments while mounting the smaller miniature-disk specimen. With further development, it is hoped that the miniature-disk specimen can be used as a screening test to quickly scope fatigue behavior of irradiated materials.

Conclusions

1. A miniature-disk bending fatigue specimen was developed to scope cyclic properties of irradiated materials. The specimen has the dimensions of a 3-mm-diameter transmission electron microscope specimen. A slightly larger rectangular specimen was also developed. The specimens, made of annealed type 316 stainless steel, were tested at 25, 550, and 650°C.
2. Strain values for both specimens were estimated analytically using specimen geometry and material properties. For the rectangular specimens, actual strain values were measured by attaching strain gauges to the specimens. The calculated strains were then calibrated to measured strains using a calibration factor.
3. Results for the rectangular specimen were in good agreement with the ASTM full-size specimen results. However, the data for the miniature-disk specimen fell below the full-size specimen results, indicating that the analytical technique used for calculating strains underestimates the actual strain values.
4. There was no clear temperature dependence evident for the miniature-disk specimen data unlike the larger specimens. The miniature-disk specimen data also show a greater scatter about the best fit curve. This was attributed to the greater sensitivity to alignment of the miniature-disk specimen.

Acknowledgment

This work was supported by the Department of Energy, Office of Fusion Energy, under grant DE-FG0585ER52139C.

References

[1] Lucas, G. E., *Metallurgical Transactions,* Vol. 21A, 1990, pp. 1105–1119.
[2] Corwin, W. R. and Lucas, G. E., in *The Use of Small-Scale Specimens for Testing Irradiated Material, ASTM STP 888,* W. R. Corwin and G. E. Lucas, Eds., September 1983, pp. 1–2.
[3] Rao, G. R., Rowcliffe, A. F., and Chin, B. A., *Journal of Nuclear Materials,* Vol. 179–181, 1991, pp. 438–440.
[4] Rao, G. R. and Chin, B. A., in *Effects of Radiation on Materials: 15th International Symposium, ASTM STP 1125,* R. E. Stoller, A. S. Kumar, and D. Gelles, Eds., American Society for Testing and Materials, Philadelphia, 1992.

[5] Szirmae, A. and Fisher, R. M. in *Techniques of Electron Microscopy, Diffraction and Microprobe Analysis, ASTM STP 372,* American Society for Testing and Materials, Philadelphia, 1965, pp. 3–9.

[6] Rao, G. R., M.S. thesis, Auburn University, Auburn, Alabama, 1988, pp. 23–32.

[7] Liu, K. C. and Grossbeck, M. L., "Use of Subsize Fatigue Specimens for Reactor Irradiation Testing," *The Use of Small-Scale Specimens for Testing Irradiated Material, ASTM STP 888,* W. R. Corwin and G. E. Lucas, Eds., American Society for Testing and Materials, Philadelphia, September 1983, pp. 276–289.

[8] Grossbeck, M. L. and Liu, K. C., *ADIP Semiannual Progress Report,* DOE/ER-0045/8, March 1982, pp. 136–140.

[9] Jaske, C. E. and Frey, N. D., *Journal of Engineering Materials and Technology,* Vol. 104, 1982, pp. 137–144.

[10] Conway, J. B., Stentz, R. H., and Berling, J. T., *Fatigue, Tensile and Relaxation Behavior of Stainless Steels,* TID-26135, U.S. Atomic Energy Commission, Washington, DC, 1975.

Shigetomo Nunomura,[1] *Shinji Noguchi,*[2] *Yuichi Okamura,*[2]
Shinji Kumai,[3] *and Shiro Jitsukawa*[4]

Two Micro Fatigue Test Methods for Irradiated Materials

REFERENCE: Nunomura, S., Noguchi, S., Okamura, Y., Kumai, S., and Jitsukawa, S., **"Two Micro Fatigue Test Methods for Irradiated Materials,"** *Small Specimen Test Techniques Applied to Nuclear Reactor Vessel Thermal Annealing and Plant Life Extension, ASTM STP 1204,* W. R. Corwin, F. M. Haggag, and W. L. Server, Eds., American Society for Testing and Materials, Philadelphia, 1993, pp. 275–288.

ABSTRACT: This paper demonstrates two miniature fatigue test methods in response to the requirements of the fusion reactor wall materials development program. It is known that the fatigue strength evaluated by the axial loading test is independent of the specimen size, while that evaluated by the bend test or torsion test is dependent upon the size of specimen. The new type of gripping system for the axial, tension-tension, fatigue testing of TEM disk[5]-size specimens that has been developed is described in this paper. An alignment tool assists in gripping the miniature specimen. The miniature tension-tension fatigue test method seems to provide reliable S-N curves for SUS304 and SUS316L stainless steels.

An indentation method has also been developed to determine fatigue properties. A hard steel ball or ceramic ball was used for cyclically loading the specimen, and an *S-N* curve was subsequently obtained. The merit of this method is primarily simple handling. *S-N* curves obtained from four materials by this indentation method compared well with those obtained from the rotary bend fatigue test employing a standard-size specimen.

KEYWORDS: small specimen, fatigue properties, tension-tension fatigue, indentation method, fusion reactor materials

Fatigue characteristics are of fundamental importance when choosing a structural material, especially when deciding upon the material for the fusion reactor wall, where long-term safety is of primary importance [*1*]. It is well known that a metal may fail under imposition of a stress considerably lower than the normal breaking stress if that stress is applied in a cyclic manner. However, the fatigue properties of highly irradiated wall materials have not been studied in detail. This is primarily due to the shortage of materials that are suitable for such studies. In an axial-type fatigue test, a larger-size specimen is required compared to other mechanical tests to minimize the gripping effect and to eliminate fatigue fracture in the grips. Nevertheless, in the case of fusion reactor wall materials, the limited irradiation space for the specimen requires the use of TEM disk-size specimens in mechanical tests to cooperate with safety regulations [*2*].

[1] Professor, Precision and Intelligence Laboratory, Tokyo Institute of Technology, Nagatsuta, Midori-ku, Yokohama, Japan 227; [2] former students of the graduate school, Tokyo Institute of Technology; [3] research associate, Precision and Intelligence Laboratory, Tokyo Institute of Technology; [4] senior researcher, Department of Fuels and Materials Research, Japan Atomic Energy Research Institute, Tokai-mura, Ibaraki-Ken, Japan 319-11.

[5] Disk-shape specimen for transmission electron microscope, about 3 mm in diameter and 0.3 mm thick.

A bending-type fatigue specimen requires less material than the axial-type specimen, but the fatigue characteristics evaluated from the fatigue bend test are strongly influenced by specimen size. Fatigue characteristics obtained from an axial fatigue test are not affected by the size of specimen [*3*]. The size effect of the specimen under bending fatigue in irradiated materials is unknown and impossible to evaluate.

In the present work, the authors have developed a new type of gripping system for the axial, tension-tension, fatigue testing of TEM-size specimens. An alignment tool assists in gripping the miniature specimen. The tension-tension fatigue test method, adopting the newly developed gripping system, seems to provide reliable *S-N* curves of SUS304 and SUS316L stainless steels.

It is desirable to use axial loading for miniature specimen fatigue testing since the effect of specimen size is less important. However, the axial loading method is less practical because of the difficulty in gripping by remote operation in the hot laboratory. The authors also have applied the cyclic indentation method to determine fatigue properties [*4*]. A hard steel ball or ceramic ball was used for cyclically loading the specimen, and an *S-N* curve was obtained from the load amplitude and the loading cycle-displacement curve. The merit of this method is primarily simple handling since no gripping problems are encountered. An advantage of the indentation method is that a complete *S-N* curve may be obtained from a single specimen, whereas alternative methods required a single specimen for each data point on the curve. *S-N* curves obtained from four materials by this indentation method agreed well with those obtained from the rotary bend fatigue test employing a standard size specimen.

In this investigation, two miniature fatigue test methods for irradiated materials are reported. One has a high reliability, and the other is a more practical technique.

Experimental Procedure

Tension-Tension Miniature Fatigue Test

A bend-type fatigue test has previously been successfully performed using the static mechanical test system for TEM disk-size specimens where no grip system was required [*5*]. However, the results were not converted to the standard size specimen test results since a relationship concerning the size effect was unknown (also a function of material properties). In a fatigue test, if there is a stress gradient near the surface, the fatigue behavior is governed by the gradient and the direction of the slip system, which depends on both the specimen size and the material characteristics [*6*]. The tension-tension fatigue test method, in the current work, has been adopted for miniaturized specimen fatigue testing to eliminate any effect of stress gradient.

The shape and size of the tension-tension fatigue specimen machined from a TEM disk is illustrated in Fig. 1. The specimen was of a "dog bone" type with a stress concentration factor of 1.21. This specimen shape was adopted primarily because of the ease of machinability. The materials used for the tests were SUS316L and SUS304 stainless steels. Some of the SUS316L stainless steel specimens were mill machined from a 3-mm-diameter rod with symmetric side slots along the rod length. A number of other specimens were made from a 0.3-mm-thick sheet by electro-spark discharge machining (EDM).

In order to alter the average grain size of the SUS304 stainless steel, solution treatments were performed at various temperatures ranging from 900 to 1300°C for 30 min, resulting in grain sizes of 20, 60, and 110 μm. The SUS316L stainless steel specimens were solution treated at 1050°C for 30 min. After heat treatment, all specimens were polished using 6-μm diamond paste.

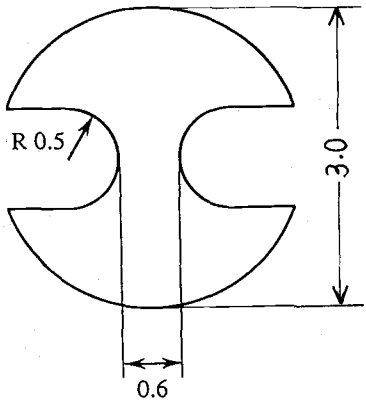

FIG. 1—*Tension-tension fatigue specimen machined from a TEM disk.*

A gripping system designed to maintain the axial alignment of the specimen was developed and consisted basically of upper and lower grips, two universal joints, and four sets of bearings. A special jig for gripping was also developed, which eliminated bending and shearing forces on the specimen during the gripping work. The gripping procedure is as shown in Fig. 2.

1. A precise vise is set on a horizontal plane.
2. The sides of the setting jig with two guide pins are precisely clamped by the vise.
3. One side of the upper grip and lower grip are set on the jig. A 1-mm gap between them is provided by two 1-mm-diameter pins on the tip of the shaft which are inserted into a bearing located on the center of the jig.
4. The miniature specimen is thrown into the proper position along the two guide pins.
5. The other sides of the grips are clamped under uniform torque. The specimen is fixed by friction between the specimen and files of the grips.
6. The complete assembly of the gripped specimen is attached to the universal joints on the fatigue testing machine, and then the vise and the jig are detached (Fig. 3).

The fatigue testing machine used was a servo-hydraulic fatigue testing machine (capacity of 9807 N). The applied load was monitored by a precise tension-compression load cell possessing a capacity of 490 N. The cyclic load was applied at a stress ratio of 0.1 and a frequency of 25 Hz under load control using a sinusoidal form wave.

The stress amplitude, S, was the nominal stress amplitude and was equal to the product of the stress concentration factor and the applied load amplitude divided by the minimum cross-sectional area.

Cyclic Indentation Loading Test Procedure

A schematic diagram of the indentation fatigue system is shown in Fig. 4. A hard ball is indented into the specimen surface that has previously been polished using 1-μm diamond paste. The test procedure is as follows. Initially, a monotonic load, P_H, is applied to the specimen surface so that the indentation depth equals the radius of the ball. The load is subsequently reduced to the mean load, P_m, and the cyclic load applied at an amplitude equal to P_a, $R = 0.1$, and $f = 20$ Hz. The fatigue-testing machine adopted also was a servo-hydraulic fatigue-testing machine which was the same as that used for the axial fatigue test.

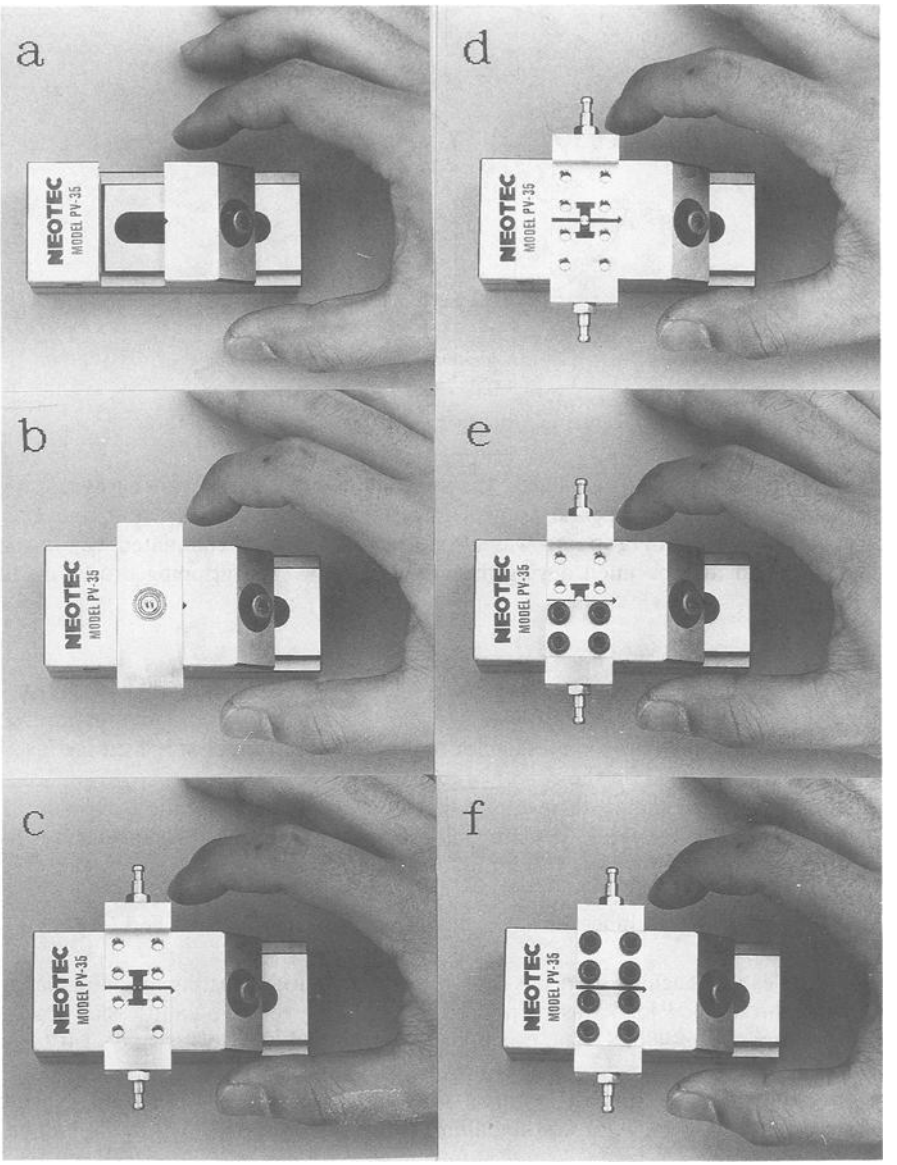

FIG. 2—*Assembling procedure;* (a) *setting a precise vise on a horizontal plane;* (b) *clamping the sides of the setting jig with two guide pins;* (c) *setting one side of the upper grip and lower grip and providing a 1-mm gap by two 1-mm-diameter pins of the jig;* (d) *the miniature specimen is thrown along the two guide pins;* (e) *clamping the other side of lower grip under uniform torque;* (f) *clamping the other side of the upper grip.*

The mean indentation displacement was monitored using a laser displacement meter (resolution of 0.5 μm).

Rectangular-shaped specimens made from 7075-T6 aluminum alloy, cold-rolled 0.45%C steel, SUS316L stainless steel, and pure copper sheet were used for the cyclic indentation

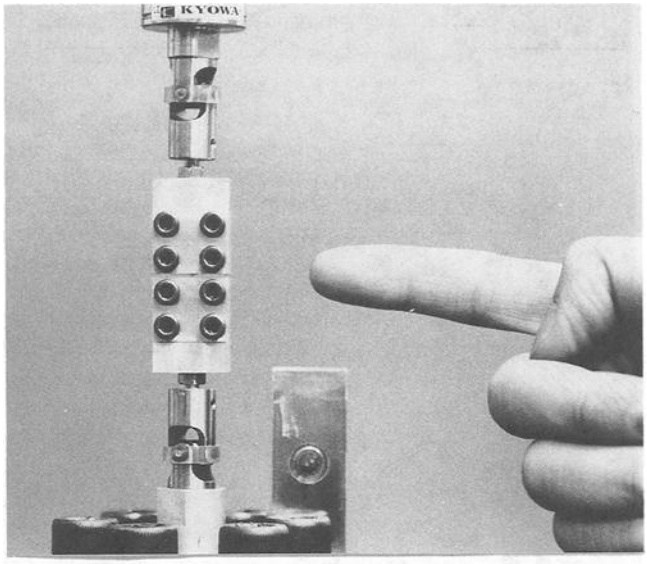

FIG. 3—*A general view of the miniature tension-tension loading unit.*

loading tests. The chemical compositions are not listed since the fatigue data obtained from standard size specimens are for comparison purposes only.

S-N *Curves in the Indentation Loading Test*

Figure 5 shows a typical example of the relationship between the vertical displacement of the indentation ball and the applied number of fatigue cycles, N. A discontinuous increase in the displacement at a specific number of cycles, N_f, is observed in all records. In general the fatigue process in metallic materials consists of the following stages: (1) formation of a persistent slip band (PSB) near the surface, (2) formation of intrusions and extrusions on the surface originating in the persistent slip band, (3) initiation of micro-cracks (Stage I fatigue growth), and (4) further growth of a dominant crack (Stage II fatigue growth). To examine whether the cyclic indentation loaded specimen experienced the fatigue process mentioned above, cyclic loading was interrupted at predetermined cycles (0.05, 0.15, 0.25, 0.5, 0.9, 1.0, 1.1, 1.5 and $2.0N_f$) and a micro-structural examination made of specimen cross sections. Areas of persistent slip bands normalized by that at $N_f = 1.0$ were plotted against N_f in Fig. 6. Early formation of PSBs, which saturated at about $0.25N_f$, are shown in the figure. A dominant growth micro-crack was observed only in the specimen after $1.0N_f$. No crack was observed in the specimen when the test was interrupted before $0.9N_f$. It is therefore considered that $1.0N_f$ corresponds to the critical stage where a dominant crack is observed [7]. If, during the fatigue life of a rotary bend specimen, no clear crack initiation process is observed, then the N_f may be regarded as equal to the fatigue life (i.e., the horizontal axis of the S-N curve). Although small discontinuities were often observed on the records due to electric noise or other sources, in most cases the N_f was distinctive from them. Figure 7 shows a fatigue crack in the specimen after 1.5 N_f.

Practical evaluation of the stress amplitude S in the S-N curve is necessary to adopt the present method as the miniaturized fatigue testing method. We considered the case of monotonic indentation where the mean indentation pressure on the contact area is S_m and

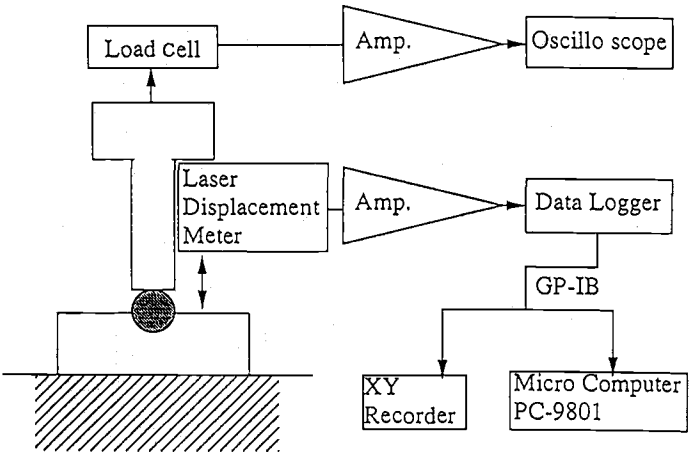

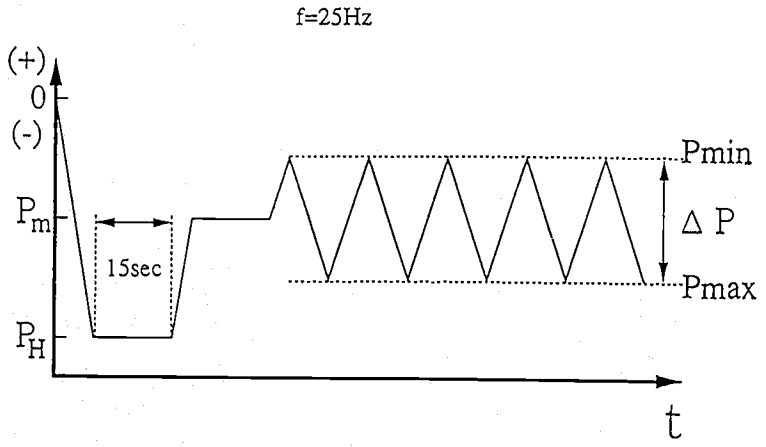

FIG. 4—*Flow diagram showing indentation fatigue testing.*

the applied load and the radius of contact are P and a, respectively. Tabor [*8*] investigated indentation flow stresses for many kinds of materials. According to his work, the stress amplitude may be written as follows

$$S = cSm = cP/\pi a^2 \tag{1}$$

where c is a function of elastic constant and yield strength and equal to 0.33 for most metallic materials.

Proof Test Results and Discussion

Tension-Tension Miniature Fatigue Test

The results of fatigue tests performed on tension-tension miniaturized specimens manufactured from SUS316L stainless steel are plotted in Fig. 8, which also shows the rotary

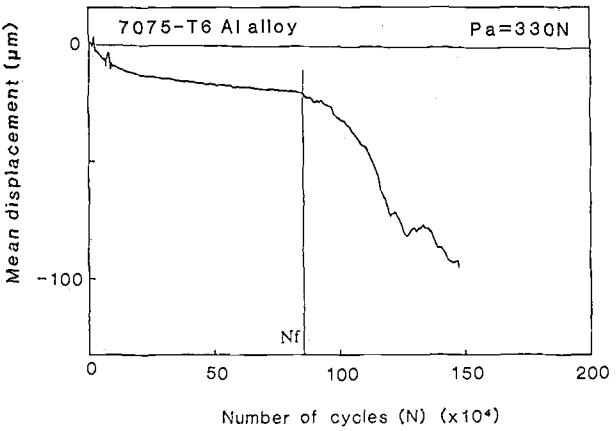

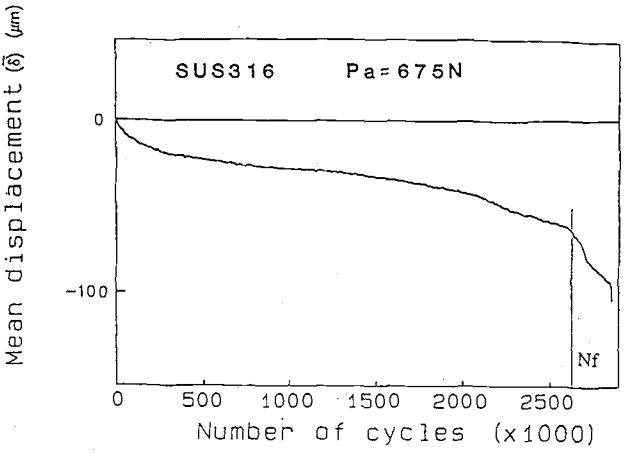

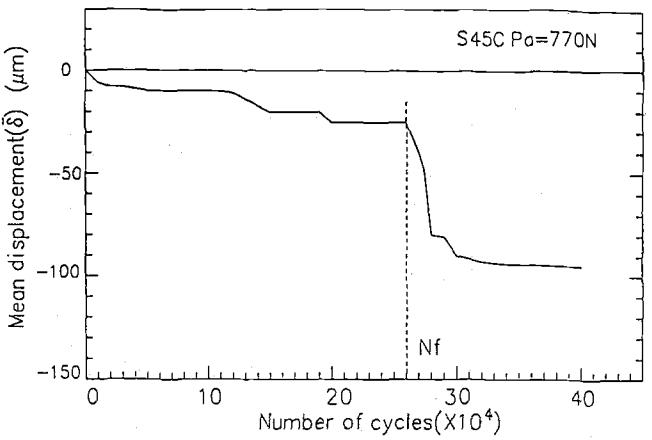

FIG. 5—*Mean displacement—relation of number of cycles shows discontinuity at* $N = N_f$.

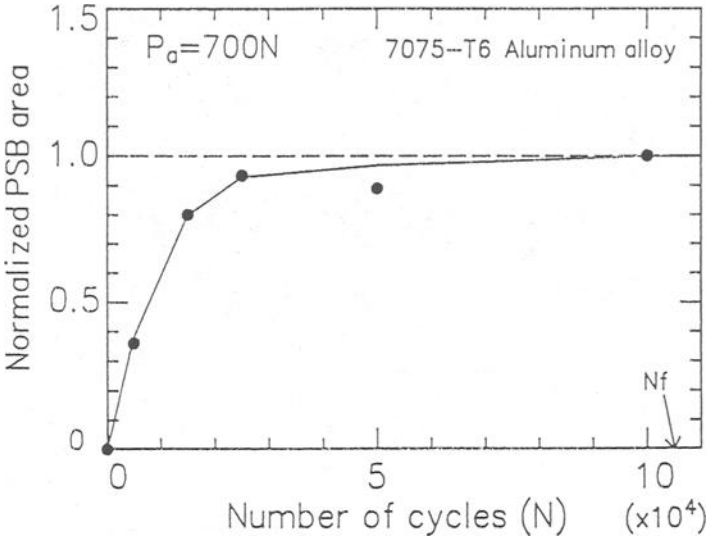

FIG. 6—*Persistent slip band (PSB) saturates in the early stage of the fatigue life.*

bend *S-N* curve for regular-size specimens of the same material [*9*]. The material from the reference was solution treated and mill finished. The open symbols in Fig. 8 represent data for solution-treated material and agree fairly well with the result from Ref *9*. Therefore, the axial loading type fatigue test using a TEM disk-size specimen can provide reasonable fatigue data, while results from the bend-type miniaturized specimen are in danger of overestimating the fatigue strength. The effect of surface finish on the miniaturized specimens was approximately the same as that in the regular-size specimen.

In the SUS304 stainless steel, fatigue tests were carried out with specimens possessing grain sizes of 20, 60, and 110 μm. Results are plotted in Fig. 9. It was found that fatigue life increased with reduction of grain size. The solid line represents results from an axial loading fatigue test where a regular-sized specimen, solution treated at 1050°C, was used [*9*]. The mismatch in results between 1050°C heat-treated specimens was attributed to surface finishing effects. The miniaturized specimen was finished using a 3-μm diamond paste,

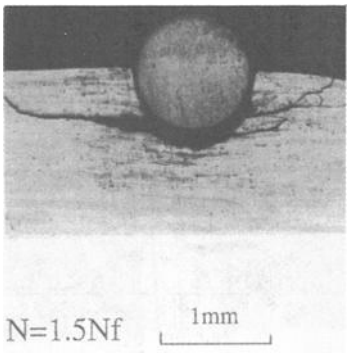

FIG. 7—*Indentation fatigue cracks at* $N = 1.5N_f$, *7075-T6 Al alloy.*

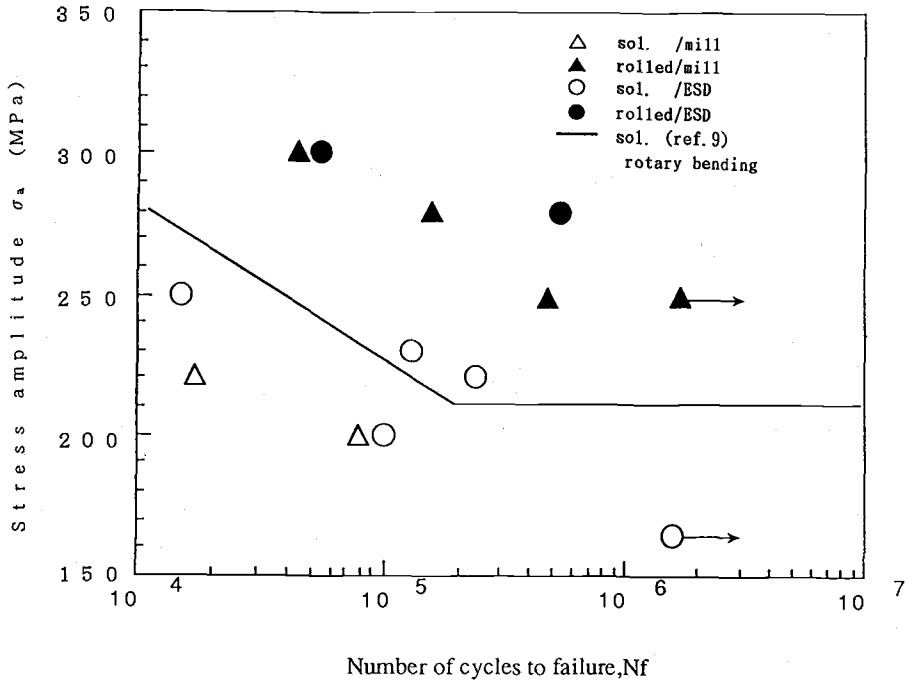

FIG. 8—*Effects of machining and metallurgical structure on fatigue life of SUS316L stainless steel.*

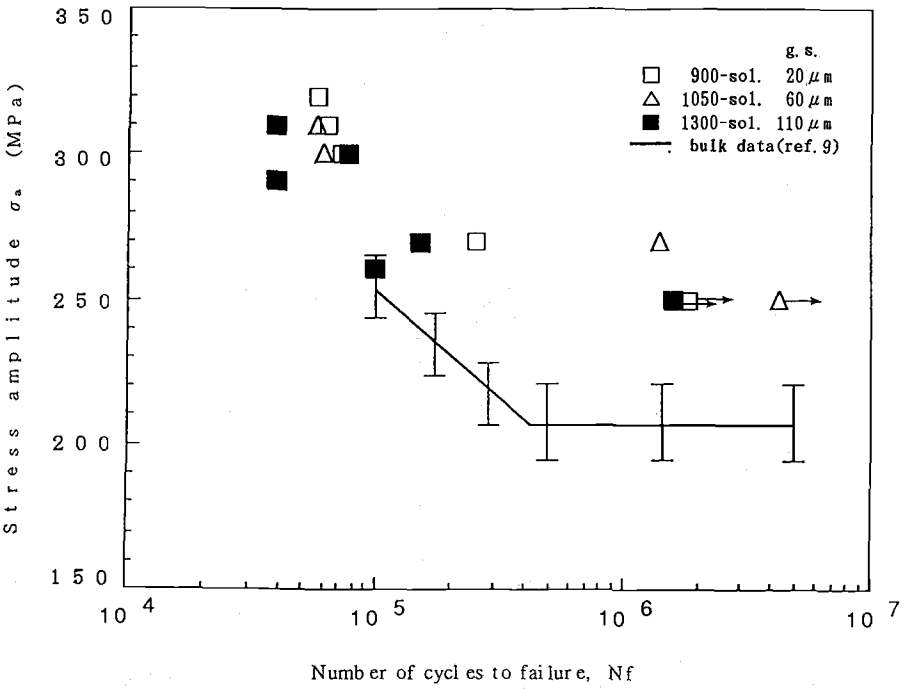

FIG. 9—*Effect of solution treatment temperature on fatigue life of SUS304 stainless steel.*

whereas the reference specimen was finished with a No. 600 emery paper. To illustrate the effect of surface roughness, a few TEM disk-size specimens were finished with the No. 600 emery paper and then tension-tension fatigue tested (Fig. 10). The difference apparently caused by specimen size (shown in Fig. 9) disappeared, illustrating the importance of the surface finish on fatigue behavior.

Figure 11 shows 10^5 times fatigue strengths of SUS304 stainless steel as a function of grain size. The dependency of fatigue behavior on grain size in both miniaturized and regular-size specimens [*10*] were in accordance with the Hall-Petch equation despite different surface finishes and other testing conditions.

Indentation Fatigue Test

The stress amplitude, S, calculated from Eq 1, and the number of cycles at N_f of (*a*) 7075-T6 aluminum alloy, (*b*) cold-rolled 0.45%C steel, (*c*) SUS316L stainless steel, and (*d*) pure copper were plotted in Fig. 12. The fatigue characteristics of these materials used for proof tests were investigated, and their S-N curves have been reported elsewhere [*11–13*]. Figure 13 shows the scatter bands of both axial and rotary bend fatigue test S-N data in the 0.45%C steel [*13*]. The solid lines in Fig. 12 represent the mean rotary bend fatigue data, which abound in quantity. The number of cycles, N, of the rotary bend fatigue S-N curve approximately equal the cycles for fatigue crack initiation since the cycles required for catastrophic propagation seem to be negligible in the rotary bend fatigue specimen. Outlines of the plots in Fig. 12 were in agreement with the rotary bend S-N curves. It may thus be concluded that the indentation loading method has a good potential as a miniaturized fatigue testing method.

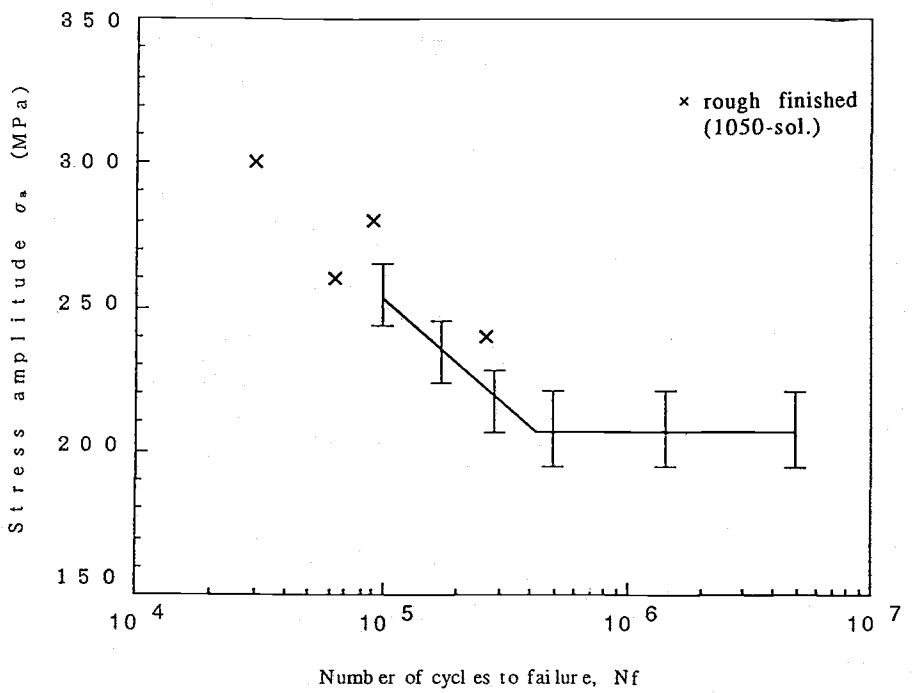

FIG. 10—*The difference due to specimen size shown in Fig. 9 disappeared when the miniature specimen was treated to a similar surface finish.*

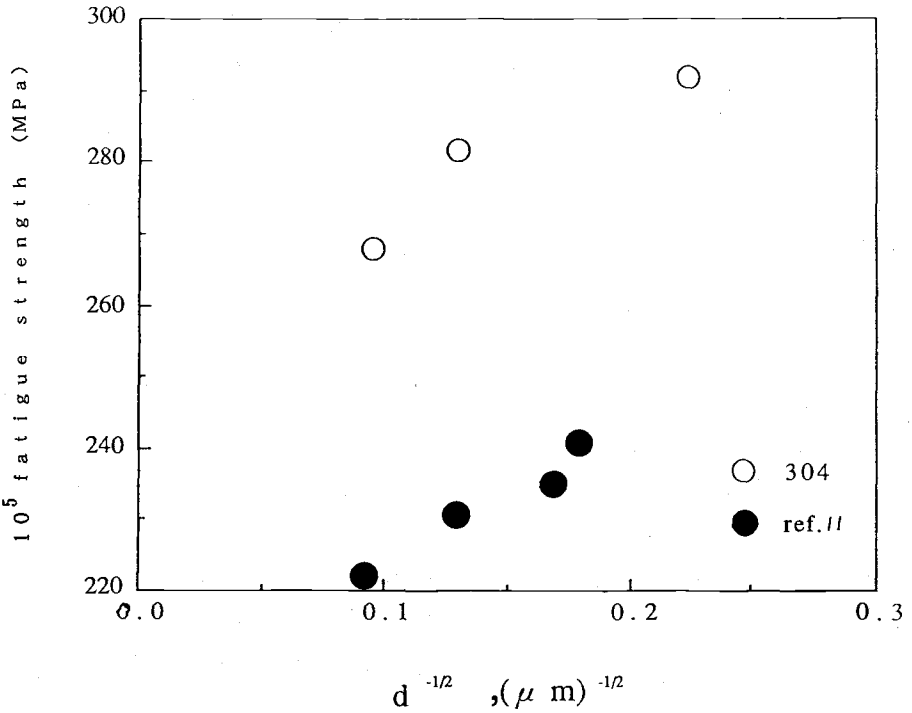

FIG. 11—*Grain-size dependence of 10^5 times the fatigue strength of SUS304 stainless steel.*

In ISO R-79 standards for hardness tests, the minimum requirements for the indentation specimen size are described. To perform a valid fatigue test using a TEM disk specimen, the diameter of the indentation ball must be less than 75 μm. It seems to be possible to test using a 75-μm-diameter ball, but in practice there are technical problems to be solved, primarily the indentation displacement monitor and the load control. The minimum ball diameter used in the present work was 300 μm, which corresponded to a 1.2-mm-thick specimen.

The crystallographic effect on the fatigue life evaluated by this method may be smaller than that by any other fatigue test technique since all crystallographic orientations exist in the contact area even if the specimen is a single crystal.

Conclusions

1. A gripping system for the axial, tension, fatigue testing of TEM-size specimens was developed. The *S-N* curves obtained agreed well with published data. This fatigue test method using a TEM disk specimen is applicable for irradiated materials, but there is a disadvantage requiring a complicated gripping operation.
2. Cyclic indentation loading also was demonstrated as a miniaturized fatigue test method for irradiated materials. The ball was indented initially into the specimen and subsequently cyclically loaded under a given load amplitude. The number of failures on the *S-N* curve was evaluated from the mean indentation displacement monitor record. According to the crystallographic analysis, the monitor record represented the cycles corresponding to fatigue

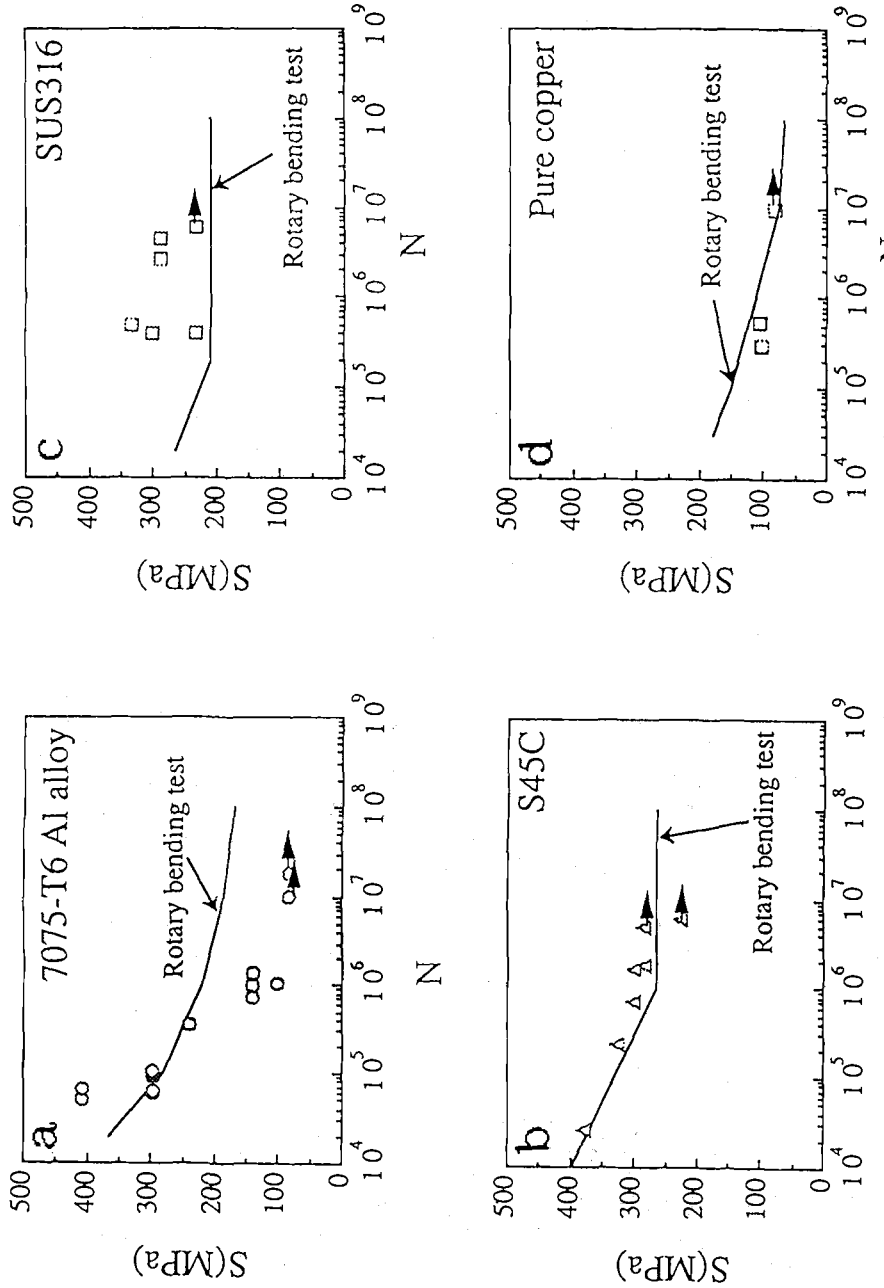

FIG. 12 —*Indentation S-N curves for* (a) *7075-T6 Al alloy,* (b) *S45C steel,* (c) *SUS316L stainless steel, and* (d) *pure copper.*

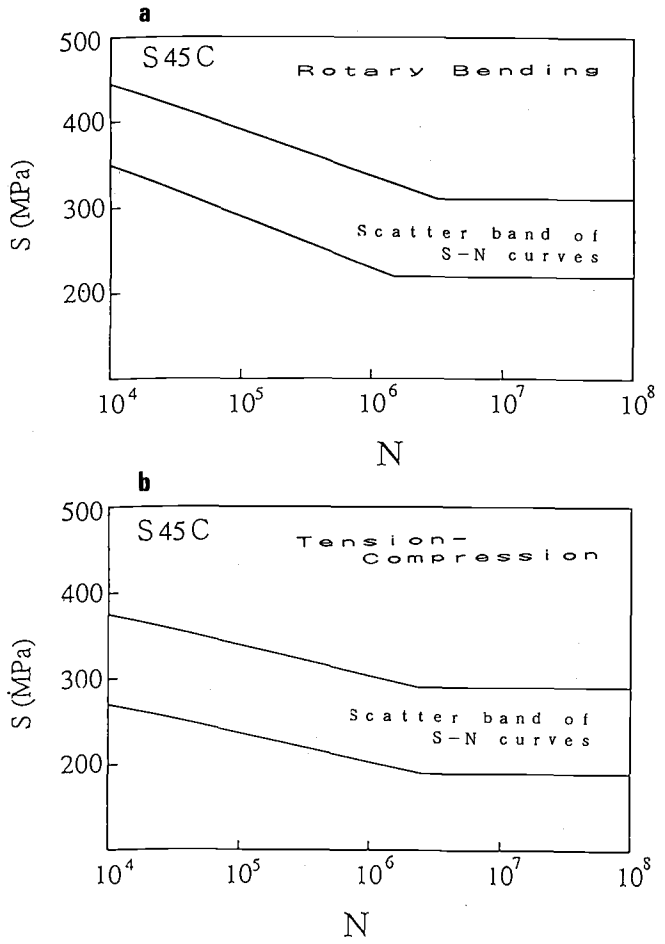

FIG. 13—*Scatter bands of S-N curves evaluated by the statistical process using more than a thousand S-N curves of carbon steel regular-size specimens (Ref* 13). *In the case of S45C steel,* (a) *87 out of 88 data from rotary bending fatigue tests and* (b) *13 out of 13 data from tension-compression fatigue tests were in the bands.*

crack initiation. The stress amplitude was deduced from Tabor's work. The *S-N* curve obtained agreed well with conventional data using a standard size specimen in four materials.

References

[*1*] *Metals and Technology,* AGNE Publishing Inc., Tokyo, 1987.
[*2*] Corwin, W. R. and Lucas, G. E. in *The Use of Small-Scale Specimens for Testing Irradiated Materials, ASTM STP 888,* American Society for Testing and Materials, Philadelphia, 1986.
[*3*] Heywood, R. B., *Designing Against Fatigue,* Chapman and Hall, London, 1962.
[*4*] Noguchi, S., Kumai, S., Higo, Y., and Nunomura, S., "Indentation Fatigue Test Method Using Miniaturized Specimen," *Proceedings,* FATIGUE90, Hawaii, Materials and Component Engineering Publications, Birmingham, 1990, p. 2291.

[5] Nunomura, S., Higo, Y., Nishijima, S., and Hishinuma, A., "Tensile Properties Evaluation Using a TEM Disk," this publication, p. 256.
[6] "Metal Fatigue," Japan Society for Materials Science, Marzen, Tokyo, 1968.
[7] Klesnil, K. and Lukas, "Fatigue of Metallic Materials," Elsevier Scientific Publishing Company, New York, 1980.
[8] Tabor, D., *The Hardness of Materials,* Clarendon Press, Oxford, 1951.
[9] "Fatigue Data Sheet," Vol. 5, Japan National Research Institute for Metals, Tokyo, 1989.
[10] Hatanaka, K. and Shimizu, S., "On the Grain Size Effect on Fatigue Properties in Stainless Steel," *Transactions of the Japan Society of Mechanical Engineers (A),* Vol. 48, 1983, p. 405.
[11] Tabor, D., in *Microindentation Techniques in Materials Science and Engineering, ASTM STP 889,* American Society for Testing and Materials, Philadelphia, 1986, p. 129.
[12] *Data Sheet, Journal of the Japan Society of Mechanical Engineers,* Vol. 58, 1955, p. 792.
[13] *Data Sheet, Journal of the Japan Society of Mechanical Engineers,* Vol. 60, 1957, p. 546.

Shiro Jitsukawa,[1] *Minoru Kizaki,*[2] *Akira Umino,*[3] *Kiyoyuki Shiba,*[1] *and Akimichi Hishinuma*[1]

Methods and Devices for Small Specimen Testing at the Japan Atomic Energy Research Institute

REFERENCE: Jitsukawa, S., Kizaki, M., Umino, A., Shiba, K., and Hishinuma, A., **"Methods and Devices for Small Specimen Testing at the Japan Atomic Energy Research Institute,"** *Small Specimen Test Techniques Applied to Nuclear Reactor Vessel Thermal Annealing and Plant Life Extension, ASTM STP 1204,* W. R. Corwin, F. M. Haggag, and W. L. Server, Eds., American Society for Testing and Materials, Philadelphia, 1993, pp. 289–307.

ABSTRACT: Devices for a punch test on annular notched specimens, small punch (SP) tests, and miniaturized tension tests in hot cells were developed. A micro-manipulator to handle small specimens and an electro-discharge machine (EDM) to extract miniaturized tension specimens and annular notched specimens from transmission electron microscopy (TEM) disks were also fabricated. These devices were designed and made for remote operation in hot cells. Preliminary tests to evaluate the applicability of test methods were carried out. Correlation between SP test results and tensile properties was not strong. Miniaturized tensile results were reasonably similar to the results with larger specimens. The ductile-brittle transition temperature (DBTT) by the punch test on annular notched specimens was higher than that obtained from the SP test. However, materials dependence of the DBTT was different from that measured by standard Charpy V-notch (CVN) tests. This may be due to a specimen size effect.

KEYWORDS: small specimen testing, TEM disk specimen, SP test, miniaturized tension test, hot cell, manipulator, fracture properties, DBTT, ductility, strength, austenitic stainless steel, ferritic steel, neutron source

Accelerator-driven deuterium-lithium (D-Li) stripping reaction-type neutron sources, such as the International Fusion Materials Irradiation Facility (IFMIF) planned by the International Atomic Energy Organization and the Energy Selective Neutron Irradiation Facility (ESNIT) planned at the Japan Atomic Energy Research Institute, are recognized as the most promising facilities to obtain test environments of high-energy neutrons for fusion reactor materials development. The limitation on the available test volume for irradiation requires development of small specimen test techniques.

Preliminary tests to evaluate feasibility of miniaturized tension tests, small punch tests, and a punch test on annular notched specimens are carried out. For most of the tests, transmission electron microscopy (TEM) disk specimens of 3 mm in diameter with thickness of 0.25 mm were used. Results of a miniaturized tension test using specimens extracted

[1] Senior researcher, researcher, and principal researcher, respectively, Department of Fuels and Materials Research, and [2] engineer, Department of Research Reactor Operation (former member of Department of JMTR operation), Japan Atomic Energy Research Institute, Tokai-Mura, Ibaraki-Ken 319-11.

[3] Engineer, Department of JMTR Operation, Japan Atomic Energy Research Institute Oarai Branch, Oaria-Machi, Ibaraki-Ken 311-13, Japan.

from TEM disks are examined in terms of specimen size effects. Results from punch tests are compared with those obtained by standard methods of tension and Charpy tests. Developed devices for hot cells are also introduced.

Small Punch (SP) Test

Test Method

Figure 1 schematically illustrates a cross-sectional view of the specimen holder with a hemispherical punch and a specimen. Prior to the test, the holder is forced to clamp the specimen rigidly to limit specimen deformation in the region at the hole of the lower fixture. Then the specimen is deformed by punching. A 3-mm-diameter transmission electron microscopy disk with a thickness of 0.25 mm and a rectangular plate of 10 mm square with 0.5-mm thickness are used as specimens. Dimensions of the radius of hemisphere of the punch, the lower holder hole diameter, and the radius at the shoulder of the lower holder for two types of specimens are also shown in Fig. 1. The clamping force on the specimen is selected to be the value that brings about an average compressive stress of about 10% of the yield stress for the materials in the annealed condition at test temperature, that is, about 120 N for TEM disk specimens of Type 316 stainless steel at room temperature.

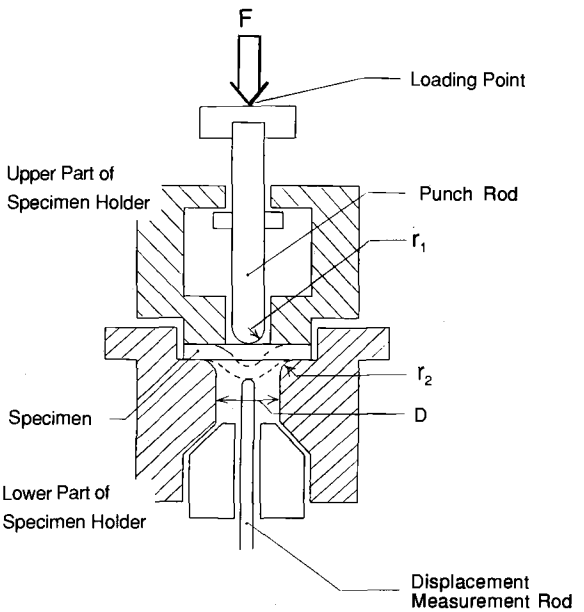

	r_1	r_2	D
TEM disk	0.5	0.2	1.5
10mm SQ.	1.2	0.2	4.0

(in mm)

FIG. 1—*Schematic illustration of test rig with a hemispherical punch and a specimen. By applying force to the loading point of the punch end, the specimen is deformed. Dimensions of the hemisphere radius of the punch, the lower holder hole diameter, and the radius of the shoulder of the lower holder for the TEM disk specimens and the 10-mm-square plate specimens are shown.*

During the test, the deformation mode of the specimen changes successively. Baik et al. [*1*] described the deformation mode change in four stages, which are: elastic bending, plastic bending, plastic membrane stretching, and plastic instability development stages. These stages are shown with a typical load displacement curve in Fig. 2. The energy to fracture, which is obtained from a load displacement curve, expresses a toughness of the materials for the SP test. Efforts have been made by many researchers to obtain correlations between the toughness (SP energy) and known fracture-related properties and between characteristics of the load-displacement curve and tensile stress-strain relationships. Baik et al. demonstrated that the temperature dependence of the energy (elastic plus plastic energy) for some ferritic alloys showed a steep decrease with decreasing temperature in a temperature range and that the transition temperature correlated well with a transition of the fracture mode; cleavage fracture had occurred at lower temperatures than the transition temperature. Suzuki et al. [*2*], McNaney et al. [*3*], and Misawa et al. [*4*] also showed that there was a simple relation between the transition temperature (SP DBTT) and the ductile brittle transition temperature (DBTT) from Charpy V-notch (CVN) tests from several different steels. Takahashi et al. [*5*] and Suzuki et al. indicated that SP energy and the minimum thickness of the specimen at fracture also correlated well with the elastic-plastic fracture toughness, J_{IC}, of the materials obtained by ASTM standard test method for J_{IC} measurement [*6*]. Okada et al. [*7*] and Suzuki et al. examined load displacement curves of irradiated and unirradiated alloys. Okada et al. pointed out that the maximum load of the punch test correlated well with tensile strength, and Suzuki et al. reported that (tensile) yield stress exhibited a similar change with the transition load from the elastic to the plastic stage (see Fig. 2) by irradiation.

Testing Device for SP Test

A test device capable of SP testing and miniaturized tension testing has been developed. As the machine is used in a hot cell, care was taken to design it for easy manipulation of

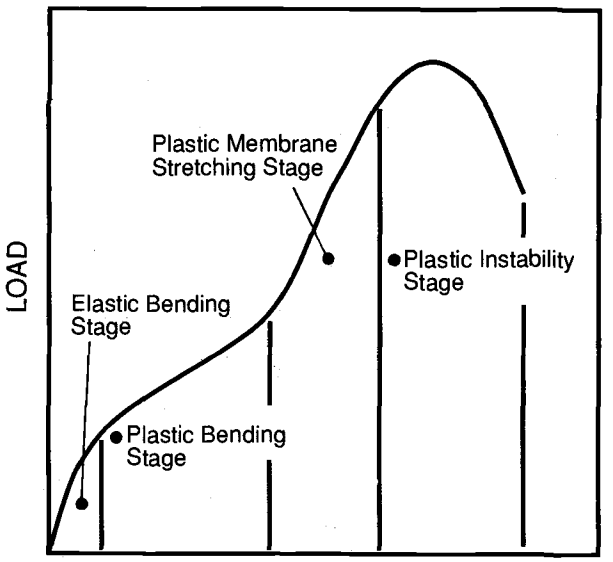

FIG. 2—*Deformation mode during SP test (after Baik et al.* [1]).

the specimen holder and operation of the machine. Figures 3 and 4 show the inside of a vacuum chamber of the machine. To conduct tests, holders with specimens are placed first into the holes in the turntable by a manipulator. Then the turntable turns to a right angle, placing exactly one of the holders above a lower rod—the lower rod travels upward to carry the holder to an upper rod. The lower rod thrusts the holder to the upper rod to apply force on the holder clamping the specimen between the upper and lower part of a holder. Finally, an actuator travels down to deform the specimen and the lower rod moves downward to place the holder on the turntable after the test. This sequence can be operated automatically by a computer until tests for twelve holders are finished.

Another feature of this test device is in displacement measurement. Displacement during an SP test is usually obtained from the travel of the punch rod at the loading point (see Fig. 4). The actuator rod of this machine is relatively long and therefore can shrink elastically by compressive testing forces. Therefore, a displacement measurement rod equipped with a LVDT is attached to the bottom surface of the specimen during the test to avoid disturbances by the deformation of the actuator rod. The effective rigidity of the load train of about 1×10^4 N/mm is not small, however.

Table 1 shows current performance of the device. Testing at a low temperature of 150 K is possible; however, it takes about 3 h to cool the holder. This is not practical, and improvement is now in progress on a temperature control system for low temperatures.

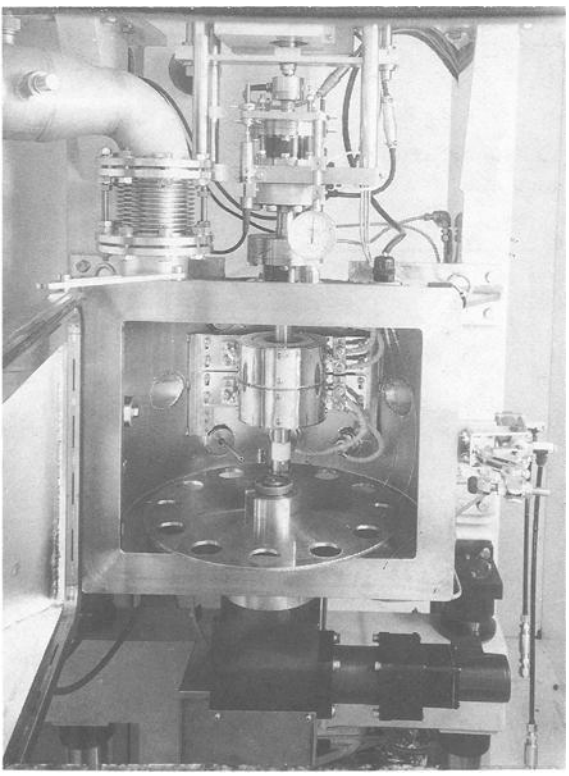

FIG. 3—*A view of the interior of the vacuum chamber of the SP and miniaturized tension testing device. A turntable with twelve holes for holder placement, a furnace, and lower and upper rods are seen in the chamber (see Fig. 4).*

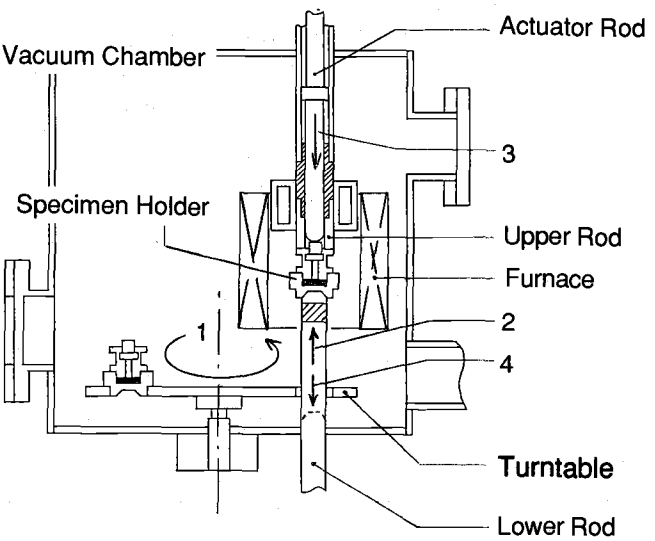

FIG. 4—*Schematic illustration of a vacuum chamber, a turntable, specimen holders, an actuator rod, and a lower and an upper rod. To conduct the test: 1: turn a turntable to a right angle to place one of the holders exactly above a lower rod; 2: a lower rod travels upward to carry a holder to an upper rod and thrusts to the upper rod to clamp a specimen between a lower and an upper part of the holder; 3: the actuator travels downward to deform the specimen, and; (4) the lower rod travels downward to place the holder into a hole in the turntable.*

Results for SP Test

Figure 5 shows two load displacement curves in the initial stage of deformation. A TEM disk specimen of an annealed Ti-modified austenitic stainless steel (JPCA) was used for this test. Mechanical properties of the alloy are similar to Type 316 stainless steel. The nominal chemical composition of the alloy is Fe-0.06C-0.5Si-14Cr-16Ni-1.5Mn-2.5Mo-0.25Ti. In the curves, displacement was obtained from the travel of the loading point of the rod actuator for Curve 1 and the travel of the lower displacement rod for Curve 2. Larger displacement at the loading point of the actuator rod indicates that the rod deformed elastically. Load was applied until Curve 1 showed yielding. Then, the load was removed and reloaded to bring about further deformation. Residual deformations after reloading A for Curve 1 and B for Curve 2 were obtained after the unloading. Deformation A was far larger than B.

TABLE 1—*Performance of test machine for SP and miniaturized tension tests.*

Test Method	Small Punch Test Miniaturized Tension Test
Load capacity/rigidity of load train	5 to 10 kN/mm
Temperature range	150 to 1073 K
Displacement rate range	1 μm/s to 10 mm/s
Maximum number of holders in the vacuum chamber	12

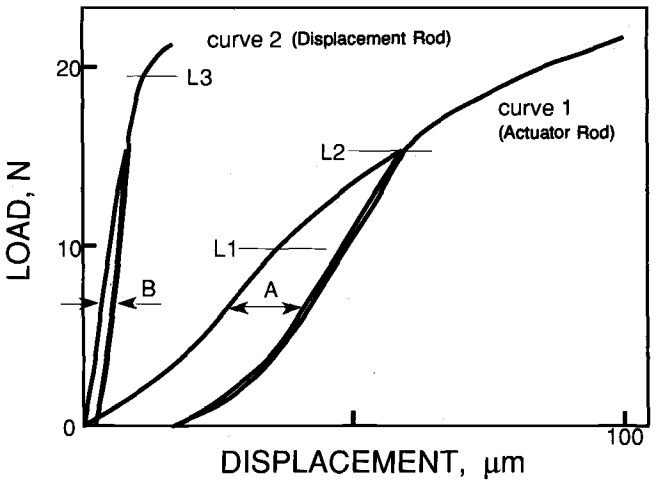

FIG. 5—*Load displacement curves of the initial stage of deformation. Displacement was obtained from the travel of the actuator rod for Curve 1 and from the displacement measurement rod for Curve 2.*

Examination of deformation on both top and bottom surfaces of the separate specimen, loaded to the same level of L1, revealed that a denting of 0.15 mm diameter by the hemispherical punch was produced on the top surface while no obvious deformation was observed on the bottom surface. This indicates that a deformation like a ball hardness test had initiated at L1. Yielding load L3 for Curve 2 was about twice as much as L1. L3 seems to indicate the load at which the plastic deformation penetrates to the bottom surface. Figure 6 shows load displacement curves for TEM disks obtained from annealed and cold rolled to 25% and 50% JPCA plates. Tensile properties of the materials with 5 by 5 mm cross section and 25-mm-long gage length specimens are shown in Table 2. The maximum load increased with the degree of cold-working rate as did the yield stress (σ_y) and ultimate tensile stress (σ_{uts}) of tension test results. However, the ratios were different: σ_{uts} for 50% cold-worked material was larger than that of the solution-annealed material by 70%. Maximum displacement was not sensitive to the cold-working rate, while uniform, total, and fracture strains by tensile results were rather sensitive to the cold working. Fracture by SP test occurred at displacements of about 0.7 mm. The stress state during the SP test changed with deformation. This may indicate that the fracture condition and plastic instability of the SP test do not strongly rely on ductility of the material. Ghosh [*8*] revealed that fracture of the thin sheet metal during punch stretching occurred by localized necking. The condition of the localized necking initiation was strongly dependent on the stress state. Localized necking occurred at minimum strains under the plane strain stretching condition, and the deformation limit during punch stretching on thin metal sheet specimens tended to be close to the strain of the localized necking initiation under the plain strain stretching condition when friction between the sheet and punch was large (the strain for the localized necking initiation becomes maximum under bi-axial stretching [*8*]). However, because the specimen for the SP test is relatively thick and the friction effect may not be very large, the stress state may deviate from bi-axial stretching to plane strain stretching during testing. Therefore, it may be said that the fracture condition for the SP test is determined not only by ductility of the material tested but is also affected by friction between the punch and the specimen.

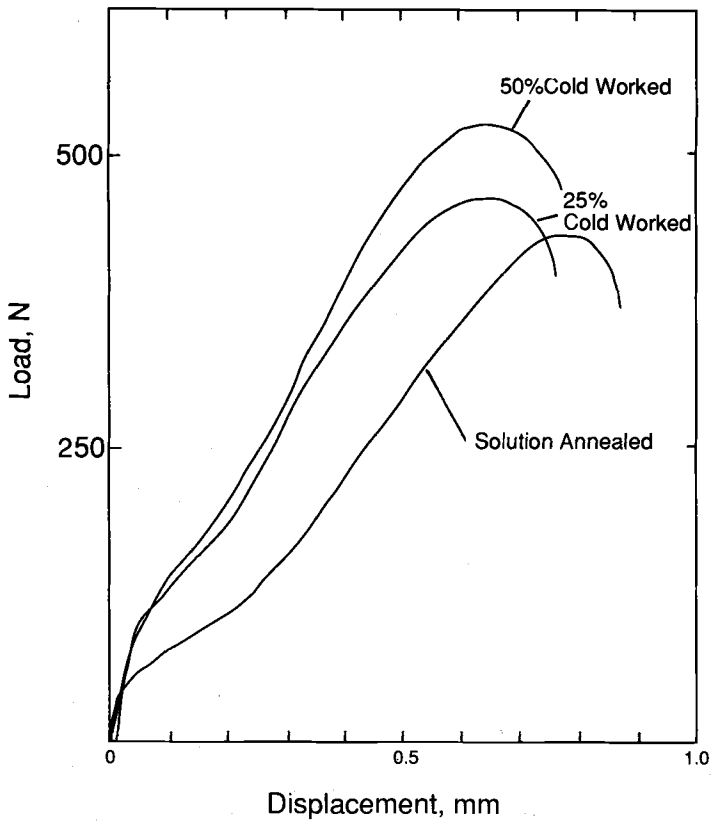

FIG. 6—*Load displacement curves of SP tests on solution-annealed, 25% cold-worked, and 50% cold-worked JPCA specimens.*

Tension Test

Specimen and Jig

Irradiation often causes a hardening of materials and a reduction in uniform elongation to close to zero [9]. Among the tensile properties for such hardened materials, ductility (measured by reduction of area, true fracture strain, etc.), yield stress, and work-hardening characteristics are the most important properties to characterize mechanical properties of

TABLE 2—*Tensile properties of solution-annealed, 25% cold-worked and 50% cold-worked JPCA obtained from specimens with gage section of 5 mm square and 25 mm long.*

Material Condition	σ_y, MPa	σ_{UTS}, MPa	σ_p, MPa	σ_f, MPa	ϵ_u, %	ϵ_t, %	ϵ_p	ϵ_f	R.A., %
SA	240	530	1210	1100	52	60	1.13	1.38	75
25% CW	703	760	1230	1020	19	27	0.85	1.05	65
50% CW	840	900	1240	1050	0.5>	7	0.72	0.89	60

materials. Ductility is a rather sensitive property to specimen configuration; in particular, the width-thickness ratio (w/t) and length-width ratio (l/w) in the gage section are important. Therefore, evaluation of the specimen configuration effect on tensile properties were examined to obtain the proper configuration at the gage section for miniaturized tension specimens.

Figure 7 shows specimen width-thickness ratio and fracture strain ($= \ln(A_0/A_f)$; A_0 and A_f are areas at minimum cross sections before and after the test, respectively). Width and length of the gage section of the specimen used for these tests were 5 and 25 mm, respectively. Materials were of solution-annealed (SA), 25% cold-worked (25% CW), and 50% cold-worked (50% CW) JPCA. The width-thickness ratio (w/t) was changed by changing specimen thickness. Fracture strain was clearly affected by w/t values; with increasing w/t, fracture strain for each material monotonically decreased. The w/t effect was relatively small at w/t between 1 and 2. Therefore, the maximum w/t value for miniaturized tension specimens was chosen to be equal or smaller than 2. As for l/w, the effects on uniform elongation

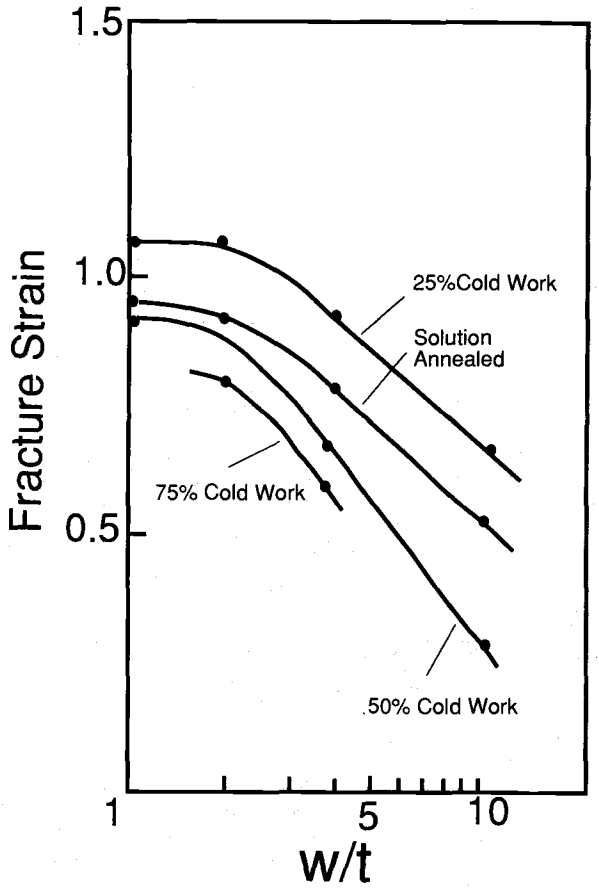

FIG. 7—*Fracture strain as functions of specimen width-thickness ratio* (w/t). *Specimens of solution-annealed 25% cold-worked, 50% cold-worked, and 75% cold-worked JPCA were tension tested. The gage length and width of the gage section were 25 and 5 mm, respectively. With increasing* (w/t), *fracture strains were monotonically decreased.*

and the displacement produced during neck development were not large with l/w of larger than 2. The l/w ratio for miniaturized tension specimen was selected to be 2 or larger. Yield stress was not affected by l/w and w/t ratios to any appreciable level.

As indicated earlier, strain-hardening behavior is another important property expected to be extracted from miniaturized tension tests. By observing specimen shape during testing, reduction at minimum cross section may be obtained. To obtain specimen images during the test, it was preferable to develop the neck at the center of the gage length. This is because jigs for the test cover the specimen and only the central region of the gage section (about 0.5 mm long along the tensile direction) is available for width measurements. To make necking occur at the central region of the gage section, the width of the gage section was reduced by 0.4 mm. Figure 8 shows the configuration of a miniaturized tension specimen.

Testing Machine and Method of Displacement Measurement

The same testing machine as used for SP testing can be used for miniaturized tension tests. Figure 9 shows the specimen holder for the test. Both ends of the tension specimen are held by the jig at hooks. Images of the specimen were obtained with two video cameras, and the images were recorded continuously on video tapes and intermittently on magneto-optical disks. An arrangement of the cameras and a jig is shown in Fig. 9. By comparing specimen width during the test with the width before the test, the reduction at minimum cross section and the distribution of the reduction along gage length were obtained during the test. Figure 10 shows specimen images obtained before testing and just before fracture. Dimensional resolution of the image was equivalent to about 0.5% of strain.

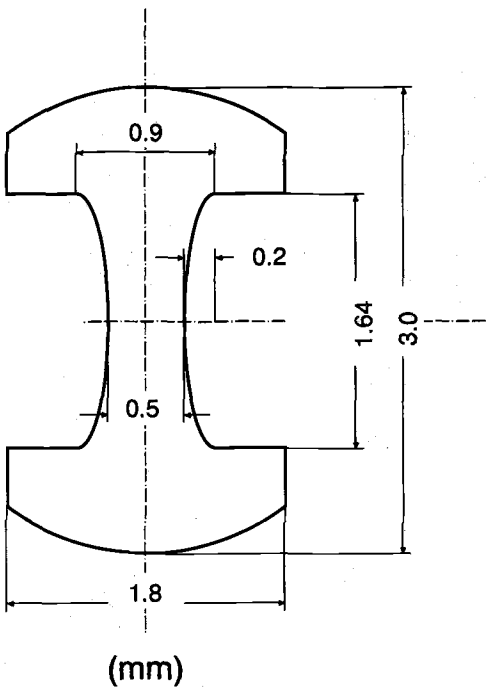

FIG. 8—*Dimensions of the miniaturized tension specimen.*

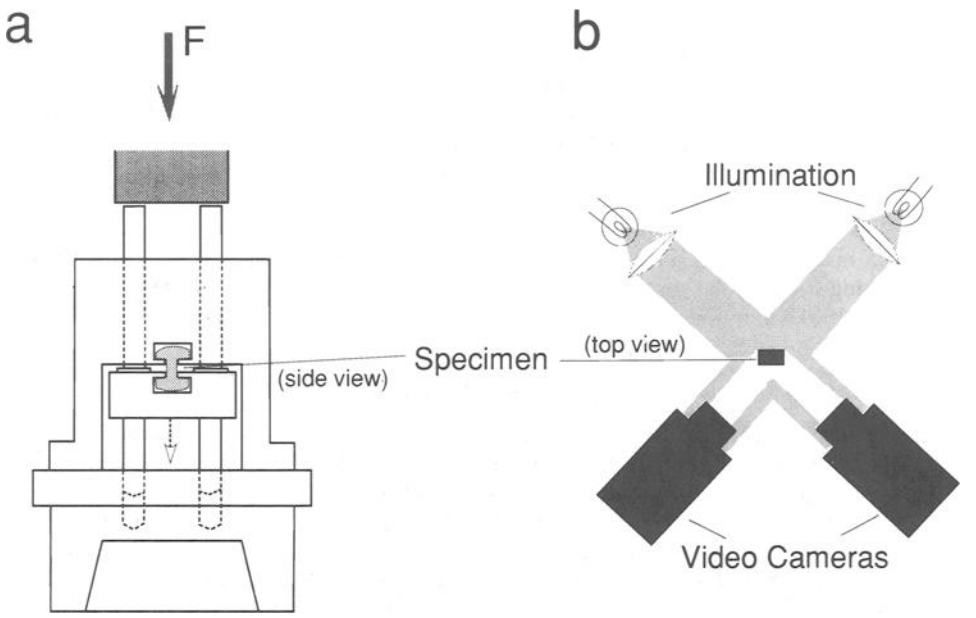

FIG. 9—(a) *Jig for the miniaturized tension specimen (see Fig. 8); F stands for the test load;* (b) *video camera arrangement for specimen width measurement; both ends of the specimen are held by the jig at its hooks.*

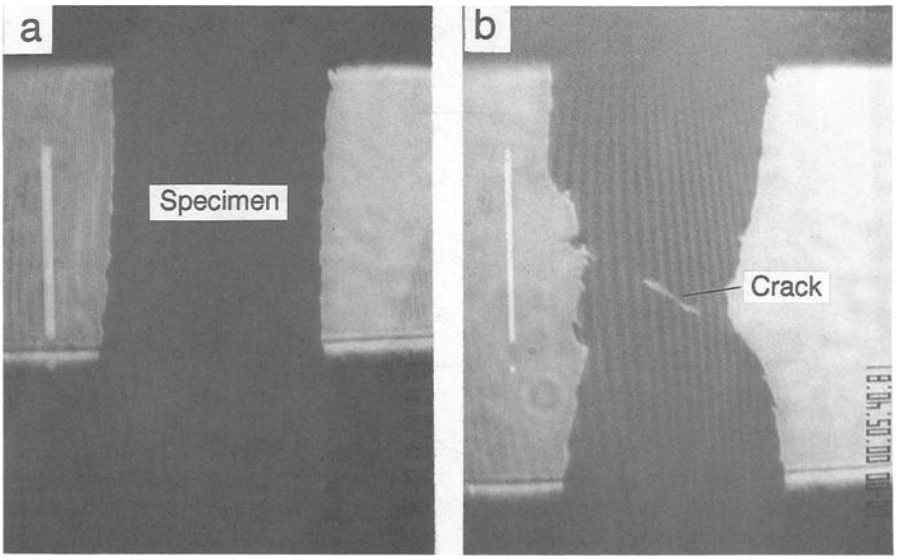

FIG. 10—*Example of images of a miniaturized tension specimen:* (a) *before the test;* (b) *after the test: necking and cracking occurred during the test. Dark parts at the top and the bottom in the photographs are images of the grips.*

Results of Miniaturized Tension Test

Specimens of SA-JPCA, 25% CW-JPCA, and 50% CW-JPCA were fabricated by electro-discharge machining (EDM). Thickness of the damaged layer by EDM was about 10 μm or less. After the EDM, specimens were electro-polished to remove about 20-μm-thick of the surface layer. Helium (He) atoms were implanted in some of the 25%-CW JPCA specimens to concentration levels of 1 and 50 appm. A cyclotron at the NRIM operated at 16 MeV and equipped with a degrader was used to implant He atoms uniformly in the specimen. During the implantation, specimen temperature was monitored and kept below 473 K. Tests were carried out at room temperature.

Figure 11 shows nominal stress strain curves and true stress-strain curves of the specimens. Results for unirradiated miniaturized tension specimens agreed well with the results from larger specimens, except for stresses and strains at peak and at fracture for 50% CW specimens. Results for the larger specimens are shown in Table 2. Helium implantation caused slight hardening.

The results indicate that specimen miniaturization did not introduce marked change on tensile properties for the materials tested.

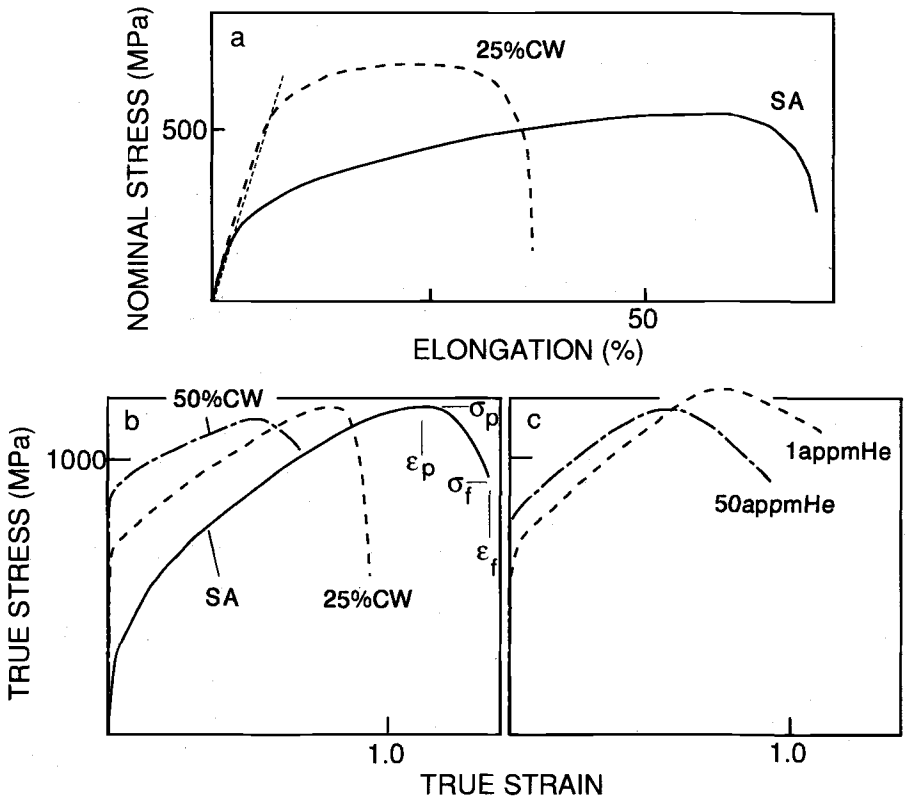

FIG. 11—(a) *Nominal stress-strain curves of solution-annealed (SA) and 25% cold-worked (25% CW) specimens;* (b) *true stress-strain curves of SA, 25% CW, and 50% cold-worked (50% CW) specimens;* (c) *true stress-strain curves of helium (He) implanted specimens. Helium was implanted to 1 and 50 appm in 25% cold-worked specimens prior to the tests. These stress-strain curves were obtained from miniaturized tension specimens.*

Shear Punch Test on Annular Notched Specimen

Test Method for Shear Punch Test on Annular Notched Specimen

Ductile to brittle transition temperature (DBTT) may be obtained from small specimens; however, small specimen DBTT is often far lower than that obtained from a standard CVN test. The lower DBTT causes difficulty in conducting the tests; the lower test temperature requires a longer time to conduct the test. It is well recognized that DBTT is sensitive to the strain rate in the specimen. A notch can increase the strain rate at the notch root. The shear punch [*10*] test is one of the best methods to bring about deformation at a high strain rate because the volume in the specimen to be subjected to the deformation is relatively small. The maximum strain rate in the specimen may be increased by introducing an annular notch on TEM specimens for shear punch tests.

Figure 12 shows a schematic view of the test method. A larger gap between the punch and die compared with the original shear punch [*10*] was employed to allow brittle crack propagation.

Punch Testing Machine on Annular Notched Specimen

Figure 13 shows a punch testing machine for annular notched specimens. The mechanism and test sequence are similar to the testing machine for SP and miniaturized tensile specimens except that the upper and the lower rod contact to fix the specimen directly and the liner

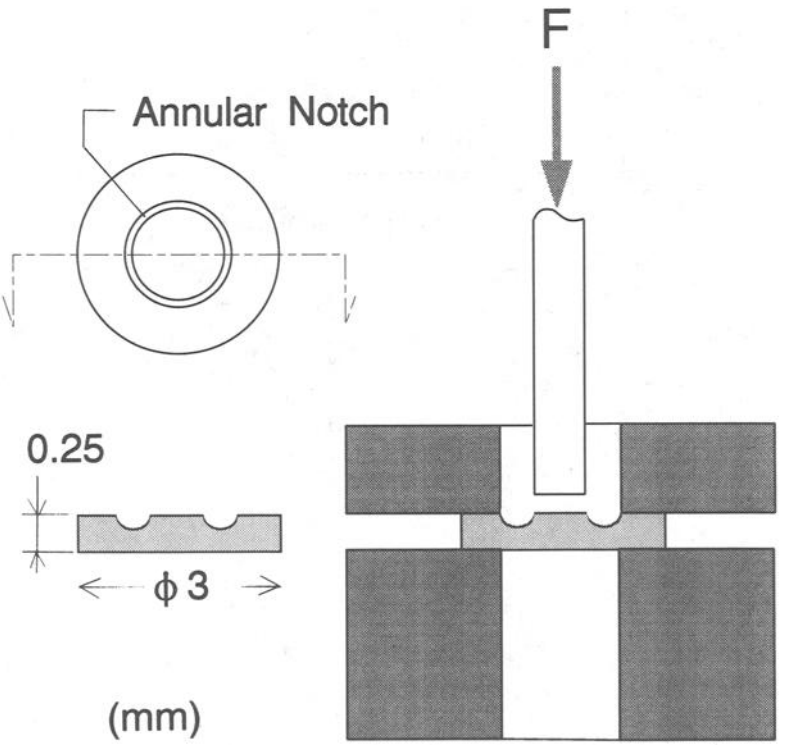

FIG. 12—*Schematic illustration of the shear punch test on annular notched TEM disk specimen. Depth of the annular notch was about half of the specimen thickness. F stands for test load.*

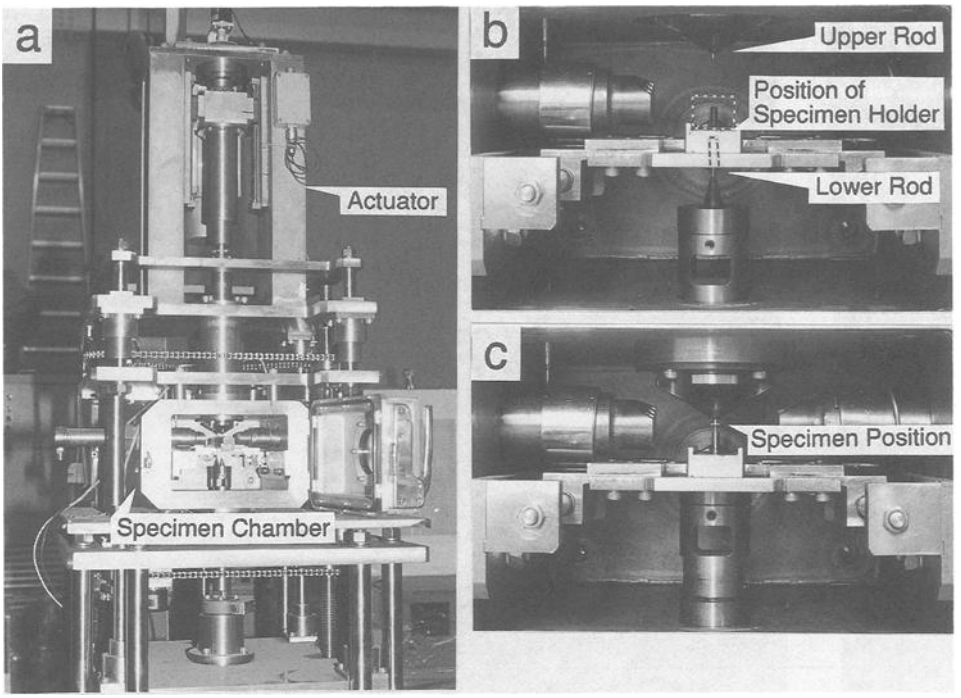

FIG. 13—*Photographs of the testing machine for the shear punch test on annular notched TEM disk specimens:* (a) *a specimen chamber and an actuator;* (b) *positions of upper and lower rods during specimen exchange* (*position of the specimen holder is indicated*); (c) *during the test* (*specimen is clamped between upper and lower rods*).

traveling specimen holder is employed instead of the turntable. Maximum displacement rate is 1 m/s, which is about 1000 times larger than the machine for the SP test. A load cell with a free resonance frequency of over 50 kHz was used; the time to punch out the specimen was 0.2 ms or smaller and 50-kHz resonance frequency of the load cell is at the lower end of available resonance frequency for the test. Installation of a temperature control system is now in progress.

The machine was also designed to conduct miniaturized Charpy tests with specimens of 20-mm-long, 1.5 by 1.5 mm cross section by changing jigs.

Results of the Annular Notched Shear Punch Test

TEM disk specimens of tempered 2¼Cr-1Mo, 8Cr-2WTa, and HT-9 ferritic steels were used for the test. Tests were conducted at a displacement rate of 2 mm/s; as the temperature control system was not equipped yet to the machine fabricated for this test, an Instron-type tension testing machine with a cooling bath was used for the test. Time-load curves were recorded using digital memory.

Figure 14 shows time-load curves and a temperature dependence of absorbed energy for 8Cr-2WTa steel. Absorbed energies were calculated from the area beneath the time-load curves and the nominal displacement rate. Absorbed energies dropped clearly with decreasing temperature from 200 to 100 K. Specimen deformation, which is illustrated also in Fig. 14, changed corresponding to the temperature dependence of the absorbed energy. Scanning

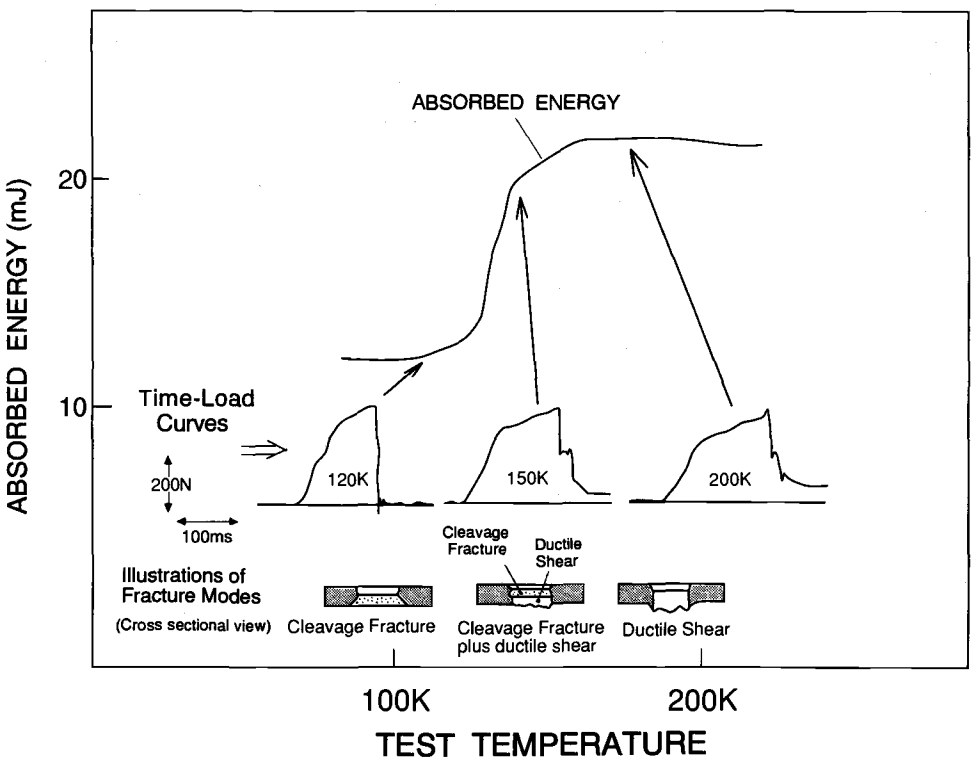

FIG. 14—*Temperature dependence of absorbed energy of the shear punch test on annular notched TEM disk specimens of 8Cr-2WTa ferritic steel. Load-time curves and illustrations (cross-sectional view) of fracture modes at temperatures for cleavage fracture (see Fig. 15*a *and 15*b*), cleavage fracture plus ductile shearing (see Fig. 15*c *and 15*d*) and ductile shear (see Fig. 15*e *and 15*f*) are shown.*

electron micrographs (Fig. 15) of fractured surfaces also show the transition of the fracture mode: cleavage (15*a* and 15*b*), cleavage plus ductile shear (15*c* and 15*d*), and ductile shear (15*e* and 15*f*). At lower temperatures below the transition temperature region, specimens failed by brittle cleavage fracture. In the transition temperature region, fracture occurred by mixture of cleavage fracture and ductile shearing. As illustrated in Fig. 14 (at 150 K) and seen in the fracture surface in Fig. 15*d*, fracture occurred at the notch root and propagated producing a cleavage fractured surface. Then, brittle crack propagation was stopped and the rest of the specimen failed by ductile shear. This arrest of the cleavage crack propagation may indicate that the stress state at the crack tip changed when the thickness of the ligament became smaller than some critical size. When the plastic zone size became comparable or larger than ligament size, stress was reduced to arrest further brittle crack propagation. The thickness of the region failed by ductile shear may have a correlation with the plastic zone size at the temperature.

Figure 16 shows temperature dependence of absorbed energy for 8Cr-2WTa steel and HT-9. Results by SP [*11*] and CVN tests are also shown in the figure. DBTT by this test is clearly higher than that by the SP test for 8Cr-2WTa steel and was reasonably close to that by CVN test. On the other hand, the difference between DBTTs for 8Cr-2WTa steel and HT-9 was about 79 K by CVN tests while the difference by this method was only 4 K.

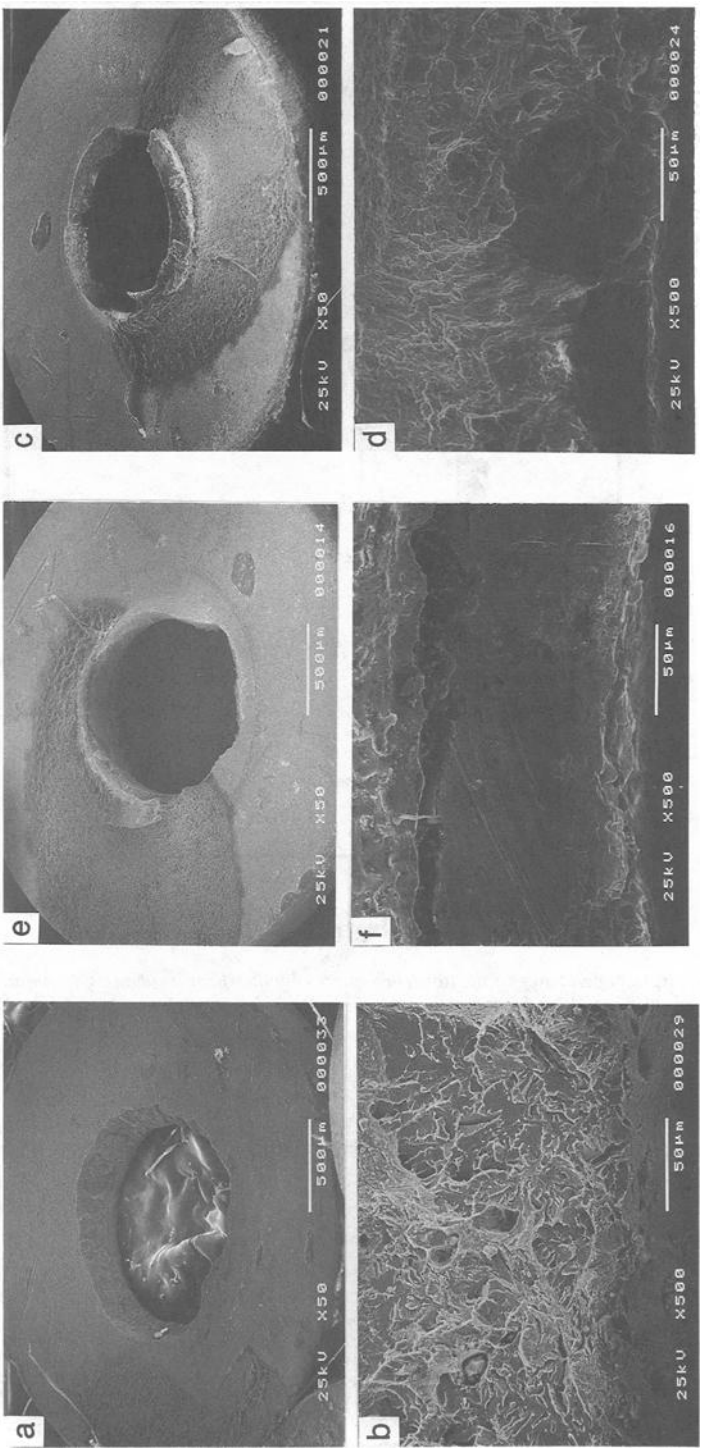

FIG. 15—*Scanning electron micrographs of fracture surface by the shear punch test on annular notched TEM disk specimen of HT-9 steel. Specimens are placed upside down to show fracture surfaces (annular notches are not seen). The specimens were tested at* (a, b) *150 K;* (c, d) *166 K; and* (e, f) *210 K.*

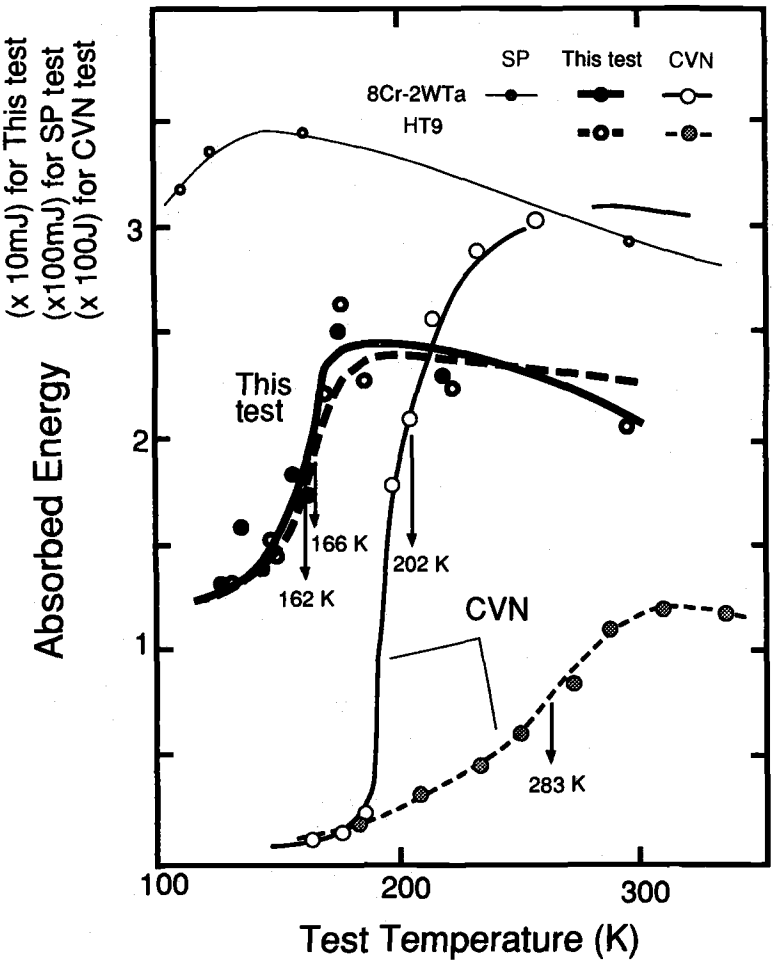

FIG. 16—*Temperature dependence of the absorbed energy by the shear punch test on annular notched TEM disk specimens of 8Cr-2WTa ferritic steel and HT-9 steel. Results by standard CVN and SP tests* [11] *on TEM disks are also plotted.*

The difference in the results by CVN and by this method may be interpreted by the relation between plastic zone size and ligament size. Smaller CVN energy in the transition region and upper shelf region for HT-9 may be the result of smaller fracture toughness of the steel. As the yield stresses for both steels were not largely different [*11*], plastic zone size for 8Cr-2WTa steel might be larger than that for HT-9, and this could be the cause of the different CVN behavior. However, the plastic zone size for HT-9 was small, and it might be comparable or larger than the ligament size of an annular notched specimen at, for example, 200 K, in this method. If this was so, DBTT by this method for both steels would not be much different, as has been seen. If the analysis above is valid, it will be very difficult to overcome specimen size effect for DBTT measurement. Examination of size dependence may be important to understand DBTT property for these steels.

Manipulator for Small Specimens and a Device for Electro-Discharge Machining

Micro-Manipulator

Development of devices to manipulate, examine, and machine is also an important subject. A micro-manipulator to handle specimens and to use for the examination of specimens before and after the tests is now under development. An EDM for small specimens to obtain miniaturized tension specimens and annular notched specimens has been made.

In the manipulation process, it is frequently required to mount randomly dispersed specimens on a table into specimen holders. A computer-controlled manipulator was designed to do this operation. Figure 17 shows the manipulator. To insert specimens in vials into holders, first the specimens are dispersed on the tray by a conventional manipulator. A video camera is equipped over the tray to obtain digitized images of the specimen in the tray. By pointing at a digitized image of each specimen, signals corresponding to the position are sent to the computer to move the X-Y-Z arm to pick up the specimen. The arm is equipped with vacuum tweezers. The position of the specimen holder has been also supplied as digital data into a computer program prior to the operation, and the arm carries the specimen to the holder and puts the specimen into the holder. This device also has mechanisms to turn the specimen over and to turn the specimen (a turntable) to obtain the wall thickness distribution after a SP test with an X-ray source and an X-ray camera.

EDM is also computer controlled to machine specimens in the holder (twelve specimens can be inserted in a holder) sequentially. Figure 18 shows the EDM for small specimens. As EDM is to be operated remotely and the required machining accuracy is to be high enough for small specimens, the consumption rate of the machining electrode and the surface

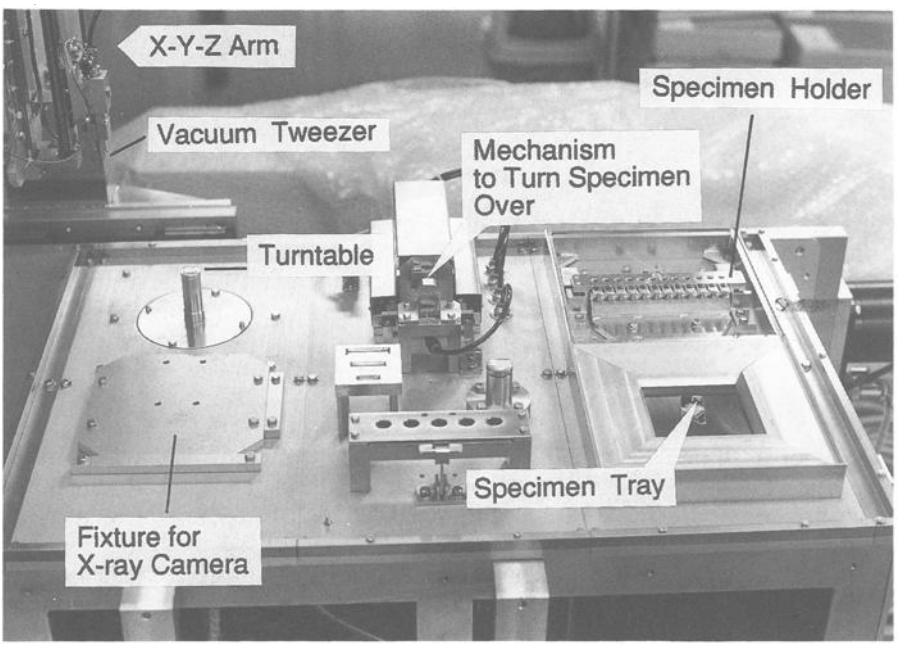

FIG. 17—*A photograph of micro-manipulator. Specimen tray (black plate on the right), X-Y-Z arm with a vacuum tweezers, and a specimen holder for EDM device are shown.*

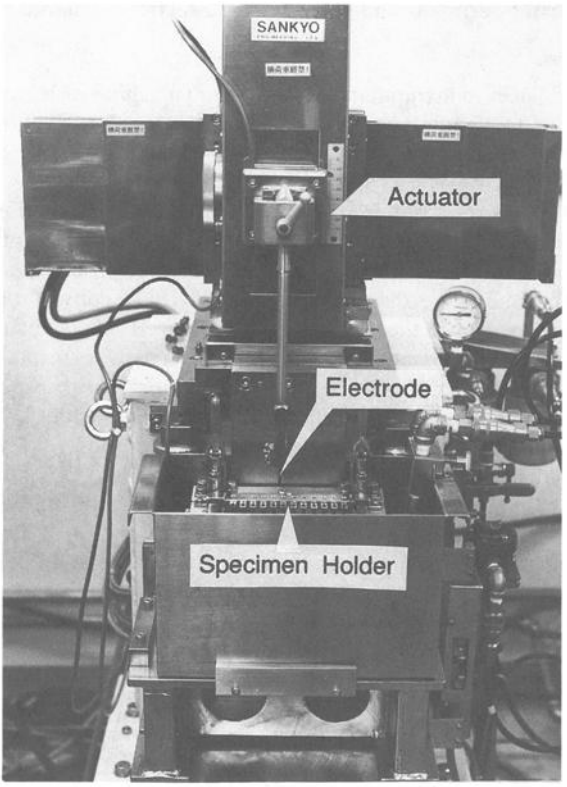

FIG. 18—*A photograph of an electro-discharge machining device. A specimen holder, a machining electrode, and an actuator for the electrode are shown.*

roughness after the machining are particularly important for practical use. An electronic machining power supply is designed to apply negative bias voltage to minimize the consumption rate and surface roughness by minimizing arcing between an electrode and a specimen. The consumption rate of 3% and surface roughness of less than 5 μm has been achieved for the machining of carbon steel.

Summary

Devices for small specimen testing that have been and will be installed in hot cells of the Japan Atomic Energy Research Institute are briefly introduced. Test methods for the devices are also introduced. Preliminary results of the test methods were presented and discussed:

1. *SP test.* Tensile properties of solution-annealed and cold-worked austenitic stainless steel were compared with SP test results obtained by a testing device developed for hot cell use. SP results were not sensitive to the cold work rate of the materials in contrast to the tensile results.
2. *Miniaturized tension test.* Reasonable correlations between the tensile results with larger size specimens and those with miniaturized specimens have been obtained.

3. *Shear punch test on annular notched specimen for DBTT measurement.* DBTT by this method was higher than that obtained by the other method with TEM disks. Measured DBTT dependence on materials was different from that by CVN test. This may be due to specimen size effects.
4. *Devices developed for small specimen tests.* Devices developed for small specimen tests are a testing machine for SP and miniaturized tension tests, a testing machine for DBTT evaluation from TEM disks and miniaturized Charpy specimens, a micro-manipulator for handling specimens, and a device for electro-discharge machining to obtain miniaturized tension and annular notched specimens from TEM disks.

References

[1] Baik, J.-M., Kameda, J., and Buck, O., "Development of Small Punch Tests for Ductile-Brittle Transition Temperature Measurement of Temper Embrittled Ni-Cr Steels," *The Use of Small Scale Specimens for Testing Irradiated Material, ASTM STP 888*, W. R. Corwin and G. E. Lucas, Eds., American Society for Testing and Materials, Philadelphia, 1986, pp. 92–111.

[2] Suzuki, M., Eto, M., Fukaya, K., Nishiyama, Y., Kodaira, T., Oku, T., Adachi, M., Umino, A., Takahashi, I., Misawa, T., and Hamaguchi, Y., "Evaluation of toughness degradation by small punch (SP) tests for neutron-irradiated 2¼Cr-1Mo steel," *Journal of Nuclear Materials*, Vols. 179–181, 1991, pp. 441–444.

[3] McNaney, J., Lucas, G. E., and Odette, G. R., "Application of Ball Punch Tests to Evaluating Fracture Mode Transition in Ferritic Steels," *Journal of Nuclear Materials*, Vols. 179–181, 1991, pp. 429–433.

[4] Misawa, T., Suzuki, K., Saito, M., and Hamaguchi, Y., "Determination of the Minimum Quantity of Irradiated Ferritic Steel Specimens for Small Punch DBTT Testing," *Journal of Nuclear Materials*, Vols. 179–181, 1991, pp. 421–424.

[5] Takahashi, H., Shoji, T., Mao, X., Hamaguchi, Y., Misawa, T., Saito, M., Oku, T., Kodaira, T., Fukaya, K., Nishi, H., and Suzuki, M., "Standardization of SP test (in Japanese)," JAERI-M 88-172, Japan Atomic Energy Research Institute, Ibaraki, Japan, 1988.

[6] Standard Test Method for J_{IC}, A Measure of Fracture Toughness, ASTM E 813-88, *Annual Book of ASTM Standards*, Vol. 03.01., American Society for Testing and Materials, Philadelphia, 1988, pp. 698–712.

[7] Okada, A., Hamilton, M. L., and Garner, F. A., "Microbulge Testing Applied to Neutron Irradiated Materials," *Journal of Nuclear Materials*, Vols. 179–181, 1991, pp. 445–448.

[8] Ghosh, A. K., *Mechanics of Sheet Metal Forming*, D. P. Koistinen and N.-W. Wang, Eds., Plenum Press, New York, 1978, pp. 287–312.

[9] Jitsukawa, S., Grossbeck, M. L., and Hishinuma, A., "Stress-Strain Relations of HFIR-Irradiated Austenitic Stainless Steels," *Journal of Nuclear Materials*, Vols. 179–181, 1991, pp. 563–567.

[10] Lucas, G. E., Odette, G. R., and Sheckherd, J. W., "Shear Punch and Microhardness Tests for Strength and Ductility," *The Use of Small Scale Specimens for Testing Irradiated Material, ASTM STP 888*, W. R. Corwin and G. E. Lucas, Eds., American Society for Testing and Materials, Philadelphia, 1986, pp. 112–140.

[11] Suzuki, M., et al., "Small Specimen Test Techniques for the Evaluation of Toughness Degradation," *Journal of Nuclear Materials*, Vols. 191–194, 1992, pp. 1023–1027.

Tension Testing

Enrico Lucon,[1] *Valerio Bicego,*[1] *Davide D'Angelo,*[2] *and Carlo Fossati*[1]

Evaluating a Service-Exposed Component's Mechanical Properties by Means of Subsized and Miniature Specimens

REFERENCE: Lucon, E., Bicego, V., D'Angelo, D.,and Fossati, C., **"Evaluating a Service-Exposed Component's Mechanical Properties by Means of Subsized and Miniature Specimens,"** *Small Specimen Test Techniques Applied to Nuclear Reactor Vessel Thermal Annealing and Plant Life Extension, ASTM STP 1204,* W. R. Corwin, F. M. Haggag, and W. L. Server, Eds., American Society for Testing and Materials, Philadelphia, 1993, pp. 311–323.

ABSTRACT: Estimating the mechanical properties of a service-exposed component in a quasi-nondestructive manner implies sampling as little material as possible from the component itself. Different subsized or miniature specimens to be employed in the various fields of mechanical testing are presented and discussed:

1. Cylindrical specimens with circumferential crack for fracture toughness testing in the brittle regime and miniature disk-shaped specimens for the upper-shelf ductile regime.
2. Miniature reconstructed specimens for residual creep strength evaluation by means of isostress temperature-accelerated tests.
3. Small-size specimens for low-cycle fatigue testing with enhanced cycle frequency.

Data significance and transferability to actual components, as well as accuracy of results, are discussed. Particular emphasis is devoted to usually favorable comparisons obtained with respect to larger, conventional specimens considered by ASTM test standards.

KEYWORDS: residual life evaluation, life extension, subsized specimens, miniature specimens, fracture toughness testing, cylindrical specimens, disk-shaped specimens, residual creep strength evaluation, low-cycle fatigue testing

Knowing the mechanical properties of the structural materials of plant components is one of the starting points for reliable integrity assessments and correct residual life predictions. In recent years, the introduction of a damage-tolerant philosophy for assessing service-exposed plants has enhanced the need for a comprehensive knowledge of the material's crack growth characteristics, such as fracture toughness (FT), fatigue, low-cycle fatigue (LCF), creep, fatigue crack growth (FCG) and creep crack growth (CCG). These data are usually unavailable for the oldest plants, which require more careful assessment for continued operation. On the other hand, even if data for the as-received materials were available, their significance and usefulness would be questionable since actual service conditions and related damage mechanisms can deeply affect the materials' behavior. It is therefore necessary to obtain data from the component itself so that both metallurgical conditions and residual mechanical properties can be directly assessed.

[1] Chief of Fracture Mechanics Laboratory, chief of Fatigue and Creep Laboratory, and chief of Mechanics and Microstructural Section, respectively, Material and Technology Division, CISE SpA, via Reggio Emilia 39, 20090 Segrate (Milano), Italy.

[2] Chief of Materials Office, ENEL-CRTN, via Rubattino 21, 20133 Milano, Italy.

Excluding microstructural characterization, which can be completely nondestructive in case of accessible surfaces, the evaluation of the mechanical properties requires sampling material from the component (with the exception of hardness measurements). Sampling can usually be performed only when the sample size is so small that easy repairing or even no repairing at all is eventually needed. This requirement implies the use of very small specimens, usually not complying with the size requirements imposed by ASTM test standards.

Presently, an intense effort is being carried out in many test laboratories to set up reliable testing procedures and data reduction methods for material characterization by means of subsized and miniaturized specimens. Several aspects are of particular concern:

1. Significance of test data, which must retain full theoretical validity and be comparable with standard test results.
2. Data transferability to actual components.
3. Appropriate data reduction techniques.
4. Data accuracy with respect to available laboratory instrumentation.

In the framework of ENEL (Italian Electricity Board) activities aimed at assessing the integrity of critical components in fossil-fueled power stations, a considerable amount of experimental work has been performed at CISE and ENEL-CRTN in the field of miniature specimen testing; particular attention has been devoted to fracture mechanics, low-cycle fatigue, creep, and fatigue crack growth testing.

In the present paper, details on different subsized and miniature specimen geometries, testing techniques, and test results on different steels are presented; data significance and transferability are subsequently discussed.

Fracture Mechanics Testing

Cylindrical Specimens with Circumferential Crack

Fracture toughness testing in the linear elastic regime normally requires large and expensive specimens if one wants to comply with the dimensional requirements imposed by widely used standards like ASTM Test Method for Plane-Strain Fracture Toughness of Metallic Materials (E 399-90). For the residual life evaluation of a service-exposed component, the main problem is the unavailability of large amounts of sample material, thus forcing the need to consider alternative specimens to the conventional compact tension [C(T)] or single edge notched bend [SEN(B)] geometries.

The cylindrical specimen with circumferential notch, precracked by rotary fatigue and tested in tension, represents a valuable solution for K_{Ic} testing: its geometry is shown in Fig. 1. Its main advantages with respect to conventional specimens are the following:

1. Machining is simpler, quicker, and considerably cheaper.
2. A small amount of sample material is required (the possibility of enhancing material saving by reconstruction is currently being investigated).
3. The circumferential crack guarantees plane-strain conditions at the tip through a triaxial stress distribution induced by its particular configuration.
4. The actual test is just a straightforward tension test and requires no extensometer or strain gages on the specimen.

A series of tests at room temperature have been conducted using three proportional sizes of this specimen; the material was a 1Cr-1Mo-0.25V steam turbine rotor steel (ASTM A 370 Grade B). Comparisons were eventually made with K_{Ic} values obtained on C(T) specimens tested according to the requirements of ASTM E 399.

Precracking—A circumferential crack of controlled depth was achieved at the root of the machined notch on a rotary fatigue machine applying a four-point bending moment to the

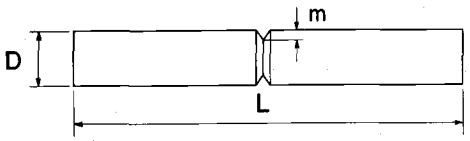

Specimen type	A	B	C
D	6	9.4	12
m	1.09	1.7	2.17
L	48.5	76	97

FIG. 1—*Cylindrical specimen with circumferential crack for fracture toughness testing (dimensions in mm).*

specimen. Precracking load was chosen so that the applied K during precracking corresponded to approximately 50% of the expected K_{Ic}. Crack depth was monitored by a magnetic transducer mounted above the notch, sensing specimen deflection caused by crack growth; specimen deflection was eventually associated to crack depth by a simple best-fit procedure. Ideal conditions, defined after some attempts, yielded precracking times of approximately 30 min (≈150 000 cycles with a rotational speed of 5000 rpm). More details on the precracking of cylindrical specimens have been given elsewhere [*1*].

Test Results—Only the load at fracture was required for calculating the K_{Ic} value according to the formula [*2,3*]

$$K_{Ic} = \frac{P}{D^{3/2}} \cdot F\left(\frac{d}{D}\right) \tag{1}$$

where

P = load at fracture, N,
D = specimen outer diameter, mm,
d = inner diameter (accounting for the crack), mm, and
$F(d/D)$ = dimensionless geometrical factor.

An effective crack length, given by the measured value plus a correction factor related to the plastic radius at the crack tip [*4*] was used in Eq 1. Test results are summarized in Table 1, where a straightforward comparison is presented with K_{Ic} values obtained according to E 399 on C(T) specimens with B = 25.4 mm thickness. More tests and statistical analyses are now needed for assessing the real significance of K_{Ic} differences between cylindrical and conventional C(T) specimens.

Miniature Disk-Shaped Specimens

The disk-shaped compact, DC(T), is one of the specimens considered by ASTM standard E 399-90 for fracture toughness testing in the linear elastic regime. Although no mention of it is made by other standards relating to the upper-shelf regime, like ASTM Standard Test Method for J_{Ic}, a Measure of Fracture Toughness (E 813-89), this specimen has been used for some years at CISE for evaluating the ductile fracture resistance of a service-exposed component [*5*] using the C(T) formulas for J-integral calculations. Thanks to its miniaturized dimensions (diameter 16 to 20 mm, see Fig. 2), it can easily be machined out of plugs obtained in the residual life evaluation of a plant.

TABLE 1—*Test results for cylindrical specimens and comparison with K_{Ic} data obtained from C(T) specimens (material: 1Cr-1Mo-0.25V steam turbine rotor steel, ASTM A370 Grade B).*

Specimen Type	Specimen Size	Number of Tests	K_{Ic},[a] MPa$\sqrt{m}$
Cylindrical	D = 6 mm	5	52.3 ± 3.1
Cylindrical	D = 9.4 mm	10	54.9 ± 3.5
Cylindrical	D = 12 mm	9	58.8 ± 5.1
Compact-tension	B = 25.4 mm	3	58.5 ± 6.7

[a] Average values, with standard deviation.

The inapplicability of a conventional clip gage on such a small specimen has been successfully overcome by utilizing an indirect methodology for deriving load-line displacement; extraneous displacements due to of load system compliance and elastic deformations in the grips and specimen are measured by testing an unnotched specimen and eventually subtracted from the crosshead displacement during the actual test. This method is similar to other techniques commonly used for SEN(B) specimens, like the one described in ASTM E 813-89, Annex A1.

The miniaturized DC(T) specimens should not be used in cases where the investigated material is in the brittle or brittle/ductile regime, since they most likely fail to meet the dimensional requirements of the standards and are likely to significantly overestimate the real fracture toughness of the component unless their thickness coincides with that of the component itself. On the other hand, in the upper-shelf regime they can provide sufficient J-capacity for most ferritic steels to be used for toughness characterization within the limits imposed by the standards; their results compare very favorably with data obtained on larger, conventional specimens, both in terms of fracture parameters (J_{Ic}) and resistance curves. Figure 3 shows an example in which J-Δa data from B = 25.4 mm C(T) and D = 16 mm DC(T) specimens are compared with relevant R-curves; the material is the same CrMoV rotor steel already considered for the

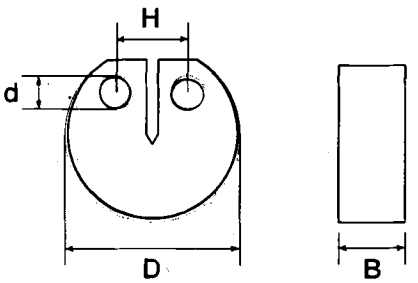

Specimen type	A	B	C
D	16	18	20
d	3.2	3.4	4
H	6.5	7.3	8.14
B	5.92	6.67	7.4

FIG. 2—*Miniature disk-shaped specimen for fracture toughness testing (dimensions in mm).*

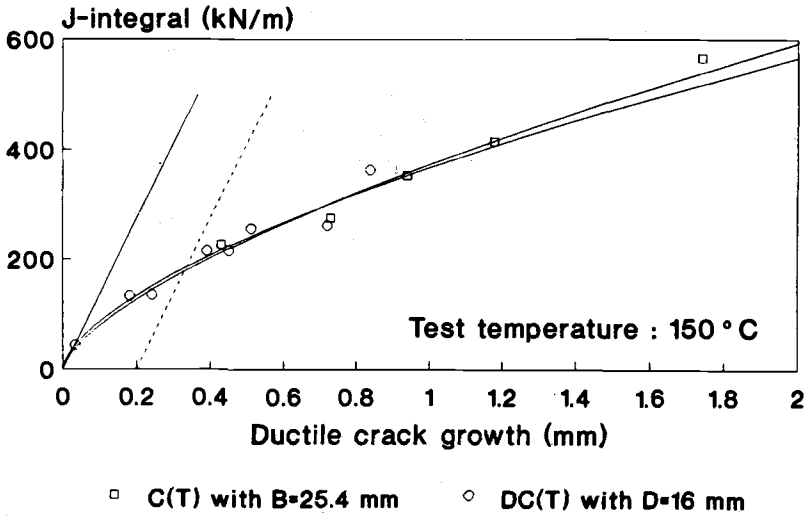

FIG. 3—*J-R curves obtained from miniature disk-shaped and conventional C(T) specimens (material: 1Cr-1Mo-0.25V).*

cylindrical specimens. Fracture resistance curves are also being obtained on a single-specimen basis employing the reversing direct current electrical potential drop (RDCEPD) technique [*6*] for monitoring crack growth in the specimen.

Miniaturized RDCEPD-instrumented DC(T) specimens have also been used for fatigue crack growth testing, showing satisfactory trends with respect to larger specimens. However, their very small size tends to restrict the experimental ΔK range too much, thus missing out the first and some of the second stage of crack growth. Further investigations are currently underway.

Creep Testing

ENEL has been developing, since 1972, methods for residual life assessment of high-temperature components of thermal power plants [*7*]. Different stages have been considered: theoretical analysis, nondestructive controls, metallographic examination, and post-exposure testing. At first, steam pipes were considered, then superheaters and reheater boiler tubes, as well as steam turbine components. From 1986 on, ENEL began monitoring headers operating at elevated temperatures to verify life extension in terms of reliable and safe operation [*8*].

Among the various techniques for the determination of the remaining life of components working in creep conditions, one of the most quantitatively reliable is the creep-rupture strength evaluation by means of tests on service-exposed materials cut from the component [*9*]: but the direct application of such methodologies to steam headers is not possible because of the inapplicability of cutting out large spool pieces.

Suitable methods for quantitative estimation of residual life have been developed and validated, such as cutting small samples through the header shell, preparing miniature and reconstructed specimens by specific welding procedures, and setting up the experimental system and methodology for creep-rupture testing in argon with a temperature accelerated isostress extrapolation [*10*]. The specimen dimensions for these creep-rupture tests depend on the ex-service cutouts available. Whenever a plug could be sampled in the shell thickness of the header, creep-rupture tests could be performed in argon on subsized semi-standard specimens (Fig. 4*a*). Moreover, if just a small boat sample was machined on the thin shell

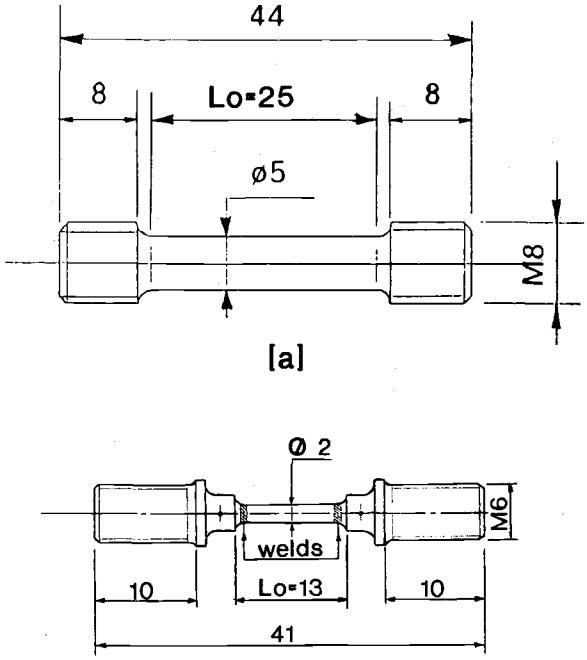

FIG. 4—*Small-size specimens for creep testing:* (a) *subsize semi-standard specimen;* (b) *miniature weld-reconstructed specimen* (*dimensions in mm*).

of the header, miniature specimens for creep-rupture testing in argon can be adopted, reconstructing them by electron-beam welding techniques and using service-exposed material for the gauge zone and joining matching materials for the specimen heads (Fig. 4*b*).

Creep-rupture tests on subsized (5 by 25 mm) specimens of a 2¼Cr-1Mo (ASTM A335 P22) header ex-service steel have been performed mainly to compare the rupture times in air with those in argon. Table 2 illustrates testing parameters and results: a reduction of

TABLE 2—*Test parameters and results for creep-rupture tests on subsized specimens (material: 2¼Cr-1Mo).*

Environment	Stress, MPa	Temper., °C	t_r,[a] hours	Elong., %	Red. of area, %	P_{LM}[b]	$\dot{\epsilon}_{min}$,[c] %/hour
Argon	45.1	700	110.6	70	95	21448	$1.08 \cdot 10^{-1}$
Argon	45.1	680	228.0	46.6	91.4	21307	$1.16 \cdot 10^{-2}$
Argon	45.1	670	700.5	80	96	21543	$1.26 \cdot 10^{-2}$
Air	45.1	670	442.4	54	94	21355	$1.07 \cdot 10^{-2}$
Air	36.5	670	1094.4	32	96	21726	$1.12 \cdot 10^{-3}$
Argon	45.1	655	1447.4	52	92	21493	$3.65 \cdot 10^{-3}$
Air	36.5	650	4551.6	...	...	21836	$8.76 \cdot 10^{-4}$
Argon	45.1	635	3928.0	46	89	21423	$8.87 \cdot 10^{-4}$
Air	45.1	635	2673.0	37	95	21272	$2.53 \cdot 10^{-5}$

[a] t_r = rupture time.
[b] P_{LM} = Larson-Miller parameter.
[c] $\dot{\epsilon}_{min}$ = minimum creep rate.

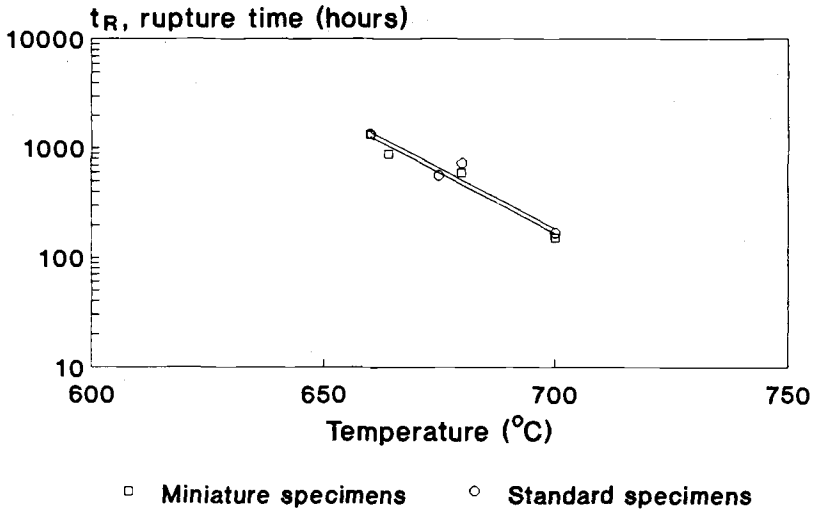

FIG. 5—*Creep test results from standard and miniature specimens (material: 2¼Cr-1Mo).*

rupture times, caused by specimen surface oxidation, can be observed; moreover, whenever a direct comparison could be made between tests performed at the same temperature and stress value, a reduction factor of approximately 1.5 in rupture times was found.

Miniature specimens (2 by 10 mm) of the same steel (2¼Cr-1Mo, ASTM A 335 P22) have been creep tested in argon. A comparison of rupture times (Fig. 5), ductility, and minimum creep rate between subsized and standard specimens has been made to verify the significance and accuracy of data, with respect to the transferability to the component behavior and to the suitability of the laboratory procedure. Results obtained up to present (Table 3 and Fig. 5) support the feasibility of obtaining the actual creep strength of the service-exposed materials and, therefore, deducing the remaining component life by means of the critical isostress extrapolation to the header operating temperature.

Low-Cycle Fatigue Testing

LCF resistance of a material is the result of complex time-dependent phenomena produced by the combined action of cyclic plasticity, creep, and environmental attack (mainly oxidation in the case of structural steels for plant components of power industry). Material metallurgical instability during long-term operation is also relevant. As far as LCF tests are concerned

TABLE 3—*Comparison between test results on miniature and standard creep specimens (material: 2¼Cr-1Mo).*

Specimen Type	Stress, MPa	Temperature, °C	t_r, h	Deformation at Rupture, %	$\dot{\epsilon}_{min}$, %/h
Miniature	44.5	700	152	92.48	$5.5 \cdot 10^{-2}$
	44.5	680	595	68.27	$1.5 \cdot 10^{-2}$
	44.5	664	883	67.72	$5.3 \cdot 10^{-3}$
	44.5	660	1319	71.00	$4.8 \cdot 10^{-3}$
Standard	44.5	700	168	52.24	$4.9 \cdot 10^{-2}$
	44.5	680	724	45.68	$9.2 \cdot 10^{-3}$
	44.5	675	560	39.00	$1.2 \cdot 10^{-2}$
	44.5	660	1332	37.31	$4.2 \cdot 10^{-3}$

on service-exposed materials taken from plant for residual life evaluation purposes, these tests must inherently involve a strong acceleration in time with respect to realistic times of transients in plants and in view of the fact that utilities need short-time answers. Extrapolation of accelerated test data is always a problem in LCF, as no model exists treating with appropriate reliability (in view of the long extrapolations involved) the complex combined effects of cyclic plasticity, creep, oxidation, and metallurgical instability. Therefore, LCF predictions up to now have mostly been based on calculations, using reference data on virgin material, analysis of component history, and damage models. However, even with a less ambitious aim (as for instance with pure creep, where a real estimate of the creep residual life is derived, e.g., from isostress tests), LCF tests on samples taken from service-exposed components have also been carried out during the last few years at CISE. This work is mainly to get indications about material LCF damage situations. Essentially what one expects from these tests is a comparison with the endurance data of the original material (if available) or at least with nominal LCF curves considered in design. The classical LCF waveforms considered at CISE for these tests therefore involve: (1) strain control with constant amplitude, (2) continuous cycling (triangular cycles), or (3) cycles with a hold time (HT) of 1 h at maximum tensile strain. In standard testing for LCF material characterization, two basic configurations of round specimens were considered in the past at CISE: (1) hourglass specimens with axial strains evaluated from measurements taken with diametral extensometers (Fig. 6*a*), and (2) cylindrical specimens (Fig. 6*b*). Alignment and compressive stability are

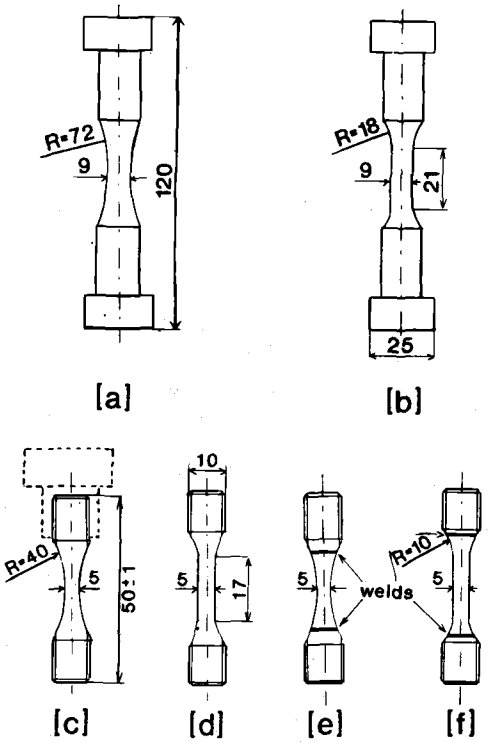

FIG. 6—*Standard and miniature specimens for low cycle fatigue testing:* (a) *standard, hourglass;* (b) *standard, cylindrical;* (c) *miniature, hourglass;* (d) *miniature, cylindrical;* (e) *miniature reconstructed, hourglass;* (f) *miniature reconstructed, cylindrical* (*dimensions in mm*).

important aspects. As far as this latter point is concerned, an hourglass geometry is preferred when ductile materials are to be tested at high strain ranges (5%), especially if a compressive HT is present; use of cylindrical specimens is essential when testing nonisotropic materials and welded joints (CISE's experience indicates approximately 80% shorter LCF lives are obtained for cylindrical with respect to hourglass specimens). A large specimen minimum diameter is beneficial for a fixed specimen length for compressive stability: in the standard CISE specimens a value of $D = 9$ mm is used. Proper alignment (maximum bending strain below $5 \cdot 10^{-6}$) is obtained by the use of flat button heads, 25 mm in diameter. In testing service-exposed material, the rather large size of these specimens, particularly in view of the wide button heads, is a problem, not only because of the amount of material which is needed for machining the five or six specimens necessary to develop a typical fatigue curve, but also because material at the center of the specimen is unavoidably far from the position where thermal fatigue is expected to be highest in the component (i.e., at the surface). Therefore, the possible use of miniature specimens was considered having 5-mm minimum diameter (below this dimension oxidation would become excessive for ferritic steels) and 10-mm-diameter threaded ends (Figs. 6*c* and 6*d*, utilizing a volume of material which is only 8% of the volume needed for specimens 6*a* and 6*b*); more recently, the use of weld-reconstructed miniature specimens was also investigated (Figs. 6*e* and 6*f*, with 2.3% volume of material with respect to conventional specimens; material waste during sampling and machining operations is not considered in these figures).

The main aspects considered were: strength of the thread-button head couplings (a nickel-based superalloy provides reusability of this part), alignment and compressive stability, significance of miniature specimen data with respect to standard specimen data. As far as this last point is concerned, perfect identity must not be expected, as size dependency is a typical feature of LCF testing (because of oxidation, essentially dependent on the surface-to-volume ratio, and because of the different extent of plane stress/plane strain regions in the samples). Instead of trying to get a universal rationale for this size dependency of results, the activity described here was intended to provide, with reference to typical steels and typical test conditions, experimentally determined corrective factors applied to miniature specimen data to get estimates of conventional LCF curves. Up to now a comparative series of tests utilizing the specimen geometries in Figs. 6*a* to 6*e* have been concluded on the same 1Cr-1Mo-0.25V rotor steel already considered for fracture tests, with $T = 540$°C, $\dot{\epsilon} = 3 \cdot 10^{-4}\,s^{-1}$, tensile HT = 0 and 1 h. The reference LCF data on the conventional size specimens ($D = 9$ mm) considered in this analysis are from a previous extensive characterization activity on this rotor material [*11*]. Use of miniature specimens was found at risk of failure in the threaded end connections coupled to button heads (3 failures out of 27 specimens), with less risk in HT tests as expected (this being mainly a pure fatigue problem). Compressive stability of the miniature cylindrical specimens was a problem in one test only; however, tests at large strains were intentionally avoided in this work. The strength of the welds in the reconstructed miniature specimens was always adequate.

Comparisons of conventional versus miniature specimen endurance data are shown in Figs. 7*a* to 7*d*. Differences are only moderate; but systematically inferior lives of the miniature specimens with respect to the normal size specimens may be noted. No alteration of the core material, due to the weld cycle, of the weld-reconstructed miniature specimens was found, and such data compare well with the results of the other (sound, unwelded) miniature specimens. From a closer examination of results, it seems that life reductions tend to decrease slightly in the HT tests, whereas no particular trend is visible in relation to strain range levels and use of cylindrical versus hourglass geometry. Independently of possible uncertainties, a conservative life reduction factor of 2/3 has been determined for the LCF data range (cyclic life, $N_f \leq 10\,000$), which accounts for the worst cases experienced in testing

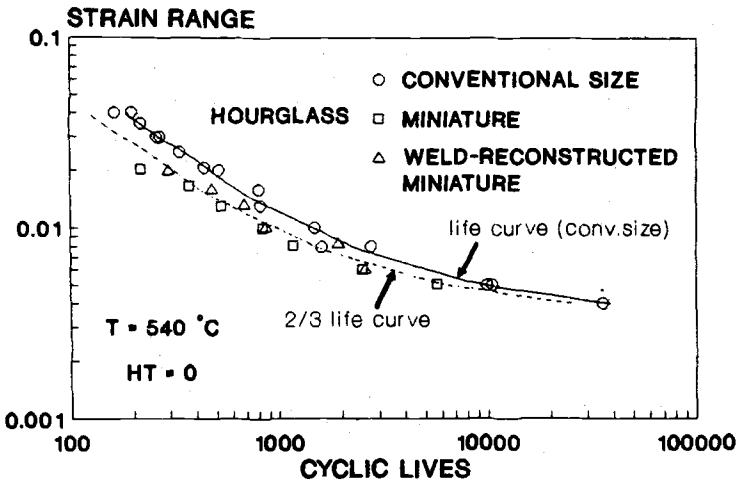

(a)

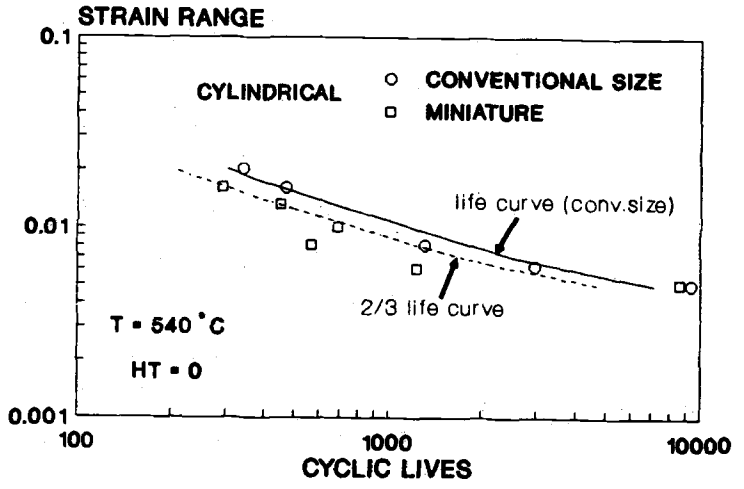

(b)

FIG. 7—*LCF test results on standard and miniature specimens:* (a) *hourglass, HT = 0;* (b) *cylindrical, HT = 0;* (c) *hourglass, HT = 1 h;* (d) *cylindrical, HT = 1 h* (*material: 1Cr-1Mo-0.25V*).

practice. This has become the corrective factor utilized at CISE for LCF integrity assessment studies of service-exposed components of the same steel (even welds) by tests on miniature specimens: in other words, the damage analysis considers tests on miniature specimens, cylindrical or hourglass, with the fatigue life numbers multiplied by 3/2, and then a comparison is made with reference LCF data (often reference is made to the famous curves for rotor steels from Timo [*12*]).

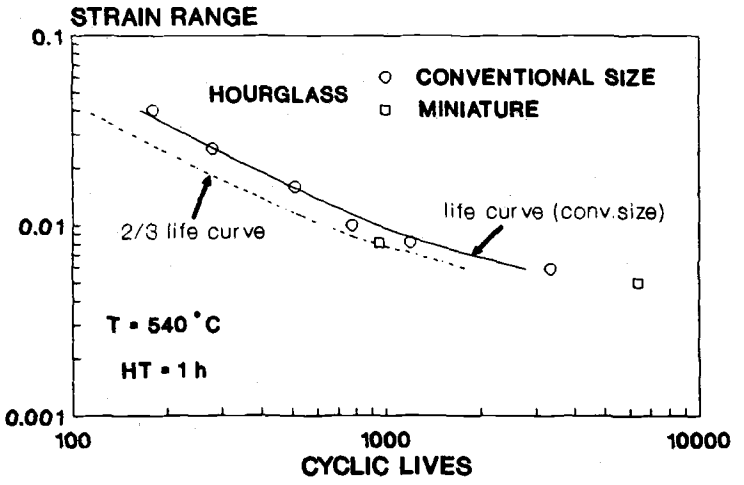

(c)

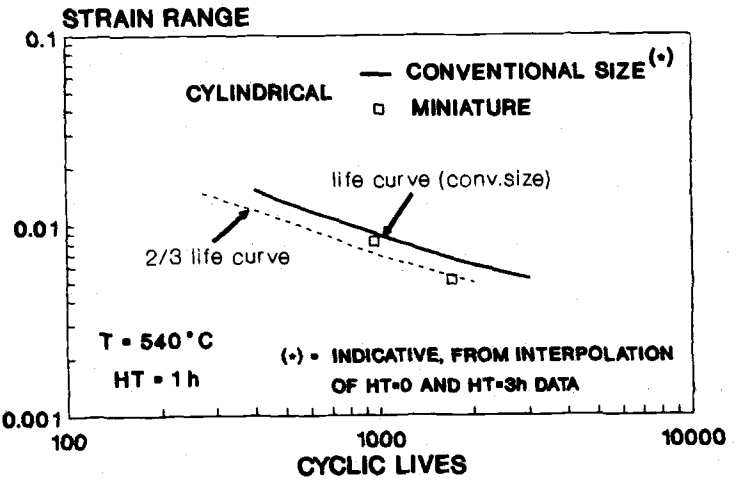

(d)

FIG. 7—*Continued.*

Conclusion

A series of subsized and miniature specimens have been described for mechanical testing in the frame of the residual life evaluation of service-exposed components. The various aspects of fracture mechanics, creep, low-cycle fatigue, and fatigue crack growth testing using small-size specimens have been discussed, with particular emphasis given to the remarkably favorable comparisons with test data obtained on large, conventional specimens.

Weld-reconstruction techniques have also been addressed in view of the further material saving they can provide. More investigation is still needed to improve scientific correlations and experimental procedures: the object is enhancing data significance and transferability to actual service-exposed components.

Acknowledgments

All fracture toughness and low-cycle fatigue tests have been performed at CISE under the sponsorship of ENEL. The authors would also like to thank their colleague Nigel Taylor for his precious collaboration in editing this paper.

References

[*1*] Lucon, E., "Fracture Toughness Testing Using Small Cylindrical Specimens with Ring-Shaped Cracks," *Fracture Behavior and Design of Materials and Structures,* Proceedings of ECF8, 8th Biennial European Conference on Fracture, D. Firrao, Ed., Vol. II, EMAS, London, 1990, pp. 1077–1082.

[*2*] Sih, G. C., "Handbook of Stress-Intensity Factors for Researchers and Engineers," Lehigh University, Bethlehem, PA, 1973.

[*3*] Tada, H., Paris, P., and Irwin, G., "The Stress Analysis of Cracks Handbook," Del Research Corporation, Hellertown, PA, 1973.

[*4*] Wei, S. et al., "Fracture Toughness Measurement by Cylindrical Specimen with Ring-Shaped Crack," *Engineering Fracture Mechanics,* Vol. 16, No. 1, 1982, pp. 69–82.

[*5*] Bicego, V., Lucon, E., and Ragazzoni, S., "Fracture Toughness Testing of Subsized and Weld-Reconstructed Specimens," *Defect Assessment in Components—Fundamentals and Application,* ESIS/EGF9 1991, Mechanical Engineering Publications, London.

[*6*] Bicego, V., Liviero, D., Fossati, C., and Lucon, E., "J-R Curve Testing Utilizing the Reversing Direct Current Electrical Potential Drop Method," *Applications of Automation Technology to Fatigue and Fracture Testing, ASTM STP 1092,* American Society for Testing and Materials, Philadelphia, PA, 1990, pp. 143–166.

[*7*] Castani, C., D'Angelo, D., and Michelizzi, C., "Methods for Residual Life Prediction of Power Plant Components," *Proceedings,* seminar at Institution of Mechanical Engineers on Remaining Life of High Temperature Plants, London, UK, 1983.

[*8*] Angeli, F., D'Angelo, D., and Fedeli, G., "ENEL's Approaches and Experiences in the Field of Life Assessment and Extension of High Temperature Power Plant Components," *Proceedings,* International Conference on Residual Life of Power Plant Equipment: Prediction and Extension, Hyderabad, India, 23–25 Jan. 1989.

[*9*] Angeli, F., D'Angelo, D., Fedeli, G., and Livraghi, M., "Methods for Residual Life Assessment of Elevated Temperature Components," *Proceedings,* International Conference on Life Assessment and Extension, The Hague, Netherlands, June 1988.

[*10*] Cane, B. J., Ellis, F. V., Roberts, B. W., and Townsend, R. D., "Remaining Life Estimation by Metallographic and Miniature Specimen Methods," *Proceedings,* Workshop Notebook on Fossil Plant Life Extension, Washington, DC, June 1984.

[*11*] Bicego, V., D'Angelo, D., and Ragazzoni, S., "High Temperature Fatigue and Creep Cracking of a 1CrMoV Steam Turbine Rotor," *Proceedings,* International Conference on High Temperature Materials for Power Engineering, Liège, September 1990.

[*12*] Timo, D. P., "Designing Turbine Components for Low Cycle Fatigue," *Proceedings,* International Conference on Thermal Stress and Thermal Fatigue, Berkeley, September 1969, Butterworth, London, 1969, pp. 453–468.

DISCUSSION

M. Brumovsky[1] *(written discussion)*—How do you evaluate tests of cylindrical specimens (for fracture toughness) in cases with eccentric cracks, and how large is their effect on test results? Do you apply similar correction formula as in the Gost (Soviet) Standard?

[1] SKODA Concern, Nuclear Machining Plant, 31600 Plzen, Czechoslovakia.

E. Lucon, V. Bicego, D. D'Angelo, and C. Fossati (authors' closure)—No different evaluation procedure is needed for tests on cylindrical specimens showing eccentric cracks since no detectable effect was found on overall results whatsoever. We feel that no correction formula is therefore required.

W. Schmitt[2] *(written discussion)*—How do you explain the fact that for cylindrical specimens low toughness was obtained from smaller specimen dimensions (D).

E. Lucon, V. Bicego, D. D'Angelo, and C. Fossati (authors' closure)—At the time this paper was written, no explanation had been given to the fact that toughness values seemed to decrease with specimen size, instead of increasing as with conventional specimens. Not enough tests had then been performed in order to assess the significance of this effect. Subsequently, more tests on even smaller cylindrical specimens were carried out just to investigate specimen size influence and this trend was confirmed. Some physical considerations and a few preliminary FEM calculations showed that this might be related to the considerable amount of plastic deformation undergoing in the small-size specimen ligament before fracture: this should prevent the use of an LEFM formula, like the one found in the literature, to calculate critical K_C values. More details on this are to be found in Ref *1* of the Discussion Section.

W. R. Corwin[3] *(written discussion)*—The apparent lack of significant effect of eccentricity of fatigue precracking is very important for the use of the notched rolled subsize specimen for irradiated testing in assuring reproducibility of results. It would be valuable to describe details of any dependency (or the lack thereof) on fatigue precrack eccentricity.

E. Lucon, V. Bicego, D. D'Angelo, and C. Fossati (authors' closure)—More tests on cylindrical specimens of different size have been performed at CISE after this paper was written. An overall evaluation of test results clearly showed that no detectable influence of fatigue precrack eccentricity was found on toughness values, which were randomly distributed around the mean value. More details of this are to be found in Ref *1* of the Discussion Section.

G. R. Odette[4] *(written discussion)*—Was the fracture mode the same for all specimens? Was it cleavage?

E. Lucon, V. Bicego, D. D'Angelo, and C. Fossati (authors' closure)—Yes, the fracture mode was the same for all cylindrical specimens tested, irrespective of their size; the observation of the fracture surfaces with an optical microscope (magnification $\times 7$) revealed typical brittle fracture features, although for some of the smaller specimens ($D = 6$ mm) the load/displacement trace showed evidence of a slight plastic deformation (loss of linearity) before fracture.

Reference

[*1*] Lucon, E., "Cylindrical Specimens for Evaluating a Serviced Component's Fracture Toughness Properties," presented at the Ninth European Conference on Fracture, ECF9, Varna (Bulgaria), 21–25 Sept. 1992.

[2] Fraunhofer Institut für Werkstoffmechanik, Freiburg, Germany.
[3] Oak Ridge National Laboratory, Oak Ridge, TN.
[4] University of California at Santa Barbara, Santa Barbara, CA.

Akira Okada[1]

Tension Test System for Irradiated Small Specimens Operated by Remote Control

REFERENCE: Okada, A., **"Tension Test System for Irradiated Small Specimens Operated by Remote Control,"** *Small Specimen Test Techniques Applied to Nuclear Reactor Vessel Thermal Annealing and Plant Life Extension, ASTM STP 1204,* W. R. Corwin, F. M. Haggag, and W. L. Server, Eds., American Society for Testing and Materials, Philadelphia, 1993, pp. 324–335.

ABSTRACT: A robot-based tension test system has been developed to aid in the mechanical testing of highly radioactive specimens. This system reduces radiation hazards from specimens and allows for the uniform precision of testing results independent of experimenters' skills. The robot system is designed to accommodate a miniaturized tension specimen with a gage section 5.5 by 1.2 mm, with a total length and width of 12.5 and 2.3 mm, respectively, and thickness of about 0.2 mm. The system is composed of a manipulating robot, a vibrational-type specimen feeder, a rotating-type specimen tray, a specimen observation system, a simulated tension test fixture, and a microcomputer for controlling the system. This system accomplishes specimen arrangement in the specimen tray, specimen transportation and loading to the test fixture and testing, and removal of the broken specimen from the fixture. These procedures are performed quickly, safely, and with uniform testing precision by computer control remotely by an unskilled experimenter.

KEYWORDS: tension test, miniature specimen, neutron irradiation, robot manipulating system, remote control

The development of mechanical test techniques using small specimens is a primary task for fusion reactor materials research and also for fission reactor materials research. For the safe performance of experiments and for obtaining systematic irradiation experimental data, it is necessary to reduce the specimen size in order to lower the hazards of radiation from radioactive specimens and for the effective utilization of the limited volume of irradiation facilities. The development of various kinds of small specimen techniques for mechanical testing has been pursued over a decade since the fabrication of the FMIT facility (Fusion Materials Irradiation Test Facility in the United States) was planned [*1,2*]. Papers on small specimen techniques for irradiated materials were compiled in a book edited by Corwin and Lucas [*3*]. A variety of small specimen mechanical testing techniques were also reviewed by Kohyama and Igata [*4*] and Lucas [*5*]. The correlation among several kinds of small specimen techniques were discussed by Okada [*6*]. The successful establishment of these small specimen techniques for irradiation experiments strongly depends on the development of facilities.

Specimen miniaturization for post-irradiation experiments has advantages for the experimenter. However, contrary to belief, this often brings more hazards. Because the specimens are so small, an experimenter tends to come too close to them and to need more time to

[1] Associate professor, Department of Precision Engineering, Faculty of Engineering, Hokkaido University, Sapporo 060, Japan.

sort and place them in testing fixtures than in the case of conventional-sized specimens. At the present time, the handling of small specimens is usually done with bare hands, even though the radioactivity of the specimens is very high. This makes the quality of precision of the testing results low because an experimenter may feel anxious about the radiation level during specimen handling—the precision of the testing results may strongly depend on the experimenter's skill and patience. With the development of research in Japan, the number of specimens to be examined has increased daily, and the radioactivity of the specimens also has increased. Although the specimen sizes are small (a typical small specimen has a volume 1000 times smaller than conventional-sized specimens), the radioactivity of heavily irradiated specimens has become too high to handle with bare hands. Specimen sizes also are too small to handle easily with a conventional manipulator in a hot cell, even though it is controlled by a skilled operator.

At present, facilities designed for miniaturized specimens are very limited. The development of specific facilities to assist the post-irradiation experiments is urgently required for the development of research work on irradiated materials. The development of facilities for assisting laboratory research seems delayed compared with that of manufacturing facilities. Quite recently, a manipulating robot system and an automated testing machine for small-sized radioactive specimens have been developed independently by Okada [7] and Kohyama [8], respectively. In the present work, a remote-controlled tension testing system for radioactive specimens has been developed for miniaturized specimens to demonstrate the feasibility of the application of a robot system to post-irradiation experiments on small tension specimens.

System Design

Requirements for the Tension Test System

In Japan and elsewhere, miniaturized tension specimens are widely employed for irradiation experiments. In Japan, the gage section is 5.5 by 1.2 mm, total length is 12.5 mm, and thickness is about 0.2 mm. The system described in this paper was designed to accommodate miniaturized specimens of these dimensions.

The following procedures are required for the system. A number of disordered specimens with high radioactivity should be arranged in a specimen tray prior to the experiment. Specimens should be identified with a suitable observation system. Then an arbitrary specimen is picked up from the tray and loaded to a testing fixture. During this process, the specimen should be treated carefully to avoid damage. After testing, two pieces of the broken specimen should be unloaded from the fixture and transported to a specimen container.

The Construction of the System

In order to respond to these requirements, a system was designed composed of a manipulating robot, a specimen feeder, an observation system for specimen identification, a specimen tray, a tension test fixture, and a microcomputer. A diagram of the system is shown in Fig. 1. It is basically composed of a specimen-manipulating system (right half of the diagram) and a specimen identification system (left half). An experimenter can select one of the job commands listed on a computer CRT to execute various steps of the system. The direction of specimen flow is shown by arrows in the figure. The specimen information, including specimen identification (ID) code and remarks on observation results, are entered from the keyboard and stored in the computer—they can be recalled on the CRT at any time.

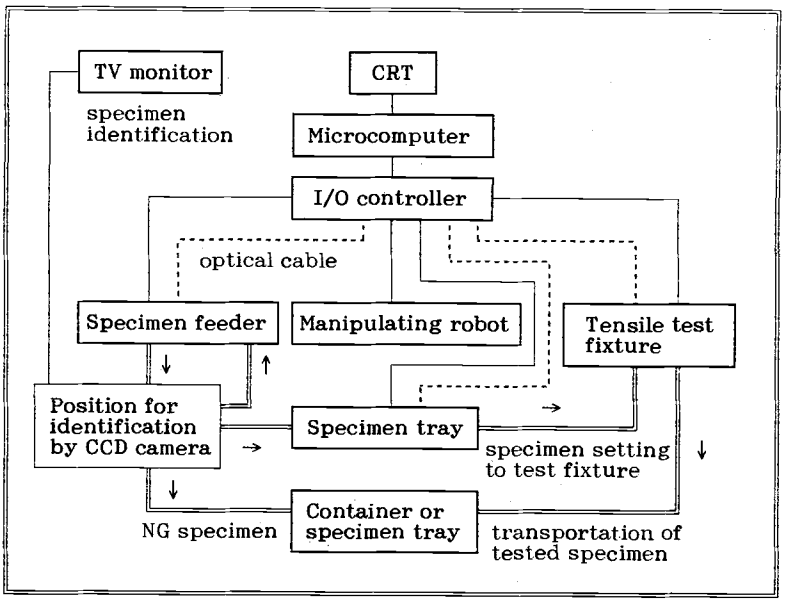

FIG. 1—*Block diagram of the system. Each assembly is connected with optical cables as shown by dotted lines, and light signals are sent to the computer via an input/output controller. Arrows indicate the direction of specimen flow.*

Setup of the System

The setup of this system is shown in Fig. 2. The top surface of the base frame is 1200 by 650 mm and 600 mm high. Each of the assemblies is shown in Figs. 3 through Fig. 6, respectively. A five-joint robot was employed for the transportation of a specimen from an assembly to the next assembly.

Specimen Feeder

The specimen feeder is shown in Fig. 3. This is composed of a commercially made vibrational-type bowl feeder and a linear feeder; both are actuated by electromagnets at a frequency of 100 Hz. A specimen is fed along a spiral track of the bowl feeder and transported to the positioning plate attached to the exit of the linear feeder. The specimen feed speed can be changed by varying the amplitude of the vibration. A pressure plate is located at the terminal end of the linear feeder to hold a specimen in the correct position.

Specimen Tray

The specimen tray is mounted on a turntable driven by a stepping motor as shown in Fig. 4. There are 30 numbered slits cut along the radial direction, one for each specimen. One of the slits' ends is open, so that the outer end of the specimen in the slit is pushed until it comes to the correct position in its axial direction. The width of the slit is 1 mm, including an allowance for the error of robot arm positioning, and the depth is 2 mm.

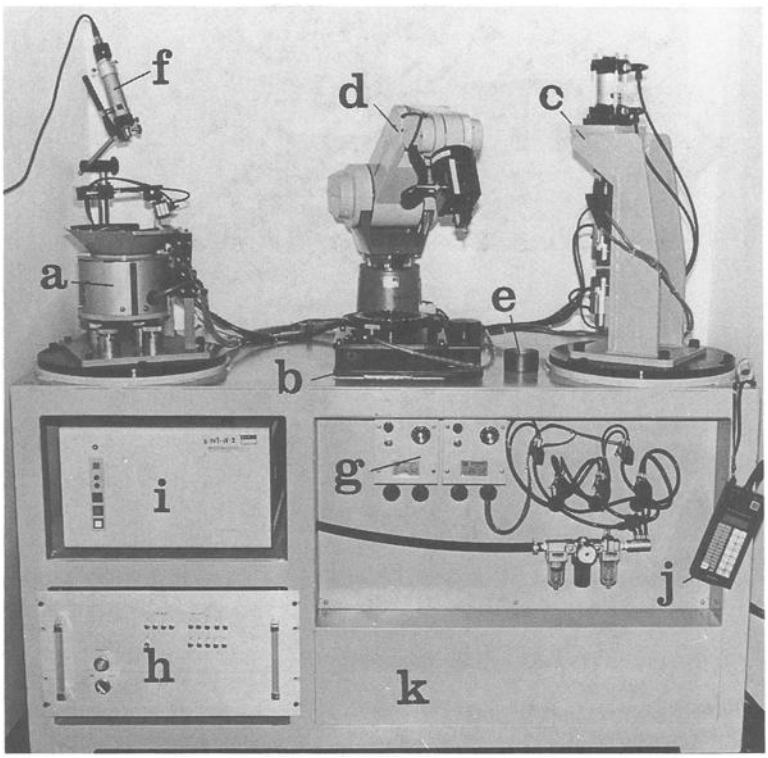

FIG. 2—*Setup of the tension test system:* (a) *specimen feeder,* (b) *specimen tray on turntable,* (c) *simulated tension test fixture,* (d) *manipulating robot,* (e) *specimen container,* (f) *specimen identification system,* (g) *feeder controller,* (h) *input/output controller,* (i) *servo unit,* (j) *manual operation panel, and* (k) *base frame. A small air compressor is in the base frame but cannot be seen in the figure.*

Specimen Observation System

The specimen should be inspected to determine whether it is good for testing and whether its position in the robot fingers is correct. The specimen ID code marked on the gripping ends of the specimen is read on a color TV monitor via a charge coupled device (CCD)-type TV camera. This is located at a position between the specimen feeder and specimen tray, as seen in Fig. 5. The specimen image can be observed on a 14-in. TV monitor at a magnification of 50. The exact specimen position can be checked on the TV monitor.

Tension Testing Fixture

In order to simulate tension testing, a fixture shown in Fig. 6 was fabricated. At present, this fixture has no measuring systems for displacement and load because it is only designed to extend a specimen. This fixture will be replaced by a real test machine for actual testing in the future.

Microcomputer and Controlling System

This test system is controlled by entering parameters with a keyboard responding to messages appearing on a computer CRT. All of the above active assemblies except for the

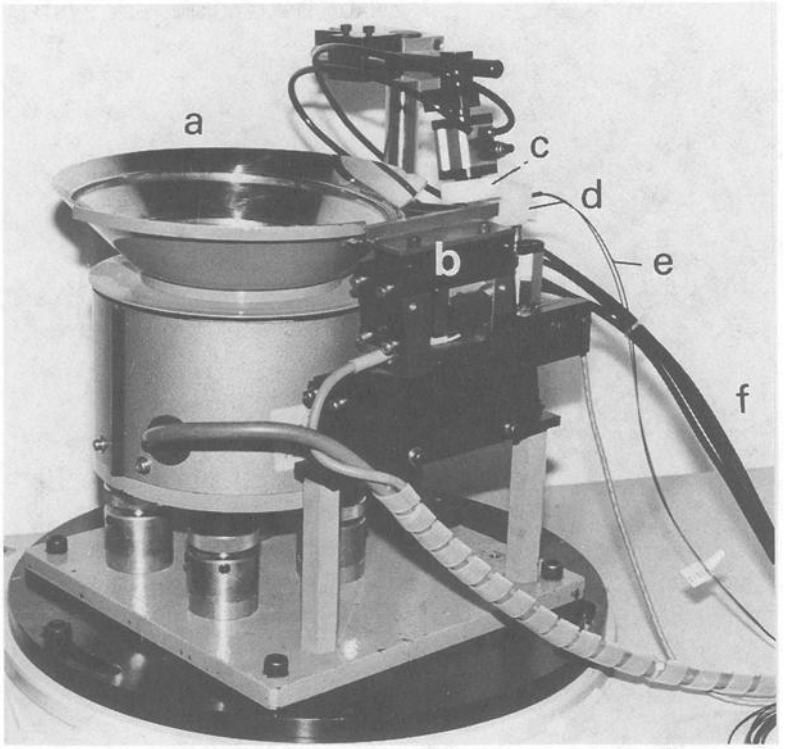

FIG. 3—*Vibration-type specimen feeder:* (a) *bowl feeder,* (b) *linear feeder,* (c) *pressure plate,* (d) *specimen positioning plate with optical sensor,* (e) *optical cables, and* (f) *air tubes. The pressure plate and specimen positioning plate move upward and downward.*

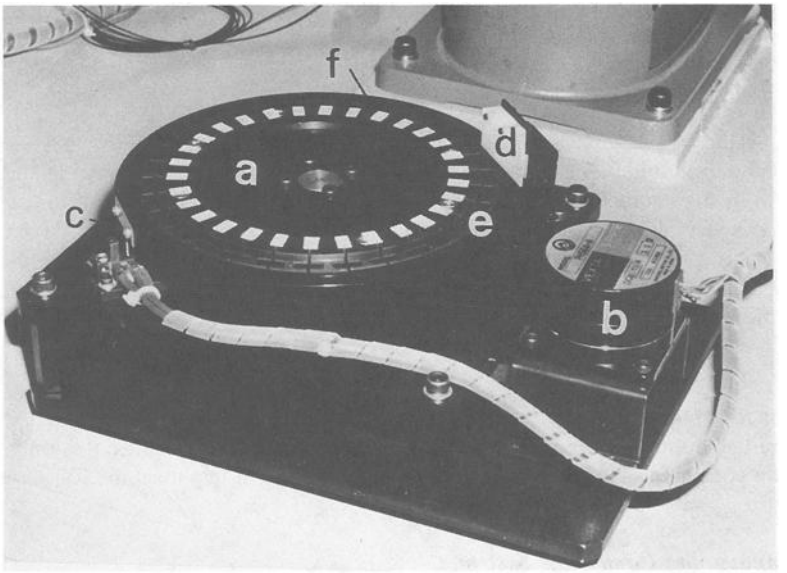

FIG. 4—*Rotary-type specimen tray:* (a) *specimen tray with 30 slits that rotates counterclockwise,* (b) *stepping motor,* (c) *positioning sensor for setting the starting point,* (d) *specimen-adjusting plate,* (e) *loading position, and* (f) *specimen pick-up position.*

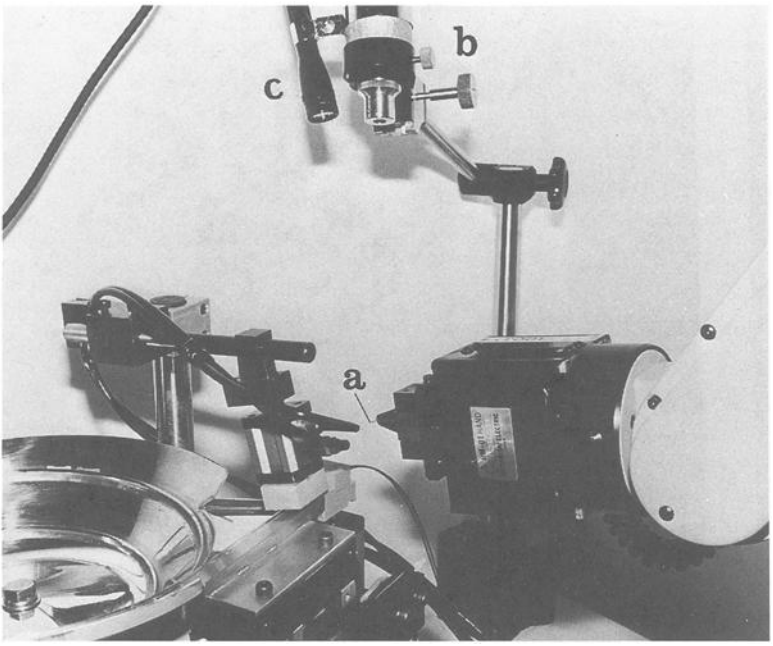

FIG. 5—*Specimen observation system. The specimen is observed with a specimen identification system in Position* a. *Specimens to be tested are loaded in the tray by entering the specimen tray location together with the specimen ID:* (a) *specimen,* (b) *optical microscope and CCD camera, and* (c) *illumination light.*

manipulating robot are connected with optical cables to detect and send light signals to the computer via an input/output controller for controlling the sequence of motion of every part of the system. If necessary, the robot can be operated in manual mode with a control panel.

Power Source for Actuating Active Assemblies

A small air compressor is employed to actuate the pressure plate, specimen positioning plate, robot fingers, grips, and upper crosshead of the tensile fixture. The compressor generates a pressure of 0.7 MPa.

System

Specimen Transportation and Arrangement in the Specimen Tray

Before starting the operation of the system, specimens are deposited in the specimen feeder bowl by either a manipulator or another robot hand. The specimen-feeding sequence in the specimen feeder is shown in Fig. 7*A*, *B*, *C*, and *D*. By the vibration motion of the feeder, specimens are fed along a spiral track of the bowl feeder (*A*) and transported one by one along a linear track of the linear feeder to the specimen-positioning plate attached to the terminal end of the linear feeder (*B*) and (*C*). As soon as one of the gripping ends of a specimen comes to the position, a pressure plate moves down to hold the specimen in this position (*D*). Then the specimen-positioning plate is retracted downward to yield a

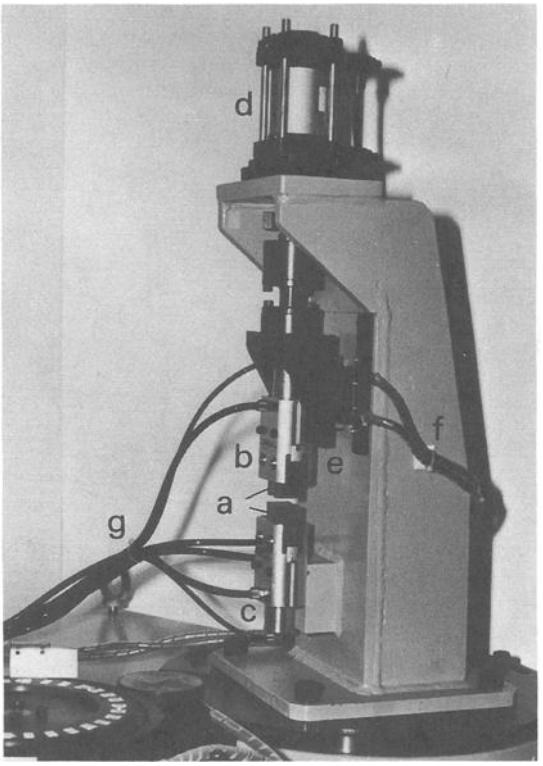

FIG. 6—*Tension test fixture:* (a) *a pair of grips,* (b) *upper crosshead,* (c) *lower crosshead,* (d) *pneumatic cylinder for driving upper crosshead,* (e) *positioning sensor for upper crosshead,* (f) *optical cables, and* (g) *air tubes.*

space for the entry of the robot fingers. In order to hold a specimen softly, the pressure plate surface is covered with a soft rubber sheet. After the center of the specimen is gripped by the robot fingers, the pressure plate moves up to release the specimen, and it is transported to a specimen observation position shown in Fig. 5. An experimenter can then identify the specimen and observe the specimen condition on a TV monitor via a CCD camera. The distance between the CCD sensor and the specimen is about 0.3 m; an objective lens is at the midpoint.

In the next step, an experimenter is supposed to select one of three directions of specimen flow. Namely, if a specimen is not held correctly by the robot fingers, it should be sent back to the specimen feeder bowl; otherwise the specimen cannot be inserted in the slit. If a specimen is not good for testing, it is transported to a container. Specimens to be tested are loaded in the tray by entering specimen information such as specimen ID code, material, comments, and so on and, finally, location of the specimen tray. Then the specimen is transported to the loading position.

Corresponding to the entered slit number, the turntable rotates until the slit of this number appears at the loading position and the specimen is inserted in the slit on its side edge as shown in Fig. 8. For reading the specimen ID code easily and correctly with a TV system, the ID code should be marked by laser engraving. Scratching with a needle point is not

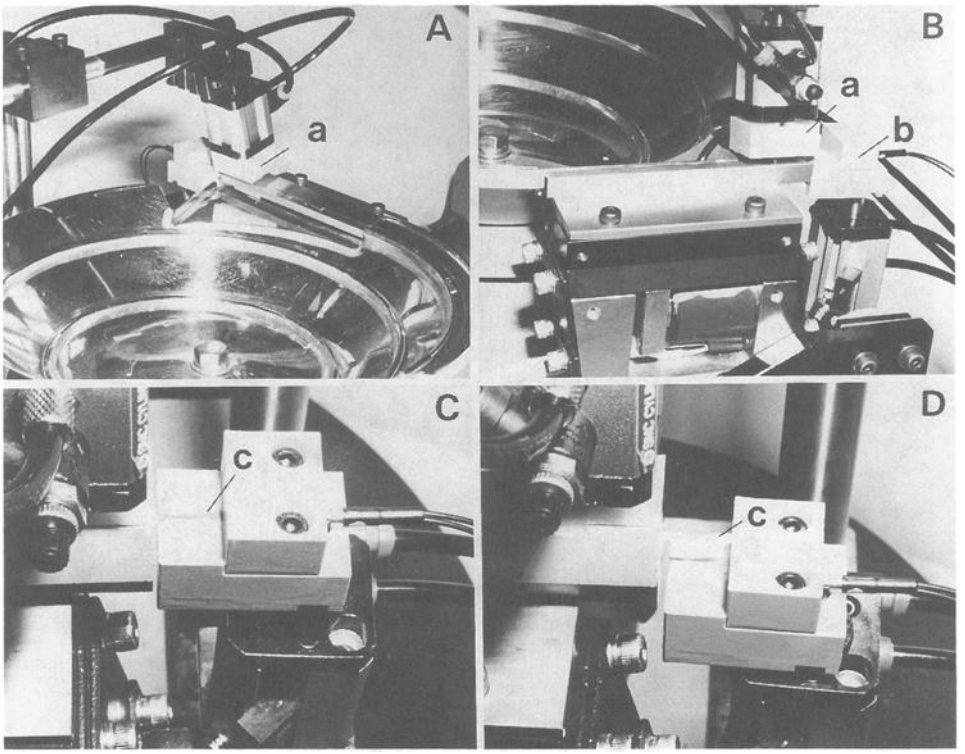

FIG. 7—*Specimen feeding sequence.* (A, B): *The specimen is fed to the specimen positioning plate. A light signal is sent to the computer from the specimen feed sensor.* (C): *The pressure plate moves down to hold the specimen.* (D): *The positioning plate moves down to yield the entry of robot fingers. Apparatus:* (a) *pressure plate,* (b) *specimen positioning plate, and* (c) *specimen.*

recommended, even though this can be read with a telescope for freshly produced specimens. These markings cannot be easily read after irradiation at elevated temperatures, however.

Specimen Loading to the Tension Test Fixture

An experimenter enters the slit number of the specimen tray, and the turntable rotates until the specimen to be tested reaches the pick-up position (Fig. 9). Just before the specimen arrives at this position, the outer end of the specimen in the slit is pushed automatically until it comes to the correct position in the slit by the action of the counterclockwise rotation of the turntable past a stationary position adjusting plate (Fig. 9) to eliminate the displacement from the exact position in the specimen axis direction. Precision of positioning in the specimen axis direction can be kept to an error of ±0.1 mm. This is smaller than the resolution of robot arm positioning.

The specimen is then picked up from the specimen tray by the robot fingers and transported to a loading position of the fixture, as seen in Fig. 10*A*. The testing fixture has two pairs of grips: the upper grip is mounted on a movable upper crosshead, and the lower grip is fixed to a stationary lower crosshead. The upper grip is open and waits at a loading position.

FIG. 8—*Specimen arrangement in specimen tray. The turntable rotates until a slit of an entered number comes into position and a specimen is inserted into the slit.*

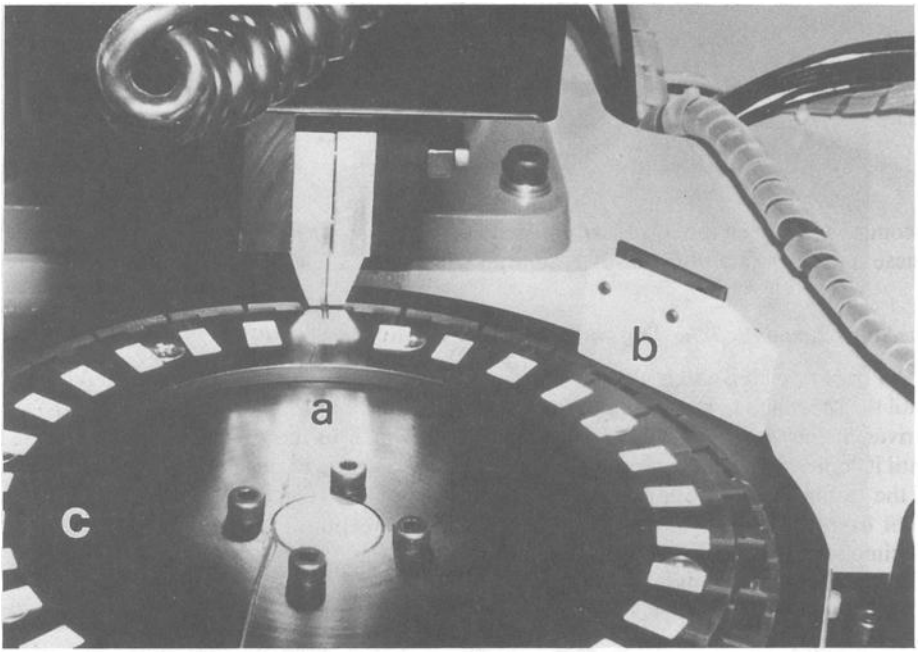

FIG. 9—*Specimen pickup from the specimen tray for testing. Before a specimen comes into position* (a), *its position in the slit is adjusted by an adjusting plate* (b) *by rotation of the turntable* (c).

After the upper grip holds the top end of the specimen, the robot finger releases it, and then the lower grip holds the bottom end so that a specimen is not gripped by more than two points at the same time, as shown in Fig. 10*B*. This procedure reduces the possibility of deformation of the specimen due to misalignment between the axis of the test fixture and the specimen axis in the robot fingers.

Tension Testing Simulation

The upper crosshead moves to test the specimen. After the specimen is broken, the crosshead moves to an unloading position. The unloading sequence is shown in Fig. 10*C*. The two pieces of broken specimen are then removed from the grips and transported to a specimen container.

Programming for the System Control

The program for controlling the system, composed of about 1000 steps, is written in BASIC for the convenience of changing the parameters of robot hand movement. The robot motion is dictated by specifying the coordinates in three-dimensional space of points to which the hand is to move. These can be entered and saved as a data file for any specific task or set of tasks. Robot motion from a specified point to another specified point can also be written as a set of commands used in conjunction with the path data. The computer sends commands to the following assembly after receiving signals from the leading assembly via optical cables.

Performance of the System Operation

All functions of the system were confirmed to run well, and it was easy to operate the system by following the messages appearing on the CRT. The gripping force of the specimen grips and the pulling force of the crosshead generated by an air pressure of 0.7 MPa are

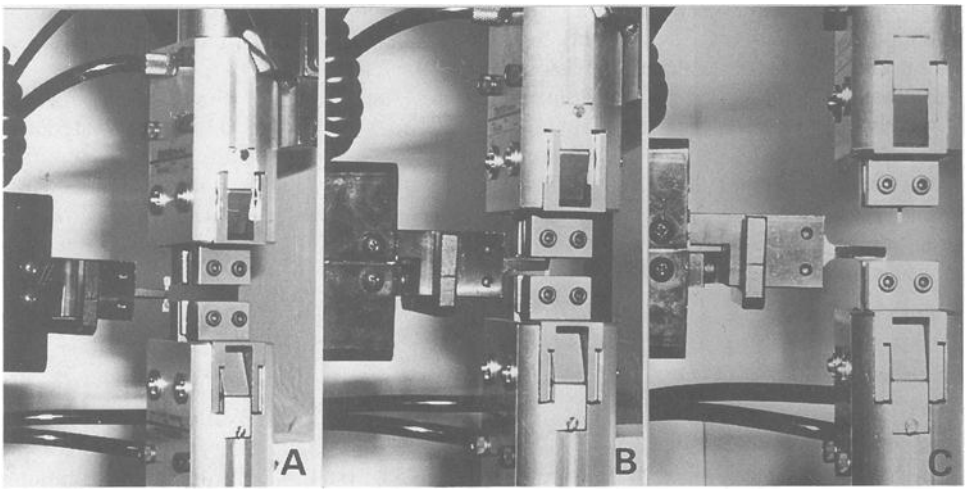

FIG. 10—*Specimen loading to the test fixture and unloading:* (A, B) *specimen loading into the grips of the test fixture, and* (C) *unloading of the two pieces of the broken specimen.*

enough for testing miniaturized specimens of alloy steel even with a tensile strength larger than 1500 MPa. Although the robot is operated at a medium speed at present, it takes about 30 s for specimen arrangement, excluding the time for entering specimen information from the keyboard, and another 90 s for transportation of a specimen from the tray to the test fixture and to the container, excluding a testing time which depends on the test conditions. The total time for the specimen handling for testing is thus 120 s per specimen; this is one half to one quarter the time required for manual operation. Although the reduction of time is not great, the most important factor is the almost complete elimination of personal hazards during this process.

The most important issue for obtaining reliable tension test results is the alignment of the specimen axis in the robot fingers with the axis of the tension test fixture because a specimen will be bent by any misalignment during loading, which affects the accuracy of the testing precision. The resolution of the positioning of the present robot is about ±0.3 mm for the full expansion of the robot arm. In the present system, the arm is operated within a half expansion so the misalignment can be kept within ±0.3 mm. The misalignment by the resolution of the robot arm itself is inevitable. For the misalignment coming from the limit of robot arm resolution, the robot finger position of the present system can be adjusted. When the robot fingers were positioned carefully by the manual control panel before testing, deformation by misalignment was not observed for alloy steel specimens. So far, positional adjustment of the assemblies was not necessary for our alloy specimens. In this case, the rigidity of the specimen is high enough to accommodate a small amount of misalignment due to the resolution of the positioning of the robot because of the deformation of rubber pads of robot fingertips and a small deflection of a robot arm due to its compliance for a small deflection. In the case of soft materials with low yield strength, however, misalignment can be serious. The rubber pads of the robot fingers should be replaced by softer material and the robot finger structure changed to avoid misalignment from the limit of the resolution.

Conclusion and Future Plans

The present robot system is a prototype testing system to confirm the feasibility of using robot operation for a tension testing system. It was demonstrated that miniaturized tension testing can be done safely and quickly by a robot system even when controlled remotely by an unskilled operator. Uniform precision can also be expected.

A change in the experimental setup will allow testing at low or elevated temperatures with this robot system. By using a shielding panel for the radiation, this testing system can be operated outside a hot cell. This is convenient for recovery procedures if the system fails and for its maintenance. Required improvements of the system are the addition of a recovery system for failures and the protection of the electronic devices and optical systems from the radiation of specimens. Eventually this system will be coupled to a real miniature tension test machine for the testing of radioactive specimens.

Acknowledgments

The author would like to express thanks to Messrs. M. Nanbu of Nanbu Mechatoro Design for the system design, E. Matsumoto of Matsumoto Machinery Co. Ltd. for the fabrication of assemblies, and T. Komachi of Sanken System Co. Ltd. for the computer programming. This work is financially supported by the Grant-in-Aid for Scientific Research, The Ministry of Education, Science and Culture, Japan.

References

[1] Nygren, R. E. and Opperman, E. K., Eds., FMIT Test Assemblies Progress Report, HEDL-TME 78-65 UC-20c, Hanford Engineering Development Laboratory, Richland, WA, August 1978.
[2] Burke, R. J. and Holmes, J. J., *Journal of Nuclear Materials,* Vols. 133 and 134, 1985, pp. 869–872.
[3] Corwin, W. R. and Lucas, G. E., Eds., *The Use of Small-Scale Specimens for Testing Irradiated Materials, ASTM STP 888,* American Society for Testing and Materials, Philadelphia, 1986.
[4] Kohyama, A. and Igata, N., *Journal of Atomic Energy Society of Japan,* Vol. 25, 1983, pp. 329–336.
[5] Lucas, G. E., *Metal Transactions,* Vol. A, No. 21A, 1990, pp. 1105–1119.
[6] Okada, A., Yoshiie, T., Kojima, S., and Kiritani, M., *Journal of Nuclear Materials,* Vols. 133 and 134, 1985, pp. 321–325.
[7] Okada, A., Igarashi, S., and Kakazu, Y., *Fusion Engineering and Design,* Vol. 18, 1991, pp. 525–529.
[8] Kohyama, A., Sato, S., and Hamada, K., *Journal of Nuclear Materials,* Vols. 191–194, 1992, pp. 1033–1037.

DISCUSSION

G. Lucas[1] *(written discussion)*—What kind of positional resolution does the robot arm have? Is this adequate to ensure alignment of your specimens in the groups?

A. Okada (author's closure)—The total positional resolution of the center of the robot fingers is within ±0.3 mm. The deviation of 0.3 mm in the direction of the specimen axis creates no problem for testing. Even for Fe-based dilute alloys (rigidity is not so high), the offset of the specimen axis of 0.3 mm from the tension axis can be accommodated by the deformation of soft rubber pads covering the robot finger surfaces in order to hold specimens softly. The resolution of the alignment of the system can be considered enough for our specimens. However, when the specimen is very soft such as pure Cu, small deformation due to the offset may be inevitable.

[1] University of California at Santa Barbara.

Frank A. Garner,[1] *Margaret L. Hamilton,*[1]
Howard L. Heinisch,[1] *and Arvind S. Kumar*[2]

Application of Miniature Tension Specimens to Studies of Radiation Damage in Metals

REFERENCE: Garner, F. A., Hamilton, M. L., Heinisch, H. L., and Kumar, A. S., **"Application of Miniature Tension Specimens to Studies of Radiation Damage in Metals,"** *Small Specimen Test Techniques Applied to Nuclear Reactor Vessel Thermal Annealing and Plant Life Extension, ASTM STP 1204,* W. R. Corwin, F. M. Haggag, and W. L. Server, Eds., American Society for Testing and Materials, Philadelphia, 1993, pp. 336–355.

ABSTRACT: Miniature sheet-type tension specimens are currently being used in a variety of radiation damage studies conducted in a number of different reactors. Although these specimens are very small (12.7 mm long, 0.25 mm thick, 1.0 mm gage width), they have proven successful in addressing issues encountered in both thermal reactors and anticipated fusion reactors. This paper reviews the results of a number of recent studies that illustrate the range of applicability of these small specimens. When combined with other types of specimens and other types of measurements made prior to tension testing, miniature tension specimens have been found to serve as very useful tools for application to both fundamental studies and alloy screening studies.

KEYWORDS: tension specimens, miniaturization, radiation effects, neutrons, property-property correlations, neutron spectra, displacement rate, size effects

Irradiation experiments directed toward the neutron-induced embrittlement of pressure vessel steels often involve the use of both tension and Charpy impact specimens, but miniature versions of both types of specimens are usually required to compensate for the small test volumes available in various test reactors. It is difficult, however, to decrease the size of Charpy specimens below one half or one third of the standard size specified by ASTM Test Methods for Notched Bar Impact Testing of Metallic Materials (E 23-86) and obtain meaningful data. Even with subsize Charpy specimens, it is often difficult to irradiate enough specimens to cover the full range of environmental interest, especially for a pressure vessel annealing program involving an extensive time-temperature matrix. It is proposed in this paper that the simultaneous irradiation of both miniature tension and miniature Charpy specimens allows an expansion of the specimen matrix, provided that suitable property-property correlations are developed and that the smallest practical miniature tension specimens are used.

One of the smallest sheet-type tension specimens is being used in a variety of radiation damage studies conducted by the authors in a number of different reactors. Figure 1 illustrates the small scale of both the specimens and the tension frame. Although these specimens are very small (12.7 mm long, 0.25 mm thick, 1.0 mm gage width), they have proven successful in addressing issues relevant to both operating fission reactors and anticipated fusion reactors.

[1] Staff scientist, senior scientist, and senior scientist, respectively, at Pacific Northwest Laboratory, P.O. Box 999, MS P8-15 Richland, WA 99352.

[2] Professor, University of Missouri, Materials Research Center, Rolla, MO 65401.

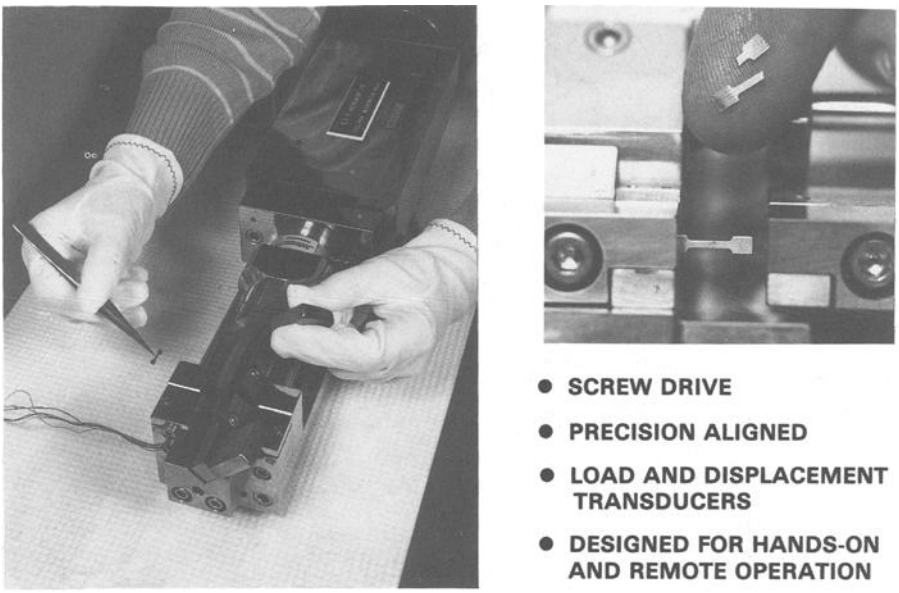

FIG. 1—*Horizontal test frame and miniature sheet-type tension specimens employed in a large variety of radiation damage studies* [1]. *Since the specimens are held in wedge grips, all strain is confined to the gage section of the miniature specimens.*

This paper reviews the results of a number of recent studies that illustrate the range of applicability of these small specimens. When combined with other types of measurements made prior to tension testing, these miniature tension specimens have been found to serve as very useful tools for application to both fundamental studies and alloy screening studies. The production of the specimens, their testing, and the analysis of the tension data are described in Refs *1* and *2*.

Type of Radiation Studies Using Minitensiles

Several categories of studies are in progress. One category involves the use of miniature tension specimens to develop and test models describing the microstructural origins of radiation damage in different materials and diverse irradiation environments. The second category addresses the factors that must be considered before data derived from such specimens can be confidently applied to the solution of any given problem. Size effects are important here, but it should be noted that most irradiation studies proceed at accelerated displacement rates and often in different neutron spectra than are found in the environment where the radiation damage problem arose. Thus, fundamentally oriented studies are required on the effects of size, displacement, rate, neutron spectra, and temperature/flux history.

The third category involves the application of miniature tension specimens to specific material's problems. This includes broad exploratory studies, more specific alloy screening and optimization studies, development of property-property correlations, and data base development for selected candidate materials.

Microstructurally Oriented Studies

Side-by-side irradiation of miniature tension specimens and 3-mm microscopy disks allows the examination of the microstructural origins of the radiation-induced changes in tension

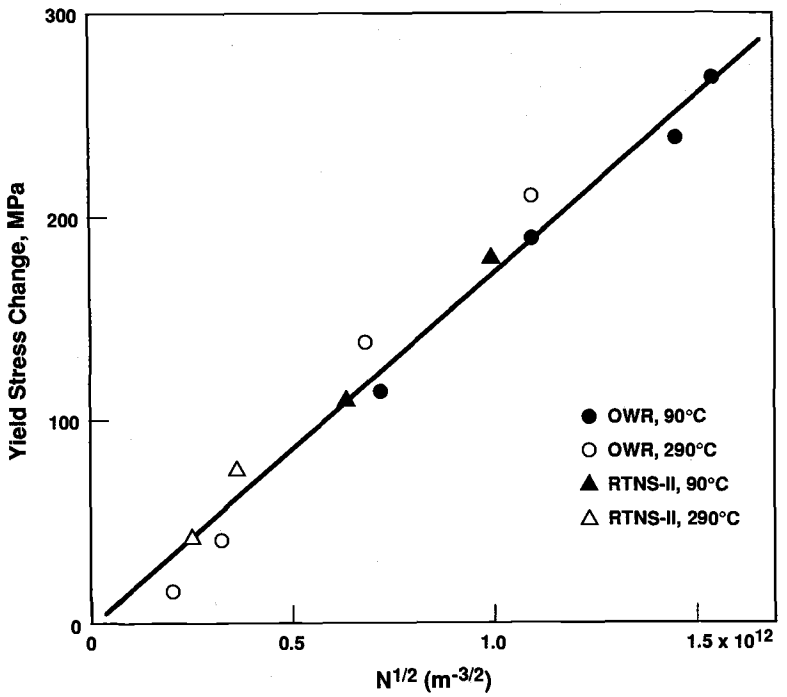

FIG. 2—*Plot of yield strength change versus the square root of defect density for solution-annealed 316 stainless steel irradiated in two diverse irradiation facilities at two temperatures* [4,5].

properties while avoiding problems associated with gradients in neutron flux or temperature. Microscopy specimens can also be made from the end tabs of untested specimens. This side-by-side approach is important because the microstructural components that lead to hardening or softening vary not only with the materials being studied but also with the irradiation environment, particularly temperature and atomic displacement rate.

For annealed metals irradiated at relatively low temperatures to very low displacement levels ($\ll$1 dpa),[3] the radiation damage usually consists of small clusters of interstitial atoms coexisting with small vacancy clusters. These clusters can reorganize themselves into dislocation loops or stacking fault tetrahedra, but all serve as obstacles to dislocation motion. The resultant changes in yield strength are postulated to vary as the square root of the cluster density [*3*]. Using both miniature tension specimens and microscopy disks cut from their end tabs, Yoshida, Heinisch, et al. [*4,5*] showed that this relationship was consistent for microscopy-visible clusters at two temperatures (363 and 563 K) for annealed 316 stainless steel when irradiated in two different neutron spectra (OWR and RTNS-II),[4] as shown in Fig. 2. Muroga, Heinisch, et al. [*6*] also confirmed the applicability of this model to annealed pure copper irradiated at 316 to 363 K in three quite different spectra, that of OWR, RTNS-II, and LASREF[5].

[3] dpa = displacements per atom, a standardized damage exposure parameter.
[4] Omega West Reactor and Rotating Target Neutron Source-II.
[5] Los Alamos Spallation Radiation Effects Facility.

At higher irradiation temperatures and high dose levels, the microstructural evolution can be much more complex, involving the relaxation or alteration of pre-existing microstructural components and the simultaneous formation of precipitates, bubbles, voids, dislocation loops, and network dislocations. The matrix composition can also change significantly as a function of precipitation and/or transmutation in some alloys. In one series of studies conducted in FFTF[6] on three FeCrNi alloys at 638 to 873 K, for example, it was shown that the influence of alloy composition, metallurgical starting condition, helium generation rate, and irradiation conditions on the radiation-induced evolution of room temperature tension properties could be described by conventional hardening theory involving the interaction of the radiation-dependent dislocation network with the various long range and short range obstacles [*7–9*]. In another series of studies on copper alloys irradiated at ~673 K in FFTF to very large exposures (16 to 150 dpa), it was shown that the quite different tension response at room temperature of various irradiated copper alloys could be explained in terms of microstructural processes that were strongly influenced by atomic displacements, leading to enhanced diffusion, void growth, precipitate aging and/or dissolution. These processes were also sometimes influenced by the large level of solid transmutants formed [*10–13*].

It has also been shown that miniature tension tests can be used as a microstructural probe to identify the existence of hardening contributions that are not easily imaged using electron microscopy. Examples of such contributions are short-range order, spinodal decomposition on a fine scale, and sub-resolvable defect clusters. For example, Brager, Garner, and Hamilton [*14*] found using miniature specimens that a significant and unresolved component of hardening developed in Fe-Cr-Ni alloys in the Invar compositional regime. They proposed that the hardening was a consequence of radiation-induced spinodal-like oscillations on a scale smaller than could be resolved using energy dispersive X-ray microchemical analysis. These oscillations are otherwise invisible using transmission electron microscopy. Subsequent studies later demonstrated that spinodal-like decomposition indeed occurred in these alloys [*15–17*]. It was later shown by Aïdí et al. [*18*] that similar hardening developed in Fe-16Cr-Ni alloys at higher nickel levels not only during electron irradiation, but also during thermal aging. The hardening was attributed to local ordering.

Grossbeck et al. [*19*] recently found that tension change data on an irradiated titanium-modified stainless steel could only be explained if an unresolved component of hardening developed at the higher end (603 to 673 K) of the 333 to 673 K temperature range explored. Several potential hardening components were identified by Grossbeck as requiring further study.

Sekimura, Garner, and Griffin [*20*] also showed that the increased hardening observed in the ORR[7] reactor compared to that in EBR-II[8] was indeed the direct result of an unprecedented refinement of cavity microstructure that resulted from an unanticipated interaction of the reactor's rather unique temperature history with the high helium generation rate produced in these materials by the ORR neutron spectrum.

In some cases, however, the concurrent use of other techniques can aid the microscopy analysis to identify and describe the unresolvable hardening components indicated by the tension results. Brager, Garner, and Panayotou [*21*] used coupled microhardness and microscopy measurements in a very low dose ($\leq$0.003 dpa at 298 K) study of neutron-irradiated copper alloys to conclude that ~70% of the defect clusters were smaller than resolvable by

[6] Fast Flux Test Facility in Richland, WA.
[7] Oak Ridge Research Reactor.
[8] Experimental Breeder Reactor.

microscopy (~1 nm), thereby explaining the disparity between microstructure-based predictions and miniature tension data. This large fraction of unresolvable clusters was thought at the time to present a significant problem in the tension-microstructural correlations under development by Heinisch et al. in an extensive study on the effects of neutron spectrum on damage development [*22–25*]. Since Heinisch's studies proceeded at higher temperatures (363 and 563 K) and to larger doses, where the cluster sizes were larger, the fraction of unresolved clusters was much smaller than those at 298 K. Thus, the resolution problems in his studies were found to be smaller than originally anticipated.

Zinkle and Kulcinski [*26*] later extended the study of Brager et al. at 298 K, adding resistivity measurements to those of microhardness and microscopy [*25*]. Since resistivity is much more sensitive than microhardness to smaller defect clusters, it became possible to provide a much better description of the cluster distribution and to relate this distribution to the hardness and tension property changes typically observed at low dpa levels and temperatures.

In the copper irradiation studies conducted at much higher temperatures (673 to 793 K) by Garner, Hamilton, Edwards et al. [*10–13, 27–31*], electrical resistivity (performed on the gage portion of the minitension prior to the tension test), density change measurements, and fractography were also used to complement the results of tension tests and thereby unravel the details of the microstructural and microchemical evolution in each alloy.

Size Effects Studies

The confident application of such small tension specimens requires that some estimate be made of the validity of the tension measurements and of the relationship between the measured bulk and small specimen values when the two diverge. Panayotou et al. [*1*] demonstrated that the miniature tension specimens used in the majority of the studies described in this paper yielded representative strength and ductility data at room temperature for three unirradiated alloys (20% cold-worked 316, austenized and tempered HT9, and the age-hardenable copper alloy CuBeNi) when compared to other commonly used larger specimen sizes and geometries. The assumption was made at that time that representative values would also be obtained from irradiated specimens.

Igata et al. [*32*] explored in some detail the dependence of room temperature tension properties of 304 and 316 stainless steel for *very* thin unirradiated specimens and found that the properties exhibited a dependence on both grain size and specimen thickness, but above a critical ratio of specimen thickness to grain size, the 0.2% yield strength was equal to the bulk value. Igata also found that a thickness of 200 μm was required before the total elongation was equal to the bulk value for these steels. Conclusions similar to those of Igata were reached by Rickerby et al. [*33*] for annealed type 316 stainless steel in the range 297 to 1123 K, providing the thickness was greater than ~2.5 times the grain size, with the total elongation falling with decreasing thickness for very thin foils.

Kohyama et al. [*34–36*] later showed that the yield stress at room temperature of ferritic alloys exposed to relatively low doses of 14 MeV neutrons at 300, 473, and 673 K was not dependent on specimen thickness as long as the thickness was larger than 0.1 mm. It was also shown, however, that the ultimate strength and uniform strain were somewhat dependent on specimen size, the difference varying with total displacement level. The smallest specimen employed in Kohyama's studies was thinner (0.15 mm versus 0.25 mm) but otherwise comparable to that employed by the authors of this paper.

The applicability of miniature tension specimens to materials irradiated to very high displacement levels and at much higher irradiation temperatures is currently being studied jointly in FFTF by Kohyama's group and the authors of this paper, using a wide range of

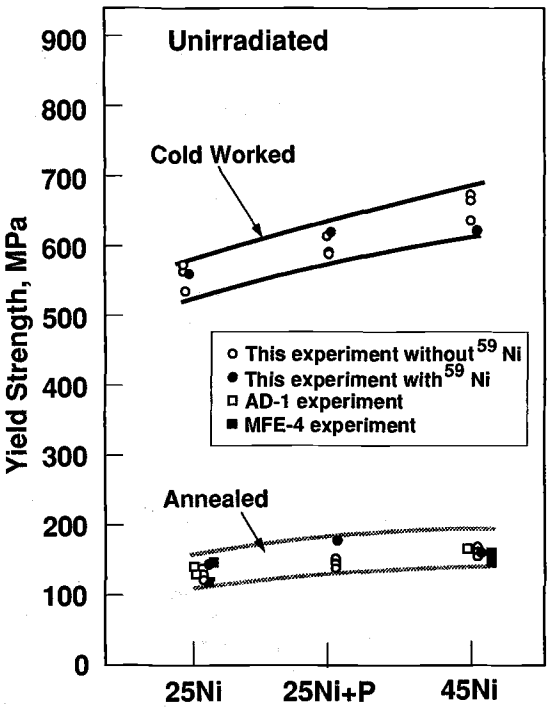

FIG. 3—*Comparison of the yield strengths observed in unirradiated Fe-15Cr-25Ni, Fe-15Cr-25Ni-0.04P, and Fe-15Cr-45Ni minitensions employed in the ^{59}Ni isotopic doping experiment in FFTF-MOTA with the larger specimens used in earlier experiments* [38,40].

specimen thicknesses and two specimen sizes. Two well-characterized alloys, one austenitic and one ferritic/martensitic in nature, are involved in this irradiation series. An automated tension machine will be used to explore the influence of size effects on tension properties during either room temperature or elevated temperature testing [*37*].

As shown in Fig. 3, Garner, Hamilton, et al. [*38,39*] demonstrated that unirradiated minitension specimens employed in their study of Fe-Cr-Ni austenitic alloys yielded room temperature tension properties that were comparable to those derived from much larger specimens used in several earlier studies [*40*]. Both annealed and cold-worked specimens were employed in these studies. The data on irradiated specimens will be covered in a later section.

It appears, therefore, that the tension specimens of the size shown in Fig. 1 can provide representative yield strengths and reasonably representative elongations for some materials but not others, depending not only on the material but also on the irradiation conditions. Some fraction of the divergence in the various studies quoted in this section may be due to the specimen preparation technique, as discussed in Ref *2*.

Environmentally Oriented Studies

One of the major uses to date of the miniature specimens shown in Fig. 1 has been the examination of the effects of neutron spectra and displacement rate on damage accumulation. Understanding of the role of these parameters is required for interpretation of surveillance

data for pressure vessel steels and for the use of fission reactors as surrogates to generate data for design of fusion reactors. Heinisch et al. [*22–25*] have conducted a number of studies directed toward understanding the influence of these important variables.

In the early days of fusion reactor materials development there was a concern that high-energy neutrons resulting from the D-T fusion reaction might produce displacement cascades in irradiated materials that were significantly different from those produced by fission neutrons. Heinisch et al. [*22–25*] irradiated miniature tension specimens of various metals and alloys to low doses in three widely disparate neutron spectra that encompass the range between pure fusion (14 MeV) and several typical spectra used for radiation experiments. Tension tests conducted on these irradiated specimens at room temperature showed that similar damage was produced by 14 MeV (fusion) and fission reactor neutrons when correlated using the dpa concept. Computer simulations by Heinisch [*41*] showed that such correlations work because of the formation of subcascades at high cascade energies. Based on the results of these and other studies [*42–44*], the following conclusions can be drawn concerning the effects of neutron spectra on radiation-induced changes in tension properties:

1. If a large fraction of the displacement damage arises from the high-energy cascade-producing neutrons, the irradiation-induced hardening of *alloys* correlates very well using dpa as a correlation parameter, as shown in Fig. 4. This conclusion does not always hold in pure metals, however, as demonstrated for pure copper in Fig. 5. This difference in behavior is not yet fully understood. Copper alloyed with 5 wt% of Mn, Ni, or Al, or 0.25 wt% of Al_2O_3 does not exhibit such a disparity [*24*].
2. If a significant fraction of the displacement damage is produced by epithermal and thermal neutrons, dpa may not be a good correlation parameter. A damage parameter based on the production of "available" or "freely migrating" defects may be more appropriate [*42–43*].

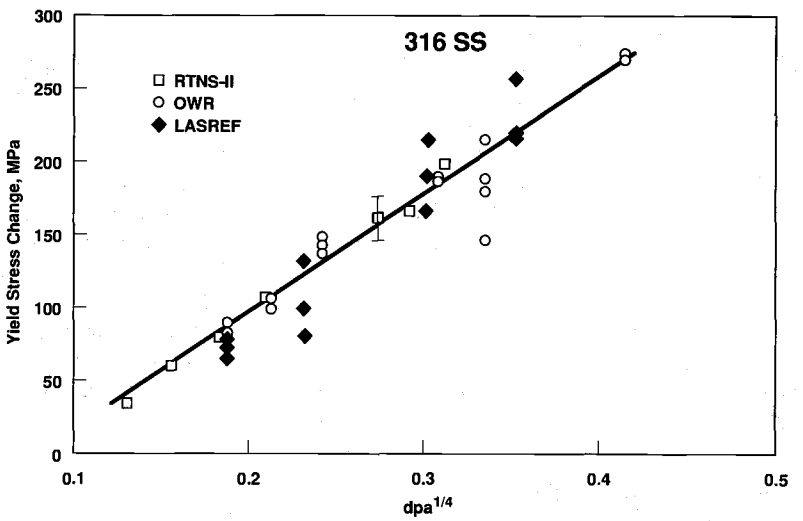

FIG. 4—*Yield strength changes for annealed Type 316 stainless steel irradiated in three disparate neutron spectra at significantly different displacement rates at 328 to 363 K, showing suitability of displacements per atom (dpa), as an effective correlation parameter* [25]. *Similar behavior was observed in most alloys.*

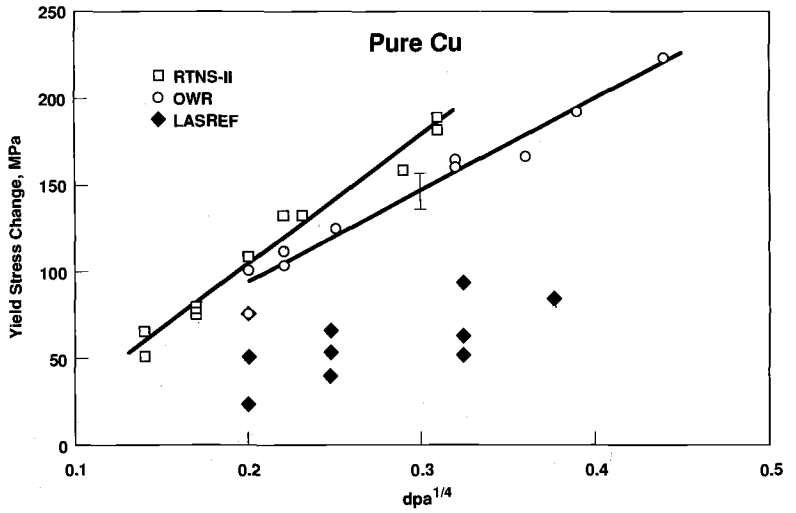

FIG. 5—*Yield strength behavior of pure copper in the same experiment as that of Fig. 4. In some pure metals, dpa was found not to be an effective correlation parameter* [25].

3. The influence of displacement rate on hardening and embrittlement does not appear to be significant for relatively low irradiation temperatures, comparable to those experienced by pressure vessels [*44*]. For high-dose and high-temperature irradiations typical of fusion or breeder reactors, this conclusion is not true, and rate effects can be very important, particularly in the transient regime of microstructural evolution [*45*].

The latter conclusion concerning low-temperature irradiation arises from the lack of influence of the wide range of displacement rates associated with the data of Figs. 4 and 5 and also from a similar comparative study by Hamilton and Heinisch [*44*] involving A302B and A212B pressure vessel steels shown in Fig. 6. The range of displacement rates involved in the pressure vessel study of Hamilton and Heinisch relative to those of the recent HFIR pressure vessel embrittlement problem [*46*] is shown in Fig. 7.

There are other aspects of the neutron spectrum that are of interest when "surrogate" spectra are employed in radiation damage studies, particularly at high neutron exposure levels [*45–48*]. These are the solid and gaseous transmutation products that can form at very high levels in some materials. The production rates of most transmutation products are very sensitive to neutron spectrum. While helium is the most important gaseous product, hydrogen production is large in some materials, although hydrogen has not received as much attention as helium. Solid transmutation products have not been found to be very important in typical structural steels, but they are important in other alloys such as those based on copper [*45*], aluminum [*49*], and vanadium base alloys [*50,51*].

The following sections present some results from two ongoing studies that employ miniature tension specimens to study the effects of transmutants. One of these addresses the influence of helium in austenitic steels and the other is directed toward the impact of solid transmutation products in copper alloys during irradiation.

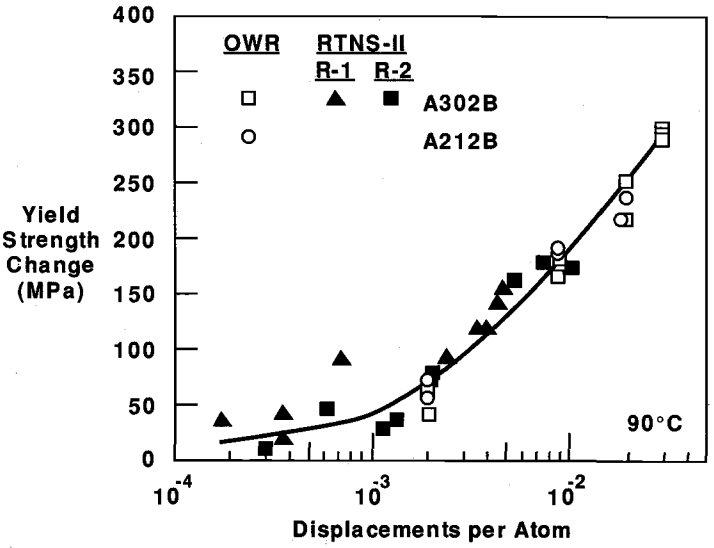

FIG. 6—*Yield strength changes in A212B and A302B following irradiation at 363 K in RTNS-II and OWR. R-1 and R-2 refer to separate RTNS-II irradiations, which proceeded at slightly different ranges of displacement rate* [44].

Isotopic Tailoring Experiments in FFTF

Until recently it has been impossible to conduct experiments in which spectrum-related parameters such as the helium/dpa ratio were varied without also accepting variations in other important parameters, such as displacement rate or temperature history. A technique currently being used, however, allows the study of the influence of helium alone on density change, microstructural evolution, and tension properties. This technique utilizes isotopic tailoring to vary the helium production rate without introducing changes in neutron spectrum or displacement rate [*52,53*]. It is possible to generate substantial variations in helium/dpa ratio without varying any other important parameter by using alloys whose only difference

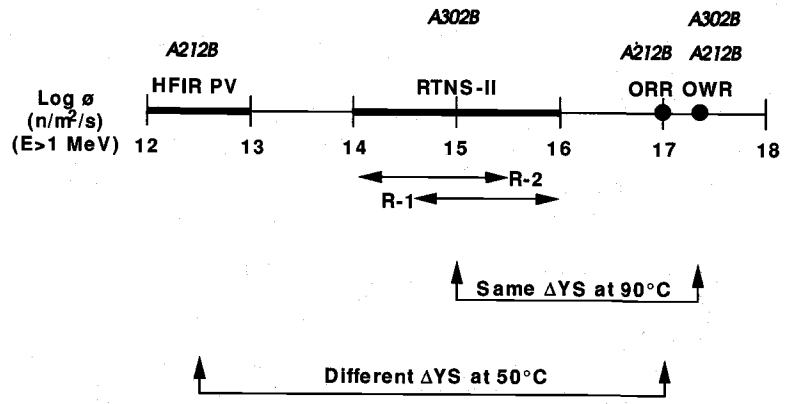

FIG. 7—*Schematic representation of the dependence on displacement rate of yield strength changes observed in the study of Hamilton and Heinisch compared to those observed in HFIR and ORR* [44].

is in either the $^{58}Ni/^{60}Ni$ ratio or the presence or absence of ^{59}Ni, an isotope that does not occur naturally. The isotopically different specimens are then irradiated side by side in the appropriate reactor spectra. A series of such experiments involving ^{59}Ni doping have been undergoing irradiation in the FFTF reactor using the Materials Open Test Assembly (MOTA), in which temperatures are controlled to ±5°C [*52*].

A particular advantage of comparative isotopic doping experiments is that one need not be concerned with the details of temperature history, which are now known to strongly influence the outcome of some fission-fusion correlation experiments [*54*]. Since both doped (^{59}Ni added) and undoped specimens are irradiated side by side, the primary variable is the helium/dpa ratio. In FFTF the production rate of helium in doped specimens is also nearly constant throughout the experiment provided that no changes occur in the neutron environment. Relatively small variations in helium production rate do occur, however, in both sets of alloys in response to burn-in or burn-out of ^{59}Ni [*55*].

The alloys employed in this study were Fe-15Cr-25Ni, Fe-15Cr-25Ni-0.04P and Fe-15Cr-45Ni (wt%) in both the cold-worked and annealed conditions. The acquisition of the ^{59}Ni, the production of the ^{59}Ni-doped tension specimens, and their irradiation conditions were described by Simons et al. [*52*]. Microscopy disks were also prepared and irradiated; the results of transmission electron microscopy (TEM) examinations are described in detail in Refs *7–9*. The miniature tension specimens were tested at room temperature at a strain rate of 4.7×10^{-4} s^{-1} in the horizontal test frame described in Ref *1*.

Although the experiment was conducted at four irradiation temperatures [*38,39*], only the results at two temperatures will be shown in this paper to demonstrate the utility of the isotopic doping technique. Figure 8 shows that, in the absence of variations in displacement rate or temperature, the yield strength of each of the three alloys during isothermal irradiation at 365°C converged at a saturation level that was independent of both the thermomechanical starting condition and the helium generation rate, which in this case varied from 0.5 to 15 appm/dpa. The total elongation of the alloys also converged to a saturation value independent of these variables. Similar behavior was also observed at two other irradiation temperatures, but the saturation level of the yield strength fell with increasing irradiation temperature, and the saturation level for the total elongation increased with irradiation temperature.

It is also possible to study temperature history effects using this technique, although in the following example the experiment took advantage of an experimental accident that caused a significant difference in temperature history. The original experiment was initiated in MOTA 1D in FFTF Cycle 7, but a short (~50 min) and severe temperature excursion referred to as an "overtemperature event" compromised the integrity of many of the experiments in the MOTA. A decision was made, therefore, to run the MOTA in the helium-purged mode for the remainder of FFTF Cycles 7 and 8 while a series of reactivity feedback tests were conducted during which the majority of the MOTA canisters operated at variable but *lower*-than-targeted temperatures until the end of MOTA 1D.

Irradiation of the compromised sequence at 495°C was continued into MOTA 1E and beyond, along with a replacement series that had not experienced the nonisothermal history. At 495°C only annealed tension specimens were irradiated, and it is therefore not possible to confirm from tension tests alone that convergence occurs at this temperature. TEM disks were irradiated at 495°C in both the annealed and cold-worked conditions, and convergent microstructures appear to have developed in both, regardless of helium generation or thermomechanical starting condition [*7–9*]. The data at 495°C do demonstrate another type of convergence, however. Note in Fig. 9 that the strength of the original compromised specimens (i.e., those that were subjected to the overtemperature and subsequent low-temperature irradiation) initially reached a very high level and then fell to lower levels during the

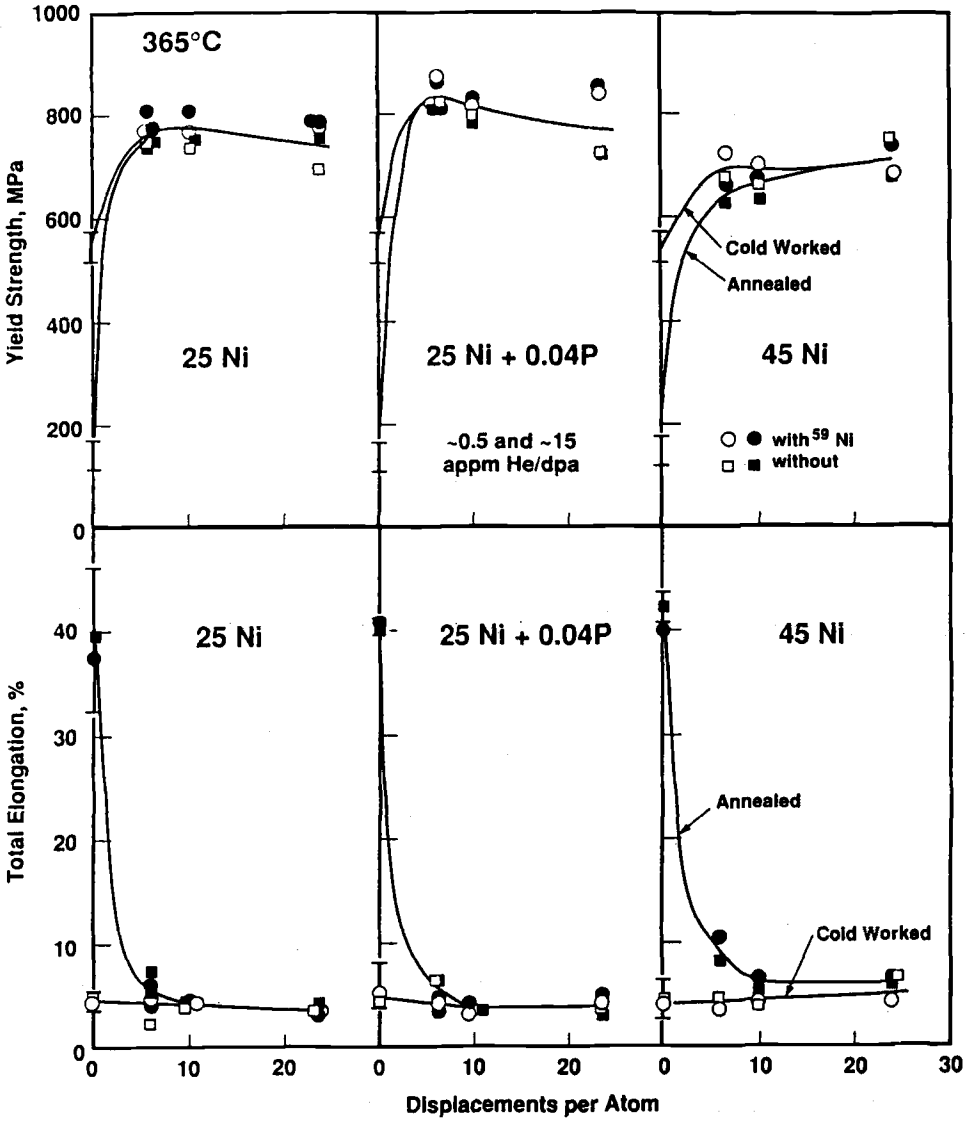

FIG. 8—*Influence of thermomechanical starting state and isotopic doping on yield strength and elongation of three Fe-15Cr-Ni alloys irradiated in FFTF-MOTA at 365°C. Filled and open symbols denote annealed and cold-worked specimens, respectively* [39].

second and third irradiation sequences. The specimens in the replacement sequence, however, reached the same lower levels directly. Similar but inverted behavior is evident in the corresponding elongation data at 495°C, as also shown in Fig. 9. The specimens exhibited lower ductility levels initially, followed by higher ductility levels when the originally intended irradiation temperature was reestablished. Thus, both the microstructure and the tension properties converge at levels dependent more on the recent irradiation temperature than on earlier temperature history.

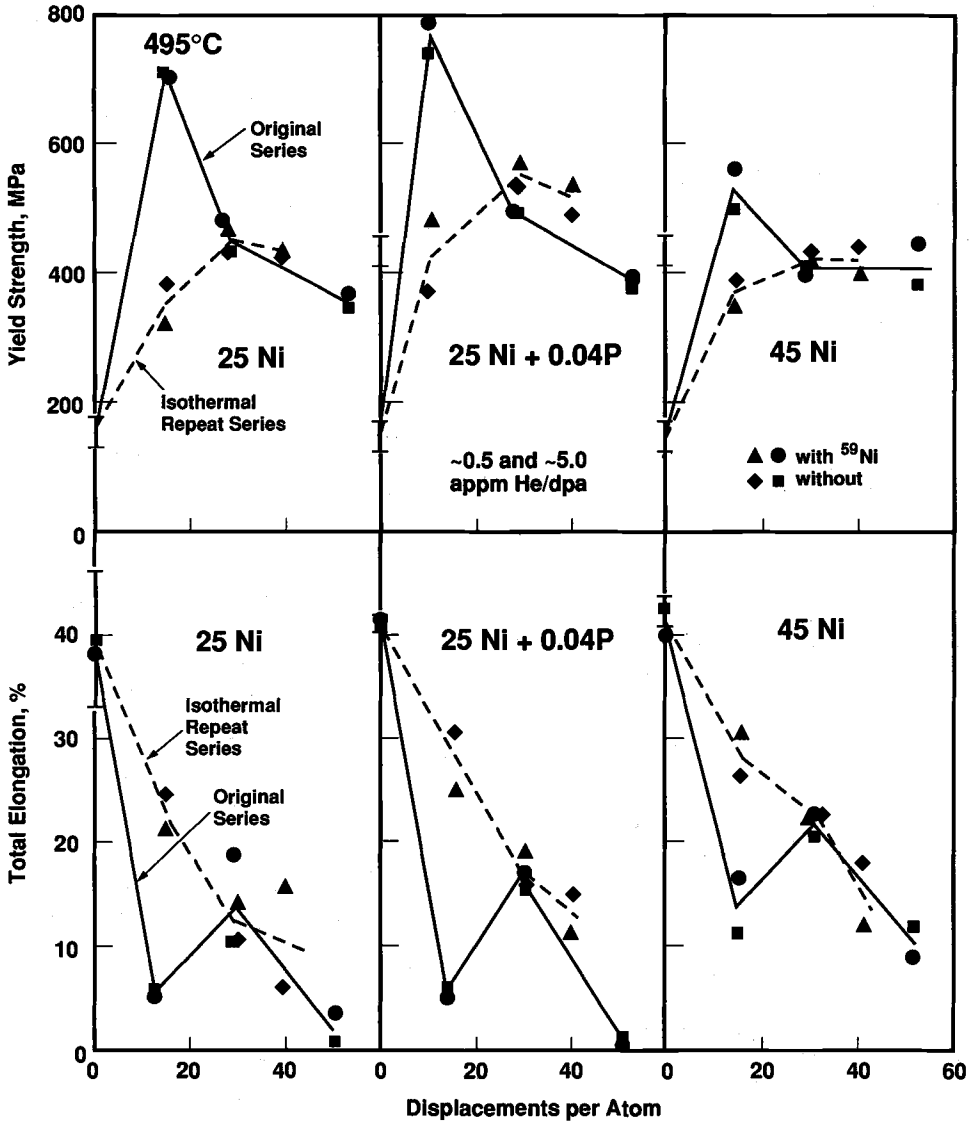

FIG. 9—*Influence of isotopic doping and temperature history on the yield strength and elongation of annealed Fe-15Cr-Ni alloys following irradiation in FFTF-MOTA at 495°C. The dotted line corresponds to the isothermal repeat sequence* [39].

The high-strength levels that were reached originally did not arise from the temperature excursion itself, however, but from the prolonged irradiation at the lower temperatures during Cycle 8 that followed the overtemperature event. The higher density of microstructural features and the resulting higher strength and lower ductility that developed at the lower temperatures were then replaced by microstructures and tension properties more appropriate to the temperatures achieved in the second and third irradiation segments.

The most significant feature of the isotopic tailoring data shown in Figs. 8 and 9 as well as in other irradiation sequences [*39*] is the relative unimportance of isotopic doping at all

test temperatures in determining the yield strength. Also significant is the tendency toward convergence of the data for both annealed and cold-worked specimens to saturation levels that depend only on alloy composition and irradiation temperature. A similar convergence was observed previously in 316 stainless steel over a wide range of irradiation temperatures, with convergence levels dependent on both temperature and displacement rate [*45,56*].

It appears that the helium generation rate in this experiment is of minimal importance compared with the other variables studied. In the absence of variations in displacement rate, the influence of helium is minor. A similar conclusion was reached by Mansur and Grossbeck [*57*] in a comparison of data from EBR-II and the High Flux Isotope Reactor (HFIR) on PCA, the prime candidate alloy of the fusion materials program. Although the displacement rates in the two reactors were comparable, the differences in helium generation rates in that comparison were even larger than in the current experiment.

Copper Irradiation Experiments in FFTF

For construction of the International Thermonuclear Experimental Reactor (ITER), relatively pure copper and oxide dispersion strengthened (ODS) copper have been selected to serve as the high heat flux materials and structural materials, respectively, for the diverter assembly. Copper alloys may also serve in commercial fusion reactors. The choice of the ODS type of copper alloy was a direct result of a series of tests conducted on miniature tension specimens and microscopy disks irradiated in FFTF/MOTA [*10–13, 27–30*]. Earlier candidates such as CuNiBe and MZC alloys were assigned a less favorable rating after being examined in these studies. Typical stress-strain curves are shown in Fig. 10.

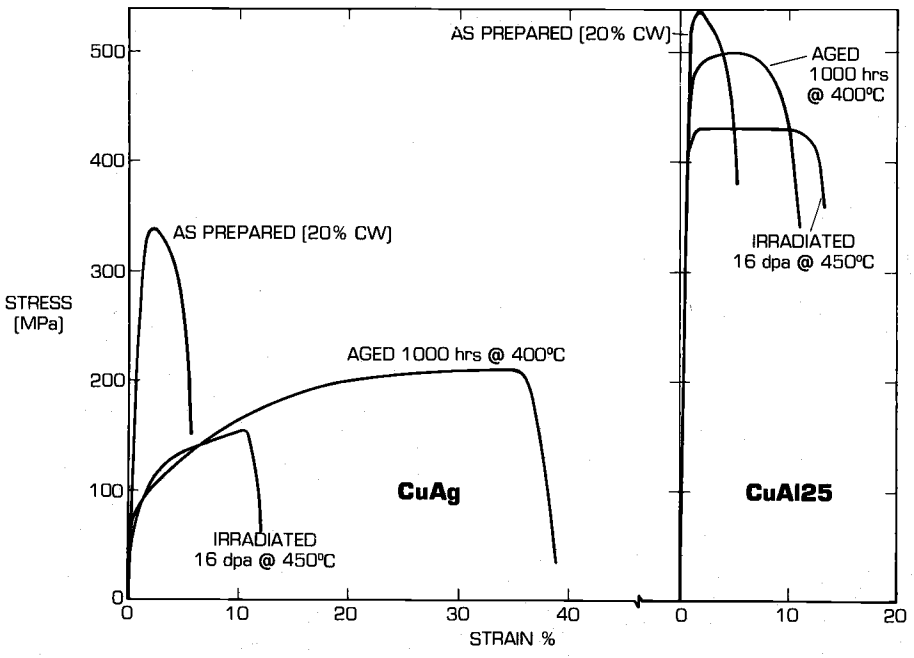

FIG. 10—*Typical stress-strain curves observed in two copper alloys after either thermal aging or irradiation in FFTF. CuAl25 is an oxide dispersion strengthened alloy chosen for fusion high heat flux service.*

One major complication in these studies is the highly spectrum-dependent transmutation of copper to nickel, zinc, and cobalt (in order of decreasing formation rate), reaching 5% Ni, 0.6% Zn, and 0.2% Co after five years of operation under proposed commercial fusion reactor conditions [*45*]. As shown in Fig. 11, the addition of nickel to copper by transmutation in FFTF, or by prior inclusion, causes large changes to its electrical conductivity, although its impact on void swelling and tension properties is not very significant. The conductivity also falls strongly with the onset of void swelling, which is larger at ~400°C than at 529°C. The large level of swelling that occurs in copper also leads to a very unusual fracture behavior, as shown in Fig. 12.

The interaction between transmutants, solutes, cold work-induced dislocations, and aging of pre-existing precipitates can be rather complex in copper alloys and may be different for each property measured. The quite different behaviors of Cu-2Be and CuNiBe shown in Fig. 13 demonstrate this complexity very well. Note, for instance, that Cu-2Be does not decline in conductivity with continued irradiation in the manner shown by CuNiBe (Cu-

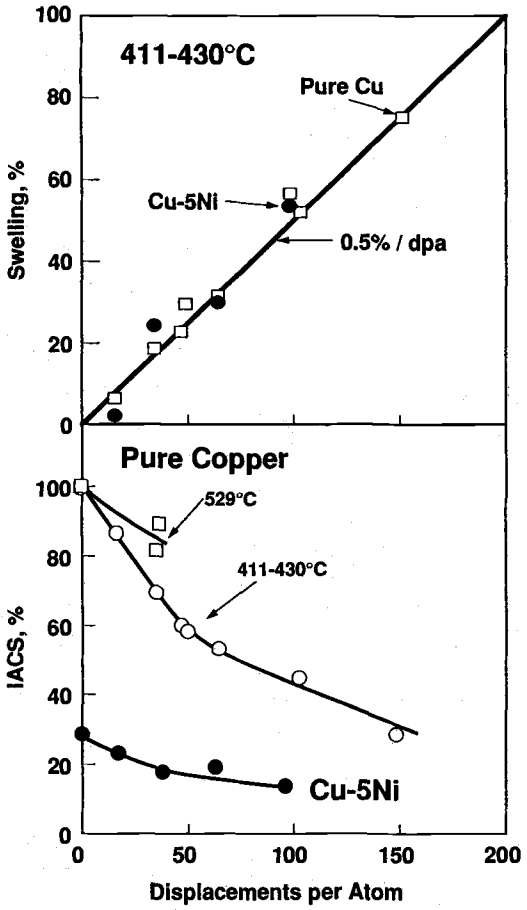

FIG. 11—*Comparison of swelling and conductivity changes of pure copper and Cu-5Ni observed after FFTF irradiation* [27].

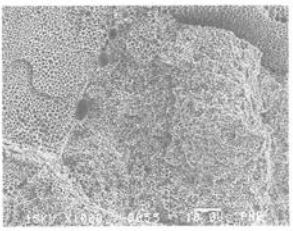

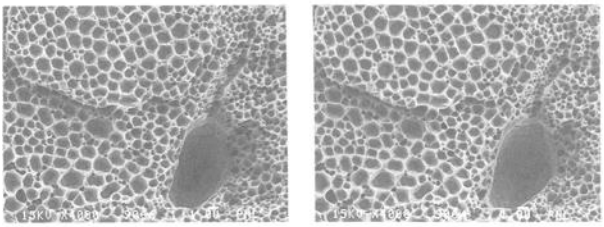

Stereo Pair 8° Tilt

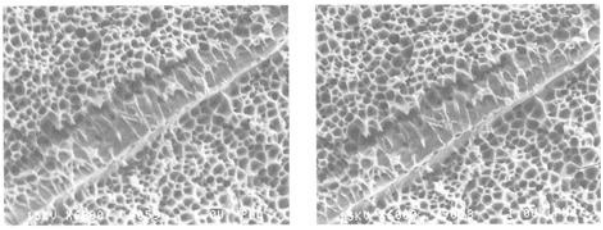

Stereo Pair 8° Tilt

FIG. 12—*Unusual fracture surfaces observed in highly voided pure copper irradiated in FFTF-MOTA to 50 dpa at 411°C* [11]. *The lower figure shows a grain boundary region.*

1.8Ni-0.3Be). Using the combined techniques of microscopy, electrical resistivity, tension testing, and fractography, it was found that the progressive addition of transmuted nickel drives residual Be out of solution, forming a greater amount of beryllide precipitates. The impact on the electrical conductivity of the gradual loss of Be from the alloy matrix is balanced out by the continuous addition of Ni. In CuNiBe the Be was already driven out of solution by the large level (1.8%) nickel existing prior to irradiation. The absence of Be in solution in CuNiBe also leads to larger swelling, thus causing a greater drop in the conductivity.

Other Types of Studies

Several studies involving miniature tension specimens are in progress to determine the suitability of the FeCrMn austenitic alloys and FeCrWV ferritic/martensitic alloys as re-

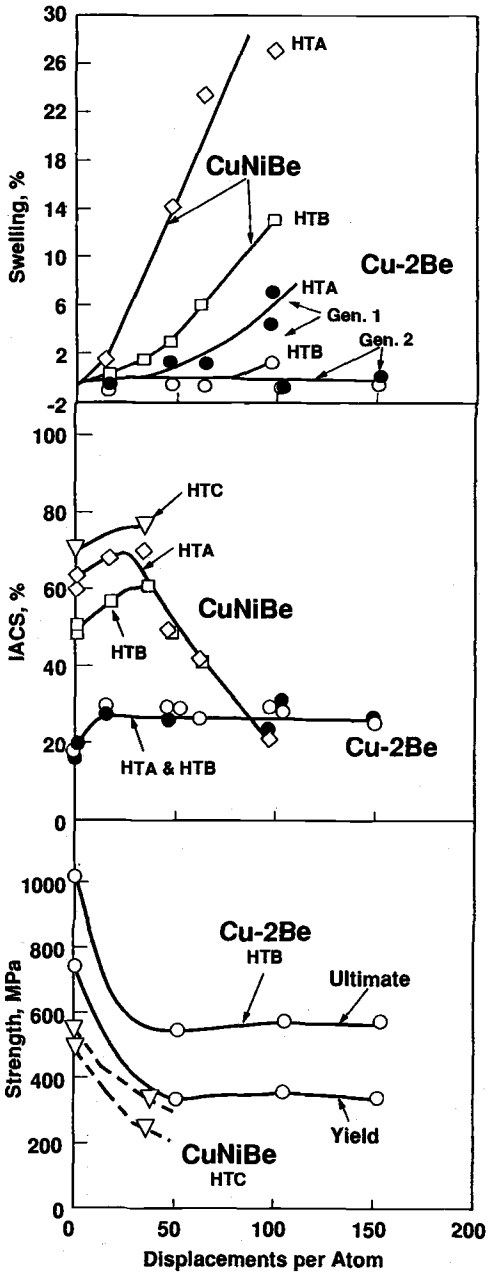

FIG. 13—*Swelling, conductivity, and tension strength measured in beryllium-containing alloys after irradiation at 411 to 430°C. Gen. 1 and Gen. 2 refer to the first and second irradiation series in FFTF-MOTA, respectively* [27].

placements for conventional alloys that exhibit a much higher level of long-term radioactivation [*58–60*]. Various fundamental studies are also in progress in a variety of reactors. A typical example is directed toward the composition dependence of irradiation-induced hardening in Fe-(3-18)Cr binary alloys in FFTF [*61*]. Another study involves the side-by-side irradiation of miniature tension specimens and low-cycle fatigue specimens in the DR-3 reactor (RISØ, Denmark) as well as in EBR-II.

Now that the spectral effects studies of Heinisch et al. have shown that the correlation of hardening data using dpa as the correlation parameter is valid for the LASREF facility as well as for other facilities, a series of tests are in progress or are being planned to take advantage of the unique advantages of the LASREF facility [*62*]. These tests involve: (a) the influence of copper level on embrittlement of A533B pressure vessel steel; (b) the dose and temperature dependence of pressure vessel embrittlement, exploring the question of damage saturation; and (c) an extensive property-property correlation experiment utilizing side-by-side irradiation of microscopy disks, miniature tensions, sub-size Charpy specimens, and sub-size fracture toughness specimens.

Conclusions

A large variety of experiments have shown the wide utility of miniature tension specimens for irradiation tests, particularly when combined with concurrent irradiation of other types of specimens and when subjected to other test techniques. The application of miniature tension specimens to pressure vessel embrittlement and annealing studies appears to offer significant advantages for future experiments.

References

[*1*] Panayotou, N. F., Atkin, S. D., Puigh, R. J., and Chin, B. A., "Design and Use of Nonstandard Tension Specimens for Irradiated Materials Testing," *The Use of Small Scale Specimens for Testing Irradiated Material, ASTM STP 888*, W. R. Corwin and G. E. Lucas, Eds., American Society for Testing and Materials, Philadelphia, 1986, pp. 201–219.

[*2*] Hamilton, M. L., Edwards, D. J., and Blotter, M. A., this publication, p. 368.

[*3*] Fleischer, R. L., *Acta Metallurgica*, Vol. 10, 1962, p. 835.

[*4*] Yoshida, N., *Journal of Nuclear Materials*, Vol. 174, 1990, pp. 220–228.

[*5*] Yoshida, N., Heinisch, H. L., Muroga, T., Araki, K., and Kiritani, M., *Journal of Nuclear Materials*, Vols. 179–181, 1991, pp. 1078–1082.

[*6*] Muroga, T., Heinisch, H. L., Sommer, W. F., and Ferguson, P. D., *Journal of Nuclear Materials*, Vols. 191–194, 1992, pp. 1150–1154.

[*7*] Stubbins, J. F. and Garner, F. A., *Journal of Nuclear Materials*, Vols. 179–181, 1991, pp. 523–525.

[*8*] Kawanishi, H., Garner, F. A., and Simons, R. L., *Journal of Nuclear Materials*, Vols. 179–181, 1991, pp. 511–514.

[*9*] Stubbins, J. F. and Garner, F. A., *Journal of Nuclear Materials*, Vols. 191–194, 1992, pp. 1300–1304.

[*10*] Anderson, K. R., Garner, F. A., Hamilton, M. L., and Stubbins, J. F., "Mechanical Property Changes and Microstructures of Dispersion-Strengthened Copper Alloys After Neutron Irradiation at 411 and 529°C," *Effects of Radiation on Materials, 15th International Symposium, ASTM STP 1125*, American Society for Testing and Materials, Philadelphia, 1992, pp. 854–874.

[*11*] Anderson, K. R., Garner, F. A., Stubbins, J. F., "Unusual Tensile and Fracture Behavior of Pure Copper at High Levels of Neutron-Induced Swelling," *Effects of Radiation on Materials, 15th International Symposium, ASTM STP 1125*, American Society for Testing and Materials, Philadelphia, 1992, pp. 835–845.

[12] Shikama, T., Garner, F. A., Hamilton, M. L., and Anderson, K. R., "Tension and Fracture Behavior of Cu-5Ni and Various Precipitation-Strengthened Copper Alloys After High Neutron Fluence," *Effects of Radiation on Materials, 15th International Symposium, ASTM STP 1125,* American Society for Testing and Materials, Philadelphia, 1992, pp. 846–853.

[13] Anderson, K. R., Stubbins, J. F., and Garner, F. A., "The Properties of Selected Spinodally Strengthened Copper Alloys Following High Temperature Neutron Irradiation," *Nuclear Science and Engineering,* Vol. 110, 1992, pp. 394–407.

[14] Brager, H. R., Garner, F. A., and Hamilton, M. L., *Journal of Nuclear Materials,* Vols. 133 & 134, 1985, pp. 594–598.

[15] Garner, F. A., Brager, H. R., and McCarthy, J. M., "Neutron-Induced Spinodal-like Decomposition of Fe-Ni and Fe-Ni-Cr Alloys" in *Radiation-Induced Changes in Microstructure: 13th International Symposium (Part 1), ASTM STP 955,* F. A. Garner, N. H. Packan, and A. S. Kumar, Eds., ASTM, Philadelphia, PA., 1987, pp. 775–787.

[16] Garner, F. A., Brager, H. R., Dodd, R. A. and Lauritzen, T., *Nuclear Instruments and Methods in Physics Research,* Vol. B16, 1986, pp. 244–250.

[17] Garner, F. A. and McCarthy, J. M., "Spinodal-Like Decomposition of Fe-Ni and Fe-Ni-Cr Invar Alloys During Neutron or Ion Irradiation," *Physical Metallurgy of Controlled Expansion Invar-Type Alloys,* K. C. Russell and D. F. Smith, Eds., The Minerals, Metals and Materials Society, Warrendale, PA, 1990, pp. 189–206.

[18] Aïdí, B., Viltange, M., and Dimitrov, O., *Journal of Nuclear Materials,* Vol. 175, 1990, pp. 96–106.

[19] Grossbeck, M. L., Maziasz, P. J. and Rowcliffe, A. F., *Journal of Nuclear Materials,* Vols. 191–194, 1992, pp. 808–812.

[20] Sekimura, N., Garner, F. A., and Griffin, R. D., *Journal of Nuclear Materials,* Vols. 191–194, pp. 1234–1237.

[21] Brager, H. R., Garner, F. A., and Panayotou, N. F., *Journal of Nuclear Materials,* Vols. 103 & 104, 1981, pp. 955–960.

[22] Heinisch, H. L., Atkin, S. D., and Martinez, C., *Journal of Nuclear Materials,* Vols. 141–143, 1986, pp. 807–815.

[23] Heinisch, H. L. and Martinez, C., *Journal of Nuclear Materials,* Vols. 141–143, 1986, pp. 883–887.

[24] Heinisch, H. L., *Journal of Nuclear Materials,* Vols. 155–157, 1988, pp. 121–129, also pp. 1159–1163.

[25] Heinisch, H. L., Hamilton, M. L., Sommer, W. F., and Ferguson, P. D., *Journal of Nuclear Materials,* Vols. 191–194, 1992, pp. 1177–1182.

[26] Zinkle, S. J. and Kulcinski, G. L., *Journal of Nuclear Materials,* Vols. 122 & 123, 1984, pp. 449–454.

[27] Garner, F. A., Brager, H. R., and Anderson, K. R., *Journal of Nuclear Materials,* Vols. 189–191, 1991, pp. 250–253.

[28] Garner, F. A., Hamilton, M. L., Shikama, T., Edwards, D. J., and Newkirk, J. W., "Response of Solute and Precipitation-Strengthened Copper Alloys at High Neutron Fluence," *Journal of Nuclear Materials,* Vols. 191–194, 1992, pp. 386–390.

[29] Edwards, D. J., Anderson, K. R., Garner, F. A., Hamilton, M. L., Stubbins, J. F., and Kumar, A. S., "Irradiation Performance of Oxide Dispersion-Strengthened Copper Alloys to 150 dpa at 415°C," *Journal of Nuclear Materials,* Vols. 191–194, 1992, pp. 416–420.

[30] Garner, F. A., Hamilton, M. L., Brager, H. R., Anderson, K. R., Stubbins, J. F., and Singh, B. N., "Overview of Copper Irradiation Programs in FFTF," *Proceedings,* International Conference on Radiation Materials Science, Alushta, USSR, 22–25 May 1990, Vol. 1, pp. 82–92.

[31] Garner, F. A. and Zinkle, S. J., "Radiation Response of Copper Alloys at High Exposure Levels," *Proceedings,* International Conference on Effects of Irradiation on Materials of Fusion Reactors, Leningrad, USSR, 18–20 September 1990, in press.

[32] Igata, N., Miyahara, K., Uda, T., and Asada, S., *The Use of Small Scale Specimens for Testing Irradiated Material, ASTM STP 888,* W. R. Corwin and G. E. Lucas, Eds., American Society for Testing and Materials, Philadelphia, 1986, pp. 161–170.

[33] Rickerby, D. G., Fenici, P., Jung, P., Piatti, G., and Schiller, P., *The Use of Small Scale Specimens*

for Testing Irradiated Material, ASTM STP 888, W. R. Corwin and G. E. Lucas, Eds., American Society for Testing and Materials, Philadelphia, 1986, pp. 220–232.

[*34*] Kohyama, A., Asano, K. and Igata, N. in *Influence of Radiation on Materials Properties: 15th International Symposium (Part II), ASTM STP 956,* F. A. Garner, C. H. Henager, Jr., and N. Igata, Eds., American Society for Testing and Materials, Philadelphia, 1987, pp. 111–122.

[*35*] Kohyama, A., Asakura, K., and Igata, N., *Journal of Nuclear Materials,* Vols. 141–143, 1986, pp. 921–925.

[*36*] Kohyama, A., Hamada, K., and Matsui, H., *Journal of Nuclear Materials,* Vols. 179–181, 1991, pp. 417–420.

[*37*] Kohyama, A., Sato, S., and Hamada, K., *Journal of Nuclear Materials,* Vols. 191–194, pp. 1033–1037.

[*38*] Garner, F. A., Hamilton, M. L., Simons, R. L., and Maxon, M. K., *Journal of Nuclear Materials,* Vols. 179–181, 1991, pp. 54–557.

[*39*] Hamilton, M. L. and Garner, F. A., *Journal of Nuclear Materials,* Vols. 191–194, 1992, pp. 1239–1243.

[*40*] Hamilton, M. L., Okada, A., and Garner, F. A., *Journal of Nuclear Materials,* Vols. 179–181, 1991, pp. 558–562.

[*41*] Heinisch, H. L., *Radiation Effects and Defects in Solids,* Vol. 113, 1990, pp. 53–73.

[*42*] Greenwood, L. R., Garner, F. A., and Heinisch, H. L., *Journal of Nuclear Materials,* Vols. 191–194, 1992, pp. 1096–1100.

[*43*] Heinisch, H. L., *Journal of Nuclear Materials,* Vol. 178, 1991, pp. 19–26.

[*44*] Hamilton, M. L. and Heinisch, H. L., "Tension Properties of Neutron-Irradiated A212B Pressure Vessel Steel," *Effects of Radiation on Materials: 14th International Symposium (Volume II), ASTM STP 1046,* N. H. Packan, R. E. Stoller, and A. S. Kumar, Eds., ASTM, Philadelphia, 1990, pp. 45–54.

[*45*] Garner, F. A., Heinisch, H. L., Simons, R. L., and Mann, F. M., *Radiation Effects and Defects in Solids,* Vol. 113, 1990, pp. 229–255.

[*46*] Cheverton, R. D., Merkle, J. G., and Nanstad, R. K., *Evaluation of HFIR Pressure-Vessel Integrity Considering Radiation Embrittlement, ORNL/TM-10444,* Oak Ridge National Laboratory, Oak Ridge, TN, September 1987.

[*47*] Garner, F. A., *Journal of Nuclear Materials,* Vol. 174, 1990, pp. 229–239.

[*48*] Garner, F. A., *Journal of Nuclear Materials,* Vols. 179–181, 1991, pp. 111–117.

[*49*] Farrell, K. in *Dimensional Stability and Mechanical Behaviour of Irradiated Metals and Alloys,* British Nuclear Engineering Society, London, 1983, Vol. 1, pp. 73–76.

[*50*] Bates, J. F., Garner, F. A., and Mann, F. M., *Journal of Nuclear Materials,* Vols. 103 & 104, 1981, pp. 999–1004.

[*51*] Brager, H. R. and Garner, F. A., *Journal of Nuclear Materials,* Vols. 108 & 109, 1982, pp. 347–358.

[*52*] Simons, R. L., Brager, H. R., and Matsumoto, W. Y., *Journal of Nuclear Materials,* Vols. 141–143, 1986, pp. 1057–1060.

[*53*] Odette, G. R., *Journal of Nuclear Materials,* Vols. 141–143, 1986, pp. 1011–1017.

[*54*] Kiritani, M., *Journal of Nuclear Materials,* Vol. 160, 1988, pp. 135–141.

[*55*] Greenwood, L. R., Garner, F. A., and Oliver, B. M., *Journal of Nuclear Materials,* Vols. 191–194, 1992, pp. 1051–1055.

[*56*] Garner, F. A., Hamilton, M. L., Panayotou, N. F., and Johnson, G. D., *Journal of Nuclear Materials,* Vols. 103 & 104, 1981, pp. 803–808.

[*57*] Mansur, L. K. and Grossbeck, M. L., *Journal of Nuclear Materials,* Vols. 155–157, 1988, pp. 130–147.

[*58*] Brager, H. R., Garner, F. A., Gelles, D. S., and Hamilton, M. L., *Journal of Nuclear Materials,* Vols. 133 & 134, 1985, pp. 907–911.

[*59*] Garner, F. A. and McCarthy, J. M., "An Assessment of Fe-Cr-Mn Austenitic Alloys for Fusion Reactor Irradiation," *Reduced Activation Materials for Fusion Reactors, ASTM STP 1047,* R. L. Klueh, D. S. Gelles, M. Okada, and N. H. Packan, Eds., ASTM, Philadelphia, 1990, pp. 19–29.

[*60*] Klueh, R. L., Gelles, D. S., and Lechtenberg, T. A., *Journal of Nuclear Materials,* Vols. 141–143, 1986, pp. 1081–1087.

[61] Hamilton, M. L., Gelles, D. S., and Gardner, P. L., to be published in the Proceedings of the 16th ASTM International Symposium on Effects of Radiation on Materials, Denver, CO, June 1992 (ASTM STP 1175).

[62] Sommer, W. F., Lohmann, W., Graf, K., Taylor, J. K., and Chavez, R. M., "Operating Experience at the Los Alamos Spallation Radiation Effects Facility at LAMPF," *Influence of Radiation on Materials Properties: 13th International Symposium Part II, ASTM STP 956*, F. A. Garner, C. H. Henager, Jr. and N. Igata, Eds., ASTM, Philadelphia, 1987, pp. 718–729.

Akira Kohyama,[1] *Shinji Sato,*[1] *and Kenichi Hamada*[1]

An Automated Tensile Machine for Small Specimens Heavily Neutron Irradiated in FFTF/MOTA

REFERENCE: Kohyama, A., Sato, S., and Hamada, K., **"An Automated Tensile Machine for Small Specimens Heavily Neutron Irradiated in FFTF/MOTA,"** *Small Specimen Test Techniques Applied to Nuclear Reactor Vessel Thermal Annealing and Plant Life Extension, ASTM STP 1204,* W. R. Corwin, F. M. Haggag, and W. L. Server, Eds., American Society for Testing and Materials, Philadelphia, 1993, pp. 356–367.

ABSTRACT: The objective of this work is to develop a fully automated tensile machine for post-irradiation examination (PIE) of Fast Flux Test Facility (FFTF)/Materials Open Test Assembly (MOTA) irradiated miniature tension specimens. The anticipated merit of the automated tensile machine is to reduce damage to specimens during specimen handling for PIE and to reduce exposure to radioactive specimens. This machine is designed for testing at elevated temperatures, up to 873 K, in a vacuum or in an inert gas environment. Twelve specimen assemblies are placed in the vacuum chamber that can be tested successively in a fully automated manner.

A unique automated tensile machine for the PIE of FFTF/MOTA irradiated specimens, the Monbusho Automated Tensile Machine (MATRON) consists of a test frame with controlling units and an automated specimen-loading apparatus. The qualification of the test frame has been completed, and the results have satisfied the machine specifications. The preliminary tests utilizing unirradiated specimens reproduced duplicated data with those from an Instron-type testing machine. An automated specimen-loading apparatus has also been developed, and the qualification of the functions of this apparatus has been completed. The further improvements, which add flexibility to accept deformed specimens that do not fit the original dimensions, will also be reported.

The capabilities of producing creep and relaxation data have been demonstrated for Cu, Al, 316SS, and ferritic steels. The specimen holders for the three-point bending test and the small bulge test (small punch test; SP test) were also designed and produced. These fixtures are currently being tested to verify the validity of the material test results.

KEYWORDS: post-irradiation examination, tension test, small specimen test technique, automated machine, bend test, creep test, relaxation test

There is a strong demand to establish a good method for performing post-irradiation mechanical testing, especially for heavily irradiated and highly radio-activated materials utilizing small specimens [*1–4*]. The major motivations to establish small specimen test techniques are: limitations in irradiation volume, cost of irradiation and post-irradiation testing, and radiation dose to personnel during post-irradiation specimen handling and tests. Recent efforts in fusion reactor materials research and development have led to standard specimen geometries in each national program or international collaboration program [*5,6*]. In the Japanese Monbusho fusion materials program, a standard small tension specimen with gage section dimensions of 1.2 by 5.0 by 0.25 mm (Japanese Type S) has been proposed

[1] Department of Materials Science, The University of Tokyo, Hongo, Bunkyo-ku, Tokyo 113, Japan.

and utilized in the irradiation programs Rotating Target Neutron Source-II (RTNS-II), JOYO, Japan Materials Testing Reactor (JMTR), and FFTF/MOTA by major participants from Japanese universities. This specimen is much smaller than the SS-3 specimens used in the U.S. fusion program. In the Japan/U.S. collaboration program utilizing FFTF/MOTA, a large number of tension specimens with a variety of materials and thermomechanical treatments have been irradiated, and there is still more to come from FFTF. In order to accomplish this amount of PIE, an automated tensile machine has been under development.

In this paper, a newly designed and fabricated fully automated tensile machine, MATRON, which stands for Monbusho Automated Tensile Machine, will be described together with representative results.

Design Concept and Specifications of MATRON

The automated tensile machine was designed to satisfy the following requirements.

1. To have specimen size flexibility by changing the specimen holder geometry, which enables testing U.S. SS-3 and Japanese Type S specimens.
2. To have a test temperature range from room temperature to 873 K.
3. To have a test environment that can be either a vacuum or an inert gas.
4. To have specimen setting and unloading from the specimen holder done in a semi-automatic mode by remote control.
5. To have the test carried out by remote operation out of the hot cell where the test frame is located.

Specimen Holder

To simplify the test sequence, the specimen holder was designed to convert the pushing motion of the pushing rod into a pulling motion on the specimen to test by tensile action. Figure 1 shows two specimen holders, one with a new specimen and the other with a broken one. The tension specimen is assembled with pins, spacers, and washers and is clumped to the holder. Machinable Si_3N_4, Macor tubes are placed surrounding the sliding shafts of the holder to prevent sticking and to reduce friction at elevated temperatures. The maximum elongation is 100% for the Type S specimen. The designs to perform three-point bend testing, compression testing, small bulge testing, and small punch testing have also been completed in a manner to accommodate the rotating table of MATRON. Thus, it is quite easy to perform this variety of tests with only a change in specimen holders.

Specimen Loading and Unloading Apparatus

Specimen loading in the specimen holder prior to the test and unloading after the test can be done automatically by the specimen loading and unloading apparatus, as shown in Fig. 2*a*. The first step is to place the specimen holder in the right position in the apparatus, as shown in Fig. 2*b* (plane view) and Fig. 2*c* (side view). The next step is to select auto mode and push the start switch: the apparatus feeds pins to the holder, then feeds washers, a specimen, washers, spacers, and screws successively to set the specimen to the holder. The torque for the screw insertion to the holder can be adjusted by a dial selection. The sequence to assemble the specimen holder with the specimen is a process with about 60 step motions of bowl feeders, line feeders, air tweezers, and a pneumatic screwdriver. The whole operation takes about 10 min. The unloading procedure is done in a reversal way. The

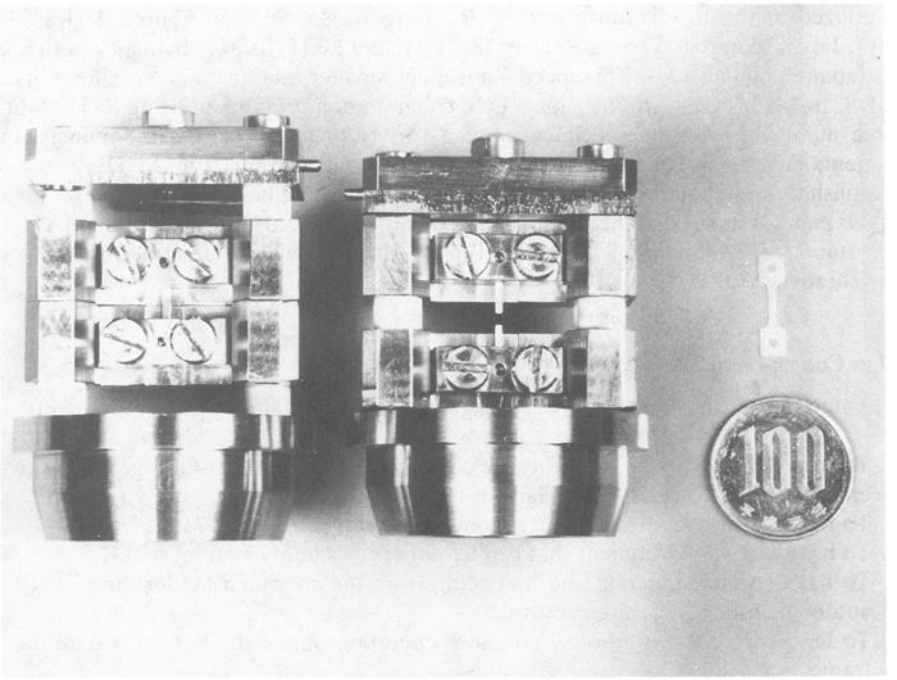

FIG. 1—*The specimen holders prior to and after tension testing.*

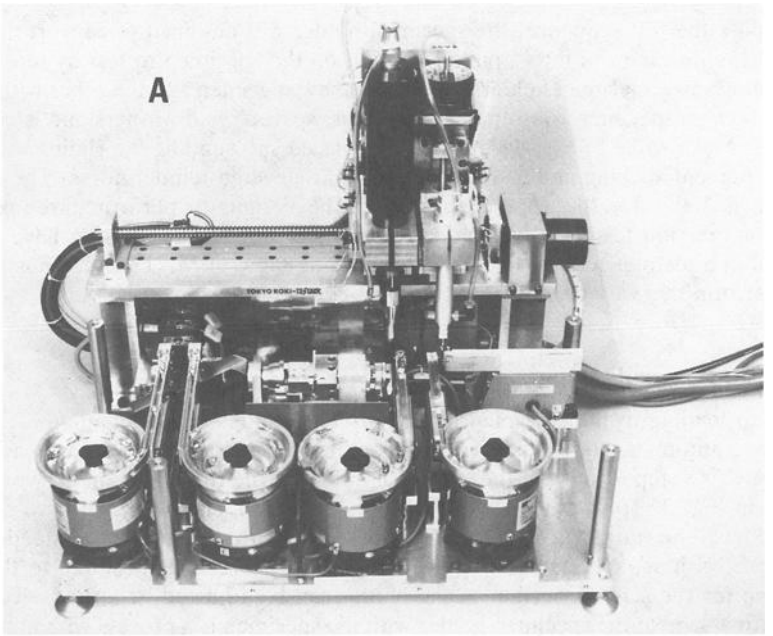

FIG. 2—(a) *The automated specimen loading and unloading apparatus and its schematic illustrations;* (b) *plane view; and* (c) *side view.*

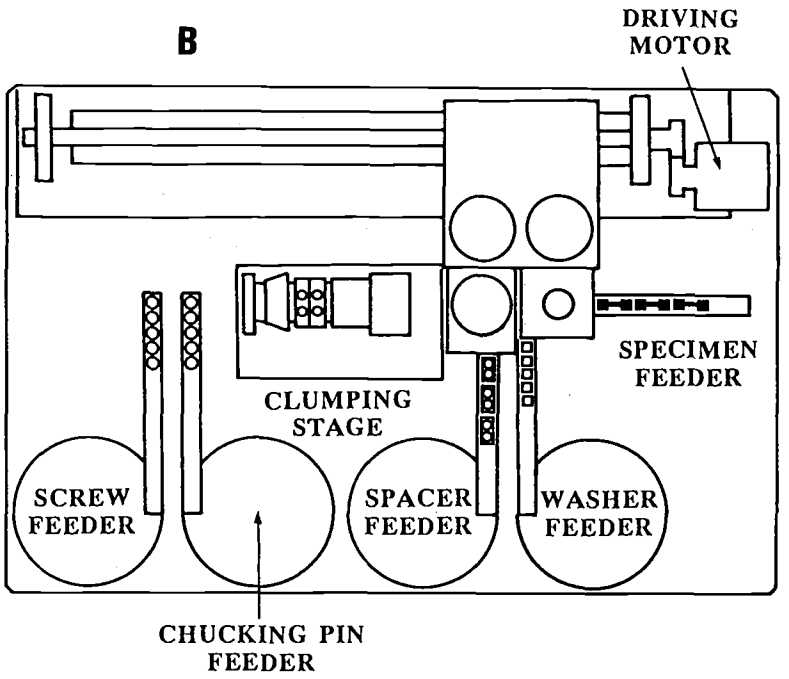

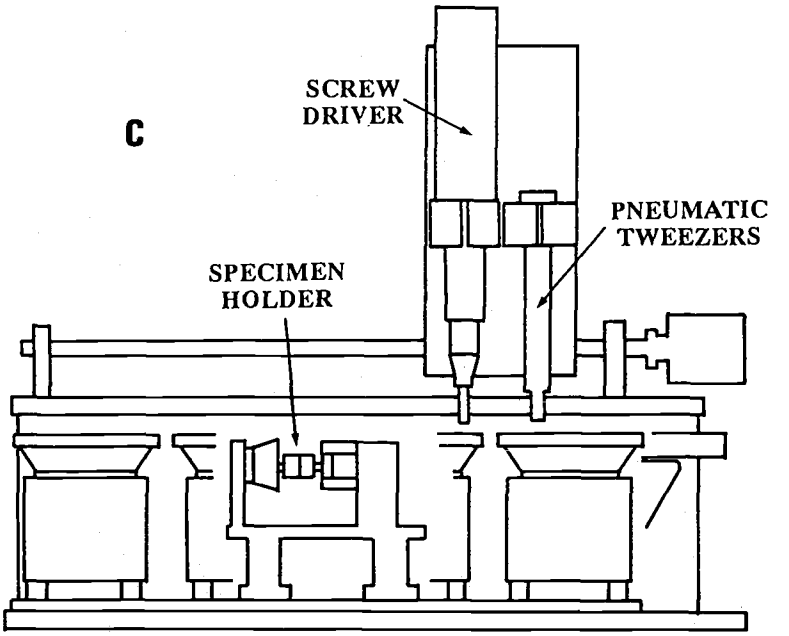

FIG. 2—*Continued.*

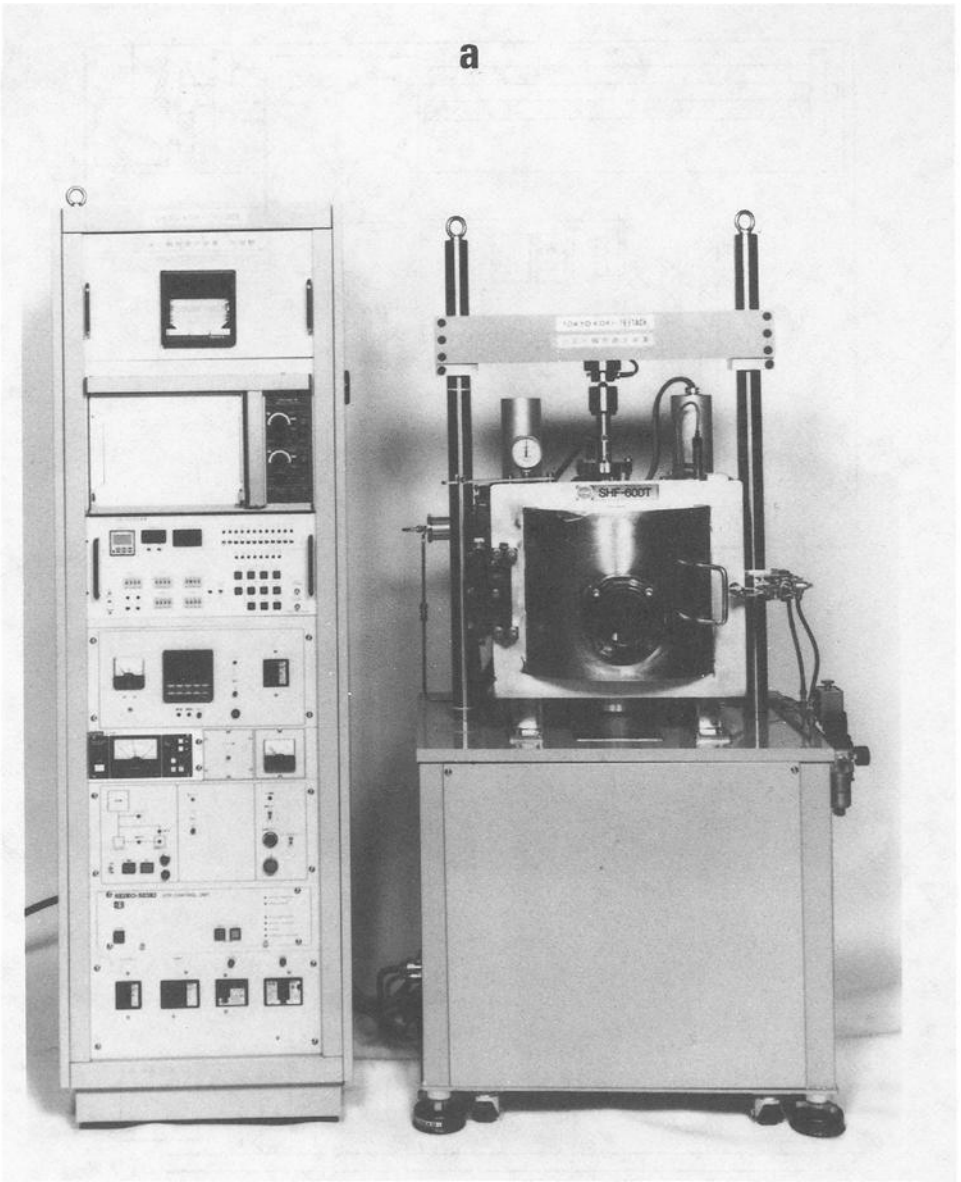

FIG. 3—(left) *MATRON and* (right) *its system diagram.*

broken tension specimen and other fixture parts are retrieved separately and deposited in baskets. The baskets can then be removed from the apparatus.

The apparatus works satisfactorily in auto mode for the mini-size tension specimens with their original dimensions. To improve flexibility and to be in a position to accept deformed or swelled specimens which do not have the original dimensions, manual modes have been introduced. One is a full-manual mode, where every motion is controlled under visual

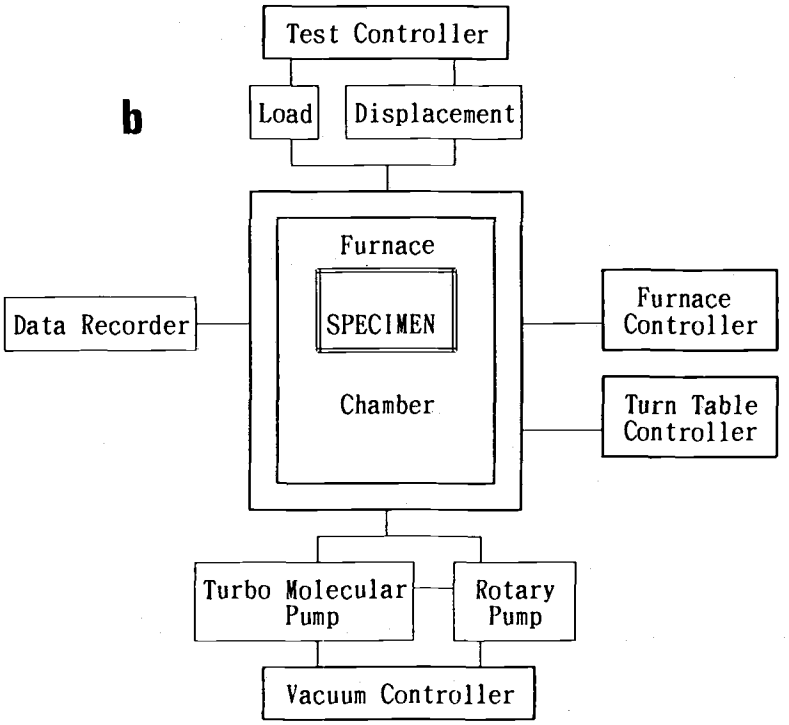

FIG. 3—*Continued.*

observation. The other is a preset mode, where each specimen dimension is conveyed to the controller prior to the start of the apparatus.

Test Frame and Operation System

The test frame and the control panel of MATRON are shown in Fig. 3*a*, with the system diagram in Fig. 3*b*. The main unit of MATRON is schematically illustrated in Fig. 4, which consists of a test chamber, vacuum system, and main frame with a displacement operation system.

The test chamber is made of Type 304 stainless steel and is comprised of an electric furnace and a turntable with twelve positions for specimen assemblies. The chamber is a front-loading type with a view window in the front door. A turbo-molecular pump with the capacity of 300 L/min and a rotary pump are installed as the evacuating system. The upper limit of the test temperature is 873 K with the vacuum of 6×10^{-5} Pa and 5×10^{-4} Pa at room temperature and 873 K, respectively. The temperature history during the test can be controlled upon the selection of one of the 19 temperature history patterns memorized. Each temperature history pattern is preset up to 99 steps as a function of the furnace controller.

The pretest motion of the machine starts with the rotation of the turntable so as to align the specimen and the specimen holder with the test axis. The pushing rod pushes up the specimen holder to the center of the electric furnace with the transfer speed of 25 mm/min. Then the test can be started with a displacement speed between 0.0001 and 0.9999 mm/min, which is a strain rate from 3.3×10^{-7}/s to 3.3×10^{-3}/s for the case of the Type S

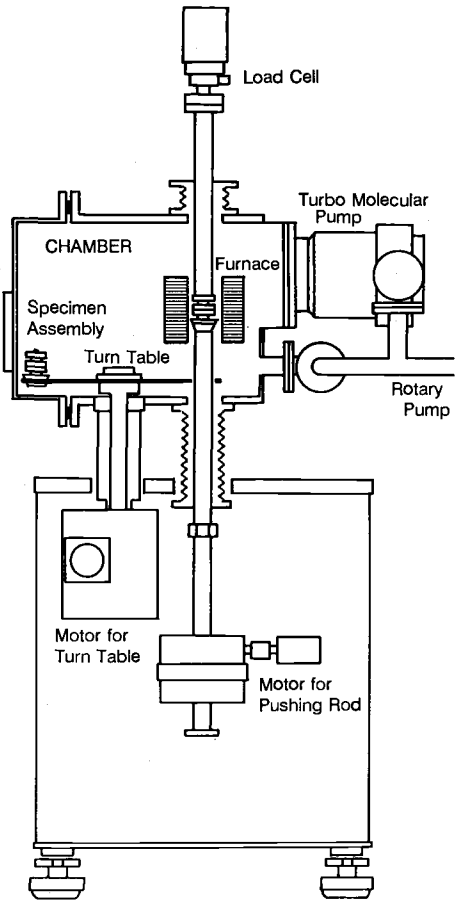

FIG. 4—*The main unit of MATRON in a cross-cut illustration.*

specimen. The maximum test load is designed to be 50 kg, which corresponds to a maximum applied stress of 140 kg/mm^2 for the case of a standard Type S specimen.

The tests may be performed by presetting the twelve test conditions of the twelve specimens. MATRON can be operated under either applied load or displacement control. Therefore, MATRON has the capability of performing creep, relaxation, and fatigue tests.

Representative Test Results

Regarding specimen size effects, previous studies have provided a fairly weak size dependence on the yield strength and a strong size dependence on both the ultimate strength and the total elongation of both unirradiated and neutron-irradiated materials [*6,7*]. In this study, the Type S specimens of Japan ferritic/martensitic steel (JFMS, 10Cr-1Mo-1Ni dual phase steel) annealed at 973 K for 30 min were tested with Instron-type tensile machines, Tensilon (trade name), and with the MATRON. As shown in Fig. 5, there is no difference between the strain rate dependence of the tensile properties as determined by MATRON and by Tensilon. These results suggest that the potential friction problem in the sliding

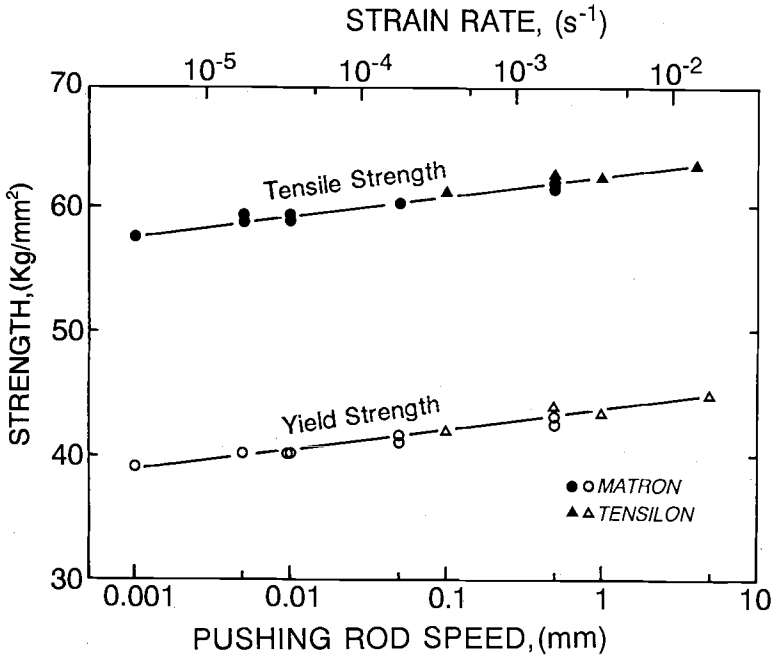

FIG. 5—*Strain rate dependence of tensile properties obtained from MATRON and Tensilon.*

mechanism of the specimen holder is negligibly small for the case of JFMS and for the cases of metals and alloys with similar strength levels [*8*]. A typical example of temperature dependence obtained from MATRON is shown in Fig. 6, which is nearly identical with that from Tensilon. For the test at elevated temperature, the Macor tube has to be essentially applied to reduce or prevent the problem, otherwise the results become inconsistent with that from Tensilon [*8*].

Yield strengths are known to be thickness independent for thicknesses larger than the critical thickness, t_c [*9*]. The critical thickness for ferrous materials is about six to ten times the average grain size. Figure 7 shows the specimen thickness dependence of both the tensile strength and the yield strength for JFMS tested with MATRON. In this study, the thickness dependence could not be observed as the average grain size of these specimens was about 15 μm and each specimen thickness was ten or more times this size.

Future Application

Utilizing the same specimen holder as for the tension test, creep tests can be carried out with MATRON. For creep tests, not only the specimen holder but also the pushing rod must be in a heat equilibrium state. Figure 8 shows a creep test result for a 0.25-mm-thick specimen of JFMS at 873 K. In this test, the creep load was 6 kg, and the resulting creep rate was 6×10^{-5}/s.

For the three-point bending test, a prototype specimen holder was designed and evaluated. Figure 9 depicts the holder, where the outer dimensions of the lower component are identical with those for tension test and the whole dimensions of the three-point bend test holder is

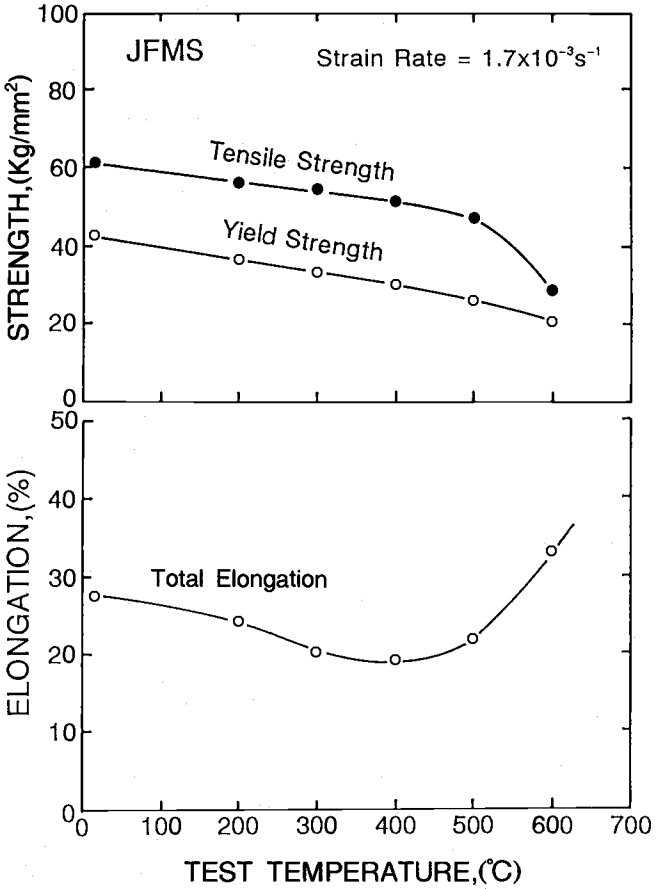

FIG. 6—*Temperature dependence of tensile properties for JFMS annealed at 973 K for 30 min obtained from MATRON.*

accommodated with the MATRON test frame. The support span, the radii of a loading and support noses, and specimen dimensions are set to be 12.5, 1, and 2 by 2 by 20 mm, respectively. Figure 10 shows, as an example of the soundness of the holder, the three point-bend test results at room temperature using the prototype holder for the carbon/carbon composite. Heat treatment at 873 K for 30 min improved flexural strength, which has been also demonstrated with a standard three-point bend test jig and has been interpreted to be due to outgassing by the heat treatment [*10*].

Conclusions

A unique automated tensile machine for the PIE of FFTF/MOTA irradiated specimens, the Monbusho Automated Tensile Machine (MATRON), consisting of a test frame with controlling units and an automated specimen-loading apparatus, was designed and fabricated. This machine is designed for testing at elevated temperatures, up to 873 K, in a vacuum or in an inert gas environment. Twelve specimen assemblies are placed in the vacuum

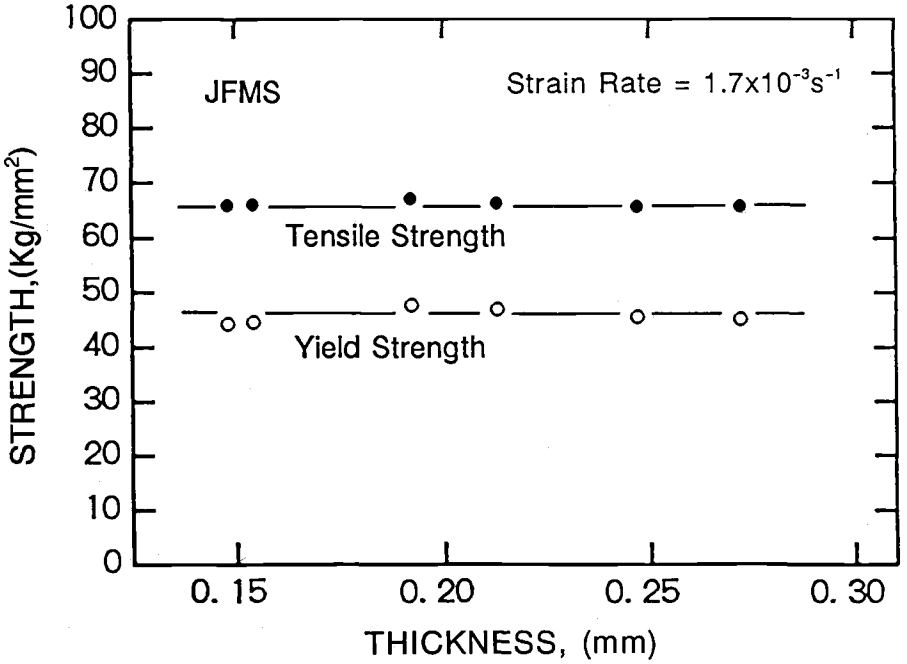

FIG. 7—*Specimen thickness dependence of tensile properties of JFMS tested with MATRON.*

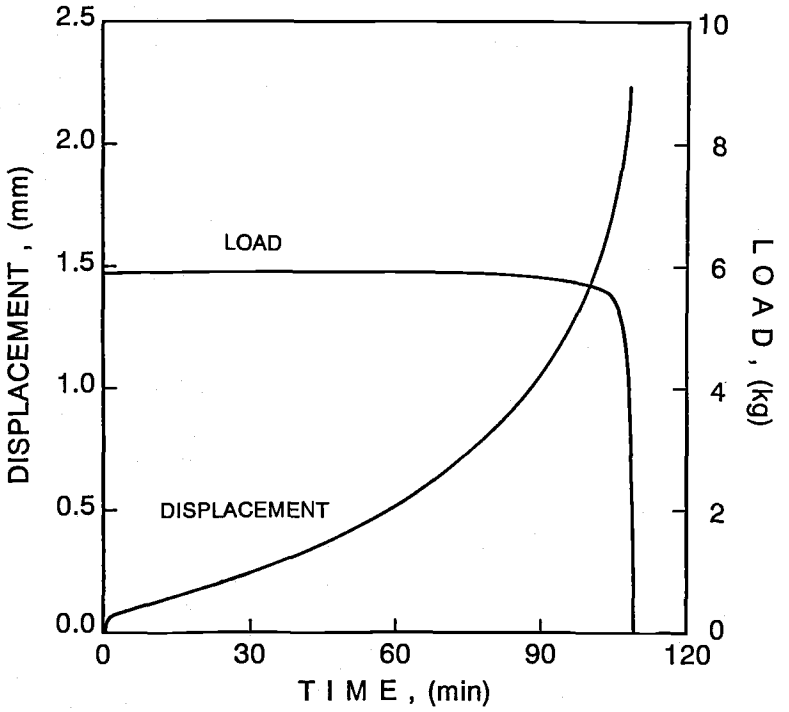

FIG. 8—*Time-displacement and time-load curves obtained from creep test of JFMS at 873 K with MATRON.*

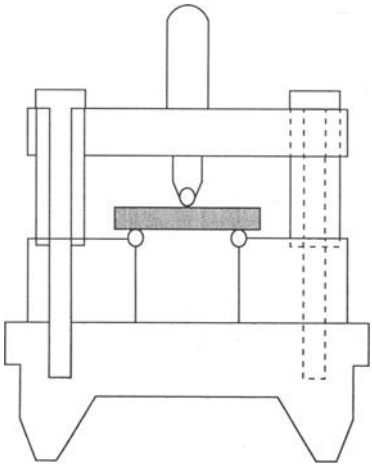

FIG. 9—*A schematic illustration of the specimen holder for three-point bending test.*

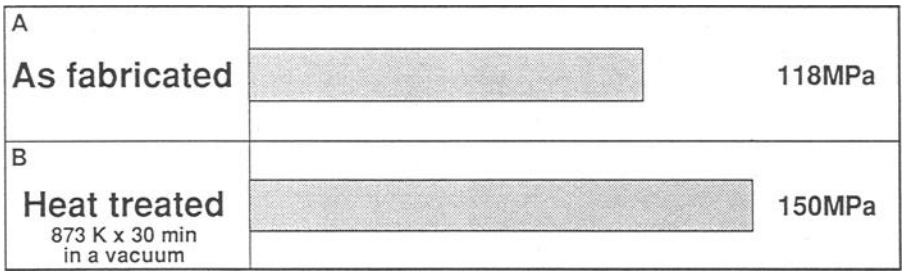

FIG. 10—*Representing results about flexural strength of C/C composites, as fabricated and with heat treatment.*

chamber and tested successively in a fully automated manner. The preliminary tests utilizing unirradiated specimens reproduced duplicated data with those from an Instron-type testing machine. As a result, the qualification tests of the frame have been reported in this paper and the results have satisfied the machine specifications.

Acknowledgments

The support by the Japan/U.S.A. collaboration program utilizing FFTF/MOTA, sponsored by Monbusho for the research and development of MATRON is acknowledged. The authors would like to express their appreciation to the participants of this program with their special thanks to Profs. S. Ishino, H. Matsui, and K. Abe for their kind discussions and help. They are grateful to Ms. M. L. Hamilton for her kind discussions and efforts to install MATRON in the hot cell of Battelle Pacific Northwest Laboratories, Richland, Washington.

References

[*1*] Panayotou, N. F., *Journal of Nuclear Material,* Vols. 108–109, 1982, p. 456.
[*2*] *The Use of Small Scale Specimens for Testing Irradiated Materials, ASTM STP 888,* G. W. Corwin and G. E Lucas, Eds., American Society for Testing and Materials, Philadelphia, 1986.

[3] Ho, E. T. C. and MacEwen, S. R., *Novel Techniques in Metal Deformation Testing,* TMS-AIME, New York, 1983, pp. 359–371.
[4] Panayotou, N. F., Atkins, S. D., Puigh, R. J., and Chin, B. A., in *The Use of Small Scale Specimens for Testing Irradiated Materials, ASTM STP 888,* G. W. Corwin and G. E. Lucas, Eds., American Society for Testing and Materials, Philadelphia, 1986, pp. 201–219.
[5] Hannula, S. P., Wanagel, J., and Li, C. Y., in *The Use of Small Scale Specimens for Testing Irradiated Materials, ASTM STP 888,* G. W. Corwin and G. E. Lucas, Eds., American Society for Testing and Materials, Philadelphia, 1986, pp. 233–251.
[6] Kohyama, A., Hamada, K., Asakura, K., and Matsui, H., in *Effects of Radiation on Materials: 14th International Symposium, ASTM STP 1046,* American Society for Testing and Materials, Philadelphia, 1990, pp. 404–421.
[7] Kohyama, A., Hamada, K., and Matsui, H., *Journal of Nuclear Materials,* Vol. 179–181, 1991, pp. 417–420.
[8] Nakahara, N., graduation thesis, Department of Materials Science, University of Tokyo, 1990 (in Japanese).
[9] Kohyama, A., Matsui, H., Abe, K., Hamada, K., and Asano, K., *Journal of Nuclear Materials,* Vols. 155–157, 1988, p. 1354.
[10] Hamada, K., masters thesis, Department of Materials Science, University of Tokyo, 1992 (in Japanese).

DISCUSSION

G. Lucas[1] (*written discussion*)—How are the specimens unloaded after testing?

A. Kohyama et al. (*authors' closure*)—The unloading procedure is done in a reversal way with the loading procedure. This did not work for some exceptional cases after tests at elevated temperatures.

M. Brumovsky[2] (*written discussion*)—Are you able to measure also an elongation of specimens, and if so, what method do you use for its determination (gage length or displacement of heads/fixtures)?

A. Kohyama et al. (*authors' closure*)—At present, MATRON has the capability to measure elongation by displacement of the crosshead, but it is easy to place the strain gage and connect it to the recorder.

[1] University of California, Santa Barbara.
[2] Skoda Concern, 31600 Plzen, Czechoslovakia.

Margaret L. Hamilton,[1] *Martin A. Blotter,*[2] *and Danny J. Edwards*[2]

Evaluation of Miniature Tension Specimen Fabrication Techniques and Performance

REFERENCE: Hamilton, M. L., Blotter, M. A., and Edwards, D. J., **"Evaluation of Miniature Tension Specimen Fabrication Techniques and Performance,"** *Small Specimen Test Techniques Applied to Nuclear Reactor Vessel Thermal Annealing and Plant Life Extension, ASTM STP 1204*, W. R. Corwin, F. M. Haggag, and W. L. Server, Eds., American Society for Testing and Materials, Philadelphia, 1993, pp. 368–385.

ABSTRACT: The confident application of miniature tensile specimens requires adequate control over their fabrication and is facilitated by automated test and analysis techniques. Three fabrication processes—punching, chemical milling, and electrical discharge machining (EDM)—were recently evaluated, leading to the replacement of the previously used punching technique with a wire EDM technique. The automated data acquisition system was upgraded, and an interactive data analysis program was developed.

KEYWORDS: miniature tension specimen, specimen fabrication, EDM, tensile data analysis, automated data analysis, punching, chemical milling, automated data acquisition

Design of the structural components of nuclear reactors requires knowledge of the changes in strength and toughness that occur during irradiation at elevated temperatures. In order to supply design or surveillance data from limited experimental irradiation volumes, it has often been necessary to use miniaturized specimens. One of the smallest specimens currently used for determination of tensile properties is a sheet-type specimen 12.7 mm long and 0.25 mm thick [*1*]. Miniature specimens such as this have been a mainstay of the fusion materials program for many years and will continue to be used extensively in future research.

Periodic review and improvement in fabrication, testing, and analysis techniques are necessary to ensure that such specimens continue to produce valid data. The specimens were originally developed to be punched from sheet stock that had been rolled to the desired specimen thickness. The primary advantages of this technique were its rapidity and its low cost [*1*]. Specimens were fabricated on site without the delays associated with using an offsite vendor or the expense of machining or tooling up for each production batch.

The main disadvantage of fabrication by punching is that the act of punching produces unavoidable deformation in the specimen; even under optimum conditions, the best specimens are likely to exhibit some cupping. Although such problems are worst in very soft or very tough materials, their effects can frequently be ameliorated by performing the required heat treatments after the punching operation. Despite some difficulties with punched specimens, it was possible to generate reproducible results for the changes in tensile behavior caused by irradiation [*2*], particularly when punching was coupled with a polishing operation to deburr the specimens.

[1] Pacific Northwest Laboratory, Richland, WA 99352. Pacific Northwest Laboratory (PNL) is operated for the U.S. Department of Energy by Battelle Memorial Institute under Contract DE-AC06-76RLO 1830.

[2] University of Missouri, Rolla, MO 65401.

To produce good specimens consistently, the punch and die must be kept sharp. In addition, the clearance between punch and die must be appropriate for the material being punched. If the punch clearance and sharpness are not optimum, the cupping can be more severe and a burr will remain that must be polished away. Punches can be sharpened only a limited number of times and are subject to damage during handling. The choice of punching for specimen fabrication was therefore reevaluated. Two other techniques were considered potentially feasible on the basis of both cost and ease of fabrication: chemical milling and electrical discharge machining (EDM).

Chemical milling is a photo-chemical etching technique frequently used to make high-precision components for a number of industries and was attractive due to its low cost and relatively rapid turnaround time for the production of large numbers of specimens. It entails masking the surface, stripping the mask from the areas to be etched away, chemically etching away the undesired regions, and removing the mask. While part outlines can be achieved with a large degree of accuracy, the edges eaten away are known to be somewhat uneven and undercut depending on material, shape, size, and thickness.

EDM is the most expensive of the three techniques on a per-specimen basis, but held the most promise for distortion-free, reproducible specimens. EDM is a means of shaping conductive materials by arc erosion. It is particularly well suited to cutting internal shapes and delicate pieces. A tool is held a small distance from the workpiece while an electrical input builds up a charge and raises the voltage across the gap between the two, which is filled with a dielectric fluid. When the potential reaches a certain level, a discharge occurs between the closest points on the two surfaces. A minute amount of metal is melted and expelled in a globular form where the spark strikes the workpiece, leaving a small crater. This is repeated 20 000 to 300 000 times per second with the spark positioned by a servo-control device.

Control specimens, used for verification of the test system operation at the start of each testing sequence, were originally punched from solution-annealed 304 stainless steel. The fabrication of new control specimens was used as a convenient means of evaluating fabrication techniques. The specimen dimensions are shown in Fig. 1.

The automation of both data acquisition and analysis were of interest for a number of reasons, including the elimination of human error that can occur during the manual analysis of tensile charts. In addition, automated analysis makes it easier to compare data from different specimens by making it possible to plot data at the same scales. Earlier unsuccessful efforts at automated analysis attempted to build in sufficient judgement that the computer could determine the major tensile properties without user involvement. The current effort focused on a more flexible, user-interactive analysis that left all judgment for the interpretation of the tensile chart in the hands of the user.

Experimental Procedure

Specimen Fabrication Technique

Two punch and die sets of hardened D2 tool steel were obtained to allow consideration of different clearances that might be appropriate for different materials of interest. Tolerances of 0.0076 and 0.0254 mm (0.0003 and 0.001 in.) were selected for the two sets. The set with the larger clearance was used to punch specimens from the same sheet of 304 stainless steel that had been used to punch the earlier control specimens. Punched specimens were used in an as-punched condition because the polishing operation typically used to deburr the miniature tensile specimens is known to remove some of the artifacts of punching that were of interest here; polishing the specimens in this case would therefore have introduced additional variability.

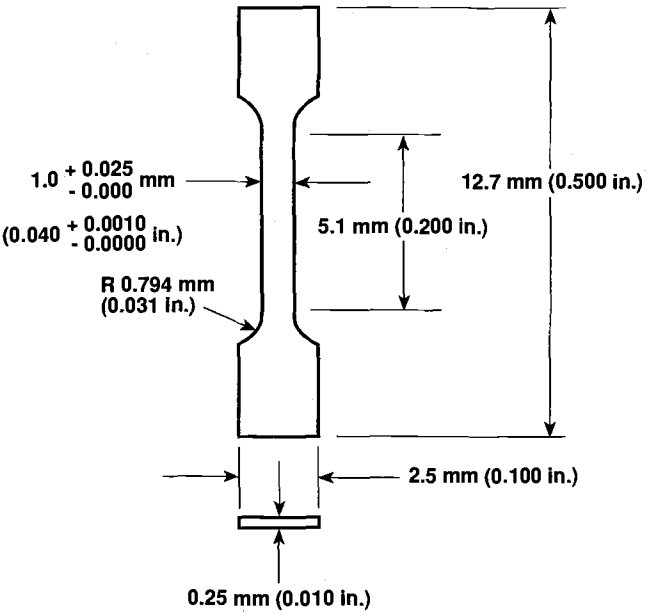

FIG. 1—*Dimensions of miniature tension specimen.*

The original drawing specified a width of 1.016 mm + 0.0254/−0.0000 mm (0.040 + 0.0010/−0.0000 in.). Only one company of the several contacted (Hutchinson Technology in Hutchinson, MN) was willing to make chemically milled specimens on a prototype basis, and then only after the tolerance on the gauge width was increased to +0.0381/−0.0000 mm (+0.0015/−0.0000 in.). Due to a paucity of the original 304 stainless steel sheet stock, only a small number of chemically milled specimens were made from the original solution-annealed sheet stock. A number of additional specimens were made from vendor-supplied 304 stainless steel to investigate more thoroughly the viability of the fabrication technique. The vendor indicated that the vendor-supplied 304 was in a "fully hardened" condition.

A wire EDM process was used to fabricate specimens at JW Industries of Albuquerque, NM, who claimed that dimensions could be held to within 0.0051 mm (0.0002 in.). The wire EDM process leaves only a small layer of disturbed metal and is therefore generally superior to other methods. Specimens were made only from the original 304 sheet stock. In anticipation of the success of the EDM technique, enough specimens were made to provide control specimens for a number of upcoming test sequences.

Three types of examinations were performed on each specimen type to determine the effect of production process on the quality of the specimens. The gauge dimensions were measured to determine the gauge measurements that would typically be used for calculation of the cross-sectional area in tensile tests. Optical microscopy was performed on transverse specimen sections to determine (1) whether there was evidence of microstructural change at the specimen edges, and (2) the variability in specimen cross section associated with each technique. Quantitative evidence for material distortion was obtained by comparing Knoop

hardness measurements taken on the transverse specimen sections at both the cut edge and in the body of the specimen.

Tensile tests were performed in a unique horizontal test frame [*1*] on each specimen type to determine the effect of the production process on the subsequent tensile data. The variability of the tensile data was evaluated for each production process. The tests were performed at room temperature at a strain rate of about 4×10^{-4} s^{-1}. The specimens are held in a wedge grip arrangement; one side of the wedge grip on each specimen end has a square grid of small teeth machined into it to improve the bite of the machine into the specimen tab ends. Load is monitored while the grips are being tightened to prevent the application of a tensile load prior to the start of the test.

Automation

Data acquisition was automated with the assistance of a National Instruments LAB PC board installed in an IBM PC/AT computer. The board was programmed in Quick Basic using the LABWINDOWS software system, also from National Instruments. It provides multichannel, double-buffered, analog input over a 10-V range (±5 V), with a maximum single channel acquisition rate of up to 62.5 Khz. The outputs of the load cell and linear variable differential transformer (LVDT), which are ±10 V, are fed through a simple voltage divider to reduce them to the range of the LAB PC board. Each output line includes a capacitive filter to minimize the fluctuations in the signal due to electrical noise. Since no extensometry is attached to the gauge length of miniature specimens such as these, the LVDT output that monitors crosshead travel is taken to be the specimen extension.

Data are acquired on two channels at sampling intervals ranging from 0.25 to 3 s. With a maximum of 4000 data points available per channel, the maximum test length over which data can be obtained at a 0.5-s sampling interval, for example, is 33 min. To assure that all test data are acquired, data acquisition is begun just before a test is started and continues until shortly after the specimen fails. A real-time display of the data is provided on the PC monitor, which shows the test trace graphically as well as the corresponding values of load and displacement in terms of both transducer voltage and the physical units of pounds and inches. In the event of a computer failure, a backup chart recorder output is also generated during the test.

An interactive program for analysis of the tensile data was also written in Quick Basic. It provides numerous options to edit and smooth the data at the discretion of the user prior to calculating the tensile properties of interest. The user chooses the slope of the straight line used to define the elastic portion of the trace. The user also has the freedom to accept or change the locations at which the program calculates the standard tensile values.

The data acquisition and analysis program was used to analyze the results of 56 tests performed on specimens irradiated to low doses in the Los Alamos Spallation Radiation Effects Facility (LASREF). The irradiation experiment is described in detail in Ref *4*. The specimens were made from both relatively strong and soft materials, including 316 stainless steel and several copper alloys. Yield strengths ranged from about 25 to 600 MPa, while ultimate strengths ranged from 150 to 700 MPa. The corresponding ductilities ranged from 0 to 55%.

Results

Specimen Fabrication Technique

Dimensional Measurements—Three measurements each of the gauge thickness and width were obtained [using a digital micrometer accurate to 0.00127 mm (0.00005 in.)] on five

specimens produced by each technique. The contact surfaces of the micrometer were a cone point and a knife edge, which allowed accurate thickness measurements to be made even on the punched specimens. The cone point was placed inside the punched "cup" while the knife edge was placed on the convex specimen surface to eliminate any potential distortion in the measurement caused by the burr. The micrometer was equipped with a ratchet stop, ensuring that the same contacting force was exerted for each measurement. The average dimensions and their variability are given in Table 1.

It is evident that while punching produced the most uniform measurements of specimen width, it also gave rise to the largest variability in measured gauge thickness, presumably due to the cupping of the specimen during the punching operation. Conversely, chemical milling produced the least distortion in the measured specimen thickness but the largest variability in gauge width. The latter result arises because chemical milling is accomplished by photographically etching the sheet stock from both sides, producing a slight bevel from each surface to the center of the sheet thickness. It is worth noting that the variability in width produced by chemical milling is more significant for hardened steel than for solution-annealed steel, most likely because the larger stored energy of the hardened steel increases the nonuniformity of the etching process.

Optical Metallography—The same five specimens of each type used for the dimensional measurements were sectioned, mounted, and polished to reveal a transverse section through the gauge section. Figure 2 shows the appearance of the edges on the transverse sections for each fabrication process. The punched edges shown in Fig. 2*a* are obviously somewhat deformed, although they are not in need of deburring, demonstrating that the clearance between the punch and die is reasonable for the 304 steel. The chemically etched specimens exhibit a wavy, nonuniform surface that appears to be more variable in the solution-annealed specimens (Fig. 2*c*) than in the hardened specimens (Fig. 2*d*). This observation is consistent with the tendency of finer-grained materials to etch more smoothly [*3*]. The EDM specimens shown in Fig. 2*b* exhibit a relatively good squared-off edge with a minimal amount of what is probably nonadherent debris in the vicinity of the edge. Such debris can result when material at the melted edge of the specimen does not fall away from the specimen completely. The debris was more visible when the metallographic mount was examined under the microscope than it is in the photograph. Neither the chemically milled nor the EDM specimens show evidence of microstructural change at the machined edges.

Hardness Measurements—Knoop hardness was measured (using a 200-g load) on the transverse metallography sections at both a specimen edge and the specimen center. Two measurements were made on each specimen at each location. The average hardness values are given in Table 1. The hardness measurements are almost identical at the edges and centers of the annealed specimens produced by chemical milling and by EDM. It is evident that the punching operation severely deformed the microstructure at the edges of the specimens, even for the relatively good specimens that were produced with the new punch and die. The punching operation also caused the hardness in the center of the annealed specimens to increase slightly relative to the center of the specimens produced by the other two techniques. It appears from the data that both EDM and chemical milling cause a small difference in hardness between the center and the machined edge. The reason for this decrease is not immediately obvious, although it is probably related to the relaxation of the microstructure allowed by the melting or etching that occurred at the specimen edges.

Variability in Cross Sectional Area Determination—Strength calculations require an accurate determination of the cross-sectional area of a specimen. Some error is typically associated with standard measurement techniques applied to punched specimens, given the tendency for such specimens to become cupped during punching and the potential nonuniformity of the deburring operation that usually follows punching. Several types of area

TABLE 1—*Average dimensions, hardness, and cross sectional area of miniature tension specimens.*

Production Process	Dimensions		Hardness		Deviation in Cross Sectional Area, %
	Thickness, mm	Width, mm	Edge, KHN	Center, KHN	
	PNL-Supplied Material (Solution-Annealed 304 Stainless Steel)				
Punching	0.259 ± 0.003	1.027 ± 0.001	357 ± 18	173 ± 5	3.8 ± 1.6
EDM	0.265 ± 0.001	1.035 ± 0.003	157 ± 8	163 ± 2	0.8 ± 0.4
Chemical milling	0.260 ± 0.001	1.025 ± 0.005	151 ± 5	161 ± 4	1.4 ± 0.9
	Vendor-Supplied Material (Hardened 304 Stainless Steel)				
Chemical milling	0.251 ± 0.001	1.033 ± 0.006	402 ± 9	428 ± 9	1.7 ± 0.4

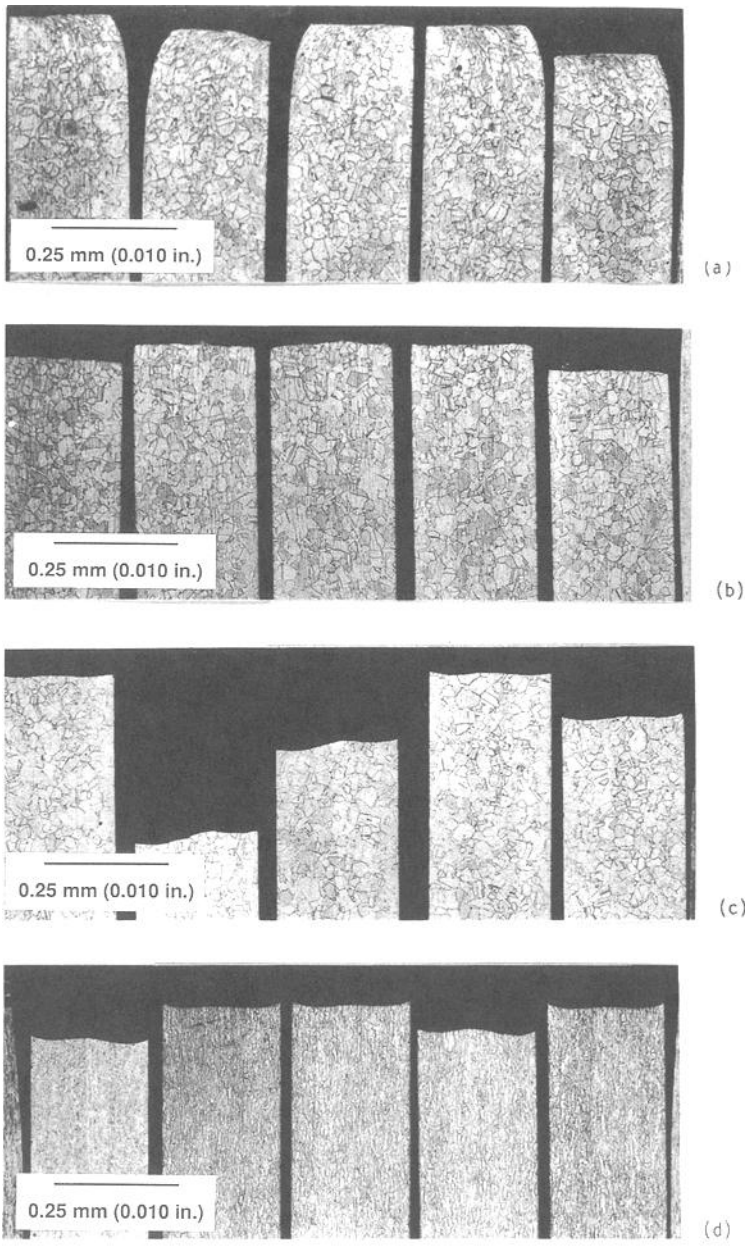

FIG. 2—*Transverse sections showing specimen edges for each fabrication type at* ×*100, ordered by decreasing edge quality:* (a) *punched,* (b) *EDM,* (c) *chemically milled (PNL-supplied material), and* (d) *chemically milled (vendor-supplied material).*

calculations were performed to assess both the variability in the actual cross-sectional area and the validity of the standard area calculation (i.e., the product of measured thickness and width) for each fabrication technique.

Photomicrographs at $\times 100$ of the transverse specimen sections shown in Fig. 2 were xeroxed to enlargements of $\times 150$. Cutouts from the xerox paper corresponding to the cross-sectional area at the maximum measured width were weighed and compared to cutouts corresponding to the actual cross-sectional area. The average percentage difference between the two represents the deviation in area, ΔA_0, that would occur for area calculations using the dimensional measurements obtained prior to a tension test, assuming that the measurement device contacts the points of greatest thickness. These deviations are also given in Table 1. The largest error in cross-sectional area was obtained with punched specimens, while the least was obtained with EDM specimens. The error in cross-sectional area associated with chemical milling was intermediate and was virtually the same for solution-annealed or cold-worked material. If the area deviation were large, as is the case for the punched specimens, the value $1 - \Delta A_0$ could be used as a multiplicative normalization factor that might provide a better determination of cross-sectional area than that calculated directly from the dimensional measurements if a value for ΔA_0 were obtained for each batch of specimens fabricated.

Tensile Data—Tension tests were performed on five specimens of each type. A nominal gauge length of 5.08 mm (0.2 in.) was assumed for all specimens. The tensile data are given in Table 2. While the ultimate strength of the punched specimens is almost identical to that of the EDM and chemically milled specimens, the yield strength is about 15% higher and the ductility is significantly lower.

The values of gauge width and thickness were determined for each specimen as the average of three measurements each. The measurements were performed between ball surfaces in a contacting LVDT device that was generally used to obtain such measurements. The dimensions obtained in this manner were not consistent with those obtained with the cone point and knife edge micrometer and exhibited more variability as well. The width measurement was particularly difficult to obtain between ball surfaces since the positioning is not stable and requires continuous operator contact, an undesirable condition with irradiated specimens. For these reasons, although the ball surfaces were used for the measurements on these specimens, the use of the ball surfaces for dimensional measurements was discontinued for future testing and replaced with a conventional micrometer.

Automation

The data acquisition system is quite reliable and reproducibly generates the error-free data files required by the data analysis program. The voltage dividers and capacitive filters consistently produce data in the ±5-V range with very low noise levels. The voltage signals typically fluctuate by about ±0.048 V, which corresponds to about 2.135 N (±0.48 lb) and 0.001 mm (±0.00005 in.) on the load cell and LVDT, respectively. Data acquisition is sensitive to other activities occurring on the same lab bench during testing; care must therefore be taken to limit simultaneous activities.

The smoothing technique was developed to eliminate the noise in the data, thereby simplifying the determination of the initial linear elastic slope. Each averaging iteration was applied to an entire curve, taking the average of three points at a time, advancing one point at a time; that is, the first averaged data point was the average of the first, second, and third data points; the second averaged data point was the average of the second, third, and fourth data points, and so on. Smoothed curves generated in this manner exhibited excellent agreement with the original data, as was frequently verified by plotting the smoothed and original data simultaneously.

TABLE 2—*Average tensile data determined on miniature tension specimens of 304 stainless steel.*

Production Process	Yield Strength, MPa	Ultimate Strength, MPa	Uniform Elongation, %	Total Elongation, %	Equivalent Cold Work Level, %
		PNL-Supplied Material (Solution-Annealed 304 Stainless Steel)			
Punching	306 ± 17	637 ± 6	46.6 ± 1.4	49.9 ± 1.4	3
Chemical milling	261 ± 3	630 ± 4	66.5 ± 3.3	73.2 ± 2.8	1
EDM	263 ± 9	626 ± 2	59.6 ± 1.7	68.0 ± 2.5	1
Previously punched	383 ± 17	700 ± 8	35.5 ± 2.9	38.5 ± 3.0	5
		Vendor-Supplied Material (Hardened 304 Stainless Steel)			
Chemical milling	752 ± 38	924 ± 10	7.1 ± 1.3	7.1 ± 1.3	25

Extraneous data acquired before the test started and after the specimens failed were easily deleted. The data traces for each specimen were typically averaged from one to four times to obtain smooth curves in which the linear elastic portions were easily defined.

The data obtained on the LASREF specimens (using the user-interactive program) are reported in Ref *4*. The tensile values calculated using the automated user-interactive program were compared to the values determined by manual analysis of the charts. These comparisons are shown in Fig. 3 for both strength and elongation, with the difference between the two values plotted as a function of the value determined using the program. The values of strength and elongation determined by using the program were generally quite consistent with the values determined manually, but they were calculated much more quickly. In addition, the values determined using the program were actually more accurate than those determined manually in the several cases exhibiting the largest deviations in Fig. 3, where the X-axis scale chosen for the chart recorder produced such compressed charts that the 0.2% offset fell within the thickness of the ink line.

Discussion

Specimen Fabrication Technique

The measured widths given in Table 1 for the 304 specimens are all within the specifications of the drawing shown in Fig. 1. In the worst case, a 1% variability in the thickness was introduced during the punching operation. From a dimensional standpoint alone, therefore, all three of the fabrication techniques could be considered acceptable. The punched specimens produced in this experiment, however, are known to be superior in quality to others in a variety of materials produced more typically using this equipment (see Fig. 4) [*2,5*] in that they exhibited virtually no cupping or burring. The latter occur because the clearance between the punch and die is not necessarily appropriate for other alloys, and the choice of punching for specimen production from a variety of alloys would require multiple punch and die sets and some effort at optimization of the clearances for the range of alloys of interest. Using a single punch and die set to produce specimens of all alloys of interest, it is likely that the dimensional quality of the specimens would degrade with time in a way similar to that observed previously. The necessary addition of a polishing operation to deburr punched specimens, as has been done previously to compensate for nonoptimum clearances, would introduce even more variability in specimen dimensions due to the difficulty of uniformly and reproducibly deburring specimens. Thus punching the specimens was considered the least desirable option from the standpoint of dimensional control and reproducibility for the wide variety of materials of interest.

If the sharpness of the punch and the clearance between punch and die are not optimized, the edges of the specimens can crack or be deformed excessively, potentially invalidating the tensile results. Both of these phenomena have been observed when use of the existing punch and die set was extended to punch materials for which they were not designed. Cracked specimens can lead to premature failure [*2*], while smeared edges represent regions of different microstructure with potentially different tensile behavior [*3*]. Post-fabrication heat treatment can be used to remove the microstructural effects of fabrication-induced deformation, but only if the final heat treatment of interest involves a normalization or annealing treatment. Such remediation is therefore not possible for materials in which the final condition of interest is cold worked.

Excessive smearing and cupping were observed when a punch and die developed for use on materials similar to 304 stainless steel were used to punch specimens from Nimonic PE16, a nickel-based superalloy strengthened by the precipitation of gamma prime. In the PE16 specimen shown in Fig. 4*a*, post-fabrication annealing and aging were applied. No difference

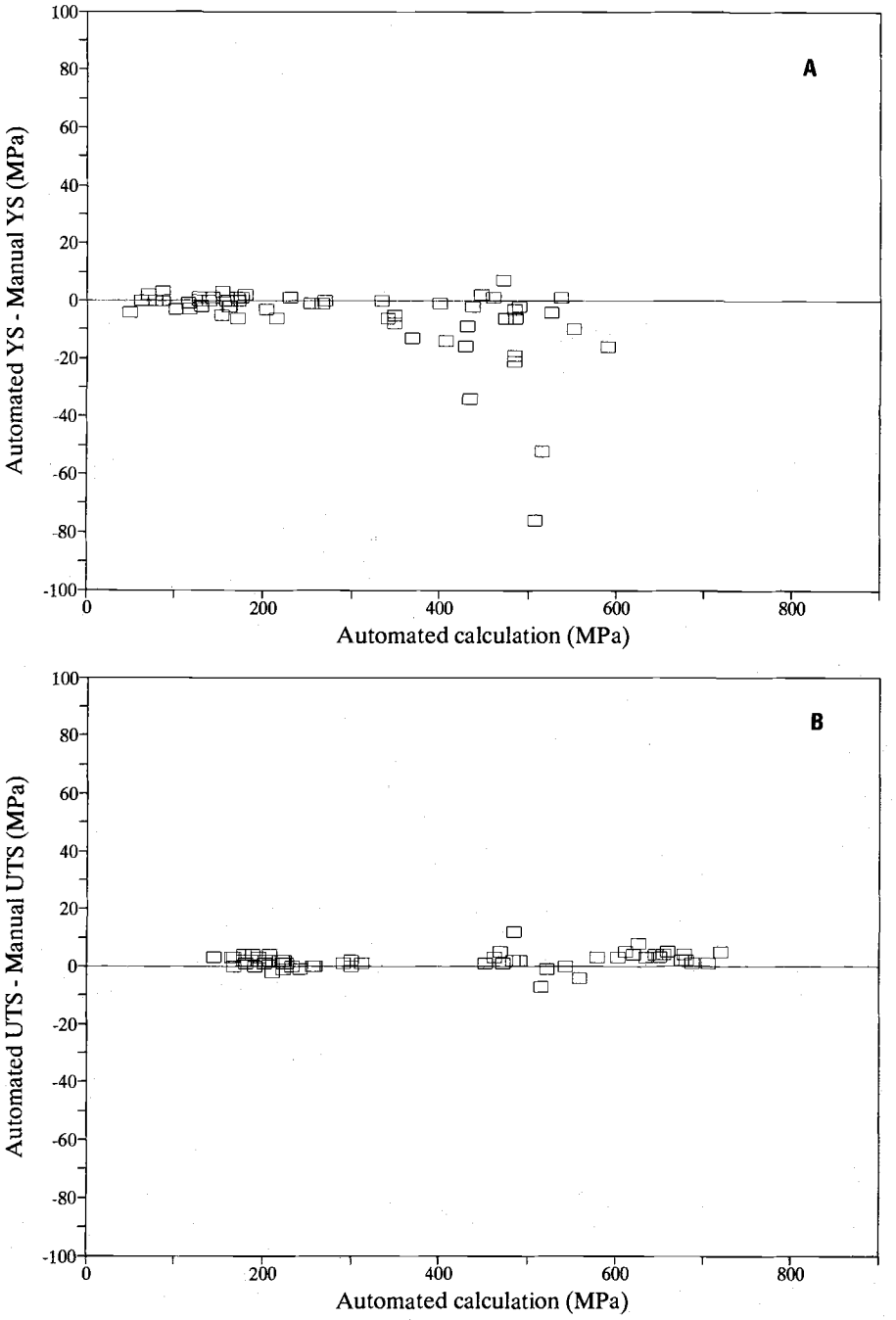

FIG. 3—*Comparison between tensile properties calculated manually and using the automated analysis program; the difference given on the ordinate was calculated in each case by subtracting the manually determined value from the value determined using the user-interactive analysis program:* (a) *yield strength variability,* (b) *ultimate strength variability,* (c) *uniform elongation variability, and* (d) *total elongation variability.*

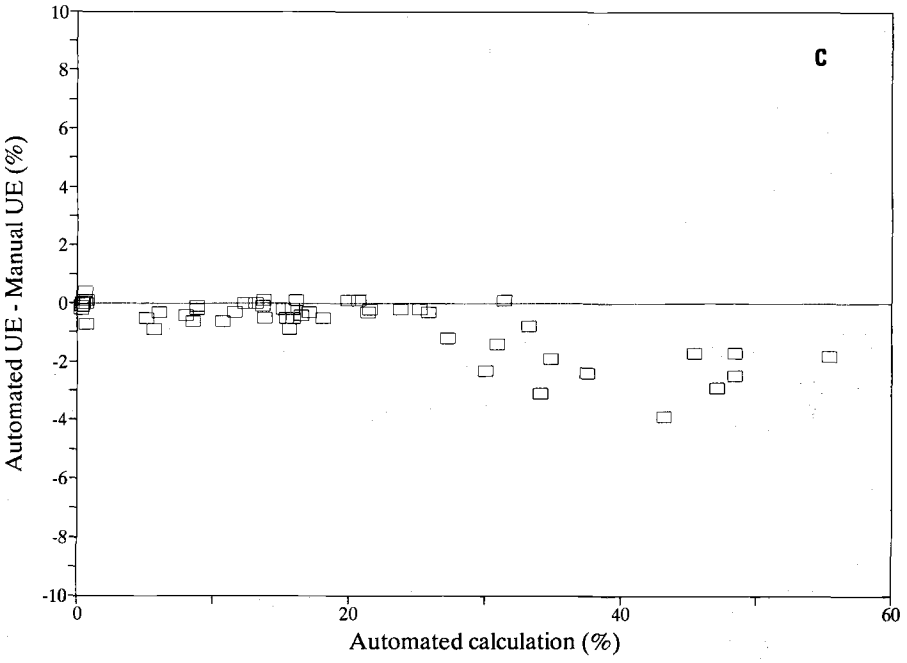

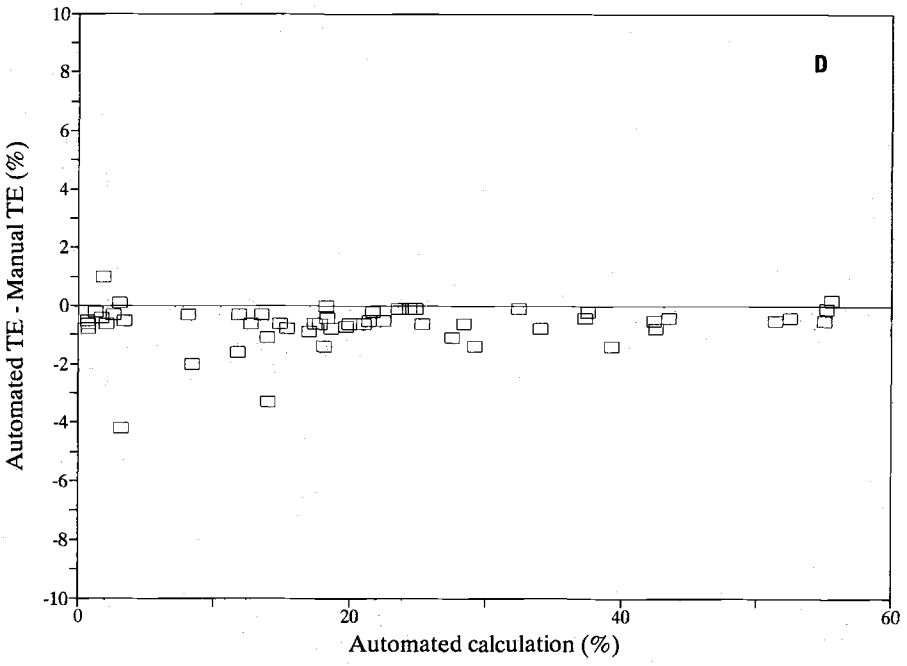

FIG. 3—*Continued.*

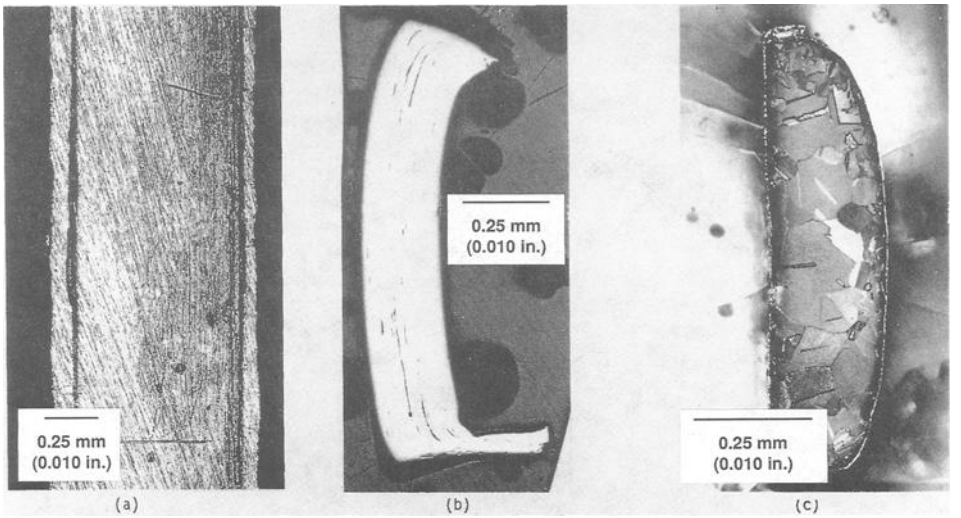

FIG. 4—(*a*) *and* (*b*) *miniature tension specimen of Nimonic PE16 showing* (a) *band delineating the size of the sheared zone that resulted from punching;* (b) *the degree of cupping that leads to the sheared zone;* (c) *Marz copper specimen showing nonuniformity of curved edges.*

in hardness was observed after heat treatment between the specimen edge and center, despite the obvious band that remained as an artifact indicating the size of the sheared zone produced during the punching operation [*3*]. The burr that existed prior to polishing in these specimens is shown in Fig. 4*b*.

While annealing treatments applied after the punching operation can restore the microstructure of specimens deformed during punching, soft ductile specimens tend to smear and cup excessively when they are punched, resulting in signficantly nonuniform cross sections. An example is given in Fig. 4*c*, which shows a deburred specimen of Marz copper with large differences between the two curved edges. The nonuniform, nonsquare edges shown in the specimens in Fig. 4 can lead to errors in cross-sectional area determinations of up to several percent.

The metallography shown in Figs. 2 and 4 and the hardness and tensile data given in Tables 1 and 2 demonstrate that punching is likely to alter the structure at the edges of the specimens. Punching could therefore only be considered acceptable if the specimens produced were heat treated following fabrication to remove the deformation remaining at the specimen edges after punching.

It is difficult to assess the effects of cracks that can be produced at the specimen edges; certainly it is impossible to remove them after they are introduced. One example of such cracks, produced in specimens of A212B, is given in Fig. 5 (before deburring) [*2*]. Although such cracks do not typically lead to errors in the determination of the cross-sectional area, they are likely to lead to premature fracture of the specimen.

The condition of the 304 sheet stock supplied to the vendors by PNL was not known precisely; the sheet stock was initally believed to be in a slightly cold-worked condition on the basis of tensile data obtained previously from miniature tensile specimens punched from the same sheet. The current data were evaluated to determine whether this belief was correct. The variability in the tensile data on the 304 specimens was assessed in terms of equivalent cold work level using Fig. 6 as follows: Trend lines were drawn through the strength data provided in Refs *6* and *7* as a function of cold work level. Only minimum values from the

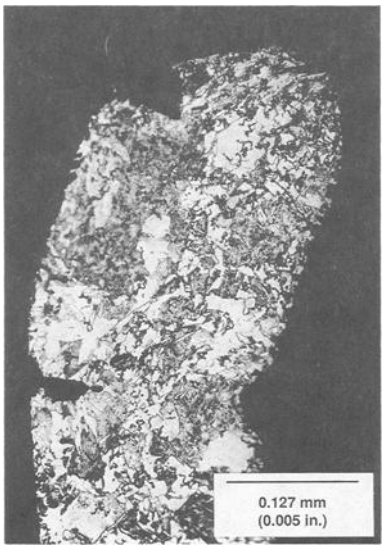

FIG. 5—*Cracks produced during punching of miniature tension specimens of A212B pressure vessel steel.*

ASTM specification were available for the solution-annealed condition (i.e., 0% cold work level). No information on variability was available for these data. The tensile values from the current experiment were then located on these trend lines; an equivalent cold work level was extracted as the abscissa coordinate corresponding to the yield strength on the trend line. The equivalent cold work values are given in Table 2. Error bars are shown only for those cases where the error was larger than the size of the data point itself. The fact that the ultimate strengths were somewhat higher than would be expected for the cold work level that was determined is consistent with the observations of earlier experimenters [*1*].

The tensile data generated in this experiment indicated that the sheet stock provided by PNL was probably nominally in the solution-annealed condition. The yield strength data from the EDM and chemically milled specimens suggest that the 304 sheet stock supplied by PNL was in a solution-annealed condition since the value given for the 0% cold work level in Fig. 6 is merely the ASTM specification for the minimum strength of 304 stainless steel. The tensile data on the new punched specimens imply that punching even the best quality 304 specimens achievable induces the equivalent of about 1% cold work, whereas the data on the old punched specimens imply that the punching process previously in use more typically induced the equivalent of about 5% cold work. In addition, more scatter was observed in the tensile data generated from punched specimens than from EDM or chemically milled specimens. Similar behavior is undoubtedly exhibited by other materials, particularly when the punch and die clearances are not optimized.

The final factor to be considered in the selection of an improved fabrication process was cost. Punching is obviously the cheapest if no optimization of punch and die clearances is explored, but the optimization that should be explored with this technique has the potential for being quite costly in both dollars and man-hours. It should be possible to punch specimens from any material and produce specimens of at least the same quality as obtained in the current work if the clearances are optimized. The cost for EDM specimens depends on the number of specimens being made, but appears to be roughly $10 each. Chemical milling

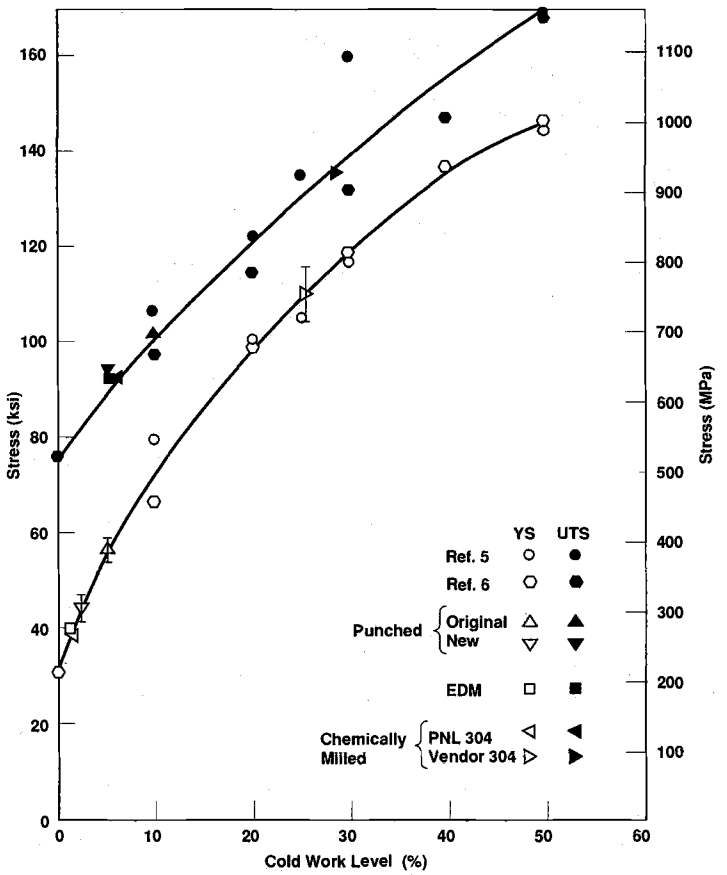

FIG. 6—*Assignment of equivalent cold work levels for specimens relative to strengths given in Refs* 6 *and* 7.

involved a set-up charge of about $500 and would cost about $500 for each future batch of specimens for lots of up to 1000 specimens. Since only small numbers of these specimens are typically manufactured at any one time, the cost savings potentially available with chemical milling would not be realized, and this process would conceivably be more expensive than the EDM technique. Thus the technique selected for the fabrication of all future miniature tensile specimens is EDM.

Automation

The use of the automated user-interactive analysis program speeds up the analysis of tensile data significantly. Data from a single test can be completely analyzed in about 10 min. This is a considerable improvement, particularly for those cases where manual interpretation of chart recorder output is not straightforward.

The automated determination of yield strength was typically within about 10 MPa of the manually determined yield strength. Larger deviations were observed only for highly compressed charts, which occurred only for specimens that were stronger than expected. The difference between the two types of ultimate strength values was much smaller, typically

less than 5 MPa, irrespective of the magnitude of the ultimate strength. This reflects the relative ease with which a maximum value can be chosen on a chart trace.

The automated determination of uniform elongation was generally within about 1% of the value determined manually. Larger differences were observed for those specimens that exhibited a long plateau at the maximum load, where it is difficult manually to pick out on a chart trace precisely the location of maximum load. The two types of total elongation values were typically within 2% of each other. The larger variability is attributed to the difficulty of establishing on a chart trace exactly when a specimen fails.

Conclusions

After three fabrication processes (punching, chemical milling, and EDM) were evaluated, the EDM technique was selected for future fabrication of miniature tension specimens. This choice was based on an evaluation that included dimensional inspection and optical metallography as well as hardness and tensile measurements. The automated data acquisition system was upgraded, increasing its reliability and minimizing the magnitude and frequency of electrical noise, and an automated, user-interactive data analysis program was developed to facilitate the analysis of the tensile data.

References

[1] Panayotou, N. F., Atkin, S. D., Puigh, R. J., and Chin, B. A., "Design and Use of Nonstandard Tensile Specimens for Irradiated Materials Testing," *The Use of Small-Scale Specimens for Testing Irradiated Material, ASTM STP 888,* W. R. Corwin and G.E. Lucas, Eds., ASTM, Philadelphia, 1986, pp. 201–219.

[2] Hamilton, M. L. and Heinisch, H. L., "Tensile Properties of Neutron Irradiated A212B Pressure Vessel Steel," *Effects of Radiation on Materials: 14th International Symposium (Volume II), ASTM STP 1046,* N. H. Packan, R. E. Stoller, and A. S. Kumar, Eds., American Society for Testing and Materials, Philadelphia, 1990, pp. 45–54.

[3] Doyle, L. E., Manufacturing Processes and Materials for Engineers, 2nd ed., Prentice-Hall, Englewood Cliffs, NJ, 1969.

[4] Heinisch, H. L., Hamilton, M. L., Sommer, W. F., and Ferguson, P. D., "Tensile Property Changes of Metals Irradiated to Low Doses with Fission, Fusion and Spallation Neutrons," *Journal of Nuclear Materials,* Vols. 191–194, 1992, pp. 1177–1182.

[5] Hamilton, M. L., "Precipitation Strengthening in a Nickel-Base Superalloy," master's thesis, Washington State University, Pullman, WA, 1985.

[6] Peckner, D. and Bernstein, I. M., *Handbook of Stainless Steels,* McGraw-Hill, New York, 1977.

[7] Moen, R. A. and Duncan, D. R., "Cold Work Effects: A Compilation of Data for Types 304 and 316 Stainless Steel," HEDL-TI-76005, Westinghouse Hanford Co., Richland, WA, March 1976.

DISCUSSION

G. Lucas[1] *(written discussion)*—

Comment 1: We use a SA 300-series austenitic material as a standard to monitor changes in the punch-and-die because it is so sensitive to changes in the punch. We see degradation in total ductility well in advance of changes in strength in either the stainless steel or carbon steel samples, and hence use this to signal time to resharpen punch and die.

[1] University of California at Santa Barbara.

Comment 2: The effects of punching increase with decreasing specimen size. Ours are somewhat bigger than yours and hence somewhat more forgiving to punch effects.

Question: Did you make hardness measurements on both sides of the specimens? If there is cupping, you can get differences between the convex and concave sides.

M. L. Hamilton, M. A. Blotter, and D. J. Edwards (authors' closure)—Yes, a specimen size difference could explain some of the decreased reliability we have experienced in punching tensile specimens, relative to your experience. And no, hardness measurements were not taken on both sides of the specimens. The Nimonic PE16 specimens referred to had already been normalized and given aging treatments after the punching was performed, so presumably the difference in hardness that you refer to would already have been obliterated. Hardness measurements were only taken on the specimen surface which exhibited the residual linear demarcation of the cupping problem, which was believed to be the side that had been concave.

E. Lucas[2] *(written discussion)*—You obviously don't use any elongation-measuring device mounted on the specimen, and what you actually measure is just machine crosshead displacement. Don't you think it's a significant approximation to derive from that quantity and not from the actual strain such tensile parameters as 0.2% proof yield strength and total elongation?

M. L. Hamilton, M. A. Blotter, and D. J. Edwards (authors' closure)—You are correct that the crosshead travel is used as a measure of specimen strain. While a more accurate measurement could obviously be obtained and would be desirable, both the residual radioactivity of the specimens and their small size preclude attachment of any device that measures specimen strain directly. The assumption that crosshead travel is a reasonable approximation of specimen strain is quite prevalent within the community of scientists testing miniaturized, radioactive specimens.

G. R. Odette[3] *(written discussion)*—How much does it cost to EDM a specimen?

M. L. Hamilton, M. A. Blotter, and D. J. Edwards (authors' closure)—It costs us between $6 and $10 to EDM a miniature tensile specimen.

A. Kohyama[4] *(written discussion)*—Although you didn't mention another process to produce specimens from bulk material, I would like to stress the importance of applying this method to precise microstructure-controlled materials. I mean, it is almost impossible to reproduce identical structure in already thinned materials to that produced in bulk specimen. My question is: (1) how to make this type of specimen from a bulk specimen? and (2) what is your concern when you use this type of specimen.

M. L. Hamilton, M. A. Blotter, and D. J. Edwards (authors' closure)—If it were judged necessary to EDM miniature specimens from bulk material, slices of the desired thickness would need to be made first. These could be EDM'd as well and the surfaces lapped if there were some concern with the presence of a recast layer on the specimen surfaces. We have not considered this an important variable since most of the materials we are interested in

[2] CISE Spa, P.O. Box 12081, 20134 Milano (Italy).
[3] University of California at Santa Barbara.
[4] University of Tokyo, Tokyo, Japan.

are produced by cold working, and the distribution of cold work through a piece will actually be more uniform in a thinner sheet than in a thicker plate that could be considered more representative of "bulk" material.

M. Valo[5] (*written discussion*)—When using EDM machining, are you afraid of loading the specimen with hydrogen?

M. L. Hamilton, M. A. Blotter, and D. J. Edwards (*authors' closure*)—In materials that are typically of interest to our programs, hydrogen is not an issue, so we have not been concerned with its introduction during EDMing of a specimen. Since we have begun to do some work on pressure vessel steels, which are known to be sensitive to hydrogen embrittlement, it is an issue that must be investigated.

[5] Technical Research Centre of Finland, 02150 Espoo, Finland.

William N. Sharpe, Jr.[1] *and Richard O. Fowler*[1]

A Novel Miniature Tension Test Machine

REFERENCE: Sharpe, W. N., Jr. and Fowler, R. O., **"A Novel Miniature Tension Test Machine,"** *Small Specimen Test Techniques Applied to Nuclear Reactor Vessel Thermal Annealing and Plant Life Extension, ASTM STP 1204,* W. R. Corwin, F. M. Haggag, and W. L. Server, Eds., American Society for Testing and Materials, Philadelphia, 1993, pp. 386–401.

ABSTRACT: Tensile stress-strain curves can be measured on specimens with an overall length of 3 mm using this new approach. The square test section of the specimens is 0.2 mm on each side.

The load frame is made from stainless steel by electrical discharge machining (EDM) and is 20 mm wide by 12 mm high and 3 mm thick. Load is applied and measured with an external translation stage and the load cell connected to the load frame with a fine wire. The load frame has wedge-shaped grips into which the ends of the specimen fit. The specimens have a "dog-bone" shape and are also manufactured by EDM.

Strain is measured directly on the specimen with laser-based interferometry from two tiny indentations placed in the specimen with a Vickers microhardness tester. Motion of the interference fringes emanating from the indentations is measured with two linear diode arrays and a microcomputer to enable real time strain measurement.

Preliminary tests have been conducted on brass samples to demonstrate the test technique. The relative uncertainty in stress measurement is high in these tests, but that arises from lack of precision in measuring the area. The relative uncertainty of strain is also high because of the crude mounts for the diodes. This paper demonstrates that the approach is feasible; straightforward refinements in the procedures will reduce the uncertainties.

KEYWORDS: small specimens, interferometry, mechanical properties, test methods

Several aspects of small specimen testing are more difficult than large specimen testing. Specimen preparation, handling, and gripping tend to be more complicated. Grain-size effects, inhomogeneities, and surface preparation become more important, although in some cases a study of them is the reason for using small specimens. Perhaps the most difficult aspect is the measurement of the strain in the specimen. Mechanical extensometers and foil resistance strain gages are too large for strain measurement on specimens with dimensions on the order of millimeters. Measurement of crosshead displacement is unsatisfactory because of deformation and slipping of the specimen in the grips. This paper describes a miniature tension test machine with the capability of measuring strain directly on the specimen.

Figure 1 is a photograph of the load frame of the testing machine, which is made from stainless steel by electrical discharge machining. Load is applied by a thin wire (visible in the figure) looped around the upper grip; this grip is supported by a thin cross member to maintain its alignment. The ends of the specimen, which has a "dog-bone" shape, fit into the upper and lower grips (the wedge-shaped slots of the grips do not pass all the way through the thickness). The specimen and machine are designed so that a strain of several percent can be attained before the upper grip hits the stops adjacent to the wire.

[1] Professor and senior student, respectively, Department of Mechanical Engineering, The Johns Hopkins University, Baltimore, MD 21218.

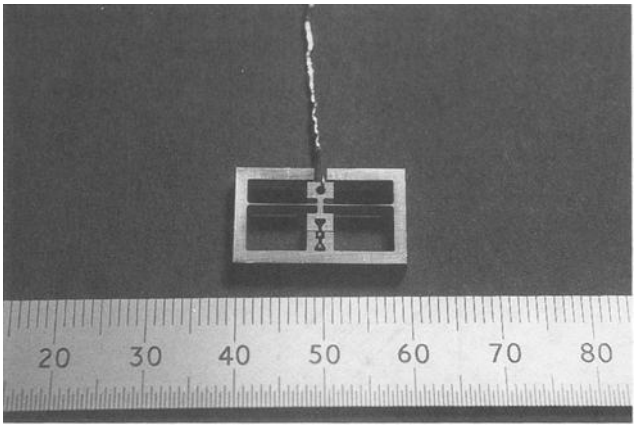

FIG. 1—*Photograph of the load frame of the miniature test machine. The scale is in millimeters, and the frame is 3 mm thick.*

The novel feature of this microsample testing machine is the capability of measuring strain directly on a specimen. Strain is measured with the interferometric strain/displacement gage (ISDG), which uses laser-based interferometry between two tiny indentations placed in the specimen surface. A laser is aligned onto the central portion of the specimen after it is placed in the load frame. Fringe patterns emanate from the indentations, and their motion is monitored to measure the strain in real time.

The laser-based system has been used by the senior author and others for various studies of strains and displacements. A review article of 1982 [*1*] covers mostly work of the author, but the number of users has increased since then. This paper describes the first application of the technique to very small specimens. The design, construction, and use of the microsample test machine is described in some detail. However, only two specimens have been tested; hence, the results must be regarded as preliminary. The objective of this work was to demonstrate that strain can be measured directly on small tension specimens. That has been accomplished, we believe, and the next step is a more thorough study of the reproducibility, size effects, etc. for particular materials.

A mechanical testing machine consists of three parts: a load frame for gripping the specimen and deforming it, a means of measuring the applied forces, and a means for measuring the resulting strains. Since the measurement system centers around the ISDG, the next section briefly explains its basics. Design and manufacture of the microsample load frame is then presented, followed by a description of the specimen. The system for deforming the specimen and measuring the load is then described. Next, the microcomputer-controlled system for monitoring the fringe motions and thus determining the strain is presented, rather briefly because it is a relatively mature technology. The demonstration tests are then presented in detail. Finally, advantages, disadvantages, and possible improvements are discussed.

Principle of the ISDG

The interferometric strain/displacement gage or ISDG is very simple in concept, and the basic principle is briefly explained in this section. A more thorough explanation is available in Ref *2*, which also includes practical considerations.

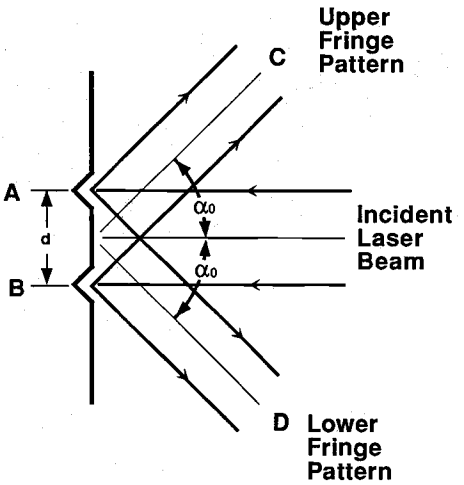

FIG. 2—*Schematic of the ISDG. Reflective indentations are located at A and B.*

The basic optical principle underlying the ISDG is illustrated schematically in Fig. 2. Two tiny indentations are made in the surface of a specimen at positions A and B with a Vickers microhardness tester. When a coherent, monochromatic light source is incident upon them, the reflected light is diffracted because of the small size of the indentations. The two cones of light emanating from A and B intersect and form interference fringes in space at positions C and D. Two other interference patterns are formed since the indentations have four sides, but these are not used in uniaxial strain measurement. (Biaxial strains can be measured by using three indentations [*3*].) As the distance between A and B changes because of loading of the specimen, the fringes at C and D move and this motion is related to the relative displacement between the two indentations.

Two typical indentations are shown in Fig. 3 along with a photograph of a fringe pattern such as would be seen at C or D in Fig. 2. The indentations in Fig. 3 are 25 μm on a side and the distance between them is 100 μm. It is this small size of the "gage" that enables the ISDG to be used for measuring strain on small specimens.

The optical principle is simply Young's two-slit interference phenomenon from elementary optics [*4*] except that it is in reflection from two indentations instead of transmission through two slits or pinholes. Both diffraction and interference are involved to create the fringes. First, the impinging light is diffracted by the reflecting facets of the indentations. The wavelength of a He-Ne laser is 0.6328 μm, whereas dimensions of the reflecting facets are on the order of 20 μm; this ratio of wavelength to "slit width" of ~0.03 is small enough to cause appreciable spreading by diffraction. Second, these reflected rays of light interfere because they are coherent and have been shifted along the lines between B and C or A and D by an amount $d \sin\alpha$, where d is the distance between the indentations and α is the angle between the incident laser beam and the observation positions C or D. If one places a screen at C or D, straight, parallel fringes will be seen because the angle α changes slightly at different positions on the screen. The governing equation is therefore

$$d \sin\alpha = m\lambda \tag{1}$$

where λ is the wavelength of light and m is a positive or negative integer.

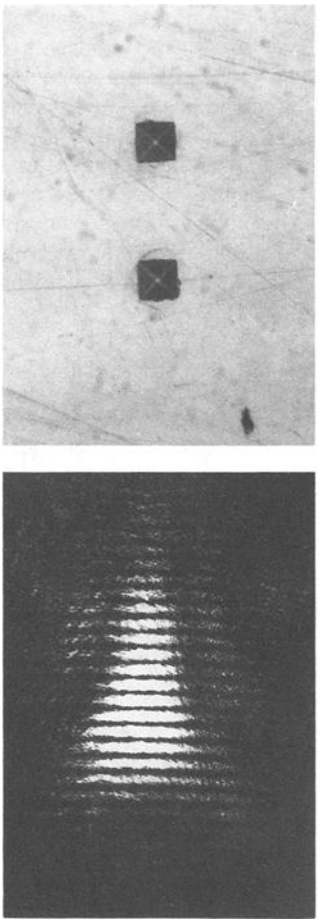

FIG. 3—*Photomicrograph of a set of indentations* (top) *and a photograph of an interference fringe pattern* (bottom). *The centers of the indentations are 100 μm apart.*

The shape and structure of the fringe pattern in Fig. 3 shows these two aspects of the optical phenomenon. The triangular overall shape of the pattern arises from diffraction from the triangular reflecting facets of the pyramidal indentations. The fringe pattern inside it arises from the interference effect and moves as the distance between the indentations changes. This point is important; it is the motion of the fringes and not the change in spacing between them that is monitored in the ISDG. The spacing between fringes does change somewhat as the indentations move, but this is considered in the calculations of relative displacement.

The equation giving the relative displacement, Δd, from the fringe movements, Δm, is

$$\Delta d = \Delta m \frac{\lambda}{\sin\alpha_0} \tag{2}$$

The angle α_0 is the angle between the incident laser beam and a fixed measurement position (at C or D in Fig. 2) and is approximately 42° because of the shape of the Vickers diamond.

So the "calibration factor," $\lambda/\sin\alpha_0$ is ~1 μm. A fringe shift of one, i.e., a fringe moving to occupy the position of a neighbor, corresponds to a relative displacement between the two indentations of ~1 μm.

It is obvious that if the specimen moves in a rigid-body manner, the fringes will also move. It is very difficult to construct a test machine in which the specimen does not move vertically as the load is applied, so that motion must be accounted for. If the specimen moves up (see Fig. 2), then the fringe pattern at C moves away from the incident laser beam and the one at D moves toward the incident beam. If fringe motion toward the incident laser beam is defined as positive, then the vertical rigid body effects can be averaged out. This definition of sign means that increasing distance between the indentations is recorded as positive. Other rigid-body motions are not averaged out; however, they can be minimized by a carefully aligned test machine.

So, the equation that is used to measure strain, $\Delta d/d_0$, with the ISDG is

$$\epsilon = \frac{\Delta m_1 + \Delta m_2}{2d_0} \frac{\lambda}{\sin\alpha_0} \tag{3}$$

where Δm_1 and Δm_2 are the fringe movements at the two observation positions and d_0 the original gage length between the two indentations.

If the gage length is 100 μm and a fringe movement of one spacing is 1 μm, then a strain of 1% will have been measured. That is too coarse for elastic strain measurement, so a fringe measurement system that can resolve fractions of a fringe movement is needed. One such system is described below after other aspects of the microsample testing machine are presented.

The ISDG can indeed be used to measure strain in a test specimen. Figure 4 shows the results of a tension test in which strain in an aluminum specimen was measured by the ISDG, a clip gage, and two foil gages. The specimen, cut from sheet material, was 2.5 mm thick and 25 mm wide with the ISDG indentations 200 μm apart on one edge, the 25 mm clip gage on the other edge, and one foil resistance strain gage on each flat side. The results of Fig. 4 show that the presence of the two indentations does not adversely affect the local strain field.

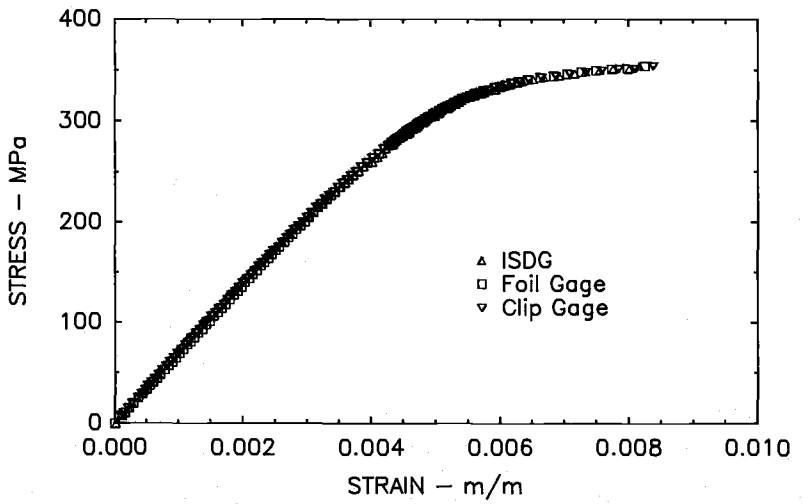

FIG. 4—*Stress-strain curve of a 2024-T3 aluminum specimen with strain measured by three methods.*

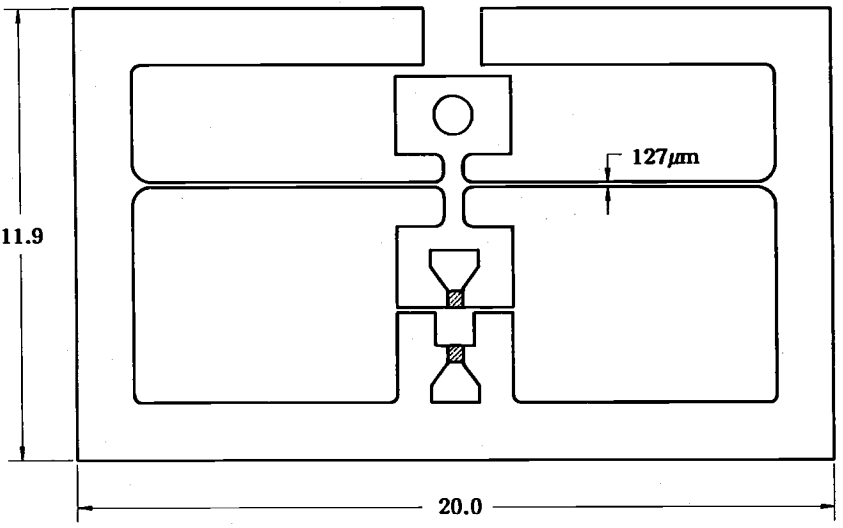

FIG. 5—*Drawing of the load frame of the test machine, which is 3 mm thick. Dimensions are in millimeters and micrometers.*

Microsample Load Frame

Figure 5 is a drawing of the microsample load frame, and Fig. 6 is a magnified view of its grips. These drawings are to scale, and only representative dimensions have been given to make the figures neater. The thickness of the load frame is 3.0 mm.

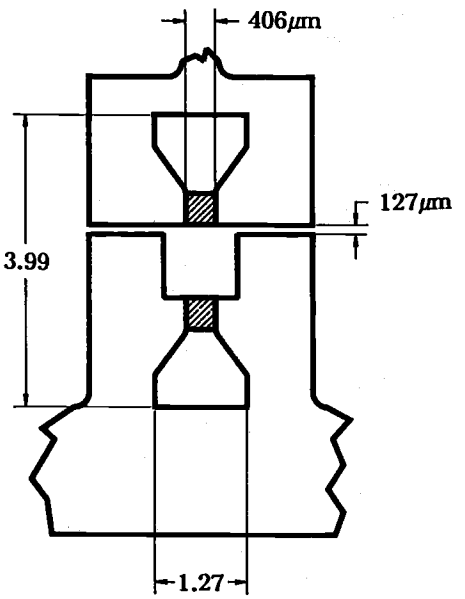

FIG. 6—*Detail drawing of the grips of the load frame with dimensions in millimeters and micrometers. The shaded areas are "shelves" for the specimen.*

The concept is quite straightforward. A "dog-bone" shaped microsample is placed in the wedge-shaped grips. A thin wire is fastened through the hole in the upper grip and pulled to displace it; load in the wire is measured. The upper grip is held in place laterally by the thin cross member. Permanent damage to the load frame is prevented by the two stops above the upper grip.

Referring to Fig. 6, note that the upper and lower wedge-shaped regions are punched completely through the load frame's thickness. The cross-hatched areas are not; they are machined down 1.60 mm. The cross-hatched areas provide a "shelf" for the specimen to rest upon. One simply drops the specimen, which is approximately 3.1 mm in total length, into the slotted grips. The tolerances on the manufacture of the grip portion of the load frame and on the specimens must be close enough that the specimen is fully engaged in the grips before the stops are hit.

It is the force applied to the ring of the load frame, not the force applied to the specimen, that is measured. The measured force, F, is equal to the force on the specimen, P, plus the force, C, necessary to displace the cross member an amount corresponding to the deformation of the specimen. If there is no specimen in the load frame, $F = C$ and the stiffness of the crossmember, K_{cm}, can be determined if its deflection, δ_{cm}, can be measured. This deflection could be measured by the ISDG with indentations placed across the 127-μm gap in Fig. 6.

The force in the specimen, P, can be written as

$$P = K_{sp} \times \delta_{sp} \tag{4}$$

where K_{sp} is its stiffness, δ_{sp} is its displacement, and the specimen remains elastic. Therefore, the measured force in an elastic specimen is

$$F = P + C = K_{cm} \times \delta_{cm} \tag{5}$$

The elongation of the specimen and the displacement of the cross member are the same, i.e., $\delta_{sp} = \delta_{cm}$; therefore Eqs 4 and 5 show that

$$P = \frac{F}{1 + K_{cm}/K_{sp}} \tag{6}$$

So there are two approaches that can be taken to get an accurate measurement of force in the specimen:

1. Measure the displacement of the cross member while simultaneously measuring the strain of the specimen and compute the force from $P = F - K_{cm}\delta_{cm}$.
2. Design the load frame so that K_{cm}/K_{sp}, is small. Of course these calculations are based on elastic behavior; the stiffness of the specimen decreases in the plastic region.

The first approach could be taken by using two ISDG systems with indentations on the specimen and across the grips. Overlapping of the fringe patterns could be prevented by tilting one of the sets of indentations [5].

The second approach has been taken here by making the cross-member pieces relatively long and thin. Calculations from a "strength-of-materials" approach show that the initial stiffness ratio is approximately 0.0012 for the load frame and brass specimen used. The error in specimen force measurement is only about 0.12% in the elastic region of these preliminary tests.

Despite the small cross-sectional area of the specimens, loads on the order of several pounds may be required for yielding. If the specimen were to fail, the cross member could be subjected to a large displacement and possible damage, but this damage is prevented by rigid stops above the cross member. Finite-element and strength-of-materials calculations indicate the cross member can withstand a deflection of 225 μm at the center before the onset of permanent damage. Considering tolerancing and the conservative calculations, the gap between the ring and stop is 300 μm in Fig. 5. Small pieces of shim stock can be inserted to reduce the gap to a smaller size.

The current load frame, shown in Fig. 1, was manufactured at The Johns Hopkins Applied Physics Laboratory using ram and wire electric discharge machining (EDM). The ram EDM operates by sinking a die into a blank; electric discharge between the graphite die and conducting blank essentially erodes away the material leaving a very smooth and stress-free surface. The wire EDM operates on the same principle in a manner similar to a bandsaw. A 100-μm-diameter wire was used to cut the entire testing machine. The ram EDM was used to cut out the 1.6-mm-deep depression in the grips, creating the shelves on which the specimen rests. The load frame was designed with a drafting program which enables direct transfer to the numerically controlled EDM machine. Modifications of the load frame to accommodate a particular specimen are therefore easy.

Specimen and Material

Figure 7 is a drawing of the specimen. Note that the test section is cut with a rather large radius in order to constrain plastic yielding to the central region. Measurements of the strain are made directly on the specimen by applying the two indentations in the polished surface at the minimum cross section. The width of the minimum cross section is 200 μm, and the thickness is approximately the same. The distance between the indentations is 200 μm for higher strain resolution.

The test section of the specimen is approximately 100 times longer than required for a snug fit in the load frame grips. This allows for a tolerance of 25 μm on each mating surface. The specimens each fit easily into the grips; the manufacturing process exhibits excellent reproducibility.

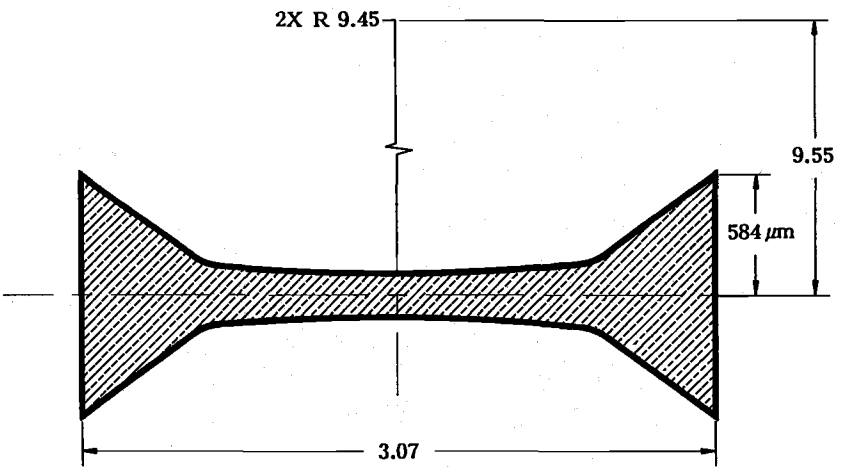

FIG. 7—*Drawing of the specimen; dimensions are in millimeters and micrometers.*

For these preliminary tests, a material with a smooth transition into the plastic region was needed. The ISDG system, as used here, takes strain data every 4 s and there was concern that it would be unable to follow the sudden extension associated with a yield point such as observed in a mild steel. A different version of the ISDG can take data at the rate of 10 points per second [*6*], which would be adequate for testing materials with sharp yield points.

Brass shim stock, 250 μm thick, was annealed for 1 h at 300°C to soften it without increasing the grain size, which was approximately 20 μm. The small piece of material was then polished using typical metallurgical sample preparation techniques with the final polish a 0.25-μm diamond paste. Specimens were cut out using the wire EDM machine.

Figure 8 is a photograph of a specimen while it is mounted in the load frame (the load frame is not visible because it is out of focus). The two indentations are visible in the center of the test section, but the ends of the specimen are not shown. There are two scratches on the left-hand side of the specimen.

Load Application and Measurement

An overall view of the microsample testing setup is given in Fig. 9. Note that the load frame, load cell, and displacement stage lie in a horizontal plane. On the right is a translation stage used to displace the end of the load application linkage. It has a resolution of approximately 1 μm and is an X-Y-Z stage; of course, only one translation axis is needed.

The translation stage is connected to the load frame through a load cell by a fine wire. The load is measured by an 18-cm-diameter spring steel load cell. A small framework supports the load cell at three places with sewing thread to raise the load cell to the same level as the translation stage and load frame. Four foil strain gages, two on the interior surface of the loop and two on the outside surface, are mounted on the ring. They are connected to a strain gage signal conditioner and sent directly to the microcomputer monitoring the ISDG system. The resolution of the load cell is approximately 0.01 N, and it was calibrated with hanging weights. The load cell undergoes a deflection across its diameter

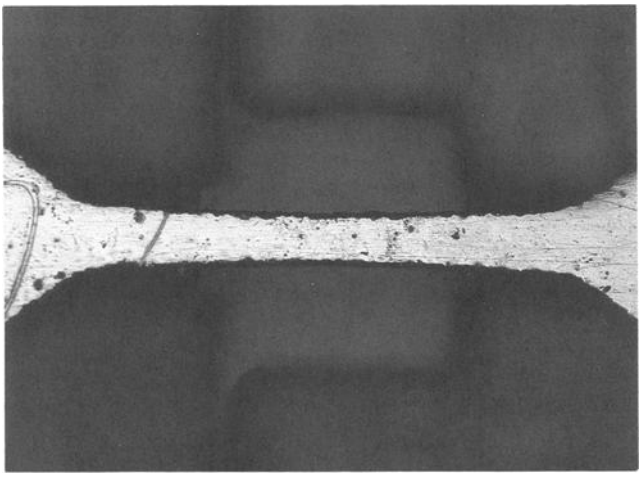

FIG. 8—*Photograph of a brass specimen mounted in the test machine. The width of the specimen is 200 μm at the center, and the two indentations are visible in the central portion.*

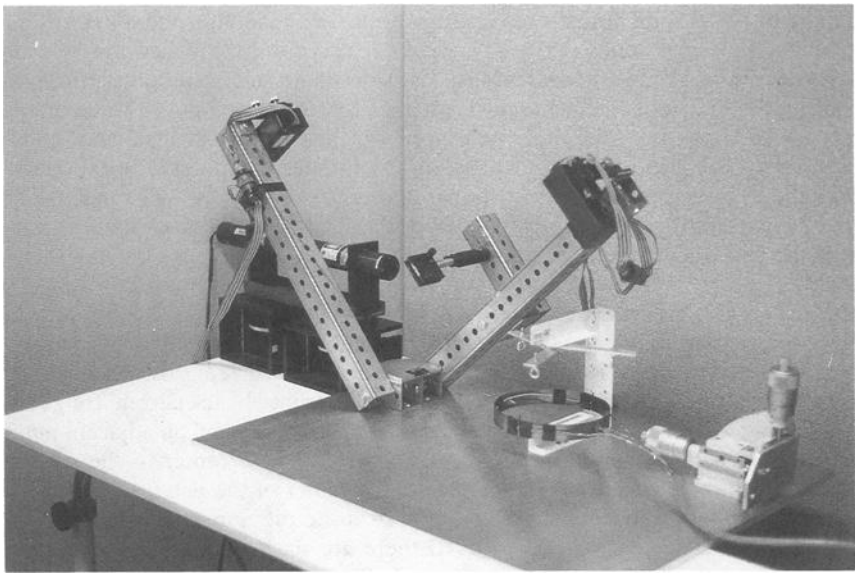

FIG. 9—*Photograph of the test machine. The load frame is mounted on a small platform on the left edge of the aluminum base plate. The translation stage for elongating the specimen is on the right edge of the base plate; it is attached to the load ring which is, in turn, attached to the load frame. The 10-mW laser is on the left, and the two diode arrays are mounted in plastic boxes attached to the support rods.*

of 12 mm when loaded to its design capacity of 45 N. This deflection leads to a slight nonlinearity in the load-voltage relation which could be corrected in the data reduction.

ISDG System

Figure 9 shows the ISDG system on the left of the table. The beam from a 10-mW He-Ne laser is directed downward onto the microsample test machine by a steering mirror and stage. The two pieces of square tubing at 45° hold linear diode arrays mounted inside plastic miniboxes and attached to small X-Y stages.

The linear diode arrays have 512 elements on 25-μm centers; each element is 2.5 mm wide. Each diode is mounted on a satellite board which carries control and preamplifying circuitry. A master circuit board for each diode contains the scanning circuitry, and the two boards are mounted on a chassis along with the necessary power supplies; this component is not visible in the figure but the connecting cables are.

The geometrical setup allows 5 to 6 fringes to impinge on each diode. That number is determined by the distance from the specimen to the diode and by the spacing between indentations. Because of the diffraction, the width of the middle of the fringe pattern (parallel to the fringes; see Fig. 3) is approximately 10 mm wide at the diodes. The fringe pattern can be compressed by mounting a cylindrical lens in front of the diode with its axis perpendicular to the fringes. This not only increases the intensity of the pattern but compresses the speckles that are seen in Fig. 3. Speckle patterns add noise to the fringe signal because they are on the same order of size as the small dimension of the individual diode elements. A technique used to reduce the speckle is to cover the diode with a layer of diffuse cellophane tape; that smooths the pattern incident on the diodes. The X-Y stages allow positioning of the diodes in the middle of the fringe patterns.

Scanning of the two diodes is controlled by a function generator and a microcomputer. The function generator sends out a TTL clock signal whose frequency can be varied to adjust the output from the diodes because the slower the scan, the longer the radiation impinges on the individual element and the higher the voltage output. The second master board is slaved to the first; the first one triggers off the TTL clock signal and sends out a trigger signal to both the second master board and to the microcomputer. The data acquisition board in the microcomputer records the two patterns sequentially—Channel 1 and then Channel 2—and also records the voltage from the load cell. A two-channel oscilloscope monitors the two fringe pattern signals during the setup phase.

Once the voltage as a function of diode element location is temporarily stored in the microcomputer, it is processed to generate a strain data point. This was accomplished by a FORTRAN program that finds the three middle minimums in each fringe pattern. The relative fringe motion, Δm, is calculated by comparing the current position of the middle minimum with its previous position and dividing that difference by the current fringe spacing, which is computed as the distance between the middle minimum and an adjacent minimum. If the minimum being followed moves too far away from the center of the pattern, the program shifts to the adjacent minimum nearest the center of the pattern.

In the above discussion, "minimum" is inferred to be the number of a diode element, i.e., a minimum at element No. 267, say. If there are six minimums in the 512 element array, the spacing between them is approximately 85. Therefore the least-count resolution of a fringe motion is 1/85. Taking the calibration constant $\lambda/\sin\alpha_0$ as 1 μm and an indentation spacing of 200 μm, this translates into a least-count strain resolution of 1/85 divided by 2 × 200 (see Eq 3) or 30 microstrain, which is acceptable, but a more sophisticated approach is taken. Each minimum is determined by fitting the raw data surrounding it (ten values from individual elements on either side for a total of 21 points) to a parabola and computing the minimum of the fitted curve. This procedure increases the resolution of Δm by a factor of 100 and produces a least-count strain resolution of 0.3 microstrain. The actual strain resolution is not this small; there are other factors such as optical and electronic noise that contribute. As will be seen, the strain resolution of the ISDG is more than adequate in this setup.

The program used to monitor fringe motion is also being used for creep strain measurement at 250°C [*7*]. For those tests, there is some degradation of the fringe pattern as the specimen oxidizes over the 1000-h test. The program was therefore arranged to store both fringe patterns associated with each data point. Furthermore, all the data were written to a diskette as each point was taken. This slows the sampling rate down so that a data point is taken only every 4 s.

The characteristics of the ISDG strain measurement as it is used here are:

1. *Resolution*—1.0 microstrain is a conservative estimate. One bit output of strain corresponds to 0.3 microstrain.
2. *Sampling rate*—A sample every 4 s; but rates of 10/s are routinely used in other applications. ISDG measurements on fatigue specimens cycling at a rate of 30 Hz have been taken using a pulsed laser diode [*8*].
3. *Range*—The range is limited by the deformation and rotation of the grains where the indentations are placed. Typically, 5 to 10% strain can be recorded directly on fine-grained specimens in test machines which permit large displacements.
4. *Relative uncertainty*—Strain uncertainty is approximately 6% in this setup; normally it is ±3% [*6*]. The original gage length can be measured to ±1%, and the relative uncertainty in locating minimums is also ±1%. The angles, α_0, are measured to only ±2° in the crude support frame; that contributes ±4% to the uncertainty.

Preliminary Tests

Preliminary tests on two brass specimens are presented in Figs. 10 and 11. Figure 10 is actually two tests, the first one loading the specimen from its initial unstrained state. That test was terminated at a little more than 0.5% strain without recording the unloading. The second test was simply a repeat of the first one; the data have been shifted along the strain axis to coincide with the last point of the first test. The second test stopped when the strain increment was too great for the ISDG system to follow. The specimen was elongated by turning the micrometer screw by hand. That is an uneven process which is exhibited in the figure by the irregular spacing of the data points in the plastic region.

When the specimen is first loaded, it must become seated in the grips. As shown in the figure, a small initial stress was applied to make initial contact between the wedge-shaped ends of the specimen and the sides of the grips. Another specimen was pulled without the ISDG measurement but with the motion observed through a low power stereo microscope. That specimen made first contact between one of the wedge sides on each end and the side of the grip. Then a second side made contact on one end, followed by final contact of the fourth side on the other end. At times the sides of the wedge ends of the specimen slide along the sides of the grips; this sliding contributes to the wavy nature of the initial portion of the stress-strain curve. Note that the elastic region is much smoother in the second test because the specimen is already seated in the grips.

Figure 11 shows the results from the second specimen, which was subjected to one continuous load-unload-reload cycle. Again, there is some waviness in the initial loading, but the unloading is very linear. The reloading curve is similar in shape to the initial loading curve. There is a marked hysteresis in the unloading-reloading cycle. That hysteresis is not believed to come from the load cell, which was cycled several times during its calibration. Yet, the stress level in the plastic region is higher upon reloading in both Figs. 10 and 11.

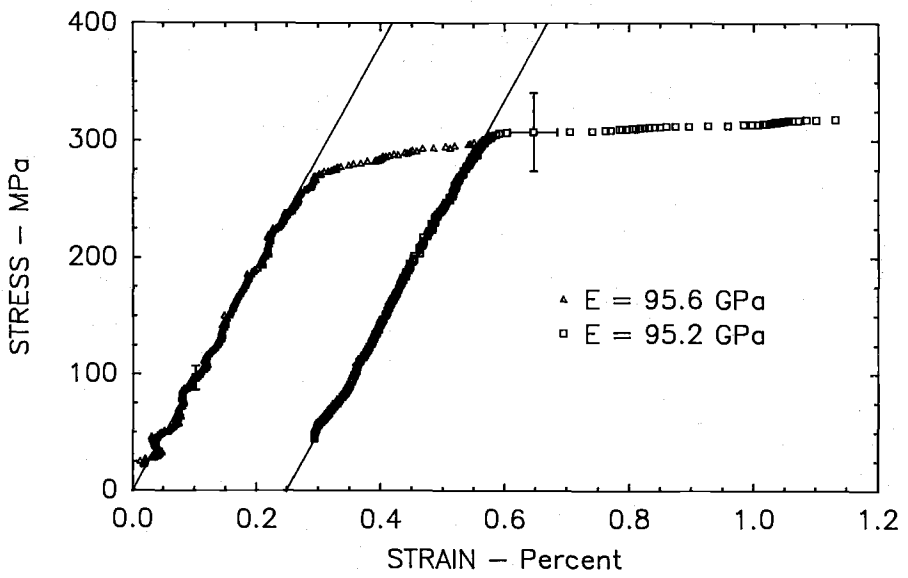

FIG. 10—*Stress-strain curve of a brass microsample. The specimen was loaded to approximately 0.5% strain and then unloaded without recording. It was then reloaded and elongated to over 1% strain. Uncertainty bars are shown at 0.1 and 0.6% strain.*

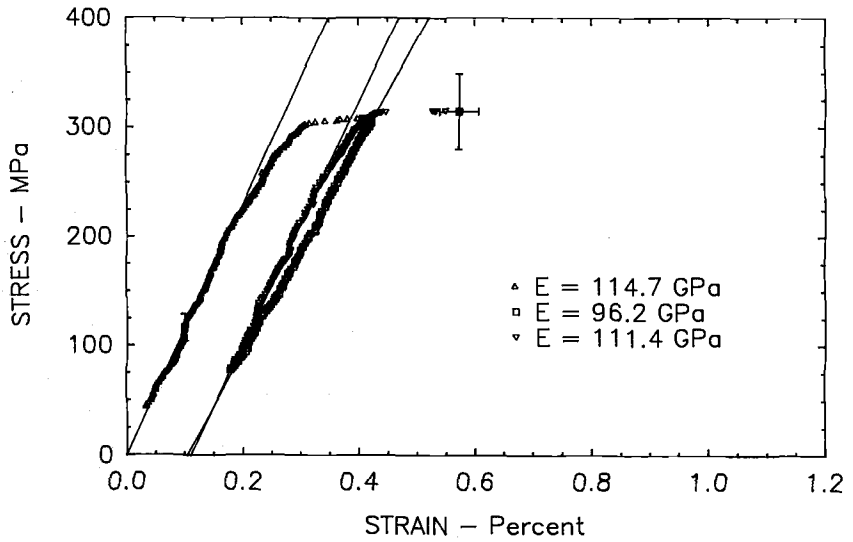

FIG. 11—*Stress-strain curve of a second brass microsample. The specimen was loaded to approximately 0.4% strain and then unloaded and reloaded. Uncertainty bars are shown at 0.1 and 0.6% strain.*

When tests are set up for cyclic strain measurement with the ISDG, elastic tests are always run to check out the system before loading into the plastic regime and show no hysteresis in the strain measured. The hysteresis appears to be a material response.

The elastic modulii are given on the plots. A typical value for brass is 103 MPa—midway between the values measured. Apart from possible material differences between the two specimens, a major source of error is the measurement of the cross-section area of the specimen. Relative uncertainty bars are shown on the two plots at strains of approximately 0.1 and 0.6%.

The specimen thickness was measured on the polished blank before the specimens were cut out of it. A micrometer with a resolution of 10 μm was used and a value of 220 ± 10 μm was obtained. The width of each specimen was measured with the translation stage of the Vickers microhardness tester; the values were 190 ± 10 μm. Thus the relative uncertainty in the area is ±10%, and this is the major source of uncertainty in the stress. More careful measurements of the dimensions of each specimen (e.g., with a scanning electron microscope) would be necessary to lower this uncertainty.

The relative uncertainty of the strain measurement is ±6% (this does not include errors generated by the motion of the specimen). The original gage length can be measured to ±1%, and the relative uncertainty in locating minimums is also ±1%. If α_0 is located to only ±2°, it contributes 4% to the uncertainty. The support frame for the diodes could easily be constructed to enable a more precise determination of α_0. The elastic modulus measured with the ISDG in Fig. 4 is 4% higher than that measured by the foil gages.

Discussion

The approach taken in this preliminary work is that the ISDG is a valid technique for measuring strain over very short gage lengths and can therefore be used in the tension testing of very small specimens. A suitably small load frame can be manufactured, and specimens with minimum dimensions on the order of 200 μm can be prepared, handled, and tested.

This preliminary work is not an application of this test method to the study of a particular material; it is simply a demonstration that stress-strain curves can be measured directly on microsamples.

Some Advantages

This procedure is not useful in all small specimen testing, but it does have potential advantages.

1. It is easy and fast, which permits replication. Once the systems are set up, one simply drops the specimen in the load frame and runs the test.
2. The load frame can be matched to the particular material and geometry of interest. Since its manufacture is numerically controlled, modifications in the computer-aided design are easily realized. A load frame for fracture toughness testing of microcompact-tension specimens would be feasible.
3. The load frame can be scaled up or down. Up is obviously easy, but down will require more care. Other manufacturing techniques such as selective etching would then be required.
4. Tests could be conducted at high or low temperatures if a windowed chamber is used. The ISDG has been used at 1200°C [*9*].
5. Tests could also be conducted in a corrosive gas or liquid environment provided the corroding agent was transparent. It might be necessary to coat the indentations with a protective layer of nonoxidizing material. Creep tests of zirconium at 250°C are underway in which the indentations are protected with an anodized layer [*7*].

Some Disadvantages

The ISDG is an optical technique that requires targets on the specimen and control of specimen motion. Apart from the difficulties of manufacturing and handling small specimens, some of the disadvantages are:

1. Application of the indentations is no problem, but their presence may be. Many ceramics crack locally around the indentations, which would clearly affect the response of a small specimen. The effect of the indentations on the material response could be examined by testing with indentations of different sizes.
2. Some surfaces may not be reflective. In that case, it may be possible to glue on acetate replicas with reflective pyramids or thin foils into which indents can be placed [*10*].
3. The strain range is limited by the allowable deflection of the crosshead. This could be remedied by a different configuration of the load frame.
4. The rigid body motion of the specimen must be controlled. The preliminary setup described here was mounted on a drafting table. Stiffer mounts between the various components are obviously needed.
5. A commercial version of the system is not available. However, a NASA report [*2*] contains sufficient information (including FORTRAN programs) for building an ISDG.

Suggested Improvements

There are obvious suggestions for improving these first tests:

1. The mechanism for elongating the specimen should be automated. Motor-driven translation stages or piezoelectric devices are candidates and would allow cyclic loading.

2. A commercial load cell with a larger stiffness is desirable. This would not only improve the linearity of the force-voltage output, but would make the entire setup more compact.
3. If the elastic response is a primary interest, the ends of the specimen could be fixed with an adhesive to prevent the initial movement in the grips. The load frame and specimen could be soaked in a solvent after each test to separate them and prepare for the next test.
4. A second set of indentations across the grips and a second ISDG system would be useful. This would reduce the uncertainty in the force measurement.
5. The biaxial version of the ISDG would enable measurement of Poisson's ratio on microsamples.
6. Smaller indentations and shorter gage lengths can be used. Indentations as small as 7 μm on a side have been used [*11*], but ones as small as 1 μm may be possible which would require a more powerful laser.
7. The sampling rate should be increased that is straightforward; rates of 10 and 30 points/s have been demonstrated.

In conclusion, it is hoped that this proposed test method will not only be useful in its own right, but will stimulate new ideas for microsample testing.

Acknowledgments

The authors wish to acknowledge the important help of Dr. Harry Charles at the Applied Physics Laboratory, who provided a summer job for the junior author and arranged the fabrication of the load frame. The several suggestions of graduate students Rob Tregoning and C. H. Yang and the assistance of H. Zeng with the tests are appreciated.

References

[*1*] Sharpe, W. N., Jr., "Applications of the Interferometric Strain/Displacement Gage," *Optical Engineering*, Vol. 21, 1982, pp. 483–488.
[*2*] Sharpe, W. N., Jr., "An Interferometric Strain/Displacement Measurement System," NASA Technical Memorandum 101638, August 1989.
[*3*] Sharpe, W. N., Jr. and Wang, K. C., "Evaluation of a Modified Monotonic Neuber Relation," *Journal of Engineering Materials and Technology*, Vol. 113, 1991, pp. 1–8.
[*4*] Jenkins, F. A. and White, H. E., *Fundamentals of Optics*, McGraw-Hill Book Company, New York, 1957.
[*5*] Sharpe, W. N., Jr., Waclawiw, Z., and Douglas, A. S., "Dynamic Measurement of CTOD," *Fracture Mechanics: Nineteenth Symposium, ASTM STP 969*, American Society for Testing and Materials, Philadelphia, 1988, pp. 466–481.
[*6*] Guillot, M. W. and Sharpe, W. N., "A Technique for Cyclic Plastic Notch Strain Measurement," *Experimental Mechanics*, Vol. 23, 1983, pp. 354–360.
[*7*] Sharpe, W. N., Jr. and Zeng, H., "Creep-Strain Measurement at Notch Roots in Zirconium Pressure-Tube Material," *Materials Evaluation*, Vol. 49, 1991, pp. 1303–1307.
[*8*] Akiniwa, Y., Harada, S., and Fukushima, Y., "Dynamic Measurement of Crack Closure Behaviour of Small Fatigue Cracks by Interferometric Strain/Displacement Gage with a Laser Diode," *Fatigue and Fracture of Engineering Materials and Structures*, Vol. 14, 1990, pp. 317–328.
[*9*] Jenkins, M. G., Kobayashi, A. S., Sakai, M., White, H. W., and Bradt, R. C., "Fracture Toughness Testing of Ceramics Using a Laser Interferometric Strain Gage," *Ceramic Bulletin*, Vol. 66, 1987, pp. 1734–1738.
[*10*] Sharpe, W. N., Jr. and Wang, K. C., "Small Attachable Interferometric Strain Gages," *Experimental Mechanics*, Vol. 28, 1988, pp. 136–141.
[*11*] Sharpe, W. N., Jr. and Su, X., "Closure Measurements of Naturally Initiating Small Cracks," *Engineering Fracture Mechanics*, Vol. 30, 1988, pp. 275–294.

DISCUSSION

M. L. Hamilton[1] (*written discussion*)—What size are the indents? Would strain fields around the indents affect the flow behavior of the tension specimens?

W. N. Sharpe, Jr. and Richard O. Fowler (*authors' closure*)—The indentations are approximately 25 μm on a side, but they can be as small as 7 μm or less. Calibration experiments on smooth specimens as well as comparison with finite element predictions for notched specimens show little impact of the indents on the plastic strain measurement.

G. R. Odette[2] (*written discussion*)—(1) What spacing of indents/mirrors is possible? (2) Can you scan multiple indents/mirrors? (3) What is the dimensional resolution?

W. N. Sharpe, Jr. and Richard O. Fowler (*authors' closure*)—(1) The indentations can be as close as 25 μm or as far apart as 300 μm with no special arrangements. Measurements have been made with indents ¼ in. apart by splitting the laser beam. Of course, this means that the spacing between fringes is very fine. (2) Pairs of indentations approximately ½ μm apart can be interrogated by moving the laser beam; this distance could be smaller if the laser beam is focused. To scan along a row of indentation pairs requires moving the laser and the detectors, which has been done manually in studies of crack profiles. Conceivably this could be automated. (3) The resolution is on the order of 0.2 nm.

[1] PNL, Richland, WA.
[2] University of California at Santa Barbara.

Applications

Stan T. Rosinski,[1] *Arvind S. Kumar,*[2] *N. Scott Cannon,*[3] *and Margaret L. Hamilton*[4]

Application of Subsize Specimens in Nuclear Plant Life Extension

REFERENCE: Rosinski, S. T., Kumar, A. S., Cannon, N. S., and Hamilton, M. L., **"Application of Subsize Specimens in Nuclear Plant Life Extension,"** *Small Specimen Test Techniques Applied to Nuclear Reactor Vessel Thermal Annealing and Plant Life Extension, ASTM STP 1204,* W. R. Corwin, F. M. Haggag, and W. L. Server, Eds., American Society for Testing and Materials, Philadelphia, 1993, pp. 405–416.

ABSTRACT: The U.S. Department of Energy is sponsoring a research effort through Sandia National Laboratories and the University of Missouri-Rolla to test a correlation for the upper shelf energy (USE) values obtained from the impact testing of subsize Charpy V-notch specimens to those obtained from the testing of full-size samples. The program involves the impact testing of unirradiated and irradiated full-, half-, and third-size Charpy V-notch specimens. A correlation between subsize and full-size testing results has been developed in an earlier effort and tested on HT-9 material utilized in fusion reactor applications. To verify the applicability of the correlation on LWR materials, unirradiated and irradiated full-, half-, and third-size Charpy V-notch specimens of a commercial pressure vessel steel (ASTM A533 Grade B) will be tested. The correlation methodology is based on the partitioning of the USE into crack initiation and crack propagation energies. To accomplish this partition, both precracked and notched-only specimens will be used. Whereas the USE of notched-only specimens is the sum of both crack initiation and crack propagation energies, the USE of precracked specimens reflects only the crack propagation component. The difference in the USE of the two types of specimens represents a measure of the crack initiation energy. Normalizing the values of the crack initiation energy to the fracture volume of the sample produces similar values for the full-, half-, and third-size specimens. In addition, the ratios of the USE and the crack propagation energy are also in agreement for full-, half-, and third-size specimens. These two observations will be used to predict the USE of full-size specimens based on subsize USE data. This paper will provide details of the program and present results obtained from the application of the developed correlation methodology to the impact testing of the unirradiated full-, half-, and third-size A533 Grade B Charpy V-notch specimens.

KEYWORDS: ferritic steel, A533B, upper shelf, size effect, Charpy, embrittlement, correlation, energy partition

As commercial light water reactors consider extended operation under the option of license renewal, the detailed characterization of material condition will continue to be an important factor in the determination of component integrity. For reactor pressure vessels (RPVs), this may include additional development of material data bases on the effects of neutron irradiation on the embrittlement of RPV materials over a longer than 40-year duration. This will also likely involve a continuation (and expansion) of surveillance programs into the life

[1] Senior member of technical staff, Sandia National Laboratories, Albuquerque, NM 87185.
[2] Professor, University of Missouri, Rolla, MO 65401.
[3] Principal engineer, Westinghouse Hanford Company, Richland, WA 99352.
[4] Senior scientist, Pacific Northwest Laboratory, Richland, WA 99352.

extension period, especially if thermal annealing of the RPV is considered. Difficulties may exist in acquiring a long-term comprehensive data base on RPV steels due to the somewhat limited irradiation volume available in the commercial reactor or in test reactors. Also of concern is the potentially decreasing amount of original pressure vessel archive material available from which to manufacture sufficient full-size Charpy V-notch (CVN) surveillance samples. The relatively large size of the full-size CVN specimen not only limits the number of samples that can be irradiated in a given volume but also introduces the potential for neutron flux and temperature variations among the large-size specimens. An alternative to the impracticality of irradiating a large number of standard CVN samples from a limited amount of available archive material is the use of subsize CVN samples.

Although the use of subsize specimens will allow for a larger number of samples to be irradiated in a given volume, size-related consequences of their use exist that influence the usefulness of the data. Full-size specimens exhibit a state of mainly plane strain below the notch root at the beginning of testing. This state tends to promote brittle fracture. Reducing the specimen cross-sectional area alters the stress state under the notch by increasing the percentage of specimen cross-section that is close to a plane stress state. This condition promotes a relatively ductile fracture in subsize specimens at a given temperature compared with that of standard full-size specimens and makes the material appear to be more ductile, thus decreasing the ductile-brittle transition temperature (DBTT). Also, the smaller volume of the subsize specimen that is involved in the fracture process reduces the CVN upper shelf energy (USE) of the specimen.

Several attempts have been made to correlate the USE of full-size and subsize specimens [*1–7*] by defining a normalized USE as the ratio of the experimentally measured USE to a normalization factor. The normalized values of the USE for full- and subsize CVN specimens should be equal for a valid correlation.

The normalization factor used in previous USE correlations has been based either on the fracture volume below the notch root [*1,2, 4–6*] or on the dimensions of the entire specimen as well as the stress concentration factor at the notch root, which incorporates notch geometry effects [*7*]. Correlations based on a normalization factor that considers only the fracture volume below the notch root have been found to be satisfactory for relatively ductile steels having a USE above 150 J. The correlation based on a normalization factor that considers all specimen dimensions including the notch geometry and the stress concentration factor has been found to work satisfactorily for steels in a relatively brittle condition (USE $<$ 100 J). This condition is more characteristic of irradiated RPV materials.

The above-mentioned correlations are not suitable, however, for predicting full-size CVN results when a normally ductile material (USE $>$ 200 J) becomes embrittled during irradiation such that the USE falls considerably below 200 J. An earlier stage of the present effort [*8*] investigated a methodology for the correlation of full-size and subsize USE values that is applicable to steels in the irradiated or unirradiated state. The methodology was based on the partitioning of the USE into two components, that required for crack initiation and that for crack propagation. Both precracked and notched-only CVN specimens were used to facilitate this partition. The USE of notched-only specimens represented the sum of the crack initiation and propagation energies. The USE of precracked specimens, however, characterized only the crack propagation energy. Testing of the two types of specimens, therefore, gave a measure of the crack initiation energy. The developed methodology, tested on HT-9 steel CVN specimens, satisfactorily predicted full-size CVN values from subsize specimen data.

The purpose of the present study was to test the developed USE correlation methodology on a commercial RPV material in the unirradiated condition using full-, half-, and third-size CVN specimens. This will help establish the applicability of the USE correlation over

a range of steel materials. Additional efforts are currently underway to apply the USE correlation used in this study to irradiated samples of the same RPV material.

Experimental Procedure

All specimens used in this study were machined from A533B plate material and were obtained from the Electric Power Research Institute. The chemical composition of this material is 0.22 C, 1.35 Mn, 0.012 S, 0.010 P, 0.18 Si, 0.53 Mo, 0.62 Ni, and 0.14 Cu. The microstructural analysis, described below, showed no directionality. Therefore, the Charpy impact test results should be independent of specimen orientation. The metallographic examination, precracking, and Charpy impact test procedures are described below.

Dimensions for both full-size and subsize specimens are given in Fig. 1. The full-size specimen dimensions are in accordance with ASTM Test Methods for Notched Bar Impact Testing of Metallic Materials (E 23-86). While there are no standards available for subsize specimens that consider changes in the dimensions of cross section, length, notch angle, and notch radius, the dimensions used in this study for half- and third-size specimens are similar to those used in other investigations [*1–8*].

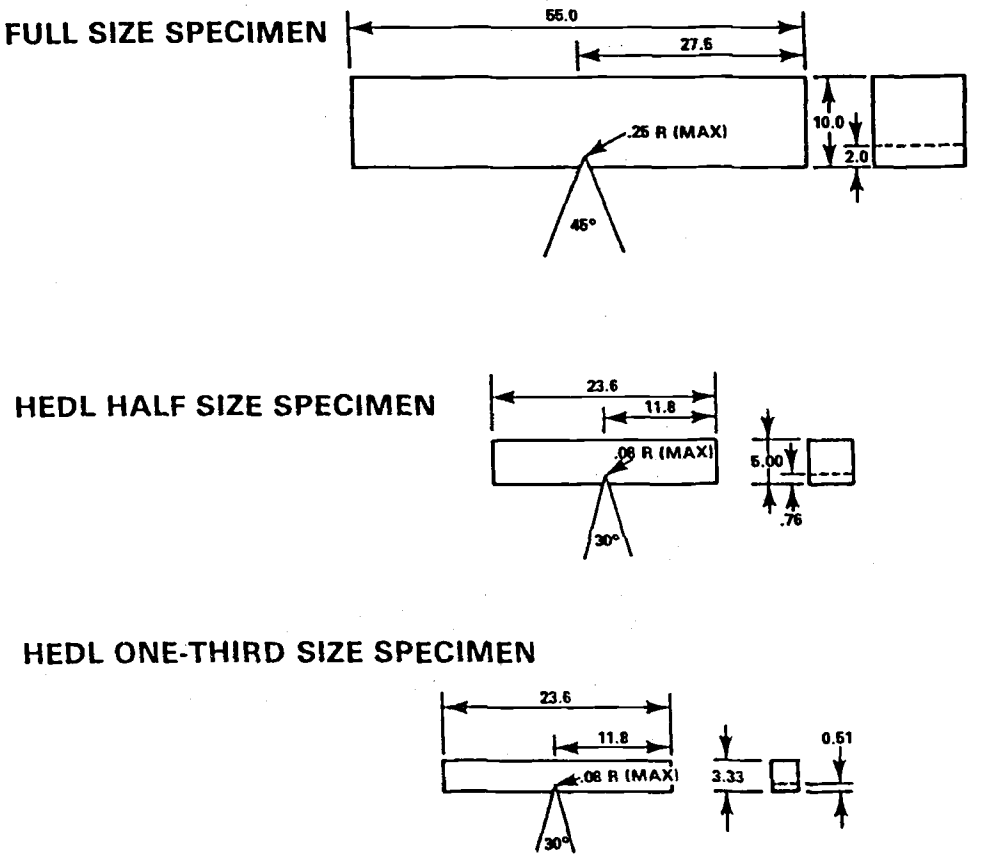

FIG. 1—*Specimen configurations of full-, half-, and third-size specimens. All dimensions are in millimetres.*

Metallographic Examination

Three samples representing the outer surfaces of Charpy specimens were selected from the steel plate and prepared to a 0.05-μm final polish. The samples were then examined prior to etching to evaluate the degree of directionality imparted to nonmetallic inclusions (oxides, sulfides, silicates) during the fabrication processes of the steel plate. This examination revealed a very slight degree (negligible) of orientation of elongated (stringer type) inclusions. The material contained relatively few nonmetallic inclusions.

Evaluation of the steel microstructure was accomplished by chemical etching with 2% Nital. Figure 2 provides a low-magnification (×50) view of the rather large prior austenite grain size defined by white ferrite bounding cells of what appear to be lath martensite. Actual measurement of the prior austenite grain size was determined by comparison of the ×100 photomicrographs to ASTM Test Methods for Determining the Average Grain Size (E 112). Figure 2 also provides a means of evaluating possible microstructural orientation (banding of pearlite and ferrite) due to macro-segregation imparted during hot forming. Figure 3, at ×400 magnification, provides a closer view of the lath (martensite) type structure and the grain size of the ferrite surrounding it. Very little directionality in the microstructure was observed. Therefore, the Charpy impact test results should be independent of specimen orientation.

Microhardness tests were conducted with a Leco DM-400 microhardness tester using a Vickers (DPH) indenter, with a 500-g force applied load. An average of five indents were obtained from the center of each specimen while in the unetched condition. The average Vickers hardness was determined to be 257.

Precracking

Precracked specimens were prepared by loading the notched specimens in a three-point bend arrangement and subjecting them to an oscillating load (15 Hz) in a closed loop hydraulic system. The minimum and maximum loads for the oscillations were determined in advance according to ASTM Test Method for Plain-Strain Fracture Toughness of Metallic Materials (E 399) modified for miniature specimens. The maximum loads at the start of the

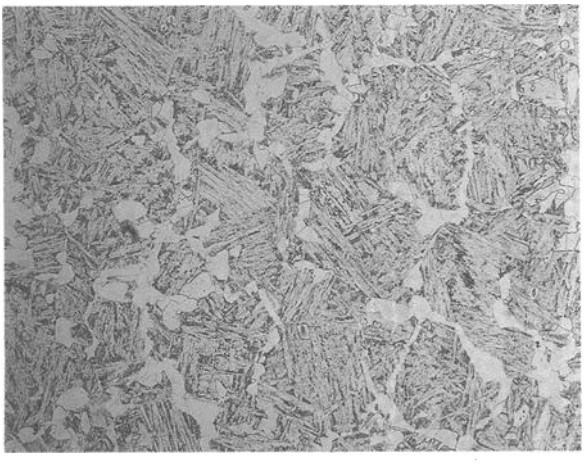

FIG. 2—*Low magnification (×50) view of the microstructure showing prior austenite grain size.*

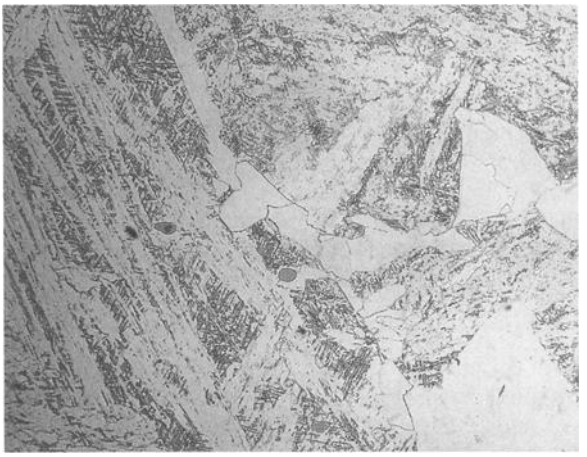

FIG. 3—*Microstructure showing lath martensite structure* (×*400*).

precracking were approximately 550, 180, and 60 kg for full-, half-, and third-size specimens, respectively. The load was reduced every time the crack progressed approximately 250 μm. The minimum loads were maintained at one tenth of the maximum load during the precracking process. To precrack to the desired lengths, it took approximately 100 000 cycles were required for full-size and approximately 30 000 cycles for half- and third-size specimens. In every case the remaining ligament size of precracked specimens was approximately half the width of the notched specimen.

Charpy Impact Testing

All the specimens were tested in the same instrumented drop tower utilizing an anvil with two test locations for the two specimen lengths and a moveable striker. Note that the half-size and third-size specimens have the same length. Data from each test were recorded on a digital oscilloscope and transferred to an IBM PC AT for storage and analysis.

Two load cells (4500 kg for full size and 1600 kg for subsize) were used to increase the sensitivity over the lower load ranges that were relevant to the subsize specimens. Both load cells were calibrated statically to ensure that their response was linear over the desired range. Dynamic calibration of the instrumented tup was performed for both load cells by adjusting the load signal gain so that the maximum load obtained during dynamic testing was the same as the maximum load determined during the slow bend testing of 6061 aluminum in the T651 condition, which is a strain-rate insensitive condition.

The impact velocity of the crosshead was calibrated for each specimen size by attaching a flag of known dimension to the crosshead positioned so that the flag passed an infrared sensor just prior to impact, causing a change in voltage during interruption by the flag. The duration of this change was measured on the oscilloscope and the velocity calculated. Velocity was determined as the average of at least five calibration runs.

Temperature control for all specimens was accomplished in a conditioning chamber where high temperatures were attained with a heated stream of argon and low temperatures were achieved by using cold nitrogen gas. Temperature control was achieved by adjusting the rate of gas flow into the conditioning chamber. Independent temperature calibrations were performed for each specimen size; four thermocouples were attached at various locations

along the length of the specimen to quantify the variability in temperature. Each specimen was kept at the test temperature for approximately 5 min prior to testing to ensure temperature stabilization.

Specimen placement was achieved by pneumatically driven pistons that moved the specimen from its initial position, into the conditioning chamber, and out of the chamber onto a positioning arm. A stepping motor was used to rotate the arm, dropping the specimen into the appropriate position on the anvil for testing. The elapsed time between the exit of the sample from the conditioning chamber and the impact was 1 to 2 s, well within the maximum 5-s delay permitted by ASTM standard E 23-86.

Correlation Methodologies

The methodology of correlating the upper shelf energies (USE) of full- and subsize specimens developed by Kumar et al. [*8*] is presented below. The methodology was used successfully by Kumar et al. on the USE of HT-9. This paper compares the previously developed methodology with those of Louden et al. [*7*], Corwin et al. [*1,2*], and Lucas et al. [*5,6*], presented below.

All of the methodologies compare the normalized values of the upper shelf energies for full- and subsize specimens. The normalized values are defined as the ratio of the USE and a normalization factor.

Methodology of Corwin et al.

Corwin et al. [*1,2*] used a normalization factor equal to the extent of the plastic deformation (i.e., the fracture volume below the notch root). The fracture volume is approximated as $[B(W - A)]^{3/2}$, where B is the thickness and $(W - A)$ is the ligament size below the notch root. This methodology works well for ductile materials having USE larger than 150 J.

Methodology of Lucas et al.

This methodology [*5,6*] is similar to that of Corwin et al. except that the fracture volume is approximated as $B(W - A)^2$. This methodology also works well for ductile materials having USE larger than 150 J.

Methodology of Louden et al.

The methodology of Louden et al. [*7*] accommodates all of the specimen dimensions and the notch geometry in the normalization factor. The normalization factor is given by $[B(W - A)^2/LK_t]$, where the numerator is the fracture volume, L is the span, and K_t is the stress concentration factor at the notch root. This methodology works well for brittle materials having USE less than 100 J.

Methodology of Kumar et al.

This methodology [*8*] is based on the partitioning of the USE into energies for macro-crack initiation and crack propagation. The macro-crack initiation energy is expended in plastic deformation and strain hardening to raise the maximum normal stress to the fracture stress below the notch root of a notched specimen. The total USE is the sum of the macro-crack initiation energy and the energy required to propagate the crack (i.e., the crack propagation energy). In a precracked specimen, however, the energy spent in breaking the

specimen represents the crack propagation energy only. The difference between the USE of notched and precracked specimens (ΔUSE) represents the macro-crack initiation energy and is expended in the deformation of the material in the fracture volume. Therefore, ΔUSE normalized over the fracture volume must be equal for full and subsize specimens. The fracture volume is approximated as $B(W - A)^2$.

Results and Discussion

The results of the Charpy impact test results are shown in Figs. 4, 5, and 6. Each figure shows the actual energies absorbed for both notched and precracked specimens. Table 1 provides the *USE* of notched and precracked specimens and their ratios for each specimen size. The difference between the upper shelf energies of notched and precracked specimens (Δ*USE*) is normalized by the fracture volume (Kumar et al.—Ref *8*) and is presented in Table 2. *USE* of notched specimens normalized by the methods of Louden et al. [*7*], Lucas et al. [*5,6*], and Corwin et al. [*1,2*] is also presented in Table 2.

The actual energies plotted in the figures are obtained from apparent energies as determined from the experimental data using the method of Ireland [*9*]. In order to obtain the actual energies, corrections are provided for the changes in velocity of the tup during the time it is in contact with the impacted specimen, variations in the ligament size of precracked specimens, and the load calibration factor for each size specimen.

Figure 4 shows that the upper shelf energies of full-size notched and precracked specimens are 58.6 and 17.1 J, respectively. The test material received from the Electric Power Research Institute, Nondestructive Evaluation Center, appears to be very brittle (not the condition

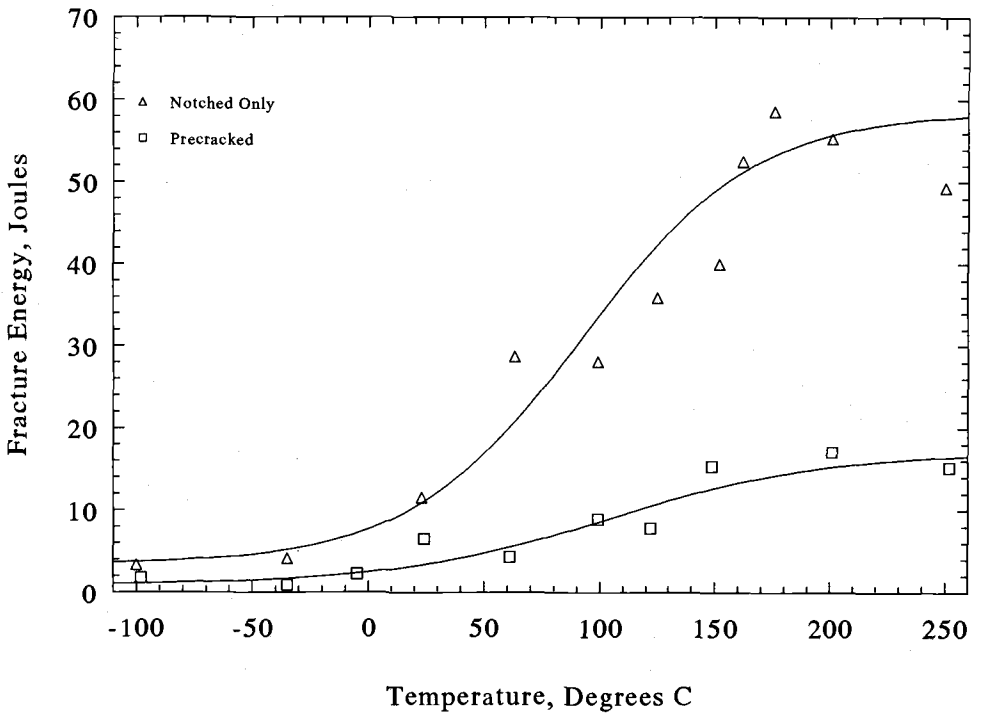

FIG. 4—*Charpy data—full-size samples.*

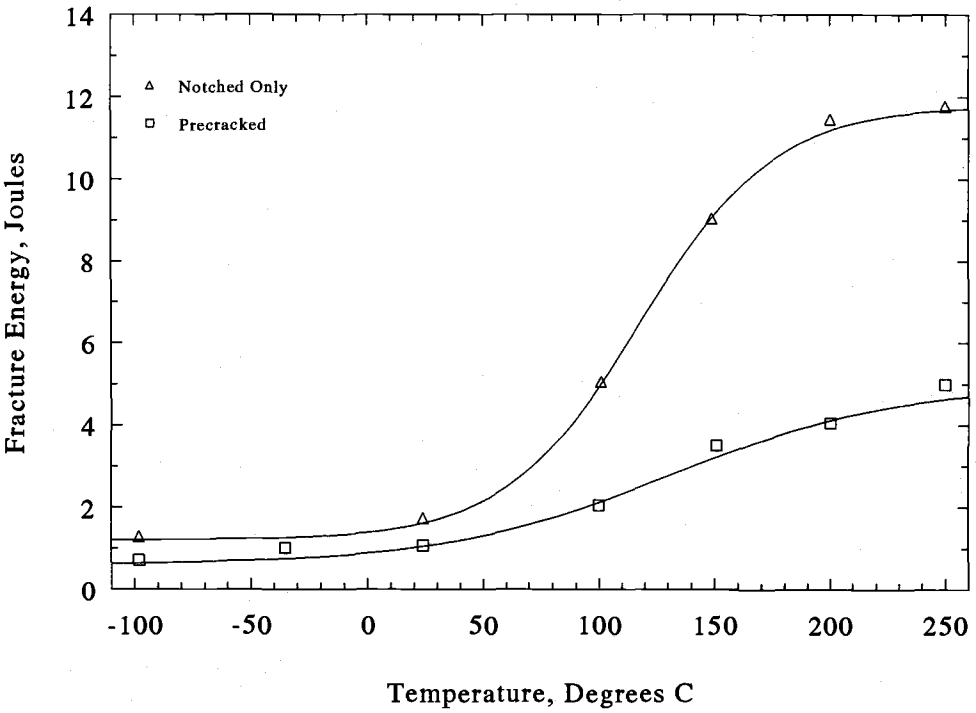

FIG. 5—*Charpy data—half-size samples.*

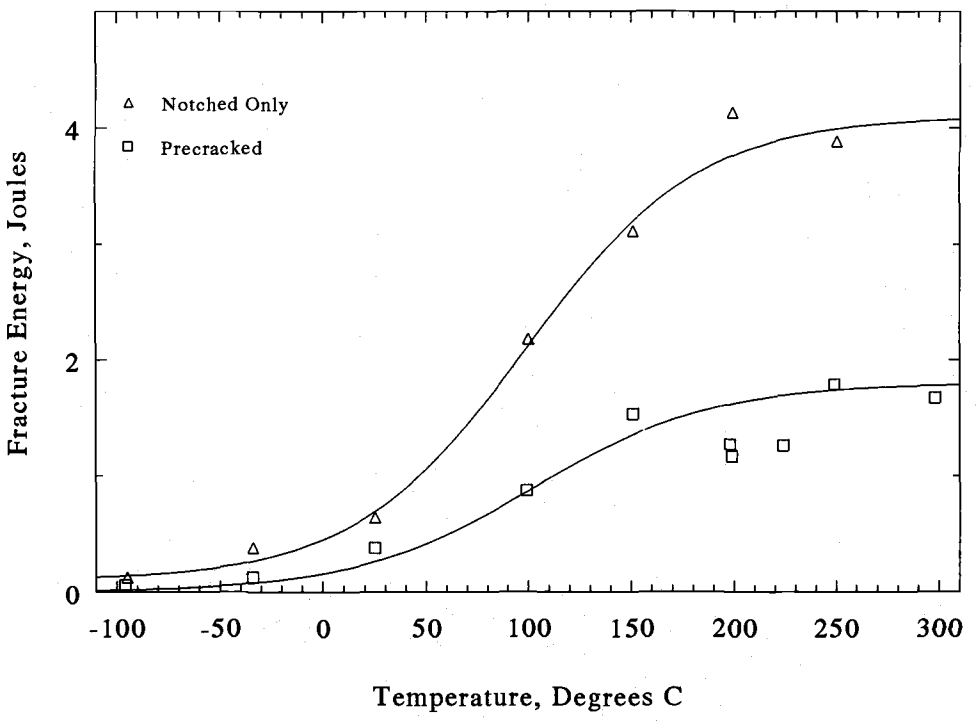

FIG. 6—*Charpy data—third-size samples.*

TABLE 1—*A533B Charpy data—USE.*

	USE, J			
	Notched Only	Precracked	Ratio[a]	ΔUSE[b]
Full size	58.6	17.1	3.4	41.5
Half size	11.9	5.0	2.4	6.9
Third size	4.2	1.9	2.2	2.3

[a] Ratio = *notched USE*/precracked *USE*.
[b] ΔUSE = notched *USE* − precracked *USE*.

utilized for nuclear power plant operation). Furthermore, the prior austenite grain sizes as shown in Fig. 2 were rather large (~250 μm). There were roughly 30 grains below the notch root and 20 grains below the crack tip of the precracked full-size specimens. The number of grains across the width is roughly 40. Therefore, the fracture in a full-size specimen resembles a polycrystalline material. As we will see later, the situation is quite different for half- and third-size specimens. There are only approximately 10 grains below the notch of a third-size specimen. Therefore, in addition to the normal reduction in the constraints to deformation of subsize specimens, fewer grain boundaries present yet another factor that results in the strain energy not being uniformly distributed throughout the fracture volume. The smaller specimens appear to be more ductile. Therefore, we expect that the normalized values of the differences between USE of notched and precracked specimens (ΔUSE) to increase as the specimen size decreases.

For full-size specimens, ΔUSE is 41.5 J. The normalized value is 65 J/cm^3. The ΔUSE of half-size and third-size specimens are 6.9 and 2.3 J, respectively. The corresponding normalized values of ΔUSE lie within the range of 76 ± 10 J/cm^3. This amounts to a variation of 14% about the mid-value. Based on the work of Kumar et al. [*8*], it was expected that the variation would be within 10%. It is proposed that the larger than expected variation in the normalized values of ΔUSE is due to the fact that the fracture in full-size specimens represents that of a polycrystalline specimen. The fracture of subsize specimens, on the other hand, represents the behavior of fewer grains. The smaller the specimen size, the smaller is the number of grains in the fracture surface. The apparent ductility represented by the normalized value of USE increases with decreasing specimen size. Currently there is a program under way at the University of Missouri-Rolla to test the dependence of the normalized USE on grain size.

The Charpy impact data obtained in this program were also tested against the correlations of Louden et al. [7] developed at the University of Missouri-Rolla, of Corwin et al. [*1,2*] at Oak Ridge National Laboratory, and of Lucas et al. [*5,6*] at the University of California—Santa Barbara. The comparison of these correlations is shown in Table 2.

TABLE 2—*Comparison of the normalized value of USE.*

	Kumar et al. [*8*]	Louden et al. [7]	Lucas et al. [5,6]	Corwin et al. [*1,2*]
Full size	65 J/cm^3	1759 J/cm^3	91 J/cm^3	82 J/cm^3
Half size	76 J/cm^3	2009 J/cm^3	132 J/cm^3	122 J/cm^3
Third size	86 J/cm^3	1968 J/cm^3	158 J/cm^3	146 J/cm^3
Range	76 ± 14%	1912 ± 8%	127 ± 28%	116 ± 25%

For the Louden et al. [7] correlation, the normalized values are within 8% of the average of the normalized values for full-, half-, and third-size specimens. The ranges for the correlations of Lucas et al. [5,6] and of Corwin et al. [1,2] are 28 and 25%, respectively.

Since the USE of full-size specimens is only 58.6 J (<100 J), the correlations of Lucas et al. [5,6] and of Corwin et al. [1,2] were not expected to work satisfactorily. The volume normalizations of *USE* used by these investigators work very well for ductile materials whose *USE* exceeds 150 J. The correlation of Louden et al. [7], on the other hand, is especially suited for brittle materials whose USE falls below 100 J. This is the case with the material tested in this program. For brittle materials, the stress concentration factor and the length of specimen have a strong influence on *USE*. The correlation factor of Louden et al. takes these factors into account. However, had the tested material been more ductile (USE > 150 J) the Louden et al. [7] correlation would not have been satisfactory.

A comparison of all the correlations shows that the correlations of both Louden et al. [7] and Kumar et al. [8] are acceptable for this material (A533B) with low USE. It is anticipated that the correlation of Kumar et al. will improve with the choice of smaller grain-size materials normally used in commercial pressure vessel steels. The correlation of Kumar et al. worked very well with HT-9, which had a USE of 124 J and a grain size of ASTM 5 as opposed to ASTM 0.5 for A533B in this work [8].

Conclusions

1. The difference between *USE* for notched-only and precracked specimens can be correlated with fracture volume.
2. Partition of *USE* extends the validity of the correlation to a wide range of *USE* values.

Based on previous thermal aging experiments [7], the correlation should also be applicable to both unirradiated and neutron-irradiated materials. This will be further verified in the continuation of this study.

Acknowledgments

This work was supported by the United States Department of Energy under contract DE-AC04-76DP00789.

References

[1] Corwin, W. R., Klueh, R. L., and Vitek, J. M., *Journal of Nuclear Materials*, Vols. 122–123, 1984, p. 343.

[2] Corwin, W. R. and Hougland, A. M., *The Use of Small Scale Specimens for Testing Irradiated Material, ASTM STP 888*, W. R. Corwin and G. E. Lucas, Eds., American Society for Testing and Materials, Philadelphia, 1986, p. 325.

[3] Ferguson, B. L., *Proceedings*, American Institute of Mining, Metallurgical, and Petroleum Engineers (AIME), Annual Meeting on "What Does the Charpy Test Really Tell Us?", Denver, CO, February 1978, A. R. Rosenfield et al., Eds., American Society for Metals, Metals Park, OH, pp. 90–107.

[4] Abe, F., Noda, T., Araki, H., Okada, M., Narai, M., and Kayano, H., *Journal of Nuclear Materials*, Vol. 150, 1987, pp. 292–301.

[5] Lucas, G. E., Odette, G. R., Sheckherd, J. W., McConnell, P., and Perrin, J., *The Use of Small-Scale Specimens for Testing Irradiated Material, ASTM STP 888*, W. R. Corwin and G. E. Lucas, Eds., American Society for Testing and Materials, Philadelphia, 1986, p. 305.

[6] Lucas, G. E., Odette, G. R., Sheckherd, J. W., and Krishnadev, M. R., *Fusion Technology*, Vol. 10, 1986, p. 728.

[7] Louden, B. S., Kumar, A.S., Garner, F.A., Hamilton, M.L., and Hu, W. L., *Journal of Nuclear Materials,* Vols. 155 to 157, 1988, pp. 662–667.
[8] Kumar, A. S., Garner, F. A., and Hamilton, M. L., in *Effects of Radiation on Materials: 14th International Symposium (Volume II), ASTM STP 1046,* N. H. Packan, R. E. Stoller, and A. S. Kumar, Eds., American Society for Testing and Materials, Philadelphia, 1990, pp. 487–495.
[9] Ireland, D. R., *Instrumented Impact Testing, ASTM STP 563,* American Society for Testing and Materials, Philadelphia, 1974, p. 3.

DISCUSSION

M. L. Hamilton[1] (*written comment*)—The small specimens are also valuable for the fusion materials program, where alloy development for structural components is still an issue. The Japanese program in this area considers specimens as small as 1 to 1.5 mm on a side.

S. T. Rosinski, A. S. Kumar, N. S. Cannon, and M. L. Hamilton (*authors' closure*)—We agree with this comment.

M. P. Manahan[2] (*written discussion*)—In your paper you use fracture volume to normalize the upper shelf energy for various specimen geometries. The fracture volume formulation uses the ligament squared. Why have you chosen this particular formulation and how sensitive is the normalization to the choice of fracture volume equation?

S. T. Rosinski, A. S. Kumar, N. S. Cannon, and M. L. Hamilton (*authors' closure*)—The form of the fracture volume used in this study was chosen to place emphasis on the impact of the ligament size on the overall fracture process. We feel that the remaining ligament size has a larger impact on the fracture process than the sample thickness. This is reflected in our definition of fracture volume: $B(W - A)^2$, where $(W - A)$ reflects the ligament of material under the notch. Although this form was chosen, it does not appear that the normalization is significantly sensitive to the form of the fracture volume equation.

A. Kohyama[3] (*written discussion*)—What is your present status of the phase-2 experiment, the neutron irradiation experiment?

S. T. Rosinski, A. S. Kumar, N. S. Cannon, and M. L. Hamilton (*authors' closure*)—The phase-2 portion of our program is presently underway. Full-, half-, and third-size Charpy V-notch samples are presently being irradiated to a fluence of approximately 2×10^{19} n/cm^2, $E > 1$ MeV. The irradiations and subsequent testing should be completed soon.

W. R. Corwin[4] (*written discussion*)—How do your correlations compare with other similar European and Russian methods for 3 by 4 mm and 5 by 5 mm subsized CVN specimens?

S. T. Rosinski, A. S. Kumar, N. S. Cannon, and M. L. Hamilton (*authors' closure*)—Our program is still in progress and, to date, comparisons have not yet been made between our correlation and those from similar Russian and European methods for 3 by 4 mm and 5 by 5 mm subsize CVN specimens. As additional data become available from the Russian and European methods, as well as additional information from this program, more detailed comparisons will be made.

[1] PNL, Box 999, P8-15, Richland, WA 99352.
[2] MPM Research & Consulting, 213 Teaberry Circle, State College, PA 16803.
[3] University of Tokyo, Hongo, Bunkyo-ku, Tokyo 113, Japan.
[4] ORNL, P.O. Box 2008, Oak Ridge, TN 37831-6151.

B. Server[5] *(written discussion)*—What was the selection criterion for the A533B steel chosen for this study? The properties of the A533B steel appear to be poor and not representative of actual production RPV steels.

S. T. Rosinski, A. S. Kumar, N. S. Cannon, and M. L. Hamilton (authors' closure)—The material properties of the A533B steel selected for this study were not fully characterized prior to selection. It is our hypothesis, however, that the choice of material should not affect the application of the correlation methodology.

[5] ATI Consulting, 2010 Crow Canyon Pl., Suite 160, San Ramon, CA 94583.

Alexander M. Kryukov[1] *and Mikhail A. Sokolov*[1]

Investigation of Material Behavior Under Reirradiation after Annealing Using Subsize Specimens

REFERENCE: Kryukov, A. M. and Sokolov, M. A., **"Investigation of Material Behavior Under Reirradiation after Annealing Using Subsize Specimens,"** *Small Specimen Test Techniques Applied to Nuclear Reactor Vessel Thermal Annealing and Plant Life Extension, ASTM STP 1204,* W. R. Corwin, F. M. Haggag, and W. L. Server, Eds., American Society for Testing and Materials, Philadelphia, 1993, pp. 417–423.

ABSTRACT: Experimental results are presented from a study of changes in the ductile-to-brittle transition temperature of VVER-440 base and weld metals under cyclic irradiation and recovery. The transition temperatures were determined from the results of subsize V-notch impact specimens measuring 5 by 5 by 27.5 mm. Specimen irradiation was carried out in a commercial reactor at a temperature of 270°C in three irradiation and recovery cycles. Annealing of specimens was performed at 340, 420, and 460°C. The shift in the transition temperature of subsize specimen data in the first irradiation cycle was compared to the transition temperature shift determined from tests using standard Charpy specimens.

KEYWORDS: Charpy, reirradiation, annealing, ductile-to-brittle transition temperature (DBBT)

Irradiation embrittlement (IE) of reactor pressure vessel (RPV) steels, which results in increased ductile-to-brittle transition temperatures (DBTT) and reduced fracture toughness, may lead, and in some cases has led, to a reduction of the RPV service life. However, the IE effect can be largely mitigated or even eliminated by annealing the irradiated metal. The recovery level of the metal properties depends on annealing temperature and time [*1–4*]. Annealing the irradiated reactor vessel creates a possibility, which seems to be the only one so far, of extending the radiation service life of vessels which have reached the brittle fracture-resistance limit.

The technology of reactor vessel annealing has been developed and widely implemented for the first Soviet VVER-440 reactors. In establishing the temperature range of material property recovery, it is important to determine the relationship between concentrations of various microstructural defects, their distribution in size, and distances between them. These parameters of the defect structure depend, in turn, on many metallurgical factors and irradiation conditions. Therefore, the temperature-time conditions required for recovery of the irradiated material properties are functions both of the irradiation conditions and individual characteristics of the material. The results of full-size Charpy specimens tests were used to substantiate the temperature-time regime utilized [*1,2*]. The main experiments were carried out using either surveillance specimens or commercial metal specimens irradiated in the reactor vessel channels after removal of surveillance specimens. These experiments

[1] Deputy head of laboratory and senior researcher, respectively, I. V. Kurchatov Institute of Atomic Energy, Moscow, Russia.

permitted the characterization of different factors affecting annealing recovery of the irradiated metal properties to be established [*1*].

These full-size specimen studies relate to experiments on reirradiation of annealed steel. However, the reirradiation experiments are more complicated technically since they require irradiation of a great number of specimens under the same conditions, intermediate annealing of specimens, and testing of a part of the specimens after the first irradiation cycle. Use of subsize specimens permits a significantly greater number of specimens to be simultaneously irradiated within the available experimental capabilities. Consideration of the test results of full-size and subsize specimens must be extended to an understanding of material behavior after reirradiation.

This paper presents the results of studies of reembrittlement of the reactor vessel steels based on the data obtained from impact tests of full-size and subsize specimens.

Selection of Specimen Size

Subsize specimens were chosen as geometrically similar to full-size Charpy impact specimens. The subsize specimens were 5 by 5 by 27.5 mm, having a 45°, 1-mm-deep notch and a notch radius of 0.25 mm [*5*]. Change in a specimen's size inevitably affects its scale factor. For impact tests this is a complicated problem. In this case it is reasonable to use subsize specimens for the estimation of the influence of any factors on the steel sensitivity to irradiation, annealing, etc. For establishing the general tendency of material behavior in this kind of study, the change in the ductile-to-brittle transition temperature (DBTT), rather than the absolute DBTT value, is of primary interest.

Results

One may assume in first approximation that irradiation-induced shift of DBTT is similar for subsize and full-size specimens. The base metal of 15Kh2MFA steel (P = 0.020% and Cu = 0.11%) and its weld metal (P = 0.023%; Cu = 0.12%) were irradiated to a neutron fluence of $1 \cdot 10^{20}$ n/cm^2 ($E > 0.5$ MeV). The specimens were irradiated in the reactor vessel of a nuclear power plant (NPP) at 270°C in the channels from which surveillance specimens had been removed. The DBTT shift was 55°C for the base metal and 85°C for the weld metal as measured with subsize specimens. Both subsize specimens and full-size specimens from the base and weld metals investigated were irradiated. The irradiation conditions were the same for the two types of specimens. The full-size specimens' DBTT shift for the weld metal was 70°C and that for the base metal was 50°C. With allowance for the error in determination of the DBTT shift, these results agree with other data on DBTT shift determination for subsize and full-size specimens [*5*]. Though these data are scarce, they can serve as experimental support of the assumption that the irradiation-induced DBTT shifts determined by tests with subsize and full-size specimens are similar.

After irradiation, the two materials were subjected to annealing at 340, 420, and 460°C. Some of the specimens were tested, while the rest of the specimens were subjected to reirradiation. The reirradiation neutron fluence was 0.8×10^{20} n/cm^2. Recovery of the metal properties and reembrittlement at annealing temperatures of 420 and 460°C were found to be the same. Figures 1 and 2 present changes in the DBTT of the base and weld metals at intermediate annealing temperatures of 340 and 460°C. The shift of the weld metal DBTT after the first irradiation was 85°C (see Fig. 1). Annealing at 340°C reduced the DBTT of the metal irradiated by 15°C while the initial DBTT was fully recovered after annealing at 420 and 460°C. Following reirradiation, the metal annealed at 340°C exhibited an additional DBTT shift of 10°C. Annealing at 340°C after reirradiation did not lead to further changes

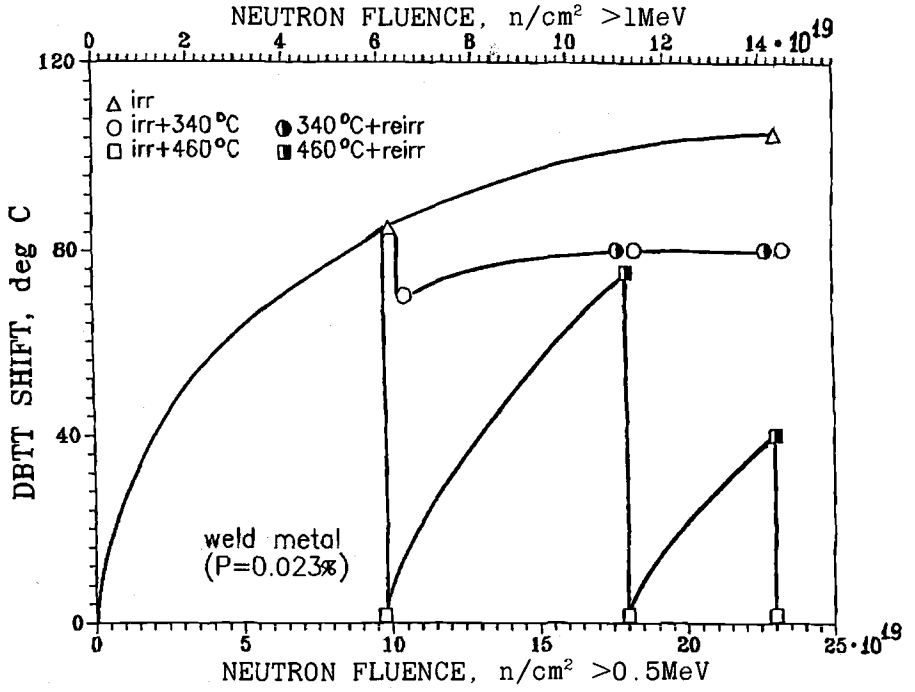

FIG. 1—*Change of DBTT of weld metal after irradiation-anneal-reirradiations (subsize specimens).*

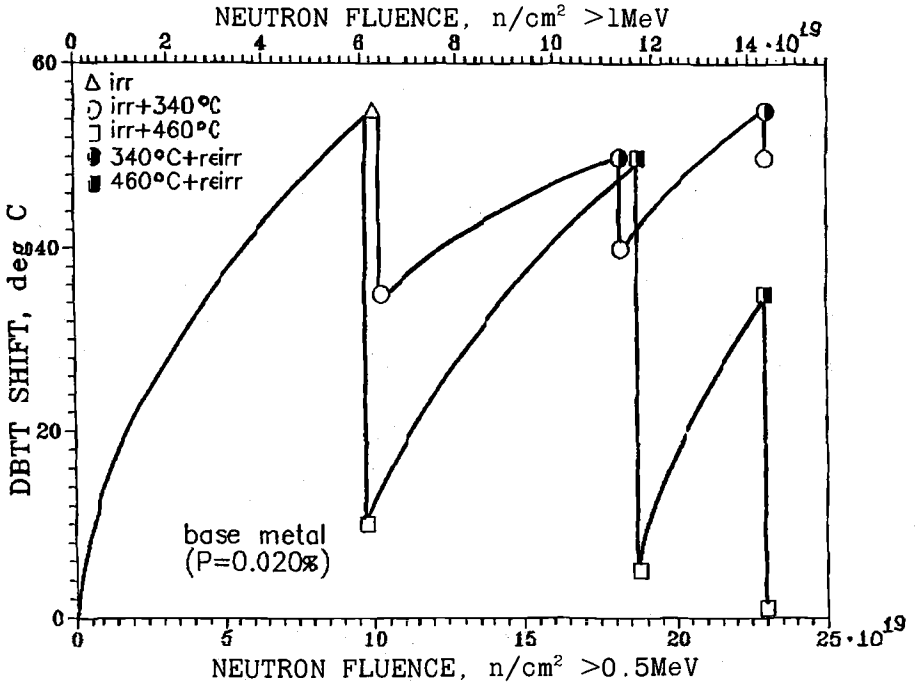

FIG. 2—*Change of DBTT of base metal after irradiation-anneal-reirradiations (subsize specimens).*

in the DBTT of the metal. After reirradiation, the metal annealed at 460°C showed a DBTT shift of 75°C. Annealing at 460°C after the second irradiation fully restored its DBTT as in Case 1. These metals were also subjected to irradiation after the second annealing. The third increment of irradiation fluence was $5 \cdot 10^{19}$ n/cm^2.

One batch of specimens was irradiated during all three irradiation cycles without intermediate annealing. The total shift in this case was 105°C.

As far as the 15Kh2MFA steel base metal is concerned, the shift of its DBTT after the first irradiation cycle was 55°C (see Fig. 2). Annealing at 340°C reduced the DBTT of the irradiated metal by 20°C and at 420 and 460°C by 45°C (the residual embrittlement being as low as 10°C). As in the case of the weld metal, the base metal annealed at 340°C exhibited an insignificant additional DBTT shift (15°C) following reirradiation. Annealing after the second irradiation restored the DBTT by 10°C. Upon the third irradiation, the DBTT increased by 15°C and annealing after the third irradiation restored the DBTT only by 5°C. The base metal subjected to annealing at 420°C after the first irradiation exhibited an additional DBTT shift of 35°C after reirradiation. Annealing after the second irradiation restored the DBTT by 35°C.

The base metal which was subjected to annealing at 460°C after the first irradiation exhibited an additional DBTT shift of 40°C following reirradiation. Annealing after the second irradiation restored the DBTT by 45°C, and the third irradiation increased the DBTT by 30°C. The final annealing fully recovered the DBTT.

The experimental results show that both for the base and weld metals the DBTT shift following reirradiation (after annealing) depends on the temperature of intermediate annealing. An increase in the annealing temperature results in a higher percentage of DBTT recovery. However, the DBTT shift following reirradiation ($\Delta DBTT_{add}$), which is equal to the difference between the DBTT after reirradiation and the DBTT of the metal after intermediate annealing (prior to reirradiation), is smaller for lower annealing temperatures.

Similar results were obtained in studying full-size specimens of the weld metal containing 0.033 to 0.035% of phosphorus (see Fig. 3). The irradiation conditions were identical. After the first irradiation, the DBTT shift was 105°C. Intermediate annealings were carried out at 340, 380, 420, and 460°C. The specimens that had undergone annealing at 460°C were not subjected to reirradiation. Some of the specimens were irradiated without intermediate annealing.

The least recovery of DBTT (as little as by 15°C) was exhibited by the material annealed at 340°C. However, in reirradiation this material had no additional DBTT shift compared to the post annealing DBTT. An additional shift of the transition temperature after reirradiation ($\Delta DBTT_{add}$) for the weld metal subjected to intermediate annealing at 380°C was 45°C; for the metal which underwent intermediate annealing at 420°C, it was 65°C. In other words, as in the first experiment, the largest DBTT shift in reirradiation corresponds to the highest annealing temperature.

After annealing at 340°C, the DBTT rises slightly during reirradiation, which is followed by an insignificant recovery of the DBTT by annealing. Figure 3 shows no increase in DBTT after reirradiation. It may be assumed that during low-temperature annealing the faulted structure formed in the initial irradiation seems to stabilize. Reirradiation of this material with the neutron fluence as high as in the initial irradiation does not essentially change the DBTT. Taking into account the results of Ref *1*, it may be supposed that the defects related to phosphorus are determining this effect. However, this demands more detailed study, which is beyond the scope of this paper.

In practice the fact that in all cases the transition temperature of post-annealed steel does not exceed that of steel irradiated with the similar total neutron fluence but without intermediate annealing is very important.

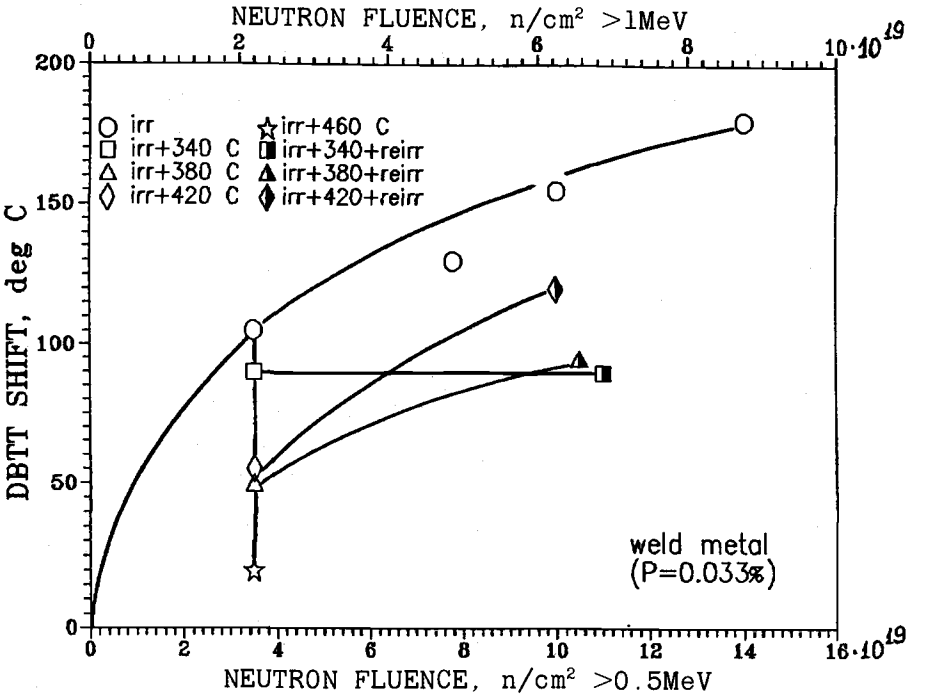

FIG. 3—*Change of DBTT of weld metal after irradiation-anneal-reirradiations (full-size specimens).*

It is known that the shift of the DBTT of the VVER-440 vessel materials after irradiation is reasonably described by the relation [*6*]

$$\Delta\text{DBTT} = A_F \cdot F^{1/3} \tag{1}$$

where

A_F = the irradiation embrittlement coefficient, and
F = the fast neutron fluence, 10^{18} n/cm² ($E > 0.5$ MeV).

At higher annealing temperatures (420 and 460°C), the irradiation embrittlement in reirradiation (after annealing) is well described in Ref *7*

$$\Delta\text{DBTT}_{sum} = (\Delta\text{DBTT}_{res}^3 + A_F^3 F_2)^{1/3} \tag{2}$$

where

ΔDBTT_{sum} = the total shift of the transition temperature after reirradiation compared to the initial state,
ΔDBTT_{res} = the residual (after annealing) embrittlement of the steel, the difference between the transition temperatures in the post-annealed and initial states,
A_F = the steel embrittlement coefficient according to Ref *1*, and
F_2 = the fast neutron fluence in reirradiation.

Dependence of the shift of transition temperature during reirradiation (ΔDBTT_{add}) can be plotted as in Fig. 4. For each material the slope of the curve in Fig. 4 is determined by impurity contents.

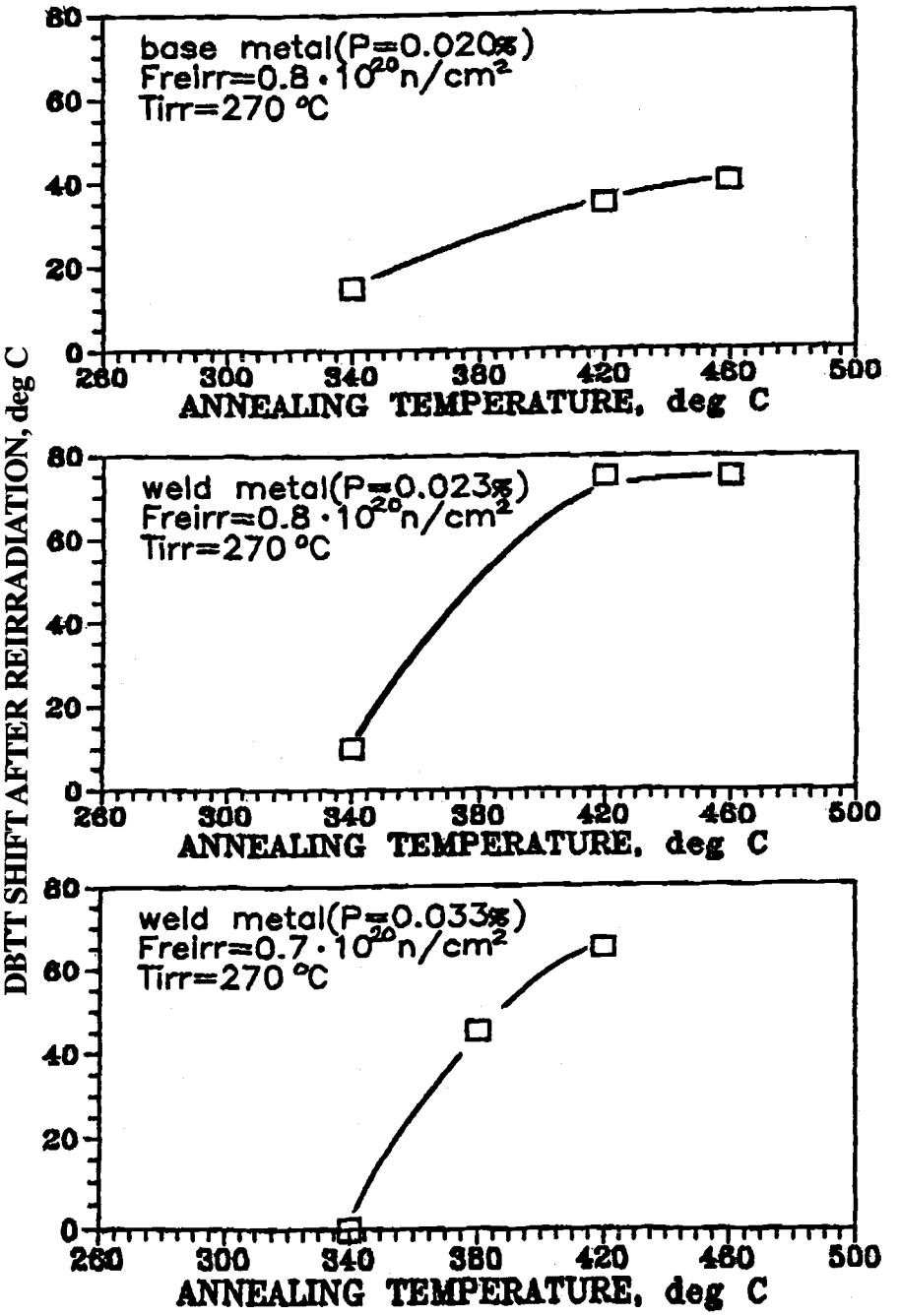

FIG. 4—*Dependence of DBTT shift after reirradiation* ($\Delta DBTT_{add}$) on annealing temperature.

Conclusion

Annealing of irradiated metal is an efficient method for recovery of the properties of VVER-440 vessel materials. Reirradiation of annealed steel does not result in an increased rate of irradiation embrittlement compared to the initial irradiation, which permits several annealings to be performed, if necessary.

Changes in the transition temperature as a result of reirradiation depend both on the intermediate annealing temperature and on the chemical composition of the metal, in particular, on the phosphorus content.

It has been found that the greatest shift of the DBTT following reirradiation corresponds to the highest temperature of annealing.

References

[1] Amayev, A. D., Kryukov, A. M., and Sokolov, M. A., "Recovery of the Transition Temperature of Irradiated VVER-440 Vessel Metal by Annealing," *Radiation Embrittlement of Nuclear Reactor Pressure Vessel Steels: An International Review (Fourth Volume), ASTM STP 1170,* L. E. Steele, Ed., American Society for Testing and Materials, Philadelphia, 1993.

[2] Amayev, A. D., Kryukov, A. M., Sokolov, M. A., Badanin, B. I., and Nikolayev, V. A., "Investigation of the Mechanical Properties Processes of the Irradiated Pressure Vessel Steels by Annealing," *Proceedings,* International Conference on Radiation Materials Science, Alyshta, USSR, Vol. 4, Khorkov, May 1990, pp. 25–32 (in Russian).

[3] Hawthorne, J. R., "Steel Impurity Element Effects on Post-irradiation Properties by Annealing," *Influence of Radiation on Material Properties: 13th International Symposium (Part II), ASTM STP 956,* American Society for Testing and Materials, Philadelphia, 1987, pp. 461–479.

[4] Lott, R. G., Mager, T. R., Shogan, R. P., and Yanichko, S. E., "Annealing and Reirradiation Response of Irradiated Pressure Vessel Steels," *Radiation Embrittlement of Nuclear Reactor Pressure Vessel Steels: an International Review (Second Volume), ASTM STP 909,* L. E. Steele, Ed., American Society for Testing and Materials, Philadelphia, 1986, pp. 242–259.

[5] Amayev, A. D., Kryukov, A. M., Sokolov, M. A., Badanin, B. I., Nikolayev, V. A., and Rogov, M. F., "Use of Subsize Specimens for Determination of Radiation Embrittlement of Operating Reactor Pressure Vessels," this publication, pp. 424–439.

[6] Amayev, A. D., Kryukov, A. M., Levit, V. I., and Sokolov, M. A., "Radiation Stability of VVER-440 Vessel Materials," *Radiation Embrittlement of Nuclear Reactor Pressure Vessel Steels: An International Review (Fourth Volume), ASTM STP 1170,* L. E. Steele, Ed., American Society for Testing and Materials, Philadelphia, 1993.

[7] Nikolayev, V. A., Badanin, V. I., and Morozov, A. M., "Summing of Damages in Annealing and Reirradiation of Reactor Vessel Steel," *Atomnaya Energia,* Vol. 57, No. 3, 1984, pp. 165–167 (in Russian).

Amir D. Amayev,[1] *Vladimir I. Badanin,*[2] *Alexander M. Kryukov,*[1] *Vladimir A. Nikolayev,*[2] *Mikhail F. Rogov,*[3] *and Mikhail A. Sokolov*[1]

Use of Subsize Specimens for Determination of Radiation Embrittlement of Operating Reactor Pressure Vessels

REFERENCE: Amayev, A. D., Badanin, V. I., Kryukov, A. M., Nikolayev, V. A., Rogov, M. F., and Sokolov, M. A., **"Use of Subsize Specimens for Determination of Radiation Embrittlement of Operating Reactor Pressure Vessels,"** *Small Specimen Techniques Applied to Nuclear Reactor Vessel Thermal Annealing and Plant Life Extension, ASTM STP 1204,* W. R. Corwin, F. M. Haggag, and W. L. Server, Eds., American Society for Testing and Materials, Philadelphia, 1993, pp. 424–439.

ABSTRACT: This paper presents groundwork for determining the ductile-to-brittle transition temperature (DBTT) from subsize specimens (5 by 5 by 27.5 and 3 by 4 by 27.0 mm) and describes the correlation between the DBTT obtained from tests of standard Charpy specimens and subsize specimens. A method for taking samples from the inside surface of reactor pressure vessels and fabricating small specimens from them was developed in the USSR. This method is used to assess the effectiveness of pressure vessel recovery by annealing. Some results of the DBTT evaluation for the base and weld metal before and after recovery are given.

KEYWORDS: Charpy, reactor pressure vessel, annealing, ductile-to-brittle transition temperature (DBTT)

To assess the recovery of the ductile-to-brittle transition temperature (DBTT) of annealed pressure vessels that have no surveillance specimens, a method of taking samples (templets) from the inside surface of the vessel and to fabricate subsize specimens for impact tests has been developed. The requirements of pressure vessel integrity after sampling place substantial restrictions on the geometrical dimensions of the samples taken. In fact, it is possible to produce specimens with the dimensions of 5 by 5 by 27.5 or 3 by 4 by 27 mm. The 5 by 5-mm specimens were selected on the basis of geometrical similarity with standard Charpy specimens. Specimens of this size were cut out of a weld metal that had a weld pad on the internal surface of the pressure vessel. The thickness of the samples cut from the base metal is not sufficient to produce specimens of these dimensions. For this reason 3 by 4 by 27-mm specimens were used that comply with German Standard DIN 50 115: Testing of Metallic Materials—Notched Bar Impact Bending Test, 1991. Experience with specimens of these dimensions has been accumulated [*1*] in similar investigations. Figure 1 shows sample sizes and the orientation of cutting specimens.

[1] Head of laboratory, deputy head of laboratory, and senior researcher, respectively, I. V. Kurchatov Institute of Atomic Energy, 123182 Moscow, Russia.

[2] Senior researcher and head of laboratory, respectively, Central Research Institute of Structural Materials, 133024 St. Petersburg, Russia.

[3] Head of division, OKB "Gidropress," 142103 Podolsk, Moscow region, Russia.

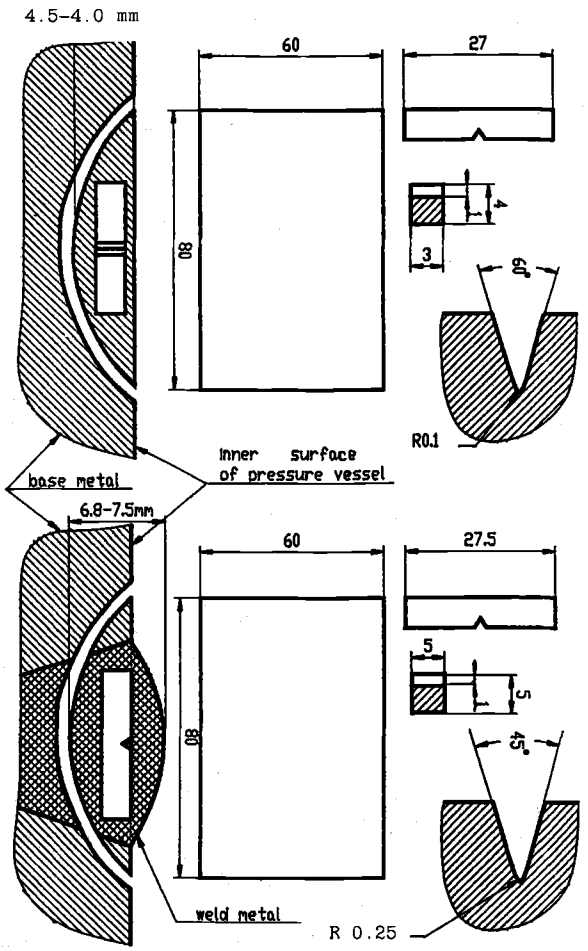

FIG. 1—*Scheme of sample cutting from the inner surface of the reactor vessel. Sizes and orientation of subsize specimens.*

A 50-J impact machine with DIN tup geometry and impact velocity 3.87 m/s was used for the tests. The loading span was 20 and 22 mm for the 5 by 5 by 27.5 and 3 by 4 by 27-mm specimens, respectively.

The objective of the present investigation was to establish a correlation between the values of ductile-to-brittle transition temperature obtained from tests of subsize and standard specimens, as well as to use the correlations for the assessment of the extent of recovery of operated reactor pressure vessels.

To establish a relevant correlation with the test results for the 3 by 4, 5 by 5 and 10 by 10-mm cross-section specimens of grade 15Kh2MFA steel and its weld metals with different impurity contents were summarized and analyzed. In addition, specimens of A533 steel supplied by the IAEA were also tested (see Tables 1 through 3). Due to the fact that the normal condition of the materials does not provide a sufficiently wide variation of DBTT, an additional material (grade 15Kh2MFA steel) was used and subjected to quenching and tempering under laboratory conditions in various off-normal regimes, including a low-temperature (500°C) regime, which yielded DBTT values of 80 to 100°C. A total of ten different

TABLE 1a—*Results of unirradiated full-size and 3 by 4 by 27 Charpy specimen impact tests.*

Metal	Specimen Cross-Section, mm	USE, J	USE(10)/USE(3)
15Kh2MFA	10 x 10	168	
No. 109534	3 x 4	8	21
No. 109868	10 x 10	153	
No. 109868	3 x 4	6.3	24.3
No. 103672	10 x 10	195	
No. 103672	3 x 4	8.4	23.2
15Kh2MFAA	10 x 10	195	
No. 105731	3 x 4	8	24.4
A533B (JRQ)	10 x 10	163	
A533B (JRQ)	3 x 4	7.7	21.2
A533B (JPI)	10 x 10	205	
A533B (JPI)	3 x 4	8	25.6
Weld metal	10 x 10	148	
No. 25	3 x 4	7.2	20.6
No. 20	10 x 10	104	
No. 20	3 x 4	6.7	15.5
No. 502	10 x 10	128	
No. 502	3 x 4	5	25.6
No. 10	10 x 10	144	
No. 10	3 x 4	6.3	22.9
No. 28	10 x 10	135	
No. 28	3 x 4	6	22.5

regimes of heat treatment were employed. With a view to using this procedure for specimens produced from samples cut out of operating VVER-440 reactor pressure vessels, some of the materials were irradiated. Both standard and subsize specimens were irradiated in identical conditions. The irradiation temperature was 270°C, and the fast neutron fluence incident on the specimens was $1 \cdot 10^{20}$ n/cm^2 ($E > 0.5$ MeV).

Establishment of the Criteria Values of Absorbed Energy and Lateral Expansion

The problem of absorbed energy criteria selection may be solved by using the notion of the scale factor in ductile fracture. This approach is based on the following considerations. It the DBTT in the impact tests is determined from a fixed level of absorbed energy, it is logical to assume that for specimens of different scale the similarity of the criterion may be ensured only when this level is constant in relation to the energy of fully ductile fracture (in the area of the upper shelf), that is, when

$$\frac{A_{pi}}{\text{USE}} = \text{Constant} \tag{1}$$

where

A_{pi} = criteria level of the absorbed energy used for the determination of DBTT, J, and
USE = the upper-shelf energy, J.

Since we have the fixed value of A_{pi} for a standard specimen, the task of determining the critical level of the absorbed energy for subsized specimens is reduced to finding the dependence of the upper-shelf value on the scale.

TABLE 1b—*Results of unirradiated standard and 5 by 5 by 27.5 Charpy specimen impact tests.*

Metal	Specimen Cross-Section, mm	USE, J	USE(10)/USE(5)
15Kh2MFA	10 x 10	168	
No. 109534	5 x 5	18	9.3
No. 109868	10 x 10	153	
No. 109868	5 x 5	20	7.7
No. 103672	10 x 10	195	
No. 103672	5 x 5	31.5	6.2
15Kh2MFAA	10 x 10	195	
No. 105731	5 x 5	29	6.7
A533B (JRQ)	10 x 10	163	
A533B (JRQ)	5 x 5	24	6.8
A533B (JPI)	10 x 10	205	
A533B (JPI)	5 x 5	30	6.8
15Kh2MFA	10 x 10	96	
15Kh2MFA	5 x 5	12	8
15Kh2MFA	10 x 10	89	
15Kh2MFA	5 x 5	12	7.4
15Kh2MFA	10 x 10	144	
15Kh2MFA	5 x 5	16	9
15Kh2MFA	10 x 10	212	
15Kh2MFA	5 x 5	18	11.8
15Kh2MFA	10 x 10	200	
15Kh2MFA	5 x 5	19	10.5
15Kh2MFA	10 x 10	200	
15Kh2MFA	5 x 5	18.6	10.8
Weld metal	10 x 10	148	
No. 25	5 x 5	16.4	9
No. 20	10 x 10	104	
No. 20	5 x 5	16	6.5
No. 502	10 x 10	128	
No. 502	5 x 5	15	8.5
No. 10	10 x 10	144	
No. 10	5 x 5	16	9
No. 28	10 x 10	135	
No. 28	5 x 5	21.5	6.3
No. 24	10 x 10	147	
No. 24	5 x 5	17	8.7
No. 27	10 x 10	162	
No. 27	5 x 5	16.4	9.9
9713	10 x 10	140	
9713	5 x 5	18.6	7.5
9713	10 x 10	136	
9713	5 x 5	18.4	7.4
9936	10 x 10	148	
9936	5 x 5	16	9.3
9938	10 x 10	120	
9938	5 x 5	17.6	6.8
9939	10 x 10	126	
9939	5 x 5	18	7
9941	10 x 10	152	
9941	5 x 5	18.4	8.3
9942	10 x 10	120	
9942	5 x 5	18.4	6.5
9937	10 x 10	120	
9937	5 x 5	17	7.1

TABLE 2—*Results of irradiated* ($F = 1 \cdot 10^{20}$ *n/cm²*) *Charpy and subsize specimen impact tests.*

Metal	Specimen Cross-section, mm	USE, J	USE(10)/USE(5)	USE(10)/USE(3)
15Kh2MFA	10 x 10	102		
No. 109868	5 x 5	17	6.0	
No. 109868	3 x 4	5.4		18.9
15Kh2MFA	10 x 10	190		
No. 103672	5 x 5	31.5	6.0	
No. 103672	3 x 4	7.7		24.7
15Kh2MFAA	10 x 10	190		
No. 105731	5 x 5	25	7.6	
No. 105731	3 x 4	7.7		24.7
Weld metal	10 x 10	94		
No. 28	5 x 5	16.7	5.7	
No. 28	3 x 4	3.5		26.9
A533 (JRQ)	10 x 10	94		
A533 (JRQ)	5 x 5	17	5.5	
A533 (JRQ)	3 x 4	5		18.8
A533 (JPI)	10 x 10	205		
A533 (JPI)	5 x 5	30	6.8	
A533 (JPI)	3 x 4	8		25.6

Statistical treatment of the database demonstrated that the following ratio existed between the upper-shelf levels for 5 by 5 and 10 by 10-mm specimens

$$\frac{\text{USE(10)}}{\text{USE(5)}} = 7.75 \tag{2}$$

For 3 by 4 and 10 by 10-mm specimens, it was

$$\frac{\text{USE(10)}}{\text{USE(3)}} = 22.8 \tag{3}$$

where the figure in parentheses is the characteristic dimensions of the specimen cross section.

TABLE 3—*Results of irradiated* ($F = 1 \cdot 10^{20}$ *n/cm²*) *and annealed at 460°C for 100 h Charpy and subsize specimen tests.*

Metal	Specimen Cross-section, mm	USE, J	USE(10)/USE(5)	USE(10)/USE(3)
15Kh2MFA	5 x 5	20	...	...
No. 109868	3 x 4	6.3	...	...
15Kh2MFA	5 x 5	31.5	...	...
No. 103672	3 x 4	8.4	...	...
15Kh2MFAA	5 x 5	29	...	...
No. 105731	3 x 4	9	...	...
Weld metal				
No. 28	3 x 4	6.5	...	...
ASTM (JRQ)	10 x 10	105	...	...
ASTM (JRQ)	5 x 5	26	7.1	...
ASTM (JRQ)	3 x 4	7.7	...	24.0

Considering that deformation in the first order approximation is proportional to the volume, V, being deformed, there are grounds to believe that the upper-shelf energy depends on the linear dimension, L, raised to the third power. It should be pointed out here that the experimental value obtained from Eq 2 correlates within the precision of the experiment with the value of 8 that follows from the geometrical similarity of 5 by 5 by 27.5 mm and standard specimens.

With regards to the considerations given above, the criteria value of absorbed energy that corresponds to 47 J for standard specimens [2] may be assumed equal to 6.0 J for 5 by 5-mm specimens. In accordance with Eq 1 for specimens of the 3 by 4-mm cross section, the criterial value of absorbed energy corresponding to the level of 47 J should be equal to $47/22.8 = 2.1$ J, which is very close to the value of 2.2 J assumed in Ref *1*. Due to the small difference of the compared values, and, more importantly, because the effect this difference has on the value of DBTT is small, it is desirable in our case to assume, for the sake of consistency, the absorbed energy of 2.2 J as a criterion for the determination of DBTT for 3 by 4-mm specimens. Table 4 lists criteria of the absorbed energy as required by the "Calculation standards for strength of equipment and pipes..." [2]. The required data are complemented by two additional lines for subsize 5 by 5 and 3 by 4-mm specimens.

Besides absorbed energy, there is another criterion used for the determination of DBTT, which is the value of lateral expansion of the specimen. The following approach has been used for establishing the criterion for lateral expansion. The dependence of lateral expansion of standard specimens on the value of absorbed energy is shown (Fig. 2). Using data from Fig. 2, the value of energy (E_{LE}) corresponding to the criterion for lateral expansion (0.9 mm) has been determined.

Figure 3 presents the dependence of the lateral expansion on the absorbed energy for 5 by 5-mm cross-section specimens. Using the ratio (Eq 2), the critical value of the lateral expansion for 5 by 5-mm cross-section specimens was found to be equal to 0.35 mm, as shown in Fig. 3.

The dependence of the lateral expansion on the absorbed energy for 3 by 4-mm cross-section specimens is shown in Fig. 4. The criterion of lateral expansion for 3 by 4-mm cross-section specimens was determined similarly to that of the 5 by 5-mm specimens and was found to be 0.3 mm. The obtained value is identical to the values of the level of the lateral expansion established in Ref *1*.

Dependence of the Ductile-to-Brittle Transition Temperature on Specimen Dimensions

B. B. Chechulin [3] has obtained, based on A. F. Ioffe's ductile-to-brittle transition scheme and in accordance with the notions of the statistical nature of brittle strength, a dependence of the ductile-to-brittle transition temperature, DBTT, on the specimen size, L

$$\frac{1}{\text{DBTT}} = K \ln L + B \tag{4}$$

TABLE 4—*Criteria values of the absorbed energy and the lateral expansion for full-size and subsize Charpy specimens.*

Specimen Cross-Section	Criteria Value	
	Absorbed Energy, J	Lateral Expansion, mm
10 x 10	47	...
5 x 5	6	0.35
3 x 4	2.2	0.3

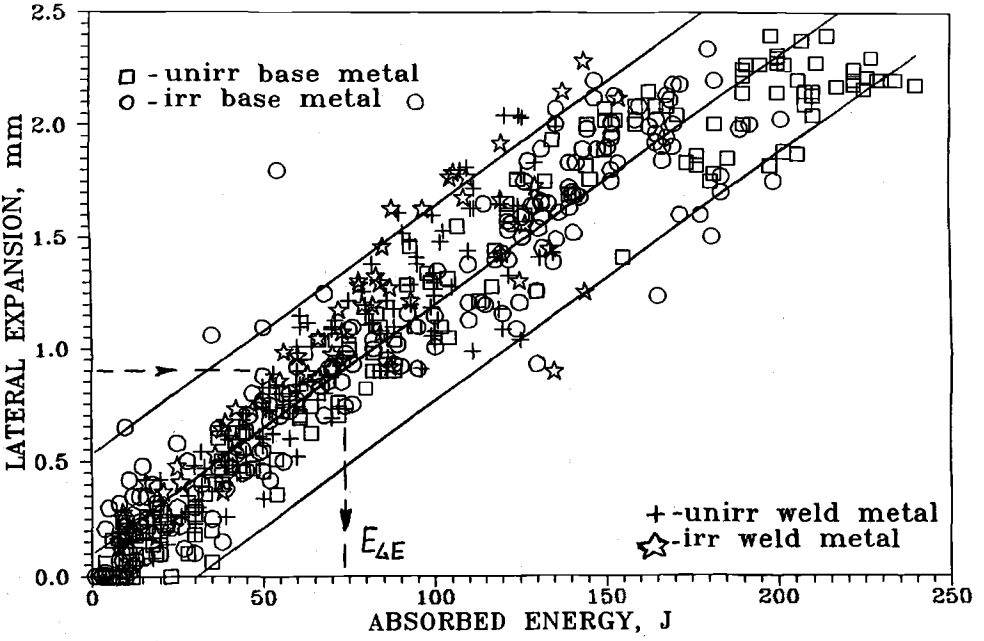

FIG. 2—*Plot of lateral expansion versus absorbed energy for full-size Charpy specimens of both base and weld metal of VVER-440 reactor pressure vessel.*

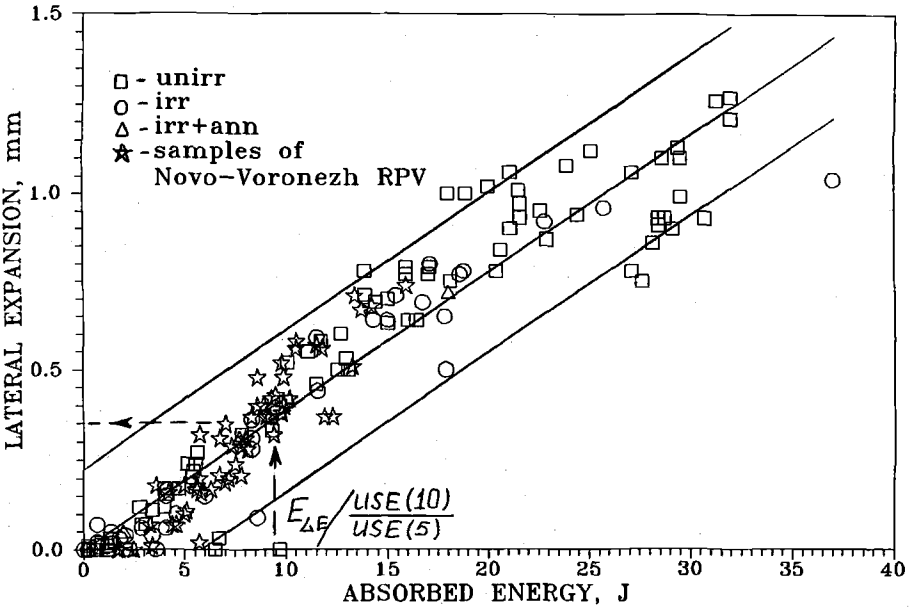

FIG. 3—*Plot of lateral expansion versus absorbed energy for subsize (5 by 5-mm) specimens of both base and weld metal of VVER-440 reactor pressure vessel.*

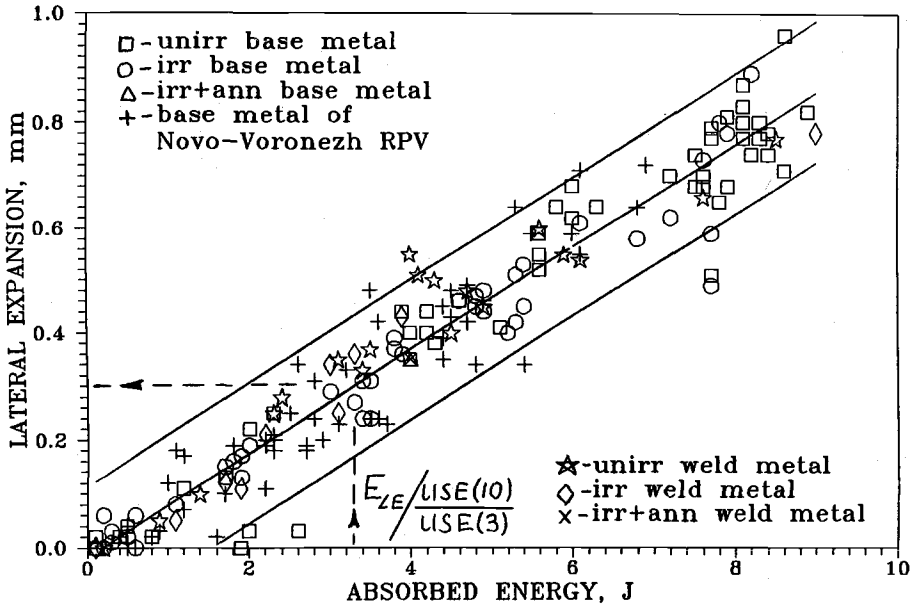

FIG. 4—*Plot of lateral expansion versus absorbed energy for subsize (3 by 4-mm) specimens of both base and weld metal of VVER-440 reactor pressure vessel.*

where DBTT is expressed in the Kelvin scale. The constants K (scale coefficient) and B depend on the nature of the metal (temperature dependence of the yield strength and statistical characteristics of the microdefect population). It was demonstrated [*3*] that Eq 4 agrees well with the experiment; the material condition may affect the general level of the ductile-to-brittle transition threshold (constant B) as well as the scale coefficient.

In establishing the empirical relationship between the DBTT of full-size and subsize specimens of particular materials, the following relation can be used

$$\text{DBTT}(F) = \text{DBTT}(S) + C \tag{5}$$

where DBTT(F) and DBTT(S) are the ductile-to-brittle transition temperatures for full- and subsize specimens, respectively, and C is a constant.

In Ref *4*, the summarized results of the comparison of the DBTT values for specimens of different sizes are given, which confirm the possibility of using Eq 5.

German researchers [*1*] have studied the correlation between DBTT, determined from standard Charpy and from subsized (3 by 4 by 27-mm) specimens. They used a number of low-alloyed steels with different heat treatments, some of which had been irradiated and some of which are weld metal. The absorbed energy levels of 41 and 68 J and the value of the expansion were selected as criteria for the determination of the DBTT of Charpy specimens. For subsized specimens the absorbed energy of 1.9 and 3.1 J and the expansion of 0.3 mm, correspondingly, were selected as criteria values. The Charpy specimen DBTT values ranged from −120 to 200°C (the bulk of the data points were confined to a range of −80 to +50°C). The results of the statistical analysis showed a linear dependence between the compared DBTT values and a shift value of 65 K

$$\text{DBTT}(10) = \text{DBTT}(3) + 65\ \text{K} \tag{6}$$

where DBTT(3) is the ductile-to-brittle transition temperature determined from 3 by 4-mm cross-section specimens, and DBTT(10) is the ductile-to-brittle transition temperature determined from 10 by 10-mm cross-section specimens.

As for the present work, a statistical treatment of the experimental data produced the following results. The relation between DBTT of specimens with 10 by 10-mm and 5 by 5-mm cross sections in the irradiated and unirradiated condition can be presented as follows (see Fig. 5)

$$\text{DBTT(10)} = \text{DBTT(5)} + 46, \text{°C} \tag{7}$$

For unirradiated and irradiated 10 by 10 and 3 by 4-mm specimens, the DBTT relation is (see Fig. 6)

$$\text{DBTT(10)} = \text{DBTT(3)} + 65, \text{°C} \tag{8}$$

It should be pointed out that the latter relation agrees perfectly with the independent German results [*1*]. The agreement of the results contained in this report and in Ref *1* expands the volume of the analyzed information and provides support for the validity of the established correlations. Therefore, on the basis of the data obtained and available international experience, it is recommended to use the following relation

$$\text{DBTT(10)} = \text{DBTT(3)} + 65, \text{°C} \tag{9}$$

to determine the values of DBTT(10) from the results of 3 by 4-mm cross-section specimen tests.

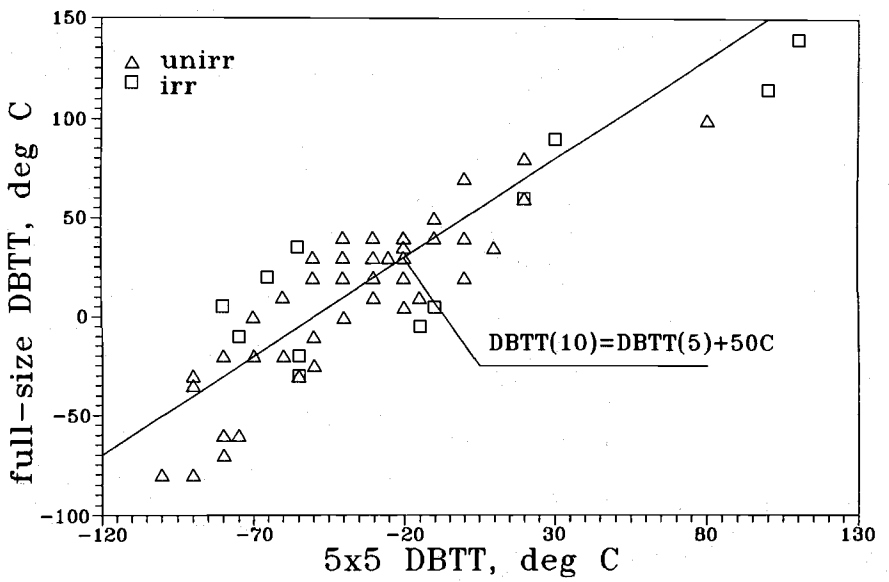

FIG. 5—*Correlation between full-size Charpy and subsize (5 by 5-mm) specimen transition temperature.*

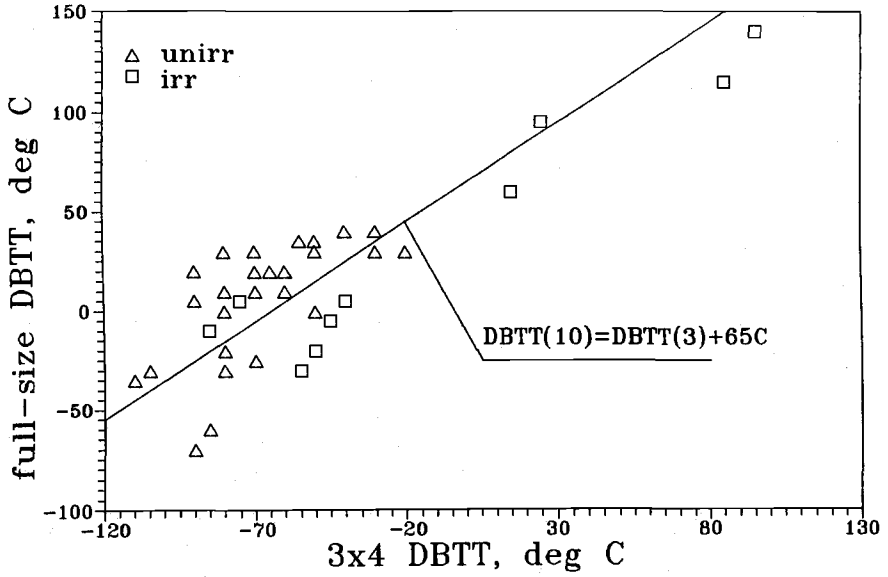

FIG. 6—*Correlation between full-size Charpy and subsize (3 by 4-mm) specimen transition temperature.*

As for the 5 by 5-mm cross-section specimens, bearing in mind the similarity of approach with regard to 3 by 4-mm specimens, it is recommended to use Eq 7, rounding the correlation constant to 50

$$\text{DBTT}(10) = \text{DBTT}(5) + 50, \text{°C} \tag{10}$$

Investigation of the Reactor Vessel Metal

In 1991, circumferential weld No. 4 of the reactor pressure vessel (RPV) at Novo Voronezh nuclear power plant Unit 3 (NVNPP-3) was subjected to reannealing. The reannealing of the NVNPP-3 RPV was carried out for the following reasons. For assurance of the design service life of the reactor vessels of VVER-440 B-230, the following measures were developed and recommended:

1. Installation of shielding assemblies in the core periphery.
2. Preheating of emergency make-up water for the primary circuit and a change in the scheme of its supply.
3. Introduction of additional interlocks and quick-acting isolation valves.
4. Annealing of weld No. 4 of the reactor vessels.

In accordance with the foregoing, in 1987 the annealing of NVNPP-3 reactor vessel was carried out at 430°C for 150 h. This would have permitted the design life of RPV to be obtained if all the other measures described above had been completed. However, the shielding assemblies and the quick-acting isolation valves were not installed at NVNPP-3, and therefore in 1991 the DBTT of the weld metal again approached the maximum permissible level. For this reason, a decision was made to perform reannealing of the NVNPP-3 reactor vessel. As mentioned above, the first annealing of the pressure vessel was carried out at 430°C.

This first annealing was successful, which permitted the subsequent annealing temperature of the RPV to be increased up to 475°C and thus the degree of recovery of the irradiated material properties to be enhanced. Therefore, annealing of the NVNPP-3 RPV was carried out at 475°C. To confirm the annealing effectiveness and to evaluate the DBTT of the weld before and after annealing, samples were taken from the inner surface of the reactor vessel wall, which were then used for fabricating subsize specimens. For taking samples, special electrodischarge machining equipment was developed and manufactured.

In accordance with the program plan, three 4-mm-thick samples of the base metal (at the core center level) and three 7.5-mm-thick samples of the weld metal were cut before annealing. After annealing, samples were cut only from the weld metal. Cutting was oriented so that samples were taken from the most irradiated areas of the reactor vessel metal. The scheme of sample cutting from the NVNPP-3 RPV is shown in Fig. 7.

Chemical Analysis of RPV Materials

Measurements of the concentrations of the impurity and alloying elements in weld No. 4 metal and in the base metal were performed using a SPECTROVAC GSG quantometer by the photoelectric spectral method. Calibration was made using standard specimens. The average measurement values are presented in Table 5. As seen from the data listed in Table 5, the average contents of phosphorus and copper in the weld metal are 0.028 and 0.12%, respectively. In the base metal these values are 0.012 and 0.16%, respectively.

The phosphorus and copper contents were also determined by the "wet" chemistry method. The average contents of phosphorus and copper in the weld metal were 0.029 and 0.12%, respectively. In the base metal the average content of phosphorus was 0.0106% and that of copper was 0.142%. Reasonable agreement of the results obtained from the chemical analysis of small amounts of impurities using different methods should be pointed out.

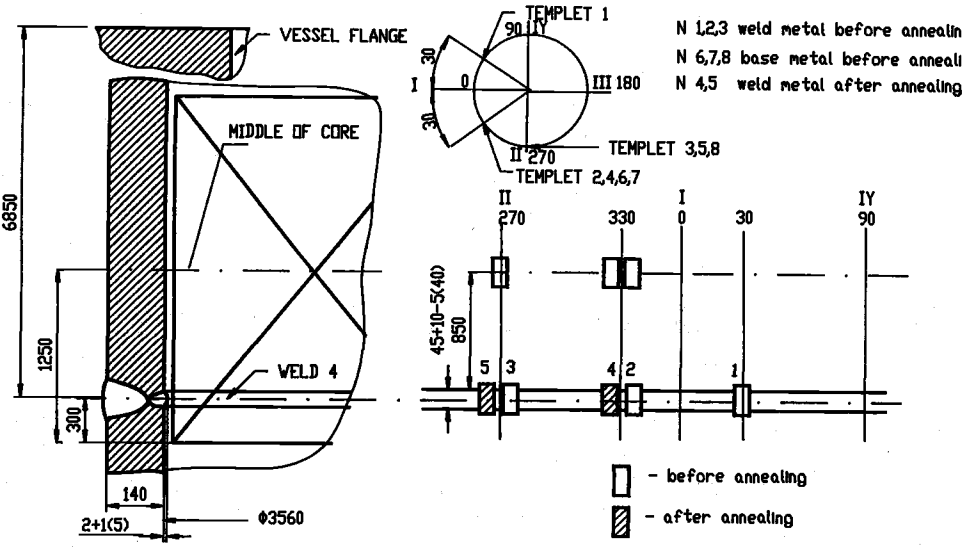

FIG. 7—*Scheme of templet cutting from the inner surface of the reactor vessel.*

TABLE 5—*Average content of the impurity and alloying elements in weld No. 4 metal and the base metal of 15Kh2MFA steel.*

Material	Contents of the Elements, mass %								
	P	Cu	Si	Cr	Mo	Ni	V	Mn	C
Weld metal	0.028	0.12	0.34	1.42	0.52	0.12	0.16	0.9	0.05
Base metal of the shell	0.012	0.16	0.30	2.65	0.68	0.2	0.28	0.44	0.14

Determination of Fast Neutron Fluence

During the fabrication of the specimens from the extracted samples, small pieces of metal were chosen for the determination of fast neutron fluxes. Neutron fluxes were determined by activity of manganese-54, which is accumulated in the RPV material as a result of a 54Fe(n,p)54Mn reaction having a threshold energy of 3 MeV. Neutron fluences for the samples were determined for different neutron fluxes and power operation histories. The neutron fluence values are listed in Table 6.

Hardness Measurements

Hardness measurements were carried out by the Rockwell method using a diamond cone with load of P = 150 kg at at least four points on the specimen surface. The following hardness values were obtained (the corresponding Brinell values are in parentheses):

1. *Before reactor vessel annealing*—Base metal: HRC = 12.5 to 13 (HB = 195 to 200 kg/mm^2); weld metal: HRC = 21 to 25 (HB = 235 to 255 kg/mm^2).
2. *After reactor vessel annealing*—Weld metal: HRC = 15.5 to 18 (HB = 210 to 230 kg/mm^2).
3. *After impact tests*—Weld metal specimens cut from the vessel before and after annealing were subjected to reannealing at 475 ± 5°C for 50 h. Both batches of specimens had the following hardness values: HRC = 15.5 to 18 (HB = 210 to 230 kg/mm^2), which agreed with the results in Item 2.

TABLE 6—*Fast neutron fluence for templets (samples) of Novo-Voronezh Unit 3 RPV.*

Templet Number	Material	Flux with Spent Fuel Assemblies, n/cm^2 · s	Flux with Normal Core, n/cm^2 · s	Total Neutron Fluence, n/cm^2 · s (E > 0.5 MeV)	Neutron Fluence in Three Last Core Lives between Annealing of RV, n/cm^2 (E > 0.5 MeV)
1	Weld metal	$1.22 \cdot 10^{11}$	$1.59 \cdot 10^{11}$	$7.1 \cdot 10^{19}$	$1.08 \cdot 10^{19}$
2	Weld metal	$1.14 \cdot 10^{11}$	$1.49 \cdot 10^{11}$	$6.61 \cdot 10^{19}$	$1.02 \cdot 10^{19}$
3	Weld metal	$1.07 \cdot 10^{11}$	$1.40 \cdot 10^{11}$	$6.2 \cdot 10^{19}$	$1.02 \cdot 10^{19}$
6	Base metal	$1.64 \cdot 10^{11}$	$2.13 \cdot 10^{11}$	$9.5 \cdot 10^{19}$	$1.45 \cdot 10^{19}$
7	Base metal	$1.80 \cdot 10^{11}$	$2.34 \cdot 10^{11}$	$10.4 \cdot 10^{19}$	$1.59 \cdot 10^{19}$
8	Base metal	$1.78 \cdot 10^{11}$	$2.32 \cdot 10^{11}$	$10.3 \cdot 10^{19}$	$1.57 \cdot 10^{19}$

Impact Tests of Subsize Specimens and Analysis of the Results

Figure 8 presents the results of weld metal sample tests for the RPV of NVNPP-3, cut before and after RPV annealing. DBTT(5) for the weld metal before annealing was +70°C and after annealing was +25°C. As there is no "archive" weld metal of the NVNPP-3 RPV, an attempt was made to simulate the original mechanical properties of the reactor vessel (at the time of the power unit startup) by a heat treatment of irradiated specimens. For this purpose the irradiated weld metal was subject to annealing at 560°C for 2 h. The results of this experiment are also shown in Fig. 8. Because of the small number of specimens, the level of the upper-shelf energy could not be determined. Later some special experiments were carried out, including those with surveillance specimens which showed that the simulating heat treatment did not adequately reproduce the initial material properties. In particular, these experiments showed that annealing at 560°C of irradiated weld metal yields Charpy data better than the initial condition, whereas annealing at 475°C [*5,6*] does not always completely recover the material's properties. Thus, the initial DBTT ($DBTT_i$) of the weld metal must be between the values of those two conditions, and therefore the $DBTT_i$ of the weld metal of NVNPP-3 RPV as measured using subsize specimens, was taken equal to +10°C (see Fig. 8, dashed line).

Figure 9 shows the results of the NVNPP-3 RPV base metal tests before annealing. The DBTT is equal to −40°C.

Figure 10 presents the scheme of irradiation embrittlement of the weld metal of NVNPP-3 RPV based on the current understanding of processes of irradiation embrittlement and annealing. The results of the specimen sample tests are used in the scheme for estimating the validity of the above representations and the degree of conservatism of the methods adopted for estimation of these parameters. In considering this problem, it was assumed that the transition temperatures corresponding to full-size Charpy specimens were

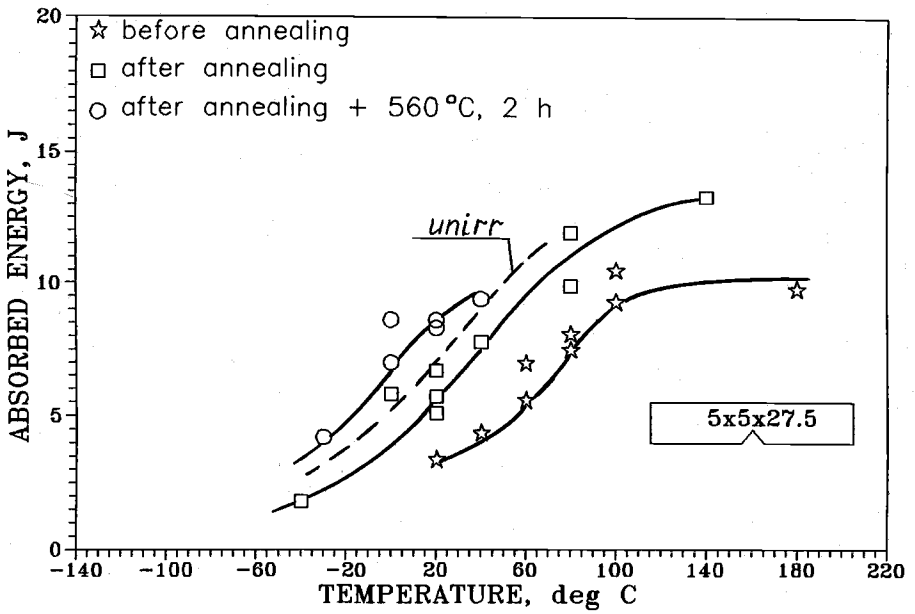

FIG. 8—*Impact tests of subsize specimens of weld metal of Novo-Voronezh Unit 3 reactor pressure vessel, cut before and after annealing of the vessel.*

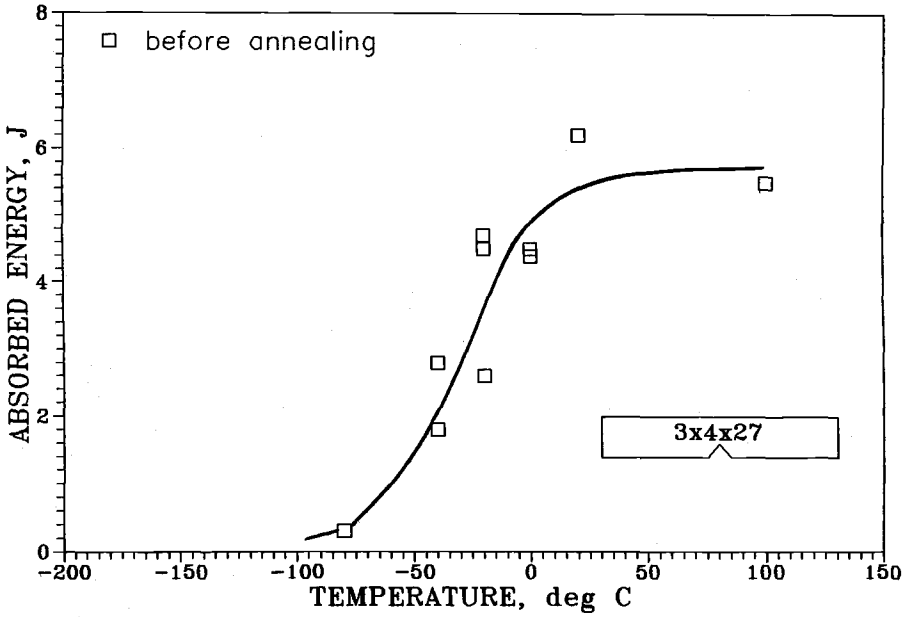

FIG. 9—*Impact tests of subsize specimens of base metal of Novo-Voronezh Unit 3 reactor pressure vessel, cut before annealing of the vessel.*

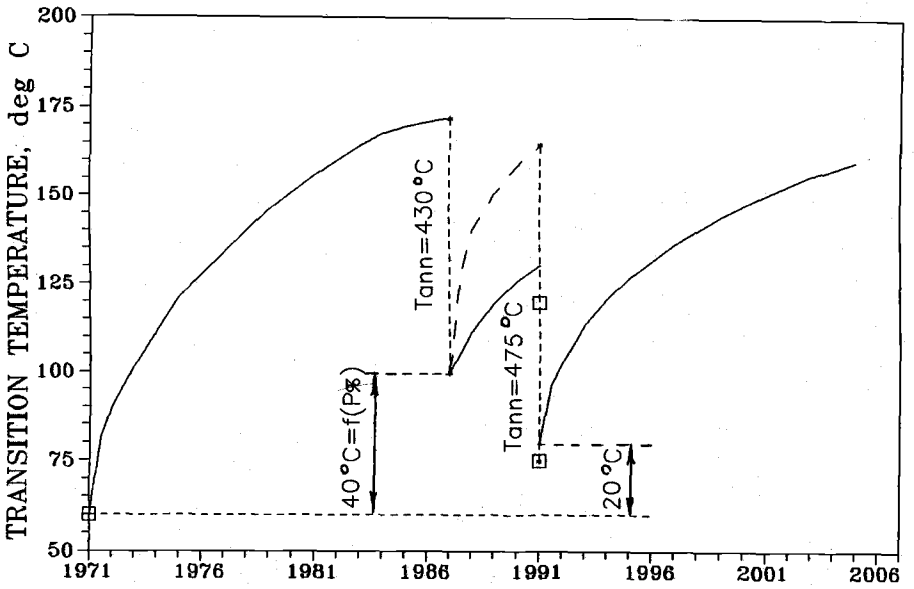

FIG. 10—*Scheme of in-operation changes in the DBTT of the weld metal of Novo-Voronezh Unit 3 reactor vessel.*

$DBTT_i = +10 + 50 = +60°C$ (according to Eq 10), preannealing DBTT = +70 + 50 = 120°C, and postannealing DBTT = +25 + 50 = 75°C. The average content of phosphorus in the weld metal was 0.029% and 0.12% for copper. In 1987 the neutron fluence on the weld metal was $6 \cdot 10^{19}$ n/cm^2, and between annealings it was $1.02 \cdot 10^{19}$ n/cm^2. According to the standards [2] currently in force, the shift in the DBTT is determined by the equation

$$\Delta DBTT_F = A_F(F/F_0)^{1/3}, °C \tag{11}$$

where

$$\begin{aligned} A_F &= 800\ (P + 0.07\ Cu), \\ F &= \text{fast neutron fluence at } E > 0.5 \text{ MeV n/cm}^2, \text{ and} \\ F_0 &= 10^{18} \text{ n/cm}^2. \end{aligned} \tag{12}$$

It is seen from the experience gained that, after annealing at 430°C, the residual shift of DBTT at this phosphorus content [5] should be 40°C. Thus, the DBTT of the weld metal after annealing is estimated to be 100°C. According to the method of estimation of the DBTT after the annealing of the RPV, currently in force in the USSR, a further change in the DBTT of the metal would be predicted in the following way. The postannealing value of DBTT of the metal is taken as the starting one, while its further change is determined by Eq 11 as shown in Fig. 10 by the dashed line. At the same time the whole set of the available information on reirradiation of annealed specimens indicates that the best agreement with the experimental data is reached using the approach of the so-called lateral shift [see the ASTM Guide for In-Service Annealing of Water-Cooled Nuclear Reactor Vessels (E 509–86)]. The estimation of change in the DBTT by this approach is shown by the solid line in Fig. 10. Of interest is the fact that the experimentally determined value of preannealing DBTT is close to the prediction by the lateral shift approach. After annealing at 475°C was carried out in 1991, the residual shift of the DBTT should be no higher than 20°C [5]. The results of metal sample tests after RPV annealing confirmed this estimate, too.

The estimate of changes in DBTT of the weld metal after annealing in 1991 is given using the scheme of lateral shift.

Conclusion

The impact tests of full-size Charpy specimens and 5 by 5 by 27.5-mm and 3 by 4 by 27-mm subsize specimens manufactured from the VVER-440 vessel materials have been carried out. The criterion energy level for determination of the DBTT of the chosen subsize specimens was determined. The empirical relationship between the ductile-to-brittle transition temperature of full-sized and subsized specimens has been established based on the analysis of the experimental data. The dependencies obtained were used in the investigation of the metal samples taken from the inner surface of the reactor vessel before and after annealing. The tests of metal samples cut in 1991 before and after annealing of the Novo-Voronezh NPP Unit 3 reactor vessel showed that annealing at 475 ± 15°C is an effective means for recovery of the ductile-to-brittle transition temperature and the upper-shelf energy of the VVER-440 reactor pressure vessel steel.

References

[1] Ahlstrand, R., Klausnitzer, E., Lange, D., Leitz, C., Pastor, D., and Valo, M., "Evaluation of the Recovery Annealing of the Reactor Pressure Vessel of NPP Nord (Greifswald) Units 1 and 2

by Means of Subsize Impact Specimens," *Radiation Embrittlement of Nuclear Reactor Pressure Vessel Steels: An International Review (Fourth Volume), ASTM STP 1170,* L. E. Steele, Ed., American Society for Testing and Materials, Philadelphia, 1993.

[2] Calculation Standards for Strength of Equipment and Pipes of Nuclear Power Units, PNAE-G-7-002-86, Energoatomizdat, NGA-01-85-1, NIKIET, 1989, in Russian.

[3] Chechulin, B. B., "The Size Factor and Statistical Nature of Metal Strength," *Metallurgizdat,* Moscow, 1963, in Russian.

[4] Alexander, D. J. and Klueh, R. L., "Specimen Size Effects in Charpy Impact Testing," *Charpy Impact Test: Factors and Variables, ASTM STP 1072,* J. M. Holt, Ed., American Society for Testing and Materials, Philadelphia, 1990, pp. 179–191.

[5] Amayev, A. D., Kryukov, A. M., and Sokolov, M. A., "Recovery of the Transition Temperature of Irradiated VVER-440 Vessel Metal by Annealing," *Radiation Embrittlement of Nuclear Reactor Pressure Vessel Steels: An International Review (Fourth Volume), ASTM STP 1170,* L. E. Steele, Ed., American Society for Testing and Materials, Philadelphia, 1993.

[6] Amayev, A. D., Kryukov, A. M., Sokolov, M. A., Badanin, V. I., and Nikolayev, V. A., "Investigation of the Mechanical Properties Recovery Processes of the Irradiated Pressure Vessel Steels by Annealing," *Proceedings,* International Conference on Radiation Materials Science, Alushta, 22–25 May 1990, Vol. 4, Kharkov-1990, in Russian, pp. 25–32.

Matti Valo[1] *and Ralf Ahlstrand*[2]

Application of Reconstitution Welding Technique for Studying Base Metal of a Novovoronesh Unit-1 Trepan Sample

REFERENCE: Valo, M. and Ahlstrand, R., **"Application of Reconstitution Welding Technique for Studying Base Metal of a Novovoronesh Unit-1 Trepan Sample,"** *Small Specimen Test Techniques Applied to Nuclear Reactor Vessel Thermal Annealing and Plant Life Extension, ASTM STP 1204,* W. R. Corwin, F. M. Haggag, and W. L. Server, Eds., American Society for Testing and Materials, Philadelphia, 1993, pp. 440–456.

ABSTRACT: The toughness of a through-wall trepan sample cutout from the shut-down Novovoronesh Unit-1 was characterized with reconstituted specimens. The trepan sample was taken from the core weld and also contained base metal from the upper and lower forged rings. Because the sample is relatively small, with a diameter of 110 mm and a height of 120 mm, effective use of the material is of vital importance. Standard Charpy specimen size was chosen to be used throughout the sample. All the specimens were reconstituted from 10 by 10 by 16-mm unit volumes. Both Charpy-V impact and Charpy-size three-point bending (3-PB) specimens were used. The validation of specimen preparation technique includes Charpy-V impact and static 3-PB tests with reference and irradiated materials and is described in detail. The results for one base metal, including the vessel wall condition and annealed conditions at 470°C/168 h and 650°C/2 h, are reported and discussed.

KEYWORDS: pressure vessel steel, irradiation embrittlement, annealing, specimen reconstitution, vessel wall sampling

Irradiation embrittlement of pressure vessel steel is an important safety-related phenomenon in older nuclear power plants. It may limit the lifetime of the plant and is often encountered when plant life extension measures are considered. Thermal annealing of the pressure vessel is a straightforward and effective means of restoring the toughness properties of the vessel.

Vessel annealing has been applied many times for Soviet-designed VVER-440 plants [*1*]. However, there is not much surveillance-type data available on the material behavior in annealing, reirradiation, or in multiple annealing-reirradiation cycles. Often the lack of archive or surveillance material is a serious drawback in older plants.

The most relevant data on pressure vessel wall properties is obtained by taking and studying in-situ vessel wall samples. Small samples have been taken from operating power plants [*2*] and larger samples from closed units like Gundremmingen [*3*] and Novovoronesh-1.

The pressure vessel wall is inhomogeneous in many respects, and the measurement of a brittle-ductile transition curve requires at least ten specimens. Consequently, the effective use of the available material is a primary requirement, and a proper specimen preparation technique can increase the attainable information from a vessel wall sample.

[1] Senior research scientist, VTT (Technical Research Center of Finland), Reactor Laboratory, P.O. Box 200, SF-02151 Espoo, Finland.
[2] Manager, Imatran Voima Oy, P.O. Box 112, SF-01601 Vantaa, Finland.

Because specimen size is an inherent quality factor in toughness testing, standard Charpy specimen size was chosen instead of subsize specimens. In fracture mechanics tests, Charpy-size specimens usually violate specimen size criteria—in this respect they are subsize specimens. The number of available specimens were optimized by reconstituting all specimens from small active center sections. The use of the chosen center section length of 16 mm has proven to be acceptable. The applied specimen preparation technique and its verification are described in detail.

The Power Plant

Novovoronesh Unit-1 belongs to the first generation of Soviet-made pressurized water reactors. Its nominal electric output was 220 MW, it was operated for 20 years as originally planned, and it was shut down in 1984. The steel type used in the vessel is the same as in the VVER-440 units, namely 15Kh2MFA. The pressure vessel temperature of the operating unit has been 250°C, somewhat lower than 265°C of the VVER-440 units. The total vessel wall thickness is 120 mm including a 20-mm-thick cladding.

Specimen Preparation Techniques

The essential tools used for specimen preparation are an electric wire discharge machine and a reconstitution welding apparatus. The discharge machine allows keeping the cutting tolerances of the trepan block minimal and guarantees the dimensional quality of the specimens.

Discharge Cutting

An electric discharge cutting machine is an accurate numerically controlled tool, which produces the final surface quality and has a cutting waste of material of only 0.3 mm. Other advantages are the absence of reaction forces in the cutting process and the residual stress-free surface that is produced.

The machine is used for sectioning the trepan block, for removing the oversized end tabs and weld seams from the welded specimens, and for machining the V-grooves, the side-grooves, and the integral clip-gauge seats in the specimen. The only drawback is the slow cutting speed.

Reconstitution Welding

The specimens were reconstituted with the stud arch welding technique. The preparation sequence is shown in Fig. 1, and the welding parameters are given in Table 1. Discharge time and voltage were measured with a transient recorder. The current given is the nominal one for the equipment. The length of 16 mm chosen for the active center insert is near the minimum which fulfils the requirements given in ASTM E 1253-88, "Guide for Reconstitution of Irradiated Charpy Specimens" for Charpy-V specimens. Because the parallel alignment of the end tab and the center insert is often distorted in welding by unsymmetric seam formation or uneven seam cooling, oversized end tabs of 10.5 by 10.5-mm cross section with subsequent machining were used.

The main concern in specimen preparation by welding is the risk of thermally annealing the irradiated material. Excessive temperature transient is avoided by applying a low-energy weld pulse and by using copper heat sinks. Temperature transient due to welding is discussed later on. If the active center section length is of the order of the specimen thickness, other

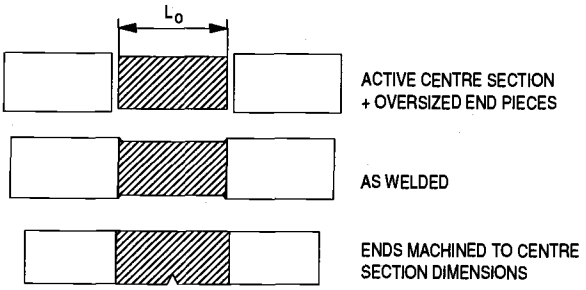

FIG. 1—*Specimen preparation sequence.*

factors like the distortion of the deformation field in the specimen by the hard weld seams and residual stresses of the weld seams will have an effect on the test value. The chosen insert length of 16 mm is considered to hold for the deformed area of the specimen.

The quality of the weld seam is not ideal. The weld usually contains small gas bubbles but still stands the test load. In a few cases, the weld seam has failed. This occurred with reconstituted specimens annealed for 650°C/2 h apparently because a brittle zone was formed in the weld during annealing. Failure did not occur when the specimens were reconstituted after annealing. It was also necessary to remove the tight magnetite layer formed during annealing from the surfaces to be welded in order to guarantee a full surface weld seam.

Testing

Test Methods

The test methods for the Charpy-type specimens comprise normal instrumented impact testing of Charpy-V specimens and static elastic-plastic fracture toughness measurements with Charpy-size 3-PB specimens.

The instrumented impact tests were performed according to DIN 50115. The hammer uses a pneumatic mechanism for specimen transfer and electric recording of impact energy and has a transient recorder for load-time recording. The impact velocity is 5.4 m/s.

The static *J-R* curve testing was performed as far as applicable according to ASTM Test Method for J_{Ic}: A Measure of Fracture Toughness (E 813-89). The crack length is measured with a partial unloading compliance technique. All specimens used for *J-R* curve testing were 20% side-grooved. Most of the specimens were tested in the transition region where valid K_{Ic} or J_{Ic} values cannot be obtained. Then the fracture toughness was defined as the value of J at the onset of cleavage fracture.

TABLE 1—*The welding parameters.*

Discharge time of the arch	ca. 70 ms
Arch voltage	ca. 24 V
Current	ca. 700 A
Energy	ca. 1.2 KJ

The results usually violate the specimen size criteria and are to be considered as non-standard.

Analyzing Methods

The results of Charpy-V tests are represented in the form of energy-temperature transition curves defined by hyperbolic tangent function fittings of the form

$$E = 0.5 \times B \{1 + \text{TANH} [(T - T_{50})/C]\} \quad (1)$$

where B corresponds to the upper shelf energy, T_{50} to the 50% upper shelf energy transition temperature, and C is a fitting parameter. The lower shelf energy has been approximated to zero. In the fitting process, the square of the absolute differences has been minimized. Transition temperature values have been calculated from the fitted curves.

The fracture toughness values corresponding to cleavage fracture initiation are presented in the form of K_{Jc} values and are treated as described below.

The scatter in the brittle fracture toughness values can be described with the equation

$$P_f = 1 - \exp\{-[(K_I - K_{\min})/(K_0 - K_{\min})]^4\} \quad (2)$$

where P_f is the cumulative failure probability at a stress intensity factor level, K_I, K_0 is a specimen thickness and temperature-dependent normalization parameter, and $K_{\min}$ is the lower bound fracture toughness which for steels is close to 20 MPa$\sqrt{m}$. As described in Ref 6, the temperature dependence of parameter K_0 can be expressed for Charpy-size specimens in the form

$$K_0 = 34 + 97 \exp [0.019 (T - T_0)] \quad (3)$$

where T_0 is the temperature at which the mean fracture toughness is 100 MPa$\sqrt{m}$. The above given functional form is found to be universal for many kinds of steels [7].

The experimental results were analyzed by combining Eqs 2 and 3 for determination of the transition temperature values and for drawing the scatter bands.

The unirradiated and irradiated test results can be analyzed jointly by describing the fluence dependence of the irradiation embrittlement temperature shift explicitly, usually in the form

$$T_0 = T_{01} + A \, (\text{fluence}/10^{-18})^B \quad (4)$$

where A and B are free parameters. The data in Fig. 8 have been analyzed according to this formula.

Validation of Specimen Preparation Technique

Validation of specimen preparation technique consists of two kinds of experiments. First, the temperature transient in the specimen due to welding is measured carefully in order to prove that the use of the chosen center section length is conservative concerning the possibility of thermal anneal in welding. Secondly, a comparison of the original specimen test values with reconstituted specimen test values is performed for the test methods applied in the study.

The validating tests for Charpy-V and 3-PB fracture mechanics specimens were done with 15Kh2MFA-type Loviisa surveillance material or A533B-type material JRQ [*4*], which is a Japanese plate used in the IAEA Coordinated Research Program for "Optimizing of Reactor Pressure Vessel Surveillance Programmes and Their Analyses," Phase 3.

Temperature Transient in the Specimen due to Welding

A conservative criterion for the irradiated material to be unaffected by welding is that the temperature due to welding does not exceed the original reactor irradiation temperature. The measurements show that this criterion is exceeded within about a 3-mm distance from the weld surface for the 250°C reactor vessel wall temperature.

During welding the temperature profile in the center section was measured with special instrumented bars. The bar is shown in Fig. 2. It is made of two split bar halves with a borehole in the center. The distance between the surface to be welded and the borehole bottom is measured, a Copper-Constantane thermocouple with uninsulated wire end tips is placed in the hole, the halves are subsequently pressed together for flattening the wires, and finally they are spot welded at four points under compression. The residual stresses of the welds keep the halves tightly pressed together and guarantee a good thermal contact between the thermocouple wire ends and the specimen. These instrumented specimens were welded like the other specimens, and the thermocouple signal was recorded with a transient recorder. The recorded temperature maximum in different distances from the weld surface is given in Fig. 3 for different welding energies. About 1.2 kJ is used for preparing the specimens. The cooling time of the specimen after welding is also short. The time the specimen temperature is higher than ca. 250°C is only a fraction of a second.

Charpy-V Specimen Tests

Charpy-V specimens were reconstituted from broken Loviisa surveillance base metal specimens in the reference and irradiated conditions. The fluence of the irradiated specimens was 1.4×10^{20} n/cm^2, $E > 1$ MeV. The specimens were originally irradiated in the surveillance position of Loviisa nuclear power plant. The center section length used for reconstitution was 16 mm. Because the test matrix of the Novovoronesh-1 trepan included a simulated reference condition produced by a 650°C/2 h annealing, the same heat treatment was given also to some irradiated and reference surveillance specimens.

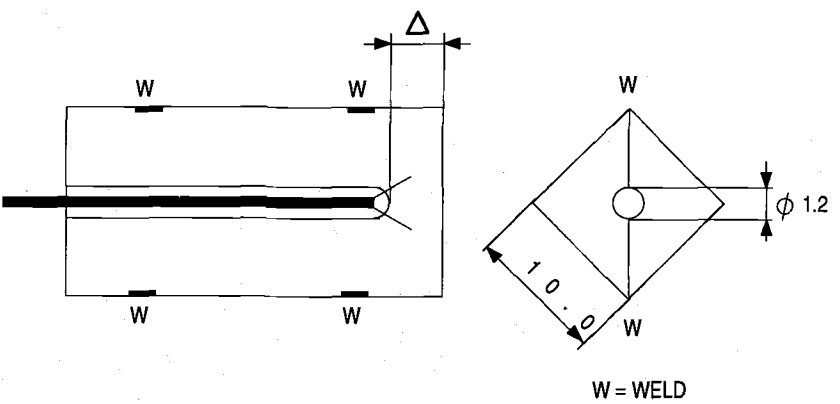

FIG. 2—*An instrumented split bar for temperature measurement.*

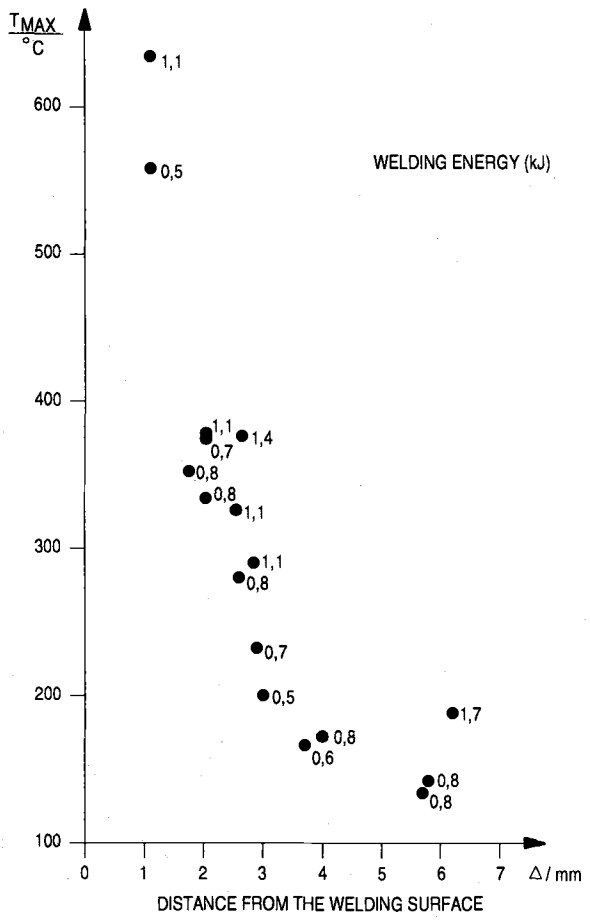

FIG. 3—*The measured temperature maximum in the specimen due to welding at different distances from the weld surface.*

Figure 4 shows the measured Charpy-V transition curves for the original full size for the reconstituted and for the annealed specimens. The transition temperature values from hyperbolic tangent curve fittings are given in Table 2.

According to Fig. 4, the transition curve for reference specimens is reproduced by reconstituted specimens almost ideally. For irradiated specimens, the original transition curve and the curve measured with reconstituted specimens differ slightly. The difference in the irradiated specimen transition curve estimations is considered to be within the experimental scatter and explained by the rather large intrinsic scatter in the material impact values and by the small number of reconstituted specimens. However, the reconstituted upper shelf value is slightly lower than the original value.

The transition curve measured with irradiated, 650°C/2 h heat-treated specimens given in Fig. 4 is not connected with validation of specimen preparation technique. This heat treatment, called a simulated reference heat treatment, was used to evaluate the unknown material properties of the unirradiated vessel wall. The measured transition curve has a

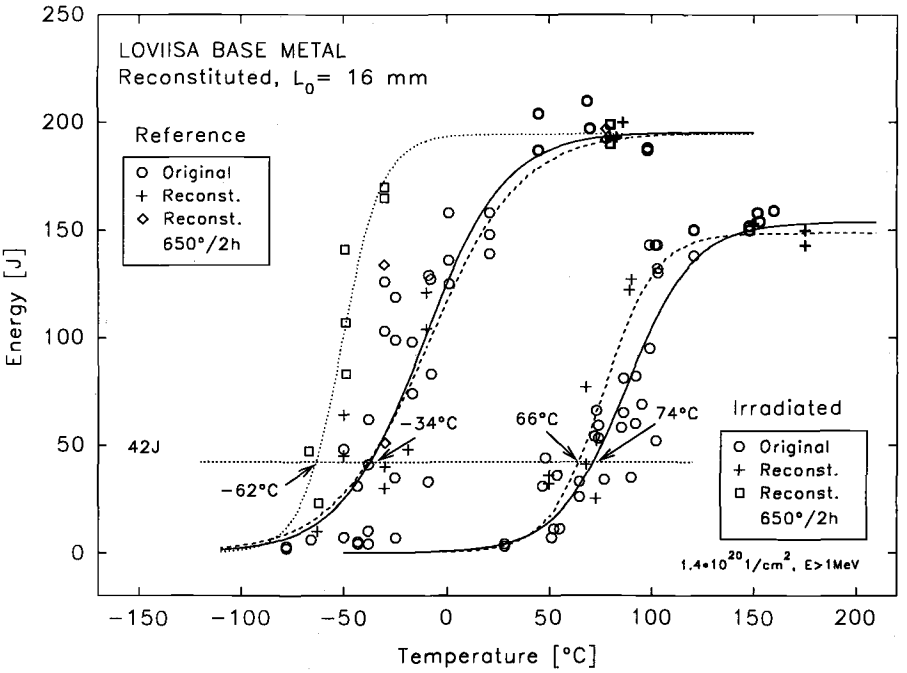

FIG. 4—*Original and reconstituted specimen Charpy-V transition curves for Loviisa base metal in different conditions.*

different curve shape and a lower transition temperature than the original reference condition. Only the upper shelf energy seems to recover correctly. Hence the conception of a simulated reference heat treatment, at least using these parameters, does not work.

3-PB Fracture Mechanics Specimen Tests

The geometry of 3-PB specimens used for validation as well as for studying the trepan is given in Fig. 5. The clip gauge for measuring the crack mouth opening displacement is seated on the 1-mm-deep sharp integral edge machined on the specimen surface.

Ductile Tearing—The fracture resistance curves describing the ductile tearing behavior have little scatter from specimen to specimen. Because only few specimens are needed, the

TABLE 2—*T_{42J}-transition temperatures for Loviisa surveillance base metal used for validation experiments.*

	T_{42J}/°C
Original reference	−34
Reconstituted reference	−34
Original irradiated	74
Reconstituted irradiated	66
Reconstituted irradiated, annealed (650°C/2 h)	−62

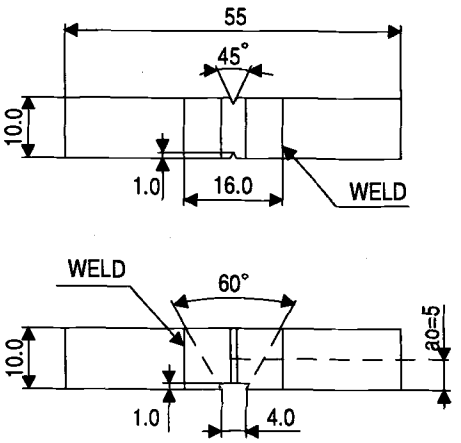

FIG. 5—*The reconstituted 3-PB fracture mechanics specimen.*

aim was to find out experimentally the lower limit of an acceptable center section length. For JRQ material, neutron irradiation clearly effects the ductile tearing behavior [5].

The fracture resistance curves measured at 180°C for reference material are given in Fig. 6 and for irradiated material in Fig. 7. The figures reveal that the original fracture resistance curves can be reproduced with reconstituted specimens using only short center section lengths of about 6 mm for reference specimens and about 5 mm for irradiated specimens. The

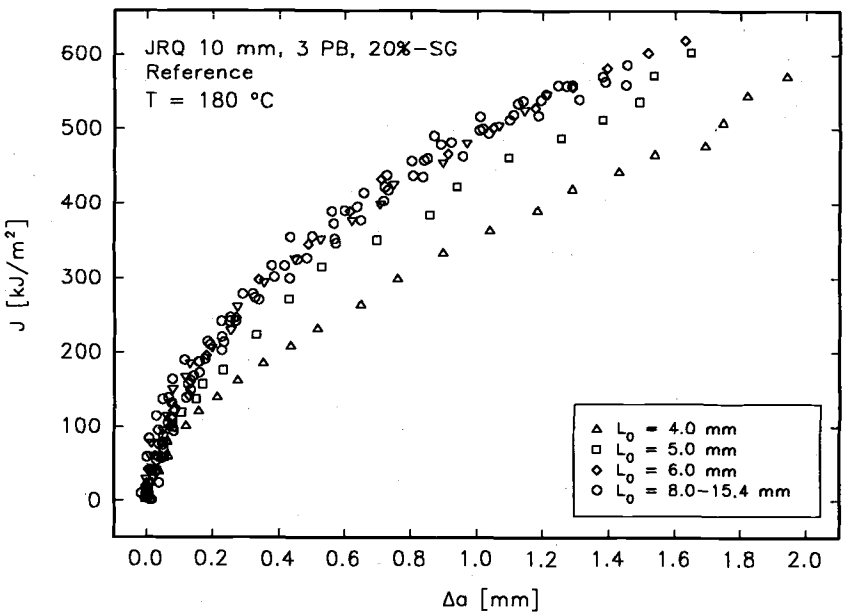

FIG. 6—*Fracture resistance curves for reconstituted unirradiated JRQ specimens.*

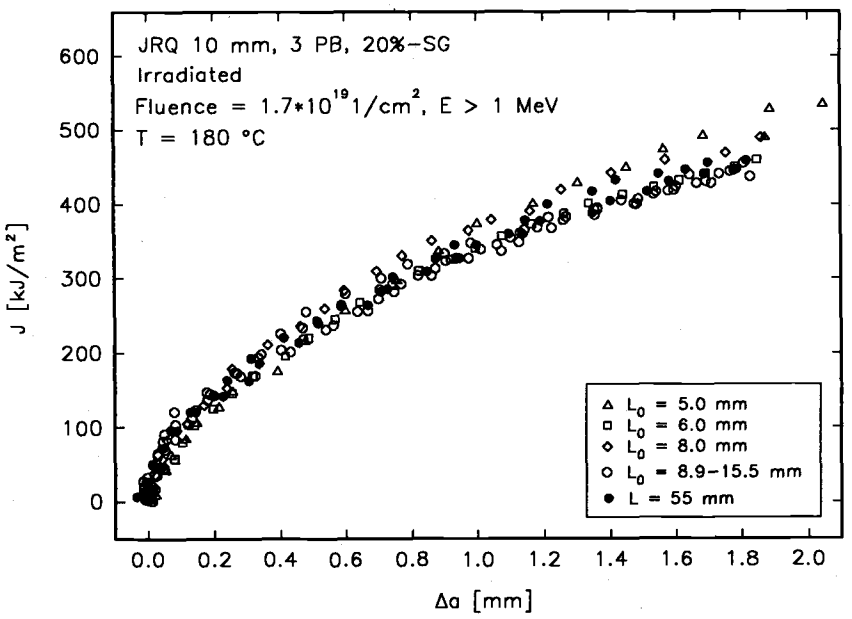

FIG. 7—*Fracture resistance curves for reconstituted irradiated JRQ specimens.*

experiments indicate that the deformation field in a precracked, side-grooved specimen do not extend outside the central portion of about 5-mm length because the reconstituted specimens with hard weld seams 5 mm apart from each other give the same test result as the original specimen. The fracture resistance curve is not especially sensitive to thermal annealing either because, according to Fig. 3, the temperature in the center of the specimen has reached about 350°C. Center section lengths shorter than about 10 mm should not be used for irradiated specimens because of the risk of exceeding the irradiation temperature in the center of the specimen during welding and because the uncertainty in defining the exact weld seam positions will be rather large with short sections. The deformation zone size increases when the material becomes softer, and longer center sections are then necessary. For this reason, shorter center sections work for irradiated material than for unirradiated material as demonstrated by Figs. 6 and 7.

Brittle Fracture Initiation—The measured brittle fracture initiation values have relatively high scatter, and hence the verification is done only for a few center section lengths. The lengths of 10 and 12 mm were chosen, as the ductile tearing suggests that relatively short lengths might be acceptable with precracked specimens.

JRQ material is used for the tests. The brittle fracture initiation values K_{Jc} for this material previously measured with 3-PB Charpy size specimens and RCT specimens of 12-mm thickness [5] are given in Fig. 8. In this figure, a single curve is fitted to the unirradiated and irradiated specimen values. The results from the reconstituted specimen tests are given in Fig. 9 with the same scatter bands as in Fig. 8. The test temperature of the unirradiated specimens was −40°C and that of the irradiated specimens +100°C.

The considerable scatter in the brittle fracture initiation values and the small number of reconstituted specimens make the comparison of original and reconstituted specimen test values to some extent uncertain. However, the toughness values measured with reconstituted specimens are well centered around the average curve, and the number of points outside

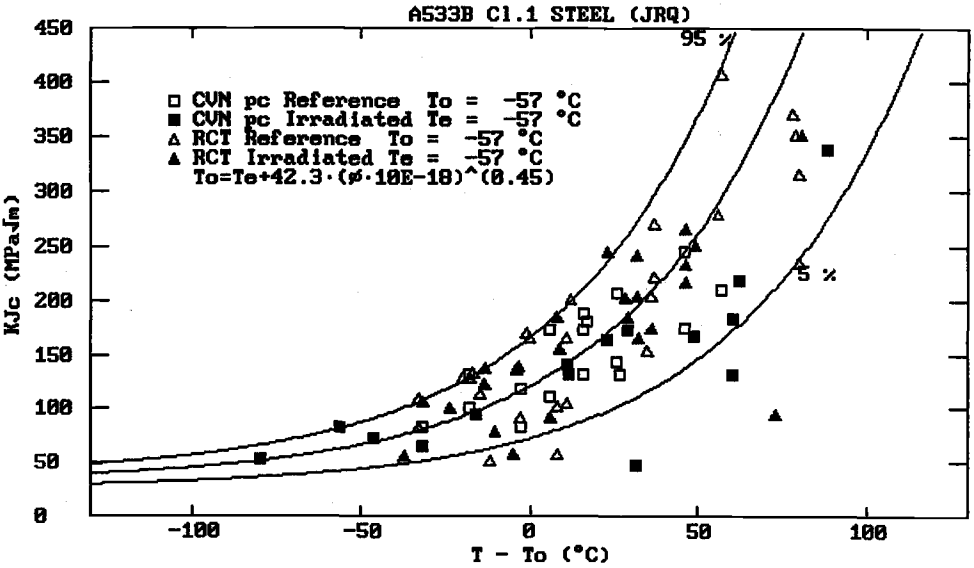

FIG. 8—*Brittle fracture initiation toughness for JRQ material measured with original 3-PB specimens and RCT specimens.*

the 5% offset curves is as expected. The values are not biased according to the center section lengths, i.e., 10 and 12 mm, which indicates that 10 mm is not a critical center section length. It should be also noted that the reference and irradiated specimen test temperatures differ by 140°C. Hence, in the case of incorrect specimen preparation, a large potential temperature shift due to specimen annealing exists but no shift is observed.

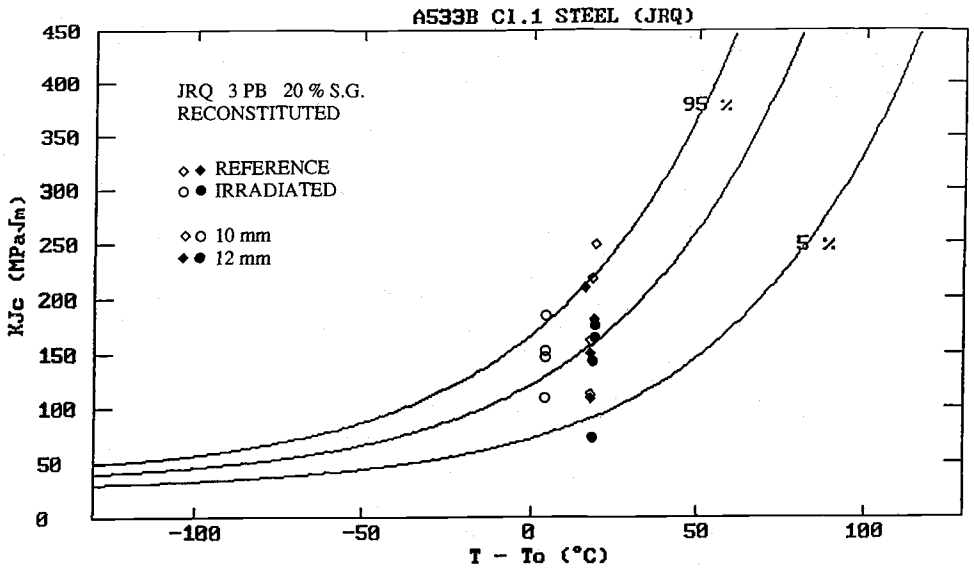

FIG. 9—*Brittle fracture initiation toughness for JRQ material measured with reconstituted 3-PB specimens. The fitted curves of Fig. 8 are redrawn.*

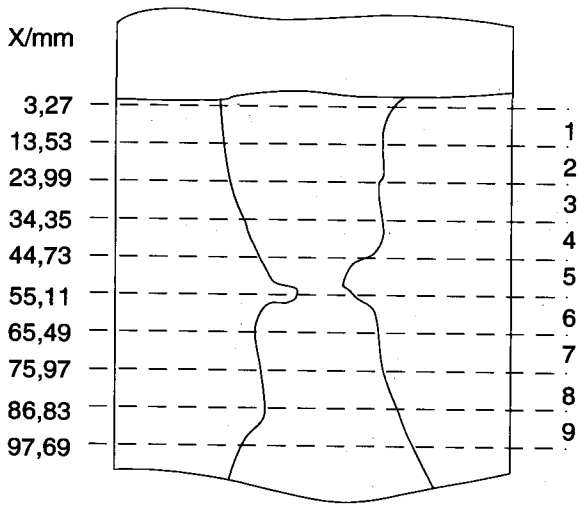

FIG. 10—*The weld seam profile on the trepan sample, coding of the disks, and the coordinates of the cutting lines.*

Characterization of the Trepan Base Metal-2 Material

Sectioning of the Trepan Block

Before sectioning the trepan block, the position and shape of the weld seam was identified by polishing and etching the cylindrical block surface. The profile of the weld is shown in Fig. 10. Before the final sectioning, two thin side strips extending from the inner surface to the outer surface were cut from the cylindrical block surface, one for chemical analyses and the other for neutron dosimetry.

The sectioning of the block was started by cutting the block into disks. The coordinates of the cutting lines are given in Fig. 10. Before cutting the disks into smaller units, the positions of the weld fusion lines on the disks were identified by polishing, etching, and

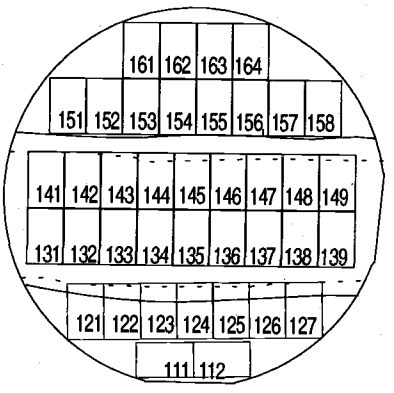

FIG. 11—*Sectioning of Disk 1 viewed from the vessel inner surface side. Weld fusion lines are drawn on the disk inner surface with a solid line and on the outer surface with a dashed line. Base metal-2 is on the lower side of the figure.*

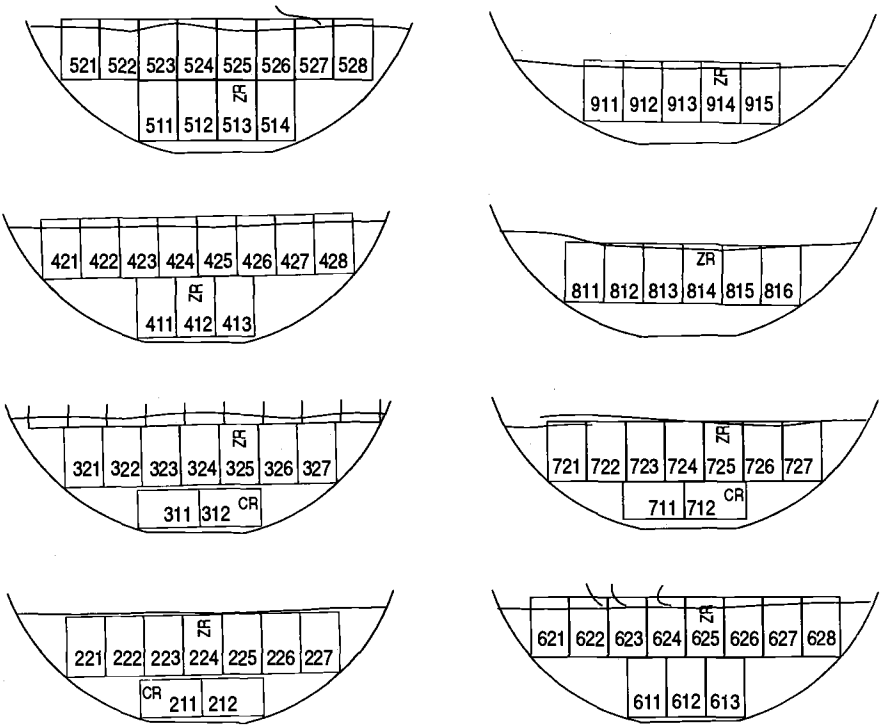

FIG. 12—*Sectioning of base metal-2 areas in Disks 2-9.*

photographing the surfaces. The cutting lines in Disk 1 are shown in Fig. 11 and for base metal-2 samples in other disks in Fig. 12.

The V-grooves were machined and the fatigue cracks made on the vessel outer surface sides of the disks except for Disks 1 and 4, where the grooves were on the disk inner surface.

Test Matrix

The test matrix for base metal-2 samples is given in Table 3. Only the specimens in ZR orientation (TS) are included in the matrix.

Neutron Fluence and Chemical Analyses

The neutron fluence evaluation [7] is based on measured specific 54 Mn activities, on neutron spectra given by the plant owner, on IRDF-90 (IAEA, 1990) cross-section data, and on electric power output statistics of the plant. The fluence gradient in the wall is nearly radial. The gradient in the vessel cylindrical direction is only 1.2%/50 mm and even less in the circumferential direction.

The numerical neutron fluence values for different disks are included in Table 3 using the unit $E > 1$ MeV, and in Tables 5 and 6 in units $E > 0.5$ MeV.

Chemical analysis was made with optical emission spectroscopy. The values for base metal-2 are given in Table 4.

TABLE 3—*Test matrix for trepan base metal-2.*

Disk	Fluence, 10^{19} n/cm², $E > 1$ MeV	Number of Specimens					
		Charpy-V			3-PB specimens		
		I	A	R	I	A	R
1	1.37	7					
2	1.20				7		
3	1.05			7			
4	0.91	8	4				
5	0.79				12		
6	0.68						11
7	0.58	7					
8	0.49		6				
9	0.41	5					

where
I = pressure vessel wall condition.
A = annealed 470°C/168 h.
R = simulated reference, annealed 650°C/2 h.

TABLE 4—*Chemical analyses of trepan base metal-2 in atomic percentages.*

C	Si	Mn	P	S	Cr	Ni	Mo	Al	Cu	V
0.14	0.33	0.43	0.015	0.009	2.66	0.096	0.68	0.005	0.094	0.34

TABLE 5—*The Charpy-V transition temperatures of trepan base metal-2.*

Disk	Fluence, 10^{19} n/cm², $E > 0.5$ MeV	Condition	T_{47J}, °C	$T_{LE0.9mm}$, °C
1	2.71	Vessel wall	41	38
4	1.93	Vessel wall	35	40
7	1.28	Vessel wall	25	26
9	0.89	Vessel wall	28	31
4	1.93	470°C/168 h	8	8
8	1.08	470°C/168 h	7	10
3	2.18	650°C/2 h	−25	−22

TABLE 6—*Fracture toughness transition temperatures of trepan base metal-2.*

Disk	Fluence, 10^{19} n/cm², $E > 0.5$ MeV	Condition	$T_{100MPa\sqrt{m}}$, °C
2	2.43	Vessel wall	−59
5	1.70	Vessel wall	−56
6	1.48	650°C/2 h	−118

Test Results

The measured Charpy-V transition curves are shown in Figs. 13 and 14. The measured fracture toughness values, K_{Jc}, based on brittle fracture initiation, are given in Fig. 15. All the test results were obtained with reconstituted specimens. No size correction is made for the test values. The measured Charpy-V transition temperatures are given in Table 5 and the fracture toughness transition temperatures in Table 6.

Discussion

Reconstitution technique and its validation was already discussed with the validation tests. The data on the fracture properties are shown in Figs. 13, 14, and 15. The vessel wall condition was measured with Charpy-V specimens for Disks 1, 4, 7, and 9, and with fracture mechanics specimens for Disks 2 and 5. If the first disk layer is excluded, the toughness changes through the wall gradually and the total gradient is about 10°C. This difference is measured with Charpy specimens; with the small number of fracture mechanics specimens prepared from Disks 2 and 5, a difference in the transition temperatures between these layers could not be seen. The measured toughness gradient is small and raises no safety-related concerns. The Charpy transition curve of the first disk layer deviates from the other layers. Its upper shelf energy value is only half of the other layer values, but the transition temperature is nearly the same. Evidently the material of these specimens has been affected by a heat treatment during the production of vessel wall weld seam or cladding. The V-grooves for the first layer specimens were machined on the side of the vessel wall inner surface. The nearest distance from the V-groove bottom to the weld fusion line was about 6 mm and to the cladding fusion line about 5 mm. The weld geometry is such that the distance between the weld fusion line and the growing crack will increase when the specimen is tearing in the test.

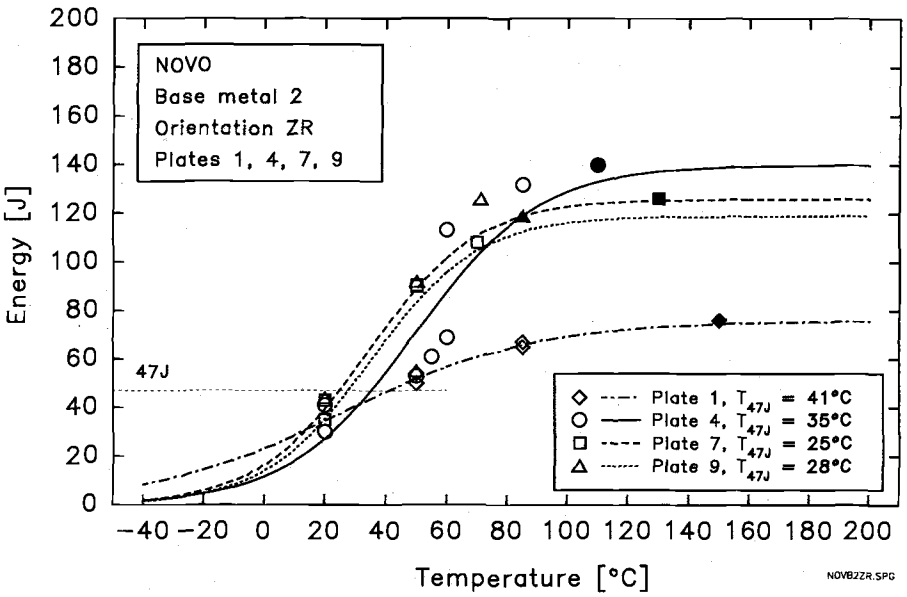

FIG. 13—*Charpy-V transition curves for trepan base metal-2 in the vessel wall condition. Closed points indicate upper shelf behavior.*

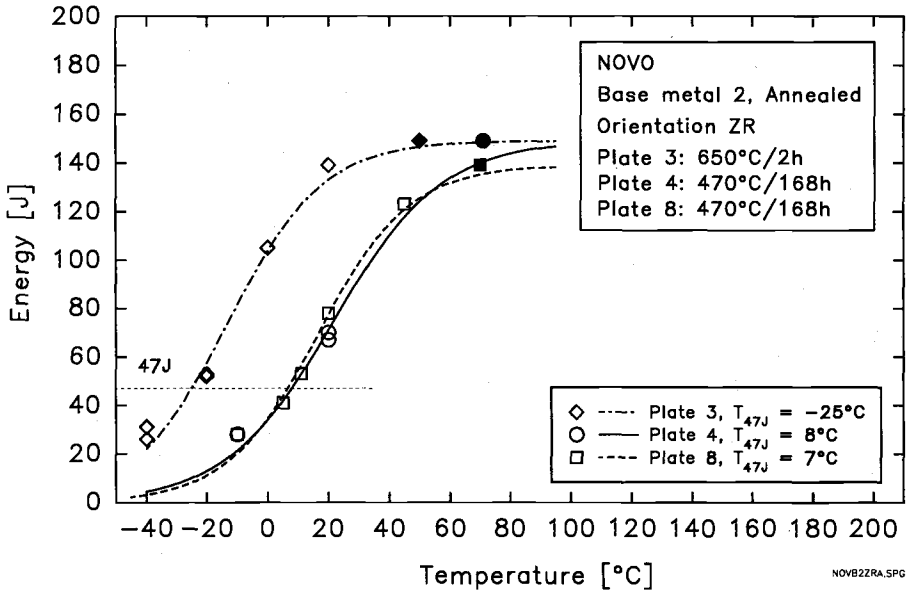

FIG. 14—*Charpy-V transition curves for trepan base metal-2 in annealed conditions. Closed points indicate upper shelf behavior.*

The annealing behavior of base metal-2 in vessel wall condition was studied by applying a 470°C/168 h heat treatment on Disks 4 and 8. Both layers showed the same post-heat treatment transition temperature. The temperature shift recovery by annealing was about 17°C. A small recovery in the upper shelf energy was also measured.

The evaluation of irradiation embrittlement sensitivity of the material is not directly possible because the unirradiated material transition temperature is not known and archive

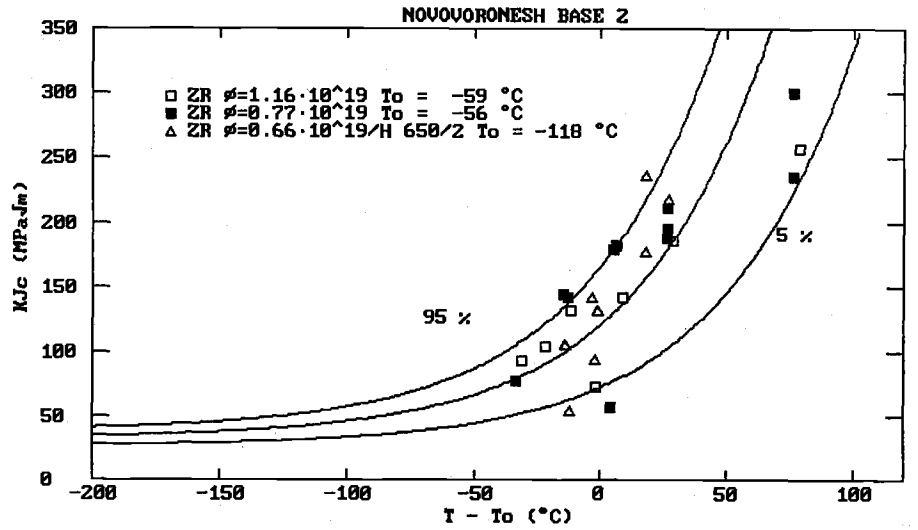

FIG. 15—*Fracture toughness transition curves for trepan base metal-2.*

material do not exist. The unirradiated reference condition was estimated by a simulating heat treatment 650°C/2 h, but, as shown in Fig. 4, this procedure overrecovers the toughness of Loviisa surveillance base metal. The difference in transition temperatures between the simulated reference and the true reference conditions for Loviisa surveillance base metal was 28°C and between the simulated reference and the 470°C/168 h annealed conditions for trepan base metal was 32°C. These values are equal, but the amount of overannealing might well depend on the neutron fluence of the material, which for Loviisa surveillance base metal was nearly ten times higher than for the trepan sample. Hence, it cannot be concluded that the transition temperature of trepan base metal recovers completely in a 470°C/168 h annealing.

In the Soviet standard [*8*], radiation embrittlement is described by the formula

$$\Delta T = A_f \times [\text{fluence}/10^{18}]^{1/3} \tag{5}$$

where A_f is 22 for base metal in 250°C irradiation and fluence is given in units $E > 0.5$ MeV.

If the 470°C/168 h annealed condition in Fig. 14 is assumed to be the reference condition and parameter A_f is calculated for Disk 4 and Disk 8 (average of Disks 7 and 9), one gets $A_f = 9$ and $A_f = 10$, respectively. If the simulated reference is used as the reference condition, one gets $A_f = 22$ for Disks 4 and 8.

The real value of the embrittlement coefficient A_f is between these two estimates and remains below the norm value.

Charpy-V and fracture mechanics specimens give equal transition temperature shifts for this material. Transition temperature shifts between the simulated reference conditions and the vessel wall conditions, Disk 4 for Charpy specimens and Disk 5 for fracture mechanics specimens, are both 60°C.

Conclusions

Specimen reconstitution technique, including reconstitution welding and discharge machining operations, was validated for Charpy-V and Charpy size 3-PB specimens using unirradiated and irradiated pressure vessel steel materials. Specimens reconstituted from 16-mm center section lengths were proven to give test results equivalent to original homogeneous specimen values. Specimen preparation technique was applied for toughness characterization of a large trepan sample. The Charpy-V transition temperature of the base metal in the trepan was near room temperature in the irradiated pressure vessel wall condition, and the transition temperature gradient through the vessel wall was found to be gradual and small, giving rise to no safety-related concern. The irradiation sensitivity of the base metal material could not be directly measured due to unknown reference condition. The sensitivity is estimated to be below the value given in the Soviet norm.

Acknowledgments

The authors are grateful to Dr. Kim Wallin for valuable discussions and to various Soviet organizations for making the trepan sample available.

References

[*1*] "Report on Annealing of the Novovoronesh Unit 3 Reactor Vessel in the USSR," prepared by N. M. Cole and T. Friedrichs, NUREG/CR-5760, MPR-1230, NRC, Washington, DC, July 1991.

[*2*] Ahlstrand, R., Klausnitzer, E., Lange, D., Leitz, C., Pastor, D., and Valo, M., "Evaluation of the Recovery Annealing of the Reactor Pressure Vessel of NPP Nord (Greifwald) Units 1 and 2

by Means of Subsize Impact Specimens," *Radiation Embrittlement of Nuclear Reactor Pressure Vessel Steels: An International Review (Fourth Volume), ASTM STP 1170*, L. E. Steele, Ed., American Society for Testing and Materials, Philadelphia, 1993.

[3] Hawthorne, J. R., "Gundremmingen RPV Embrittlement Investigation," presentation to NRC Vessel Integrity Group Meeting, American Museum of Science and Energy, Oak Ridge, TN, 2–3 Dec. 1986.

[4] "Manufacturing History and Mechanical Properties of Japanese Materials Provided for the International Atomic Energy Agency," CRP subcommittee report, Atomic Energy Research Committee, Japan Welding Engineering Society, October 1986.

[5] Valo, M., Wallin, K., Törrönen, K., and Ahlstrand, R., "Irradiation Response of the New IAEA Correlation Monitor Material JRQ Measured by Fracture Mechanical Properties," *Effects of Radiation on Materials: 15th International Symposium, ASTM STP 1125*, ASTM, Philadelphia, 1992.

[6] Wallin, K., "Fracture Toughness Transition Curve Shape for Ferritic Structural Steels," *Fracture of Engineering Materials and Structures*, S. H. Toeh and K. H. Lee, Eds., Elsevier Applied Science, London and New York, 1991.

[7] Bärs, B., "Neutron Fluence Evaluation of the Novovoronesh Trepan Sample," to be published.

[8] *Norms for Strength Calculations of Equipment and Pipelines of Nuclear Power Plants*, Energoatomizdat, Moscow, 1989.

Author Index

Subject Index

ISBN 0-8031-1869-4